ISSN 0288-4534
CODEN: KONAE7

KONA

POWDER AND PARTICLE

No.24 (2006)

Published by Hosokawa Powder Technology Foundation

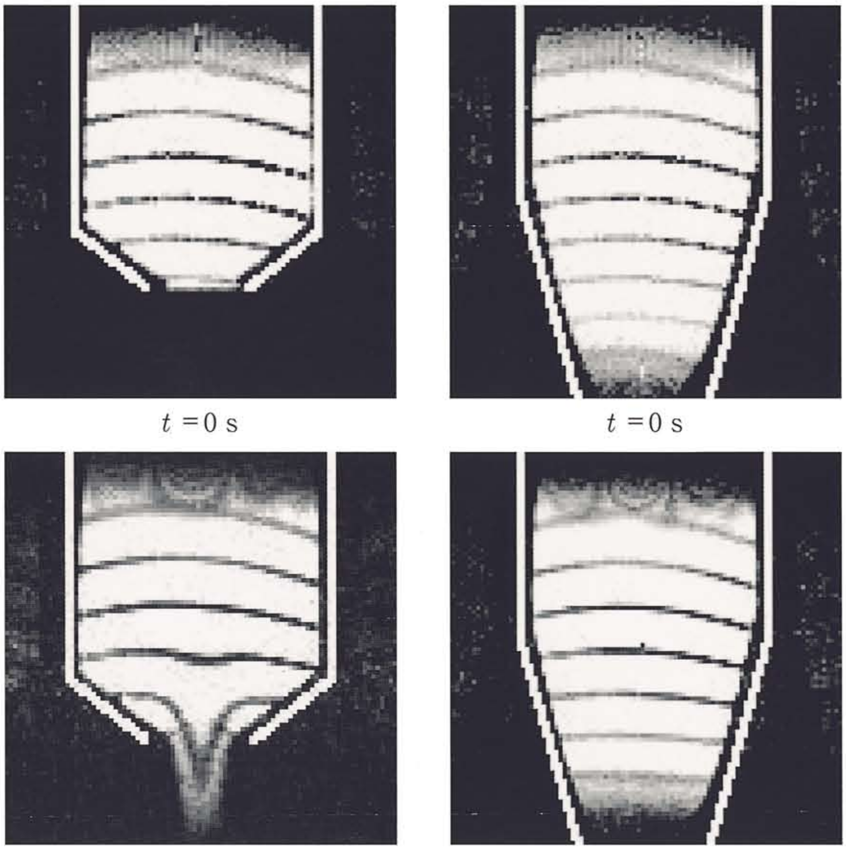

t = 0 s

t = 0 s

t = 100 ms

t = 100 ms

Funnel flow in a cylindrical hopper visualized by MRI tagging

now available online – www.kona.or.jp

KONA

POWDER AND PARTICLE

http://www.kona.or.jp

KONA is a refereed scientific journal that publishes articles on powder and particle sciences and technology. KONA has been published annually since 1983 in Japan. KONA is distributed to researchers, members of the scientific community, universities and research libraries throughout the world.

About the Cover of Journal “KONA”

The Chinese character “粉” is pronounced “KONA” in Japanese, and means “Powder”. The hand written “粉” is after the late Mr. Eiichi Hosokawa, founder of the Hosokawa Micron Corporation.

Hosokawa Micron Corporation and its R&D Center

Editorial Board

Y. Tsuji	Editor-in-Chief (Osaka Univ., JAPAN)

Asia / Oceania Editorial Board

Y. Kousaka	(Professor Emeritus of Osaka Prefecture Univ., JAPAN)
H. Masuda	(Kyoto Univ., JAPAN)
H. Emi	(Professor Emeritus of Kanazawa Univ., JAPAN)
K. Higashitani	(Kyoto Univ., JAPAN)
K. Nogi	(Osaka Univ., JAPAN)
Y. Fukumori	(Kobe Gakuin Univ., JAPAN)
J. Hidaka	(Doshisha Univ., JAPAN)
M. Takahashi	(Nagoya Institute of Technology, JAPAN)
M. Rhodes	(Monash Univ., AUSTRALIA)
Y. Kang	(Chungnam National Univ., KOREA)
W. Tanthapanichakoon	(National Science and Technology Development Agency, THAILAND)
T. Yokoyama	(Hosokawa Powder Technology Research Institute, JAPAN)
M. Naito	(Osaka Univ., JAPAN)
Secretariat	
T. Kawamura	(Hosokawa Powder Technology Foundation, JAPAN)

Europe / Africa Editorial Board

E. Forssberg	Chairman (Univ. Lulea, SWEDEN)
W. Peukert	(Univ. Erlangen, GERMANY)
S.E. Pratsinis	(ETH Zürich, SWITZERLAND)
H. Kalman	(Ben Gurion Univ., ISRAEL)
J.F. Large	(Univ. de Tech. de Compiégne, FRANCE)
N.Z. Lyakhov	(Institute of Solid State Chemistry, RUSSIA)
M. Ghadiri	(Univ. of Leeds, UNITED KINGDOM)
Secretariat	
P. van der Wel	(Hosokawa Micron B.V. NETHERLANDS)
P. Krubeck	(Hosokawa Micron GmbH, GERMANY)

Americas Editorial Board

B.M. Moudgil	Chairman (Univ. of Florida., U.S.A.)
D.W. Fuerstenau	Vice Chairman (Univ. of California, U.S.A.)
R. Flagan	(California Institute of Technology, U.S.A.)
R. Hogg	(Pennsylvania State Univ., U.S.A.)
A.I. Hickey	(Univ. of North Carolina, U.S.A.)
F. Concha	(Univ. of Concepción, CHILE)
S.B. Savage	(McGill Univ., CANADA)
Secretariat	
C.C. Huang	(Hosokawa Micron Powder Systems, U.S.A.)

■**Publication Office**

Hosokawa Powder Technology Foundation (Japan) in Hosokawa Micron Corporation
No. 9, 1-chome, Shoudai Tajika, Hirakata-shi, Osaka 573-1132, Japan

■**Notes**

○Hosokawa Powder Technology Foundation has entrusted the editorial duty to the editorial board organized by the Council of Powder Technology, Japan.

(Complimentary Copy)

Printed in Japan

KONA Powder and Particie No. 24 (2006)

CONTENTS

<Review Papers>

<Original Research Papers>

<Translated Research Papers>

<Information Articles>

<Academic publication concerning powder technology in Japan (2005)(2006)>

The Letter from the Editor

Yutaka Tsuji
Editor-in-Chief

As is well known, powder technology or particle technology is a typical example of interdisciplinary fields. People concerned with KONA, the readers, contributors and reviewers have various disciplinary backgrounds such as chemical engineering, pharmaceutical engineering, mechanical engineering, civil engineering, material engineering, material science, metallurgy, chemistry, physics and so on. These fields are regarded as a basis of science and engineering today. Education systems in higher educational institutions like universities and colleges are categorized according to those disciplines. Thus, engineers and researchers have graduated from the departments, names of which are accompanied by the words expressing these disciplines. The same classification can be applied to industries.

KONA is a place where people with different backgrounds meet through the printed articles. It is pleasant to interact with people with different backgrounds, but sometimes we feel difficulties in understanding each other. The difficulties are caused by the difference in culture and ways of thinking of different areas. Sometimes misunderstanding happens. The secret of success of such interdisciplinary journals lies in respecting research methods developed in other fields. Though the research target is the same, the approach is often different. We should recognize that basic fields described above have long histories while histories of interdisciplinary fields are relatively short in general. Methods or approaches authorized in some fields have reasons why such methods have been authorized. We should not criticize methods used in other fields lightly. Criticism itself is not bad but it is good to study hard by competing with each other. If we lose the spirit of criticism, we can not expect growth and progress in any field. What I would like to emphasize here is that if you try to criticize, first consider the background and then criticize carefully. Through knowing other fields, our views will be naturally wider. This is the very benefit that we can get from interdisciplinary journals. It is our pleasure that KONA continues to play such a role.

Finally I must inform a sad news here. Prof. David Grant, an editorial board member of the KONA American Block, passed away on Dec.9, 2005. Almost one year has passed since this sad news was spread in the world. When we knew it, KONA issued last year was already in printing. David rendered numerous services to KONA for many years. We shall not forget his great contributions.

Y. Tsuji

Comment of the Cover Photograph

Visualization and velocity measurement of granular flow in hopper by use of MRI

Toshihiro Kawaguchi
Department of Mechanical Engineering
Graduate School of Engineering
Osaka University

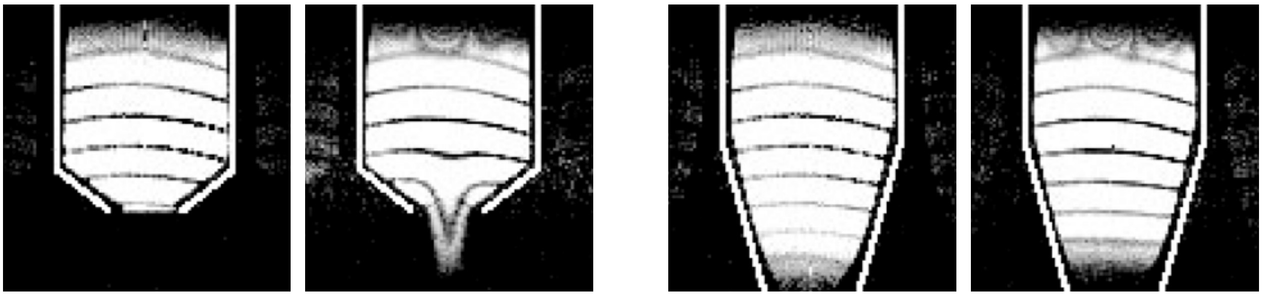

(a) funnel flow (b) mass flow

Fig. 1 Deformation of particle layer

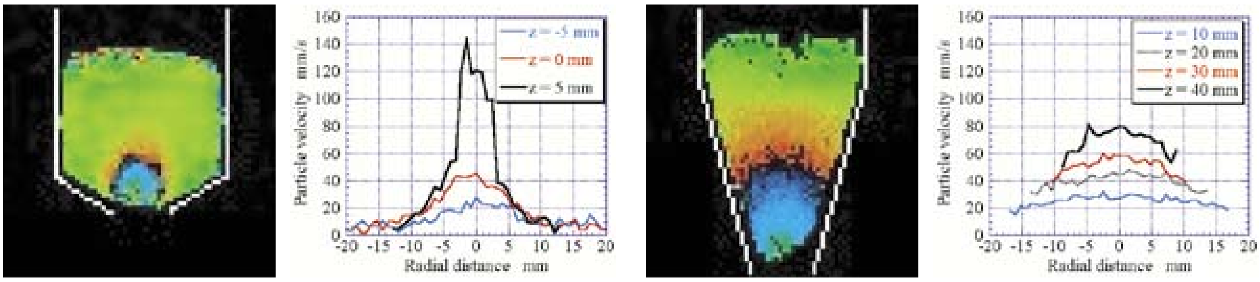

(a) funnel flow (b) mass flow

Fig. 2 Distribution of particle velocity

MRI (Magnetic Resonance Imaging) is one of the non-invasive techniques to observe the inside of granular flows. MRI can measure the velocity field, which is a pronounced advantage over the other non-invasive techniques such as X-ray or electrical capacitance tomography.

Figure 1 shows MRI images of the granular flow inside a cylindrical hopper. Band-like magnetic spatial tags generated at the initial state allow the direct observation of the deformation of the particle layer; this technique is referred to as the *tagging method*. The time interval is 100 ms. Since MRI detects the NMR (Nuclear Magnetic Resonance) signals from protons (H^+), the measuring particles need to contain the proton. Thus, we employ a specially ordered capsule particle, which is liquid vitamin E covered with a gelatin spherical shell. The mean diameter of the capsule particles is 1 mm and the hopper diameter is 40 mm. The funnel flow and the mass flow are clearly distinguished by the tagging method.

Figure 2 shows the distribution of the particle velocity measured by MRI. When a nuclear spin moves through a gradient magnetic field, a phase shift takes place. The phase shift is proportional to the velocity. Therefore the particle velocity distribution can be obtained by detecting the distribution of the phase shift of the protons; this technique of velocity measurement is referred to as the *phase method*. The difference between the funnel flow and the mass flow can be quantitatively evaluated.

Gas Fluidisation of Nano-particle Assemblies: Modified Geldart classification to account for multiple-scale fluidisation of agglomerates and clusters[†]

Ö. Gündoğdu and U. Tüzün[1]
Chemical and Process Engineering,
School of Engineering,
University of Surrey[*]

Abstract

Recent literature of the past several years has borne out gas fluidisation phenomena of nano-particle beds and assemblies quite unlike the conventional behaviour observed in fluidisation of micron size or larger particles. A review is presented of the recent publications in the field in comparison with more recent studies of nano-particle assembly fluidisation at Surrey University with the use of high resolution and high speed microtomography techniques. These studies support well the previously published observations in incipiently fluidised 2-D and 3-D beds as well as providing further insight into the highly expanding behaviour of dynamic nano-particle clusters observed at fluidisation velocities much in excess of the incipient fluidisation velocity of a packed bed. It has proved possible to explain the observed behaviour of nano-particle agglomerates in incipiently fluidised beds and those expanding dynamic clusters observed in high gas velocities by extending the established framework of the Geldart Classification to sub-micron particle sizes and to immersed bulk densities as low as 100th of the solid density. Further quantification studies are underway to establish the various long and short range force contributions to the observed dynamic force fields of nano-particle assemblies over a wide range of percolating gas velocities.

Keywords: Nano-particles, Gas fluidisation, Multiple-scale agglomerates, Dynamic clusters, Geldart classification

1. Introduction

The fluidisation phenomenon is best explained by the balance of short and long range forces evaluated in a given powder assembly. The long range body forces include gravity, solid friction, buoyancy, interstitial fluid drag to include both the viscous (skin) friction and the form drag. The short-range forces, also known as particle surface-active forces can be due to physical (e.g. van der Waals, capillary, electrostatics) or chemical (e.g hydrogen bonding) or electrochemical effects such as electrophoretics. The relative magnitudes of the short-range and long-range forces are in turn determined by the physical properties of the solid particles such as particle size, particle shape and solid density and the properties of the carrier fluid such as fluid density, fluid viscosity and surface tension. It is well-known that with small particles in the sub-millimeter size range, the interstitial fluid effects dominate when the immersed weight becomes of the same order as the fluid drag forces which scale inversely proportionally to particle size.

Geldart's well-known graphical classification [1, 2] of the fluidization behaviour is a very effective way of mapping the balance of forces onto measurable particle and fluid properties that determine the relative magnitudes of the immersed weight and the fluid drag forces in a fluidised particle assembly; see **Fig.1** below.

As seen in **Fig.1**, the fluidization behaviour is dominated by gravity effects for solid particles in the millimetre range or above (B and D type), and governed by the interstitial fluid permeability effects for

---

[†] Accepted July 24, 2006

[*] Guildford, GU2 7XH, UK

[1] Corresponding author Ugur Tüzün
TEL:+44-1483-686587
FAX:+44-1483-686591
E-mail:U.Tuzun@surrey.ac.uk

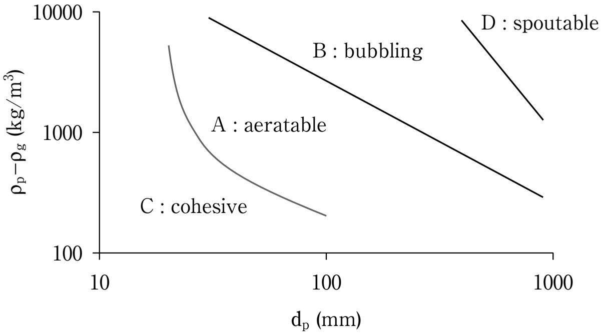

Fig. 1 Geldart's Classification of the fluidisation behaviour of powders.

sub-millimeter particles down to about 50 microns (A type). Below 50 microns, the particle surface forces begin to dominate giving rise to significant bulk cohesion that causes significant reduction in the permeability of the particle assembly by the interstitial fluid. Little or no information is presented for particles below 10 microns in size that are believed to give rise to assemblies that behave as “stable cakes” due to much increased particle surface forces per unit bulk volume such as due to Van der Walls, capillary and electrostatic attractions. Fine cohesive powders (Group C) fluidize poorly, exhibiting channelling, lifting as a plug, and forming “wormholes” when aerated.

According to the above classification, sub-micron and nanoparticles are at the extreme end of Group C particles suggesting at first sight that that fluidisation would prove impossible due to the much higher surface active forces. However, the very high magnitudes of the short-range surface interactions in a sub-micron powder assembly has been found to yield in certain cases dynamically stable agglomerate structures made up of the constitutive nano-particles that can then grow to sizes in the micron and millimetre size ranges and thus whose fluidization behaviour could very well fall within groups A and B as well as C. Recent literature of the past five years or so cites many examples of “successful” fluidization of nanoparticles by the production of dynamically stable large agglomerates; see for example [3, 4, 5, 6] to name but a few.

Ultrafine powders, including nanoparticles, have become of major interest in many industries because of new functionalities and desirable properties attributed to these particles. Special properties of nanoparticle assemblies include

- 10^{-9} reduction in mass per unit bulk volume (compared to particles in the sub-millimetre range),
- 10^{6} increase in particle surface area per unit bulk volume (compared to particles in the sub-millimetre range),
- Increased surface-to-volume atomic ratio; (e.g. exponential increase in the portion of constituent atoms at or near surfaces creating more sites for bonding, reactions with surrounding media),
- High surface charge concentration,
- High electric field strength, and
- High electrophoretic mobility.

Ceramic, plastic and metallic nano particles and the various nano-composites comprising synthetic combinations of different inorganic and organic constituents are being used increasingly in manufacturing and process industries to provide i) increased surface area for heat and mass transfer and surface catalytic reactions and ii) advanced material functionality in films, compacts and coatings due to effects that include the modification of the carrier fluid rheology, enhancement of bulk mechanical, thermal and electrical properties, provision of chemically-active adhesive bonding to solid surfaces, highly porous micro-structures that are used for targeted delivery of fluid excipients.

The very high magnitudes of the short-range surface interactions in a sub-micron powder assembly has been found to yield in certain cases dynamically stable agglomerate structures made up of the constitutive nano-particles that can then grow to sizes in the micron and millimetre size ranges and thus whose fluidization behaviour could very well fall within groups A and B as well as C. Recent literature of the past five years or so cites many examples of “successful” fluidization of nano-particles by the production of dynamically stable large agglomerates; see for example [2,3,4,5,6,7,8] to name but a few.

In a number of experimental investigations of the past few years, fluidization of ultra fine particles has been extensively studied as a possible route to particle dispersion, particle growth and particle collection processes. Some of these studies consider agglomerate bubbling fluidization (ABF). The dynamic aggregation of particles increases with decreasing particle size, which is attributed to greater inter-particle forces between particles, which attract them into aggregated groups. The existence of these micro-structured aggregates is believed to prevent the formation of cemented or stable cohesive bonds between the constituent particle surfaces and as such presenting a potential deviation from the theoretical behaviour

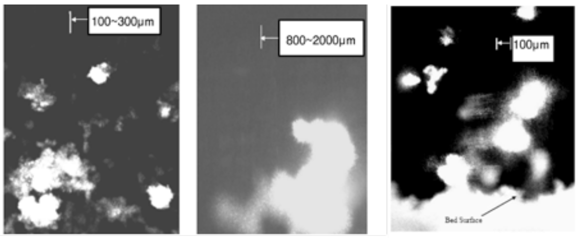

Fig. 2 Agglomerates observed by optical imaging techniques.[4, 8]

of "cohesive" materials observed in group C particles in **Fig.1** above. Experimental results show the existence of cells in a well organised structure; see **Fig.2** for examples of agglomerate structures cited in recent literature.

In the case of nano-particles, it is the agglomerates rather than individual particles that homogeneously fluidise, and this is achieved in a number of stages as described by Yao et al.[9]. Wang et al[13] state that the properties of the primary particles determine the properties of the agglomerates, which control the behaviour of the two-phase flow in a fluidized bed. SiO_2 nanoparticles with a size range of 7 to 16nm are quite different from normal Geldart-C particles and can be smoothly fluidized in a gas-solids particulate fluidization regime with a high bed expansion ratio and bubbleless behaviour via micro-structured self-agglomeration. As distinguished from the ABF of Geldart-C particles, this homogeneous fluidization phenomenon of SiO_2 nanoparticles is called agglomerate particulate fluidization (APF). A number of studies also state that unique fluidization behaviour of nano particles is due to multi-stage agglomerate (MSA) structure.

To increase understanding of APF behaviour, the relationship between the intrinsic characteristics of the primary particles and the agglomerate properties and macroscopic flow behaviour would have to be studied. It is for this reason density, size, porous structure and size of agglomerates need to be measured. The current theoretical and modelling studies all require direct measurement of voidage, local solids concentration, particle size measurements, agglomerate size and distribution, agglomerate structure and porosity. In all the studies on ultrafine/nanoparticle fluidization reported in the literature, physical properties of the particles were either estimated by making some simple theoretical assumptions or using other tentative imaging techniques or used intrusive measures such as local probes which would interfere with the flow around them. There is therefore, a serious need to determine these parameters dynamically and non-intrusively.

2. X-Ray Microtomography

The application of x-ray imaging techniques for fluidised beds has existed for around fifty years. One of the earliest recorded occurrences of this was by Grohse[26] using x-ray absorption to calculate density profiles. According to Simons[25] and Chaouki et al.[18] much of the work carried out on fluidised beds using x-ray systems has been conducted by Rowe, Yates and co-workers at University College London. The original work conducted by Rowe and Partridge[27] involved the observation of bubble behaviour using x-ray imaging, as this method involves using a single source and detector a small range of gas velocities had to be used to maintain an accurate 2D image. In further experimentation Yates et al.[28] investigated the voidage distribution around a rising bubble within a fluidised bed. The technique follows earlier work by Rowe and Partridge[27] that shows that there is not a straight division between the bubble and the surrounding emulsion phase. end van Dijk et al.[29] employed the use of x-ray imaging on a three-dimensional apparatus to allow bubbles to rise unhindered investigating the effects of the presence of an internal baffle. Kantzas et al.[30] demonstrates the practical benefit of a CAT system by utilising the technology to observe channelling in a polyethylene fluid bed. Lehner and Wirth[31] have utilised an X-ray computed tomography system in order to obtain solids distribution data on a downer reactor under a variety of conditions. They have stated that the spatial resolution of this system is 0.7 x 0.7mm with a 10% error in a standard sample compared to the actual concentration. Kai et al.[32] have used a fast CT unit to capture both a high spatial and time resolution. The use of x-ray imaging techniques on industrial sized fluidized beds is also a well-researched field. Recent developments in x-ray sources and detectors now allow fluidized beds to be studied at length scales down to 400nm and with temporal resolutions of 1 ms. X-ray imaging also has the advantage of studying the bulk of the fluidized bed, rather than the surface, in a nondestructive and dynamic manner.

The X-ray microtomography technique developed at Surrey University in collaboration with the Department of Physics[5,14] is providing valuable in-situ, non-destructive structural information on the morphological changes that take place nano fluidisation of powder samples. We can look into changes of agglomerates dynamically and examine the final microstructural features. Unlike other available imaging techniques which are usually surface techniques, X-ray microtomography imaging allows us to see through the sample and allow us to reconstruct 3-D internal structure of the sample. This powerful techniques allows us to identify processing routes that would provide better preserved nanostructural features [5,15]. Combining high spatial resolution X-ray micro-tomography with fast radiographic imaging (i.e. 40 milliseconds), dynamic changes in the agglomerate structure and density can clearly be seen with different fluidisation conditions. The structure of three-dimensional assemblies of nanoparticles can be examined using high resolution x-ray microtomography apparatus, details of this technique have previously been described[15]. The apparatus was used with the following operating parameters for these experiments: x-ray tube voltage 60kVp and current 0.1mA from a molybdenum transmission target with a 100mm zirconium filter. The magnification used resulted in the reconstruction of a $(1024)^3$ cube of data with a linear dimension of 4.5mm.

Metallic oxide particles such as zinc and copper oxides were used in 2-D and 3-D fluidisation experiments at different gas velocities and the resulting internal bed microstructures were compared before and after fluidisation. The mean diameter of the ZnO nanoparticles (Tetronics, UK) were measured as 50nm using a Scanning Electron Microscope. The X-ray microtomography equipment provides the 3-D agglomerate size distribution as shown in **Fig. 3**. This is used for calibration of the bed contents prior to fluidisation. The agglomeration of these nanoparticles was studied using X-ray microtomography. High resolution X-ray microtomography enables us to evaluate rate of change of agglomerate size under different fluidization conditions.

The zinc oxide nanoparticles were placed in a small fluidized 2D bed of dimensions 4mm by 40mm and 300mm in height and in a 3D bed with a 10mm diameter. Homogeneous air distribution was ensured by using an area of free space below a sintered metal plate filter at the bottom of the bed. Nitrogen from a pressurized cylinder was used as the source gas to minimize the possibilities of capillary forces from air moisture. The gas flow velocity was controlled using a Brooks Instrument model 5850S mass flow controller. Different gas flow velocities were used.

The strong cohesive nature due to electrostatic and van der Waals interparticle forces of the nanoparticles leads to the production of even up to millimeter-sized agglomerates; the mean size and distribution of these agglomerates were determined using the 3D microtomography data. The agglomerate volume distribution is shown in **Fig. 3 b**.

The distribution was fitted to a log-normal distribution with a mean value of $0.695 \times 10^9 \mu m^3$ and a variance of $3.56 \times 10^{21} (\mu m^3)^2$ for the agglomeration volume. It can be seen that nanoparticles are capable of creating observable agglomerate structures even

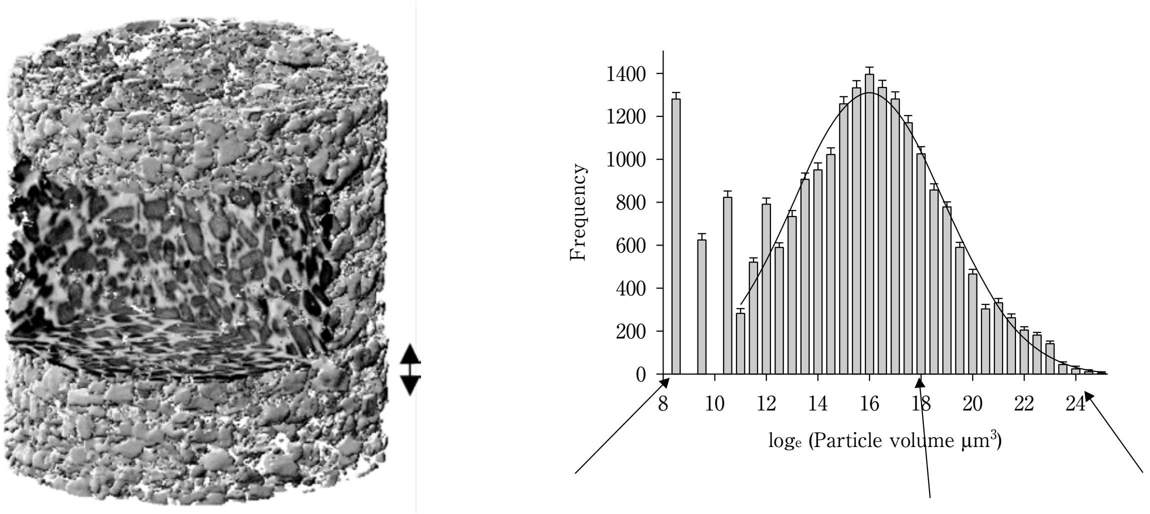

(a) (b)

Fig. 3 a) Microtomographic scan of 3-D static bed. b) Agglomerate size distribution within the 3-D static bed.

on the millimetre length scale.

A histogram of the natural logarithm of the agglomerate volume versus frequency resulted in a distribution closely resembling a log-normal distribution. A description of the statistical features associated with log-normal distributions of coalescing particles is described by Granqvist and Buhrman[13]. The mean of the agglomerate volume distribution μ and the variance, σ^2, can be extracted from a mean of the normal distribution fit, M and the variance V to $\log_e$(agglomerate volume) using the Equation 1.

$$\mu = e^{\left(\frac{2M+V}{2}\right)} \text{ and } \sigma = \mu\sqrt{e^V - 1} \qquad (1)$$

A log-normal distribution fit to $\log_e$ (agglomerate volume) yields $M = 15.95$ and $V = (2.97)^2$, which implies a mean value of $0.7 \times 10^9 \mu m^3$ (corresponding to an agglomerate mean size of about 700μm). It is clear from the log-normal distribution that there is a diverse range of agglomerate sizes with some extending into the millimeter size range.

Fig. 4 shows the detail of multi-modality of small agglomerate sizes determined below 75 μm down to less than 5microns. Here the peaks correspond to the indigenous (primary) structures of nanoparticles which are subsequently are seen to be dispersed into the dilute suspension phase above the fluid-bed at increasing fluidisation velocities. It is believed that the cloud formations observed in the x-ray images seen in **Figs. 5** and **6** below support networks of individual clusters of less than 5 micron in size. This aspect needs further detailed study using a finer scrutiny of length scale examination than the one presented in **Figs. 3** and **4** above.

As a further future, the three dimensional tomographic data presented above also allows the density of the agglomerates to be determined directly from the tomographic measurements; see reference 5) for details. Here, by calibrating the reconstructed data against data of reference materials, the mean bulk density of the ZnO agglomerates was found to be 2900 kgm^{-3} compared to the 5600 kgm^{-3} of the specific solid density of the individual nanoparticles. This result implies an internal porosity of agglomerates of about 0.5 which compares well with the incipient fluidisation state of the packed bed. However, once the agglomerates are introduced to the suspension phase above the bed, then other literature reports internal porosities as low as 0.1; see for example, reference 9).

The images presented in **Figs. 5** and **6** below are taken from an X-ray projection video with a spatial resolution of 30 microns and a temporal resolution of 40 milliseconds.

Fig. 5 below shows snapshots of X-ray images during fluidisation of 50 nm mean size CuO nano particles at different superficial gas velocities using a planar (2-D) fluidised bed.

As seen in **Fig.6**, at lower gas flow velocities ($<0.052 ms^{-1}$) the nanoparticle agglomerates act

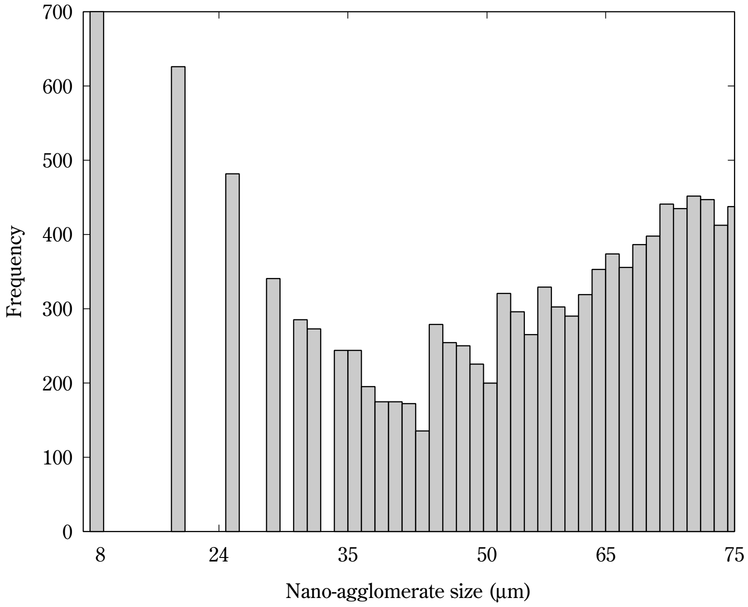

Fig. 4 Histogram of smaller size range nano-particle agglomerates showing discrete modality.

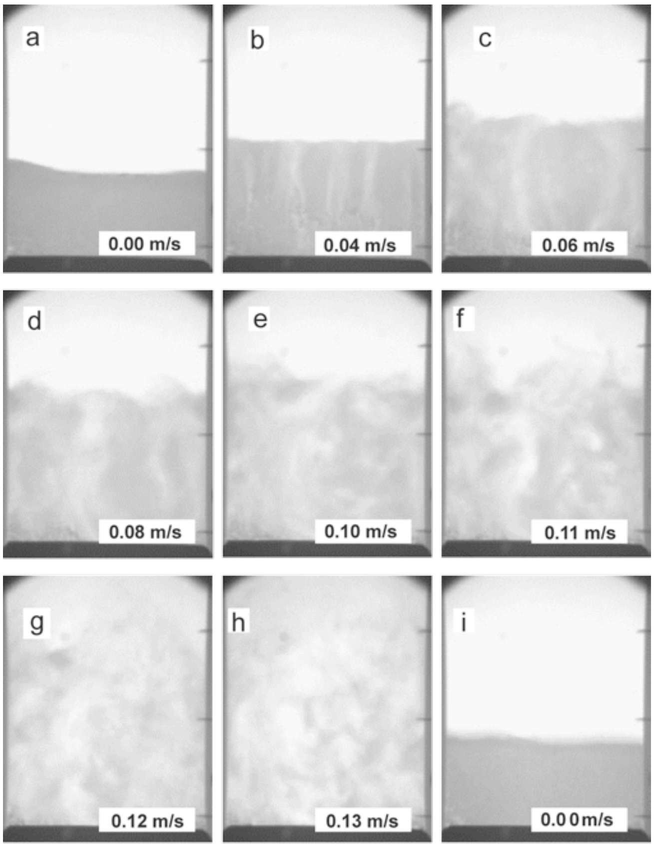

Fig. 5 X-ray images of CuO nanoparticle fluidization. a) static bed. b-c) incipient fluidisation, d-e) bed expansion post incipient fluidisation f) onset of aggregative fluidisation g-h) aggregative fluidisation with homogeneous expansion. i) return to static bed condition.

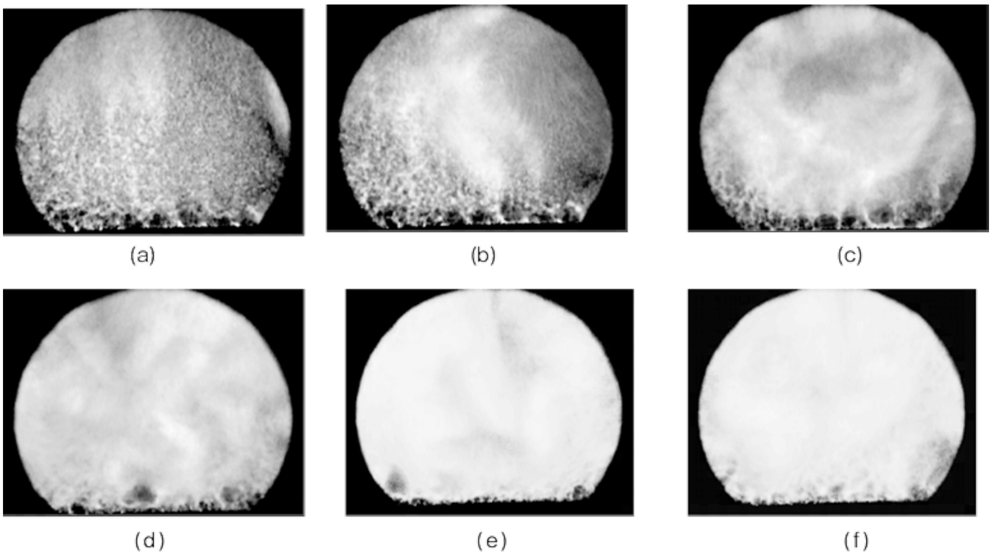
(a) (b) (c)
(d) (e) (f)

Fig. 6 X-ray images taken during planar (2-D) fluidisation at gas flow velocities:
a) 0.026 ms^{-1} b) 0.052 ms^{-1} c) 0.078 ms^{-1} d) 0.104 ms^{-1} e) 0.208 ms^{-1} f) 0.313 ms^{-1}.

as Geldart class A (aeratable) / B (bubbling) type systems, the fluidized bed exhibits a region of fixed larger agglomerates, through which channeling of the gas is occurring, below a region of fluidization of smaller and medium sized agglomerates, in which bubbling and turbulent flow is occurring, as observed by Wang *et al* [13]. Agglomerates which are representative of the mean volume can be seen a few millimeters above the larger agglomerates at the base of the fluidized bed in **Fig. 6**(a). It can be seen in **Fig. 6**(c) that as the gas velocity is raised above 0.078ms^{-1} that the collision energy of the particles is enough to break them apart to sizes below the imaging resolution.

The dynamic process of larger agglomerates being broken down and then re-agglomerating due to cohesive forces is shown in a series of images extracted from the original data sets collected with a temporal resolution of 40ms in **Fig. 7**. Future work will, instead of making simple assumptions about the bulk properties of the agglomerate system, track down colliding agglomerates measure their spatial and temporal properties used to understand how different sized agglomerates behave. The agglomerate, labeled (a), in **Fig. 7** can be seen to break down, due to collisions in the fluidized bed. In the same region a similar sized agglomerate, labeled (b), reforms, all within approximately 440ms.

3. Determination of break-up energy of agglomerates from tomographic data

If the agglomerates are assumed to have the mean volume, μ, and density, ρ, obtained from the tomographic data (μ=0.695×10^9μm^3 and r=2900 kgm^{-3}) seen in **Fig. 3(b)** above, and are travelling at the gas velocity, v_g, before colliding with effectively stationary agglomerates of the same size, that the break-up energy, E_b, can simply be calculated from the kinetic energy of the moving agglomerate. This gives a break-up energy of 2×10^{-8}J for the average size of ZnO nanoparticle agglomerates in the system examined if an internal porosity of 0.5 is assumed. The corresponding magnitude of the break up energy needed for agglomerates with an internal porosity of 0.1 will be about 4x 10^{-9} J. A more detailed model for calculating the break-up energy is provided by Morooka et al [16] which suggests for powder agglomerates with a volume of 0.695×10^9μm^3, the energy required to break the agglomerate is of the order of 10^{-8}J. The range of values calculated for agglomerates of different internal porosity appear to agree well with this figure reported in previous literature.

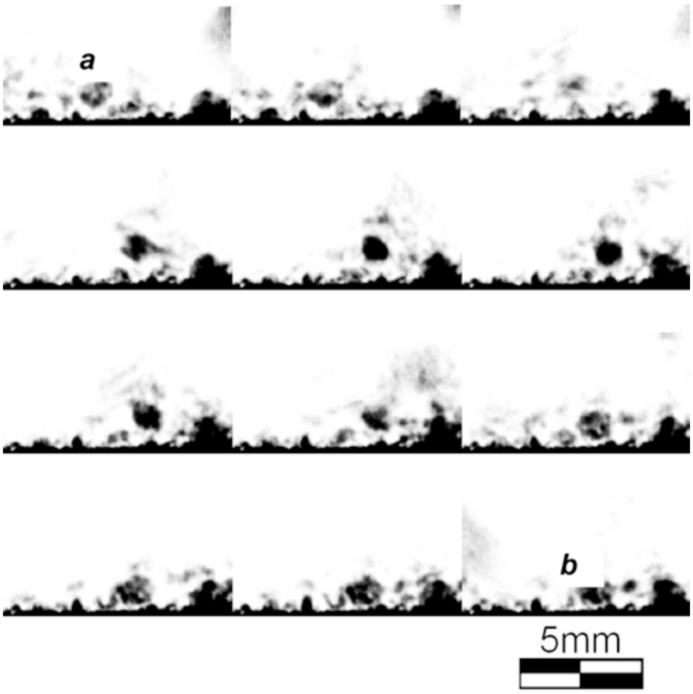

Fig. 7 Consecutive X-ray images of the planar fluidized bed above the distributor at a gas flow velocity of 0.313 ms^{-1}; the time between images is 40 ms. N.B. The images should be viewed in sequence from top left to bottom right.

The fluidized beds seen in **Figs. 5** and **6** exhibit regions of stationary larger agglomerates, through which channelling of the gas is occurring, below a region of fluidization of smaller and medium sized agglomerates, in which bubbling and turbulent flow is occurring, as observed by Wang et al. 17). Furthermore, comparison of the images shown in **Figs. 6** and **7** reveal that at sufficiently high gas flow velocities, the collision energy between the agglomerates exceeds that of the cohesive forces as predicted by Morooka et al 16) and the larger agglomerates are broken down into a distribution of individual nanoparticles and smaller agglomerates. This dynamic process of larger agglomerates being broken down and then re-agglomerating due to cohesive forces is clearly visible in the series of images extracted from the original data sets collected with a temporal resolution of 40ms as seen in **Fig. 7**. Our experiments with axially-symmetric (3-D) beds have also revealed similar processes which are currently under investigation.

Morooka et al.16) studied fluidity of several kinds of submicron particles and reported that all tested ultrafine particles form agglomerates during fluidization. The energy balance model was proposed for estimating agglomerate size. Iwadate and Horio 12) developed the force balance model to predict agglomerate size in a bubbling system. Two models have been proposed to predict the size of agglomerates in fluidized beds of Geldart C group powders by Iwadata and Horio 12). Chaouki 20) assumed that the drag force due to gas flow, which is approximately equal to gravity force acting on an agglomerate, is equal to van der Waals force of attraction between primary particles. Morooka et al 16) assumed that agglomerate breaks if the collision energy exceeds the energy that is required to break it into two parts. However, no bubble dynamics has been considered in these two different models. Iwadate and Horio 22) put forward a model that considers the bubble dynamics by including the particle pressure around the bubble. They then consider the cohesion force between the two agglomerates and use an expression for cohesive rupture force and make use of the bubble dynamics and work out the agglomerate breakage and agglomerate size estimation. However, for this or any other physical model validation, in-situ dynamic measurements of agglomerate size evaluation is needed. However, in the absence of direct measurements, most researchers use the minimum fluidization velocity and incipiently-fuidised bed bulk density as the value for the mean agglomerate density in their calculations. Sugihara 19) measured the bed pressure drop to determine the minimum fluidization velocity and utilizing the Carman's equation, he obtained the agglomerate sizes. However, it was assumed that agglomerate density ρ_a was equal to primary particle density ρ_p instead of $\rho_a=\rho_p\ (1-\varepsilon_a)$. Since neither ρ_a nor ε_a were measured, the predicted size values were much lower that the observed ones. Chaouki et.al.20) assumes that the drag force due to gas flow, which is approximately equal to gravity force acting on the agglomerate, is equal to the van der Waals force of attraction between the primary particles. Morooka et.al.16) assumes that the agglomerate will break down if the collision energy exceeds the energy that is required to break it into two parts. In fact, these two models are not very different from each other.

There is a serious need to determine the agglomerate size and density at resolutions not attained in previous X-ray applications to determine dynamically and non-intrusively the agglomerate size, agglomerate density, agglomerate porosity, inter agglomerate voidage and local solids fraction and its dependency, bubble evolution as the hydrodynamic effect of bubbles on the behaviour of particles also needs to be considered by using high resolution x-ray microtomography. In all the studies on ultrafine/nanoparticle fluidization studies reported in the literature, these parameters were either estimated by making some simple theoretical assumptions or using other tentative imaging techniques. This technique would also make it possible to measure the amount of agglomeration of primary particles due to the tendency of nanoparticles to agglomerate before the fluidization. In some of the reported studies for example this was achieved by sieving the powders before the fluidization process. It is therefore crucially important to determine these parameters through dynamic measurements in situ.

The fluidised beds were also used to measure the tappings placed at the walls interstitial pore pressure drop as a function of the fluidising velocity using pressure tapings placed at the walls; see **Fig. 8** for a typical set of results.

From these graphs, it has been possible to obtain a mean value of the "pseudo-agglomerate" size using the conventional Carman-Kozeny equation as applies to the incipient fluidisation conditions.

$$d=\sqrt{\frac{E(1-\varepsilon)^{V}\mu U}{(\Delta \mathrm{p}/\mathrm{l})\ \varepsilon^{3}}} \tag{2}$$

The fluidization parameters are $E=180$, $\Delta p/\mathrm{l}=$

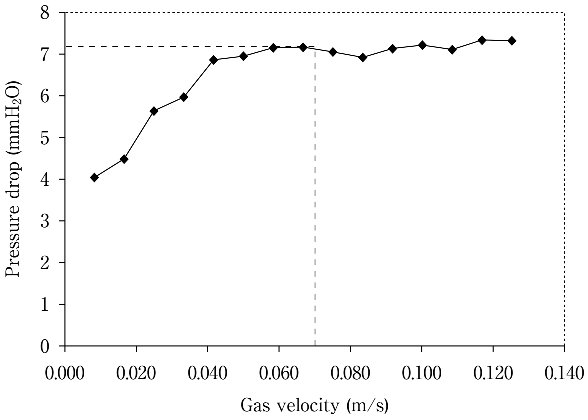

Fig. 8 Pressure drop of the fluidized bed with ZnO nanoparticles with mean size of 50nm.

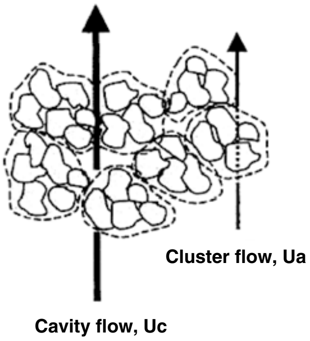

Fig. 9 Multiple scales of interstitial voidage and gas percolation in nano-agglomerate fluidization [23].

$0.28 kpam^{-1}$, $U_{mf} = 0.07 m/s$ and $\varepsilon = 0.45-0.55$. By putting these values back into Carman-Kozeny equation, the mean agglomerate size is found to be between 700mm and 1mm. This mean agglomerate size is in good agreement with the results obtained from the application of 3-D high resolution X-ray microtomography shown earlier in **Fig. 3**.

The predicted values of the mean effective agglomerate sizes compare well with the size distribution of agglomerates observed during x-ray imaging of the static and incipiently fluidised beds; refer to **Fig. 3** above. Further work is underway to characterise the dynamics of growth and decay of agglomerates above the distributor as a function of the fluidisation velocity, particle loading and fluidising gas density and viscosity; see **Fig. 5** above. Measurements of the bed expansion following the onset of the aggregative fluidisation has resulted in values of the mean dynamic voidage of the bed according to

$$\frac{H_2}{H_m} = \frac{(1-\varepsilon_{mf})}{(1-\varepsilon_2)} \tag{3}$$

which results in values of 0.7 - 0.8 as predicted by the Richardson and Zaki correlation at the limit of particle terminal velocities;-

$$U_D = U_1 \varepsilon_D^n \tag{4}$$

in which U_D and ε_D are the superficial gas velocity and the bed voidage, respectively, and U_1 and n are the two adjustable parameters of the equation. The exponential index n assumes a nearly constant value of 4.65 for Group A powders. The Richardson-Zaki equation is particularly useful for high-bed voidage ranges. The Richardson-Zaki equation and all other existing bubble-free bed hydrodynamic models assume that the bed is homogeneous and its void structure is represented by a single characteristic voidage. However, this view represents only an approximation to the real cavity structure that is heterogeneous, consisting of strings of clustered particles and interstitial cavities of gas. A comprehensive characterization of the cavity structure would require two or more characteristic voidages as seen below.

Castellanos et.al [21] have investigated the settling of fine powders to find that existing equations to describe these phenomena need to be extended in order to account for aggregates that form due to strong inter-particle attraction. Aggregates form up to an order of 100μm which is significant given the size of a single particle. They state that despite the simplicity of Richardson-Zaki equation, at high solidosity values, it has no theoretical justification. They propose a modified Richardson-Zaki equation for complex agglomerates along with a straightforward criterion using a force balance. Using, particle volume fraction φ,

$$\frac{U_D}{U_1^*} = (1-\varphi^*)^n \tag{5}$$

where $U^*_1 = U_1 N/k$ is the settling velocity of an individual agglomerate and $\varphi^* = \varphi k^3/N$. They modelled the fluidized bed as an ideal system of simple agglomerates each one consisting of N primary particles and with a radius of gyration RG equal to the hydrodynamic radius R_H (let us define k $=2R_G/dp$).

$$\frac{U_D}{U_1} = \frac{N}{k}\left(1-\frac{k^3}{N}\varphi^*\right)^n \tag{6}$$

However, complex agglomerate structures should be considered in the evaluation of this equation. As stated above, smaller agglomerates themselves form bigger agglomerates in different shapes i.e. Multistage Agglomeration (MSA). Nam et.al.[33] makes use of this modified model to adapt to multiscale, multistage agglomerate structures. In an attempt to include these multistage agglomeration, a new version of Eqn. (5) is put forward as by Valverde and Castellanos [6] and (private communication):

$$\frac{v_s}{v_{p0}} = \frac{N}{k}\frac{N^*}{k^*}\left(1-\frac{k^3}{N}\frac{(k^*)^3}{N^*}\varphi\right)^n \qquad (7)$$

4. Modelling of dynamic clustering effects

A closer examination of the clustering and aggregation of nano-particles above the fluidised bed by x-ray micro-radiography is found to reveal a very high degree of mobility of individual particle separations; refer to **Fig. 5g-h** above. This is believed to be due to the manifestation of the "cohesive energy" produced by electric field strength at large contact separations. Jung and Gidaspow [2] provide discussions of such effects in fluidisation of ultra-fine particles with reference to the existence of highly thermalised, dynamic clusters held together by long-range Van der Waals and electrophoretic forces. This result is in stark contrast to the established observations of the Geldart C Type behaviour. Particles in the micron size range are often found to exhibit cohesive/adhesive force bonding of (almost) touching contacts marked by very low degree of mobility of particle contact separations. The presence of strong short-range Van der Waals or capillary type forces often result in dense agglomerate structures which can be further compacted to "stable cakes" at quite small compressive forces as in powders in the micron size-range; see for example reference 2).

In the studies presented here, the formation and preservation of dynamic agglomerates and clusters of nano-particles in the 100 micron −1 mm size range allows homogeneous bed expansion coupled with increased aggregation of the particle assembly as the fluidising gas velocity is increased; refer to **Fig. 5** above. Hence, with nano-particle clusters in high fluidising velocities much in excess of the minimum fluidisation velocity, the fluidisation behaviour is described by continuous expansion similar to Group A behaviour in stark contrast to the group C behaviour observed typically with particles in the micron size-range; see modified Geldart diagram below incorporating dynamic clustering effects observed in the expansive suspension phase in nano-agglomerate fluidisation.

Further on-going studies of the dynamic clustering effects are likely to reveal further evidence of the sustainability of long-range clustering at very small values of the immersed weight $(\rho_p-\rho_f)\cong 10-10^2$ kg m^{-3} of the clusters as seen in **Fig. 10**.

With varying particle and carrier fluid properties, it is believed that it would be possible to represent the aggregative fluidisation of these nano-particle assemblies with continuous and homogeneous expansion without bubbling (i.e. Geldart A-type behaviour) by allowing gas percolation through the bed contents at multiple porosity length scales as depicted by the schematic in **Fig. 9** above. Therefore, we add this region where dynamic nanoparticle clusters are observed as "E: expandable" in the modified Geldart diagram presented in **Fig. 10**. It is also important to establish here the effects of 2-D and 3-D bed ge-

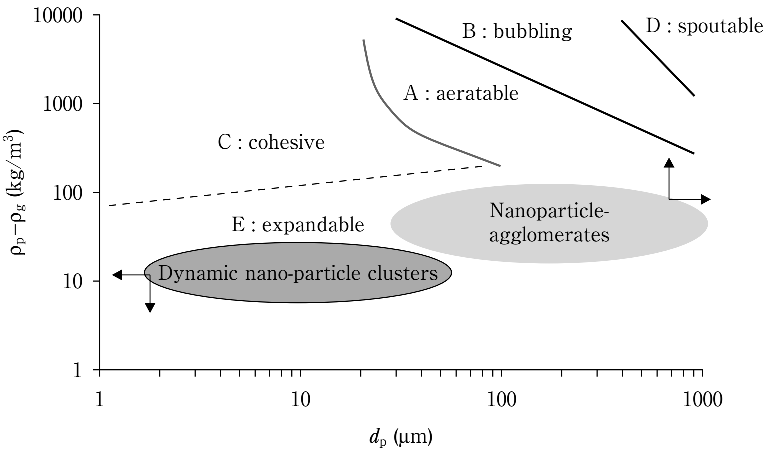

Fig. 10 Proposed modification of Geldart's classification to incorporate nano-particle fluidization regimes (dp=particle/agglomerate size and ($\rho_p-\rho_g$) is the immersed solids density)

ometry on the observed transitions from particulate to aggregative states of fluidisation both within the agglomerates as well as with in the cavity space between the "effective" agglomerates in the bed. The other very recent literature cited above in 3-D beds[24] suggests that the transitions from particulate fluidisation to aggregative and/ or bubbling regime is markedly different in 2-D and 3-D geometries. All of these phenomena could be fitted into the Geldart classification above by a further systematic study of the dynamics of the agglomerate/cluster growth and decay processes in 2-D and 3-D fluidised beds.

5. Conclusions

Through the use of novel x-ray micro imaging techniques, highly accurate data are produced of the mean size and shape of nano-agglomerates in incipiently fluidised beds and in expanding clusters above the bed region. In the latter regime, the multi-scale nature of the interstitial voidage and gas percolation has been demonstrated to produce nano-agglomerates of substantial size (5- 75 microns) as seen in **Fig. 4** with immersed cluster/agglomerate densities of a factor of 10 of the density of the gas phase whilst within an incipiently fluidised bed, denser and more stable agglomerate sizes were found to grow to the millimetre scale; as seen in **Fig. 3b** above. Tomographic data to date presented here is indicative of the way that such data could be used to predict quite accurately the size and internal porosity of the said agglomerate structures. The uncertainties associated with tomographic calibrations will no doubt be reduced substantially with ever increasing spatial and temporal resolutions afforded by further state-of-the-art scanner hardware developments.

A modified Geldart chart is proposed to take in to effect the dynamics of the expanding dynamic clusters observed at high fluidisation velocities which result in E type expandable dynamic cluster behaviour in stark contrast to the much more dense agglomerates observed with particles in the micron size range in conventional Group C type fluidisation behaviour. The literature to date attributes the differences to the predominance of different long and short range forces in sub-micron particle assemblies. It therefore remains very important to establish the effects of the physical and chemical properties of the different particle species on the magnitude and the nature of these force fields. Current investigations are underway to quantify the contributions to the nanoparticle cluster force fields from long range van der Waals, electrostatic and electrophoretic forces.

Acknowledgements

Authors would like to thank Dr P.M. Jenneson of University of Surrey for playing a pivotal role in X-ray imaging and Dr M. Wise of Tetronics Ltd., UK for his help with the supply of nanopowder samples.

References

1) Geldart, D.,Powder Technology, 7, 287 (1973)
2) Jung JW, Gidaspow D, Journal of Nanoparticle Research, 4 (6), 483 (2002).
3) Hakim LF, Portman JL, Casper MD, Weimer AW, Powder Technol, 160, 149 (2005).
4) Dukhin S., Zhu C., Dave R.N., Yu Q., Adv. in Colloid and Interface Sci. 114 (2005).
5) Jenneson PM, Gundogdu O, Appl. Phys. Lett., 88, 034103 (2006).
6) Valverde JM, Castellanos A., AIChE Journal 52 (2): 838-842 (2006).
7) C. Zhu, G. Lui, Q. Yu, R. Pfeffer, R. N. Dave, and C. H. Nam, Powder Technol., 141, 119 (2004).
8) Valverde J.M. et al., Physics Review, E , 67, 051305 (2003).
9) Yao W., Gu G., Wei Fei, Wu J., 2002, Powder Technology, 124, 152 (2002).
10) Matsuda S., Hatano H., Muramoto M., Tsutsumi A., AIChE Journal, 50 (2004).
11) Kwauk M., Li J., Liu D., Powder Technology, 111, 3 (2000).
12) Granqvist C.G.and Buhrman R.A., Appl. Phys. Lett., 693 (1975).
13) Wang, M. Kwauk, and H. Li, Chem. Eng. Sci. 53, 377 (1998).
14) Jenneson P.M., Luggar R.D., Morton E.J., Gundogdu O., Tuzun U, J. Appl. Phys., 96, 2889 (2004).
15) Zhu C et al, Powder Technology, 141, 119 (2004).
16) Morooka S., K. Kusakabe, A. Kobato, and Y. J. Kato, Chem. Eng. Jpn., 28, 41 (1988).
17) Y. Wang, F. Wei, G. Luo, H. Yu, and G. Gu, Chemical Physics Letters, 364,568 (2002).
18) Chaouki J., Larachi F. and Dudukoni- M. P., Ind. Emg. Chem. Res., 36, 4476 (1997).
19) Sugihara M., J. Res. Assoc. Powder Technol., Jpn., 3, 21 (1966).
20) Chaouki J., Chaverier C., Klvana D., Pajonok G., Powder Technol., 43, 117 (1985).
21) Castellanos A, Valverde J. M., Quintanilla M. A. S, Phys. Rev. E, 64 (2001).
22) Iwadate Y., Horio M., Powder Technol. 100, 223 (1998)
23) Park, YJ., Chemical Engineering Science, 58,193 (2003).
24) Peirano, E., Delloume, V, Leckner B, Chem. Eng. Sci., 56, 4787 (2001).

25) Simons, S. J. R., Chem. Eng J, 56, 83-93 (1995).
26) Grohse, E. W., AIChE J., 1, 358-365 (1955).
27) Rowe, P. N., Partridge, B. A, Trans. Instn. Chem. Engrs., **43**, T157-T175 (1965).
28) Yates J. G., Ruiz-Martinez R. S., Cheeseman D. J., Chem. Eng. Sci. **45** 1105-1111 (1990).
29) van Dijk J.J., Hoffmann A.C, Cheesman D., Yates J.G., Powder Techaology, 98, 273-278 (1998).
30) Kantzas A., Wright I., Kalogerakis N., Chem. Eng. Sci. **52**, 2023-2035 (1997).
31) Lehner P. and Wirth K., J., Chem. Eng. **77** 199-206 (1999).
32) Kai T., Misawa M., Takahashi T., Tiseanu I., Ichikawa N. and Takada N. J., Chem. Eng. Jpn., **33**, 906-909 (2000).

Author's short biography

Dr. Özcan Gündogdu

Dr Gündogdu received his PhD in Applied Physics from the University of Birmingham where he developed novel Positron Emission Tomography (PET) multiple particle tracking techniques for powder processing and particle interactions. He then worked on developing novel filtration techniques exploring complex multiphase systems, developing theoretical models. He has been working as senior research fellow at the University of Surrey since 2003, in nano-powder processing, polymer-nano hybrid systems, nanocomposites and developing novel imaging and theoretical models which will prove crucial to exploit exciting properties nanopowders and nanotechnology offer. He has a wide range of research interests from tomographic imaging techniques to zone plates and holography, optics, radiation physics, cluster analysis, fractal and percolation models, image processing and especially nanoparticle interactions and processing in multiphase systems. He has been awarded the most prestigious "2003 Gold Medal" given biennially by International Filtration Society for his work on novel filtration systems with Prof. Curt Koenders at Kingston University prior to his arrival at the University of Surrey.

Prof. Ugur Tüzün

Professor Ugur Tüzün, C.Eng, C.Sci, FIChemE, FRSA is a professor of chemical and process engineering in the School of Engineering of Surrey University. He heads a large research group studying the mechanics of particulate and multiphase flow systems. During the last decade, this group has been instrumental in developing a significant number of mathematical models (and software) using novel computational simulation techniques (e.g. CFD, FEM, MD, SPH, LGA) relating the microscopic properties of particles to the assembly behaviour in complex fluid rheologies and complex device configurations. Alongside the model development, Prof. Tüzün and his colleagues have been responsible for pioneering work on the development of novel 3D tomographic techniques to image multi-phase flows and multi-component particle systems in process equipment. Most recent applications include imaging and modelling of nano-particle compaction and fluidisation processes with applications in advanced materials and pharmaceutical industries. Prof. Tüzün also has considerable experience of continuum modelling of bulk solids velocity and stress fields with experimental validations in pilot plant equipment. Prof. Tüzün's research has attracted research funding over £1.7M with output of some 80+ research publications and over 10 PhD's during the past decade. Prof. Tüzün was honoured with the Nisshin Engineering (Japan) Distinguished Professor in Particle Technology Award in 2001.

Use of Particle Tracking Velocimetry for Measurements of Granular Flows: Review and Application[†]

—Particle Tracking Velocimetry for Granular Flow Measurements—

N. Jesuthasan, B.R. Baliga
*Department of Mechanical Engineering, McGill University**
and S.B. Savage[1]
*Department of Civil Engineering and Applied Mechanics, McGill University**

ABSTRACT

A brief review of publications that deal with particle image velocimetry (PIV) and particle tracking velocimetry (PTV) is presented first in this paper. It is followed by a brief review of papers that discuss the applications of PIV and PTV to granular flows. Next, the application of PTV to granular flows is demonstrated in the context of an experimental investigation of free-surface flows of almost spherical, slightly polydisperse, ceramic particles immersed in air. Flows of this granular material down the upper inclined surface of a wedge-shaped static pile of the same material, formed naturally and contained in a narrow channel between two parallel vertical glass plates are considered. Some sample results obtained from PTV measurements of these flows in the statistically steady and fully developed region are presented.

Keywords: Particle tracking velocimetry, Granular flows, Ensemble average velocity, Granular temperature

1. INTRODUCTION

Granular flows are commonly encountered in the materials, metallurgical, cement, fertilizer, chemical, coal, food, and pharmaceuticals industries. Examples of granular flows in geophysical contexts include formation and dispersion of sand dunes in deserts, sediment transport in oceans and rivers, debris flows, and snow avalanches. In general, granular flows involve one or more of three broad regimes: (1) static, (2) slowly deforming or quasi-static flows, and (3) rapid flows. Discussions of these and additional regimes of granular flows have been presented by Bagnold (1954), Savage (1984, 1993), Campbell (1990, 2006), Iverson and Vallance (2001), Goldhirsch (2003), and Hutter (2005) among others.

Over the last half-century or so, there have been numerous analytical, experimental, and numerical studies of granular flows. Typical examples of such studies include the works of Bagnold (1954), Savage and Sayed (1984), Lun and Savage (1987), Johnson and Jackson (1987), Jenkins (1987), Sinclair and Jackson (1989), Kobayashi et al. (1989), Campbell (1990), Jaeger and Nagel (1992), Ohyama et al. (1993), Okamoto et al. (1995), Savage (1998), Sela and Goldhirsch (1998), Oda and Iwashita (1999), Ottino and Khakhar (2000), Chou (2000), Komatsu et al. (2001), Bonamy et al. (2002), Jop et al. (2005), and Campbell (2006). However, mathematical models of these flows are not yet fully established. Furthermore, a single (unified) model of all of the aforementioned regimes of granular flow is not available, except for some ad hoc efforts aimed at patching together available models of the individual regimes. Efforts to formulate such models are continuing, and there is a need

---

[†] Accepted July 24, 2006

[*] 817 Sherbrooke St. W., Montreal, Quebec H3A 2K6, Canada

[1] Corresponding author
TEL: 514-398-6864
FAX: 514-398-7361
E-mail: stuart.savage@mcgill.ca

for experimental data that can be used for the verification of such models. The work presented in this paper is a part of a recently completed investigation which was undertaken to obtain experimental data for a flow that spanned the three above-mentioned flow regimes [Jesuthasan (2005)].

The use of particle tracking velocimetry for measurements of granular flows is discussed in this paper. A brief review of publications that deal with particle image velocimetry (PIV) and particle tracking velocimetry (PTV) is presented first. It is followed by a brief review of papers that discuss the applications of PIV and PTV to granular flows. Next, the application of PTV to granular flows is demonstrated in the context of a recently completed experimental investigation of free-surface flows of almost spherical, slightly polydisperse, ceramic particles immersed in air [Jesuthasan (2005)]. Flows of this granular material down the upper inclined surface of a wedge-shaped static pile of the same material, formed naturally and contained in a narrow channel between two parallel vertical glass plates, as shown photographically in **Fig. 1**, are considered here. These free-surface granular flows are relatively simple and affordable to set up in a university research context, but they encompass all three of the aforementioned regimes. PTV allows non-invasive measurements of such flows, and the results could be used to aid fundamental works aimed at the formulation, testing, and refinement of a unified theory (one that covers the whole range of static, slowly deforming, and rapid flow regimes), at least for dry cohesionless materials. This was the primary motivation for the work on which this paper is based [Jesuthasan (2005)]. Some sample results obtained from PTV measurements of these flows in the statistically steady and fully developed region are presented in this paper.

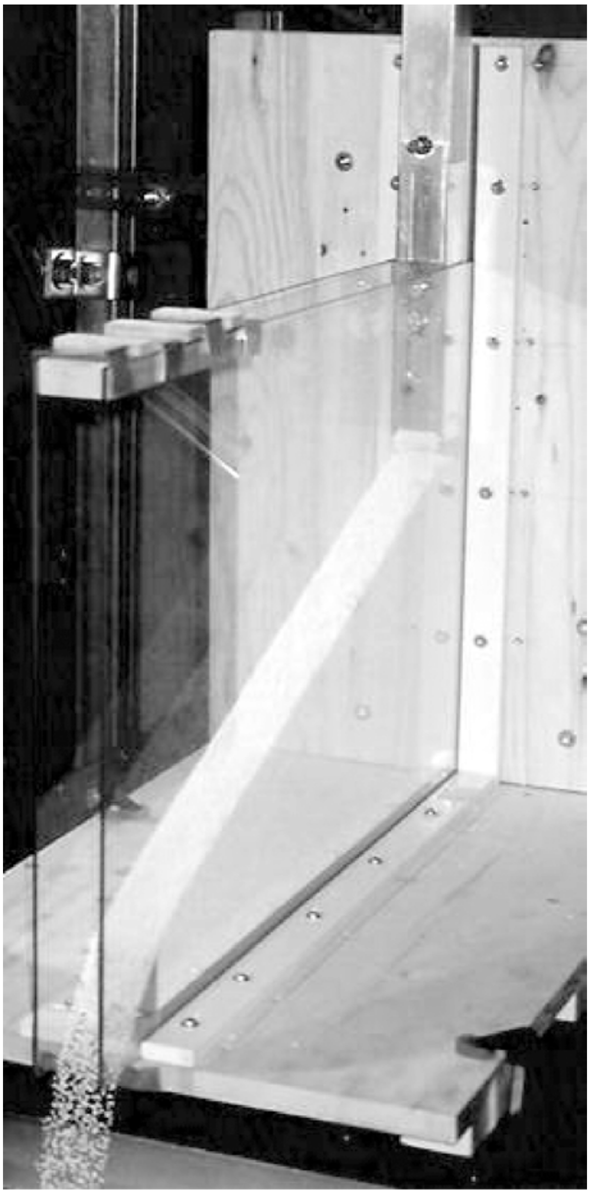

Fig. 1 Photograph of the free-surface granular flow investigated in this work.

2. REVIEW OF PIV AND PTV TECHNIQUES

PIV and PTV techniques have been used for measurements of single-phase fluid flows for the last 15-20 years. Reviews of PIV in this context have been presented by Adrian (1991), Willert and Gharib (1991), and Raffel et al. (1998). PIV is a technique where the whole flow field is visualized (measured) at a multitude of points by seeding it with suitable tracer particles, illuminating these particles with a sheet of laser light that is pulsed, obtaining images of these particles on photographic film or a video array detector, transferring these images to a computer, and using suitable computational algorithms and procedures to deduce the velocity field and related information. If the particle images are digitally acquired and stored, using a high-speed digital camera, rather than recorded on conventional photographic film, then this technique is sometimes referred to as digital particle image velocimetry (DPIV) [Willert and Gharib (1991)].

Adrian (1991) classifies low-image density PIV as PTV. In PTV, images of the flow obtained with multiple exposures are used to track particle displacements that are short compared to the mean spacing between individual particles tracks; furthermore, since the number of particle displacements per unit area of the image is relatively small, it is feasible to track individual particles. As observed by Adrian (1991), PTV has its roots in flow-visualization techniques such as particle-streak photography and stroboscopic photography [Van Dyke (1982)]. In modern PTV, the quantitative results are obtained using computerized analyses of the seed-particle images. PTV is effective for investigations of flows with large velocity gradients, a condition that is known to pose problems for conventional PIV methods [Huang et al. (1993a and 1993b)].

Two well-established PTV algorithms are the four-frame in-line tracking method [Kobayashi et al. (1989); Hassan and Canaan (1991)], that uses four consecutive images of the tracked particles, and the binary image cross-correlation method [Uemura et al. (1989)], which makes use of only two such consecutive images. In the four-frame tracking algorithm, the movement of the tracer particles is detected frame-by-frame, while evaluating the geometrical consistency of every particle path. Typically, an iterative scheme is used to select the best-match particle trajectory, involving extrapolation of the particle displacement and searching for the nearest neighbor. On the other hand, the binary image cross-correlation technique is viewed as a variation of the standard cross-correlation PIV, in which the correlation functions are computed for each interrogation window centered on the first frame of particles using an adaptive shifting scheme.

Additional two-frame algorithms that employ a particle-cluster matching concept have been proposed [Okamoto et al. (1995), Ishikawa et al. (1997)]. In this method, particles from the first and second frame are conceived to form a cluster with their respective neighboring particles, and the selection of the best match particles is conducted on the basis of a deformation index defined for the relationship between the clusters in the two frames. Another two-frame technique is based on the use of a suitable cost function in particle tracking algorithms: An example is the algorithm proposed by Ohyama et al. (1993), in which the best-match particle pairs are determined by using a fitness function that minimizes the total sum of the squares of particle displacements. The neural-network PTV proposed by Labonté (1999) can also be classified in this category of algorithms. Although time consuming, this algorithm seems more efficient (reliable) in identifying and tackling unpaired particles between the frames.

3. REVIEW OF APPLICATIONS OF PIV AND PTV TO GRANULAR FLOWS

Over the last 15 years, continual improvements of computer hardware and software have greatly facilitated the use of PIV and PTV for measurements of granular flows. Today, digital PIV and PTV systems and procedures, and modern high-speed digital cameras, enable the speedy acquisition and processing of massive amounts of data with excellent spatial resolution.

As was mentioned earlier, PTV is better suited than PIV for handling flows with steep velocity gradients, such as those commonly encountered in granular flows. Nevertheless, PIV has been used successfully for measurements of granular flows. Examples of such efforts include the works of Warr et al. (1994), Lueptow et al (2000), Hanes and Walton (2000), and Tischer et al. (2001). Jain et al. (2002) have discussed the difficulties associated with the application of PIV to thin granular shear layers. In their rotating-drum experiments, the granular shear layers adjacent to the free surface were only 5-10 particle diameters deep, leading to relatively steep velocity gradients. Thus, they resorted to the use of a hybrid PTV/PIV technique proposed by Cowen and Monsmith (1997).

Larcher (2002) has performed experiments on suspensions of solid particle in liquids flowing down inclined chutes. He measured mean streamwise velocities of the particles, granular temperature, and solids fraction profiles over the depth of the flow. Larcher also described his attempts to use PIV techniques to determine the mean velocity profiles. However, at high shear rates, problems of the kind discussed by Jain et al. (2002) were encountered. Larcher also used a particle-tracking technique based on Voronoï diagrams around the particle centers in paired frames: The particles in one frame and the next were paired based on a goodness of match between the shapes of the Voronoï cells. The particle velocities were found by dividing the corresponding particle displacements by the time interval between the frames. Larcher (2002) found this Voronoï approach to work effectively at shear rates higher than those possible with the standard PIV method. A detailed description of particle tracking based on Voronoï imaging methods is presented in Capart et al. (2002). An extension of these ideas to a three-dimensional Voronoï imaging method is given in Spinewine et al. (2003).

Over the last ten years or so, there have been several experimental investigations of free-surface granular flows in which optical techniques have been used to obtain measurements of particle velocities, and, in some cases, also their fluctuations. Two different experimental set-ups have been primarily used in these studies. In one, the granular material flows down a static pile (or heap) of the same material, usually contained between two vertical walls. The granular material is released from a hopper on top of the pile, and its flow rate out of the hopper is controlled: examples include the works of Komatsu et al. (2001) and Khakhar et al. (2001), and also the recent work of Jop et al. (2005). In the second set-up, a cylindrical tumbler, or drum, whose axis is horizontal (with respect to the gravitational acceleration vector), is half-filled with the granular material and rotated about its axis at a controlled angular speed to create the free-surface granular flow: examples include the works of Jain et al. (2002) and Bonamy et al. (2002). The rotating-tumbler arrangement is very convenient experimentally, since with a finite mass of particles, the steady-state free-surface flow can be continued indefinitely for all practical purposes. However, in the work of Jesuthasan (2005), on which this paper is based, the granular flow down a static pile was the chosen configuration for the experimental set-up (**Fig. 1**). The motivation for this choice is that under statistically steady conditions, the free-surface granular flow down a static pile can achieve a thickness of the flowing layer that is independent of the distance from the hopper (fully developed condition), whereas in the rotating-tumbler set-up, this thickness varies continually along the direction of the flow. Furthermore, PTV was selected for measurements of the granular flows of interest. Full details of this technique and the related procedures are available in Jesuthasan (2005).

4. APPLICATION OF PTV TO A FREE-SURFACE GRANULAR FLOW

PTV measurements of a free-surface granular flow down the upper inclined surface of a wedge-shaped static pile of the same material, contained in a narrow channel between two parallel vertical glass plates, were undertaken in this work. A photographic illustration of this flow is given in **Fig. 1**. In the design of the experimental set-up, some ideas contained in the works of Komatsu et al. (2001) and Khakhar et al. (2001) were borrowed and extended. An overview of the experimental apparatus and techniques, a synopsis of the PTV procedures, and some sample results from this investigation are presented in this section. For full details of this research, the readers are referred to the work of Jesuthasan (2005).

4.1 Overview of the Experimental Apparatus and PTV set-up

A photograph of the experimental apparatus is provided in **Fig. 2**. It consists of the following main elements located in sequence along the flow path of the granular material: (i) a reservoir hopper that was designed to safely hold a sufficiently large amount (up to 20 L) of the granular material; (ii) a height-adjustable spout with a double-slider gate mechanism (schematically illustrated in **Fig. 3**) which was used to control the flow rate of the granular material; (iii) a test section in which the free-surface flow was set up and measured (see **Fig. 1**); and (iv) a discharge hopper. The granular material used in this work consisted of slightly polydisperse, almost spherical, ceramic (zirconium silicate) beads: mean effective diameter of 1.59 mm (standard deviation of 0.034 mm) and mass density of 4071 kg/m^3 (±28 kg/m^3) [Jesuthasan (2005); Jesuthasan et al. (2005)]. Each of the two vertical glass plates that were used to create the channel for the flow of the granular material was 610 mm long, 350 mm high, and 3.175 mm thick. Three different values of the normal separation distance between these plates were investigated: 25.4 mm,

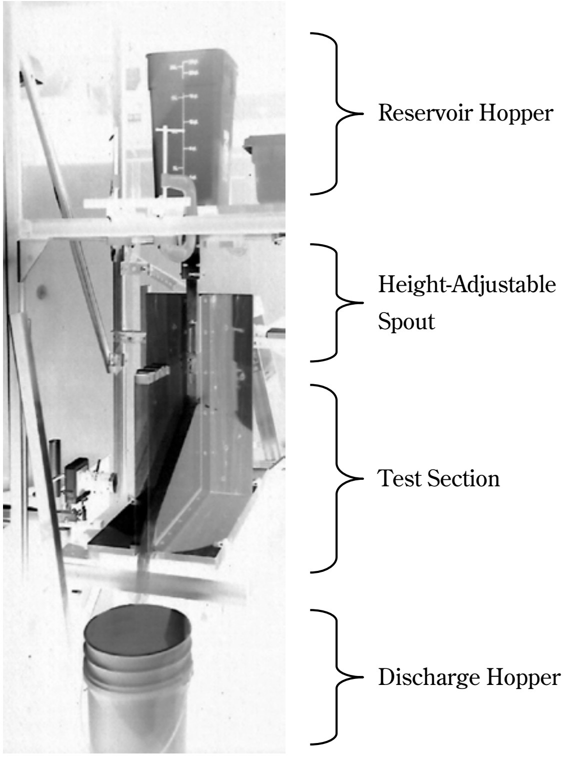

Fig. 2 Photograph of the experimental set-up.

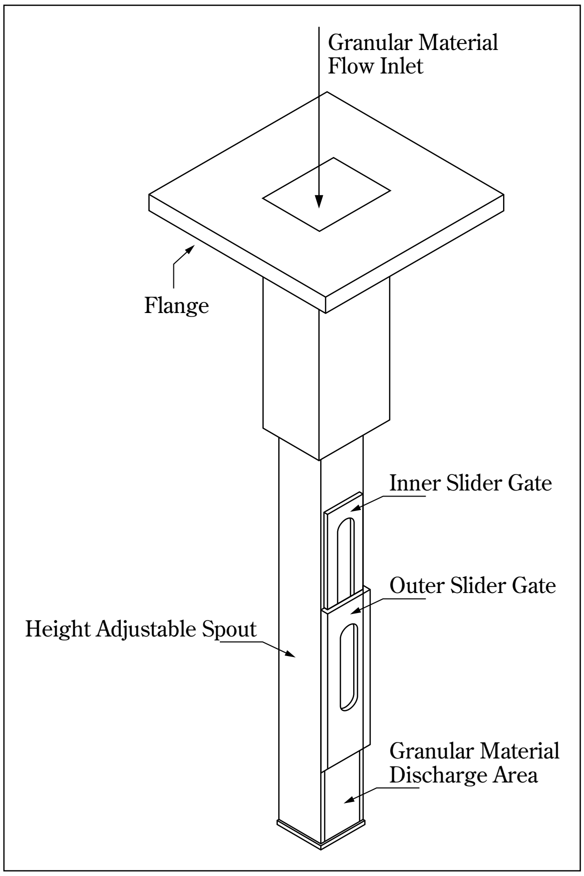

Fig. 3 Schematic illustration of the flange, height-adjustable spout, and the double-slider gate mechanism.

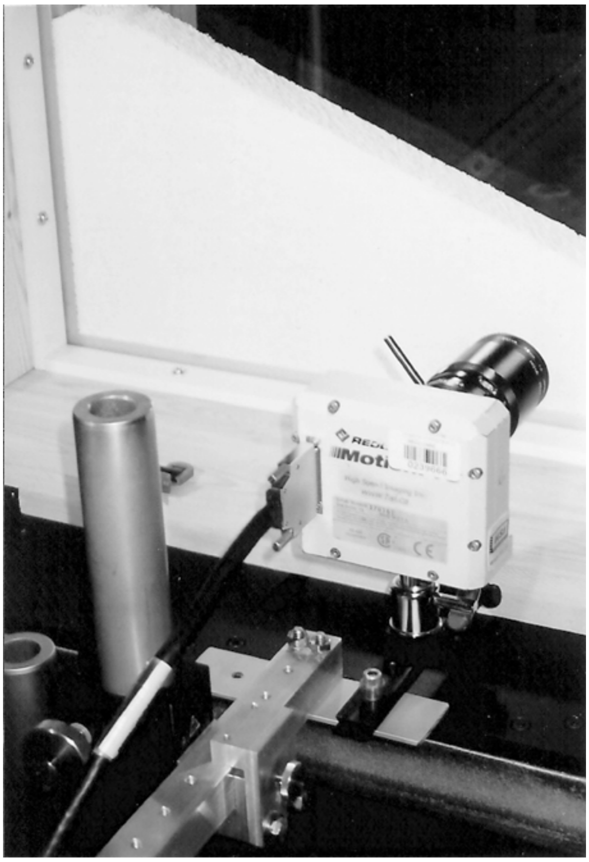

Fig. 4 Photograph of the high-speed camera and its mounting and traversing system.

38.1 mm, and 50.8 mm. For each of these separation distances, the following three values (nominal) of the mass flow rate per unit width were considered: 0.811 kg/s-m, 1.847 kg/s-m, and 3.332 kg/s-m. For these ranges of dimensional parameters, statistically-steady fully developed flows were established inside the test section in a reliable and repeatable manner [Jesuthasan (2005)].

A high-speed camera system (Redlake MotionPro 10000) was used to acquire digital images of the granular flows of interest in the fully developed region. A photograph of this high-speed camera and the system that was used to mount and traverse it is shown in **Fig. 4**. Illumination of the front surface of the granular flows of interest was done using two 250 W halogen photoflood variable-intensity lights (Lowel Pro-Light). Image processing and a commercial PTV software package (DiaTrackPro 2.3) were used to obtain the particle trajectories, and special programs were written in Matlab to obtain the corresponding instantaneous and ensemble-averaged velocity distributions and related results.

4.2 Synopsis of the PTV Procedures

The high-speed digital camera, after it was properly positioned and aligned to capture images of the granular flows, was first used to acquire images of a plumb ball and a ruler placed on the inside surface of the front glass plate of the test section. The images of the plumb ball were used to establish the orientation of the camera with respect to the horizontal, and then the static angle of repose of the granular particles was determined. The images of the ruler were employed to determine a conversion factor for relating data in pixels counts to physical length dimensions. These analyses were done using an image-processing computer program called ImageTool, which is available on the Internet at http://ddsdx.uthscsa.edu/dig/itdesc.html. This program allows angular measurements with a precision of about ± 0.05°.

As was stated above, a commercial PTV software package (DiaTrackPro 2.3, developed and distributed by Semasopht, Swizterland) was purchased and used in this work. The initial step in the PTV analysis using this software package is to load the first image frame (of a sequence of such frames) in the application window. The image is then convoluted by a Gaussian filter of variable strength such that centers and boundaries of the particles are highlighted [Willert and Gharib (1991)]. The locations of the center of mass of the particles in the image are then identified based on local brightness maxima. Incorrectly identified particles are selected and eliminated by imposing suitable image thresholds [Jain et al. (2002); Larcher (2002)]. Once this is done for the first image frame, the aforementioned processing steps are automatically applied to all successive image frames in the sequence. At this point, the tracking algorithm is initiated and particles in each pair of successive frames are sequentially matched [Adrian (1991); Cowen and Monismith (1997); Larcher (2002)] to produce a series of particle displacement vectors. This sequence of steps is illustrated by the images provided in **Fig. 5**.

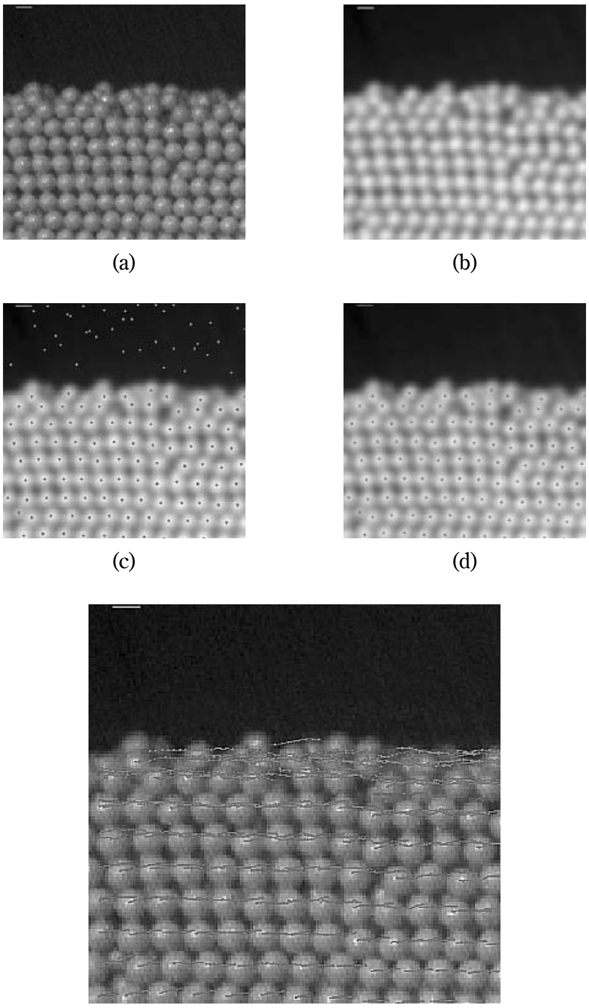
(a)
(b)
(c)
(d)
(e)

Fig. 5 Results of PTV operations performed using DiaTrackPro 2.3: (a) loaded raw image; (b) filtered image; (c) particle identification; (d) final image after particle selection; (e) superimposed particle displacement vectors after PTV analysis.

The PTV data processing procedures are summarized in the flow diagram given in **Fig. 6**. First, the high-speed digital camera is used to acquire sequential images of the granular flow. Then the acquired raw digital images are rotated and cropped, using programs written in Matlab, to aid the PTV analyses using DiaTrackPro 2.3. Finally, specific data processing for the granular flows of interest is done, again using programs written in Matlab.

4.3 Data Processing

Upon successful completion of PTV analysis via DiaTrackPro 2.3, the resulting particle displacement data were used to compute the corresponding instantaneous velocities. The following simple approximation was used in this step:

$$\frac{\vec{V}_i^{(m)}=\vec{r}_i^{(m+1)}-\vec{r}_i^{(m)}}{\Delta t} \qquad (1)$$

where $\vec{r}_i^{(m+1)}=(x_i^{(m)}, y_i^{(m)})$ is the position of the i^{th} particle in the measurement plane at time $t^{(m)}$, $\vec{V}_i^{(m)}=(u_i^{(m)}, v_i^{(m)})$ is the corresponding in-plane velocity, and x and y are oriented in the directions parallel and perpendicular to the mean flow direction, respectively. The particle displacements yielded by the PTV analysis are in pixels counts: The conversion factor mentioned in the previous subsection was used to relate the image pixel counts to physical lengths.

Once the instantaneous velocities were computed and stored for each image pair in the sequence, a program written in Matlab was used to compute the following granular flow field properties: mean velocities, mean-square velocity fluctuations, granular temperature, and the Savage-Jeffrey parameter.

First, the flow region of interest was subdivided

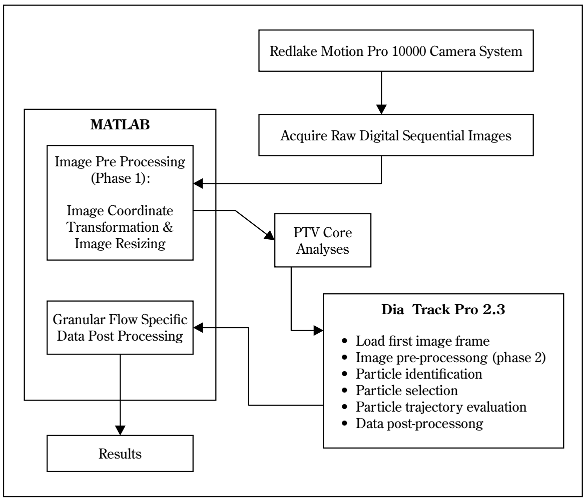

Fig. 6 Flow diagram of the PTV and data processing procedures.

into non-overlapping horizontal slices (or bins) of thickness, δ, equal to one particle diameter, as shown schematically in **Fig. 7**. The coordinates of the centers of the measured particle displacement vectors were used to distribute them into these bins. They were then processed to obtained ensemble-averaged results for each bin.

The ensemble-averaged streamwise velocity, $\bar{u}_k$, and transverse velocity, $\bar{v}_k$, within the k^{th} bin, at its centroid, Y_k, were calculated as follows:

$$U=\bar{u}_k=\bar{u}(Y_k)=\frac{\sum_{i=1}^{N_k}(u_i)_k}{N_k}\ ;\ V=\bar{v}_k=\bar{v}(Y_k)=\frac{\sum_{i=1}^{N_k}(v_i)_k}{N_k} \qquad (2)$$

In this equation, N_k is the total number of displacement vectors in the k^{th} bin.

Second-order statistics such as the square of the velocity fluctuations, the granular temperature, and the Savage-Jeffrey parameter were then evaluated. Within each bin, the streamwise and transverse fluctuating velocities were defined as follows:

$$(u_i')_k=(u_i)_k-\bar{u}_k\ ;\ (v_i')_k=(v_i)_k-\bar{v}_k \qquad (3)$$

The means of the squares of the streamwise and transverse velocity fluctuations were then calculated as follows for each bin:

$$<(u')^2>_k=\frac{\sum_{i=1}^{N_k}[(u_i')^2]_k}{N_k}\ ;\ <(v')^2>_k=\frac{\sum_{i=1}^{N_k}[(v_i')^2]_k}{N_k} \qquad (4)$$

In this work, the z-direction fluctuating velocity component was assumed to be comparable in magnitude to the y-direction fluctuating velocity component, and the granular temperature was calculated as follows:

$$[T]_k=\{[(u')^2]_k+2[(v')^2]_k\}/3 \qquad (5)$$

The Savage-Jeffrey parameter, R, was calculated as shown below:

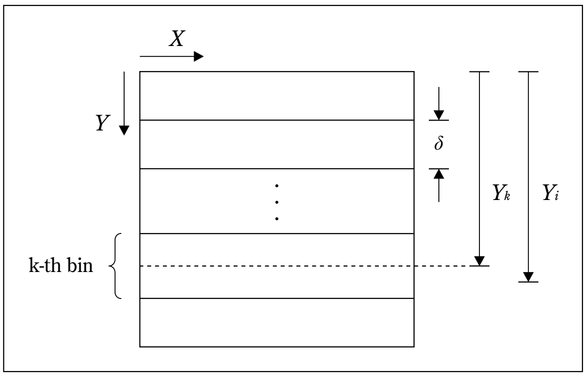

Fig. 7 Schematic illustration of the binning operation.

$$R_k=\frac{d\left|\frac{\mathrm{d}U}{\mathrm{d}Y}\right|_k}{\sqrt{(T)_k}} \qquad (6)$$

In this equation, d is the mean particle diameter. The streamwise velocity gradient in Eq. (6) was determined using cubic-spline interpolation of the binned ensemble-averaged velocity data.

4.4 Sources of Error and Benchmarking

The PTV operations are prone to errors. Particle identification from one frame to the next could be erroneous. Limited accuracy in particle positions induces physically unrealistic disturbances to the velocity data. Particle mismatch between successive frames due to incorrect tracking leads to so-called “outliers”. As a result, erroneous and/or spurious velocity vectors could contaminate the field data.

Another set of errors is associated with the experimental set-up. The high-speed digital camera and related optics, as well as the lighting system, operate within their own levels of uncertainties. The camera lens and zoom level can contribute to image distortions, compromising the accuracy of the acquired images. An appropriate choice of frame speeds in image recording is also important. Long time steps between successive images damps high-frequency fluctuations. On the other hand, short time steps lead to small displacements and large pixel errors.

For detailed and authoritative discussions of errors involved in PTV measurements, the reader is referred to the works of Adrian (1991), Willert and Gharib (1991), and Cowen and Monismith (1997).

Benchmarking of the PTV software, experimental set-up, and procedures is needed in order to evaluate the effects of the aforementioned errors on the measurements. In this work, the PTV software was validated via standard digital images obtained from the Japanese Standard Image Project, following the recommendations of Okamoto et al. (2000). These standard image sets are offered free of charge on the website of the Visualization Society of Japan (http://www.vsj.or.jp/piv). Additional details of these and related benchmarking procedures are available in the work of Jesuthasan (2005).

4.5 Sample Results

In this subsection, the intention is to demonstrate the type of results that can be obtained using PTV measurements of granular flows. Thus, with reference to the test section shown in **Fig. 1**, sample results are presented only for one normal separation distance, W=25.4 mm, between the vertical glass plates, and the following three different mass flow rates per unit width: $\dot{m}/W$=0.775 kg/s·m, 1.799 kg/s·m, and 3.288 kg/s·m. For additional results and related discussions, the readers are referred to the work of Jesuthasan (2005). The static angle of repose for the separation distance of W=25.4mm was determined to be θ_{rep}=20.55° (standard deviation of 0.44°).

The results presented in this subsection are based on measurements acquired and ensemble-averaged over a sampling period of 10 s. It was established by Jesuthasan (2005) that this sampling period is sufficient to provide statistically repeatable results for four different frame speeds: 250 fps, 333 fps, 500 fps, and 1000 fps. Furthermore, Jesuthasan (2005) determined that the optimal frame speeds for the cases considered here are the following: 333 fps for $\dot{m}/W$=0.775 kg/s·m; 333 fps for $\dot{m}/W$=1.799 kg/s·m; and 500 fps for $\dot{m}/W$=3.288 kg/s·m.

In the presentation of the sample results, X denotes the streamwise coordinate; and Y is the coordinate normal to X, directed into the flowing layer towards the underlying static pile, and zero at the free surface. The ensemble-averaged free surface velocity is denoted by U_{surf}, and the angle of inclination of the free surface of the flowing granular material is denoted by θ_{fs}.

The X-component of the velocity of the flowing layer has its maximum values at the free surface (U_{surf}) and it decays to zero with increasing Y. The exact Y location where this velocity component reaches zero is difficult to determine from the PTV measurements. It was assumed here (somewhat arbitrarily) that the bottom of the flowing layer of granular material (Y=H) corresponds to the position where U/U_{surf} =0.001.

Distributions of the mean (ensemble-averaged) streamwise and transverse velocity components (U and V) with Y are given in **Figs. 8a and 8b**, respectively. As was discussed earlier, U reaches its maximum value at the surface (Y=0) and decays down to zero with increasing Y. The transverse mean velocity component, V, is zero throughout, for all practical purposes, indicating that the ensemble-averaged flow of the granular material is parallel to the X direction. Values of the tangent of the angle of inclination of the free surface, θ_{fs}, the depth of the flowing layer of granular material, H, as defined in Equation (7), and the maximum velocity, U_{max}=U_{surf}, are given in **Table 1**. Distributions of the mean-square velocity fluctuations in the X and Y directions ($<(u')^2>$and$<(v')^2>$) and the granular temperature, T, as defined in Equation (5), are given in **Figs. 9a, 9b, and 9c**, respectively: Each of these ensemble-average quantities achieves its maximum value at the free surface and decays to zero with increasing Y; at corresponding locations, the values of $<(v')^2>$ are lower than $<(u')^2>$ by a factor of two to three; and all of these quantities increase with increasing values of $\dot{m}/W$.

Distributions of the Savage-Jeffrey parameter, R, are presented in **Fig. 10**. The calculation of this di-

Table 1 Values of tan(θ_{fs}), H, and U_{max}

W [m]	$\dot{m}/W$ [kg/s·m]	tan(θ_{fs})	H [m]	U_{max} [m/s]
2.54E-02	7.750E-01	3.823E-01	1.924E-02	4.204E-02
	1.799E+00	4.192E-01	2.067E-02	8.241E-02
	3.288E+00	4.346E-01	2.321E-02	1.345E-01

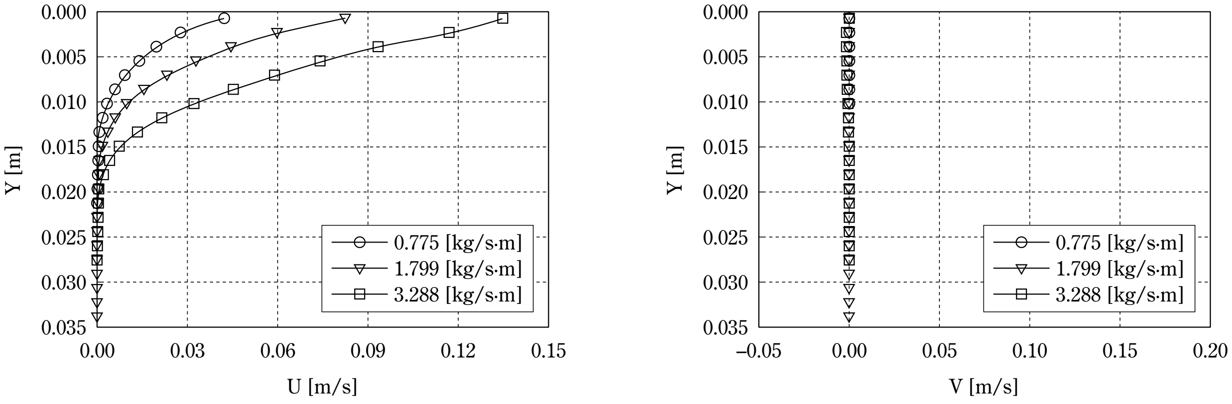

(a) (b)

Fig. 8 Distributions of mean velocity in (a) streamwise and (b) transverse directions.

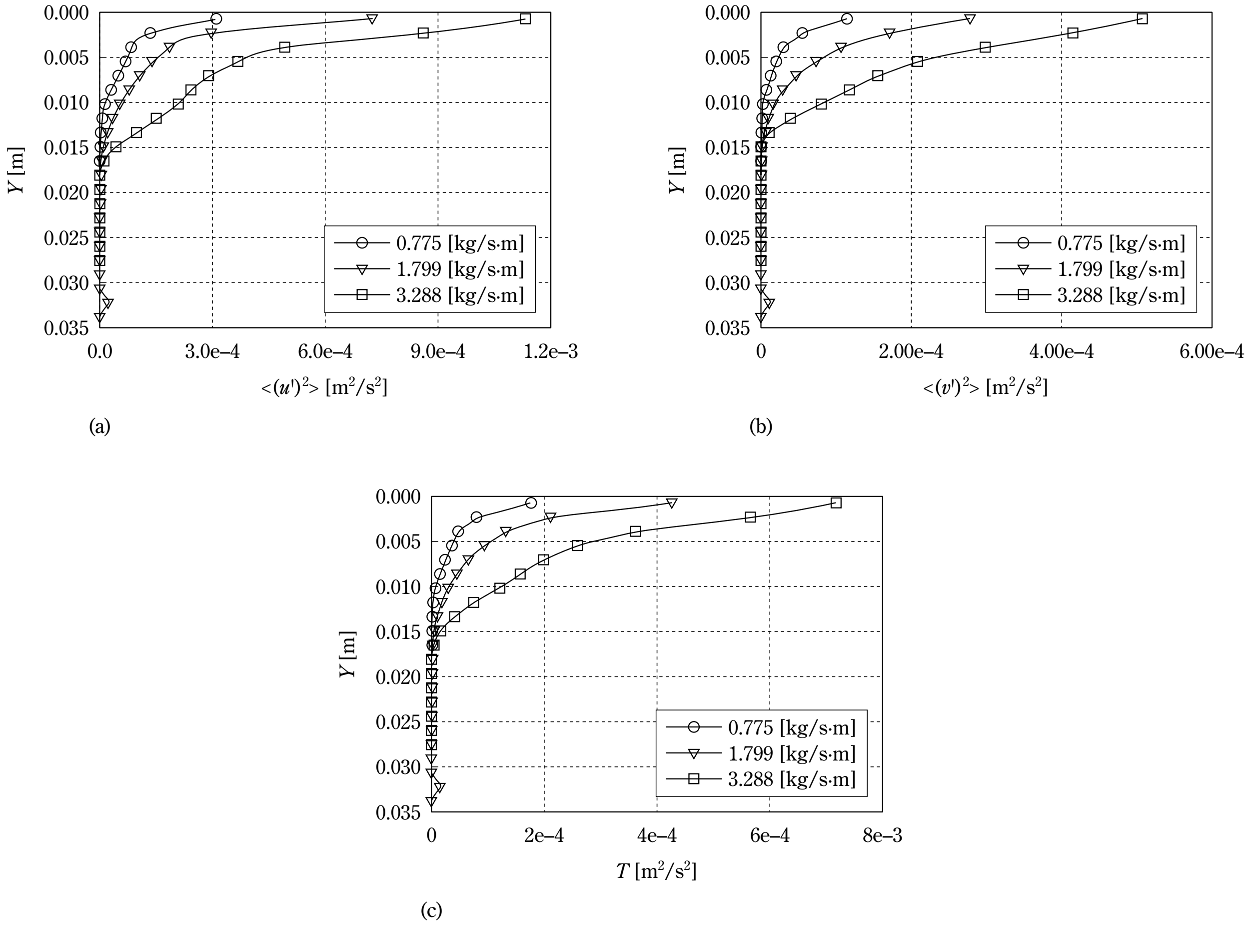

Fig. 9 Distributions of mean-square velocity fluctuations in (a) streamwise and (b) transverse directions, and (c) granular temperature.

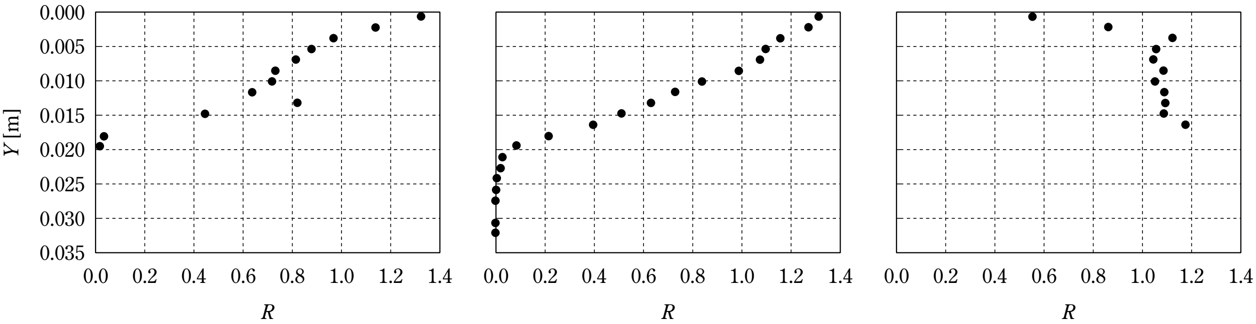

(a) 0.775 [kg/s·m] (b) 1.799 [kg/s·m] (c) 3.288 [kg/s·m]

Fig. 10 Distributions of the Savage-Jeffrey parameter.

mensionless parameter requires inputs of the gradient of the streamwise velocity, $U_{X,Y}$, and the square-root of the granular temperature, $T^{1/2}$, as shown in Equation (6). The values of $U_{X,Y}$, were calculated using cubic-spline fits to the nodal values of streamwise velocity, U_k, available at the centroids of the bins, Y_k. In the vicinity of the free-surface and also as the static pile is approached, the errors in these calculated velocity gradients could be substantial. Furthermore, as the static pile is approached, both the velocity gradients and the granular temperature go to zero, thus the calculation of R using Equation (6) could invoke large uncertainties. In this context, the values of R in the regions immediately adjacent to the free surface and the static pile are unreliable. If these regions are ignored, a trend is discernable in the plots of R presented in **Fig. 10**: The variation of R with Y is linear at the lower mass flow rates per unit width; and at the highest mass flow rate per unit width, R assumes an essentially constant value. These results seem to indicate that for the free-surface granular flows considered in this work, when the wall friction effects are significant (with respect to the shear and normal stresses in the interior of the granular flow) R vs. Y is almost linear; and R is essentially constant for the other cases.

5. CONCLUDING REMARKS

A brief review of publications related to PIV and PTV techniques was presented first in this paper. That was followed by a brief review of papers on the applications of these techniques to granular flows. The application of PTV to a demonstration problem involving a free surface granular flow was presented next, along with some sample results. The aforementioned reviews and results show that PTV is a convenient and reliable technique for non-invasive measurements of granular flows, and these measurements can be processed to obtain results that could be useful for checking and refining mathematical models of such flows.

NOMENCLATURE

d	Mean diameter of the particles
H	Thickness of the flowing layer of granular material, Equation (7)
$\dot{m}$	Mass flow rate of the granular material
R	The Savage-Jeffrey parameter, Equation (6)
T	Granular temperature, Equation (5)
u	Instantaneous velocity component in the X direction (streamwise)
u'	Fluctuating velocity component in the X direction
$<(u')^2>$	Mean-square fluctuating streamwise velocity component
U	Mean velocity component in the X direction (streamwise)
U_{surf}	Free-surface velocity (U at Y=0)
U_X	Mean velocity component in the X direction (same as U)
$U_{X,Y}$	Gradient of U_X in the Y direction
v	Instantaneous velocity component in the Y direction (transverse)
v'	Fluctuating velocity component in the Y direction
$<(v')^2>$	Mean-square fluctuating transverse velocity component
$(<(v')^2>)^{1/2}$	Root-mean-square of the transverse fluctuating velocity
V	Mean velocity component in the Y direction (transverse)
W	Separation distance between the vertical glass plates (gap width)
X	Streamwise coordinate oriented along mean flow direction (same as x)
Y	Coordinate normal to X, directed into the flowing layer (same as y)
Z	Transverse coordinate to the flow, directed from the front glass wall to the back glass wall (same as z)
θ_{fs}	Free-surface inclination angle with the horizontal
θ_{rep}	Static angle of repose of the granular material

ACKNOWLEDGMENTS

The authors gratefully acknowledge sponsorship of this work by Natural Resources Canada (NRCan), under the auspices of the Climate Change Technology Innovation Initiative, through a project on granular multiphase flow directed by the Canadian Hydraulics Centre (CHC) of the National Research Council (NRC). Thanks are also due to the Natural Sciences and Engineering Research Council of Canada (NSERC) for a scholarship to the first author and research grants to the second and third authors.

REFERENCES

Adrian, R.J. (1991), Particle imaging techniques for experimental fluid mechanics, *Annu. Rev. Fluid Mech.*, Vol. 23, pp. 261-304.

Bagnold, R. A. (1954), Experiments on a gravity free dispersion of large solid spheres in a Newtonian fluid under shear, *Proc. R. Soc. London, Ser.* A., Vol. 225, pp. 49-63.

Bonamy, D., Daviaud, F., and Laurent, L. (2002), Experimental study of granular flows via a fast camera: A continuous description, *Phys. Fluids.*, Vol. 14, pp. 1666-1673.

Campbell, C. S. (1990), Rapid granular flows, *Annu. Rev. Fluid Mech.*, Vol. 22, pp. 57-92.

Campbell, C.S. (2006), Granular material flows - An overview, *Powder Technol.*, Vol. 162, pp. 208-229.

Capart, H., Young, D. L., and Zech, Y. (2002), Voronoï imaging methods for the measurements of granular flows, *Exp. Fluids.*, Vol. 32, pp. 121-135.

Chou, C. S. (2000), Research on rapid granular flows of highly inelastic particles, *Proc. Natl. Sci. Counc. ROC(A)*, Vol. 24, pp. 317-329.

Cowen, E. A. and Monismith, S. G. (1997), A hybrid digital particle velocimetry technique, *Exp. Fluids.*, Vol. 22, pp.

199-211.

Goldhirsch, I. (2003), Rapid Granular Flows, *Annual Review of Fluid Mechanics*, Vol. 35, pp. 267-293.

Hanes, D. M. and Walton, O. R. (2000), Simulations and physical measurements of glass spheres flowing down a bumpy incline, *Powder Technol*., Vol. 109, pp. 133-144.

Hassan, Y. A. and Canaan, R. E. (1991), Full-field bubbly flow velocity measurements using a multiframe particle tracking technique, *Exp. Fluids*., Vol. 12, pp. 49-60.

Huang, H. T., Fiedler, H. E., and Wang, J. J. (1993a), Limitation of PIV-part 1: limitation of conventional techniques due to deformation of particle image patterns, *Exp. Fluids*., Vol. 15, pp. 168-174.

Huang, H. T., Fiedler, H. E., and Wang, J. J. (1993b), Limitation of PIV-part 2: particle image distortion, a novel technique, *Exp. Fluids*, Vol. 15, pp. 263-273.

Hutter, K. (2005), Geophysical granular and particle-laden flows: review of the field, *Philos. Transact. Series A, Math. Phys. Eng. Sci*., Vol. 363, pp. 1497-1505.

Ishikawa, M., Yamamoto, F., Murai, Y., Iguchi, M., and Wada, A. (1997), A novel PIV algorithm using velocity gradient tensor, in *Proc. Second International Workshop on PIV' 97*-Fukui, T. Kobayashi and F. Yamamoto (Eds.), Visualization Society of Japan, pp. 51-56.

Iverson,-R. M. and Vallance,-J. W. (2001), New views of granular mass flows, *Geology*, Vol. 29, pp. 115-118.

Jaeger, H. M. and Nagel, S. R. (1992), Physics of the granular state, *Science*, Vol. 255, pp. 1523-1531.

Jain, N., Ottino, J. M., and Lueptow, R. M. (2002), An experimental study of the flowing granular layer in rotating tumbler. *Phys. Fluids*, Vol. 14, pp. 572-582.

Jenkins, J. T. (1987), *Rapid Flows of Granular Materials* in Non-Classical Continuum Mechanics, R. Knops and A. Lacey (Eds.), Cambridge University Press, Cambridge, U.K., pp. 213-225.

Jesuthasan, N. (2005), Optical measurements of a free-surface granular flow, *M.Eng. Thesis*, Department of Mechanical Engineering, McGill University, Montreal, Quebec, Canada.

Jesuthasan, N., Baliga, B. R., and Savage, S. B. (2005), Particle sizing using elements of a particle tracking velocimetry system for granular flows, accepted for publication, *Proc. 20th Canadian Congress of Applied Mechanics* (*CANCAM 2005*), May 30 - June 3, Montreal, Canada.

Johnson, P. C. and Jackson, R. (1987), Frictional-collisional equations of motion for particulate flows with applications to chutes and shear cells, *J. Fluid Mech*., Vol. 176, pp. 67-93.

Jop, P., Forterre, Y., and Pouliquen, O. (2005), Crucial role of side walls for granular surface flows: consequences for the rheology, *J. Fluid Mech., (under consideration)*.

Khakhar, D. V., Orpe, A. V., Andresén, P., and Ottino, J. M. (2001), Surface flow of granular materials: Model and experiments in heap formation. *J. Fluid Mech*., Vol. 441, 255-264.

Kobayashi, T., Saga, T., and Segawa, S. (1989), Multipoint velocity measurement for unsteady flow field by digital image processing, in *Flow Visualization V*, R. Reznicek (Ed.), Hemisphere, New York, pp. 197-202.

Komatsu, T. S., Inagaki, S., Nakagawa, N., and Nasuno, S. (2001), Creep motion in a granular pile exhibiting steady surface flow, *Phys. Rev. Lett*., Vol. 86, 1757-1760.

Labonté, G. (1999), A new neural network for particle-tracking velocimetry, *Exp. Fluids*., Vol. 26, pp. 340-346.

Larcher, M. (2002), Vertical structure of high-concentration liquid-granular flows, *Ph.D. Thesis*, Department of Civil and Environmental Engineering, University of Padova, Italy.

Lueptow, R.M., Akonur, A., and Shinbrot, T. (2000), PIV for granular flows, *Exp. Fluids*., Vol. 28, pp. 183-186.

Lun, C. K. K. and Savage, S. B. (1987), A simple kinetic theory for granular flow of rough, inelastic spherical particles, *J. Appl. Mech*., Vol. 54, pp. 47-53.

Oda, M. and Iwashita, K. (1999), *Mechanics of Granular Materials*, Balkema Publishers, Rotterdam, Netherlands.

Ohyama, R., Takagi, T., Tsukiji, T., Nakanishi, S., and Kaneko, K. (1993), Particle tracking technique and velocity measurement of visualized flow fields by means of genetic algorithm, *J. Visualization Soc*. Japan, Vol. 13, pp. 35-38.

Okamoto, K., Hassan, Y.A., and Schmidt, W.D. (1995), New Tracking Algorithm for Particle Image Velocimetry, *Exp. Fluids*., Vol. 19, pp. 342-347.

Okamoto, K., Nishio, S., Saga, T., and Kobayashi, T. (2000), Standard Images for Particle-Image Velocimetry, *Meas. Sci. Technol*., Vol. 11, pp. 685-691.

Ottino, J. M. and Khakhar, D. V. (2000), Mixing and segregation of granular materials, *Annu. Rev. Fluid Mech*., Vol. 32, pp. 55-91.

Raffel, M., Willert, C. E., and Kompenhans, J. (1998), *Particle Image Velocimetry: A Practical Primer*, Springer-Verlag, New York.

Savage, S. B. (1984), The mechanics of rapid granular flows, *Adv. Appl. Mech*., Vol. 24, pp. 289-366.

Savage, S.B. (1993), Mechanics of granular flows, in *Continuum Mechanics in Environmental Sciences and Geophysics*, K. Hutter (ed.), CISM No. 337, Springer, New York, pp. 467-522.

Savage, S. B. (1998), Analyses of slow high-concentration flows of granular materials, *J. Fluid Mech*., Vol. 377, pp. 1-26.

Savage, S.B. and Jeffrey, D.J. (1981), The stress tensor in a granular flow at high shear rates, J. Fluid Mech., Vol. 110, pp. 255-272.

Savage, S. B. and Sayed, M. (1984), Stresses developed by dry cohesionless granular materials sheared in an annular shear cell, *J. Fluid Mech*., Vol. 142, pp. 391-430.

Sela, N. and Goldhirsch, I. (1998), Hydrodynamic Equations for Rapid Flows of Smooth Inelastic Spheres, *J. Fluid Mech*., Vol. 361, pp. 41-74.

Sinclair, J. L. and Jackson, R. (1989), Gas-particle flow in a vertical pipe with particle-particle interactions, *AIChE J*., Vol. 35, pp. 1473-1486.

Spinewine, B., Capart, H., Larcher, M., and Zech, Y. (2003), Three-dimensional Voronoï imaging methods for the measurement of near-wall particulate flows, *Exp. Fluids*., Vol. 34, pp. 227-241.

Tischer, M., Bursik, M. I., and Pitman, E. B. (2001), Kinematics of sand avalanches using particle-image velocimetry, *J. Sediment Res.*, Vol. 71, pp. 355.

Uemura, T., Yamamoto, F., and Ohmi, K. (1989), A high speed algorithm of image analysis for real time measurement of two-dimensional velocity distribution, in *Flow Visualization*, B.

Khalighi, M. Braun, and C. Freitas (Eds.), ASME, NewYork, pp. 129-134.

Van Dyke, M. (1982), *An Album of Fluid* Motion, Parabolic Press, Stanford, California.

Warr, S., Jacques, G. T. H., and Huntley, J. M. (1994), Tracking the translational and rotational motion of granular particles: Use of high-speed photography and image processing, *Powder Technol.*, Vol. 81, p. 41-56.

Willert, C. E. and Gharib, M. (1991), Digital particle image velocimetry, *Exp. Fluids.*, Vol. 10, pp. 181-193.

Biographical Sketches of the Authors

Nirma Jesuthasan

Nirma Jesuthasan obtained the B.Eng. and M.Eng. degrees in Mechanical Engineering from McGill University, where is he currently working on his Ph.D. thesis. His research interests are in experimental and computational fluid dynamics and heat transfer, with applications to granular flows, heat pipes and loop heat pipes, spacecraft thermal control, compact heat exchangers, gas turbine engines, and alternative energy systems.

B. Rabi Baliga

B. Rabi Baliga obtained the B.Tech. degree from the Indian Institute of Technology, Kanpur, in 1972. He then obtained the M.A.Sc. degree, with specialization in solid propellant combustion, from Case Western Reserve University, Cleveland, Ohio, in 1974. He was awarded the Ph.D. degree in Mechanical Engineering, with specialization in heat transfer, from the University of Minnesota, Minneapolis, Minnesota, in 1978. He is currently a professor and director of the Heat Transfer Laboratory in the Department of Mechanical Engineering at McGill University. His research interests are in computational and experimental fluid dynamics and heat transfer, with applications to compact heat exchangers, heat pipes and loop heat pipes, microencapsulated phase-change material slurries, gas-solid and granular flows, porous media, internally finned ducts, thermal control, energy storage, and alternative energy systems.

Stuart B. Savage

Stuart Savage is a Professor Emeritus in the Department of Civil Engineering and Applied Mechanics, McGill University, Montreal. The main focus of his research over the past 30 years has been on mechanics of granular materials; it has involved the development of statistical and continuum theories, computer simulations, and laboratory and field experiments. This work has applications in materials handling and processing, fluidized beds, pharmaceutical and ceramics manufacturing, as well as to geophysical problems such as debris flows and rock avalanches, snow avalanches, and the motion of wind driven arctic pack ice. Prof. Savage has acted as a consultant to major corporations, consortia and various government organizations. He is a Fellow of the Royal Society of Canada, a Member of the US National Academy of Engineering, and a Life Member of Clare Hall, Cambridge University.

Control of Physical Forms of Drug Particles for Pulmonary Delivery by Spray Drying and Supercritical Fluid Processing[†]

H. H. Y. Tong[2] **and A. H. L. Chow**[1]
School of Pharmacy, Chinese University of Hong Kong[*]

Abstract

Dry powder inhalation (DPI) is an important means of pulmonary drug delivery for both local and systemic actions. Since drugs of different solid-state chemistry can influence a wide range of physical, chemical and biological properties, control of the solid-state structures and associated behaviours of drug particles is critical for DPI formulation. Current production technology of fine drug particles for pulmonary delivery utilizes sequential batch crystallization and micronization. However, this two-step manufacturing approach often causes unwanted crystallographic damage to the particles and may induce undesirable polymorphic transformation in certain materials. In recent years, spray-drying and supercritical fluid crystallization have emerged as two cost-efficient processing technologies that allow more precise control of the crystal forms and physical properties of the powders produced in a single step operation. This article presents a critical review of these latest technological developments in DPI formulation with focus on the regulation of the physical forms of inhaled drug particles.

Keywords: Physical forms, During particles, Pulmonary delivery, Spray drying, Supercritical fluids

1. Introduction

Pulmonary drug delivery has been the subject of intensive investigation by formulation scientists and respiratory medicine practitioners/specialists. In addition to producing localized effects, drugs delivered into the lungs can be absorbed across the alveolar epithelium to exert systemic actions. Among the different types of therapeutic inhalation formulations available on the market, dry powder inhaler (DPI) has become increasingly popular as a pulmonary delivery system primarily for the following reasons: (a) being in a solid form, the drug is relatively stable chemically; (b) the inhaler is environment-friendly, as it is free from chlorofluorocarbon (CFC) propellants; and (c) the delivery is breath actuated, and does not require coordination between actuation and inhalation by the patient, as does its pressurized counterparts.

Apart from particle size, particle morphology and surface properties, the crystal form of inhaled particles is probably the next crucial parameter in line for consideration in DPI formulation. It has been well documented that solid-state phenomena such as polymorphism, solvate/hydrate formation, and change of crystallinity or the level of crystal imperfections, could all exert profound influence on the physical, chemical and mechanical properties, and ultimately, on the clinical performance of solid pharmaceuticals. Consequently, a good understanding of the solid-state behaviors of pharmaceutical materials as well as

---

[†] Accepted July 24, 2006

[*] 6/F, Rm 616, Basic Medical Sciences Building
Shatin, New territories
Hong Kong SAR, China

[1] Corresponding author
TEL: (852) 26096829 FAX: (852) 26035295
E-mail: albert-chow@cuhk.edu.hk

[2] Present address
School of Health Sciences, Macao Polytechnic Institute, Macao, China

the availability of an effective means to regulate their physical forms during production are crucial for the successful formulation of inhalation dosage forms.

Drug powders used in DPI are normally prepared by batch crystallization from a suitable solvent, followed by micronization to the optimal particle size range for deep lung delivery. However, this two-step manufacturing approach often results in highly cohesive, highly charged, and crystallographically defective materials, which are difficult to process downstream. Consequently, alternative strategies for producing readily processable and dispersible powders are being actively sought. In this regard, spray-drying and supercritical fluid processing technologies appear to hold promise, primarily because of their dual abilities to generate ultra-fine powders within the respirable size range and to control the formation of particular crystal form.

Presented in this article are general background information on pulmonary drug delivery and solid-state chemistry relevant to DPI formulation together with a review on the current applications of spray-drying and supercritical fluid crystallization technologies in regulating the physical forms of ingredients used in DPI formulation.

2. Pulmonary route as an important means of drug delivery

Asthma is a pulmonary disease characterized by reversible airway obstruction, airway inflammation, and increased airway responsiveness to a variety of stimuli. Pulmonary delivery of drugs plays an indispensable role in the management of asthma. β-Adrenoceptor agonists and corticosteroids are two common classes of drugs administered via the lungs. Pulmonary drug delivery offers a number of advantages, including: (a) a small amount of drug will normally suffice for preventing or treating symptoms; (b) adverse reactions are usually much less than those produced by systemic administration; and (c) there is a rapid and predictable onset of action[1)].

Since the introduction of the first inhaled medication, *Datura ferox*, a congener of atropine, in England in 1802, the inhalation route of drug delivery has captured increasing attention in the pharmaceutical industry. Inhalation therapy is not limited to asthma, but is also of benefit to other respiratory diseases, such as chronic obstructive pulmonary disease (COPD) and bronchiectasis.

Lungs, with a large surface area, good vascularization, an immense capacity for solute exchange and an ultra-thin alveolar epithelium, have been actively explored as an effective route for systemic delivery of peptides and proteins[2)]. Of particular potential in this development is inhaled insulin, which may serve as an effective, well-tolerated, non-invasive alternative to subcutaneous regular insulin[3)]. Pulmonary route is considered an important means for both local and systemic drug delivery.

3. Dry powder inhalation formulations for pulmonary drug delivery

Typical inhalation formulations for pulmonary delivery include liquid nebulizer, metered dose inhaler (MDI) and dry powder inhaler (DPI).

3.1 Nebulizer

Nebulizer is the preferred choice of many physicians for the therapy of acute asthma in an emergency care unit or for treating patients with severe asthma at home[4)]. In jet nebulizers, the aerosol is formed by a high velocity airstream from a pressurized source directed against a thin layer of liquid solution. Ultrasonic nebulizers involve the vibration of a piezoelectric crystal aerosolizing the solution. Although nebulizer can deliver more drug to the lungs than MDI or DPI, the main drawbacks of nebulizer are lack of portability, higher costs of drug delivery as a result of the greater need for assistance from healthcare professionals, and the requirement for higher drug doses to achieve a therapeutic effect.

3.2 Metered Dose Inhaler (MDI)

MDI is the most popular device for aerosolized administration of drugs. With this method, a medication is mixed in a canister with a propellant, and the preformed mixture is expelled in precise measured amounts upon actuation of the device. Proper use of MDIs requires that patients learn how to coordinate exhalation and inhalation with actuation of the device. This can be quite difficult for the juvenile and the elderly. The use of spacer device can only solve the problem partially because the bulky size of the device can be a deterrent for patients who require use of MDIs outside their homes.

In early 1990s, attempts were actively made to reformulate MDIs as a result of the mandatory ban on the use of propellant chlorofluorocarbons (CFCs), which have been implicated in the depletion of the Earth's ozone layer. Alternative propellants, such as hydrofluoroalkane 134a (HFA-134), have been extensively investigated for their potentials to replace

CFCs since 1990s. Extensive researches are currently in progress to compare the efficacy and safety between CFCs and non-CFCs MDIs[5-6].

3.3 Dry Powder Inhaler (DPI)

Dry powder systems utilize drug alone or its blends with a suitable carrier, usually lactose, for delivery to the lungs. Drugs, carriers and devices are three important factors affecting the performance of pulmonary delivery of drugs. Unlike MDIs, delivery of medication with a DPI requires minimal patient cooperation and coordination of breathing following actuation of the device. Moreover, DPIs are small, portable devices that can be conveniently carried in a pocket or purse. Turbuhalers® and Diskhalers® are some well-known examples. There is also no need to use spacers. Furthermore, DPIs are devoid of environmentally harmful CFC propellants, as normally required in MDI formulation. Since both MDI and DPI have been shown to afford comparable efficacy in delivering the same drug and in view of the mandatory ban of CFCs use in MDIs by the United Nations, it is not surprising that DPIs have become increasingly important as a pulmonary drug delivery system over the past decade[7].

4. Solid state chemistry of dry powder inhalation formulations

Fine particles in DPIs may exist in different solid states, which include polymorphs, solvates (hydrates) and amorphous forms. Since pharmaceuticals in different solid states display widely different physical properties, understanding the solid state behaviours of drugs is of particular interest to formulation scientists, chemical engineers, materials scientists, physical chemists, industrial pharmacists, process chemists as well as regulatory affairs personnel involved at various stages of the drug development process[8]. In recent years, solid state phenomena, particularly polymorphism, have attracted considerable attention in pharmaceutical industry, where regulatory control necessitates close examination of all products under development for their solid state behaviour[9].

4.1 Polymorphism

Many solid pharmaceuticals exist as polymorphs, or crystal forms having the same chemical composition but different internal structure in the crystal lattice, i.e., different unit cell dimensions and cell packing. Steroids, sulphonamides and barbiturates are three common classes of drugs exhibiting polymorphism[8]. A casual online computer search in PubMed will easily reveal emerging polymorphs for new and existing compounds.

Polymorphs show a range of widely different physical and chemical properties, such as melting points, spectroscopic behaviour, solubility, density, hardness, crystal shapes, physical and chemical stability and dissolution profiles. Review on crystal polymorphism of drug substances in the European Pharmacopoeia has been prepared by the regulatory authority[10]. Polymorphism is of vital importance in the context of patent protection, process development and product specification in pharmaceutical industry[11]. The potential formulation problems associated with polymorphism are best exemplified by the antiviral drug, ritonavir. In the summer of 1998, Novir® (ritonavir) semi-solid capsules supplies were put on hold following the discovery of a new crystal form of ritonavir, which is much less water soluble[12]. The existence of this new polymorph was confirmed by microscopy and powder X-ray diffraction (PXRD). The sudden emergence of this drastically less soluble polymorph has created tremendous formulation hurdles for the drug company concerned. Chloramphenicol palmitate is another well-demonstrated example of polymorphism. Maximum blood levels of the two reported polymorphic forms are 3 and 22 mg/ml respectively, which represent a seven-fold difference[13]. If this problem is kept unchecked, significant dose-to-dose variations can occur. Despite such potential problems, one can still take advantage of the unique physical properties of a particular polymorph to improve drug formulation. For instances, the dry powder inhalation properties and in vitro respirable fraction of steroid KSR-592 were improved dramatically by changing its morphology from plates (α-form) to needles through polymorphic transformation to the β-form[14].

Taken pairwise, polymorphs fall into either a monotropic system or an enantiotropic system. For monotropic pairs, one polymorph is always more stable than the other. The polymorph with higher melting point has the lower Gibbs free energy at all temperatures (**Fig. 1**). Thus, change of low melter to high melter, being a non-spontaneous process, is not thermodynamically favourable. Transition point only exists above the melting points of the two polymorphs.

For enantiotropic pairs, the transition temperature exists below the melting points of both polymorphs (**Fig. 2**). At temperatures lower than transition temperature, the lower melter has lower Gibbs free

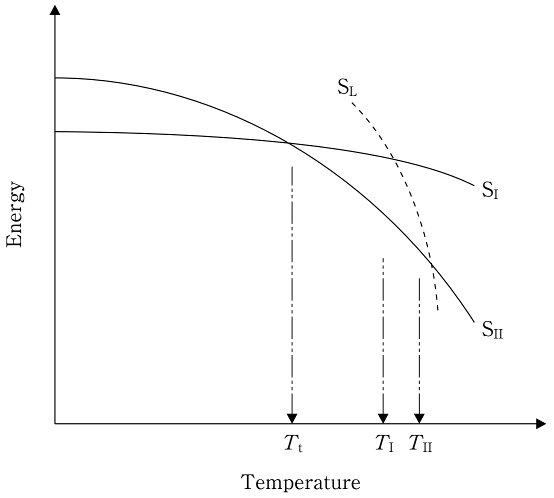

Fig. 1 Hypothetical energy diagram of an enantiotropic system (T_I and T_{II}: melting points of Forms I and II; T_t: transition temperature).

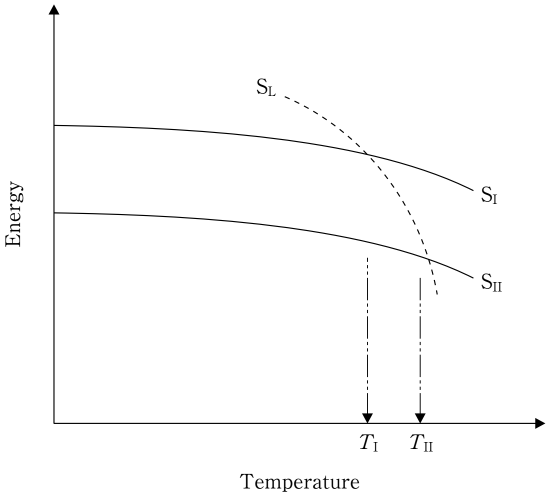

Fig. 2 Hypothetical energy diagram of a monotropic system (T_I and T_{II}: melting points of Forms I and II; T_t: transition temperature).

energy, while at temperatures higher than transition temperature, the higher melter has lower Gibbs free energy. Thus, the lower melter is the more stable form below the transition temperature while the higher melter is the more stable form above the transition temperature.

4.2 Hydrates and solvates

Solvates are crystals in which solvent molecules occupy regular positions in the crystal structure. Hydrates are a subset of solvates when the solvent molecule is water. For obvious reasons, most drug crystals that fall into the category of solvates are hydrates[8].

Physical properties of hydrates and solvates can be quite different. Solvates must be less soluble in the same solvent than their original anhydrous counterparts, otherwise there would be no thermodynamic driving force for their crystallisation[15]. For example, ampicillin anhydrate has a higher solubility and intrinsic dissolution rate than its trihydrate form[16]. A significant difference in urinary excretion rates of the drug has been demonstrated in vivo. Suspensions and capsules containing the anhydrate exhibit superior bioavailabilities to analogous formulations made from the trihydrate[16]. In the case of carbamazepine polymorphs (forms I and III) and the dihydrate, the solubilties, intrinsic dissolution rates and bioavailabilities of both anhydrous polymorphs are lower than those of the dihydrate[17].

In addition, hydrates are in dynamic equilibrium with the surrounding moisture, which can be described by the following relationships:

$$A\ (\text{solid}) + m\,\mathrm{H_2O} \overset{K_h}{\rightleftarrows} A \cdot m\,\mathrm{H_2O}\ (\text{solid}) \qquad (1.1)$$

$$K_h = \frac{a_3[A \cdot m\mathrm{H_2O}(\text{solid})]}{a_1[A(\text{solid})]\,a_2[\mathrm{H_2O}]^m} \qquad (1.2)$$

where a_1, a_2 and a_3 represent the activities of the anhydrate, water and hydrate respectively.

From the equations, it is clear that water activity and relative humidity (%RH) in a closed system are significant in influencing the hydration states of crystal forms. For example, water stoichiometry of aspartame are 0.5 below 42% and 2.5 above 58% RH[18]. Nedocromil sodium hydrate changes from monohydrate or trihydrate to heptahemihydrate as the relative humidity increases[19]. In addition, temperature will also influence the hydration status of pharmaceuticals. For instance, the kinetics of dehydration of aspartame hemihydrate to aspartame anhydrate has been studied with variable temperature powder X-ray diffractometry[20]. This may adversely affect drug potency, powder flow, content uniformity, particle morphology, dissolution rate, and possibly bioavailability[16].

4.3 Amorphous solids

Amorphous solids are devoid of crystallinity and have no long-range order. The atoms and molecules exist in a totally disordered array. Amorphous solid can be viewed as a glass characterized by a glass transition temperature (T_g), defined as the temperature below which the constituent molecules are configurationally frozen in a glassy state and lack the motion typical of those in a liquid. Above the T_g, the amorphous solid assumes a rubbery state exhibiting flow property and the molecules have substantial configurational motion.

Amorphous solids have enhanced solubility and dissolution rate in comparison to their crystalline counterparts. It has been reported that the clinical relevance of solubility enhancement associated with the amorphous form is likely to be significant, even in systems, which are only partially amorphous[21]. However, such amorphous or glassy materials are not without problems. The Gibbs free energy of amorphous solids is higher than that of their crystalline counterparts. There is always a tendency for the glassy materials to recrystallize into the stable crystalline form. In addition, due to their higher energy state, amorphous compounds have higher chemical reactivity.

Owing to technical difficulty in stabilizing the amorphous form, particularly for small organic molecules, only a limited number of amorphous pharmaceutical materials are available on the market. In the European Pharmacopoeia, more than 35 materials (both active ingredients and excipients) are described as being amorphous. There are five in the United States Pharmacopoeia and over 25 different dosage forms in the Physicians' Desk Reference that contain amorphous drug substances, including anti-infectives, anticoagulants, antiinflammatories, analgesics, hormones and preparations for both internal and external uses[22].

Most of the commercially available dry powder inhalation formulations employ stable crystalline polymorphs, such as salmeterol xinafoate[23] and fluticasone[24], and sometimes hydrates, such as pranlukast hydrate[25].

Drug products (or dosage forms) may undergo changes in technological, physicochemical or biopharmaceutical properties due to polymorphic transformation which can be induced by mechanical or heat treatment or by a change in environmental conditions, e.g., relative humidity, solvents, etc. Polymorphic transformation can also occur in a number of pharmaceutical manufacturing and quality control processes, including milling / grinding, tabletting, suspension preparation, granulation, dissolution, stability testing, spray drying, freeze-drying, and preparation of adsorbates or complexes[16]. Unforeseen changes of solid state properties can pose serious problems with regard to patent protection, process development and product specification in pharmaceutical industry[9]. Thus, a better understanding and tighter control of solid-state behavior of drugs is crucial to the development of DPI formulations.

5. Technologies for producing drug particles for dry powder inhalation formulations

Apart from solid state properties, the particle size distribution of drug powders also plays a determinant role in DPI formulations. The respirable fraction is defined by the American Conference of Governmental Industrial Hygienists (ACGIH) as the fraction of aerosolised dose in an inhalation formulation surviving the filtration and impaction mechanism of the nasopharynx. Respirable fractions of particles with different aerodynamic diameters are shown in **Fig. 3**[26].

Particles greater than about 10 μm have a respirable fraction of almost zero and deposit predominantly in the upper airways (i.e., throat and trachea) by inertial impaction. Moderate size particle can settle out from the airstream under gravitational influence. Submicron particles deposit as a result of Brownian movement mainly in the lower airways (bronchial and alveolar regions)[27]. Particles in DPI formulations should be engineered to about 5 μm or less in diameter for maximizing the deposition in the transitional and respiratory zones of the lung. Discussed below are some current powder production technologies that are potentially useful for generating drug particles within the respirable range (1-5 μm).

5.1 Micronisation

Conventionally, drug powders formulated for the inhalation route are produced by batch crystallization from a suitable solvent followed by micronization to the appropriate particle size range (1-5mm) for deep lung delivery.

It is obvious that a substantial amount of energy is used to process the substance, which may result in either a polymorphic conversion or the generation of

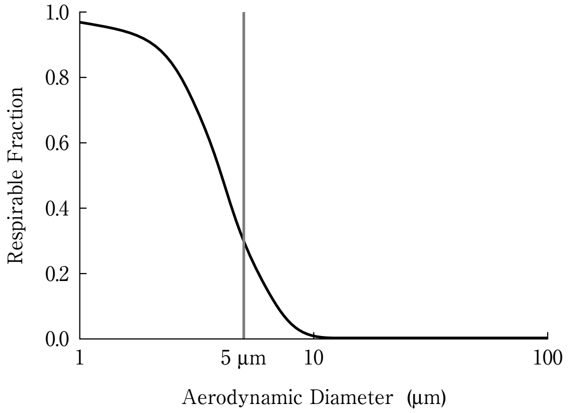

Fig. 3 Respirable fractions of particles with different aerodynamic diameters.

an amorphous substance. Polymorphic transformation of drugs has been widely reported, e.g., fostedil, chloramphenicol palmitate and phenylbutazone, to name a few(16). Generation of amorphous domains is almost unavoidable during micronization, and the extent of amorphization is highly material dependent. As regulatory authorities worldwide impose more stringent requirements in polymorph control, micronization may not be a desirable powder production method if the solid state chemistry of drug is changed significantly during the process. Therefore, a number of single-step crystallization methods, such as spray-drying and supercritical fluid crystallization, are being investigated for their applicability in powder production for DPI formulations.

5.2 Spray-Drying

Spray drying is a one-step process that converts a liquid feed into a dried particulate form via the following stages: (a) atomization of the feed solution to form a spray; (b) spray-air contact; (c) drying of the spray; and (d) separation of the dried product from the gas stream. The heating and drying of the droplets are usually performed in a chamber to which a stream of hot dry air is admitted in a co-current (i.e., in the same direction as spray) or counter-current (i.e., in the opposite direction to spray) manner. Spray drying has been used to produce solid drug particles for inhalation. The resulting materials are usually amorphous in nature(16). Since the drying is normally accomplished at elevated temperatures inside the drying chamber, chemical degradation and accompanying loss of biological activity could be a problem with thermolabile compounds, for which low-temperature drying or the alternative freeze spray drying may be considered. Examples of spray-dried pharmaceutical materials are insulin(28), salbutamol sulphate(29), sodium cromoglycate, formoterol fumarate(30) and budesonide(31).

Recently, drug particles with improved pulmonary delivery have been developed using specially formulated feed solutions for the spray-drying process. Corrugated bovine serum albumin powders thus produced display better aerosol performance than spherical particles produced under similar conditions but at higher atomizing pressure(32). It was concluded that the surface asperities of the corrugated particles could lower the area of contact between particles, and thus reduce the particle cohesiveness. Production of large hollow porous particles with improved aerosol performance by spray drying has also been reported for albuterol, estradiol and insulin(33). These spray dried samples have high respirable fractions, ranging from 49% to 92%, depending on the measurement techniques.

Spray-dried hollow porous particles based on similar concept have been commercialized as PulmoSphere™ 30). This system has been tested with cromolyn sodium, albuterol sulfate and formoterol fumarate, and they all show improved physical stability, content uniformity and aerosolization efficiency. Clinical data also demonstrated that delivery of spray-dried budesonide PulmoSphere™ powder is more efficient and reproducible than that of the micronized drug from passive DPIs(31). Interestingly, it is suitable not only for indirect systemic delivery of drug molecules via the lungs but also for more efficient and reproducible direct delivery of the drug to the lungs from passive DPIs(31, 34).

Cospraying with additives has also been explored to improve the delivery of antiasthmatic drugs to the lung, e.g., salbutamol sulphate with L-leucine in DPI formulations(35).

5.2.1 Control of physical forms by spray-drying processing

The application of spray drying to generate amorphous materials is well established(16). The technique has been employed to produce a wide range of spray-dried materials, including enzymes (e.g., trypsin, protease, lipase), antibiotics (e.g., sulphathiazole, aureomycin, streptomycin), blood serum, plasma substitute (e.g., dextran), vitamins (e.g., brewers' yeast, vitamins A/D) and pharmaceutical gums (e.g., acacia, tragacanth, sodium alginate)(36). Extensive research has been conducted to exploit the advantageous aspects of amorphous drug materials, e.g., salbutamol sulphate(37), paclitaxel(38), tolbutamide(39), clarithromycin(40), ursodeoxycholic acid(41), lactose(42) and ketoconazole(43).

Spray drying, an extremely rapid particle formation process, can be used to control the polymorphic forms of pharmaceuticals, provided that the operating parameters are carefully optimized. For instance, polymorphic forms (A, B and C) of abecarnil, a β-carboline derivative and a partial agonist of CNS benzodiazepine receptor, can be produced by spray drying using different solvents in the feed solutions(44). PXRD and DSC data showed that the resulting polymorphs are free of amorphous regions.

The pH of the feed solution has also been shown to exert a significant effect on the polymorphic forms of glycine produced by spray drying. α-Glycine was crystallized from solutions without pH adjustment (pH 6.2) while γ-glycine was the preferred polymorph formed at pH 4.0 and 8.0. The phenomenon has been attributed to the pH effect on the dimeric growth unit of α-glycine[45]. Different salt forms, such as glycine HCl and diglycine HCl, can also be generated by spray drying using low pH solutions and different inlet temperatures[45]. The formation of polymorphs during spray drying has also been demonstrated for tolbutamide (polymorph IV)[46].

5.3 Supercritical Fluid Crystallization

In recent years, supercritical fluid crystallization (SFC) technologies have gained increasing attention in the pharmaceutical industry due to their capability and versatility of producing micro-fine particles to predetermined specifications. Supercritical fluids (SFs) are those gases and liquid at temperatures and pressures above their critical points (T_C - critical temperature; P_C - critical pressure). In **Fig. 4**, the critical point is located at the upper end of the liquid / gas curves, and the phase area in excess of this point is the SF region. In this region, the SF exists as a single phase with several advantageous characteristics of both liquid and gas. SFs have density values that afford appreciable solvation power. In addition, the viscosity of solutes is lower in SFs than in liquids while the reverse is true for the diffusivity of solutes, which facilitates mass transfer. More importantly, SFs are highly compressible, particularly near the critical point, and thus their density and solvation power can be carefully controlled by slight adjustment of temperature or pressure.

Of all the gases available for use as SFs in industry, carbon dioxide is the most widely used one because of its low critical temperature (31.1℃), which makes it particularly suitable for heat sensitive materials, such as biologicals. In addition, it is non-flammable, non-toxic, inexpensive, recyclable and environment friendly.

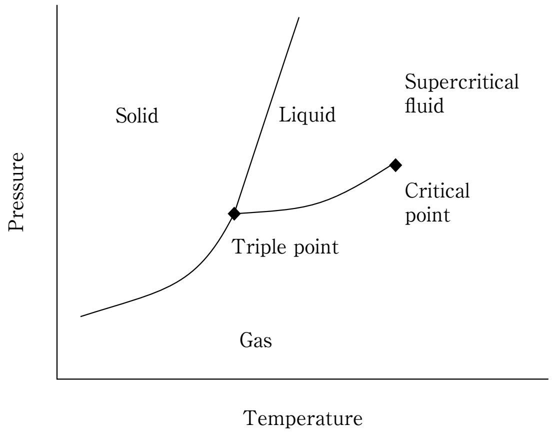

Fig. 4 Phase diagram of a pure substance.

The use of SFs to process pharmaceutical materials has proved to be a cost-efficient approach in generating high purity, micron-sized particles with defined morphology in a single-step operation[47-48]. SFs, by virtue of their attractive physical properties such as variable density and transport properties such as viscosity and diffusivity, and the relative ease by which these properties can be manipulated with temperature and pressure have created tremendous formulation opportunities for engineering drug particles with specific biological applications.

Extensive literature and patent surveys of various particle designs using supercritical fluids have been reported[49, 50]. A number of literature reviews are also available[51-52]. Broadly speaking, supercritical fluid crystallization technologies can be divided into two categories: 1. precipitation from supercritical solutions, e.g. Rapid Expansion of Supercritical Solution (RESS); 2. precipitation using SFs as non-solvents or antisolvents, e.g., Gas AntiSolvent (GAS), Supercritical AntiSolvent (SAS), Precipitation with Compressed Antisolvents (PCA), Aerosol Spray Extraction System (ASES), Solution Enhanced Dispersion by Supercritical fluids (SEDS^{TM}).

5.3.1 Precipitation from supercritical solutions

Diagrammatic representation of Rapid Expansion of Supercritical Solution (RESS) process is shown in **Fig. 5**. The solute is first dissolved in SF to form a solution, which is then allowed to undergo expansion through an orifice to create extremely high supersaturation for effecting homogeneous nucleation and subsequent particle formation in the precipitation unit. It relies on the fact that solvent strength can be reduced drastically by decreasing the SF density through the rapid expansion of the fluid. Processing equipment requires a source of SF, which passes through an extractor unit to a restricted orifice positioned in a particle collection/precipitation vessel held at a lower temperature and pressure (often ambient) than the extractor unit. Primary factors influencing the particle properties include solute solubility in SF, dimensions of orifice (expansion device), expansion time scale, operating pressure/temperature in precipitator, agglomeration during SF expansion and the subsequent phase process path. Examples of materials processed by RESS include griseofulvin[53] and salicylic acid[54].

RESS is the technology that has been rigorously investigated. Debenedetti and his coworkers have

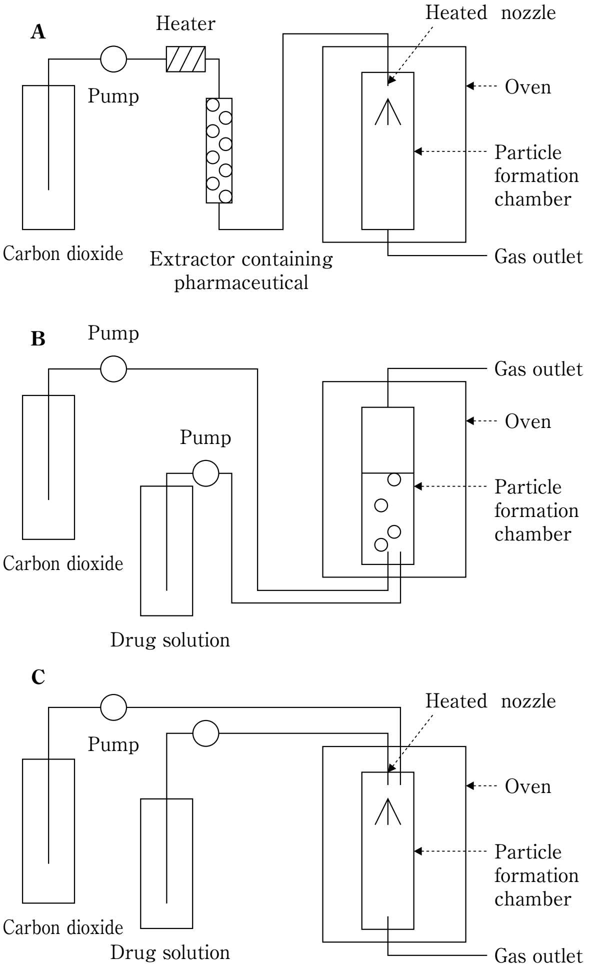

Fig. 5 Schematic diagrams of the (A) RESS, (B) GAS, and (C) PCA/SAS/ASES crystallizers.

reported several theoretical works in relating particle properties to the RESS processing conditions[55-59]. A number of mathematical simulations and models relating to particle formation in the RESS process have also been published[60, 61].

5.3.2 Precipitation using supercritical fluids as non-solvents or antisolvents

These methods utilize a similar concept to the use of antisolvents in traditional solvent-based crystallization processes. The relatively low solubilities of drug compounds in unmodified carbon dioxide are exploited in this process wherein the solute of interest (a drug, a polymer, or both) is dissolved in a conventional solvent to form a solution[51]. The preferred ternary phase behaviour is such that the solute is virtually insoluble in dense carbon dioxide while the solvent is completely miscible with dense carbon dioxide at the recrystallization temperature and pressure[51]. The solute is recrystallized from solution in one of the three ways discussed below.

In the first method, the volume of the solution containing the solute of interest is expanded several fold by mixing with dense carbon dioxide in a vessel. Since the expanded carbon dioxide solvent has a lower solvent strength than the pure solvent, the mixture becomes supersaturated, forcing the solute to precipitate or crystallize as microparticles. This process is termed Gas AntiSolvent (GAS) recrystallization[62]. Schematic diagram of the GAS process is shown in **Fig. 5.** GAS was originally applied to nitroguanidine, an explosive, for which conventional comminution to reduce particle size is considered not feasible[62]. The GAS process has been applied to a number of pharmaceutical materials, including hyaluronic acid ethyl ester / protein[63], sodium cromoglycate[64] and lobenzarit[65].

The second method involves spraying the solution through a nozzle as fine droplets into compressed carbon dioxide. A schematic diagram illustrating the technique is shown in **Fig. 5**. This process is commonly named 'Precipitation with Compressed Antisolvent' (PCA) technique and employs either organic solvent or a supercritical fluid as the antisolvent[66]. Examples of PCA processed materials are indomethacin[67], methylprednisolone acetate and hydrocortisone acetate[68]. When a supercritical fluid is used as antisolvent, the spray process is termed 'Supercritical AntiSolvent' (SAS) process or 'Aerosol Spray Extraction System' (ASES)[51]. It has been postulated that microparticles formation results from gas phase nucleation and growth within the expanding plume, rather than nucleation within discrete liquid droplets[69]. Examples of SAS-processed drug materials are salbutamol sulphate[70] and griseofulvin[71] and materials prepared by ASES process include lysozyme[72], fluticasone[73] and polylactide/hyoscine butylbromide[74].

The third method, known as 'Solution Enhanced Dispersion by Supercritical Fluids' (SEDS^{TM}), utilizes a coaxial nozzle design with a mixing chamber. The arrangement provides a means whereby the drug in organic solvent solution interacts and mixes with the SF antisolvent in the mixing chamber of the nozzle prior to dispersion via a restricted orifice into a particle-formation vessel[75]. High mass transfer rates are achieved with a high ratio of SF to solvent, and high velocity of the SF facilitates break up of solution feed[75].

In a single step operation, the SEDS^{TM} technique has been demonstrated to possess the ability to produce micron-sized particles which are solvent-free, crystalline and within a narrow size range, indicating that the crystal form can be controlled simply by varying the processing parameters. A wide range of pharmaceutical materials have been prepared as micron and submicron particles using the SEDS™ process, such as lactose[76)], nicotinic acid[77)] and paracetamol[78)].

5.3.3 Control of physical forms by supercritical fluid crystallization

The potential applications of SFC technologies in the controlled production of particular physical forms of pharmaceutical materials have attracted considerable commercial and academic interests in recent years. Although existing publications in this field are relatively few and have limited scope, they can serve as a useful lead and guide to more elaborate and extensive studies in the future.

(1) Polymorphs

Fluticasone propionate exists in two polymorphic forms (I and II). Conventional crystallization and standard spray drying techniques readily yield form I. Form II, obtainable only by SFC (e.g. SEDS™ technique), has completely different PXRD pattern from that of form I [24, 79)]. By fine-tuning the operating variables, different proportions of forms I and II can be produced in a controlled manner. In addition, the supercritically-processed form II of fluticasone propionate has lower dynamic bulk density, higher fluidisability and better flow properties than the conventionally prepared form I sample, both before and after micronisation.

Three crystal forms (two polymorphs and one hydrate) of an oxazolidone antimicrobial, RWJ-337813, could be prepared by means of the SEDS™ technique[80)]. Forms A and B are anhydrous and are monotropic to each other, with A being the stable form at ambient conditions. Form C is a hemi-hydrate. All the three crystal forms of RWJ-337813 exhibit high physical purity and high chemical integrity.

Chlorpropamide polymorphs can also be produced by the RESS process utilizing supercritical carbon dioxide ($scCO_2$) as the recrystallizing solvent[81)]. Chlorpropamide is available commercially as polymorph A (mp 129.5℃), and its metastable polymorph C (mp 122.5℃) could be prepared by recrystallization from $scCO_2$.

(2) Hydrates

Lactose monohydrate, a carrier excipient commonly used in dry powder inhalation formulation, has been prepared by SFC. When methanol or ethanol was employed as a cosolvent, processing of lactose by the SEDS™ technique afforded a mixture of the two anomeric forms α and β of lactose[76)]. This may be explained by the existence of an anomeric equilibrium between lactose monohydrate and anhydrous lactose resulting from partial conversion of the lactose monohydrate in solution.

(3) Amorphous forms

SAS processing of tetracycline resulted in an amorphous material[82)]. The observation has been attributed to an extremely rapid precipitation process, which is typical of the SAS technique. Amorphous maltose and trehalose could also be prepared by processing maltose monohydrate and α,α-trehalose dihydrate using the SEDS™ technique[83)]. However, using similar technique and operating conditions, lactose and sucrose were obtained as crystalline materials. This suggests that the tendency to form amorphous materials is highly material dependent.

5.3.4 Influence of operating variables in supercritical fluid crystallization on crystal forms produced

While fundamental thermodynamic and kinetic principles constitute the basis for the efficient design and operation of any crystallization process, very few studies have specifically considered how these principles can be utilized to control or optimize material processing in supercritical fluids at elevated pressures. Most of the reported SFC studies focus on the influence of operating parameters on material properties. Though not explicitly stated, a change in any of these parameters represents a change in the crystallization conditions in a thermodynamic and/or kinetic sense. For instance, pressure and temperature are representative factors in thermodynamics while flow rate of drug solution and supercritical fluid carries an important element in kinetics. It must be noted that most of the reported SFC works are not the result of well-controlled factorial design, and they often involve concurrent changes of more than one operating variable for individual crystallization experiment. Consequently, it would not always be possible to assess and explain the contribution of each operating parameter in relation to the others based on the available literature data. Nevertheless, gross generalization can still be made with regard to the material formation under defined operating SFC conditions.

Table 1 summarizes the operating parameters (temperature, pressure, solvent choice, flow rates of drug solution and supercritical fluid) used for processing specific crystal forms of various drug materials and their possible control mechanisms (i.e., thermodynamics or kinetics). The results clearly reflect

Table 1 Summary of the effects of vessel temperature, vessel pressure and solvent choice on crystal form produced

Compounds	Operating Conditions	Operating Variables	Physical Forms	Possible control mechanism
Influence of temperature				
Flunisolide (84)	Flow rate of scCO$_2$: 9-25 ml/min Flow rate of drug solution: 0.3 ml/min Pressure: 100 bar	Drug solvent: Acetone		
		Temperature: 80℃	I + III	T & K
		Temperature: 60℃	III	T & K
		Temperature: 40℃	III	T & K
		Drug solvent: Methanol		
		Temperature: 80℃	IV	T & K
		Temperature: 60℃	III + IV	T & K
		Temperature: 40℃	No products	T & K
Salmeterol Xinafoate (85)	Pressure: 200 bar Drug solution: 4.5% SX in methanol Drug solution flow rate: 2.0 ml/min Flow rate of scCO$_2$: 2000 NL/hr	Operating temperatures:		
		40 – 65℃	I	T
		70 – 90℃	II	T
Influence of pressure				
Salmeterol Xinafoate (85)	Pressure: 70 bar Drug solution: 4.5% SX in methanol Drug solution flow rate: 2.0 ml/min Flow rate of scCO$_2$: 2000 NL/hr	Operating temperatures:		
		50 – 135℃	I	T
		135 – 250℃	II	T
Influence of solvent choice				
Fomoterol fumarate (86)	Flow rate of scCO$_2$: 18.0 ml/min Temperature: 40℃ Pressure: 150 bar Nozzle opening: 0.2mm	2.0% (w/v) of drug in 99:1 methanol-water mixtures pumped at 0.3ml/min	Totally amorphous formoterol fumarate	K
		2.0% (w/v) of drug in methanol pumped at 0.3ml/min; Totally water-saturated CO$_2$ flushed through the particle-forming vessel after the end of the run, followed by a rinsing period where dry CO$_2$ equivalent to two volumes of the vessel	Crystalline formoterol fumarate dihydrate	K
Flunisolide (84)	Flow rate of CO$_2$: 9-25 ml/min Flow rate of drug solution: 0.3 ml/min Pressure: 100 bar	Drug solvent: Acetone	I + III (80℃) III (60 and 40℃)	T & K T & K
		Drug solvent: Methanol	IV (80℃) III + IV (60℃)	T & K T & K
		Unprocessed	II	
Stavudine (87)	Flow rate of scCO$_2$: 9 ml/min Flow rate of drug solution: 0.2 ml/min Temperature: 35℃	Pressure: 120 bar Drug solvent: 1% (w/v) stavudine in		
		10% water in isopropanolol	III	K
		5% water in isopropanolol	I & II	K
		Pressure: 90 bar Drug solvent: 0.5% (w/v) stavudine in		
		7.5% water in isopropanolol	I & II	K
		5.0% water in isopropanolol	I	K
		2.5% water in isopropanolol	II	K
Carbamazepine (88)	Flow rate of drug solution: 0.5ml/min	Drug solvent: Dichloromethane		
		Temperature: 40℃	α	T & K
		Temperature: 60℃	α and γ	T & K
		Drug solvent: Methanol		
		Temperature: 40℃; Pressure: 50 bar	α	T & K
		Temperature: 60℃; Pressure: 50 bar	β	T & K
		Temperature: 60-80℃; Pressure: 150 bar	γ	T & K
Fluticasone propionate (79)	Drug concentration: 0.5% (w/v) Pressure: 100 bar Temperature: 75℃ Flow ratio of drug solution and CO$_2$: 0.043	Solvent utilized in drug solution:		
		Acetonitrile	I	K
		Acetone	I & II	K
		Ethyl acetate	I&II	K
		Methanol	II	K
Terbutaline sulphate (89)	CO$_2$ flow rate: 18.0 ml/min	Solvent: Pure ethanol Temperature: 50℃; Pressure: 150 bar Solution flow rate: 2.4 ml/min	B	T & K
		Solvent: Methanol / Water Temperature: 45℃; Pressure: 250 bar Solution flow rate: 0.2 ml/min	Amorphous	T & K
		Solvent: Pure water Temperature: 40℃; Pressure: 250 bar Solution flow rate: 0.2 ml/min	Hydrate	T & K
		Solvent: Pure methanol Temperature: 40℃; Pressure: 250 bar Solution flow rate: 1.2 ml/min	A	T & K
Influence of flow rate of drug solution and supercritical fluid				
Sulfathiazole (90)	Pressure: 200 bar Temperatures for crystallization: 0 – 120℃ Flow rate of CO$_2$: 10ml/min Flow rate of drug solution: 0.2 – 25.6 ml/min	Drug solvent: Acetone Drug solution conc.: 1% w/w	I + Amorphous, I + IV and IV produced at different temperatures and flow ratios	K
		Drug solvent: Methanol Drug solution conc.: 1.5% w/w	I, I + III, III, III + IV and IV resulted at different temperatures and flow ratios	K

Remarks: T = Thermodynamically controlled mechanism; K = Kinetically controlled mechanism the utility of SFC in exerting precise control over the physical forms of the materials produced.

6. Conclusion

The ability of spray drying and SFC to regulate the crystal form and associated material properties has been clearly demonstrated with a number of pharmaceutical materials. In most cases, the relative composition of the physical forms produced can be precisely controlled by varying the operating parameters. While both particle production technologies appear to be comparable in terms of their capability of generating ultrafine, free flowing, non-cohesive, dispersible particles with high respirable fraction in a single step operation, spray drying processing tends to afford amorphous materials, and is apparently less effective for controlling the crystallinity of the materials produced. Additionally, SFC offers the unique flexibility of manipulating an extra operating variable, i.e. pressure/density of the supercritical fluids, which allows a wider range of crystallization conditions to be tested for the production of specific materials or crystal forms.

Despite the aforementioned advantages of SFC techniques over spray drying processing, there has not been any SFC-based inhalation dosage forms marketed to date while a few spray-dried DPI products are already available commercially. The lack of breakthrough with DPI formulation development utilizing SFC appears to stem from an insufficient understanding of the SFC process and the material-dependent limitations of individual SFC techniques. However, as more is known about SFC and the associated techniques are further refined, and as more pharmaceutical materials are being tested for formulation potential with these technologies, it will not be long before certain SFC-based products finally make their way through the development hurdle to the market.

Acknowledgements

Financial support from the Research Grant Council of Hong Kong (Earmarked Grant CUHK4244/98M) is gratefully acknowledged.

References

1) Hickey, A.J.: "Inhalation Aerosols - Physical and Biological Basis for Therapy", *Marcel Dekker Inc*, New York (1996).
2) Agu, R.U., Ugwoke, M.I., Armand, M., Kinget, R. and Verbeke, N.: "The lung as a route for systemic delivery of therapeutic proteins and peptides", *Respir. Res.*, **2**: 198-209 (2001).
3) Bindra, S., Rosenstock, J. and Cefalu, W.T.: "Inhaled insulin: a novel route for insulin delivery", *Expert. Opin. Inv. Drug*, **11**: 687-691 (2002).
4) Taburet, A.M. and Schmit, B.: "Pharmacokinetic optimization of asthma treatment", *Clin. Pharmacokinet.*, **26**: 396-418 (1994).
5) Langley, S.J., Sykes, A.P., Batty, E.P., Masterson, C.M. and Woodcock, A. : "A comparison of the efficacy and tolerability of single doses of HFA 134a albuterol and CFC albuterol in mild-to-moderate asthmatic patients", *Ann. Allerg. Asthma Im.*, **88**: 488-493 (2002).
6) Taylor, J., Kotch, A., Rice, K., Ghafouri, M., Kurland, C.L., Fagan, N.A. and Witek, T.J.: "Ipratropium bromide hydrofluoroalkane inhalation aerosol is safe and effective in patients with COPD", *Chest*, **120**: 1253-1261 (2002).
7) Virchow, J.C., Kroegel, C. and Matthys, H.: "Antiasthma drug delivery: what is on the horizon", *Clin. Pharmacokinet.*, **27**: 85-93 (1994).
8) Byrn, S.R., Pfeiffer, R.R. and Stowell, J.G.: "Solid State Chemistry of Drugs (2nd edition)", *SSCI Inc, West Lafayette, Indiana* (1999).
9) Threlfall, T.: "Crystallization of polymorphs: Thermodynamic insight into the role of solvent", *Org. Proc. Res. & Dev.*, **4**: 384-396 (2000).
10) Borka, L.: "Review on crystal polymorphism of substances in the European Pharmacopoeia", *Pharm. Acta. Helv.*, **66**: 16-22 (1991).
11) Byrn, S. R., Pfeiffer, R. R., Stephenson, G., Grant, D. J. W. and Gleason, W. B.: "Solid state pharmaceutical chemistry", *Chem. Mater.*, **6**: 1148-1158 (1996).
12) Bauer, J., Spanton, S., Henry, R., Quick, J., Dziki, W., Porter, W. and Morris, J.: "Ritonavir: an extraordinary example of conformational polymorphism", *Pharm. Res.*, **18**: 859-866 (2001).
13) Haleblian, J. and McCrone, W.: "Pharmaceutical applications of polymorphism", *J. Pharm. Sci.*, **58**: 911-929 (1969).
14) Ikegami, K, Kawashima, Y., Takeuchi, H., Yamamoto, H., Isshiki, N., Momose, D. and Ouchi, K.: "Improved inhalation behavior of steroid KSR-592 *in vitro* with Jethaler by polymorphic transformation to needle-like crystals (β-form)", *Pharm. Res.*, **19**: 1439-1445 (2002).
15) Grant, D.J.W. and Higuchi, T.: "Solubility Behavior of Organic Compounds", *John Wiley & Sons, New York* (1990).
16) Brittain, H.G. and Fiese, E.F.: "Effects of pharmaceutical processing on drug polymorphs and solvates", In Brittain, H.G. Polymorphism in Pharmaceutical Solids. Marcel Dekker Inc, New York, USA (1999).
17) Kobayashi, Y., Ito, S., Itai, S. and Yamamoto, K.: "Physicochemical properties and bioavailability of carbamazepine polymorphs and dihydrate", *Int. J. Pharm.*, **193**: 137-146 (2000).

18) Leung, S.S., Padden, B.E., Munson, E.J. and Grant, D.J.W.: "Hydration and dehydration behavior of aspartame hemihydrate", *J. Pharm. Sci.*, **87**: 508-513 (1997).

19) Khankari, R., Chen, L. and Grant, D.J.W.: "Physical characterization of nedocromil sodium hydrates", *J. Pharm. Sci.,* **87**: 1052-1061 (1998).

20) Rastogi, S., Zakrzewski, M. and Suryanarayanan, R.: "Investigation of solid-state reactions using variable temperature X-ray powder diffractometry. I. Aspartame hemihydrate", *Pharm. Res.,* **18**: 267-273 (2001).

21) Hanock, B.C. and Parks, M.: "What is the true solubility advantage for amorphous pharmaceuticals", *Pharm. Res.*, **17**: 397-404 (2000).

22) Hancock, B.C.: "Disordered drug delivery: destiny, dynamics and the Deborah number", The 138th British Pharmaceutical Conference, *Glasgow, 23th-26th September* (2001).

23) Beach, S., Latham, D., Sidgwick, C., Hanna, M. and York, P.: "Control of the physical form of salmeterol xinafoate", *Org. Proc. Res. & Dev.*, **3**: 370-376 (1999).

24) Kariuki, B.M, Psallidas, K., Harris, K.D.M., Johnston, R.L., Lancaster R.W., Staniforth S.E. and Cooper, S.M.: "Structure determination of a steroid directly from powder diffraction data", *Chem. Commun.*, **17**: 1677-1678 (1999).

25) Kawashima, Y., Serigano, T., Hino, T., Yamamoto, H. and Takeuchi, H.: "Effect of surface morphology of carrier lactose on dry powder inhalation property of pranlukast hydrate", *Int. J. Pharm.,* **172**: 179-188 (1998).

26) ACGIH.: "Threshold limit values and biological exposure indices", *ACGIH, Cincinnati*, USA (1997).

27) Martin, A.: Physical Pharmacy: Physical Chemical Principles in the Pharmaceutical Sciences (4th edition), *Lea & Febiger, Philadelphia*, USA (1993).

28) Stahl, K., Claesson, M., Lilliehorn, P., Linden, H. and Backstrom, K.: "The effects of process varib ales on the degradation and physical properties of spray dried insulin intended for inhalation", *Int. J. Pharm.*, **233**: 227-237 (2002).

29) Chawla, A., Taylor, K.M.G., Newton, J.M. and Johnson, M.C.R.: "Production of spray-dried salbutamol sulphate for use in dry powder aerosol formulation", *Int. J. Pharm.*, **108**: 233-240 (1994).

30) Dellamary, L.A., tarara, T.E., Smith, D.J., Woelk, C.H., Adractas, A., Costello, M.L., Gill, H. and Weers, J.G.: "Hollow porous particles in metered dose inhalers", *Pharm. Res.,* **17**: 168-174 (2000).

31) Duddu, S.P., Sisk, S.A., Walter, Y.H., Tarara, T.E., Trimble, K.R., Clark, A.R., Eldon, M.A., Elton, R.C., Pickford, M., Hirst, P.H., Newman, S.P. and Weers, J.G.: "Improved lung delivery from a passive dry powder inhaler using an engineered Pulmosphere® powder", *Pharm. Res.*, **19**: 689-695 (2002).

32) Chew, N.Y.K. and Chan, H.K.: "Use of solid corrugated particles to enhance powder aerosol performance", *Pharm. Res.*, **18**: 1570-1577 (2001).

33) Vanbever, R., Mintzes, J. D., Wang, J., Nice, J., Chen, D., Batycky, R., Langer, R. and Edwards, D. A.: "Formulation and physical characterization of large porous particles for inhalation", *Pharm. Res.*, **16**: 1735-1742 (1999).

34) Hirst, P.H, Pitcairn, G.R., Weers, J.G., Tarara, T.E., Clark, A.R., Dellamary, L.A., Hall, G., Shorr, J. and Newman, S.P.: "*In vivo* deposition of hollow porous particles from a pressurized metered dose inhaler", *Pharm. Res.*, **19**: 258-264 (2002).

35) Lucas, P, Anderson, K., Potter, U.J. and Staniforth, J.N.: "Enhancement of small particle size dry powder aerosol formulations using an ultra low density additive", *Pharm. Res.*, **16**: 1643-1647 (1999).

36) Masters, L.: Spray Drying Handbook (5th edition), *Longman, New York*, USA (1991).

37) Columbano, A., Buckton, G. and Wikeley, P. : "A study of the crystallisation of amorphous salbutamol sulphate using water vapour sorption and near infrared spectroscopy", *Int. J. Pharm.*, **237**: 171-178 (2002).

38) Mu, L. and Feng, S.S.: "Fabrication, characterization and in vitro release of paclitaxel (Taxol®) loaded poly (lactic-co-glycolic acid) microspheres prepared by spray drying technique with lipid/cholesterol emulsifiers", *J. Control. Release,* **76**: 239-254 (2001).

39) Kimura, K., Hirayama, F., Arima, H. and Uekama, K.: "Effects of aging on crystallization, dissolution and absorption characteristics of amorphous tolbutamide-2-hydroxypropyl-beta-cyclodextrin complex", *Chem. Pharm. Bull.*, **48**: 646-650 (2000).

40) Yonemochi, E., Kitahara, S., Maeda, S., Yamamura, S., Oguchi, T. and Yamamoto, K.: "Physicochemical properties of amorphous clarithromycin obtained by grinding and spray drying", *Eur. J. Pharm. Sci.*, **7**: 331-338 (1999).

41) Ueno, Y., Yonemochi, E., Tozuka, Y., Yamamura, S., Oguchi, T. and Yamamoto, K.: "Characterization of amorphous ursodeoxycholic acid prepared by spray-drying", *J. Pharm. Pharmacol.*, **50**: 1213-1219 (1998).

42) Chidavaenzi, O.C., Buckton, G., Koosha, F. and Pathak, R.: "The use of thermal techniques to assess the impact of feed concentration on the amorphous content and polymorphic forms present in spray dried lactose", *Int. J. Pharm.*, **159**: 67-74 (1997).

43) EsclusaDiaz, M.T., Guimaraens Mendez, M., Perez-Marcos, M.B., VilaJato, J.L. and TorresLabandeira, J.J.: "Characterization and in vitro dissolution behaviour of ketoconazole/beta- and 2-hydroxypropyl-beta-cyclodextrin inclusion compounds", *Int. J. Pharm.*, **143**: 203-210 (1996).

44) Beckmann, W. and Otto, W.H.: "Occurrence, stability, kinetics of crystallization and polymorphic transition of the A, B and C modification of abecarnil - Influence of supersaturation, temperature, solvents and impurities", *Trans. IChemE.* **74 (A)**: 750-758 (1996).

45) Yu, L. and Ng, K.: "Glycine crystallization during spray drying: the pH effect on salt and polymorphic forms", *J. Pharm. Sci.*, **91**: 2367-2375 (2002).

46) Kimura, K., Hirayama F. and Uekama, K.: "Charac-

terization of tolbutamide polymorphs (Burger's form II and IV) and polymorphic transition behaviour", *J. Pharm. Sci.,* **88**: 385-391 (1999).

47) Palakodaty, S and York, P.: "Phase behavioral effects on particle formation processes using supercritical fluids", *Pharm. Res.*, **16**: 976-985 (1999).

48) Shekunov, B.Y. and York, P.: "Crystallization processes in pharmaceutical technology and drug delivery design", *J. Crystal Growth*, **211**: 122-136 (2000).

49) Jung, J. and Perrut, M.: "Particle design using supercritical fluids: Literature and patent survey", *J. Supercrit. Fluid*, **20**: 179-219 (2001).

50) Tan, H.S., Borsadia, S.: "Particle formation using supercritical fluids: pharmaceutical applications", *Expert. Opin. Ther. Pat.*, **11**: 861-872 (2001).

51) Subramaniam, B., Rajewski, R.A. and Snavely, K.: "Pharmaceutical processing with supercritical carbon dioxide", *J. Pharm. Sci.*, **86**: 885-890 (1997).

52) Kiran, E., Debenedetti, P.G. and Peters, C.J.: Supercritical Fluids - Fundamentals and Applications, Kluwer Academic Publisher, Dordrecht, The Netherlands (2000).

53) Reverchon, E., Porta, G.D. and Taddeo, T.: "Solubility and micronization of griseofulvin in supercritical CHF_3", *Ind. Eng. Chem. Res.,* **34**: 4087-4091 (1995).

54) Reverchon, E. and Donsi, G.: "Salicylic acid solubilization in supercritical CO_2 and its micronization by RESS", *J. Supercrit. Fluids*, **6**: 241-248 (1993).

55) Mohamed, R.S., Debenedetti, P.G. and Prud'homme, R.K.: "Effects of process conditions on crystals obtained from supercritical mixtures", *AIChE. J.*, **35**: 325-328 (1989).

56) Debenedetti, P.G.: "Homogeneous nucleation in supercritical fluids", *AIChE. J.,* 36: 1289-1298 (1990).

57) Tom, J.W. and Debenedetti, P.G.: "Particle formation with supercritical fluids - A review", *J. Aerosol Sci.,* **22**: 555-584 (1991).

58) Debenedetti, P.G., Tom, J.W., Kwuak, X. and Yeo, S.D. : "Rapid expansion of superciritcal solutions (RESS): Fundamentals and applications", *Fluid Phase Equilibria*, **82**: 311-321 (1993).

59) Kwauk, X. and Debenedetti, P.G.: "The mathematical modeling of aerosol formation by rapid expansion of supercritical solutions in a converging nozzle", *J. Aerosol Sci.*, **24**: 445-469 (1993).

60) Shaub, G.R., Brennecke, J.F. and McCready, M.J.: "Radial model for particle formation from the rapid expansion of supercritical solutions", *J. Supercrit. Fluids*, **8**: 318-328 (1995).

61) Helfgen, B., Hils, P., Holzknecht, C., Turk, M. and Schaber, K.: "Simulation of particle formation during the rapid expansion of supercritical solutions", *J. Aerosol Sci.*, **32**: 295-319 (2001).

62) Gallagher, P.M., Coffey, M.P., Krukonis, V.J. and Klasutis, N.: "Gas antisolvent recrystllization: New process to recrystallize compounds insoluble in supercritical fluids. In: Supercritical Fluid Science and Technology", *ACS Symposium Series* **406**; K. P. Johnston and J M. L. Penninger., Eds.; American Chemical Society: Washington, D. C., 334-354 (1989).

63) Bertucco, A., Pallado, P. and Benedetti, L.: "Formation of biocompatible polymer microspheres for controlled drug delivery by supercritical antisolvent technique". In: *High Pressure Chemical Engineering, Process Technology Proceedings,* **12**, P. R. von Rohr and C. Trepp., Eds.; Elsevier, New York, 217-222 (1996).

64) Jaarmo, S., Rantakyla, M. and Aaltonen, O.: "Particle tailoring with supercritical fluid production of amorphous pharmaceutical particles", Proceedings of the 4th International Symposium on Supercritical Fluids, Sendai, Japan, 263-266 (1997).

65) Amaro-Gonzalez, D., Mabe, G., Zabaloy, M. and Brignole, E.A.: "Gas anti-solvent crystallization of organic salts from aqueous solutions", *J. Supercrit. Fluids*, **17**: 249-258 (2000).

66) Dixon, D.J., Johnston, K.P. and Bodmeier, R.A.: "Polymeric material formed by precipitation with a compressed fluid antisolvent", *AIChE. J.*, **39**: 127-139 (1993).

67 Bodmeier, R., Wang, H., Dixon, D.J., Mawson, S. and Johnston, K.P.: "Polymeric microspheres prepared by spraying into compressed carbon dioxide", *Pharm. Res.*, **12**: 1211-1217 (1995).

68) Schmitt, W.J., Salada, M.C., Shook, G.G. and Speaker, S.M.: "Finely divided powders by carrier solution injection into a near or supercritical fluid", *AIChE. J.,* **41**: 2746-2486 (1995).

69) Lengsfeld, C.S., Delplanque, J.P., Barocas, V.H. and Randolph, T.W.: "Mechanism governing microparticle morphology during precipitation by a compressed antisolvent: atomization vs nucleation and growth", *J. Phys. Chem. B*, **104**: 2725-2735 (2000).

70) Reverchon, E., Porta, G.D. and Pallado, P.: "Supercritical antisolvent precipitation of salbutamol microparticles", *Powder Technology*, **114**: 17-22 (2001).

71) Chattopadhyay, P. and Gupta, R.B.: "Production of griseofulvin nanoparticles using supercritical CO_2 antisolvent with enhanced mass transfer", *Int. J. Pharm.*, **228**: 19-31 (2001).

72) Bustami, R.T., Chan, H.K., Dehghani, F. and Foster, N.R..: "Generation of micro-particles of proteins for aerosol delivery using high pressure modified carbon dioxide", *Pharm. Res.*, **17**: 1360-1366 (2000).

73) Steckel, H. and Muller, B.W.: "Metered dose inhaler formulation of fluticasone-17-propionate micronized with supercritical fluid carbon dioxide using alternative propellant HFA-227", *Int. J. Pharm.*, **173**: 25-33 (1998).

74) Bleich, J., Kleinebudde, P. and Muller, B.W.: "Influence of gas density and pressure on microparticles produced with the ASES process", *Int. J. Pharm.,* **106**: 77-84 (1994).

75) York, P.: "Strategies for particle design using supercritical fluid technologies", Pharmaceutical Science and Technology Today, **2**: 430-440 (1999).

76) Palakodaty, S., York, P. and Pritchard, J.: "Supercritical

fluid processing of materials from aqueous solutions: The application of SEDS to lactose as a model substance”, *Pharm. Res.*, **15**: 1835-1843 (1998).

77) Rehman, M., Shekunov, B.Y., York, P. and Colthorpe, P.: “Solubility and precipitation of nicotinic acid in supercritical carbon dioxide”, *J. Pharm. Sci.*, **90**: 1570-1582 (2001).

78) Shekunov, B.Y., Hanna, M. and York, P.: “Crystallization process in turbulent supercritical fluid”, *J. Cryst. Growth*, **198/199**: 1345-1351 (1999).

79) Cooper, S.M.: “Orthorhombic crystalline form of fluticasone propionate and pharmaceutical composition thereof”, *United State Patent* **6**, 406, 718 (2002).

80) Gilbert, D. J., Palakodaty, S., York, P., Schultz, T. W. and Shah, D.: “Isolation of the polymorphic forms of RWJ-337813 using the solution enhanced dispersion by the supercritical fluids (SEDS) technique”, *AAPSPharmSci.,* **3 (3)** (2001).

81) Vemavarapu, C., Mollan, M. J., Ghebre-Sellassie, I. and Needham, T. E.: “Crystal engineering of chlorpropamide by recrystallization from supercritical solutions”, *AAPSPharmSci.*, **3 (3)** (2001).

82) Reverchon, E., Porta, G.D. and Falivene, M.G.: “Process parameters controlling the supercritical antisolvent micronization of some antibiotics”, Proceedings of the 6th meeting on supercritical fluids, Supercritical fluids chemistry and materials, held on 10-13 April, Nottingham, United Kingdom (1999).

83) Hanna, M. and York, P.: “Method and apparatus for the formation of particles”, International Patent Publication Number WO 96/00610 (1996).

84) Velaga, S.P., Berger, R. and Carlfors, J.: “Supercritical fluids crystallization of budesonide and flunisolide”, *Pharm. Res.,* **19**: 1564-1571 (2002).

85) Tong, H.H.Y.: “Comparative studies on the physical and surface properties of salmeterol xinafoate prepared by spray-drying and supercritical fluid processing”, Ph.D. thesis, Chinese University of Hong Kong (2003).

86) Bisrat, M., Moshashaee, S., Nyqvist, H.K. and Demirbuker, M.: “Crystallization using supercritical or subcritical fluids”, United States Patent **6**, 461, 642 (2002).

87) Bristow, S., Cocks, P.M., Harland, R. and Gandhi, R.B.: “Stavudine polymorphic form I process”, International Patent Publication Number WO 02/20538 A2 (2002).

88) Edwards, A.D., Shekunov, B.Y., Kordikowski, A., Forbes, R. and York, P.: “Crystallization of pure anhydrous polymorphs of carbamazepine by solution enhanced dispersion with supercritical fluids (SEDS^{TM})”, *J. Pharm. Sci.,* **90**: 1115-1124 (2001).

89) Rehman, M.U.: “The design and characterisation of particles of inhalation compounds prepared using supercritical fluid crystallisation”, Ph.D. thesis, University of Bradford (2002).

90) Kordikowski, A., Shekunov, T. and York, P.: “Polymorph control of sulfathiazole in supercritical CO_2”, *Pharm. Res.,* **18**: 682-688 (2001).

Author’s short biography

Henry H. Y. Tong

Henry H. Y. Tong is currently Associate Professor at the School of Health Sciences, Macao Polytechnic Institute, Macao, China. Dr. Tong received his BPharm (Hon) and PhD (Physical Pharmaceutics) degrees from the Chinese University of Hong Kong, Hong Kong, China. He is also a registered pharmacist in Hong Kong.

Albert H.L. Chow

Albert H. L. Chow is currently Professor and Associate Director for Research at the School of Pharmacy, the Chinese University of Hong Kong, Hong Kong, China. Dr. Chow received his BPharm (Hon) degree from the University of Bradford in the United Kingdom and both his MSc (Pharmaceutical Chemistry) and PhD (Physical Pharmaceutics) degrees from the University of Toronto in Canada. Prior to joining the Chinese University of Hong Kong, he had served successively as Assistant Professor at the University of British Columbia and as Senior Research Pharmacist at Glaxo Canada.

Aggregate Structures and Solid-Liquid Separation Processes[†]

S. Biggs
Institute of Particle Science and Engineering,
School of Process, Environmental and
Materials Engineering
The University of Leeds[*]

Abstract

Solid-liquid separation processes for dispersions of fine particles continue to present significant challenges in many areas. As an example, in filtration it is usually possible to achieve either fast filtration or a dry cake, but rarely both. To achieve both a compact dry cake and rapid filtration will rely upon an increased ability to control the particle network structure of the filter cake throughout the whole process, with a probable requirement being a controlled structural change from the beginning to the end of the filtration. An obvious pre-requisite is a detailed knowledge of how to control the structure of sediment beds during flocculation processes. Recent advances in measurement technology have provided unique insights of the relationship between the mechanism (bridging, depletion, charge neutralisation) and conditions of flocculation and resultant aggregate structures. As a consequence, the link between aggregate structures and sediment bed properties is also being investigated with renewed interest. Clearly, the link between flocculation, aggregate structure and sediment bed is vital in the understanding and control of solid-liquid separation processes. This paper will present a review of recent research linking aggregate formation and characterisation of solid-liquid dispersions to subsequent physical properties of the sediments and filter cakes that they produce.

Keywords: Colloid, Filtration, Sedimentation, Yield stress, Filter cake, Aggregate structure

1. Introduction

The control of solid-liquid separation processes, continues to present major challenges in a number of significant industrial sectors including water and waste-water treatment, minerals processing, paper manufacture, pharmaceuticals, and fine chemicals[1)]. It is now widely recognised that accurate control over the *macroscopic* properties of any particulate dispersion originates from a detailed understanding of the *microscopic* particle-particle interaction forces[2)]. For example, a stable dispersion can be created if a net repulsive interaction exists between the particulate objects. On the other hand, if the particles can be made attractive to one another they will aggregate forming large multi-particle units that can sediment rapidly facilitating separation of the phases. Thus, to gain good control over a particulate dispersion it is necessary to accurately characterise the strength of any inter-particle forces that may be operating.

The flocculation or coagulation of a stable dispersion to form larger aggregates is of central importance to the efficient operation of most solid-liquid separation processes, including filtration, thickening, and clarification[3)]. The relationship between aggregate properties, such as size, structure, and strength, and the efficiency of these unit operations has been recognised for many years[4)]. However, measurement and analysis limitations significantly hindered any systematic approach to understanding how aggregate properties effect these operations until comparatively recently. Whilst measurements of aggregate sizes have been available for many decades, reliable measurements of aggregate densities have only been

---

[†] Accepted: August 21, 2006

[*] Leeds LS2 9JT, UK
TEL: +113 343 2790, FAX: +113 343 2377

reported during the last decade or so[5]. The reliable measurement and analysis of sediment bed properties, such as shear and compressive yield stresses, are also a comparatively recent development[2, 6].

When considering the formation of aggregates, the inter-particle interaction forces are of central importance since these define the kinetics of aggregation and the strength of particle-particle bonds both of which ultimately influence aggregate structures. When considering the properties of sediment beds, the strength of particle bonds and the number of bonds that have to be broken, which is determined by the network structure which is in turn related to the aggregate structures, are of critical concern[2]. Hence, an understanding of what controls aggregate properties and how these properties impact on sediment bed properties is fundamental to optimising or improving basic solid-liquid separation processes.

In the sections that follow, a brief review of surface forces is given and this is followed by a discussion of how these forces impact on aggregate and sediment structures. The impact of these structural features on standard process operations such as filtration and thickening are also briefly considered.

2. Particle-Particle Surface Forces in Aqueous Systems

The stability of any aqueous particle dispersion is usually described through the so-called DLVO theory[7, 8]. This simple theory, developed in the 1940's, defines the potential energy of interaction between two particles as the summation of two independent components, one attractive and the other repulsive, according to;

$$V_{tot} = V_A + V_R = \frac{aA_H}{12H^2} + \frac{2\pi a\varepsilon_0\varepsilon\kappa\zeta^2 e^{-\kappa H}}{1+e^{-\kappa H}} \qquad (1)$$

Where V_A is the attractive component and V_R is the repulsive component. In these equations, a is the particle radius, A_H is the effective Hamaker constant, $\varepsilon$the dielectric constant of the medium, ε_0 is the permittivity of a vacuum, ζ is the particle zeta potential, H the surface-surface separation, and κ the inverse Debye length.

The attractive component arises from the bulk material properties of the particles and is caused by dipolar fluctuations of the atoms. The detail is not required here: It is sufficient to note that the strength of the attraction is essentially independent of the medium for an aqueous dispersion (ie. electrolyte type and concentration); it is always active; and, it decays very rapidly with surface-surface separation distance. The magnitude of the interaction is controlled by the Hamaker constant (A_H) which includes the dielectric information for the particles and medium.

The repulsive component to the interaction arises as a result of the attraction of counter-ions by a charged surface. It should be noted here that in an aqueous environment most surfaces can develop a charge, either by the dissociation of inherent surface charges or by specific ion adsorption[9]. Entropy considerations mean that the counter-ions to these charges are not restricted to a surface adsorbed layer but can be found anywhere within a defined volume which extends from the surface. This volume, known as the electrical double layer, ensures electrical neutrality between the particle and its counter-ions. However, when two particles approach each other, the two double layers must overlap. This results in a local non-equilibrium concentration of the counter-ions which is osmotically unfavourable and hence leads to a repulsion. The magnitude of the repulsive interaction is defined by the size of the surface charge (determines the counter-ion concentration in the double layer) and the extension of the double layer away from the surface. The double layer extension is given by the Debye length, $1/\kappa$, where;

$$\kappa \propto (z^2 c_0)^{1/2} \qquad (2)$$

and depends upon the electrolyte concentration (c_0) and counter-ion charge (z).

Thus, the concentration and the type of electrolyte play a significant role in determining the overall energy of interaction between two particles. As a function of particle-particle separation, the DLVO theory gives the following types of interaction curves;

At sufficiently high electrolyte, the primary bar-

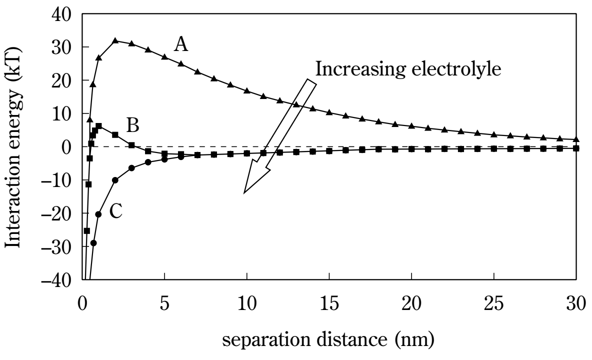

Fig.1 Energy as a function of separation distance for the interaction of two spherical particles across an aqueous electrolyte medium. Particles have a radius of 100 nm and a Hamaker constant of 1 × 10^{-20} J. The three data sets correspond to conditions of increasing electrolyte. Data set A: ψ = 22 mV and $1/\kappa$ = 10 nm. Data set B: ψ = 22 mV and $1/\kappa$= 1.5 nm. Data set C: ψ = 0 mV.

rier to coagulation is suppressed and the particles can enter the thermodynamically favoured primary minimum; the depth of this minimum determines the strength of the bonds formed. Factors such as the exact type of counter-ion and the presence of surface roughness have been shown to influence the strength of the attractive minimum although the exact mechanisms for quantifying these effects are still undecided[10-12]. It is also worth noting that aggregation can be induced even when there is a small barrier of a few kT (curve B). The presence of any repulsive barrier will be sufficient to slow the aggregation rate and here the process is considered as reaction-limited. The rate of the aggregation process is maximised when all repulsive interactions are suppressed, under these conditions the rate is purely diffusion limited (curve C).

Since the development of the DLVO theory, a large number of systems that exhibit apparently anomalous stability behaviour have been reported[13-28]. This has led to a number of other interaction forces being described. Amongst these, and relevant here, are steric polymer forces[14, 15, 19, 21, 25, 29], ionic hydration forces[16, 18, 24, 27] and hydrophobic interactions[22, 23, 26].

The adsorption of any large polymeric molecules at a particle surface can significantly affect the observed interactions. At the most basic level, an uncharged polymer can adsorb to a particle surface creating a hydrated molecular sheath. If two particles approach one another, overlap of these polymer layers leads to a loss of molecular freedom which is unfavourable and hence, a strongly repulsive interaction[30].

The distance over which this repulsion operates is dependent upon the "thickness" of the adsorbed film. This is a complex function of many parameters such as polymer molecular weight, adsorption energy, solution concentration etc.; it will suffice here to note that when the layer is sufficiently thick, the attractive dispersion forces can be permanently suppressed and a fully stable dispersion can result. Obviously, the use of charged polymers introduces a further electrostatic component into the repulsion that is strongly affected by the added electrolyte level. However, the broad analysis of the origins of stabilisation is the same as given above.

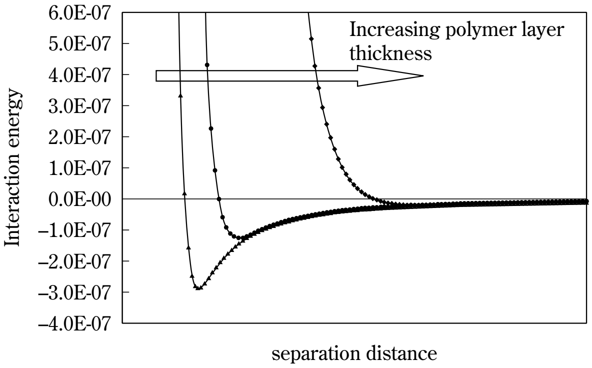

Fig. 2 Energy as a function of separation distance for the interaction of two spherical particles in the presence of a polymer coating on each particle. For simplicity, no electrical double layer interactions are included and the data shown is simply the summation of a steric polymer interaction and the van der Waals interaction. The three data sets shown correspond to an increasing thickness of the adsorbed polymer film.

The presence of different electrolyte types can also have a significant effect on particulate stability[12, 24, 27, 30, 31]. For example, it has been known for a long time that systems such as clays and silica can exhibit anomalous stability. Direct measurements using force balance techniques were used to demonstrate that this stability was caused either by the strong hydration of the surface or by the specific adsorption of strongly hydrated ions[27]. Close approach of the surfaces is prevented by the need to either de-hydrate the surface or cause ion desorption, respectively. Once again, this prevents the particle contacts from achieving close enough contact to reach the energy minimum caused by the attractive dispersion forces.

The effect of concentrated electrolyte solutions on particle-particle interactions have also been the subject of much interest recently[2, 31-35]. It has frequently been observed that simple 1-1 electrolytes at concentrations of around 1M and higher can lead to significant short-range interaction forces not described by DLVO theory. These interactions are driven by ion adsorption at the solid-liquid interface caused by the high salt concentration; the effects are seen in anomalous colloid dispersion behaviours. Despite the obvious importance of high electrolyte systems across many technologies, a unified understanding of these effects is not yet available. A number of models have been proposed to explain the observed ion adsorption data[33, 35, 65]. These are largely based around an analysis of the hydration state of the surface and the ionic species in solution. It is assumed that a "like-adsorbs-like" concept can be used to explain the adsorption of ions at a surface. Thus, a weakly hydrated surface would favour the adsorption of weakly hydrated counter-ions and vice versa. This approach satisfactorily explains the observed adsorption of ions on surfaces such as silica and alumina. Unfortunately, these hydration based approaches are unable to explain all of the data observed across all of the available particle types. It is also worth noting that in almost all cases, data were collected for a homologous series of counter-ions (whether cations or anions) adsorbing on oppositely charged substrates with little or no analysis of the role of co-ions. An exception to this is the work of Kosmulski and co-workers who have published a series of papers over the last decade in this field5). They make extensive use of the hard ion-soft ion model to explain their data since this model does allow for co-ion influences.

Finally, it is worth noting that hydrophobic particles in an aqueous medium will attract one another very strongly. Obviously, by definition they are in an unfavourable solvent environment. The exact origins of this interaction and its full quantification theoretically have yet to be resolved. However, it is accepted that a hydrophobic interaction will be attractive and will in general result in a significantly stronger and longer range interaction than is seen for the attractive dispersion forces13, 22, 23, 26).

3. Measurements and Analysis of Aggregates, Particle networks, Sludges and Slurries.

As noted above, stable particle dispersions can be destabilised in a variety of ways including through the addition of electrolyte. When an attractive particle-particle interaction force is established, any collision between two particles can result in a 'sticking event'. In this way, aggregates within dispersions can form and grow36). A fundamental parameter that is often used to characterise this process is the initial aggregation rate. As well as the interaction potential between the particles, the rate of aggregation is dependent upon factors such as particle volume fraction, medium viscosity, and whether the system is quiescent or mixed. Under quiescent conditions and in the absence of any repulsive interaction potential, the limiting rate of aggregation is given by the Smoluchowski theory as37);

$$k_R = \frac{4kT}{3\eta}$$

Where η is the viscosity of the solvent. (3)

Full characterisation of an aggregation event usually involves determination of the rate of aggregation, the aggregate size distribution (as a function of time), the sedimentation rate, and the aggregate structure36). Aggregation rate, aggregate sizes, size distributions, and densities are most frequently determined using static light scattering5, 38) although there is a significant body of research that utilises less complex turbidity measurements39). The main drawback of light scattering approaches arises from the requirement to maintain a dilute dispersion that prevents multiple scattering events. It should also be noted that determination of the aggregate densities relies upon the calculation of a so-called fractal dimension for the aggregates40). Practically, this can be obtained from measurements of the scattered intensity as a function of the scattering angle for a system of aggregates. According to relevant theories, it is critical that no multiple scattering events occur within any given aggregate: This is usually achieved for small open aggregates.

For a mass fractal aggregate consisting of monodisperse primary particles, the fractal character of an aggregate can be revealed if the primary particles satisfy the criteria of the Rayleigh-Gans-Debye (RGD) regime; the particles should behave as point scatterers and their should be no multiple scattering events. Assuming these conditions are met, the scattered intensity from the aggregate, $I(Q)$, shows a power-law behaviour, according to,

$$I(Q) \propto Q^{-D} \qquad (4)$$

provided that $1/R \ll Q \ll 1/r_0$. Here D is the aggregate mass fractal dimension, R and r_0 are the respective radii of the aggregate and the primary particles, and Q is the magnitude of the scattering wavevector. Q is a function of the scattering angle and is defined as follows:

$$Q = \frac{4\pi n_0}{\lambda_0}\sin\left(\frac{\theta}{2}\right) \qquad (5)$$

where n_0 is the refractive index of the dispersion medium, θ is the scattering angle and λ_0 is the in vacuo wavelength of the incident light. Since $1/Q$ is the length scale probed in a scattering experiment, the low and high regions of Q reveal the overall structure of the aggregate and the structure of the primary particles, respectively. The spatial arrangement of the primary particles inside an aggregate can only be probed when $1/R < Q < 1/r_0$. Typical scattering data from a fractal aggregate are shown below in **Fig. 3**.

This approach has been used to show that both the size of aggregates that form, and their density (structural compactness) can be altered by changing one or all of the particle interaction forces41), particle volume fraction42) and/or the mixing conditions43). More recently, alternative techniques that utilise ultrasonics or back scattered light have begun to be utilised to measure aggregation in situ for more concentrated dispersions44-46).

There are two main limitations on the growth of aggregates, the presence of shear43) is one and the second is sedimentation. When a shear field exists, aggregate growth is limited since large tenuous ag-

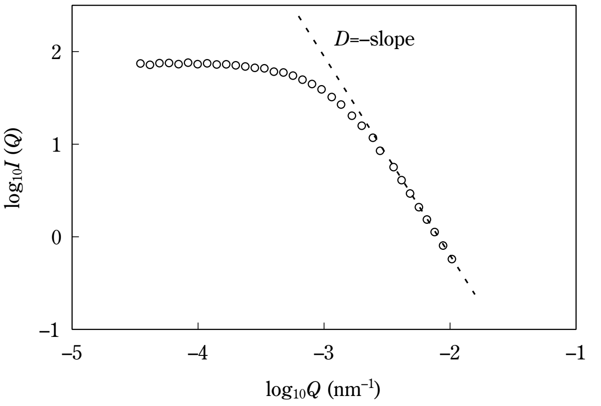

Fig. 3 Typical data of the intensity of light scattered as a function of the scattering wave vector Q. The limiting slope of these data for the higher Q values is interpreted as the fractal dimension, D, assuming that the conditions of the Rayleigh-Gans-Debye interpretation are met.

gregates can be easily disrupted leaving a system of smaller more compact aggregates. In the case of a quiescent system where there is no barrier to aggregation, if there were no sedimentation then growth of the aggregates would continue until there was only one single aggregate. This has been seen for polystyrene latex in water which is an almost neutrally buoyant system.[42] However, more typically the particles are more dense than the medium and begin to settle rapidly as the aggregates grow. This prevents them growing too large, and may also influence the average size and shape.

As we noted above, aggregate densities are characterised using the mass fractal dimension[40], D. D corresponds to the space-filling capacity of the aggregate and hence is a good measure of the structural compactness. In 3-dimensional Euclidean space, it can have values of $1 < D < 3$ where 1 corresponds to a relatively linear tenuous aggregate and 3 to a totally compact object. Fractal behaviour has been reported for a wide range of colloidal materials including latex, gold, silica, alumina, hematite, bentonite clay and carbon black[47]. Such structural characterisation has been reported for aggregates formed using a variety of aggregation mechanisms including the addition of electrolyte, polymer bridging and polymer depletion[20, 41, 42, 48]. The aggregation caused by addition of salt is by far the most understood both in experiment and theory. The theory predicts two regimes of behaviour:[49-53]In the absence of any potential energy barrier (**Fig. 1**), all collisions lead to a sticking event which results in the rapid formation of large open clusters, this is known as diffusion limited cluster-cluster aggregation (DLCA); when there is a small potential energy barrier, not all collisions lead to a sticking event and individual particles have longer to find a pathway into the core of an aggregate, this leads to smaller more compact aggregates and is known as reaction-limited cluster-cluster aggregation (RLCA). Theory and experiment have shown that for DLCA, $D = 1.7 - 1.8$, and for RLCA, $D = 2.1 - 2.2$. Examples of aggregates corresponding to these values are shown in **Fig. 4**.

In general, it has been shown that the aggregate density is a sensitive function of the ratio of the particle-particle sticking rate to the structural rearrangement rate for any aggregated particle.[47] Essentially, if the sticking rate is high, rearrangements are unlikely before further collisions (and sticking events) and an open aggregate structure becomes locked-in. Reductions in the collision rate by decreasing the particle volume fraction[42] or increasing the medium viscosity[47] have been shown to cause more compact aggregates. In general, for systems which show limited sedimentation it has been observed that aggregates which form under RLCA conditions can undergo rearrangements over long timescales which result in more compact aggregates than are initially observed.[42, 54] Such rearrangements, for aggregates with little or no settling are relevant to natural

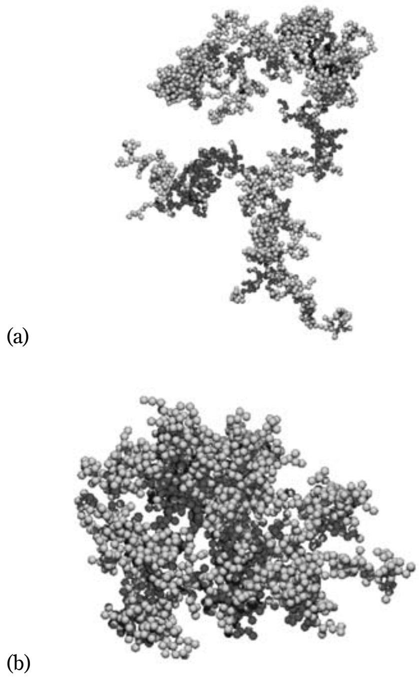

Fig. 4 Simulated aggregate structures for aggregates formed under (a) DLCA and (b) RLCA conditions. [Images kindly supplied by Dr. Graeme Bushell, Department of Chemical Engineering, UNSW].

aquatic colloids or living species such as algae that may undergo aggregation.[54-56] It has also been shown recently that there is a gradual transition between the limiting RLCA and DLCA cases across a narrow range of added electrolyte[57]; the limiting cases and this intermediate regime can be defined using the colloid stability ratio, W, which defines stability on the basis of a ratio of the observed aggregation rate to the maximum possible aggregation rate (diffusion limited). So, when $W = 1$, the system is at its maximum instability and a large value of W defines a stable system. The intermediate behaviour regime is defined as $5 < W < 100$; in this regime D was seen to gradually rise from a typical DLCA value to the RLCA limiting value.

The introduction of shear[43, 58, 59] is also an important factor and it usually results in smaller more compact aggregates. The impact of shear is affected by the primary particle size. Smaller particle sizes generate more compact aggregates through an increased level of aggregate rearrangement in the shear field. By contrast, larger particles exhibit a fragmentation and re-aggregation mechanism as a result of the breakage of tenuous features from the aggregates in the shear field.

Sedimentation rates are obviously strongly dependent upon both the aggregate sizes and their net density (a function of the primary particle density and the aggregate compactness). Typically, sedimentation rates have been investigated by recording changes in turbidity as a function of both time and height in a sedimentation column. More recently, the sedimentation rates of individual aggregates have been reported as a function of the aggregate size. Such data can be used to calculate the apparent density of an aggregate, and if the data are collected over a sufficiently broad size range they may also be used to determine the fractal dimension of the aggregates[48]. The key difficulties with this approach are associated with the porosity of the aggregates and their generally non-spherical shapes. Shape effects can be managed through the use of appropriate empirical corrections to the drag coefficient.[4] The porosity of the aggregates, and the associated flow of liquid around or through these aggregates are more difficult to understand and account for. The implications of a fractal structure are that as an aggregate gets larger, at a fixed fractal dimension, its net density must decrease and the effective porosity must increase. Furthermore, the porosity of an aggregate must increase with its radius away from the centre[60]; it seems improbable therefore that large aggregates do not show some level of liquid flow through their structure during sedimentation.[61] However, correct modelling of this flow through is difficult as a result of the complex relationship between aggregate size, fractal dimension, and porosity as a function of aggregate radius. Nonetheless, the sedimentation approach has been used to characterise fractal aggregates.[4, 48, 62] It is especially useful when the size of the aggregates leads to problems with the more common light scattering approach as a result of violations of the available RGD theory. The use of polymer flocculants usually results in such large aggregates, and it also introduces a much wider range of possible fractal dimensions[20] as a result of the increased complexity of the aggregation process and its dependence on a greater number of parameters such as polymer molecular weight, type, method of addition, and concentration.[62]

The result of particles or aggregates which sediment from a dispersion is the formation of a sediment bed (sludge). The properties of this sediment are strongly dependent on the aggregate feed properties, especially the aggregate sizes and densities.[63, 64] It is also important to understand how these aggregates interact within the sediment; for example, aggregates formed by salt coagulation will probably bind at any contact points since the salt can still be expected to have an influence continuously whereas aggregates formed by polymer bridging may not actually bind to each other and can remain as discrete objects. The size of the aggregates is important since, for any given fractal dimension, aggregates are more ‘open’ at the outer edges than they are at the core[4, 64]. Thus, in a sediment larger aggregates may generate a more porous network; it is worth noting however that the edges may be inherently weak and more compressible resulting in greater compaction of the sediment under gravity. The strength of a sediment bed is also important since this defines its resistance to compaction and ultimately has an influence on the porosity. The total strength of any sediment will depend on the strength of the particle-particle bonds and the network structure within the bed.[65] As noted above, this overall network structure will be influenced both by the structures of the individual aggregates as well as by how these aggregates interact with each other. The strength and structure of sediment beds is therefore clearly important to consolidation, filtration, and re-suspension.

The energy required for re-suspension is clearly related to the product of the bond number and average bond strength[2, 12, 66], although complications introduced by differences between bonds within aggregates and between aggregates must be considered. In the case of aggregates formed by suppression of the double layer through the addition of electrolyte, all the aggregates in the sediment bed can aggregate together forming a continuous gel network structure. The resistance of this network to an external shear field is characterised by its shear yield stress, τ_y. The shear yield stress is defined as the applied stress beyond which material will flow and is indicative of a transition between solid-like and liquid-like behaviour[67, 68]. Although the existence of a yield stress has traditionally been the subject of contention, it is now generally accepted that for a cohesive particle network τ_y has real meaning[69]. Boger and co-workers[2, 69-79] have pioneered the use of a vane technique for the characterisation of particle networks through the measurement of τ_y. The advantage of the vane for these measurements is the absence of any wall slip when performing the rheological test[69]. More commonly, it is reported that the yield stress can be obtained from an extrapolation of shear stress-shear rate data to zero shear rate[80-87]. This is often performed using a rheology model such as the Bingham, Herschel-Bulkley or Casson. This approach relies upon accurate data at low shear rates. Unfortunately, wall slip is a big problem for conventional measuring geometries (cup and bob or cone and plate) when the system has a significant yield condition. This can lead to significant errors in the flow data and hence the yield stress.

In addition to its effect on the shear yield stress, a significant inter-particle interaction can impact strongly on the compressive properties of any particle network[6, 88-95]. Compression is usually characterised through the compressive yield stress P_y. As before, P_y is defined as the compressive pressure beyond which the network consolidates inelastically. Measurement and calculation of P_y is considerably more complex[96-102] than τ_y and, as a result, there is much less data available in the literature.

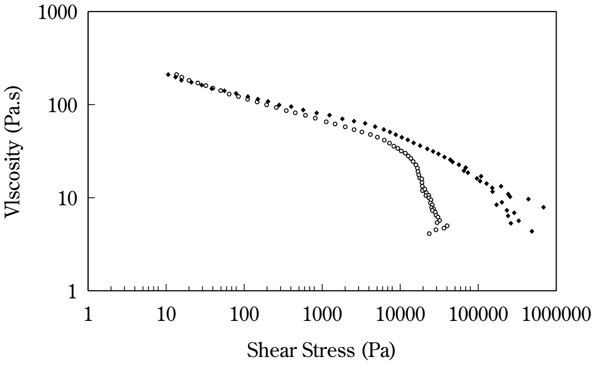

Fig. 5 Viscosity as a function of shear stress for a commercial toothpaste sample. The data were collected using a vane tool in either a smooth walled cup [open symbols] or a cup with a roughened surface [filled symbols]. The different response of these two data sets can be attributed directly to sample slip at the smooth cup surface; such slip may lead to the erroneous interpretation of a yield stress.

In general, a stronger particle-particle attraction will result in a network that has a higher yield stress (shear and compression), a more elastic character (larger storage modulus) and a lower overall particle packing density[32]. Recently, controlled rheological investigations using model mineral particles such as clean and pure alumina or silica have been used to show that there is a direct relationship between the rheological properties of a sediment bed and the net inter-particle force[2, 71, 72]. For example, Scales et al[76] have proposed that for an aqueous particle dispersion where only DLVO forces are operable, the shear yield stress can be given as;

$$\tau_y = K_{st}\left[\frac{A_H}{12H^2} - \frac{2\pi\,\varepsilon_0\varepsilon\kappa\zeta^2 e^{-\kappa H}}{1+e^{-\kappa H}}\right] \qquad (6)$$

where the terms in brackets account for the DLVO forces of interaction and K_{st} is a term that depends upon the detailed network structure, primarily the coordination number. Using the above relationship, good correlation between factors such as the zeta potential (ζ) and the shear yield stress have been demonstrated[85, 103, 104]. The influence of other interparticle forces on τ_y such as polymer bridging forces[105], hydrophobic forces[106], and polymer steric forces[104] has also been investigated and good correlation with the inter-particle forces has been demonstrated. Preliminary investigations of the influence of other factors such as particle size[66], particle size distribution[66], particle volume fraction[76], and specific ion effects[12, 31] have also been described. However, detailed understanding of their influence on the yield stress is currently not as well developed. Franks et al.[65] have examined the effect of aggregate size on the network strength using a careful series of experiments where all other features of the aggregate samples were held constant, such as bond strength, fractal dimension, and primary particle size. It was found that larger aggregates produce sediments which have a lower gel point and higher shear & compressive yield stresses when all other factors remain constant. Given that larger aggregates become more tenuous, at a fixed fractal dimension, this result seems somewhat counter-intuitive and is, as yet, not fully explained.

There is considerably less literature evidence for the relationships between inter-particle forces and compressive yield stresses[6, 90-92, 94]. Despite this, P_y is a crucial factor in understanding the properties of highly concentrated dispersions since it can indicate the maximum concentration of solids that will flow[6]. In general, knowledge of the maximum concentration for a dispersion that can still flow is highly sought after. This is particularly true in industries such as mining where the disposal of semi-dry solids is increasingly used to minimise the volume of waste. Recent theory and experiment developments have resulted in relatively rapid determinations of the compressive yield stress for settled solids using a pressure filtration approach[92, 93, 96-98, 107]. This technique also offers important complementary information about the hindered settling factor (and hence filtration efficiency). Aziz et al[94] have used such an approach to investigate the influence of inter-particle forces on the compression and filtration of a sediment. They show that a strongly repulsive inter-particle force results in a very compact dense sediment. However, there is a corresponding reduction in the filtration efficiency of this bed and a decrease in the dewaterability of the bed. Green and Boger[6] note that careful control of the compressive properties for a particle network can be used to control the final solids concentration under a given applied pressure. They also show that a highly concentrated particle system can still be pumped and, in fact, will require a lower pumping energy due to operation in a laminar regime within the pipe. Finally, they suggest that problems of start-up, as well as erosion and settling problems will be reduced if a system of more concentrated solids is used. Zukoski and co-workers have also investigated how inter-particle forces can affect the development of inhomogeneities in the sediment bed and how these flaws influence the compressibility[90, 91].

The importance of rheology for the characterisation of a sediment bed is that it can offer a direct measurement of the energies needed to re-suspend the solids under process relevant conditions. Indeed, in principle the measurement of yield stress, elastic modulus and bed structure should give direct access to the inter-particle interactions. In practice this is not easily done and more direct force balance techniques can give a much better indication of the operable forces. This detailed information is crucial for the control and manipulation of forces between particles [15-19, 29, 108].

As yet, there are few studies which combine the *macroscopic* rheology measurements of inter-particle forces with the *microscopic* data available from a technique such as AFM. One report, by Yan et al[109] shows that the two techniques are definitely complementary and in a broad sense give the same results. Burns et al[41] have also shown that rheology and AFM data can be used in combination to more completely explain the flow behaviour of a concentrated suspension. The influence of polymer steric layers on the flow properties of dispersions have also been examined using both rheology and direct force measurements[82, 87, 110, 111]. There is definitely value in exploring these links further.

4. Aggregate Properties and Solid-Liquid Separation

In considering the effect of aggregate structures on different solid-liquid processes or treatment strategies, it is important to define the range of conditions that are experienced by the particles when treated. For example, the impact of shear on aggregation and on aggregate structure is known to be important.[43, 58, 59] So, the use of mixing when adding a coagulant or flocculant can have a significant effect on the final operational performance of a given process unit.[4] The application of shear causes the formation of smaller more compact aggregates; this is seen most dramatically under DLCA conditions where larger more pendulous aggregates would be formed in a quiescent state. The diffuse arms of these large aggregates are relatively weak and easily sheared off resulting in the formation of smaller aggregates. The sheared fragments are expected to penetrate into the aggregates before re-attaching resulting in the formation of smaller more dense aggregates. It has also been noted that both the intensity of shear and the duration of its application are important control parameters for producing different size and density aggregates.[59, 112, 113]

It has also been noted previously, that the performance requirements of different solid-liquid separation processes, such as filtration or thickening, are often very different.[3, 4] As a result, the optimum aggregate properties for each are most likely very different. Furthermore, it is likely that different modes of operation within a given unit will also effect any decision about optimal aggregate properties. As noted earlier, significant progress on the analysis of aggregates and sediment bed properties has been made during the last decade. However, understanding of the impact of different aggregate properties on water treatment operations remains limited.

One of the most well developed areas is sedimentation; here researchers have demonstrated clear links between aggregate sizes and size distributions, as well as aggregate densities and sedimentation.[4, 48, 62] However, it remains unclear about how to best model an open fractal aggregate and how to define the correct drag coefficient for such an object.[4, 48] For example, will fluid flow through or around such an aggregate; given that the effective porosity of a fractal aggregate increases with aggregate size it seems likely that the opportunity for flow through the aggregate will be greatest towards its edges and decrease towards the centre. Glover et al.[48] showed that for small porous aggregates of alumina it is important to allow for some flow through the aggregates if we are to correctly interpret sedimentation data.

The links between the consolidation behaviour of sediments and aggregate properties also remain relatively poorly understood with only a limited number of reports available.

Waite and co-workers[64, 114-117] have, in a series of papers, investigated the effect of aggregate sizes and structures on the performance of ultrafiltration for colloidal solids. The relationship between fractal aggregate structures and filter cake porosity is explored in this work through application of a modified Carmen-Kozeny relationship, which is given as:

$$\alpha = \frac{180(1-\varepsilon)}{\rho_p d_p^2 \varepsilon^3} \tag{7}$$

where α is the specific resistance of the filter cake, ρ_p the density of the particles, d_p the mean diameter of the particles, and ε is the void volume of the cake. This relationship is known to be valid for cakes formed from discrete particles having porosities of less than 0.5.[61] It is clear from this expression, that the porosity (through the void volume, ε) of the cake has a strong influence on the performance of any filter cake. Hence, filter cakes that are formed from fractal aggregates of colloids will be influenced by aggregate sizes and fractal dimensions. It has been noted many times that as aggregates get larger, at a fixed fractal dimension, that they must get more porous. Hence, when they form a filter cake we might expect that the porosity of that cake would be higher. On the other hand, if the aggregates are weak they may be susceptible to collapse and the bed may consolidate under gravity resulting in a loss of porosity and hence permeability. From the work of Waite and co-workers, it seems that, in general, larger aggregates tend to form more porous filter cakes and these filter cakes are more resistant to collapse. Smaller aggregates, with a higher fractal dimension, form filter cakes that are initially of lower porosity; in addition, these cakes exhibit higher levels of consolidation with the associated poor filtration performance. Interestingly, these results appear to agree with the shear and compressive yield stress data of Franks et al. [65] which showed that larger aggregates were more resistant to an applied force. These results from filtration tests appear quite general and have been confirmed on a variety of systems including biosolids [3] and apple juice colloids. [118]

5. Conclusion

Whilst it is clear that there must exist links between the feed of aggregates and the performance of a given solid-liquid separation process, relationships between the two are still not fully developed. The last decade has seen significant advances in measurement capability and this has led to an unprecedented degree of insight into aggregation and the properties of aggregates formed. Parallel advances in the characterisation of sediments and filter cakes have also occurred using rheology and pressure filtration techniques. Despite this, links between the properties of the aggregate feed and the subsequent behaviour of a sediment bed are still poorly developed; this is primarily related to the complexity of the system and the number of inter-dependent variables that have to be controlled for a systematic study to be undertaken.

References

1) Hunter, R. J., *Introduction to Modern Colloid Science*. 1993, Oxford: Oxford University Press. 344.
2) Johnson, S.B., et al., *Surface chemistry-rheology relationships in concentrated mineral suspensions*. International Journal of Mineral Processing, 2000. **58**(1-4): p. 267-304.
3) Chau, K.W., *Investigation on effects of aggregate structure in water and wastewater treatment*. Water Science And Technology, 2004. **50**(12): p. 119-124.
4) Gregory, J., *The density of particle aggregates*. Water Science And Technology, 1997. **36**(4): p. 1-13.
5) Bushell, G.C., et al., *On techniques for the measurement of the mass fractal dimension of aggregates*. Advances in Colloid and Interface Science, 2002. **95**(1): p. 1-50.
6) Green, M.D. and D.V. Boger, *Yielding of suspensions in compression*. Industrial & Engineering Chemistry Research, 1997. **36**(11): p. 4984-4992.
7) Verwey, E.J.W. and J.T.G. Overbeek, *Theory of the stability of lyophobic colloids*. 1948, Amsterdam: Elsevier.
8) Derjaguin, B.V. and L. Landau, *Theory of the stability of strongly charged lyophobic sols and of the adhesion of strongly charged particles in solutions of electrolytes*. Acta Physicochim. URSS, 1941. **14**: p. 633-662.

9) Hunter, R.J., *Foundations of colloid science*. 2 ed. 2001, Oxford: Oxford University Press. 806.

10) Suresh, L. and J.Y. Walz, *Direct measurement of the effect of surface roughness on the colloidal forces between a particle and flat plate*. Journal of Colloid and Interface Science, 1997. **196**(2): p. 177-190.

11) Walz, J.Y. and N. Sun, *A general model for calculating the effect of surface roughness on colloidal forces*. Abstracts of Papers of the American Chemical Society, 1999. **217**: p. 207-ENVR.

12) Franks, G.V., et al., *Ion-specific strength of attractive particle networks*. Langmuir, 1999. **15**(13): p. 4411-4420.

13) Attard, P., *Long-Range Attraction between Hydrophobic Surfaces*. Journal of Physical Chemistry, 1989. **93**(17): p. 6441-6444.

14) Almog, Y. and J. Klein, *Interactions between Mica Surfaces in a Polystyrene- Cyclopentane Solution near the Theta-Temperature*. Journal of Colloid and Interface Science, 1985. **106**(1): p. 33-44.

15) Biggs, S. and T.W. Healy, *Electrosteric Stabilization of Colloidal Zirconia with Low- Molecular-Weight Polyacrylic-Acid - an Atomic-Force Microscopy Study*. Journal of the Chemical Society-Faraday Transactions, 1994. **90**(22): p. 3415-3421.

16) Biggs, S., et al., *Study of Anion Adsorption at the Gold-Aqueous Solution Interface by Atomic-Force Microscopy*. Journal of the American Chemical Society, 1994. **116**(20): p. 9150-9157.

17) Biggs, S. and P. Mulvaney, *Surfactant and polymer adsorption: Atomic Force Microscopy measurements, in Surfactant Adsorption and Surface Solubilization*. 1995, AMER CHEMICAL SOC: Washington. p. 255-266.

18) Biggs, S., et al., *Effects of Citrate Adsorption on the Interactions between Zirconia Surfaces*. Journal of the Chemical Society-Faraday Transactions, 1995. **91**(17): p. 2921-2928.

19) Biggs, S., *Steric and Bridging Forces between Surfaces Fearing Adsorbed Polymer - an Atomic-Force Microscopy Study*. Langmuir, 1995. **11**(1): p. 156-162.

20) Biggs, S., et al., *Aggregate structures formed via a bridging flocculation mechanism*. Chemical Engineering Journal, 2000. **80**(1-3): p. 13-22.

21) Costello, B.A.D., P.F. Luckham, and T.F. Tadros, *Investigation of the Interaction Forces of Polymer-Coated Surfaces Using Force Balance, Rheology, and Osmotic-Pressure Results*. Langmuir, 1992. **8**(2): p. 464-468.

22) Craig, V.S.J., B.W. Ninham, and R.M. Pashley, *Study of the long-range hydrophobic attraction in concentrated salt solutions and its implications for electrostatic models*. Langmuir, 1998. **14**(12): p. 3326-3332.

23) Craig, V.S.J., B.W. Ninham, and R.M. Pashley, *Direct measurement of hydrophobic forces: A study of dissolved gas, approach rate, and neutron irradiation. Langmuir,* 1999. **15**(4): p. 1562-1569.

24) Israelachvili, J.N. and R.M. Pashley, *Molecular Layering of Water at Surfaces and Origin of Repulsive Hydration Forces*. Nature, 1983. **306**(5940): p. 249-250.

25) Israelachvili, J.N., et al., *Forces between 2 Layers of Adsorbed Polystyrene Immersed in Cyclohexane Below and above the Theta-Temperature*. Macromolecules, 1984. **17**(2): p. 204-209.

26) Israelachvili, J.N. and R.M. Pashley, *Measurement of the Hydrophobic Interaction between 2 Hydrophobic Surfaces in Aqueous-Electrolyte Solutions*. Journal of Colloid and Interface Science, 1984. **98**(2): p. 500-514.

27) Pashley, R.M. and J.N. Israelachvili, *Dlvo and Hydration Forces between Mica Surfaces in Mg-2+, Ca- 2+, Sr-2+, and Ba-2+ Chloride Solutions*. Journal of Colloid and Interface Science, 1984. **97**(2): p. 446-455.

28) Milling, A. and S. Biggs, *Direct Measurement of the Depletion Force Using an Atomic-Force Microscope*. Journal of Colloid and Interface Science, 1995. **170**(2): p. 604-606.

29) Biggs, S., *Non-equilibrium interaction forces between adsorbed polymer layers*. Journal of the Chemical Society-Faraday Transactions, 1996. **92**(15): p. 2783-2789.

30) Napper, D.H., *Polymeric Stabilization of Colloidal Dispersions*. Colloid Science, ed. R.L. Rowell and R.H. Ottewill. 1983, London: Academic Press. 428.

31) Franks, G.V., *Zeta potentials and yield stresses of silica suspensions in concentrated monovalent electrolytes: Isoelectric point shift and additional attraction*. Journal Of Colloid And Interface Science, 2002. **249**(1): p. 44-51.

32) Colic, M., M.L. Fisher, and G.V. Franks, *Influence of ion size on short-range repulsive forces between silica surfaces*. Langmuir, 1998. **14**(21): p. 6107-6112.

33) Dumont, F., J. Warlus, and A. Watillon, *Influence Of The Point Of Zero Charge Of Titanium-Dioxide Hydrosols On The Ionic Adsorption Sequences*. Journal Of Colloid And Interface Science, 1990. **138**(2): p. 543-554.

34) Franks, G.V., et al., *Effect of interparticle forces on shear thickening of oxide suspensions*. Journal Of Rheology, 2000. **44**(4): p. 759-779.

35) Kosmulski, M. and J.B. Rosenholm, *High ionic strength electrokinetics*. Advances In Colloid And Interface Science, 2004. **112**(1-3): p. 93-107.

36) Elimelech, M., et al., *Particle Deposition and Aggregation: Measurement, Modelling and Simulation*. Colloid and Surface Engineering Series, ed. R.A. Williams. 1995, Woburn, MA: Butterworth-Heinemann. 441.

37) Smoluchowski, M., Zeitschrift fur Physichalische Chemie, 1917. **92**: p. 129.

38) Young, W.D. and D.C. Prieve, *An Improved Light-Scattering Technique for Measuring the Flocculation Rate of Colloids*. Langmuir, 1991. **7**(12): p. 2887-2892.

39) Mengual, O., et al., *Characterisation of instability of concentrated dispersions by a new optical analyser: the TURBISCAN MA 1000*. Colloids and Surfaces a-Physicochemical and Engineering Aspects, 1999. **152**(1-2): p. 111-123.

40) Mandelbrot, B.B., *The Fractal Nature of Geometry*. 1982, San Francisco: Freeman.

41) Burns, J.L., et al., *Relationship between interaction forces and the structural compactness of depletion flocculat-*

ed colloids. Colloids and Surfaces a-Physicochemical and Engineering Aspects, 2000. **162**(1-3): p. 265-277.

42) Burns, J.L., et al., *A light scattering study of the fractal aggregation behavior of a model colloidal system*. Langmuir, 1997. **13**(24): p. 6413-6420.

43) Selomulya, C., et al., *Evidence of shear rate dependence on restructuring and breakup of latex aggregates*. Journal Of Colloid And Interface Science, 2001. **236**(1): p. 67-77.

44) Haider, L., P. Snabre, and M. Boynard, *Rheo-acoustical study of the shear disruption of reversible aggregates. Ultrasound scattering from concentrated suspensions of red cell aggregates*. Journal of the Acoustical Society of America, 2000. **107**(3): p. 1715-1726.

45) Austin, J.C. and R.E. Challis, *The detection of structural transformations in kaolin suspensions by ultrasound*. Journal of Colloid and Interface Science, 1999. **220**(1): p. 6-12.

46) Snabre, P., L. Haider, and M. Boynard, *Ultrasound and light scattering from a suspension of reversible fractal clusters in shear flow*. European Physical Journal E, 2000. **1**(1): p. 41-53.

47) Yan, Y.D., et al., *Viscosity effect on the structural compactness of latex flocs formed under weak depletion attractions*. Journal of Colloid and Interface Science, 2002. **255**(1): p. 91-97.

48) Glover, S.M., et al., *Bridging flocculation studied by light scattering and settling*. Chemical Engineering Journal, 2000. **80**(1-3): p. 3-12.

49) Lin, M.Y., et al., *Universality in Colloid Aggregation*. Nature, 1989. **339**(6223): p. 360-362.

50) Lin, M.Y., et al., *The Structure of Fractal Colloidal Aggregates of Finite Extent*. Journal of Colloid and Interface Science, 1990. **137**(1): p. 263-280.

51) Lin, M.Y., et al., *Universal Diffusion-Limited Colloid Aggregation*. Journal of Physics-Condensed Matter, 1990. **2**(13): p. 3093-3113.

52) Lin, M.Y., et al., *Universal Reaction-Limited Colloid Aggregation*. Physical Review A, 1990. **41**(4): p. 2005-2020.

53) Lindsay, H.M., et al., *Properties of Fractal Colloid Aggregates*. Faraday Discussions, 1987(83): p. 153-165.

54) Chakraborti, R.K., et al., *Changes in fractal dimension during aggregation*. Water Research, 2003. **37**(4): p. 873-883.

55) Lundsgaard, C., et al., *Sources of settling material: aggregation and zooplankton mediated fluxes in the Gulf of Riga*. Journal Of Marine Systems, 1999. **23**(1-3): p. 197-210.

56) Molodkina, L.M., Y.M. Chernoberezhskii, and E.V. Golikova, *Electrokinetic properties and aggregate stability of nanosized biocolloids - Influenza virus dispersions*. Glass Physics And Chemistry, 2005. **31**(3): p. 291-300.

57) Berka, M. and J.A. Rice, *Relation between aggregation kinetics and the structure of kaolinite aggregates*. Langmuir, 2005. **21**(4): p. 1223-1229.

58) Selomulya, C., et al., *Aggregation mechanisms of latex of different particle sizes in a controlled shear environment*. Langmuir, 2002. **18**(6): p. 1974-1984.

59) Selomulya, C., et al., *Aggregate properties in relation to aggregation conditions under various applied shear environments*. International Journal Of Mineral Processing, 2004. **73**(2-4): p. 295-307.

60) Jiang, Q. and B.E. Logan, *Fractal Dimensions Of Aggregates Determined From Steady-State Size Distributions*. Environmental Science & Technology, 1991. **25**(12): p. 2031-2038.

61) Veerapaneni, S. and M.R. Wiesner, *Hydrodynamics of fractal aggregates with radially varying permeability*. Journal Of Colloid And Interface Science, 1996. **177**(1): p. 45-57.

62) Farrow, J.B., et al., *Recent developments in techniques and methodologies for improving thickener performance*. Chemical Engineering Journal, 2000. **80**(1-3): p. 149-155.

63) Waite, T.D., *Measurement and implications of floc structure in water and wastewater treatment*. Colloids And Surfaces A-Physicochemical And Engineering Aspects, 1999. **151**(1-2): p. 27-41.

64) Waite, T.D., et al., *Colloidal fouling of ultrafiltration membranes: Impact of aggregate structure and size*. Journal Of Colloid And Interface Science, 1999. **212**(2): p. 264-274.

65) Franks, G.V., et al., *Effect of aggregate size on sediment bed rheological properties*. Physical Chemistry Chemical Physics, 2004. **6**(18): p. 4490-4498.

66) Zhou, Z.W., et al., *The yield stress of concentrated flocculated suspensions of size distributed particles*. Journal of Rheology, 1999. **43**(3): p. 651-671.

67) Barnes, H.A., *The yield stress - a review or 'pi alpha nu tau alpha rho epsilon iota' - everything flows?* Journal of Non-Newtonian Fluid Mechanics, 1999. **81**(1-2): p. 133-178.

68) Cheng, D.C.H., *Yield Stress - a Time-Dependent Property and How to Measure It*. Rheologica Acta, 1986. **25**(5): p. 542-554.

69) Liddell, P.V. and D.V. Boger, *Yield stress measurements with the vane*. Journal of Non-Newtonian Fluid Mechanics, 1996. **63**(2-3): p. 235-261.

70) Barnes, H.A. and Q.D. Nguyen, *Rotating vane rheometry - a review*. Journal of Non-Newtonian Fluid Mechanics, 2001. **98**(1): p. 1-14.

71) Johnson, S.B., et al., *The binding of monovalent electrolyte ions on alpha-alumina. II. The shear yield stress of concentrated suspensions*. Langmuir, 1999. **15**(8): p. 2844-2853.

72) Johnson, S.B., D.R. Dixon, and P. J. Scales, *The electrokinetic and shear yield stress properties of kaolinite in the presence of aluminium ions*. Colloids and Surfaces a-Physicochemical and Engineering Aspects, 1999. **146**(1-3): p. 281-291.

73) Leong, Y.K., et al., *Rheology of Brown Coal-Water Suspensions*. Rheologica Acta, 1987. **26**(3): p. 291-300.

74) Leong, Y.K. and D.V. Boger, *Surface-Chemistry Effects on Concentrated Suspension Rheology*. Journal of Colloid and Interface Science, 1990. **136**(1): p. 249-258.

75) Leong, Y.K., D.V. Boger, and D. Parris, *Surface and Rheological Properties of Zirconia Suspensions.* Chemical Engineering Research & Design, 1991. **69**(5): p. 381-385.

76) Scales, P.J., et al., *Shear yield stress of partially flocculated colloidal suspensions.* Aiche Journal, 1998. **44**(3): p. 538-544.

77) Nguyen, Q.D. and D.V. Boger, *Rheological Models, for Concentrated Red Mud Suspensions*. Journal of Rheology, 1985. **29**(1): p. 114-115.

78) Nguyen, Q.D. and D.V. Boger, *Application of rheology to solving tailings disposal problems*. International Journal of Mineral Processing, 1998. **54**(3-4): p. 217-233.

79) Nguyen, Q.D. and D.V. Boger, *Characterization of Yield Stress Fluids with Concentric Cylinder Viscometers*. Rheologica Acta, 1987. **26**(6): p. 508-515.

80) Barnes, H.A., *A Review of the Slip (Wall Depletion) of Polymer-Solutions, Emulsions and Particle Suspensions in Viscometers - Its Cause, Character, and Cure.* Journal of Non-Newtonian Fluid Mechanics, 1995. **56**(3): p. 221-251.

81) Bergstrom, L., *Shear thinning and shear thickening of concentrated ceramic suspensions*. Colloids and Surfaces a-Physicochemical and Engineering Aspects, 1998. **133**(1-2): p. 151-155.

82) Luckham, P.F., et al., *The Relationship between Interparticle Forces and the Bulk Rheology of Suspensions.* Powder Technology, 1991. **65**(1-3): p. 371-379.

83) Muster, T.H. and C.A. Prestidge, *Rheological investigations of sulphide mineral slurries*. Minerals Engineering, 1995. **8**(12): p. 1541-1555.

84) Prestidge, C.A., *Rheological investigations of ultrafine galena particle slurries under flotation-related conditions*. International Journal of Mineral Processing, 1997. **51**(1-4): p. 241-254.

85) Prestidge, C.A., *Rheological investigations of galena particle interactions.* Colloids and Surfaces a-Physicochemical and Engineering Aspects, 1997. **126**(2-3): p. 75-83.

86) Prestidge, C.A., I. Ametov, and J. Addai-Mensah, *Rheological investigations of gibbsite particles in synthetic Bayer liquors*. Colloids and Surfaces a-Physicochemical and Engineering Aspects, 1999. **157**(1-3): p. 137-145.

87) Tadros, T.F., et al., *Correlation of the Rheology of Concentrated Dispersions with Interparticle Interactions.* Colloids and Surfaces a-Physicochemical and Engineering Aspects, 1993. **79**(1): p. 105-114.

88) Chang, J.C., et al., *Centrifugal Consolidation of Al2o3 and Al2o3/Zro2 Composite Slurries Vs Interparticle Potentials - Particle Packing and Mass Segregation.* Journal of the American Ceramic Society, 1991. **74**(9): p. 2201-2204.

89) Chang, J.C., et al., *Pressure Sensitivity for Particle Packing of Aqueous Al2o3 Slurries Vs Interparticle Potential.* Journal of the American Ceramic Society, 1994. **77**(5): p. 1357-1360.

90) Channell, G.M. and C.F. Zukoski, *Shear and compressive rheology of aggregated alumina suspensions.* Aiche Journal, 1997. **43**(7): p. 1700-1708.

91) Channell, G.M., K.T. Miller, and C.F. Zukoski, *Effects of microstructure on the compressive yield stress.* Aiche Journal, 2000. **46**(1): p. 72-78.

92) de Kretser, R.G., P.J. Scales, and D.V. Boger, *Surface chemistry-rheology inter-relationships in clay suspensions*. Colloids and Surfaces a-Physicochemical and Engineering Aspects, 1998. **137**(1-3): p. 307-318.

93) de Kretser, R.G., et al., *Rapid filtration measurement of dewatering design and optimization parameters.* Aiche Journal, 2001. **47**(8): p. 1758-1769.

94) Aziz, A.A.A., et al., *The characterisation of slurry dewatering*. Water Science and Technology, 2000. **41**(8): p. 9-16.

95) Green, M.D., et al., *Pressure filtration technique for complete characterization of consolidating suspensions*. Industrial & Engineering Chemistry Research, 1998. **37**(10): p. 4152-4156.

96) Landman, K.A., J.M. Stankovich, and L.R. White, *Measurement of the filtration diffusivity D(phi) of a flocculated suspension*. Aiche Journal, 1999. **45**(9): p. 1875-1882.

97) Landman, K.A. and L.R. White, *Predicting filtration time and maximizing throughput in a pressure filter.* Aiche Journal, 1997. **43**(12): p. 3147-3160.

98) Landman, K.A., L.R. White, and M. Eberl, *Pressure Filtration of Flocculated Suspensions*. Aiche Journal, 1995. **41**(7): p. 1687-1700.

99) Landman, K.A. and L.R. White, *Solid/Liquid Separation of Flocculated Suspensions*. Advances in Colloid and Interface Science, 1994. **51**: p. 175-246.

100) Landman, K.A. and L.R. White, *Determination of the Hindered Settling Factor for Flocculated Suspensions.* Aiche Journal, 1992. **38**(2): p. 184-192.

101) Landman, K.A., C. Sirakoff, and L.R. White, *Dewatering of Flocculated Suspensions by Pressure Filtration*. Physics of Fluids a-Fluid Dynamics, 1991. **3**(6): p. 1495-1509.

102) Howells, I., et al., *Time-Dependent Batch Settling of Flocculated Suspensions*. Applied Mathematical Modelling, 1990. **14**(2): p. 77-86.

103) Johnson, S.B., A.S. Russell, and P.J. Scales, *Volume fraction effects in shear rheology and electroacoustic studies of concentrated alumina and kaolin suspensions.* Colloids and Surfaces a-Physicochemical and Engineering Aspects, 1998. **141**(1): p. 119-130.

104) Leong, Y.K., et al., *Rheological Evidence of Adsorbate-Mediated Short-Range Steric Forces in Concentrated Dispersions*. Journal of the Chemical Society-Faraday Transactions, 1993. **89**(14): p. 2473-2478.

105) Leong, Y.K., et al., *Interparticle Forces Arising from Adsorbed Polyelectrolytes in Colloidal Suspensions*. Colloids and Surfaces a-Physicochemical and Engineering Aspects, 1995. **95**(1): p. 43-52.

106) Leong, Y.K., et al., *Control of the Rheology of Concentrated Aqueous Colloidal Systems by Steric and Hydrophobic Forces.* Journal of the Chemical Society-

Chemical Communications, 1993(7): p. 639-641.

107) Wakeman, R.J., M.N. Sabri, and E.S. Tarleton, *Factors Affecting the Formation and Properties of Wet Compacts.* Powder Technology, 1991. **65**(1-3): p. 283-292.

108) Biggs, S., et al., *Molecular weight dependence of the depletion interaction between silica surfaces in solutions of sodium poly(styrene sulfonate)*. Langmuir, 2000. **16**(24): p. 9242-9248.

109) Yan, Y.D., et al., *The structure and strength of depletion force induced particle aggregate*s. Chemical Engineering Journal, 2000. **80**(1-3): p. 23-30.

110) Costello, B.A.D., et al., *Experimental Investigations of the Interaction Forces in Concentrated Dispersions.* Colloids and Surfaces a-Physicochemical and Engineering Aspects, 1993. **77**(1): p. 55-63.

111) Tadros, T.F., et al., *Investigation of Interaction between Polymer Stabilized Dispersions Using Viscoelastic and Force-Distance Measurements*. Abstracts of Papers of the American Chemical Society, 1992. **203**: p. 151-COLL.

112) Farrow, J.B., et al., *Consolidation and aggregate densification during gravity thickening.* Chemical Engineering Journal, 2000. **80**(1-3): p. 141-148.

113) Flesch, J.C., P.T. Spicer, and S.E. Pratsinis, *Laminar and turbulent shear-induced flocculation of fractal aggregates.* Aiche Journal, 1999. **45**(5): p. 1114-1124.

114) Guan, J., R. Amal, and T.D. Waite, *Effect of aggregate size and structure on specific resistance of biosolids filter cakes*. Water Science And Technology, 2001. **44**(10): p. 215-220.

115) Guan, J., et al., *Rapid determination of fractal structure of bacterial assemblages in wastewater treatment: Implications to process optimisation*. Water Science And Technology, 1998. **38**(2): p. 9-15.

116) Hermawan, M., et al., *Relationship between floc short range structure and sediment compaction*. Particle & Particle Systems Characterization, 2003. **20**(5): p. 327-334.

117) Hermawan, M., et al., *Characterisation of short-range structure of silica aggregates - implication to sediment compaction*. International Journal Of Mineral Processing, 2004. **73**(2-4): p. 65-81.

118) Lencki, R.W. and K. Riedl, *Effect of fractal flocculation behavior on fouling layer resistance during apple juice microfiltration*. Food Research International, 1999. **32**(4): p. 279-288.

Author's short biography

Simon Biggs

Simon Biggs was appointed to the RAEng/BNFL Chair at the University of Leeds in September 2002. He joined the University of Leeds from The University of Newcastle (New South Wales, Australia) where he had been a staff member for 8 years. Prior to this, he developed his research career through post-doctoral positions at the Institut Charles Sadron (Strasbourg, France) and the University of Melbourne (Australia).

The main research interests of Prof. Biggs' group are in the field of colloid and interface engineering. He has a strong interest in the measurement, control, and manipulation of inter-particle forces to allow more efficient process engineering of particulate systems. In related research, his group have a growing interest in the full 3-dimensional characterisation of adsorbed surfactant or polymer layers at the solid liquid interface. This research is being used to better understand adsorption mechanisms and adsorbed layer properties for these systems. In particular, we are interested in combining in-situ imaging with direct measurements of both adsorbed amounts and adsorption kinetics. His research involves both fundamental investigations, using precision instrumentation such as light scattering and atomic force microscopy, and applied problem solving related to industrial scale issues.

Simon Biggs has been the chief investigator on numerous research projects and he is an author of over 150 publications in refereed journals.

Gas-Phase Synthesis of Nanostructured Particulate Films[†]

K. Wegner[1]
*Tethis S.r.l.**
*Particle Technology Laboratory, Institute of Process Engineering, ETH Zurich***
E. Barborini
*Tethis S.r.l.**
P. Piseri and P. Milani
*INFM-Dipartimento di Fisica and Centro Interdisciplinare Materiali e Interfacce Nanostrutturati, Universita' di Milano****

Abstract

Nanostructured films find increasing industrial application for instance in membranes, gas sensors, fuel cells, catalytic layers, biocompatible surfaces, batteries, and electronic components. The performance of these functional layers can be improved by using nanoparticles as building blocks and thereby incorporating their extraordinary physical and chemical properties into the three-dimensional film structure.

This article presents an overview of recent research on gas-phase methods for the production of such nanostructured films. Nanoparticle synthesis, methods for gas-phase particle manipulation as well as particle deposition are addressed. Emphasis is placed on flame and hot wall reactors for nanoparticle production along with cluster-beam deposition techniques. Means for gas-phase particle size selection and nanoparticle beam formation by expansion nozzles, aerodynamic lenses or electric charging are introduced. It is highlighted how the deposition process can be controlled to yield either highly porous nanostructured films or precisely ordered arrays of 1D, 2D and 3D nanostructures to fabricate microsensors, catalytic microreactors or of semiconductor nanowires.

Keywords: Thin tilms, Nanoparticles, Aerosol synthesis, Cluster-beam deposition, Nanostructured coatings

1. Introduction

A wide variety of gas-phase techniques has been developed for the fabrication of films. Apart from physical vapor deposition (PVD), the most extensively studied processes are chemical vapor deposition (CVD), spray pyrolysis (droplet deposition) and thermophoretic deposition of particles for optical fiber production[1)]. The broad range of gas-phase technologies for film generation requires a categorization and restriction of the topic which is done here by the morphology of the deposited layers. Vapor and droplet deposition techniques usually result in films that are dense at the atomic level, while particle deposition processes usually give porous nanostructures consisting of individual nanoparticles (**Fig. 1**). The latter are the focus of this article.

The generation of nanostructured particulate films involves at least two steps, the formation of solid particles and the subsequent deposition on a substrate. In many processes, gas-phase modification or manip-

---

[†] Accepted : August 14, 2006

[*] Piazzetta Bossi 4, I-20121 Milano, Italy

[**] Sonneggstrasse, CH-8092 Zurich, Switzerland

[***] Via Celoria 16, 20133 Milano, Italy

[1] Corresponding author
TEL: +39-02-3656 8349 FAX: +39-02-3656 9183
Email: karsten.wegner@tethis-lab.com

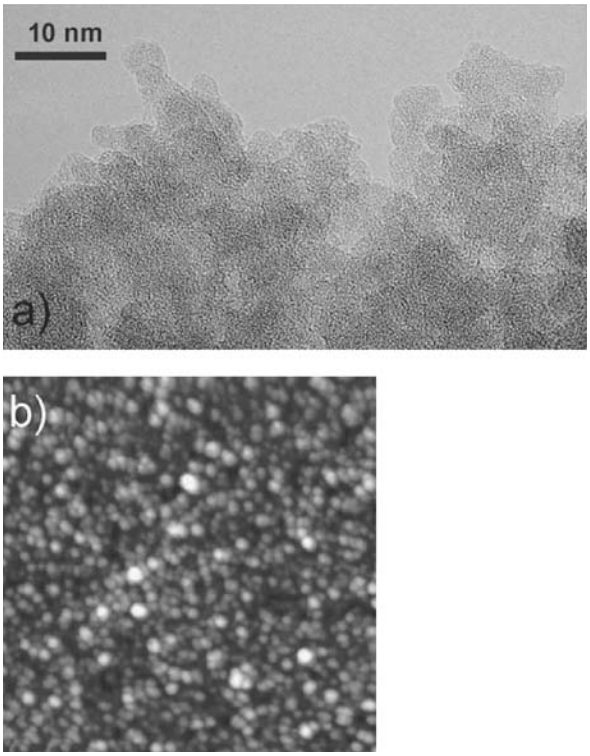

Fig. 1 Cross-sectional view of a nanostructured thin film made by cluster-beam deposition of titania nanoparticles. The transmission electron micrograph (a) and the 500 × 500 nm^2 atomic force microscopy image (b) reveal the particulate porous structure which is characteristic for films made the by gas-phase deposition of nanoparticles. Pictures adopted from Carbone et al.,[28].

ulation of the produced particles constitutes a third, intermediate step. The general term “manipulation” is used here with special reference to the following meanings: i) the ability to sort the objects in terms of a size or geometry classification; ii) the ability to control the position and sometimes the velocity of the nanoscale objects and iii) the ability to modify them physically or chemically. The need for the first ability is due to the fact that most of the available synthetic routes for the production of nanoparticles are not able to produce a perfectly monodisperse population. Depending on the specific application, a refinement of the particle population is often necessary. The second and third requisites are naturally connected with the fabrication of a class of systems exploiting the extraordinary properties of the nanoscale objects, namely the “nanodevices”. The possibility to integrate the particle production, manipulation and deposition stages into a continuous single process is one of the major advantages of the gas-phase route to nanostructured films that will be highlighted here.

Film formation by deposition of solid particles can be further categorized regarding the dominant deposition mechanism, namely inertial, thermophoretic and electrophoretic deposition. In inertial deposition, the inertia of typically accelerated particles is exploited. Thermophoretic deposition takes advantage of thermophoretic forces that act on particles when a temperature gradient is present, resulting in a momentum imbalance between the warmer and colder side of the particle and leading to particle deposition on cold surfaces. Electrophoresis is the deposition of charged particles in an electric field. Finally, a distinction can be made between vacuum and non-vacuum deposition processes.

2. Film Deposition Techniques

2.1 Non-vacuum approaches

This class of film formation routes involves gas-phase solid nanoparticle synthesis from liquid or gaseous precursors at or around atmospheric pressure and subsequent deposition on substrates. Due to deposition by thermophoresis, electrophoresis, diffusion or impaction with low kinetic energy, particles usually retain their shape so that the structural film properties depend on size and morphology control during particle synthesis.

The production of optical waveguide preforms is a prominent example for the industrial gas-phase manufacture of porous nanostructured films. Here, a flame torch is used to produce silica nanoparticles by introducing $SiCl_4$ into a CH_4/O_2 or H_2/O_2 diffusion flame. SiO_2 is synthesized by hydrolysis and/or direct oxidation, and rapidly condenses into solid primary particles which then grow by collision and coalescence to become hard agglomerates. The aerosol is then directed toward a deposition target where particles are primarily deposited by thermophoresis. The porous structures are later consolidated and drawn to form the optical fiber[2]. An alternative manufacturing route for silica optical fiber preforms is the modified chemical vapor deposition process (MCVD) [3]. Here, the reactants flow inside a tube that is heated externally by a flame moving back and forth. Reaction and particle formation occurs inside the tube at temperatures between 1500 and 1800℃. The hot aerosol then flows down the tube where the particles deposit on the wall of lower temperature[4].

An approach similar to MCVD was applied by Kodas et al.[5] for the production of thick superconducting ceramic wires and films. They sprayed a precursor solution into a hot wall reactor with oxygen carrier gas to form $Ba_2YCu_3O_7$ particles. These were deposited directly from the gas phase onto the inside surface of copper tubes and onto flat substrates to give wires and films, respectively. The advantages of this integrated gas-phase particle synthesis and deposition approach to superconducting layers over classical methods involving slurries or solid state reactions are higher purity, better chemical homogeneity, avoidance of microcrack formation and improved control of the oxygen content5).

Ostraat et al.6) designed a two-stage hot wall aerosol reactor with deposition chamber in order to integrate Si/SiO_2 nanoparticles into memory devices. Nanoparticle deposition was based on thermophoretic forces. Their deposition chamber was designed to produce a controllable particle density profile along the silicon water substrate where particles were deposited uniformly. Thereby, Ostraat et al.6) managed to overcome any concerns regarding particle contamination in microelectronic device fabrication, as particles typically create defects leading to device failure and introduce transition metal contamination that degrades performance. They successfully demonstrated that gas-phase nanoparticle and cluster production can be integrated with silicon-technology-based microelectronic device fabrication.

Also exploiting thermophoretic forces but using a flame process for particle synthesis, Skandan et al.7) directly deposited SiO_2 and SnO_2 nanoparticles on substrates placed in a stagnation flow configuration in front of the flame reactor. Both burner and substrate were placed in a low-pressure (< 5 kPa) chamber to reduce the drag force on the particles relative to atmospheric conditions. Deposition was dominated by thermophoretic forces that were as much as two orders of magnitude larger than the drag force. By controlling the substrate temperature through cooling and variation of the distance to the burner, either porous particulate deposits or dense films were formed.

Thybo et al.8) and Madler et al.9) applied atmospheric pressure flame spray pyrolysis for the production of multi-component nanoparticles that were deposited by thermophoresis on cooled substrates mounted above the flame. The highly porous layers were used as catalysts8) and gas sensors9), respectively. Madler et al.9) described film growth by a simple model accounting for particle deposition by diffusion and thermophoresis.

A gas-phase process relying on nanoparticle deposition by impaction was proposed by Kashu et al.10). Therefore, the aerosol produced by evaporation/condensation methods was expanded through a flow nozzle into a deposition chamber. Impaction occurred onto a temperature-controlled substrate that could be positioned in the chamber. Kashu et al.10) point out that the deposited films do not require any post-deposition heat treatment, as the particles made in a high-temperature gas-phase process are typically already crystalline. This has advantages especially for the production of homogeneous films consisting of several materials. Here, vacuum film deposition methods such as co-evaporation or co-sputtering would require a post-deposition heat treatment to achieve a crystalline film structure which could lead to phase segregation or rearrangement of the deposited layer.

Inertial deposition of nanoparticles was also applied by Adachi et al.11), preparing SnO nanoparticles in an aerosol flow reactor and forming gas-sensing layers on substrates equipped with electrodes. Therefore, the aerosol was expanded through a critical flow nozzle into a 30-Torr deposition chamber. The $2 \times 3\text{-mm}^2$ film had a thickness of about 40 μm and high porosity. Also, particulate zirconia-silver coatings were made using this approach12).

In electrophoretic deposition, nanoparticles are charged during or after gas-phase synthesis and brought into a region with an electric field that drives them to a surface where they deposit. The main motivation for using electrophoretic deposition is the high deposition efficiency that can be obtained1). Investigating the effect of an applied electric field on the deposition rate of flame-made silica nanoparticles, Hwang and Daily13) observed an increase of up to 35% over pure thermophoresis.

Often, electrophoretic deposition is combined with the use of a differential mobility analyzer that exploits the differences in the electrical mobility of charged particles to size-select a monodisperse fraction of a polydisperse aerosol. Wiedensohler et al.14) for instance, deposited size-selected charged Ag particles made by evaporation-condensation of silver onto InP structures for application in lasers. Kruis et al.15), Kennedy et al.16, 17) and Krinke et al.18, 19) also applied this combined size classification-electrophoretic deposition process, as is discussed in more detail in Chapter **3.1** of this article.

2.2 Vacuum techniques

Vacuum processes for solid-particle deposition usually rely on expansion techniques that pass particles in a gas through an orifice or nozzle, after which expansion takes place to give a beam of particles that can be deposited onto surfaces1). **Fig. 2** is a schematic of such a cluster-beam deposition (CBD) process. Generally, one can distinguish between neutral and ionized cluster-beam deposition. In ionized

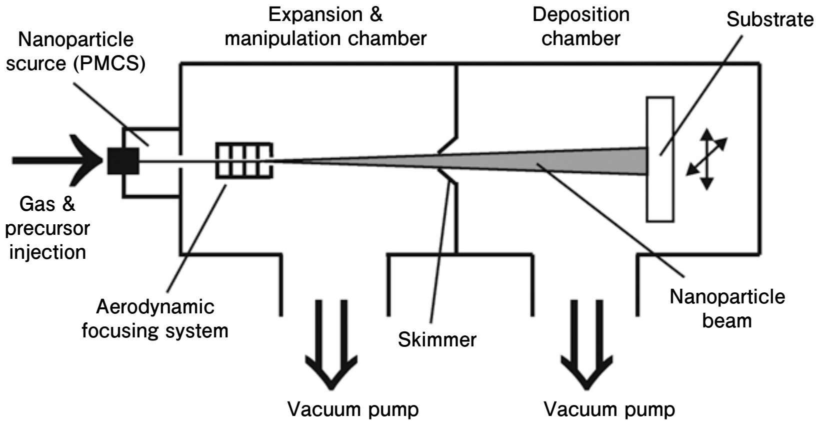

Fig. 2 Schematic of a cluster-beam deposition apparatus according to Barborini et al.[61]. Nanoparticles produced with a pulsed microplasma cluster source (PMCS, see **Fig. 3**) are first expanded through a nozzle into an expansion and manipulation chamber with aerodynamic focuser (see Chapter 3.2) and are then drawn through a skimmer into the differentially pumped deposition chamber where they are deposited onto the substrate. The substrate can be positioned in the xy-plane allowing the coating of large areas as well as position-selective deposition.

CBD, particles are formed by an expansion of a vapor into vacuum, which is followed by particle formation and subsequent charging. The charged particles are then accelerated in an electric field toward the substrate where they deposit[1]. Due to the acceleration, particles gain high kinetic energy which leads to extensive atomic migration and even breakage during impaction. The kinetic energy of the clusters can be controlled by the acceleration voltage. In neutral cluster-beam deposition, the particles are not ionized or accelerated in an electric field before deposition[1]. As a result, the particles acquire less kinetic energy and generally keep their shape upon impaction[20].

The starting vapor can be generated by a variety of means such as Joule heating of a material in a crucible, laser ablation, sputtering, or arc discharge[20, 21]. A broad range of materials including metals, metal oxides, and organics can be processed. Cluster sources can be catalogued by considering the regimes governing gas introduction and extraction: continuous or pulsed, effusive or supersonic. For cluster-beam deposition under vacuum conditions, a continuous gas flow must be compatible with stringent vacuum requirements and hence only effusive regimes are of practical interest. The realization and operation of pulsed cluster sources appears to be more complicated compared with continuous ones, but the reduced gas load has the advantage of allowing the use of a supersonic expansion regime and the compatibility with HV and UHV standards. An advantage of all CBD techniques is the separation between the particle formation region and the substrate, allowing deposition on temperature-sensitive materials such as polymers. These aspects are of fundamental importance for applications and in particular for the compatibility of CBD processes with microfabrication and planar technologies[22].

In order to improve the performance of cluster sources and to develop them toward a continuous process for fabrication of nanostructured coatings, the ablation plasma has to be confined to a well-defined target region, thus achieving high efficiency in material vaporization. Furthermore, the carrier gas load has to be kept low to avoid large pumping systems. Source geometry and dimensions should also be optimized to produce intense and stable cluster beams.

Pulsed microplasma cluster sources (PMCS) are an approach to fulfill these demands[23]. The working principle of PMCS is based on the spatially confined pulsed plasma discharge ablation of a target placed in a condensation chamber. The vaporized species is quenched by a pulse of inert gas and condenses to form clusters[24].

Schematically, the source consists of a ceramic body with a channel drilled through to perpendicularly intersect a larger cylindrical cavity (**Fig. 3**). The channel holds the target to be vaporized which typically is connected to the negative pole of a power source, thus acting as a cathode. The anode can be placed at any location inside the cavity or can also be introduced through the channel, opposite the cathode. A pulsed valve for introduction of inert carrier gas closes one side of the cavity while a nozzle is

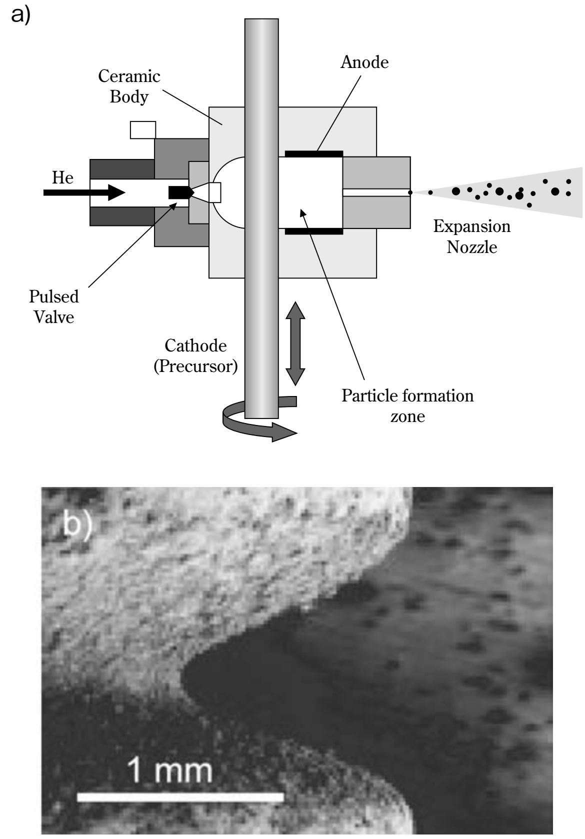

Fig. 3 Schematic of a pulsed microplasma cluster source (PMCS) according to Barborini et al.[23] (**Fig. 3a**). Inert gas is introduced through a pulsed valve into a cavity containing the target cathode. When a high voltage is applied between anode and cathode, material is sputtered from the cathode rod. The precursor vapor condenses into clusters which grow by coagulation, sintering and surface growth before they are extracted from the source through an expansion nozzle. **Fig. 3b** shows the ablation region of a rotating carbon cathode (adopted from Barborini et al. [23]). Continuous operation can be achieved by translational cathode movement.

located in the opposite cavity wall. The valve, backed with a high gas pressure, delivers inert gas pulses to the source cavity with an opening time of a few hundred microseconds. If the pulsed valve is closed, the source cavity is at the same pressure as the first vacuum chamber. Once the valve opens, the large pressure difference causes the formation of a supersonic gas jet directed against the cathode. A pulsed voltage (typical duration: 50 μs) applied between the electrodes ionizes the gas and generates a plasma. This is accelerated against the cathode and ablates the material that thermalizes and condenses to form clusters[23, 24]. Due to the aerodynamic confinement of the plasma in the cavity, the sputtering process is restricted to a cathode area of less than 1 mm^2[24]. A continuous process can be achieved by rotational and translational movement of the cathode (**Fig. 3b**). The pressure difference to the adjacent expansion chamber drives the aerosol expansion through the nozzle in the form of a supersonic beam.

For a graphite cathode, a log-normal cluster mass distribution in a range from a few tenths to several thousands of atoms per cluster with an average size of about 1000 atoms/cluster is obtained with the PMCS[25]. By operating the PMCS with a pulse frequency of 5 Hz, deposition rates of 100 μm/hour over a surface of 1 cm^2 placed at 500 mm from the exit of the nozzle can be achieved. The introduction of precursors into a PMCS, the use of alloy electrodes and the combination of several PMCS in one deposition apparatus easily allow formation of doped or multi-component films of controlled composition. By changing the particle synthesis conditions, the nanoparticle size, morphology, crystallinity and chemistry can be tuned to meet the desired film properties. Random stacking of clusters leads to a high porosity texture with mesoscale granularity characterized by pores in the range of 2-50 nm and high specific surface area[26].

PMCSs have been used for the production of devices such as supercapacitors[27], gas sensors[22, 26] or high-throughput screening arrays for biological applications[28]. PMCSs can be equipped with focalization devices as will be described in Section **3.2** in order to further improve cluster-beam intensity and patterning capabilities[29].

3. Gas-phase Manipulation and Patterning

A crucial point to be solved for a real technological breakthrough of the bottom-up approach to nanotechnology is the possibility to modify and manipulate nanoparticle building blocks prior to their assembly into nanodevices. Particle composition, crystallinity, size and morphology can be controlled to a certain extent in the synthesis step. Depending on the application, a post-synthesis functionalization or passivation of the particle surface might be necessary as well as a refinement of the particle size distribution, as gas-phase synthesis does not usually give monodisperse particles. Particle size and morphology also affect the porosity and roughness of the deposited layers, underlining the importance of size and morphology control. For the assembly of films by nanoparticle deposition, positioning of the nanoparticles on the substrate surface is of importance as it directly affects film homogeneity or the ability of patterned deposition with high lateral resolution.

3.1 Particle size separation

A narrow size fraction can be extracted from a polydisperse aerosol by a differential mobility analyzer (DMA)[30-32]. The DMA operates as an electrostatic classifier that selects charged particles of a certain size based on the balance between drag and opposing electric forces in an electric field. The size of the extracted particles can be controlled by varying the electric field strength[33, 34].

Kennedy et al.[16, 17] integrated a DMA along with an in-flight annealing zone into their process for production of nanostructured tin oxide films for gas sensing applications. Nanoparticles were produced from sublimated SnO in an aerosol flow condenser, followed by aerosol charging and DMA size fractionation. The size-classified aerosol was introduced into a second furnace for sintering, crystallization and partial oxidation to SnO_x nanoparticles that were deposited on a gas sensor substrate with interdigitized electrodes using an electrostatic precipitator or a low-pressure impactor. Nanostructured porous films of quasi monosized nanoparticles were grown and heat-treated to form conducting necks between the particles for better charge transfer in the gas-sensor application. The process of Kennedy et al.[16, 17] illustrates the possibility of integrated gas-phase production of nanostructured particulate films with a series of individually controllable particle manipulation steps. Such an integrated process was also used, e.g. by Kruis et al.[15] for the gas-phase preparation of size-classified PbS nanoparticles and by Krinke et al.[18, 19] for patterned nanoparticle deposition.

An alternative means for particle size separation in the gas phase is by exploiting aerodynamic effects. As an aerosol jet is forced by an obstacle to make a sharp (e.g. 90°) turn, particles will follow the gas flow depending on their inertia (**Fig. 4**). If the inertia exceeds the drag action of the gas flow, particles are unable to follow the stream lines and impact on the surface of the obstacle. The parameter governing particle impaction is the Stokes number which is defined as the ratio of the particle stopping distance τ at the average velocity of the initial jet U to the jet radius $D_j/2$:

$$St = \frac{\tau \cdot U}{D_j/2} = \frac{\rho_p d_p^2 U C_C}{9\eta D_j},$$

where ρ_p and d_p are the particle density and diameter, respectively, C_c is the Cunningham correction factor and η is the dynamic viscosity of the gas[33]. In aerosol science, this effect has long been used in cascade impactors for size-selective particle sampling on collection plates[33, 34].

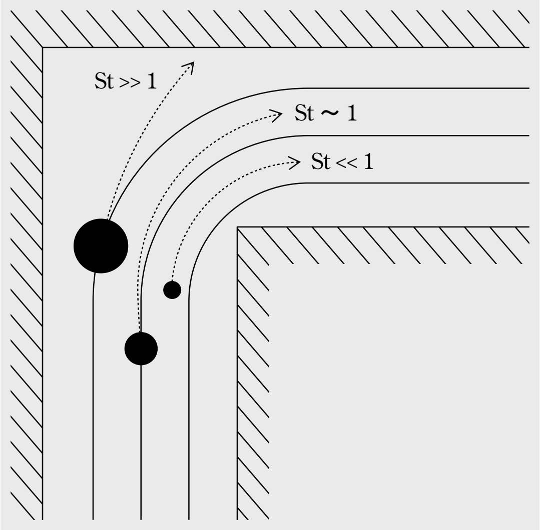

Fig. 4 Basic principle of aerodynamic size-selection and focusing. The inertia of large particles (St >> 1) exceeds the drag action of the gas, separating the particle trajectories from the gas stream lines and leading to wall deposition. Very small particles (St << 1) closely follow the flow. Intermediate size particles have trajectories only slightly decoupled from the stream lines, which can be exploited to concentrate particles at given positions in the flow field[29].

3.2 Particle focusing

Aerodynamic effects can also be used to concentrate particles at given positions in the flow field. **Fig. 5** shows that the trajectory of particles with St ≈ 1 only slightly decouples from the gas stream lines. This effect can be used to focus particles to a beam. Using only aerodynamics effects induced by nozzles, Liu et al.[35, 36] produced such an enriched stream of particles. This was achieved with a system of so-called aerodynamic lenses consisting of successive axis-symmetric contractions-enlargements of the aerosol flow passage (**Fig. 5**). The work of Liu et al.[35, 36] was inspired by the research carried out by Fernandez de la Mora and co-workers[37, 38], who revealed the possibility of particle focusing and the existence of a common focal point for the near-axis particles when expanding an aerosol through a thin-plate orifice. The novelty of the work of Liu et al.[35, 36] is that they employed thin-plate orifices in a confined passage to manipulate the spatial distribution of particles prior to the nozzle and the subsequent free jet expansion (**Fig. 5**).

The integration of an aerodynamic focusing device into CBD leads to particle beams of high directionality, collimation and intensity. Depending on the mag-

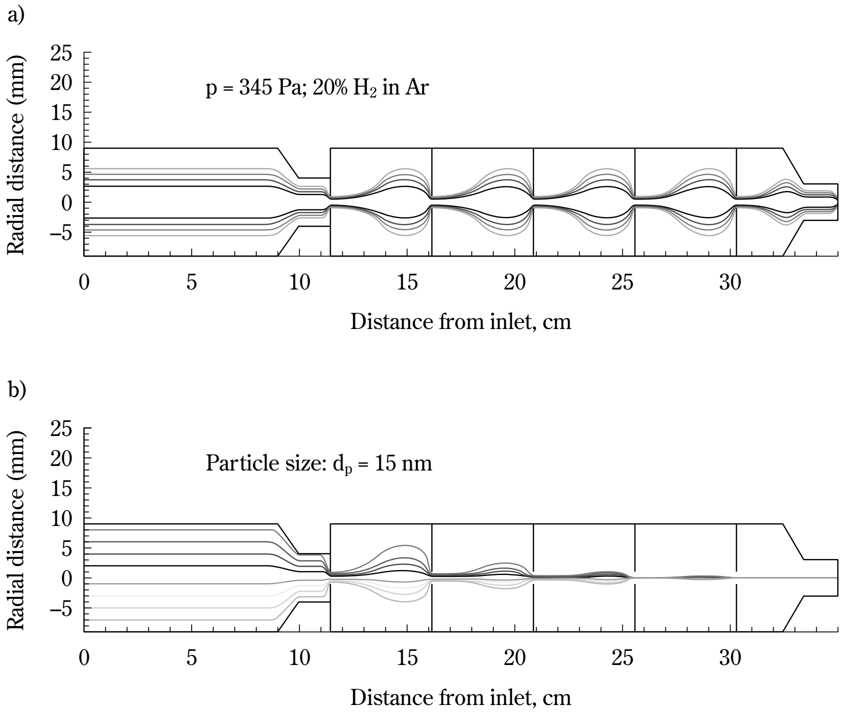

Fig. 5 Simulation of the gas flow (a) and trajectories of 15-nm particles (b) in an aerodynamic lens system[62] according to di Fonzo et al.[42]. The particles are concentrated at the center axis of the lens system, forming a beam.

nitude of focusing and the focuser-substrate distance, the beam diameter at the substrate can be reduced from several centimeters to a few millimeters. By substrate movement with a translational stage, nanostructured particulate films can be deposited over relatively large areas.

3.3 Patterned deposition

The fabrication of functional devices based on nanostructured materials often requires the ability to assemble nanoparticles in micrometer and submicrometer patterns with high precision and compatibility with planar technology. Physical and chemical vapor deposition techniques have long been used for the patterning of semiconductor, metallic and polymeric films and for the production of dot arrays[39-41]. These techniques require putting resists or stamps in contact with a substrate that undergoes different pre- or post-deposition etching or thermal treatments.

The effect of such treatments on particle-assembled films has not been investigated systematically, however, several problems due to the porosity and granularity of nanostructured layers can be expected. For nanostructured films, a non-contact patterning would thus be highly desirable, and, in principle, it would be viable, e.g. by depositing particle beams on a substrate through a stencil mask.

Due to their high directionality, collimation and intensity, supersonic cluster beams are well-suited for the patterned deposition of films through masks that are placed into the beam in front of the substrate (**Fig. 6**)[42, 43]. Structures with a high aspect ratio and controlled shape arranged in ordered arrays can be created on any kind of substrate. For instance, Milani and co-workers deposited patterns on silicon, aluminum, copper, stainless steel, and polyethylene[43,44]. Structures with heights up to several tens of micrometers could be grown on metallic and polymeric substrates while heights of several micrometers were realized on silicon[43]. The lateral resolution was in the sub-micrometer range and depended not only on the sharpness of the mask edges but also on the beam collimation. A remarkably high step sharpness was obtained by Barborini et al.[43]: the width of the step from 10% to 90% of film height was 450 nm when using a mask placed 0.33 mm in front of the substrate. The profile of the mask was reproduced even in its sub-micrometer features. Di Fonzo et al.[42] used an aerodynamic lens assembly for the deposition of SiC and Ti pillars and lines. Nanoparticles of these materials were synthesized by introducing gaseous precursors into an argon-hydrogen plasma and ex-

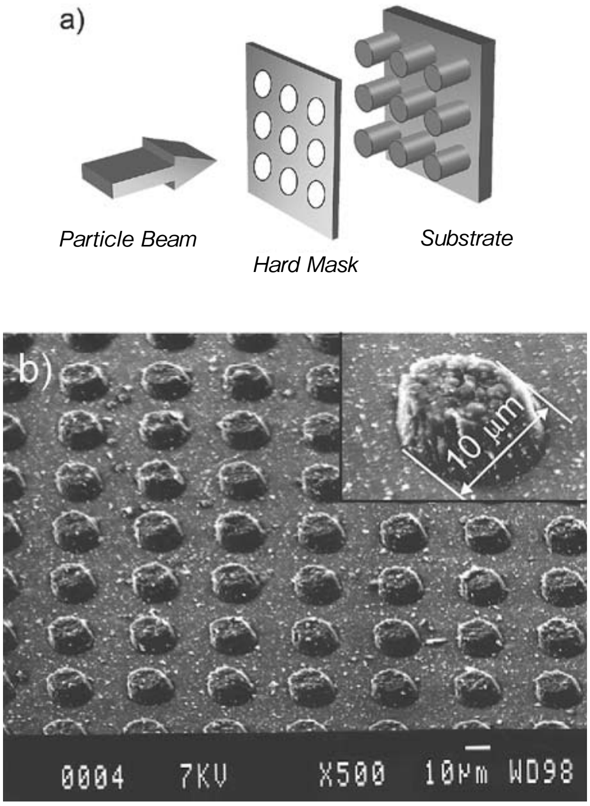

Fig. 6 Placing a hard mask into the particle beam at some distance from the substrate (a) allows the deposition of patterned films, for instance made out of carbon (b)[43].

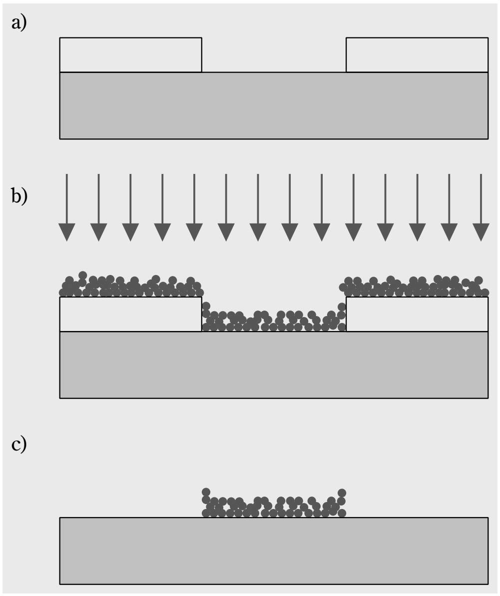

Fig. 7 Schematic for selective area coating of substrates with catalyst nanoparticles using a photoresist [8]: (a) deposition of photoresist; (b) deposition of catalyst nanoparticles on the entire surface; (c) removal of the catalyst from selected areas by dissolving the photoresist layer.

panding the plasma supersonically through a nozzle. The aerodynamic lens system was placed about 75 cm from the expansion nozzle. The highly collimated particle beam exiting the lens system was deposited on a substrate downstream of the exit nozzle without any masks.

For gas-phase deposition of nanoparticles that travel at moderate velocity rather than at supersonic conditions, other patterning mechanisms have been developed based on low-range attractive forces, i.e., thermophoretic and electrostatic forces. Patterning with hard masks has been applied for the deposition of nanoparticles from the aerosol plume of flame reactors by thermophoresis and diffusion[8, 9]. Thybo et al.[8] used a lift-off process with a standard photolithographic mask to fabricate porous nanoparticulate catalytic layers for microreactors. **Fig. 7** shows how the substrate was first spin-coated with a 1.5-μm-thick layer of photosensitive polymer where the regions for deposition were afterwards dissolved in a NaOH solution. Then, the water-cooled substrate was positioned above the flame of an aerosol reactor to deposit a porous 50-150 μm layer of nanoparticles by thermophoresis and diffusion. Finally, the photoresist was dissolved in acetone, whereby the catalyst particles on the photoresist were removed from the sample. Although the roughness of the pattern edges was below 100 μm, the submicrometer resolution of the cluster-beam deposition approach could not be reached.

An approach for the patterned deposition by electrophoresis is the creation of a charge pattern on the substrate in a first stage and the subsequent deposition of charged particles. Krinke et al.[18, 19] created charge patterns using polydimethylsiloxane (PDMS) stamps to deposit monodisperse singly charged nanoparticles on oxidized silicon surfaces. With this technique, they were able to form particle-based nanowires with a thickness down to 100 nm and spaced 2000 nm apart.

3.4 Physical and chemical modification

Basically, all gas-phase processes involving particle formation and in-situ surface coating or functionalization can be coupled with one of the deposition methods described above. Most research in the field has focused on obtaining a powder rather than a film, though. The studies of Kodas and co-workers give examples showing how the particle composition and morphology can be changed by in-situ gas-phase coating processes in hot-wall reactors[45-47]. The formation of functional coatings on oxide nanoparticles can also be achieved by introduction of multiple precursors into spray flames[48]. Such multicomponent particles were deposited on substrates directly from the gas-phase to give nanoparticulate films for gas sensing[9] or catalysis[8].

Effective post-synthesis treatment of nanoparticles has been demonstrated, for instance, for the morphology control of initially produced gold agglomerates by in-flight high temperature annealing and sintering[49, 50]. Nanda et al.[51] used this method for band-gap tuning of PbS nanoparticles in tubular flow reactors. Kennedy et al.[16, 17] and Ostraat et al.[6] integrated a post-synthesis oxidation stage to convert SnO into SnOx nanoparticles and to passivate Si nanoparticles with an oxide layer, respectively.

In-flight nanoparticle coating prior to deposition in an electrostatic precipitator was demonstrated by Karlsson et al.[52]. Here, Au nanoparticles were produced first by evaporation-condensation with subsequent annealing similar to Magnusson et al.[49], and then coated with Ga. For this purpose, a ceramic boat containing Ga metal was placed inside a third furnace downstream of the sintering furnace (**Fig. 8**). The Ga vapor was transported out of the evaporation furnace together with the flow of the Au aerosol. As the vapor left the hot zone it became supersaturated and condensed upon the Au particles. Au – Ga compound particles were thus formed through heterogeneous nucleation with the Au cores acting as condensation nuclei.

4. Applications of Nanoparticulate Films

Clusters and nanoparticles of metals, carbon and semiconductors have been extensively studied in the gas phase with particular attention to their electronic, optoelectronic, optical, and magnetic properties, as is apparent from recent comprehensive reports that also address nanostructured films[21, 53, 54]. Here, applications in catalysis and biotechnology are introduced briefly while the fabrication of gas sensors is discussed in more detail.

4.1 Gas sensors

Gas sensors are a prominent, example of functional materials where the use of nanoparticles was shown to significantly improve the performance[16]. Comparing the sensitivity of dense nanoparticulate films with that of porous films, Ogawa et al.[55] observed a greatly increased sensitivity for ethanol of the latter structure. This was explained on the basis of Hall measurements, which showed that the carrier mobility is strongly dependent on the ethanol concentration for the porous nanocrystalline films while no dependence was found for the dense film. The high specific surface area of nanostructured particulate films is usually easily accessible for gases due to the high porosity (up to 98%,[9]), allowing fast transport of the adsorbing and desorbing species. The use of masks has been demonstrated successfully, confining particle deposition to the sensing area of a single element[9, 26] or even for the production of entire libraries with 210 gas sensors in one step (**Fig. 9**)[22]. Furthermore, the possibility to obtain homogeneous and crack-free sensing layers[9] makes gas-phase nanoparticle synthesis with direct deposition a promising manufacturing route for solid state gas sensors.

Here, the fabrication of gas sensors with nano-

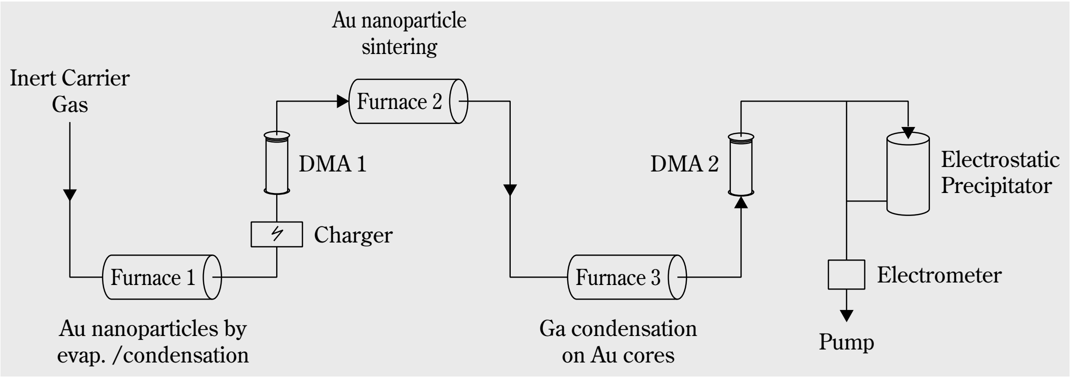

Fig. 8 Schematic of the experimental set-up used for Au-Ga alloy aerosol nanoparticle production[52]. Au nanoparticles are formed by evaporation/condensation in furnace 1. A narrow size fraction is extracted from the aerosol with a differential mosility analyzer (DMA 1) and is introduced into an in-flight sintering zone (furnace 2). Ga is evaporated in furnace 3 and condenses onto the Au particles. After a second size classification (DMA 2), the charged aerosol is deposited on substrates in an electrostatic precipitator. Schematic adopted from Karlsson et al.[52].

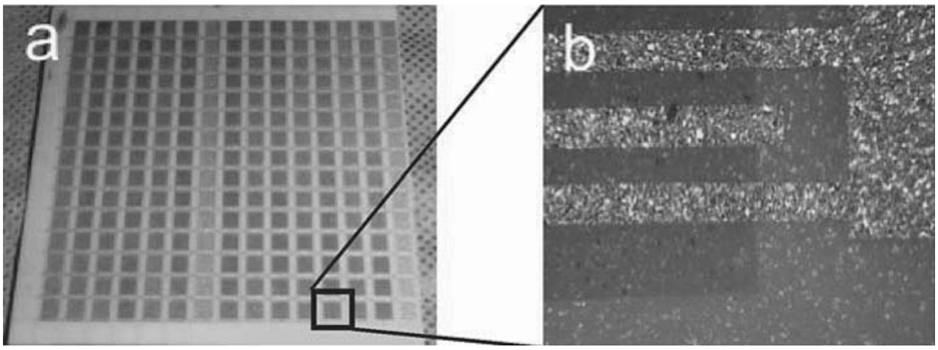

Fig. 9 Array of 210 titania gas sensors made by cluster-beam deposition with hard mask patterning[22].

structured TiO_2, WO_3 and SnO_2 sensing layers by supersonic cluster-beam deposition and their performance in the detection of volatile organic compounds (VOC) and gases related to environmental pollution (such as NOx) are reported.

A supersonic cluster-beam deposition apparatus (SCBD, **Fig. 2**) was used to generate and deposit nanoparticles on gas sensor substrates. Clusters of titanium, tungsten and tin were generated by a pulsed microplasma cluster source (PMCS)[23] as described in Section **2.2** and **Fig. 3a**. Therefore, a high-purity metal rod (6 mm diameter, approx. 10 cm length) of the material to be deposited was inserted into the PMCS cavity (diameter ~ 1.2 cm), attached to a rotational stage and connected to the negative pole of a high-voltage power supply. Pulses of argon were introduced into the cavity by means of a solenoid valve, operated at a frequency of 10 Hz. With a few hundred microseconds delay, an electric discharge triggered by the valve was used to ignite a plasma jet impinging on the metallic rod and ablating material that vaporized and condensed into metallic nanoparticles. These were entrained by the gas flux toward the PMCS exit nozzle and expended into the adjacent expansion chamber kept at differential vacuum (10^{-3} mbar).

A set of 5 aerodynamic lenses as shown in **Fig. 5**[35, 36] installed on the same axis as the expansion nozzle near the inlet of the expansion chamber was used to concentrate the nanoparticles onto the center axis, forming a collimated particle beam with less than 20 mrad divergence. The particle beam entered the differentially pumped deposition chamber through a skimmer with a 2-mm opening, impinging on the substrate through a hard mask (**Fig. 6a**). The substrate was kept at room temperature and could be positioned by a 4-axis motorized manipulator that even allowed large-area (50×220 mm^2) depositions by substrate rastering.

The sensor substrates were made of micro-machined alumina with integrated thin film heater and Pt thin-wire thermometer for temperature control during sensor operation. Micro-machined platforms having an array structure (**Fig. 10a**) were used to deposit different oxides on each single element of the array by exploiting hard mask patterning. After cluster deposition, the substrates were annealed in air at 400°C in order to obtain the proper oxide stoichiometry as well as a nanostructure and crystallinity that is stable during sensor operation up to 300°C. **Fig. 10b** shows an array of four sensing elements (TiO_2, WO_3, SnO_2 and one blank element for reference) after annealing and connected to signal read-out and analysis electronics.

The as-deposited films had an amorphous and porous structure at the nanoscale, attributed to particle impact with low kinetic energy and limited diffusion. After annealing, the amorphous grains rearranged into a crystalline structure. For example, **Fig. 11** shows transmission electron microscopy (TEM) images of as-deposited (**Fig. 11a**) and 200°C-annealed (**Fig. 11b**) tungsten oxide films. The as-deposited material was composed of nanoparticles with an average size of about 10 nm. No lattice fringes were discernible, indicating an amorphous structure. After annealing, a number of nanoparticles showed crystal lattices, indicating the transformation into a polycrystalline film, while average particle size and film morphology appeared to be largely unaffected.

The sensing properties of the films were evaluated for CO, NO, NO_2, and SO_2, as well as for ethanol. By means of an automatic mass-flow-controller-based gas mixing system, these compounds were added at trace level to pure dry air flowing into a test chamber. An electrometer was used to measure the current across the film during the test sequence. **Fig. 12** shows

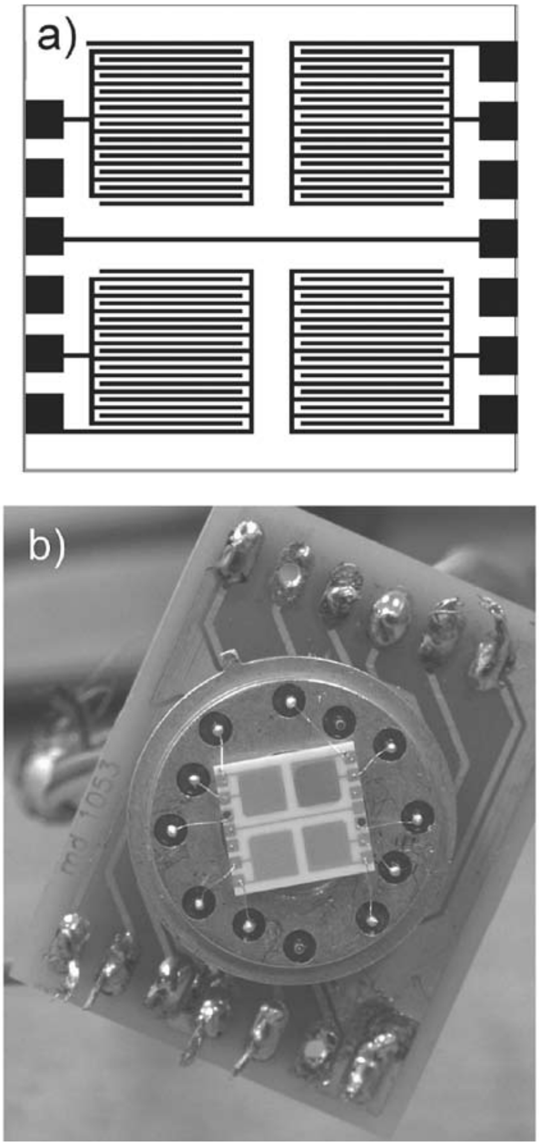

Fig. 10 (a) Schematic of the front side of a micro-machined substrate for a 2×2 gas sensor array showing the interdigitized electrodes and a Pt thin wire thermometer in the center. (b) The gas sensor array after thin film deposition and annealing with electronic connections for signal read-out.

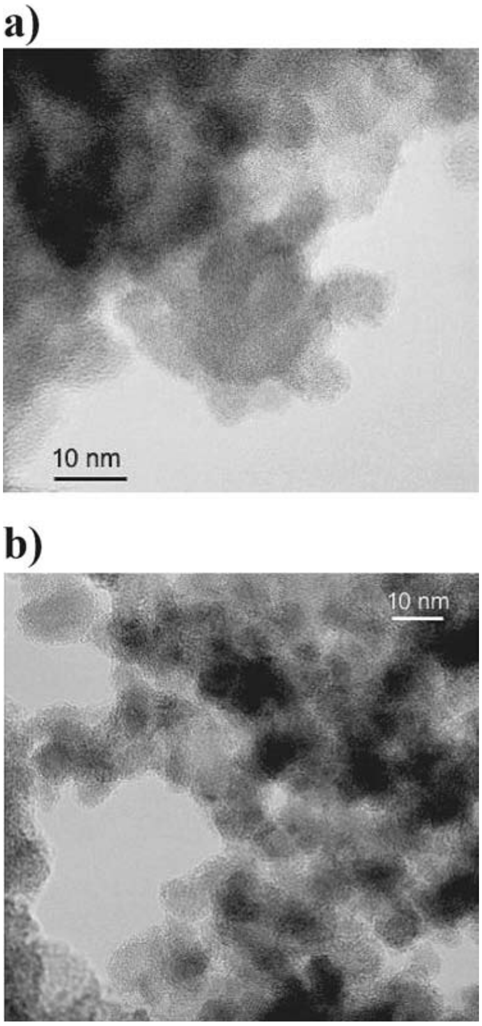

Fig. 11 (a) TEM image of the as-deposited tungsten oxide sample. The film is composed of amorphous nanoparticles having an average size of 10 nm, assembled in a porous structure. (b) The same material after annealing at 200°C. Lattice fringes appear, indicating the polycrystalline nature of nanoparticles, while average size and porous structure remain similar to those of the as-deposited material.

examples of the gas sensor performance, namely the response of the SnO_2, WO_3 and TiO_2 sensors to SO_2, NO_2, and ethanol, respectively. The titania film was doped with Pd in a two-step multi-layer deposition process involving two cluster sources. All sensors showed a fast response to trace gas injection. NO_2 was detected by WO_3 at the ppm level (**Fig. 12b**), while SO_2 and ethanol were registered with an accuracy of about 5 ppm by SnO_2 and Pd/TiO_2 sensors, as is shown in **Figs. 12a** and **12c** respectively.

The realization of complex sensor arrays with a large range of materials and material compositions by cluster-beam deposition and hard mask patterning in combination with neural network analysis for signal read-out might be a promising route to the efficient and inexpensive realization of gas microsensors, e.g. for environmental monitoring.

4.2 Catalysis

Applications in heterogeneous catalysis benefit from the high specific surface area and porosity of nanostructured particulate films[8]. Even though the coating of large-area supports has not been reported yet, methods such as flame spray deposition are promising techniques for depositing porous catalyst layers directly into microsystems by using masks[8]. Cluster-beam deposition has been used to coat 10×10 mm^2 glass substrates with Ti-Si binary oxide films

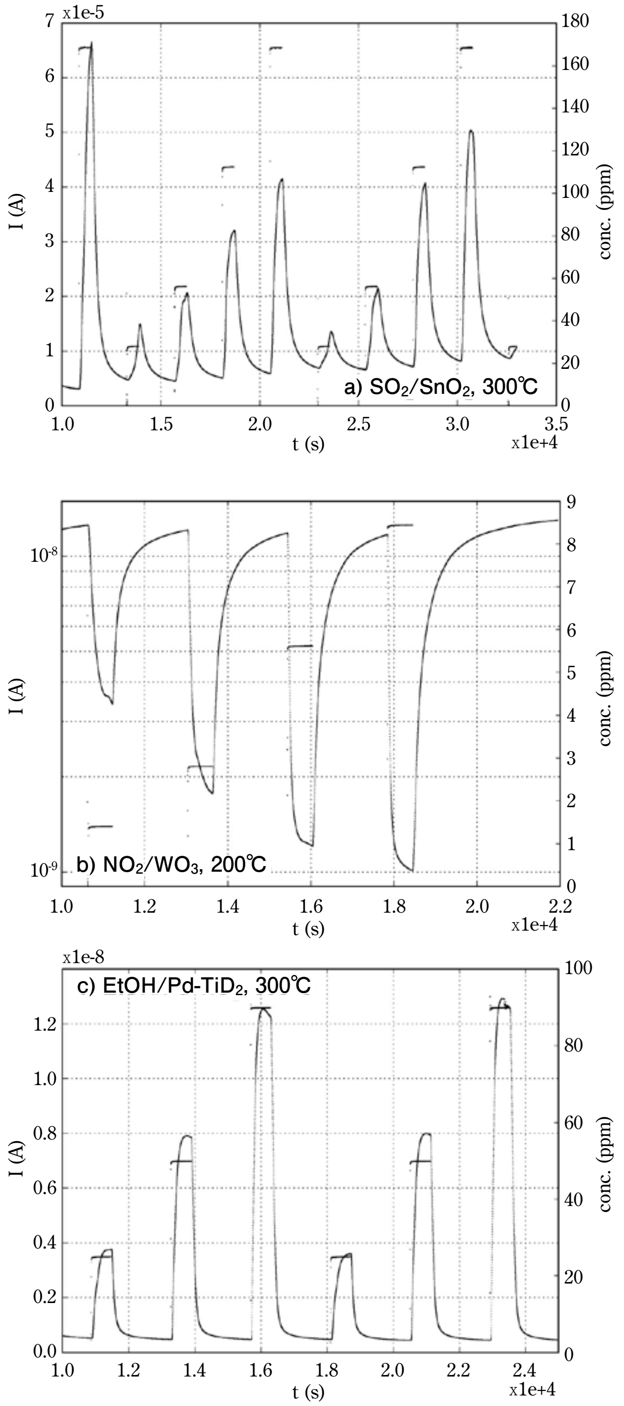

Fig. 12 Response of nanostructured films of (a) SnO_2 to SO_2 at 300°C, b) WO_3 to NO_2 at 200°C and c) Pd/TiO_2 to ethanol at 300°C. The current across the films was measured at fixed voltage by an electrometer.

for photocatalytic decomposition of NO under UV light radiation[56]. Zhou et al.[57] used combined cluster-beam deposition and metal ion implantation to produce nanostructured vanadium-doped TiO_2 films that showed photocatalytic decomposition of formic acid even under visible light radiation. Furthermore, cluster-beam deposition techniques can be employed to manufacture model catalysts by deposition of single monosize clusters for fundamental studies on heterogeneously catalyzed chemical reactions[58-60].

4.3 Biotechnology

In biotechnological applications, the surface roughness of nanostructured particulate films can be exploited. Carbone et al.[28] characterized the biocompatibility of nanostructured TiO_2 films produced by the deposition of a supersonic beam of TiO_x clusters. The cluster-assembled film supported normal growth and adhesion of primary and cancer cells with no need for coating with extracellular matrix proteins. Physical analysis showed that the films possess a nanoscale granularity and porosity mimicking that of typical extracellular matrix structures and adsorption properties that could allow surface functionalization with different macromolecules such as DNA, proteins, and peptides. Films of nanostructured titania are proposed as an optimal substrate for different applications in cell-based assays, biosensors, bioactive orthopedic, dental and vascular implants or microfabricated medical devices. Patterned deposition could be applied for the fabrication of microarrays for proteomics, genomics and post-genomic applications.

5. Conclusions

Gas-phase technology has been shown to offer versatile techniques for one-step synthesis of nanostructured particulate films. A range of gas-phase routes are available for nanoparticle synthesis such as flame, plasma or evaporation/condensation that are already employed for commercial manufacture of nanoparticles. Post-synthesis in-flight annealing, coating and functionalization has been demonstrated as well as particle size selection and focusing. Hard mask techniques adopted from microfabrication technology have been successfully applied for the generation of 1-, 2-, and 3-D nanoparticulate patterns. Deposition rates of several mm/min for non-vacuum “aerosol” approaches allow the growth of thin particulate films (< 1 μm) within seconds and also make deposition of thick films (> 10 μm) commercially feasible. Compared to standard thick film technology such as screen printing or tape casting, gas-phase techniques do not involve the intermediate steps of paste or slurry generation and are not prone to crack formation[7].

Vacuum techniques such as cluster-beam deposition offer nanoparticle deposition with high lateral resolution as well as compatibility with silicon-based microfabrication technologies. A drawback of many vacuum techniques is the low nanoparticle production rate or the requirement of huge pumping capacities. A combination of aerosol and vacuum approaches might thus lead to the integration of nanofabrication and microfabrication at an industrial level, as was indicated by the example of solid state gas sensors.

References

1) Kodas, T.T. and Hampden-Smith, M.: Aerosol Processing of Materials, Wiley-VCH, New York, 1999.
2) Bautista, J.R. and Atkins, R.M.: The formation and deposition of SiO_2 aerosols in optical fiber manufacturing torches, J. Aerosol Sci., **22**, 1991, 667-675.
3) MacChesney, J.B. and O'Connor, P.B. and Presby, H.M.: A new technique for the preparation of low-loss and graded index optical fibers, Proc. IEEE, **62**, 1974, 1280-1281.
4) Kasik, I. and Matejec, V.: New ways for influencing thermophoretic efficiency in the MCVD process, J. Aerosol Sci., **26**, 1995, 399-406.
5) Kodas, T.T., Engler, E.M. and Lee, V.Y.: Generation of thick $Ba_2YCu_3O_7$ films by aerosol deposition, Appl. Phys. Lett., **54**, 1989, 1923-1925.
6) Ostraat, M.L., De Blauwe, J.W., Green, M.L., Bell, L.D., Atwater, H.A. and Flagan, R.C.: Ultraclean two-stage aerosol reactor for production of oxide-passivated silicon nanoparticles for novel memory devices, J. Electrochem. Soc., **148**, 2001, G265-G270.
7) Skandan, G., Glumac, N., Chen, Y.-J., Cosandey, F., Heims, E. and Kear, B.H.: Low-pressure flame deposition of nanostructured oxide films, J. Am. Ceramic Soc., **81**, 1998, 2753-2756.
8) Thybo, S., Jensen, S., Johansen, J., Johannessen, T., Hansen, O. and Quaade, U.J.: Flame spray deposition of porous catalysts on surfaces and in microsystems, J. Catal., **223**, 2004, 271-277.
9) Mädler, L., Roessler, A., Pratsinis, S.E., Sahm, T., Gurlo, A., Barsan, A. and Weimar, U.: Direct formation of highly porous gas-sensing films by in situ thermophoretic deposition of flame-made Pt/SnO_2 nanoparticles, Sensors Actuators B, **114**, 2006, 283-295.
10) Kashu, S., Fuchita, E., Manabe, T. and Hayashi, C.: Deposition of ultra fine particles using a gas jet, Jap. J. Appl. Phys., **23**, 1984, L910-L912.
11) Adachi, M., Okuyama, K., Kousaka, Y. and Tanaka, H. : Preparation of gas sensitive film by deposition of ultrafine tin oxide particles, J. Aerosol Sci., **19**, 1988, 253-263.
12) Adachi, M., Okuyama, K., Moon, S., Tohge, N. and Kousaka, Y.: Preparation of ultrafine zirconium dioxide particles by thermal decomposition of zirconium alkoxide vapor, J. Mater. Sci., **24**, 1989, 2275-2280.
13) Hwang, J. and Daily, J.W.: Electric field enhanced deposition in flame synthesized materials manufacturing, J. Aerosol Sci., **26**, 1995, 5-18.
14) Wiedensohler, A., Maximov, I., Samuelson, L. and Hansson, H.-C.: Formation of nanometer-sized columns in InP using ultrafine aerosol and dry-etching techniques, J. Aerosol Sci., **24**, 1993, 555-558.
15) Kruis, F.E., Nielsch, K., Fissan, H., Rellinghaus, B. and Wassermann, E.F.: Preparation of size-classified PbS nanoparticles in the gas phase, Appl. Phys. Lett., **73**, 1998, 547-549.
16) Kennedy, M.K., Kruis, F.E. , Fissan, H., Mehta, B.R., Stappert, S. and Dumpich, G.: Tailored nanoparticle films from monosized tin oxide nanocrystals: Particle synthesis, film formation, and size-dependent gas-sensing properties, J. Appl. Phys., **93**, 2003, 551-560.
17) Kennedy, M.K., Kruis, F.E., Fissan, H., Nienhaus, H., Lorke, A. and Metzger, T.H.: Effect of in-flight annealing and deposition method on gas-sensitive SnOx films made from size-selected nanoparticles, Sensors Actuators B, **108**, 2005, 62-69.
18) Krinke, T.J., Fissan, H. and Deppert, K., Magnusson, M.H., Samuelson, L.: Positioning of nanometer-sized particles on flat surfaces by direct deposition from the gas phase, Appl. Phys. Lett., **78**, 2001, 3708-3710.
19) Krinke, T.J., Deppert, K., Magnusson, M.H. and Fissan, H.: Nanostructured deposition of nanoparticles from the gas phase, Part. Part. Syst. Char., **19**, 2002, 321-326.
20) Milani, P. and Iannotta, S.: Cluster Beam Synthesis of Nanostructured Materials, Springer, Berlin, 1999.
21) Bansmann, J., Baker, S.H., Binns, C., Blackman, J.A., Bucher, J.-P., Dorantes-Davila, J., Dupuis, V., Favre, L., Kechrakos, D., Kleibert, A., Meiwes-Broer, K.-H., Pastor, G.M., Perez, A., Toulemonde, O., Trohidou, K.N., Tuaillon, J. and Xie, Y.: Magnetic and structural properties of isolated and assembled clusters, Surf. Sci. Rep., **56**, 2005, 189-275.
22) Mazza, T., Barborini, E., Kholmanov, I.N., Piseri, P., Bongiorno, G., Vinati, S., Milani, P., Ducati, C., Cattaneo, D., Li Bassi, A., Bottani, C.E., Taurino, A.M. and Siciliano, P.: Libraries of cluster-assembled titania films for chemical sensing, Appl. Phys. Lett., **87**, 2005, 103108.
23) Barborini, E., Piseri, P. and Milani, P.: A pulsed microplasma source of high intensity supersonic carbon cluster beams, J. Phys. D: Appl Phys., **32**, 1999, L105-L109.
24) Vahedi Tafreshi, H., Piseri, P. and Benedek, G. and Milani, P.: The role of gas dynamics in operation conditions of a pulsed microplasma cluster source for nanostructured thin films deposition, J. Nanosci. Nanotechnol., **6**, 2006, 1140-1149.
25) Piseri, P., Podesta, A., Barborini, E. and Milani, P.: Production and characterization of highly intense and collimated cluster beams by inertial focusing in supersonic expansions, Rev. Sci. Instrum., **72**, 2001, 2261-2267.
26) Bruzzi, M., Miglio, S., Scaringella, M., Bongiorno, G.,

Piseri, P., Podesta, A. and Milani, P.: First study of humidity sensors based on nanostructured carbon films produced by supersonic cluster beam deposition, Sensors Actuators B, **100**, 2004, 173-176.

27) Diederich, L., Barborini, E., Piseri, P., Podesta, A., Milani, P., Schneuwly, A. and Gallay, R.: Supercapacitors based on nanostructured carbon electrodes grown by cluster-beam deposition, Appl. Phys. Lett., **75**, 1999, 2662-2664.

28) Carbone, R., Marangi, I., Zanardi, A., Giorgetti, L., Chierici, E., Berlanda, G., Podesta, A., Fiorentini, F., Bongiorno, G., Piseri, P., Pelicci, P.G. and Milani, P.: Biocompatibility of cluster-assembled nanostructured TiO_2 with primary and cancer cells, Biomaterials, **27**, 2006, 3221-3229.

29) Piseri, P., Vahedi Tafreshi, H. and Milani, P.: Manipulation of nanoparticles in supersonic beams for the production of nanostructured materials, Curr. Opinion Solid State Mater. Sci., **8**, 2004, 195-202.

30) Pui, D.Y.H. and Liu, B.Y.H.: Advances in instrumentation for atmospheric aerosol measurement, Pysica Scripta, **37**, 1988, 252-269.

31) Flagan, R.C.: History of electrical aerosol measurements, Aerosol Sci. Technol., **28**, 1998, 301-380.

32) Chen, D.-R., Pui, D.Y.H., Hummes, D., Fissan, H., Quant, F.R. and Sem, G.J.: Design and evaluation of a nanometer aerosol differential mobility analyser (Nano-DMA), J. Aerosol Sci., **29**, 1998, 497-509.

33) Hinds, W.C.: Aerosol Technology, J. Wiley, New York, 1999.

34) Friedlander, S.K.: Smoke, Dust, and Haze, Oxford University Press, New York, 2000.

35) Liu, P., Ziemann, P.J., Kittelson, D.B. and McMurry, P.H.: Generating particle beam of controlled dimensions and divergence: I. Theory of particle motion in aerodynamic lenses and nozzle expansion, Aerosol Sci. Technol., **22**, 1995, 293-313.

36) Liu, P., Ziemann, P.J., Kittelson, D.B. and McMurry, P.H.: Generating particle beam of controlled dimensions and divergence: II. Experimental evaluation of particle motion in aerodynamic lenses and nozzle expansions, Aerosol Sci. Technol., **22**, 1995, 314-324.

37) Fernandez de la Mora, J. and Riesco-Chueca, P.: Aerodynamic focusing of particles in a carrier gas, J. Fluid Mech., **195**, 1988, 1-21.

38) Fernandez de la Mora, J. and Rosell-Llompart, J.: Aerodynamic focusing of heavy molecules in seeded supersonic jets, J. Chem. Phys., **91**, 1989, 2603-2615.

39) Liu, D.C. and Lee, C.P.: Novel fabrication technique towards quantum dots, Appl. Phys. Lett., **63**, 1993, 3503-3505.

40) Rossnagel, S.M., Mikalsen, D., Kinoshita, H. and Cuomo, J.J.: Collimated magnetron sputter deposition, J. Vac. Sci. Technol. A, **9**, 1991, 261-265.

41) Xia, Y. and Whitesides, G.M.: Soft lithography, Angew. Chem. Int. Ed., **37**, 1998, 550-575.

42) Di Fonzo, F., Gidwani, A., Fan, M.H., Neumann, D., Iordanoglou, D.I., Heberlein, J.V.R., Tymiak, N., Gerberich, W.W. and Rao, N.P.: Focused nanoparticle beam deposition of patterned microstructures, Appl. Phys. Lett., **77**, 2000, 910-912.

43) Barborini, E., Piseri, P., Podesta, A. and Milani, P.: Cluster beam microfabrication of patterns of three-dimensional nanostructured objects, Appl. Phys. Lett., **77**, 2000, 1059-1061.

44) Milani, P., Piseri, P., Barborini, E., Lenardi, C., Castelnovo, C. and Podesta, A.: Cluster assembling of nanostructured carbon, in: Nanostructured carbon for advanced applications, Benedek, G., Milani, P., Ralchenko, V.G. (eds), NATO-ASI Series II, Mathematics, Physics and Chemistry, Kluwer, Dordrecht, 2001.

45) Powell, Q.H., Fotou, G.P., Kodas, T.T., Anderson, B.M. and Guo, Y.X.: Gas-phase coating of TiO_2 with SiO_2 in a continuous flow hot-wall aerosol reactor, J. Mater. Res., **12**, 1997, 552-559.

46) Powell, Q.H., Fotou, G.P., Kodas, T.T. and Anderson, B.M.: Synthesis of alumina- and alumina/silica-coated titania particles in an aerosol flow reactor, Chem. Mater., **9**, 1997, 685-693.

47) Fotou, G.P., Kodas, T.T. and Anderson, B.: Coating titania aerosol particles with ZrO_2, Al_2O_3/ZrO_2, and SiO_2/ZrO_2 in a gas-phase process, Aerosol Sci. Technol., **33**, 2000, 557-571.

48) Madler, L.: Liquid-fed aerosol reactors for one-step synthesis of nano-structured particles, KONA, **22**, 2004, 107-120.

49) Magnusson, M.H., Deppert, K., Malm, J.-O., Bovin, J.-O. and Samuelson, L.: Gold nanoparticles: Production, reshaping, and thermal charging, J. Nanopart. Res., **1**, 1999, 243-251.

50) Nakaso, K., Shimada, M., Okuyama, K. and Deppert, K.: Evaluation of the change in the morphology of gold nanoparticles during sintering, J. Aerosol Sci., **33**, 2002, 1061-1074.

51) Nanda, K.K., Kruis, F.E., Fissan, H. and Acet, H.: Band-gap tuning of PbS nanoparticles by in-flight sintering of size classified aerosols, J. Appl. Phys., **91**, 2002, 2315-2321.

52) Karlsson, M.N.A., Deppert, K., Magnusson, M.H., Karlsson, L.S. and Malm, J.-O.: Size- and composition-controlled Au – Ga aerosol nanoparticles, Aerosol Sci. Technol., **38**, 2004, 948-954.

53) Kruis, F.E., Fissan, H. and Peled, A.: Synthesis of nanoparticles in the gas phase for electronic, optical and magnetic applications – a review, J. Aerosol Sci., **29**, 1998, 511-535.

54) Binns, C., Trohidou, K.N., Bansmann, J., Baker, S.H., Blackman, J.A., Bucher, J.-P., Kechrakos, D., Kleibert, A., Louch, S., Meiwes-Broer, K.-H., Pastor, G.M., Perez, A. and Xie, Y.: The behaviour of nanostructured magnetic materials produced by depositing gas-phase nanoparticles, J. Phys. D: Appl. Phys., **38**, 2005, R357-R379.

55) Ogawa, H., Nishikawa, M. and Abe, A.: Hall measurement studies and an electrical conduction model of tin oxide ultrafine particle films, J. Appl. Phys., **53**, 1982,

4448-4455.

56) Takeuchi, M., Dohshi, S., Eura, T. and Anpo, M.: Preparation of titanium-silicon binary oxide thin film photocatalysts by an ionized cluster beam deposition method. Their photocatalytic activity and photoinduced super-hydrophilicity, J.Phys. Chem. B, **107**, 2003, 14278-14282.

57) Zhou, J., Takeuchi, M., Zhao, X.S., Ray, A.K. and Anpo, M.: Photocatalytic decomposition of formic acid under visible light irradiation over V-ion-implanted TiO_2 thin film photocatalysts prepared on quartz substrate by ionized cluster beam (ICB) deposition method, Catal. Lett., **106**, 2006, 67-70.

58) Cadete Santos Aires, F.J., Sautet, P., Rousset, J.-L., Fuchs, G. and Melion, P.: Scanning tunneling microscopy study of model catalysts obtained by cluster beam deposition of palladium onto highly oriented pyrolytic graphite, J. Vacuum Sci. Technol. B, **12**, 1994, 1776-1779.

59) Rousset, J.L., Cadete Santos Aires, F.J., Bornette, F., Cattenot, M., Pellarin, M., Stievano, L. and Renouprez, A.J.: Characterization and reactivity of Pd-Pt bimetallic supported catalysts obtained by laser vaporization of bulk alloy, Appl. Surface Sci., **164**, 2000, 163-168.

60) Abbet, S., Judai, K., Klinger, L. and Heiz, U.: Synthesis of monodispersed model catalysts using softlanding cluster deposition, Pure Appl. Chem., **74**, 2002, 1527-1535.

61) Barborini, E., Piseri, P., Li Bassi, A., Ferrari, A., Bottani, C.E. and Milani, P.: Synthesis of carbon films with controlled nanostructure by separation of neutral clusters in supersonic beams, Chem. Phys. Lett. **300**, 1999, 633-638.

62) Gidwani, A.: Ph.D. Thesis, Department of Mechanical Engineering, University of Minnesota, Minneapolis, 55455, 2003.

Author's short biography

Karsten Wegner

Karsten Wegner studied process engineering at the universities of Karlsruhe (Germany) and Cincinnati (U.S.A.). After his graduation in 1998, he joined the group of Prof. Sotiris E. Pratsinis at the Swiss Federal Institute of Technology (ETH) in Zurich to carry out his doctoral studies on gas-phase production of nanoparticles. From 2002 to 2004, he was leader of a research consortium on ceramic nanoparticles, sponsored by the Swiss Commission for Technology and Innovation (CTI). Dr. Wegner was co-founder of the start-up company “FlamePowders” that focused on industrial flame synthesis of nanopowders and was CEO and vice president of FlamePowders before working as a technology and business development consultant with Tethis (Milan). He also holds a position at ETH Zurich, where he has been lecturing mass transfer and nanotechnology courses since 2003. Dr. Wegner has co-authored over 20 scientific publications, book chapters and patents in the field of nanomaterials.

Emanuele Barborini

Emanuele Barborini graduated in Physics at the University of Milan in 1995 and received his Ph.D. in Physics from the same University in 2000. From 2001 to 2005, Dr. Barborini worked at Prof. Paolo Milani’s Laboratory of Molecular Beams and Nanocrystalline Materials (LGM) at the University of Milan, where he coordinated projects on synthesis, characterization and development of devices based on nanostructured titanium dioxide (photocatalysts, gas sensors, electronic noses). He is one of the founders of Tethis, a spin-off company marketing cluster beam deposition units and developing products based on nanostructured thin films. Today, Emanuele Barborini is senior project manager for solid state gas sensor development at Tethis. During the past ten years, Emanuele Barborini has significantly advanced the supersonic cluster beam deposition technique, as is reflected in more than 60 scientific publications in national and international journals. He is co-inventor of four international patents that today are industrially exploited.

Author's short biography

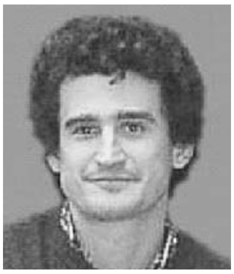

Paolo Piseri

Paolo Piseri is senior researcher and scientific manager of the Laboratory of Molecular Beams and Nanocrystalline Materials (LGM) at the Department of Physics, University of Milan, where he also graduated and obtained his PhD. He is co-founder of the spin-off company Tethis.

Dr. Piseri has been working at LGM since its establishment and has significantly contributed to the development of techniques for cluster beam generation and characterization. His research is related to generation and deposition of clusters, the development of the respective apparatus, gas phase nanoparticle manipulation as well as characterization using spectroscopic methods. He is co-inventor of five international patents in the field of nanotechnology and author of more than 70 articles published in international journals.

Paolo Milani

Paolo Milani is professor at the Department of Physics, University of Milan and head of the Laboratory of Molecular Beams and Nanocrystalline Materials (LGM). After his graduation in Physics at the University of Pavia (Italy) in 1984, Paolo Milani obtained his Ph.D. from the Swiss Federal Institute of Technology in Lausanne. From 1987 to 1991 he was research associate at the Laboratory of Molecular and Laser Physics at the University of Nijmegen (the Netherlands) and the Centro di Fisica degli Stati Aggregati (CeFSA) of the Italian National Research Center (CNR) in Trento, Italy.

In 1992, Paolo Milani joined the Physics Department of the University of Milan, where he founded the Laboratory of Molecular Beams and Nanocrystalline Materials (LGM) and where he is professor since 2000. In 2004, he was appointed director of the Center of Excellence for Nanostructured Materials and Interfaces (CIMAINA) by the Italian Ministry for University Research. Prof. Milani is co-founder and current president of Tethis.

He helds four international patents in the nanotechnology field that are currently exploited industrially and is co-author of more than 120 scientific publications, international reviews, a monography on nanostructured materials and has co-edited a volume on nanostructured carbon. Prof. Milani is member of the editorial boards of the Encyclopedia of Nanotechnology, of the American Scientific Publishers Association and of the Journal of Nanoscience and Nanotechnology. He has received the "U. Campisano" award from the Italian Institute for the Physics of Matter (INFM) in 2000 for his outstanding research contributions and the "Luigi Tartufari" Prize of the National Academy dei Lincei in 2006 as the leader of his research team.

Paolo Milani is a representative of the European Community for the topical area of "Nanotechnologies and Nanosciences" (6th Framework Program) as well as an expert for the European Commission regarding Society and Economy for Nanotechnologies.

Prof. Milani coordinates the newly formed PhD program in Medical Nanotechnology promoted by the European School of Molecular Medicine (SEMM), the Italian Institute of Technology (ITT) and the University of Milano. He is member of the board of the Italian Federation of Scientific and Technical Associations (FAST).

A Review of Thailand's Contributions to Particle Technology Research and Development[†]

T. Charinpanitkul[1], C. Klaysom, S. Monchayapisut, and S. Srinives
*Center of Excellence in Particle Technology, Faculty of Engineering, Chulalongkorn University**
W. Tanthapanichakoon
*National Nanotechnology Center, National Science and Technology Development Agency***

Abstract

This paper focuses on the review of research works contributed by Thai researchers over the last two decades. It surveys research works available in domestically issued journals, which are therefore inaccessible to any international database. Based on our survey, the spectrum of researches involving Particle Technology in Thailand covers three major categories which are 1) Fundamental research in particle synthesis and production, 2) Research and development in particle processing and handling, and 3) Research and development in particle application and utilization.

It could clearly be seen that fundamental research works have continuously been conducted while there are increasingly strong policies from governmental and funding agencies to encourage Thai researchers to pay more attention to applied research and development because there have been few successful cases of commercialized research outcomes. This is attributable to imperfect linkages among universities, industries and governmental agencies, which still lack a systemic supporting mechanism from the government, thereby resulting in research projects not amenable to commercialization.

Keywords: Thailand, Particle, Synthesis, Processing, Handling

1. Introduction

Not only around the world but also in Thailand, a sizable number of researchers and engineers who never consciously think of Particle Technology (P.T.) have contributed significantly to P.T., while accumulating a wealth of technical experiences collected from industrial workplaces and laboratories. Meantime, a growing number of Thai scholars and researchers have begun to recognize P.T. as one of the advanced technologies to facilitate academic advancement and further enhance industrial competitiveness of Thailand. Though the number of publications contributed by Thai research teams to the international database on P.T. is growing, there are still many more published only in major national and institutional journals. It is noteworthy that, due to the rapid development and diversification of P.T., it is not possible or meaningful to review all obscure publications in all domestic journals issued so far. Therefore, the authors have decided to summarize only selected P.T. research contributions over the last two decades. Major P.T.-related journals and conference proceedings will be reviewed and analyzed to give an overall picture on the current situation of P.T. R&D in Thailand.

2. Domestic contributions to P.T.

In Thailand, all major academic institutions have

[†] Accepted : August 18, 2006

* Bangkok 10330, Thailand
** Thailand Science Park, Pathumtani 12120, Thailand
[1] Corresponding Author
TEL: +66-2-218-6899 FAX: +66-2-218-6899
Email: ctawat@chula.ac.th

actively encouraged their academic personnel to focus more on research and development. Issuance of university/faculty bulletins and journals is one of the key strategies to disseminate and enhance the application potential of research outcomes. Meanwhile, it should be noted that some journals, such as Songklanakarin Journal of Science and Technology[1-45] and Science Asia[99-112], are gaining regional and international recognition. They attract contributions not only from Thai but also foreign researchers[9, 12, 135-137]. All journals dealing with conventional P.T. have recently extended their scope to cover new disciplines such as nanotechnology.

Our literature surveys cover a total of 13 journals issued by 11 major universities (Chiang Mai, King Mongkut's Institutes of Technology (Ladkrabang, and North Bangkok), King Mongkut's University of Technology (Thonburi), Mahidol, Prince of Songkla, Rachmangkala Institute of Technology, Srinakarindrwirote, Suranaree University of Technology and Thammasat) and 2 academic / professional organizations (Engineering Institute of Thailand, and National Science and Technology Development Agency). The numbers of investigated domestic papers in each category are summarized in **Table 1**. However, only some "major" papers published over the last two decades and listed in the Bibliography will be analyzed and summarized in this paper. It is noteworthy that the only journal listed in international citation database is Songklanakarin Journal of Science and Technology, which has had P.T. contributions of 7.5 per cent while KMUTT Research and Development Journal has the highest contributions of 11.1 per cent.

Among the surveyed journals, our summary shown in **Table 2** reveals that publications in Material Science and Technology have the highest contribution. This is attributable to the fact that many Thai researchers are still paying attentions to employing P.T. for the fundamentals of material synthesis and application. The second aspect, which is Civil Engineering application, corresponds to the requirement of the national infrastructure development. As expected, Industrial Applications comes third due to the encouraging strategies and policies of the funding agencies in Thailand. Particularly, research works related to rice husk and fly ash applications are comprehensively investigated. Meanwhile, dust collection and air pollution control has gained many attentions

Table 1 List of domestic journals investigated in this work

Journal title	Numbers of papers involving with P.T.	Percentages of papers involving with P.T.
1. Songklanakarin Journal of Science and Technology	45	7.5
2. Science Asia	14	3.5
3. KMUTT Research and Development Journal	31	11.1
4. Research and Development Journal of the Engineering Institute of Thailand	2	6.7
5. Engineering Journal Chiang Mai University	9	4.5
6. Suranaree Journal of Science and Technology	6	2.0
7. Mahidol University Journal of Pharmaceutical Science	3	1.0
8. The Journal of King Mongkut's Institute of Technology North Bangkok	4	1.3
9. Engineering Journal of King Mongkut's Institute of Technology Ladkrabang	3	1.3
10. Thammasat International Journal of Science and Technology	3	1.5
11. Civil Engineering Journal, EIT	1	3.3
12. Engineering Journal Kasetsart University	15	3.8
13. Srinakharinwirote Journal of Pharmaceutical Sciences	2	6.7
14. The 20th Symposium on Thai Pharmaceutical Researches	8	8.0
Total	146	

Table 2 Summary of technical aspects in particle technology papers published in domestic journals

Technical Aspects	Numbers of papers involved	Percentages of papers involved
Material Science and Technology	36	26.2
Civil Engineering	33	21.4
Industrial Applications	30	19.3
Dust Collection	20	14.5
Pharmaceutical Applications	14	10.3
Synthesis and Application of Catalysts	12	8.3

in research and development works. It could indicate that requirement of higher life quality has become a key issue in Thailand.

Besides those journals, there are several national conferences, congresses and symposia which are organized on a regular basis by various organizations such as the Engineering Institution of Thailand (EIT), the Science Society of Thailand, the National Science and Technology Development Agency (NSTDA) and its affiliated national centers as well as National Research Council of Thailand (NRCT) and Thailand Research Fund (TRF). Occasionally, P.T. is a key session in these conferences and symposia. In Chulalongkorn University, the Thai Powder Technology Center (TPTC), the Center of Excellence in Particle Technology (CEPT) and its partners have proactively organized many conferences and symposia with collaborations from many domestic and foreign organizations, such as TRF and Kasetsart University in Thailand, as well as the Association of Powder Process Industry and Engineering (APPIE), Society of Powder Technology Japan (SPTJ) and Japan Association of Aerosol Science and Technology (JAAST) in Japan. Two of the historic events are the first Asian Particle Technology (APT) in 2000 and the Asian Conference on Three-phase Fluidized Bed and Reactor (ASCON) in 2002, which attracted researchers not only within Asia but also from America, Europe and the Oceania. The 3rd APT will be organized in China in the year 2007. Since it is quite difficult to get access to these proceedings, some selected works by Thai contributors will also be introduced in the present review.

3. Categories of Major P.T. Research Works in Thailand

To the best of our knowledge, there has not been any thorough review of P.T.-related research works in Thailand. For the sake of simplicity, we adopt the following 3 main categories of research works: 1) Fundamental research in particle synthesis and production, 2) R&D in particle processing and handling, and 3) R&D in particle application and utilization.

3.1 Fundamental research in particle synthesis and production

Here development of new catalysts as well as new types of functional (nano) particles has attracted great attention of Thai researchers[79-81,86-87,99,102,118]. Catalysis covers the research topics for several research groups in both the academic institutions and petrochemical manufacturers. Synthesis of novel activated carbons from industrial wastes such as waste tires, broken anthracite, palm-oil shell or coffee beans remains one of the most popular research topics. For example, Tanthapanichakoon et al[123] as well as Boonamnuayvittaya et al[148] have selected different approaches in developing highly mesoporous activated carbons. The former team revealed that acid treatment enhances mesoporosity in activated carbons prepared from waste tires, which are useful for adsorbing large-molecule gaseous pollutants. The latter team paid more attention to the utilization of agricultural wastes such as coffee bean residues to produce activated carbons. In addition, a pilot-scale and a full-scale system for producing mesoporous activated carbons from waste tires have been investigated and designed, though not yet implemented due to shortage of investment.

Synthesis of zeolites from fly ash generated in coal-fired power plants employing indigenous lignite as main fuel has been attempted by several research teams. Research teams in Kasetsart University have made several contributions to the effective means to convert lignite fly ash to ZSM-5 and related zeolites [80,86,99]. In addition to fundamental examination, catalytic functionalization of the synthesized zeolites was investigated and reported. Interestingly Suvachittanont et al. of KU have developed and patented a method to synthesize adsorptive microcellulose particles from agricultural wastes. **Fig. 1** shows that

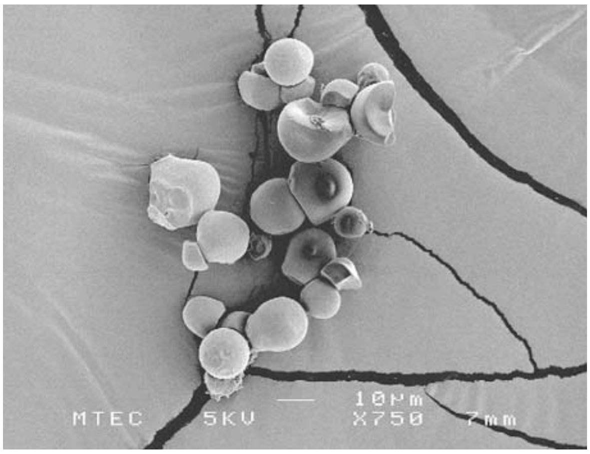

Fig. 1 Typical image of microcrystalline cellulose particles synthesized by hydrolysis of bagasse.

the synthesized microcellulose particles exhibit a narrow size distribution which is supposed to provide uniform adsorption capability. As shown in **Fig. 1**, the microcrystalline cellulose particles synthesized via hydrolysis of bagasses could provide adsorption capability on par with that of commercial products.

Recently nanomaterials, including nanoparticles, have increasingly attracted the interest for Thai researchers1,7,43,80-86,94,102,113,122). Research teams in Chiang Mai (CMU) and Chulalongkorn Universities (CU) have been exploring several techniques, such as pyrolysis, arc discharges in gas or liquid, and Chemical Vapor Deposition (CVD), for the synthesis of carbon and metal nanoparticles. Meantime, other well-known wet processes (sol-gel, microemulsion etc.) and dry processes (sputtering and flame spray pyrolysis) have also been investigated for the synthesis of nanoparticles of various metallic and semiconductive compounds. For example, Charinpanitkul et al.122) reported that the use of naphthalene as main carbon source with an additional small amount of ferrocene could yield a remarkable amount of well aligned multi-walled carbon nanotubes (MW-CNT). Meanwhile, Singjai et al. of CMU reported their success in growing CNT with the CVD technique149).

3.2 Research and development in particle processing and handling

It is noteworthy that large-scaled industrial enterprises in Thailand often adopt turn-key technologies whereas small- and medium-scaled enterprises often resort to the use of modified processes they have adopted or procured from other companies. As a consequence, process retrofitting is inevitably a key issue for all industries.

Among the relevant issues, dust collection and air pollution control are among the most frequently raised research topics. Tanthapanichakoon et al. 91,106) are among Thai chemical engineers who have contributed significantly to air filtration or industrial dust collection. Before the financial crisis in Thailand in 1997-1999, the rapid growth in national infrastructure development and construction boom has resulted in great demand for construction materials, which in turn led to fugitive dust dispersion problem and product losses. Having investigated their collection efficiencies theoretically and experimentally, several simple but effective methods, such as water droplet curtains generated by a series of nozzles106), wet screen dust collectors90), and improved wet scrubbers 130), have been designed, installed and utilized both in lab-scale and pilot-scale processes before actual applications are implemented in some industrial factories, such as rock crushing plants, windsurf manufacturer and grinding wheel producer. Moreover, high temperature dust collection using candle filters has also been investigated58).

Fly ash from some coal-fired power plants has also been investigated for concrete preparation46,51,54,60,62,77,112,116,120,121). Optimization of the incorporation of the collected fly ash into the composite concrete with regards to its characteristics, such as mechanical strength, porosity and setting time, are main topics for civil engineering researches. Works focusing on municipal waste ash have also been carried out to simultaneously tackle the environmental problem and develop an alternative resource. Some research teams in KMUTT, for instance, a team consisting of Jaturapitukkul et al.112) have investigated the classification of fly ash generated from the largest lignite-fired power plant in Thailand and the mixing of the ash with Portland cement. They reported that, in addition to changes in its chemical composition, the particle size distribution of the classified fly ash could significantly affect the compressive strength of the composite concrete.

Fluidization and its applications are also widely investigated in Thailand. For examples, at least 1 group in KMUTT and 2 groups in CU have contributed to fluidized bed drying, combustion and granulation as well as coating. Soponronnarit et al.108) have made many contributions to the drying technology for agricultural products and waste utilization, which at present have become commercially available. Damronglerd et al.150,151) in CU have conducted many investigations of solid waste combustion in fluidized beds. Similarly, Tia et al.52) attempted to utilize

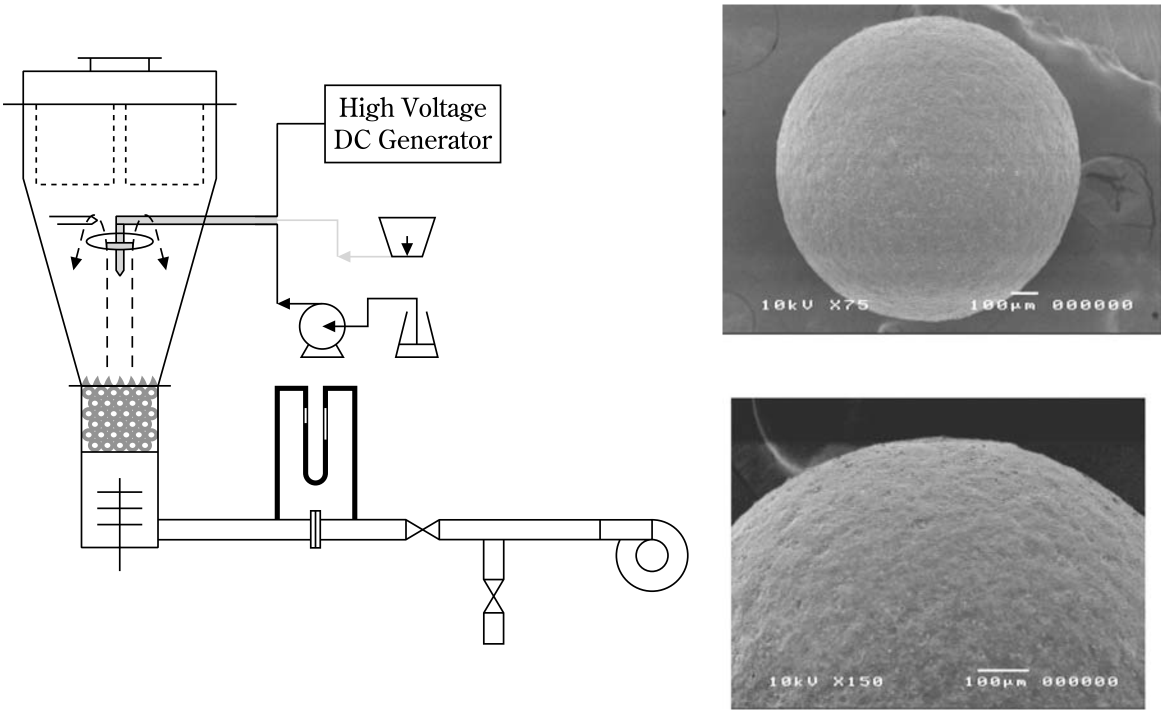

Fig. 2 Schematic diagram of the fluidizing bed coater[153] (Left), and typical images of glass bead particle coated with hydroxypropyl methylcellulose (HPMC) (Right).

a fluidized bed furnace to extract thermal energy from agricultural wastes. In CEPT, Charinpanitkul et al.[152] have developed a batch-scale fluidized-bed granulator/coater by co-opting electrostatic atomization of the binder or coating agent. **Fig. 2** reveals the schematic diagram of their coating fluidized bed with some typical examples of uniformly coated particles which could provide controlled-release functionality.

3.3 Research and development in particle application and utilization

Applications and utilizations of particulate materials are one of the most important research topics for Thai researchers. Recycle of waste materials – either in particulate or bulk forms[31,33,35], substitution of some specific materials with indigenously available natural materials[20,29-30,34,66,71], and new products development[42-43] were conducted and reported by Thai academic staffs. Typical waste materials abundant in Thailand are biomass, such as rice husks, wood shavings and sludges obtained mainly from the agricultural sector. The means to recycle these waste materials are pyrolysis for developing new products, such as zeolites and diamond films, and compositing with polymeric materials (PVC, PE or LDPE). For instance, Rimdusit et al.[153] focused on utilizing benzoxazine as matrix material and wood flour as filler in the preparation of high-quality wood composite, which could be employed as housing materials. The composites exhibit superior physical properties up to a very high filler fraction of 75%.

For other applications in environmental aspects, many research teams, such as Kiatkomol et al[113] of SUT applied montmorillonite as well as organo-clays for the removal of organic pollutants from simulated aqueous solutions. They reported that the capacity of adsorption strongly relied on the contact time between the adsorbent and adsorbate.

As an inevitable aspect of nanotechnology, the utilization and applications of nano-scale particles have also attracted great interest. Numerous attempts from various institutions employed typical nanoparticles, such as TiO_2 for wastewater treatment[118]. It has been reported that such a system has high potential to tackle wastewater with complicated molecules of dye stuffs or volatile hydrocarbon compounds which could not be handled by conventional systems.

4. Future Direction of P.T. in Thailand

Domestic and international collaborations in R&D in P.T. and its relevant fields have played an important role in their sustainable development in the whole Southeast Asian region including Thailand. Japan and other developed countries have provided technical and financial supports to Thailand, especially from APPIE Japan to TPTC and CEPT in CU. With high demands from the funding agencies for Thai researchers to conduct R&D that leads to actual applications, the use of nanoparticles in composites and sensors as well as cosmetics and advanced drug delivery would for the time being remain the focal point of P.T. research activities in Thailand.

5. Conclusions

Major contributions in P.T. of Thailand have come from Chemical, Civil and Environmental Engineering fields. Pharmaceutical scientists and technologists have contributed to the development of new methods and new recipes for specific pharmaceutical products composed of niche indigenous materials, such as rice husk and lignite. The present finding reveals that Thailand still requires more fundamental research but demand for applied research is stimulated by the policies of the government and funding agencies.

In short, Particle Technology (P.T.) is now recognized as a key technology that plays a tremendously important role in the development of Thailand's industries. In addition to the conventional aspects ranging from handling and processing to synthesis and applications of particulate materials, R&D in P.T. in Thailand has expanded to nanoparticle technology and its applications. It is believed that more researchers and engineers should study and make use of the diversity and multi-disciplinary features P.T. in their own fields to expand production capacity and develop new manufacturing practices in their factories.

Acknowledgement

Partial financial support from the Silver Jubilee Endowment Fund of Chulalongkorn University for Center of Excellence in Particle Technology is acknowledged.

References

1) Khunkitti W., Aromdee, C., Vorarat, S. and Chitropas, P. Formulation development of sunscreen lotion containing jackfruit starch and the lotion acceptance evaluation in volunteers, Songklanakarin Journal of Science and Technology, **28** (2006):137-144.
2) Khunkitti, W., Aromdee, C., Vorarat, S. and Chitropas, P. The potential of jackfruit starch for use as suspending agent and emulsifying agent, Songklanakarin Journal of Science and Technology **28** (2006):145-155.
3) Pongnoree, J. and Kongbangkerd, T. Preparation of cellulose from corncobs I: Study on cellulose extraction, Songklanakarin Journal of Science and Technology, **28** (2006): 191-199.
4) Natpinit, S., Ploypatarapinyo, P. and Jenvanitpanjakul, P. The treatment of high strength protein wastewater by UASB system, Songklanakarin Journal of Science and Technology, **28** (2006):217-226.
5) Prachayawarakorn, J. and Klairatsamee, W. Effect of solvents on properties of Bombyx mori silk grafted by methyl methacrylate (MMA) and methacrylamide (MAA), Songklanakarin Journal of Science and Technology, **27** (2005):1233-1242.
6) Laosiritaworn, Y. Mean-field calculation of some magnetic properties of rising thin-film, Songklanakarin Journal of Science and Technology, **27** (2005):1273-1284.
7) Kanna, M., Wongnawa, S., Shershoopongse, P. and Boonsin, P. Adsorption behavior of some metal ions on hydrated amorphous titanium dioxide surface, Songklanakarin Journal of Science and Technology, **27** (2005):1017-1026.
8) Chirasatitsin, S., Prasertsan, S., Wisutmethangoon, W. and Kyokong, B. Mechanism properties of rubber wood oriented strand lumber (OSL): The effect of strand length, Songklanakarin Journal of Science and Technology, **27** (2005):1047-1055.
9) Shakir Nasif, M., Morrison, G.L. and Behnia, M. Membrane and plastic heat exchangers performance, Songklanakarin Journal of Science and Technology, **27** (2005):1065-1072.
10) Rattanakawin, C. Aggregate size distributions in sweep flocculation, Songklanakarin Journal of Science and Technology, **27** (2005):1095-1101.
11) Panmatarith, T., Hayeemayang, N. and Baka-lee, N. The new types of positive temperature coefficient effect based on SnO_2 + 2CoO and SnO_2 + Cr_2O_3 ceramics used as temperature sensor, Songklanakarin Journal of Science and Technology, **27** (2005):1113-1122.
12) Bockari-Bevao, S.M., Wan Ismail, W.I., Yahya, A. and Wan, C.C. Analysis of energy consumption in lowland rice-based cropping system of Malaysia, Songklanakarin Journal of Science and Technology, **27** (2005):819-826.
13) Tongnam, C., Arkornsakul, P., Pangpat, K. and Rujijanagul, G. Effect of heating/cooling rate on the properties of $BaTiO_3$ ceramics, Songklanakarin Journal of Science and Technology, **27** (2005):839-846.
14) Puthai, W. Wanichapichart, P. and Kaewpiboon, A. Effect of polyethylene glycol on characteristics of chitosan membranes, Songklanakarin Journal of Science and Technology, **27** (2005):867-876.
15) Chetpattananondh, P., Nitipavachon, Y. and Bunyakan, C. Biofiltration of air contaminated with methanol and toluene, Songklanakarin Journal of Science and Technology, **27** (Suppl. III) (2005):762-773.
16) Prodpran, T., Chinabhark K. and Benjakul, S. Proper-

ties of composite film based on bigeye snapper surimi protein and lipids, Songklanakarin Journal of Science and Technology, **27** (Suppl. III) (2005):775-788.

17) Phiraphinyo, P., Taepakpurenat, S., Lakkanatinaporn, P., Suntornsuk, W. and Suntornsuk, L. Physical and chemical properties of fish and chicken bones as calcium source for mineral supplements, Songklanakarin Journal of Science and Technology, **28** (2006):327-335.

18) Klinpituksa, P., Chaiyotha, P. and Chaisuksan, Y. Synthesis and characterization of acrylamide/acrylic acid hydrogel and its application for crystal violet dye adsorption, Songklanakarin Journal of Science and Technology, **28** (2006):337-349.

19) Puajindanetr, S., Wisuttipaet, S. and Thammasang, D. A smart surface from natural rubber: the mechanism of entropic control at the surface monitored by contact angle measurement for rubber wood furniture part machining process, Songklanakarin Journal of Science and Technology, **28** (2006):351-359.

20) Sathitruangsak, P., Madhiyanon, T. and Soponronnarit, S. Design of an extrusion screw and solid fuel produced from coconut shell, Songklanakarin Journal of Science and Technology, **28** (2006):387-401.

21) Yudee, A., Sopadang, A., Wirojanupatump, S. and Jiansirisomboon, S. Aluminium-12 wt% silicon coating prepared by thermal spraying technique: Part1 optimization of spray condition based on a design of experiment, Songklanakarin Journal of Science and Technology, **28** (2006):431-439.

22) Yudee, A., Sopadang, A., Wirojanupatump, S., and Jiansirisomboon, S. Aluminium-12 wt% silicon coating prepared by thermal spraying technique: Part 2 microstructure and properties, Songklanakarin Journal of Science and Technology, **28** (2006):441-448.

23) Pongjanta, J., Naulbunrang, A., Kawngdang, S., Manon, T. and Thepjaikat, T. Songklanakarin Journal of Science and Technology, **28** (Suppl. 1) (2006):71-79.

24) Reungmaneepaitoon, S., Sikkhamondhol, C. and Tiangpook, C. Nutritive improvement of instant fried noodles with oat bran, Songklanakarin Journal of Science and Technology, **28** (Suppl. 1) (2006):89-97.

25) Prodpran, T. and Benjakul, S. Effect of acid and alkaline solubilization on the properties of surimi based film, Songklanakarin Journal of Science and Technology, **27** (2005):563-574.

26) Thongsang, S., Suwapanaviwat, S., Supanpesat, J., Chantawart, S., Khamphan, K. and Sombatsompop, N. Effects of recycled PVC content and processing temperature on the properties of PVC foam products. Songklanakarin Journal of Science and Technology, **27** (2005):563-574.

27) Kaewsichan, L., Sriyom, J. and Bunyakan, C. Treatment of phenolic compounds in wastewater by Fenton reaction together with CaO coagulation, Songklanakarin Journal of Science and Technology, **27** (2005):591-600.

28) Chalermyanont, T. and Arrykul, S. Compacted sand-benotnite mixtures for hydraulic containment liners, Songklanakarin Journal of Science and Technology, **27** (2005):313-323.

29) Prachayawarakorn, J. and Yaembunying, N. Effect of recycling on properties of rice husk-filled-polypropylene. Songklanakarin Journal of Science and Technology, **27** (2005):343-352.

30) Madhiyanon, T., Piriyarungroj, N. and Soponronnarit, S. A novel vortex-fluidized bed combustor with two combustion chambers for rice-husk fuel. Songklanakarin Journal of Science and Technology, **26** (2004):875-893.

31) Im-Erb, R., Bamroongrugsa, N., Kawahima, K., Amano, T. and Kato, S. Utilization of coal ash to improve acid soil. Songklanakarin Journal of Science and Technology **26** (2004):697-708.

32) Tantemsapya, N., Wirojanagud, W. and Skolchai, S. Removal of color, COD and lignin of pulp and paper wastewater using wood ash. Songklanakarin Journal of Science and Technology, **26** (Suppl. 1) (2004):1-12.

33) Rachakornkij, M., Ruangchuay, S. and Teachakulwiroj, S. Removal of reactive dyes from aqueous solution using bagasse fly ash. Songklanakarin Journal of Science and Technology, **26** (Suppl. 1) (2004):13- 4.

34) Chiarakorn, S,. Grisdanurak, N. and Miller, R.C. Analysis of nitrogen and carbon tetrachloride adsorption isotherms and pore size distribution for siliceous MCM-41 synthesized from rice husk silica. Songklanakarin Journal of Science and Technology, **26** (Suppl. 1) (2004):37-44.

35) Wirojanagud, W., Tantemsapya, N. and Tantriratna, P. Precipitation of heavy metal by lime mud waste of pulp and paper mill. Songklanakarin Journal of Science and Technology, **26** (Suppl. 1) (2004):45-53.

36) Phenrat, T., Marhaba, T.F. and Rachakornkij, M. Examination of solidified and stabilized matrices as a result of solidification and stabilization process of arsenic-containing sludge with Portland cement and lime, Songklanakarin Journal of Science and Technology, **26** (Suppl. 1) (2004):65-75.

37) Wantawin, C. and Chobthiangtham, P. Using cement, lignite fly ash and baghouse filter waste for solidification of chromium electroplating treatment sludge, Songklanakarin Journal of Science and Technology, **26** (Suppl. 1) (2004):77-84.

38) Penpolcharoen, M. Dye-adsorption capacity of bituminous fly ash and its pozzolanic property after used as dye-adsorbent, Songklanakarin Journal of Science and Technology, **26** (Suppl. 1) (2004):85-95.

39) Sopajaree, K., Kleepklang, A. and Bamrungsri, P. Effects of temperature and volumetric loading rate on phenol adsorption capacity by granular activated carbon, Songklanakarin Journal of Science and Technology, **26** (Suppl. 1) (2004):97-108.

40) Yimnirun, R., Ananta, S. and Lawratakul, P. Dielectric properties of ceramics in lead zirconate titanate − lead magnesium niobate system, Songklanakarin Journal of Science and Technology, **26** (2004):529-536.

41) Leephakpreeda, T. Dynamic control of crystallinity in

polymer film casting process, Songklanakarin Journal of Science and Technology, **26** (2004):385-391.

42) Markpin, T., Tareelap, N., Kirtikara, K. and Sombatsompop, N. Design and development of electrodeposited composite coating systems by cathode self-rotation and rotation around anode, Songklanakarin Journal of Science and Technology, **26** (2004):245-257.

43) Metanawin, T., Setasuwan, P. and Sombatsompop, N. Diamond film growth with modification properties of adhesion between substrate and diamond film, Songklanakarin Journal of Science and Technology, **26** (2004):259-268.

44) Homwuttiwong, S., Vivatanachang, N. and Jaturpitakkul, C. Effect of high volume of fly ash from 5 sources on compressive strength and acid resistance of concrete, Songklanakarin Journal of Science and Technology, **26** (2004):269-283.

45) Trachoo, N. Biofilm removal technique using sands as a research tool for accessing microbial attachment on surface, Songklanakarin Journal of Science and Technology, **26** (2004):109-115.

46) Songpiriyakij, S. and Jaturapitakkul, C. A Study of Ground Mea Moh Fly Ash as a Pozzolan for Increasing Concrete Strength, KMUTT Research and Development Journal, Vol. 18 (1995), No. 2:51-64.

47) Chayawattana, T. Desulfurization with Limestone in Fluidized Bed Coal Combustor, KMUTT Research and Development Journal, Vol. 18 (1995), No. 2:65-76.

48) Bovornsethanant, S. A Study of Lifetime of Air Cleaner Element for Vehicle in Bangkok and Suburban Area, KMUTT Research and Development Journal, Vol. 19 (1996), No. 1:17-28.

49) Boonamnuayvitaya, V., Tia, S. and Jaree, A. Study of Coal Particle Distribution in Three-Phase Spouted Bed Reactors, KMUTT Research and Development Journal, Vol. 20 (1997), No. 1:64-76.

50) Teppayayon, P., Jiraratananon, R. and Uttapap, D. The Preparation of Microfiltration Ceramic Membrane from Alumina, KMUTT Research and Development Journal, Vol. 22 (1999), No. 1:3-17.

51) Jirasit, F., Jaturapitakkul, C., Siripanichgorn, A. and Kiattikomol, K. Effects of Cement and Fly Ash Contents in Concrete against Sulfuric Acid Attack, KMUTT Research and Development Journal, Vol. 22 (1999), No. 2:27-45.

52) Tia, S., Prukamornpan, P., Jitvootthikai, P., Lao, S.S. and Chayawattana, T. Combustion of Biomass in fluidized-bed Furnace, KMUTT Research and Development Journal, Vol. 22 (1999), No. 2:47-63.

53) Kitchainukul, W., Buddhawong, S. and Chaiprasert, P. Utilization of Solid Waste from Foundries Industry as Cementious Binder in Solidification, KMUTT Research and Development Journal, Vol. 22 (1999), No. 2:79-94.

54) Chatveera, B. Durability and Compressive Strength of Mae Moh-Fly Ash Mortar, KMUTT Research and Development Journal, Vol. 23 (2000), No. 2:17-29.

55) Seanjun, B., Thaveesin, K. and Poolthong, N. Comparison of Molding Sand from Various Sources in Thailand, KMUTT Research and Development Journal, Vol. 24 (2001), No. 1:57-68.

56) Chatveera B., Mechanical Properties of Cement Paste Containing Rice Straw Ash, KMUTT Research and Development Journal, Vol. 24 (2001), No. 1:85-99.

57) Chatveera B. and Wongkamjan, W. Mechanical Behavior of Fine RHA Concrete, KMUTT Research and Development Journal, Vol. 24 (2001), No. 3:327-342.

58) Amornkitbamrung, M. Filtration Behavior and Dust Cake Detachment from Ceramic Filter Element, KMUTT Research and Development Journal, Vol. 25 (2002), No. 3:279-291.

59) Chatveera, B. and Kongsub, T. Durability of Concrete Containing Black RHA from Rice Mill, KMUTT Research and Development Journal, Vol. 25 (2002), No. 4:373-389.

60) Leekeeratikul, T., Sata, V. and Jaturapitakkul, C. Utilization of Condensed Silica Fume and Classified Fly Ash in High Strength Concrete, KMUTT Research and Development Journal, Vol. 26 (2003), No. 2:233-249.

61) Soonsin, V. and Boonamnuayvitaya, V. A Study of Solidification of Oily Sludge with Cement and Binding Agents, KMUTT Research and Development Journal, Vol. 26 (2003), No. 2:251-268.

62) Cheerarot, R., Tangpagasit, J., Jaturapitakkul, C. and Kiattikomol, K. Effect of Particle Size of Mae Moh Fly Ash on Strength Activity Index of Mortar, KMUTT Research and Development Journal, Vol. 26 (2003), No. 3:295-310.

63) Suriyachat, P. and Koadee, S. Properties of Refractory Brick Using Chainat Sand as Raw Material, KMUTT Research and Development Journal, Vol. 26 (2003), No. 4:447-457.

64) Tangchirapat, W., Tangpakasit, J., Waew-kum, S. and C. Jaturapitakkul, A New Pozzolanic Material from Palm Oil Fuel Ash, KMUTT Research and Development Journal, Vol. 26 (2003), No. 4:459-473.

65) Suriyachat, P. and Meelong, S. Geotechnical Properties of Bangkok Clay Mixed Gypsum, KMUTT Research and Development Journal, Vol. 27 (2004), No. 1:3-16.

66) Chatveera, B. and Makul, N. Effect of Curing Temperature on Mechanical Properties of Cement Mixed with White Rice Husk Ash Paste, KMUTT Research and Development Journal, Vol. 27 (2004), No. 1:49-61.

67) Nachiengtai, T. and Chim-oye, W. Undrained Shear Strength of Compacted Soft Clay Stabilized with Sand, KMUTT Research and Development Journal, Vol. 27 (2004), No. 1:117-127.

68) Chatveera, B. and Makul, N. Mechanical Properties and Durability of Portland Cement Containing Ground Slag by Los Angeles Machine, KMUTT Research and Development Journal, Vol. 27 (2004), No. 2:157-174.

69) Suriyachat, P. Friction Parameters of Interface between Sand and Concrete Foundation, KMUTT Research and Development Journal, Vol. 27 (2004), No.

2:245-252.
70) Aichayawanich, S., Nopharatana, M. and Vongsawasdi, P. Chemical, Physical and Rheological Properties of Commercial Wet-milled and Dry-milled Rice Flour, KMUTT Research and Development Journal, Vol. 27 (2004), No. 3:357-374.
71) Chatveera, B., Makul, N. and Ruxsadee, B. Use of Unground Rice Husk Ash in Concrete Block Production, KMUTT Research and Development Journal, Vol. 27 (2004), No. 4:483-496.
72) Sinsiri, T., Jaturapitakkul, C. and Chindaprasirt, P. Effect of Fly Ash Fineness on Compressive Strength, Total Pore Volume and Pore Size of Blended Cement Paste, KMUTT Research and Development Journal, Vol. 28 (2005), No. 1:17-28.
73) Srisatit, T. and Dilokkiat, N. Adsorbent Produced by Ball Clay with Coconut Shell or Palm Shell for Hexavalent Chromium Adsorption in Synthetic Wastewater, KMUTT Research and Development Journal, Vol. 28 (2005), No. 2:223-237.
74) Srisaipet, A., Jeyashoke, N. and Krisnangkura, K. Resolution of R/S-α-Hydroxy Fatty Acids by Immobilized Lipase on Rice Hull Ash, KMUTT Research and Development Journal, Vol. 28 (2005), No. 4:429-443.
75) Tangpagasit, J., Songmue, S., Jaturapitakkul, C. and Kiattikomol, K. A Study of Strength Activity Index of Mortar Due to Hydration Reaction, Packing Effect, and Pozzolanic Reaction of Rice Husk-Bark Ash and Palm Oil Fuel Ash, KMUTT Research and Development Journal, Vol. 28 (2005), No. 4:465-476.
76) Chatveera, B., Makul, N. and Rodanan, A. Durability of Cement Mortar Containing Black Rice Husk Ash under Sodium Sulfate and Magnesium Sulfate Attack, KMUTT Research and Development Journal, Vol. 29 (2006), No. 1:55-71.
77) Plang-ngern, S. and Tangtermsirikul, S. Chloride Binding Capacity in Fly Ash Concrete, Research and Development Journal of the Engineering Institute of Thailand, Vol. 10 (1999), No. 2:1-8.
78) Chatveera, B. and Makul, N. Effect of Lignite Bottom Ash on Cement Paste Properties, Research and Development Journal of the Engineering Institute of Thailand, Vol. 12 (2001), No. 4:1-8.
79) Wongsuptawee, N. and Phanawadee, P., Charoenpanich, M. A Study of Hydrogenation Reaction of CO_2 over Fe and Cu Loaded Na-ZSM-5 Zeolite Catalyst, Engineering Journal Kasetsart, Vol. 18 (2005), No. 53:12-21.
80) Vanichakit, N. and Kongnkachuichay, P. Synthesis of ZSM-5 Zeolite from China Clay, Engineering Journal Kasetsart, Vol 17 (2004), No. 50:35-41.
81) Chittanakee, W. and Kongnkachuichay, P. Synthesis of Nickel Catalytic Membrane for Oxidation of Liquid Petroleum Gas (LPG), Vol. 16 (2002), No. 47 :31-38.
82) Srinophankun, P. and Eimsumrarn, N. Treatment of Wastewater from Pulp and Paper Industry by Ozonization, Engineering Journal Kasetsart, Vol. 16 (2002), No. 47:59-68.
83) Suwanvitaya, P., Chindaprasert, P. and Pahusuwanno, S. Long Term Properties of Fly Ash Concrete, Engineering Journal Kasetsart, Vol. 16 (2002), No. 47:69-75.
84) Aumyoo, P. and Kongnkachuichay, P. Synthesis of Alumina Membrane by Sol-Gel Process, Engineering Journal Kasetsart, Vol. 16 (2002), No. 47:76-84.
85) Tungbariboon, N. Synthesis of Barium Titanate Electro-ceramic Materials, Engineering Journal Kasetsart, Vol. 16 (2002), No. 47:112-121.
86) Thaneerat, R. and Chareonpanich, M. Synthesis of Production of Y type zeolite catalyst from Lignite Fly Ash, Engineering Journal Kasetsart, Vol. 16 (2002), No. 47:150-160.
87) Phanawadee, P. and Charungmanorom, S. Determination of the Number of Active Sites of a Catalysts Sample by Multiple-Pulse-TAP-Experiment, Engineering Journal Kasetsart, Vol. 15 (2001), No. 43:85-93.
88) Maneerat, W., Nakpipat, P. and Kraiwattanawong, K. Study of Correlation of pressure to Combination Flux of Emulsion Droplets, Engineering Journal Kasetsart, Vol 15 (2001), No. 43:113-119.
89) Sukonthanit, S. and Gray, N.B. Zinc Recovery From Commercial EAF Dust by The Iron-reduction Distillation Process, Engineering Journal Kasetsart, Vol. 13 (1999), No. 41.
90) Arsingsamanunt, U. and Suvachittanont, S. Rock Mill Dust Removal by Wetted Screen, Engineering Journal Kasetsart, Vol. 13 (1999), No. 41
91) Larpsuriyakul, K., Charinpanitkul, T. and Tanthapanichakoon, W. Purification of Low-impurity Gas, with Electron-adding Reaction in Different Types of Corona Discharge Reactor, Engineering Journal Kasetsart, Vol. 12 (1998), No. 34:106-122.
92) Piromyaporn, C., Uttrapadoong, P. and Suvachittanont, S. Study of Properties of Particulate Cement, Engineering Journal Kasetsart, Vol. 11 (1997), No. 31:105-118.
93) Suvachittanont, S. and Kanaoka, C. Measurement of Specific Surface Area of Porous Media Through Pressure Drop, Engineering Journal Kasetsart, Vol. 9 (1995), No. 27.
94) Nimkulrut, S. Polymeric Nanoparticles for Drug Delivery, Srinakharinwirote Journal of Pharmaceutical Sciences, Vol. 7 (2002), No. 1.
95) Sutanthavibul, N. Sustained Release Drug Delivery System, Srinakharinwirote Journal of Pharmaceutical Sciences, Vol. 7 (2002), No. 1.
96) Vajragupta, O., La-ong, S., Bunyapraphatsara, N. and Junyaprasert, V. Pig Brain Lipids for Liposome-encapsulated Acyclovir, Mahidol University Journal of Pharmaceutical Science, Vol. 3-4 (2002):33-39.
97) Mitrevej, A. and Visavarungroj, N. Spray Dried Rice Starch: Powder Mixing in Direct Compression Formulation, Mahidol University Journal of Pharmaceutical Science, Vol. 3-4 (1998):11-16.
98) Jateleela, S. and Krisadaphong, P. Role of Surfactants in Fluidized Bed Granulation I: Effects of Various

surfactants on Physical Properties of Sulfadimidine Granulations, Mahidol University Journal of Pharmaceutical Science, Vol. 1 (1996):8-9.

99) Kongkachuichay, P. and Lohsoontorn, P. Phase Diagram of Zeolite Synthesized from Perlite and Rice Husk Ash, Science Asia, Vol. 32 (2006), No. 1:1-15.

100) Tippayawong, N. and Lee, A. Concentration and Elemental Analysis of Airborne Particulate Matter in Chiang Mai. Thailand, Science Asia, Vol. 32 (2006), No. 1:13-16.

101) Sinsiri, T., Teeramit P., Jaturapitakkul, C. and Kiattikomol, K. Effect of Finenesses of Fly Ash on Expansion of Mortars in Magnesium Sulfide, Science Asia, Vol. 32 (2006), No. 1:63-69.

102) Worayingyong, A. and Poo-arporn, Y. A Comparative Study of Toluene Catalytic Oxidation over Cerium/TiO_2 (anatase) and vanadium/TiO_2 (anatase) Catalyst, Science Asia, Vol. 30 (2004):341-349.

103) Tongsri, R. and Mcshane, H. Microstructure-Processing-Property-Relationship of Rapidly Solidified Al-Fe-(V, Si) Alloys, Science Asia, Vol. 30 (2004):25-31.

104) Tongsri, R. and Mcshane, H. Microstructure and Solidification of Al-Fe-(V, Si) Alloy Powders, Science Asia, Vol. 30 (2004):33-41.

105) Krammart, P. and Tangtermsirikul, S. A Study on Cement Made by Partially Replacing Cement Raw Materials with Municipal Solid Waste Ash and Calcium Carbide Waste, Science Asia, Vol. 29 (2003):77-84.

106) Wongsarivej, P. and Tanthapanichakoon, W. Development of Mathematical Model for Continuous Spray Evaporator/Air (De)humidifier with Nonisothermal Polydisperse Droplets, Science Asia, Vol. 29 (2003):67-75.

107) Jaiboon, N. Crystal Structure Determination of 5, 6-Dibroacenahthene from X-ray Powder Diffraction Data, Science Asia, Vol. 28(2002):271-275.

108) Soponronnarit, S. Fluidised-Bed Paddy Drying, Science Asia, Vol 25 (1999):51-56.

109) Tangtermsirikul, S. Strength Evaluation of Aggregation Made from Fly Ash, Science Asia, Vol. 25(1999):237-241.

110) Samran, J. and Amornsakchai, T. In-situ Composite Film of Thermotropic Liquid Crystalline Polymer/Polypropylene: Effect of Film Drawing on Molecular Orientation and Properties, Science Asia, Vol. 25(1999):91-97.

111) Vitidsanti, T. Production of Activated Carbon from Palm-oil Shell by Pyrolysis and Steam Activation in a Fixed Bed Reactor, Science Asia, Vol. 25 (1999):211-222.

112) Jaturapitakkul, C. A Study of Strength Activity Index of Ground Coarse fly Ash with Portland Cement, Science Asia, Vol. 25 (1999):223-229.

113) Charuwong, P. and Kiattikomol, R. Removal of Organic Compounds from Aqueous Solution by Montmorillonite Clays and Organo-clays, Engineering Journal Chiang Mai University , Vol. 11 (2003)

114) Lothongkum, A. W., Jangchud, I., Oonjittichai, W. and Channarong, W. Mechanical Properties of Untreated Natural Rubber Fibers-Reinforced Poly(vinyl chloride) Composites: Effects of Fiber Content and Diocthyl Phthalate, Engineering Journal Chiang Mai University, Vol. 10 (2002), No. 1:1-8.

115) Wittayakun, J., Watcharasiribanlue, S., Grisdanurak, N. and Mahachanon, K. Removal of Sulfur Dioxide from Flue Gas by Copper Supported on Activated Carbon, Engineering Journal Chiang Mai University , Vol. 10 (2002), No. 1:9-14.

116) Suppaviriyakit, T. and Kasemset, C. A Comparative Study of Reinforcing Steel Bond Strength and Ultimate Compressive Strength of Normal Concrete and Fly Ash Concrete after Fire Exposure, Engineering Journal Chiang Mai University, Vol. 9 (2001), No.3:1-10.

117) Charoenchuen, C. and Chaitep, S. Aerodynamic Drag Measurement of Paddy Rices, Engineering Journal Chiang Mai University, Vol. 9 (2001), No. 3:53-63.

118) Pibaljommee, S. and Sopajaree, K. Decolorization of Dyeing Wastewater by Photocatalytic Process Using Titanium Dioxide Catalyst, Engineering Journal Chiang Mai University, Vol. 9 (2001), No. 1:10-18.

119) Jaturapiree, A. and Sopajaree, K. Photocatalytic Degradation of Chlorophenol Compounds Using Batch-Recycle Reactor, Engineering Journal Chiang Mai University, Vol. 9 (2001), No. 1:19-27.

120) Thongteekar, S. and Karnchanawong, S. Solidification of Silico Jarosite Residue by Quick Lime, Limestone, Fly Ash, Cement and Lignite Ash, Engineering Journal Chiang Mai University, Vol. 9 (2001), No. 1:28-40.

121) Masruksa, P. and Kasemset, C. A Proposed Modified ACI Mix Design Method for Mae-Moh Fly Ash Concrete, Engineering Journal Chiang Mai University, Vol. 9 (2001), No. 2:106-117.

122) Charinpanitkul, T., Sano N., Puengjinda P., Muthakarn P., Kanki T., and Tanthapanichakoon W. Synthesis of carbon nanoparticles using thermal co-pyrolysis of ferrocene and naphthalene mixture, Journal of Science CMU, Vol. 32(3) (2005):379-383.

123) Lorthongkham, A.W., Sriteeravirote, T. and Tanthapanichakoon, W. Synthesis of activated carbon from coconut shell by chemical activation for adsorption of Phenol, Ladkrabang Engineering Journal, Vol. 11(2003), No. 1:18-24.

124) Piyamanocha, P. and Areerat, S. Prediction of Bubble Growth in Polyurethane Foam, Ladkrabang Engineering Journal, Vol. 12(2004), No. 3:1-6.

125) Yuangsawad, R., Kitchaiya, P. and Na-Ranong, D. Preliminary Kinetics of CO+NO Reaction over Rh/Al_2O_3, Ladkrabang Engineering Journal, Vol. 12(2004), No. 3:7-12.

126) Ratanadecho, P. Analysis of Drying Process in Porous Media (I Principle of Heat and Mass Transfer in Porous Media for Drying Process), A Publication in Thai of Thammasat University, Vol. 12(2004), No. 1: 1-11.

127) Ratanadecho, P. Analysis of Drying Process in Porous Media (II Development of Mathematical Model for Analysis of Heat and Mass Transfer in Porous Media),

A Publication in Thai of Thammasat University, Vol. 12(2004), No. 2:1-14.

128) Rukchonlatee, S., Kortrakul, T. and Cheunput, P. Influence of Rice husk Ash in Mixed Fillers on Processability and Mechanical Properties of Natural Rubber, Thammasat International Journal of Science and Technology, Vol. 12(2004), No. 3:50-59.

129) Buaklee, K. and Stitmannaithum, B. Mixing of Fly Ash-added Concrete, Civil Engineering Magazine, Vol. 15 (2003), No. 2:46-50.

130) Klinchan, S. Enhancement of Biosensor Response by Electrodeposition of Ruthenium on Platinum Electrode, Journal of King Mongkut's Institute of Technology North Bangkok, Vol.14 (2004), No. 4:38-44.

131) Changsuhan, A., Kerdsuwan, S. and Bashkin, V. N. The Efficiency of Mercury Removal in Packed-Bed Wet Scrubber from Infectious Waste Incinerator, Journal of King Mongkut's Institute of Technology North Bangkok, Vol. 13 (2003), No. 4:1-9

132) Pitiraksakul, A., Sriratchutchavan, S., Auamnoi, P. and Parnman, S. Efficiency of Particle Removal Using Continuous Dissolved Air Floatation, Journal of King Mongkut's Institute of Technology North Bangkok, Vol. 13 (2003), No. 4:16-22.

133) Moon-Pa, N. and Chaikittirattana, A. Hyperelasticity of Carbon-black Filled Rubber, Journal of King Mongkut's Institute of Technology North Bangkok, Vol. 13 (2003), No. 4:30-35.

134) Chinjaree, A., Assavapisit, S. and Khommongkol, P. Synthesis of Zeolite from Iron Smelting Slag of Cupola Furnace, Suranaree Journal of Science and Technology, Vol. 10 (2003), No. 4:181-190.

135) Baker, E., Sheikh, A., Alrahman, A. and Mahmood Mat Yunus, W. The Effect of The Annealing Time on the Optical Properties of Selenium Thin Films, Suranaree Journal of Science and Technology, Vol 8 (2001), No 1-2:37-41.

136) Rayzman, V.L., Rerkjirasawad, P. and Aturin, A. Thailand's Lignite Ash As a Raw Material For Manufacturing Alumina And Byproducts by Alkaline Hydrothermal Method, Suranaree Journal of Science and Technology, Vol. 8 (2001), No. 1-2:83-89.

137) Elshiekh Abdelrahman, A., Deraman, M. and Omer, R. X-Ray Diffraction Analysis of Carbon Prepared from KOH % Treated Self-adhesive Carbon Grain (SACG), Suranaree Journal of Science and Technology, Vol. 10 (2003), No. 4:191-197.

138) Trashoo, K. and Thepa, S. Using Silica Gel for the Evaporative Cooling System, Suranaree Journal of Science and Technology, Vol. 10 (2003), No. 4:191-197.

139) Amornnkitbamrung, M. and Kanaoka, C. Effect of Temperature on Dust Cake Formation and Detachment, Suranaree Journal of Science and Technology, Vol. 9 (2002), No. 1:8-15.

140) Pheeraphattana, J. Morphine Sulfate Sustained Release from Matrix Tablets Containing Hydroxypropylmethylcellulose, The 20th Symposium on Thai Pharmaceutical Researches, Chulalongkorn University, Thailand, December 1, 2003.

141) Sriamornsak, P. A Novel Floating Emulsion Gel Sphere For Stomach-specific Drug Delivery, The 20th Symposium on Thai Pharmaceutical Researches, Chulalongkorn University, Thailand, December 1, 2003.

142) Sangkapart, S. Application of Polyvinyl Acetate Aqueous Dispersion in Preparation of Sustained Release Matrices by Spray Drying Process, The 20th Symposium on Thai Pharmaceutical Researches, Chulalongkorn University, Thailand, December 1, 2003.

143) Chongcheroen, W. The Amphilphilicity of Thermosoftening Base (GELUCIRE) on The Release Characteristic of Diltiazem Hydrochloride Semisolid Matrix Capsule, The 20th Symposium on Thai Pharmaceutical Researches, Chulalongkorn University, Thailand, December 1, 2003.

144) Vasarach, C. Design and In Vitro Evaluation of Acylovir Sustained Release Tablet Using Hydrophilic Matrix System, The 20th Symposium on Thai Pharmaceutical Researches, Chulalongkorn University, Thailand, December 1, 2003.

145) Namwijitphan, W. Controlled Release of Chitosan Film Coated Tablets by Osmotic and Diffusion Mechanisms, The 20th Symposium on Thai Pharmaceutical Researches, Chulalongkorn University, Thailand, December 1, 2003.

146) Chantorn, S. Effect of Processing and Formulation Variables on The Properties and Release of Diclofenac Sodium From Microtablets, The 20th Symposium on Thai Pharmaceutical Researches, Chulalongkorn University, Thailand, December 1, 2003.

147) Phuvarit, P. Pregelatinized Glutinous Rice Starch As a Sustained Releasing Agent For Tablet Preparations, The 20th Symposium on Thai Pharmaceutical Researches, Chulalongkorn University, Thailand, December 1, 2003.

148) Boonamnuayvitaya, V., Chaiya, C., and Tanthapanichakoon, W. Effect of Water Vapor on the Adsorption of Toluene onto the Activated Carbon Derived from Coffee Residue, MaDParT 2005, Bangkok, Thailand, August 5, 2005.

149) Singjai, P., Changsarn, S., and Thongtem, S. Electrical resistivity of bulk multi-walled carbon nanotubes synthesized by an infusion chemical vapor deposition method, Personal contact.

150) Damronglerd, S. Patent in Fluidized-bed furnace, awarded by Department of Intellectual Properties, Thailand, patent number 8958.

151) Damronglerd, S. Patent in Fluidized-bed waste-water treatment reactor, awarded by Department of Intellectual Properties, Thailand, patent number 8958.

152) Phoonphetmongkon, Y., Kulvanich, P., Tanthapanichakoon W. and Charinpanitkul, T., Particulate coating in fluidized bed enhanced by electrostaticity, presented in The NSTDA Annual Conference 2005, Thailand, March 28-30, 2005.

153) Jubsin, C., Tanthapanichakoon, W., and Rimdusit, S. Wood-substituted Composites From Highly-filled Poly-

benzoxazene, presented The 28th Congress on Science and Technology of Thailand, Thailand, October 24-26, 2002.

Author's short biography

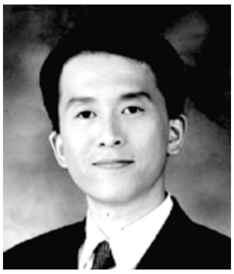

Dr. Tawatchai CHARINPANITKUL

Dr. Tawatchai CHARINPANITKUL is director of Center of Excellence in Particle Technology (CEPT), CHULALONGKORN University (CU). He received his B. Eng. in Chemical Engineering from CU. in 1986. After completing his M. Eng and D. Eng. in the same field from University of TOKYO, JAPAN in 1989 and 1992, respectively, he worked with Prof. W. TANTHAPANICHAKOON to establish a research team focusing on Particle Technology in Thailand. His research contributions are mainly concentrated on fluidization, aerosol collection and biomass utilization processes. His current research involvement is also extended to synthesis and application of nano particulate systems, in particular, Carbon Nanoparticles, Metallic Nanoparticles (i.e. Au, TiO_2, ZnO and ZnS). At the moment, he has leaded a research group which consists of about 30 young researchers with both domestic and international collaborations in JAPAN, KOREA, FRANCE and USA. etc.

Chalida Klaysom

Miss Chalida Klaysom was born on August 2, 1980 in Suratthani province, Thailand. She received the Bachelor Degree (Chemical Technology) and Master Degree in Chemical Engineering from Chulalongkorn University. Her master thesis was entitled as "Preparation, Characterization and Continuous Process Design of Activated Carbon from Waste Tires" , in which she not only prepared and characterized the carbonaceous porous materials from industrial residue like waste tires, but also designed the process to develop the products industrially. At present, with support of Thai government, she is conducting her Ph.D. in the University of Queensland, Australia, and will be working as a lecturer in Chulalongkorn University when graduation.

Siriporn MONCHAYAPISU

Siriporn MONCHAYAPISUT obtained her B. Eng. in Petrochemical and Polymeric Materials from Silpakorn University. Since 2002 to present she has joined Center of Excellence in Particle Technology (CEPT), Department of Chemical Engineering, Faculty of Engineering, Chulalongkorn University as a research assistant. Her research interest covers polymer science and technology as well as nanotechnology.

Author's short biography

Sira Srinives

Sira SRINIVES was awarded his MS. Degree in Chemical Engineering on March, 2006, from Chulalongkorn University (CU), Thailand, and has worked as a full-time research assistant in the Center of Excellence in Particle Technology, CU, since then. He experienced some back ground in the field of dust collection technology, as shown in his thesis work, "Development of rice mill dust collection system using rice husk bed" . At present, he is looking forward to a commercialization of this patented system in Thai rice mill industries. In August 2006, he was granted a scholarship from Thai government to pursue his Ph.D. in USA, in the field of Nanotechnology, and will become a lecturer in the Department of Chemical Engineering, Mahidol University, upon his return.

Wiwut TANTHAPANICHAKOON

Wiwut TANTHAPANICHAKOON obtained his PhD (U of Texas at Austin) and B. Eng. (Kyoto U) in chemical engineering. At present he is the founding Director of the National Nanotechnology Center (NANOTEC) under the umbrella of National Science and Technology Development Agency, Ministry of Science and Technology. Concurrently, he is Professor Emeritus of Chulalongkorn University (CU) and Chair Professor in particle Technology, Faculty of Engineering, CU. Since NANOTEC serves as Secretariat of the National Nanotechnology Policy Committee chaired by the Prime Minister of the Royal Thai Government, Dr. Wiwut is directly involved with the policy formulation and promotion of nanotechnology in Thailand. His life-long research interests covers particle technology, aerosol engineering (dust collection technology, air pollution control), process analysis and simulation, drying technology, energy technology, and nanotechnology.

Flake Particle Synthesis from Ductile Metal Particles Using a Novel High-speed Vibratory Mill†

Alexandros Theodore
Department of Chemical Engineering
*University of Florida**
Ki-Joon Jeon and Chang-Yu Wu[1]
Department of Environmental Engineering Sciences
*University of Florida***

Abstract

A novel particle processor was designed and built for the production of flake-shaped powders. 300 μm magnesium and 140 μm iron particles processed for 1 and 2 minutes were analyzed for dimensional, ductile, and morphological characteristics. Particle diameter distributions tended to broaden towards higher size ranges after 2 minutes of processing; the mean particle size was in the range of 400 μm for magnesium and 300 μm for iron. The flake thickness decreased over time, leading to a mean-thickness of 12 μm for the magnesium particle sample processed with 2 x 6.0 mm milling ball media after 2 minutes. The effect of particle medium showed that the milling operation had greater influences on the more ductile material. Surface morphology also became smoother as the milling time increased. Larger ball media tended to produce samples with larger particle sizes with wider size distributions, while smaller ball media produced smaller particles with narrower size distributions. Loading weights also tended to have similar trends. The novel process was demonstrated as an effective and efficient method for the production of flake-shaped metal particles which greatly reduced the amount of milling time and energy required for flake particle production.

Keywords: Flake, Vibratory Mill, Magnesium

1. Introduction

A flake-shaped particle is a particle with a high diameter-to-thickness aspect ratio. Needs for flake particles vary across a variety of applications such as: pigments and inks, electrochemical electrodes, fuel cell hydrogen storage devices, explosives, lightweight concretes and obscurences 1-6). Properties of flake-shaped particles have growing interests in the chemical and material industries, which continuously demand for increased efficiency in their processes. Flake particles are desirable from several viewpoints. Due to its high aspect ratio, a flake particle has a larger specific surface area than a spherical particle of the same volume, which can enhance chemical reactivity 5, 6). High aspect ratio metal flakes, such as those made of aluminum, have been used to increase optical obscurence characteristics so as to mimic a metallic look when used as pigment in paint 7). Additionally the use of flake powders for metal-hydride electrodes in modern batteries has shown significant improvement in electrical capacity 4, 8). Processes for the production of flake-shaped particles are relatively new and have yet to be extensively studied and mastered. Conventional methods for flake particle synthesis are attritor milling, vibratory ball milling, ball milling and wet milling 1, 2, 9).

Attritor mills generally refer to the use of a stirring rod and pin to agitate a solution of grinding media and the target particles. During such agitation, the random collisions of balls statistically occur with the target particle in between, eventually flattening the

---

† Accepted July 24, 2006

* Gainesville, FL 32611-6005 USA
** Gainesville, FL 32611-6450 USA
[1] Corresponding author
TEL: (352) 392-0845 FAX: (352) 392-3076
E-mailaddress: cywu@ufl.edu

particle after successive impactions [9]. This method, however, can take at least 5 hours to produce consistent flake particles, wasting a large amount of energy to fluid friction and fruitless collisions, and also requires milling to occur in a liquid solution, which can react with the target particle [9]. A vibratory mill operates under similar circumstances as that of the previously mentioned attritor mill; however, it produces a high frequency of randomly colliding ball media by the means of large vibrating forces, and it does not require a liquid milling solution [12]. Though this method allows for the highest kinetic transfer of those mentioned, it is also bounded by long operating times (up to 8 hours; e.g. SPEX model 8000 [12]). Ball milling methods typically require lubricants and anticoagulants such as stearic or oleic acid and/or mineral spirits to control the shape and quality of the product flake [1, 2]. These reagents are incompatible when reactive metals such as Al, Fe, Mg, and Cu must remain in their elemental form and can possibly react with the reagents during milling, especially when high energy transfers are present. Wet milling methods such as basket mills are not compatible for similar reasons. Furthermore, these conventional methods are very time-consuming, ranging in processing time from 0.5 to 60 hours [1-3, 8, 9]. As an example, Hong and Kim[2] reported that processing scrap aluminum particles in a wet ball mill system with oleic acid requires 30 hours to produce micrometer thickness flake particles.

The objective of this study was to develop a novel high-speed vibratory mill process for the production of flake particles so as to significantly reduce the milling time required to achieve micrometer thickness without the need of subsidiary milling aides. During milling operations, a cycle of particle fragmentation and reformation was observed. The effects of plastic deformation, particle-to-particle welding and flake fragmentation of this cycle on particle size distribution were examined. Several operating parameters of the milling process were studied, including milling time, particle medium (i.e. Fe, Mg), initial particle size, loading weight and ball media size.

2. Mechanisms

2.1 High Speed Orbiting of Ball Media

The milling operation occurs within a closed milling tube, where spherical particles are subjected to strong compression and shear forces produced by ball media that flatten the particles. The motion of ball media in the milling tube is illustrated in **Fig. 1(a).** Compression and shear forces are produced by ball media that roll along the smooth inner wall of the milling tube at high speeds (several thousand rotations per minute) forming sustained orbiting regions. **Fig. 1(b)** is a photograph demonstrating the orbits created by the rolling ball media that are visible as long circular blurs functioning inside a glass test-tube.

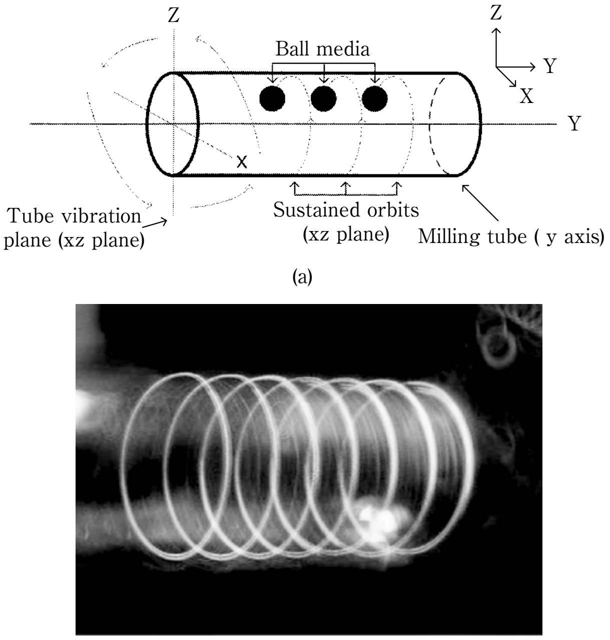

(a)

(b)

Fig. 1 (a) Schematic diagram of orbiting motion; (b) Photograph of orbiting media in glass tube (the circular blurs are trails of ball movement).

Oscillations in the xz-plane of the milling tube produce the impetus for the media motion. **Fig. 2** illustrates the frame-by-frame movements of the milling tube and the resulting movement of the containing media.

The motion of the milling tube is indicated as going in the direction from the gray position to the black position. The oscillations of the milling tube from position 1 → 2 → 3 → 4 repeated, cause an acceleration with a continuously changing direction away from the milling tube center - indicated as a gray arrow. In turn this causes the internal ball media to naturally find the opposite-most point from the direction of milling tube movement. This point is indicated by the position of the dark and filled ball media in **Fig. 2.** With a continuous change in the direction of the milling tube acceleration, the position of the ball media likewise changes continuously. Ultimately this motion causes the internal media to roll along the inside

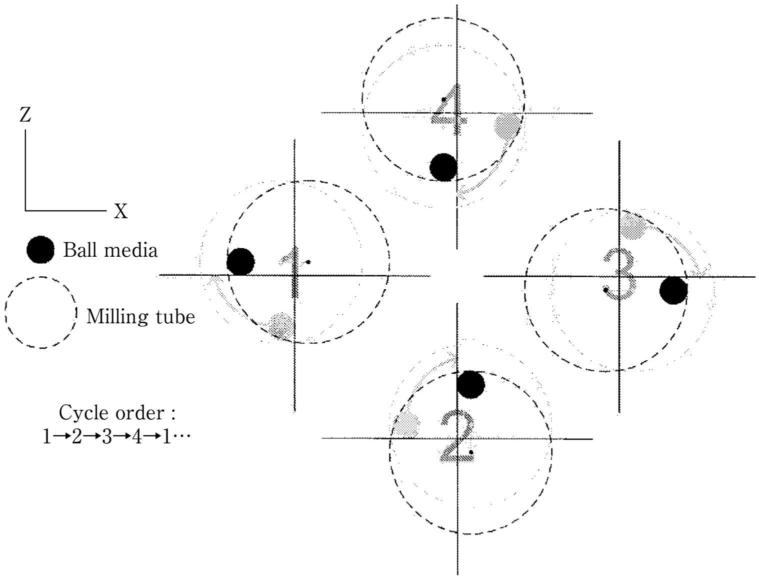

Fig. 2 Schematic diagram of basic orbiting media mechanisms.

edges of the milling tube at the same frequency as the milling tube oscillation.

2.2 Plastic Deformation and Welding Effects

In the context of the presented novel milling system, plastic deformations are shape changes occurring to the initial particle sample during milling due to the high compression and shear forces from the orbiting ball media. Deformation occurs primarily in a way that results in very thin and wide flakes. Furthermore, progressive deformation can lead to fragmentation of flake particles, resulting in many smaller flakes. Evidence of this can be seen as an increase in the fraction of smaller particles.

Due to the high frequency of orbiting media and chaotic swirling motion of particles inside the milling tube, random flake overlaps readily occur. Composite welding occurs as various flakes are joined to one another by random overlappings resulting in a single compound flake. Instances of compound flake-to-flake welding have been reported for various types of milling devices[4,7-10]. Since there are both large and very small particles accumulating, the resulting compound flake may be large or not so large, leading to a wider distribution of sizes for welding dominant systems. However, a compound flake must always be greater in size than its constituents, resulting in a shift of the particle size distribution towards larger particle size ranges.

3. EXPERIMENTAL

3.1 Experimental System

For this research, a lab scale version of the novel vibratory mill was built. A milling tube was constructed using 10 mm internal diameter aluminum tubing with a length of 50 mm. Milling tubes were mounted via plastic collars perpendicular to a high-speed vibrator, which provided 13,000 oscillations per minute (OPM) at 120 V. Chromium-Steel Cr-52100 balls (Norstone Inc.) with diameters of 2.0 4.0 and 6.0 mm were used as ball media in the milling tube. The area between the first orbiting ball and the last orbiting ball is defined as the milling zone. Whereas, the actual area which will receive the milling forces is defined as the milling area and is the sum of the ball diameter projections on the milling tube, disregarding the inter-orbit gaps, which are considered ineffectual. This method of classification is illustrated in **Fig. 3.** The milling area was fixed as being equal to a total of 12 mm for all the balls in the milling tube - such that the number of balls in each tube would be 2, 3 and 6 for the 6.0 mm, 4.0 mm and 2.0 mm sizes, respectively. This arrangement was chosen with the aim in mind to make the effective milling area approximately equal for all samples so as to replicate the effective milling area for all ball sizes. Two types of particles were tested: 300 - μm magnesium (Alfa Aesar) and 140 - μm iron (Fisher Sci.). Each milling tube was sealed under ambient atmosphere with plastic end caps to contain the ball media and particles.

Table 1 Experimental conditions

Sample	Particle medium and size	Weight loading	Ball media count and size	Milling time
1	Mg, 300 μm	25mg	2 × 6.0mm	1min
2	Mg, 300 μm	25mg	2 × 6.0mm	2min
3	Fe 140 μm	25mg	2 × 6.0mm	1min
4	Fe 140 μm	25mg	2 × 6.0mm	2min
5	Mg, 300 μm	25mg	3 × 4.0mm	2min
6	Mg, 300 μm	25mg	6 × 2.0mm	2min
7	Mg, 300 μm	15mg	2 × 6.0mm	2min
8	Mg, 300 μm	35mg	2 × 6.0mm	2min

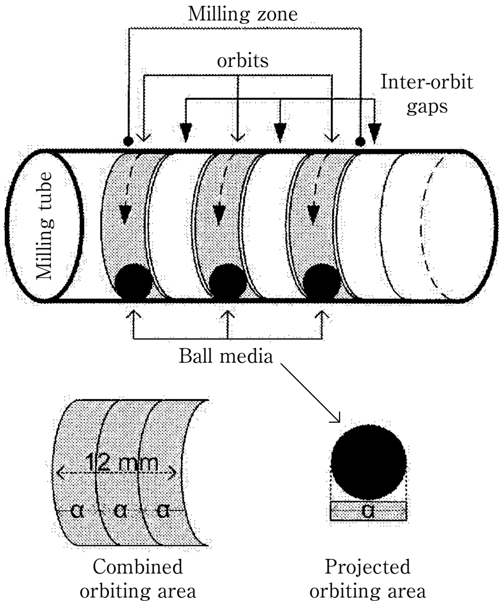

Fig. 3 Milling zone and milling Area classification.

Particles were weighed and loaded into each milling tube with the ball media in the tube. After processing, the products were separated from the ball media and then stored in labeled vials for analysis. **Table 1** displays the parameters tested for each sample.

3.2 Product Characterization

Three basic characteristics of the resulting flake particles were analyzed, including mean particle diameter, mean particle thickness and morphology. Flake particle samples were evenly distributed on glass substrates and observed under an optical microscope (Olympus BX-60) using Spot Advanced (Diagnostic Instrument, INC) image capture software to acquire sample images. The sample images were then processed with Image Pro Plus (Media Cybernetic, L.P) to calculate particle number and dimensional statistics for each sample photo batch. Martin diameter, which is defined as the length of the line parallel to a given axis that divides the particle into two equal area regions, was measured. Approximately 4000 particles were analyzed per sample. To determine the thicknesses, flake particles were suspended and solidified in an epoxy resin. The dried epoxy was then cut transversally to obtain cross sectional slices of flakes suspended in the epoxy and subsequently examined under optical microscope. Optical microscopy was also used to study the surface morphology of bare flake particles for evidence of increased surface cracks and multiple-flake layering from flake-to-flake welding.

Because of the nature of the milling process, and provided the understanding that the size distribution of particles is dependant on the fragmentation and welding qualities of the milling parameters, its distribution does not necessarily resemble a Gaussian curve. In this study, mean particle size and standard deviation were evaluated side-by-side, which can effectively signify in what regime (fragmentation/welding dominant) the sample distribution reflects.

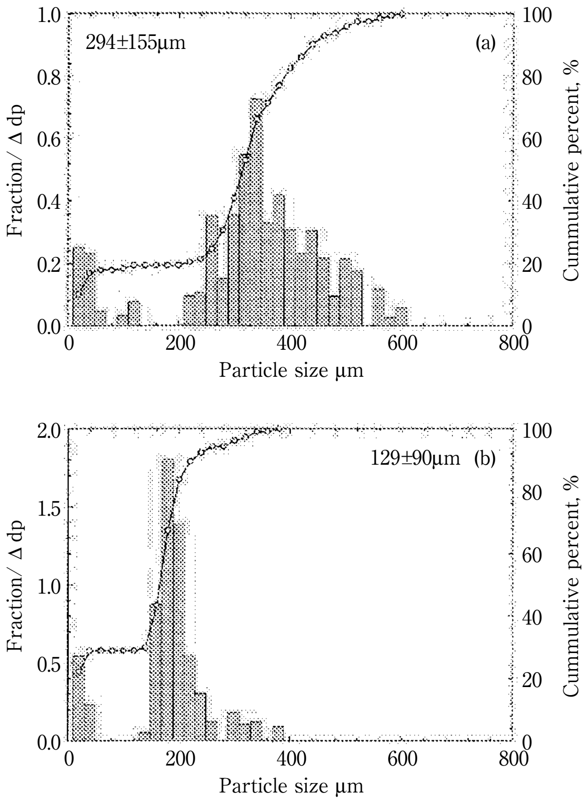

Fig. 4 Particle size distributions for original particles: (a) 300 μm Mg and (b) 140 - μm Fe.

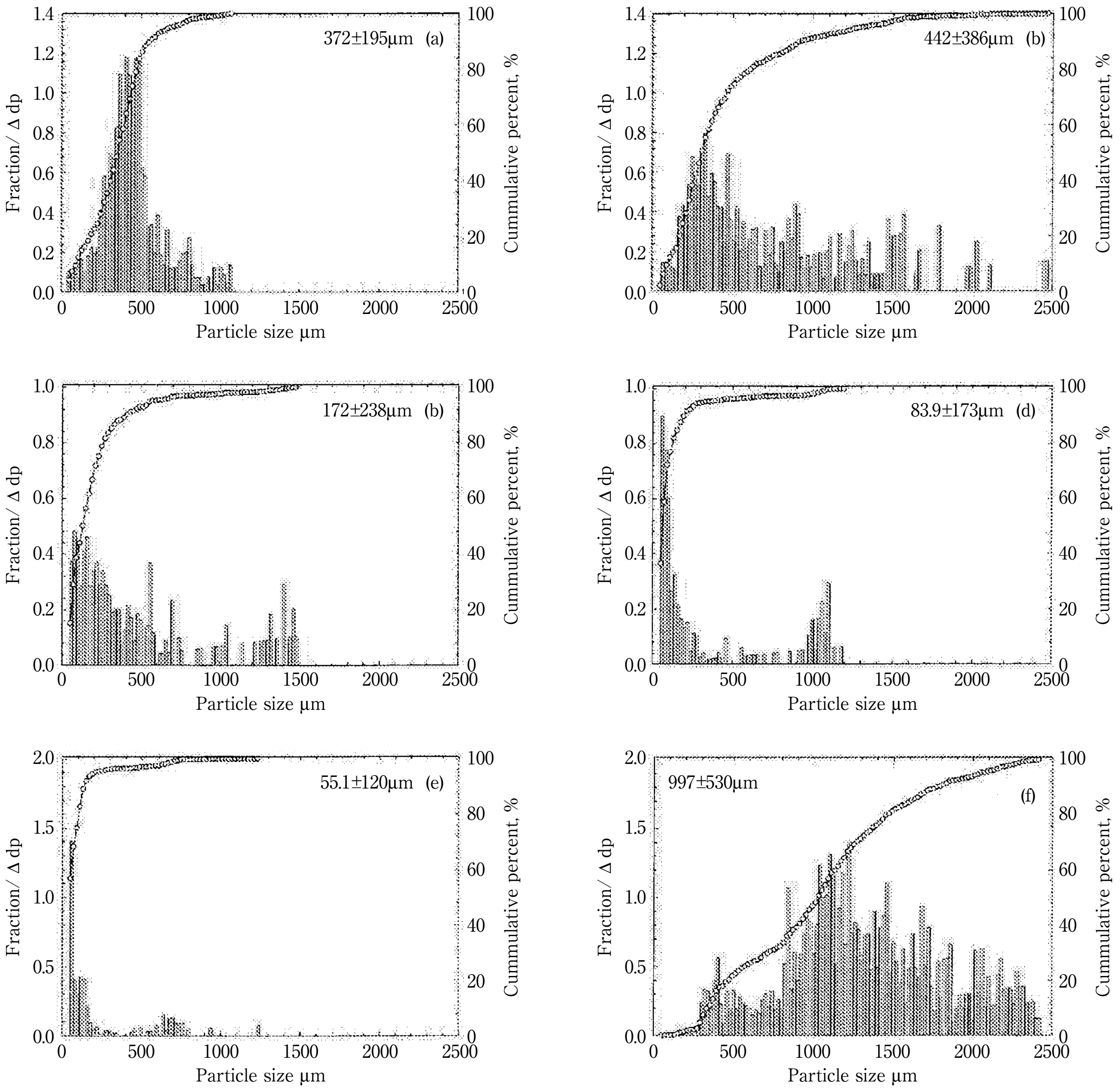

Fig. 5 Particle size distributions for Mg particle (300 μm): (a) sample 1, (b) sample 2, (c) sample 5, (d) sample 6, (e) sample 7, and (f) sample 8.

4. Results and discussions

4.1 300 μm Mg Particle

The original particle size distributions for 300 -m Mg are displayed in **Fig. 4(a)**. The effects of increased milling time on particle size distribution (Martin diameter) and thickness of 300 μm Mg particles were studied. The results for samples 1 and 2, after milling for 1 and 2 minutes respectively, are displayed in **Fig. 5(a)** and **(b)**.

The resulting mean diameters for samples 1 and 2 were 372 and 442 μm and the standard distributions were 195 and 386 respectively. As shown in **Figs. 5 (a)** and **(b)**, the majority of the sample remains near 400 μm after both 1 and 2 minutes of milling. The peak fraction in the mean size range decreased from 1.2 in sample 1 to 0.8 in sample 2, while fractions of larger particles increased. This shows that a significant amount of the particles in the mean size range were redistributed into larger particle sizes and the size distribution became broader with increased milling time. This growth and broadening in particle size distribution can be explained by plastic deformation and particle welding as described earlier. The lack of change in the smaller particle size regime implies that the particle fragmentation was not as important as welding, and that there does not seem to be a change in the dominant mechanisms between 1 and 2 minutes. It can therefore be concluded that, since the mean diameter is large and increasing and that the standard deviation is also broadening, plastic deformation and composite particle welding are the dominant mechanisms over particle fragmentation in these samples.

The change in flake thickness was analyzed using optical microscope images of epoxy resin slices containing the flake particles. **Fig. 6 (a)** displays the change in thicknesses in samples 1 and 2. With increased milling time, it can be seen that the flake thickness distribution decreases, similar to the flake diameter trend. The mean particle thickness decreased from 300 μm of unprocessed particles to approximately 35 μm after only 1 minute. Within just 2 minutes of milling, there was an even greater decrease in flake thickness, with an average flake thickness of 12 μm. Plastic deformation is responsible for this trend, since with the start of milling, flakes are continually molded thinner. It should be pointed out that due to the nature of the milling process, not all particles are milled simultaneously. During the early periods of milling, some are fully milled while others are yet to be milled. As milling time increases, the fraction of un-milled particles decreases, and the amount of milled particles arrives at the total - therefore reducing the sample discrepancy caused by the remaining un-milled particles. This explains the decrease in the flake thickness distribution in **Fig. 6 (a).** In short, the fraction of the thicker and un-milled particles greatly decreases with processing time. **Figs. 6 (b)** and **(c)** are the microscope images of representative flake cross-sections from samples 1 and 2 respectively. The results of samples 1 and 2 demonstrate the novel high-speed vibratory milling as a very effective and efficient process for the production of flake-shaped particles.

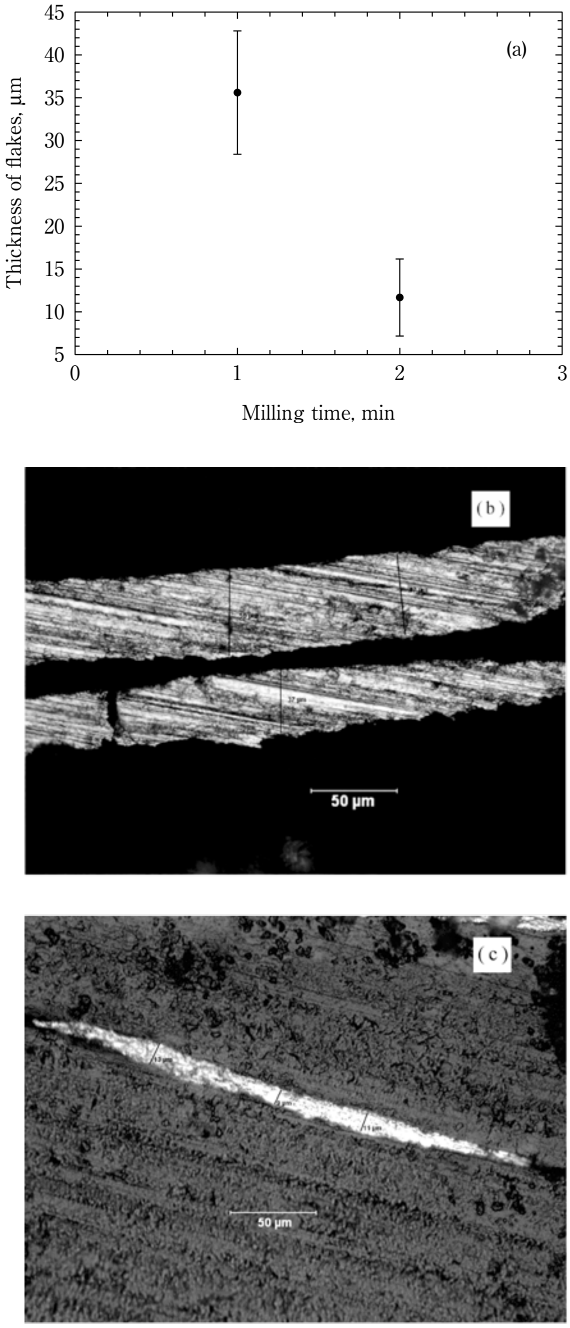

Fig. 6 Thickness of Mg particle as a function of milling time: (a) particle thickness distribution, (b) cross-sectional images for 300 μm Mg particle after 1 minute and (c) 2 minutes.

4.2 140 μm Fe Particle

Experiments were also carried out for Fe particles. The original particle size distributions for 140 - μm Fe particles are displayed in **Fig. 4 (b)** and the results for samples 3 and 4 are displayed in **Fig. 7**. The resulting mean diameters for samples 3 and 4 were 238 and 241 μm and their standard deviations 63.4 and 89.4 respectively.

It can be seen from **Figs. 7 (a)** and **(b)** that the majority of the particle size resides in the mean range of 240 μm. Similar to **Figs. 5 (a)** and **(b)**, the peak fraction decreased and larger particles developed, resulting in a wider particle size distribution. Similar to samples 1 and 2 of magnesium particles, the most possible explanation for the broadening particle size distribution is the effect of plastic deformation and particle welding - consequences of the high compression forces imposed on the flake particles inside the milling tube. In the smaller particle size range, there

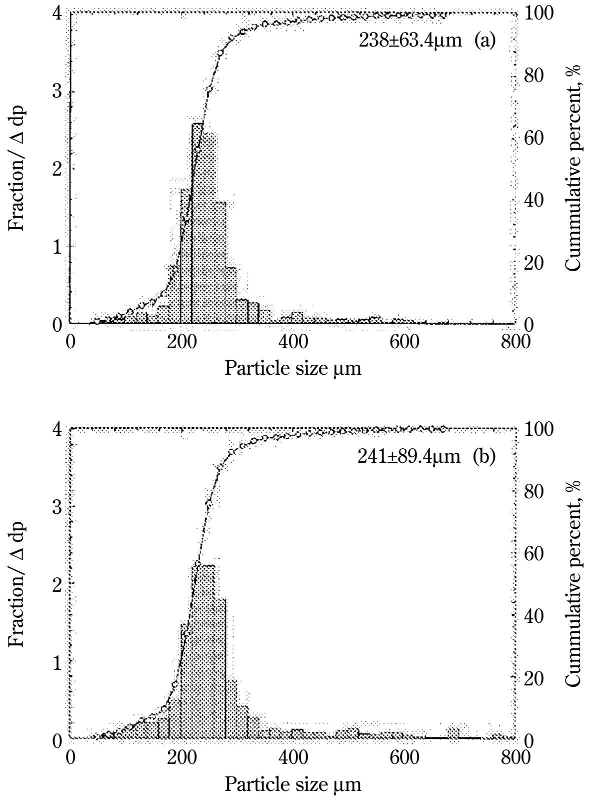

Fig. 7 Particle size distributions for iron particle (140 μm) as a function of milling time: (a) sample 3 and (b) sample 4.

is little change in particle size distribution below the mean particle size. This further affirms that samples milled up to 2 minutes do not show significant signs of particle fragmentation dominance. Rather, because of the particle size distribution shift in the larger range, welding is the dominant mechanism that influences the particle size distribution in samples 3 and 4.

Comparing the results of samples 1, 2 and 3, 4 can reveal the effects of particle material. Ductility is the primary factor that determines the sample's dimensional results. Ductile and malleable materials (those with a low Young's Modulus; Mg - 45 MPa, Fe - 211 MPa) tend to have larger particle size distribution changes over time, as they are more vulnerable to the compression and shear forces present during milling.

In addition to size characteristics, surface qualities of the flake particles were observed under optical microscope. **Fig. 8** shows the acquired images of the Fe flakes. Two main characteristics of the flakes were examined: surface morphology and evidence of flake-to-flake welding events. Comparing **Figs. 8 (a)** and **(b)**, it can be seen that the surface of these iron particles became noticeably smoother with increased time.

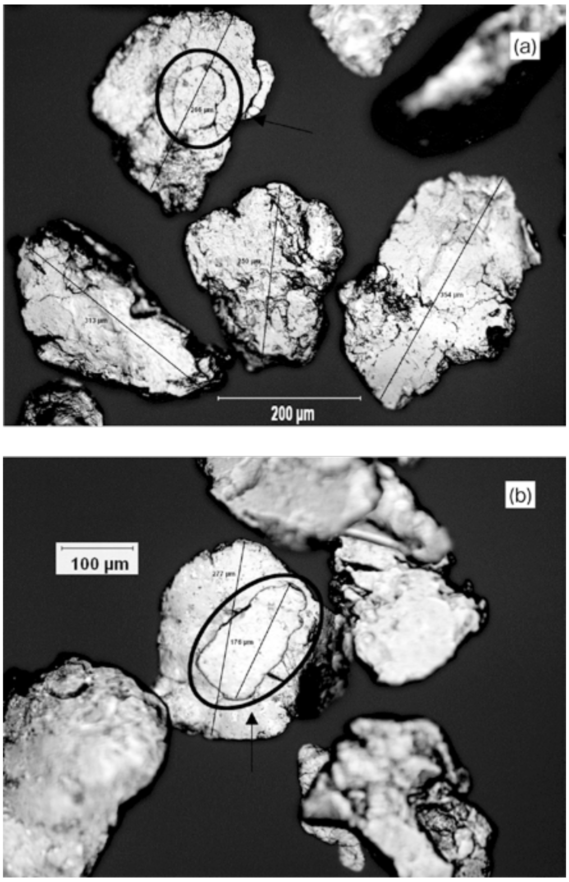

Fig. 8 Optical microscope images at 20x magnification of iron particle: (a) sample 3 and (b) sample 4.

Additionally, evidence of flake-to-flake welding can be seen (circled in both **Figs. 8 (a)** and **(b)**). The flake pieces circled are likely to be in an intermediate phase of the entire process; a loose flake is first taken up by another and then eventually milled until the two compress into each other to the point that they are indistinguishable.

4.3 Effect of Ball Size

To investigate the effect of ball size on the milling operation, in regards to mean particle size and particle size distribution, two additional samples were prepared with smaller ball sizes than that of sample 2. Samples 2, 5, and 6 can be compared for the effect of the milling ball size, with all other parameters kept constant. Their particle size distributions are graphed in **Figs. 5 (c)** and **(d)**. It can be seen clearly that a simple trend exists between the resulting mean particle size and the ball media size: as the ball size is reduced, the mean particle size reduces (442, 172 and 84 μm for 6, 4 and 2 mm ball media, respectively). This trend can be explained by the larger ball sizes creating higher compression forces due to their greater mass, resulting in thinner and wider particles.

A more detailed inspection of the particle size distributions gives clues in regards to the welding and fragmentation characteristics of each sample. As mentioned earlier, fragmentation of initial flakes, by its own nature, will result in greater numbers of smaller flakes. Conversely, welding will result in generally larger flake particles, and depending on the extent and number of weldings, can have a broad range of particle sizes. It can be seen in **Figs. 5 (c)** and **(d)** that there is a much higher fraction of smaller particles present in sample 6 (2.0 mm balls) than in sample 5 (4.0 mm balls). In other words, there is a broader midrange distribution and a lesser fraction of small particles in sample 5 (4.0 mm balls) than in sample 6 (2.0 mm balls). This indicates that smaller ball media tend to show a dominance of fragmentation over welding, while larger ball sizes tend to have a more profound welding impact, resulting in a broader distribution of particles. This vision is also supported by the standard deviation values for samples 5 and 6. The low welding qualities of sample 6 can also be resorted to the low compression forces present in smaller media, which may not be sufficient to join two flake particles. Since fragmentation is readily present even in smaller ball sizes, all milling processes that use larger ball media have fragmentation occurrences. They differ only in their welding ability, which so far has been the most influential factor of the samples' particle size distribution.

4.4 Effect of Weight Loading

The effect of weight loading of Mg in the milling tube was studied by comparing three contrasting weights. Samples 7 and 8 were 15 mg and 35 mg respectively, and were compared to the similar sample 2 of 25 mg. Their particle size distributions are displayed in **Figs. 5 (e)** and **(f)**. Comparing the trends of samples 7, 2, and 8, shows the effect of increased loading weight. As the loading weight increases, the size distribution can be seen to shift from smaller to larger particles. The mean diameter data for each sample also supports this observation (55, 442 and 997 μm for 15, 25 and 35 mg, respectively). As mentioned earlier, smaller particle sizes, like those present in sample 7, imply a dominance of fragmentation and a deficit of welding instances. Since welding can only occur when particle overlapping and milling coincide, the frequency of welding is influenced by the probability of particle overlapping, which is directly related to the particle concentration. As the loading weight of the sample is increased, the concentration increases and the probability of overlapping increases as well, resulting in a greater amount of particle-to-particle welding and ultimately a shift in the particle size distribution towards a midrange size, with a typically larger standard deviation.

5. Conclusions

Several aspects of flake characteristics produced by a novel vibratory mill process were studied, including: flake diameter, thickness, and morphology as a function of processing time, ball media count and weight loading. The results of these data showed similar particle size distribution trends in samples of magnesium and iron. With increased milling time, more particles in the larger size ranges developed. This expanding distribution can be explained largely because of the effects of plastic deformation and composite particle welding. The more ductile magnesium particles tended to show faster changes in their particle size distributions, since they were more subjective to the forces that caused the shifting distribution. Flake thickness of magnesium was found to decrease as a function of time, as did the particle thickness distribution. With compression and shear forces caused by the orbiting ball media, the flake particles were continuously milled thinner, eventually to a mean thickness of 12 μm after 2 minutes of milling. Additionally, as milling proceeded, the influence of partially milled particles reduced and welding occurrences continued thus lowered the standard deviation of flake thickness with time.

The increasing weight of the milling ball media resulted in higher compression forces, and directly affected the mean particle size and its distribution based on their greater welding effects. Smaller ball media tended to show a dominance of fragmentation over welding, while larger ball sizes tended to have a more profound welding impact, resulting in a broader distribution of particles.

Increasing the concentration of flake particles (weight loading) increased the probability of overlapping and therefore resulted in a greater amount of particle-to-particle welding. This led to a shift in the particle size distribution towards a midrange size, with a larger standard deviation.

In summary, a novel vibratory mill consisting of ball media orbiting at high revolutions inside a milling tube produced high compression and shear forces capable of processing 25 mg of 300 μm spherical magnesium particles into flakes of mean diameter 442μm and thickness of 12μm in only 2 minutes. As demonstrated, the novel high-speed vibratory mill process is a very efficient and effective process for the production of flake-shaped particles from ductile metal particles.

Acknowledgements

Alexandros Theodore is grateful to Dr. Dale Lundgren for the EPA Air Pollution Training Scholarship and to the Particle Engineering Research Center (PERC) at University of Florida for the Undergraduate Research Scholarship. Ki-Joon Jeon is grateful to the University of Florida Alumni Fellowship and Korean Science & Engineering Foundation's Graduate Study Abroad Scholarship Program (M06-2003-000-10264-0). The authors acknowledge PERC for the use of their analytical instrumentation.

References

1) Hong, S.H., Kim, B.K.: "Fabrication of aluminum flake powder from foil scrap by a wet ball milling process", *Materials Letters*, 51, 139-143, (2001).
2) Hong, S.H., Lee, D.W., Kim, B.K.: "Manufacturing of aluminum flake powder from foil scrap by dry ball milling process", *Journal of Materials Processing Technology*, 100, 105-109, (2000).
3) Lee, S.M., Yu, J.S., Lee, P.S., Lee, J.Y.: "Characteristics of surface-modified metal hydride electrode with flake Ni by the ball-milling process", *Journal of Alloys and Compounds*, 330-332, 835-840, (2002).
4) Yoshinaga, H., Arami, Y., Kajita, O., Sakai, T.: "Highly densed-MH electrode using flaky nickel powder and gas-atomized hydrogen storage alloy powder", *Journal of Alloys and Compounds*, 330-332, 846-850, (2002).
5) Trunov, M.A., Schoenitz, M., Zhu, X., Dreizin, E.L.: "Effect of polymorphic phase transformations in Al_2O_3 film on oxidation kinetics of aluminum powders", *Combustion and Flame*, 140, 310-318, (2005).
6) Cashdollar, K.L.: "Overview of dust explosibility characteristics", *Journal of Loss Prevention in the Process Industries*, 13, 183-199, (2000).
7) Smith, G.B., Gentle, A., Swift, P. D., Earp, A., Mronga, N.: "Coloured paints based on iron oxide and silicon oxide coated flakes of aluminum as the pigment, for energy efficient paint: optical and thermal experiments", Solar Energy Materials and Solar Cells, 79,179-197 (2003).
8) Yoshinaga, H., Wada, M., Sakai, T., Miyamura, H., Kuriyama, N., Uehara, I.: "Metal hydride electrodes with lamellar-type network structure", *Journal of Alloys and Compounds*, 253-254, 665-667, (1997).
9) Kilinc, Y., Ozturk, S., Ozturk, B., Uslan I.: "Investigation of milling characteristics of alumina powders milled with a newly designed vibratory horizontal attritor", *Powder Technology*, 146, 200-205, (2004).
10) Huang, J.Y., Wu, Y.K., Ye, H.Q.: "Ball milling of ductile metals", *Materials Science & Engineering*, A199, 165-172, (1995).
11) Kurrer, K.E., Gock, E., Vogt, V., Florescu, R.: "Centrifugal tube mill for finest grinding", *International Journal of Mineral Processing*, 74S, S75-S83, (2004).
12) Dunlap, R.A., Small, D.A., MacKay, G.R., O'Brien, J.W., Dahn, J.R. Cheng, Z.H.: "Materials preparation by ball milling", *Can. Journal of Physic*, 78, 211-229, (2000).
13) Suryanarayana, C.: "Mechanical alloying and milling", *Progress in Materials Science*, 46, 1-184, (2001).

Author's short biography

Dr. Chang-Yu Wu

Dr. Chang-Yu Wu is an Associate Professor in the Department of Environmental Engineering Sciences at University of Florida. He received his BS from Mechanical Engineering at National Taiwan University, both MS and PhD from Environmental Engineering at University of Cincinnati. His teaching and research interests include air pollution control, aerosol processes, nanoparticles and catalysis/photocatalysis. He has more than 40 refereed journal publications, 120 conference presentations, 16 invited lectures and 1 patent. He received 6 awards for his achievement in research and engineering education in the past 5 years.

Author's short biography

Ki-Joon Jeon

Ki-Joon Jeon received his BS and MS from Environmental Engineering at Inha University, Korea, in 2001. Currently, he is working toward a Ph.D in Environmental Engineering and Science at the University of Florida. His research interests include hydrogen storage and nanoparticle synthesis and his current project involves the kinetics of metal hydride formation.

Alexandros Theodore

Alexandros Theodore is pursuing bachelors of science in Chemical Engineering at the University of Florida. Research areas include metal-hydride storage methods, flake particle production, nano-particle coating methods and electrohydrodynamic atomization.

Experiments and Simulations on Vibration Induced Densification of Bulk Solids[†]

N. Zhang and A. D. Rosato[1]
Department of Mechanical Engineering,
Granular Science Laboratory,
New Jersey Institute of Technology[*]

Abstract

The change in bulk density or solids fraction that occurs when a vessel of granular materials is vibrated is an important, industrially-relevant process. In this paper, we present findings from experiments and discrete element simulations on the relaxation behavior of assemblies of uniform spheres that are vertically oscillated. Physical measurements of the bulk solids fraction, qualitatively reproduced in the simulations, reveal noticeable trends in the data dependent on the vibration amplitude and frequency. By carrying out extended simulations, a 'phase' chart depicting the percentage improvement in bulk density in terms of amplitude and frequency is obtained. Our results suggest that the behavior revealed in this chart may be characteristic of density relaxation in bulk solids.

Keywords: Density relaxation, Discrete element simulation, Solids fraction evolution, Vibrated bulk solids

1. INTRODUCTION

An important industrial issue in the production, transport and packaging of granular materials is the identification of those factors that affect bulk density, including how the material has been handled throughout its processing history. A common phenomenon that is not well-understood is the increase in bulk density that takes place when a container of granular materials is shaken, tapped or vibrated. There is a rather extensive literature on this topic, ranging from very fundamental investigations on the development of packing algorithms and microstructural analysis to more practical experimental and numerical studies. While it is not possible in this paper to provide a complete review of the extensive literature on this topic, a few representative papers are discussed in an attempt to provide a rough sketch.

From a certain perspective, one may think of the phenomenon of density relaxation as having its foundations in the extensive literature on the packing of spheres. (See for example reference1-15). As early as 1611, Kepler explored the geometry of the snowflake while in 1665, Robert Hook investigated circle and sphere packings. In 1694, Gregory, a Scottish astronomer, suggested that thirteen rigid uniform spheres could be packed around a sphere of the same size - a hypothesis that was only disproved by Leech some 262 years later. In 1727, Hales examined the packing of dry peas pressed into a container - an experiment that was later known as the 'peas of Buffon' based on work in 1753 by Comte de Buffon. In 1887, Thompson[16)] considered the question of how to fill Euclidean space using truncated octahedrons, while Slichter[17)] was the first to attempt to find analytical expressions for the porosity in beds of uniform spheres. There has also been interest in the alternative question of what is the minimal solids fraction ν_m of a rigid assembly of uniform spheres such that each must touch at least four others and the contact points must not lie all in one plane. Along these lines, in 1932 Hilbert[18)] found a structure for which, ν_m=0.123, while a year later, Heesch and Laves[19)] created a stable arrangement of spheres such that ν_m=0.056. It should

---

[†] Accepted: July 24, 2006

[*] Newark, New Jerey 07102, USA
[1] Corresponding author
Telephone/Fax: 973-596-5829
E-mail: rosato@njit.edu

be pointed out, however, that these geometric structures cannot be created using standard experimental procedures.

The distinction between a ‘loose’ (or poured) and ‘dense’ random packing of spheres was conceived by Oman and Watson[20] in 1944. This idea was quantified in experiments by Scott[21], in which 3mm steel ball bearings poured into cylindrical containers were subjected to two minutes of shaking. Although the vibration parameters used were not reported, he found two values of the solids fraction, i.e., $v_{\mathrm{loose}}=0.59$ and $v_{\mathrm{dense}}=0.63$ corresponding to a random close and dense configuration. Improved experiments by Scott and Kilgour[22] yielded a more precise value of the dense solids fraction $v_{\mathrm{dense}}=0.6366 \pm 0.0005$. We note that deposition experiments in viscous liquids to achieve stable loose structures have reported solids fraction values as low as $v_{\mathrm{loose}}=0.555 \pm 0.0005$ for glass spheres and $v_{\mathrm{loose}}=0.506 \pm 0.0005$ for roughened acrylic spheres[23].

The notion that a consolidated state of optimal bulk density could be achieved through the use of high frequencies and relatively small displacement amplitudes was suggested by Stewart in 1951 - a claim that found support in the 1964 experiments of Evans and Millman[24]. Several years earlier, Macrae et al.[25] proposed that bulk density was related to impact velocity, with a critical value producing optimal results. In 1967, D’Appolonia[26] performed vibration tests on dry sand within a cylindrical vessel. A mechanical shaker was employed to produce unidirectional harmonic motion of the cylinder with displacement amplitudes up to 0.254 mm and frequencies $10 \leq f \leq 60$ Hz. By measuring the volume change of the sand over a range of vibration parameters, a plot of bulk density versus dimensionless acceleration $\Gamma \equiv a\omega^2/g$ was generated, indicating that the greatest increase took place at $\Gamma \approx 2$. It was unclear from their data why increasing the acceleration beyond an optimal value resulted in decrease in bulk density. Dobry and Whitman[27], who extended D’Appolonia’s experiments, reported in 1973 that the most rapid compaction occurred when $0.9 < \Gamma < 1.1$, while a maximum bulk density was achieved for $1.1 < \Gamma < 1.3$. At higher accelerations between 1.3 and 2.0, the density either stabilized or continued to increase.

In addition to the use of continuous vibrations, there have been investigations on tapped systems, such as that by Takahashi and Suzuki[28] who studied the evolution of the volume of real powders. They described the phenomenology via a first-order rate law whose solution yielded a solids fraction $v(n)$ as a function of the number of taps n that evolved to an apparent final density v_∞ in accordance to $v(n)=v_0+(v_\infty-v_0)e^{-k/n}$. The effect of detached, vertical sinusoidal taps applied to a tall cylindrical vessel filled with 2mm mono-disperse, soda-lime glass spheres was experimentally studied by Knight et al.[29] using a noninvasive, capacitive technique to measure solids fraction. The evolution of the measured solids fraction was found to rely on the relative acceleration and on the number of taps. Experimental data was fit to a four-parameter phenomenological model of the form $v(n)=v_\infty-\dfrac{v_\infty-v_0}{1+B\ln(1+n/\tau)}$ where v_∞ is the steady-state density (dependent on the acceleration history), τ is a relaxation time, and B is an undetermined constant that depends on Γ. Linz[30] proposed an explanation of the experimental model from an analysis of the stroboscopic decay law that he derived from his physical interpretation of the compaction process. Knight et al.’s experiments were extended by Nowak et al.[31,32] to explore the frequency dependence and amplitude of the measured density fluctuations as a function of vibration intensity Γ. They found that at certain intensities the system attained a well-defined average steady-state density with large fluctuations after extended tapping. The magnitude of these fluctuations depended not only on the depth at which measurements were made, but also on Γ (eg., increasing Γ produced larger fluctuations about the mean density).

In addition to physical experiments, particle level simulations that offer insights into the micro-structural process taking place during the density relaxation process have been done. For example, Baker and Mehta[33] studied the qualitative effects of vibrations on a system of mono-disperse spheres using a hybrid simulation technique in which a real ‘shake’ was modeled by a controlled volume expansion of the assembly, a hard-sphere Monte Carlo at a low temperature to reduce the system potential energy, followed by a modified sequential random-close-packing algorithm to achieve stability. The authors carried out a careful analysis of the solids fraction and coordination number distribution as a function of their simulated shaking intensity, as well as a study of contact networks that corroborated the roles of various identified relaxation mechanisms. Rosato and Yacoub[34] carried out discrete element simulations to assess the effect low amplitude ($a/d<0.1$), vertical oscillations applied to a vessel of frictional, inelastic spheres of diameter d. They reported fairly good fits of the data with phenomenological predictions of Knight et al.[29] and the exponential decay model of Takahashi and Suzuki[28].

More recently, An et al.[35] presented discrete element results that supported the earlier findings of Zhang et al.[36,37] with regard to the effect of frequency and amplitude on solids fraction. They identified two respective densification mechanisms corresponding to low and high relative accelerations.

The physical system of interest in this paper is a model granular material comprised of acrylic spheres housed in a vertically oscillated cylindrical container. We propose a basis for trends observed in our experiments (Section 2) on the bulk solids fraction as a function of the applied vibration amplitude and frequency. Our explanation hinges on a detailed series of discrete element simulations (Sections 3 and 4) that qualitatively reproduce the experimental behavior. While the parameter space examined in the simulations is rather extensive (e.g., see reference 36)), in this paper we report on a subset of our studies that is relevant to the experiments. A phase diagram portraying 'improvement' in bulk density reveals distinct regions in the frequency-amplitude space which correlate with the experiments.

2. Experiments and Results

The containment vessel is an acrylic cylinder of diameter D formed from stacked rings that are mounted onto a B&K shaker. **Fig. 1** shows a schematic of the experimental system. An accelerometer attached to the piston provides feedback control through which precise adjustments to the frequency and amplitude could be made. The first part of the experiment involved measurements of the initial (before vibrations are applied to the piston) bulk solids fraction. Particles (acrylic spheres, d = 3.175 mm) were slowly poured into the cylinder and then the top layer was removed by sliding the top ring across. This was done to ensure that the cylinder was filled with a level surface to a height of 30d. The poured bulk solids fraction ν_0 could then be computed from the volume of the cylinder and weight of its contents. For the aspect ratio D/d=20 used in the experiments, we obtained an average value $\nu_0 \cong 0.604$ that is typically associated with a loose random packing [6].

The vibration experiments were carried out by filling the cylinder with mono-disperse acrylic spheres (d = 3.175 mm) to an undisturbed bed depth $H \approx$ 95.3 mm using the method previously described. The filled cylinder was rigidly mounted onto the shaker head, which was sinusoidally oscillated over a range of amplitudes $0.04 \leq a/d \leq 0.24$ and frequencies ω between 25Hz–100Hz, (corresponding to relative accelerations $\Gamma \equiv a\omega^2/g$ between 0.94 and 11.54). For each selected frequency and amplitude, the shaker was run for ten minutes, with each experiment repeated several times to confirm the results. In order to reduce the buildup of static charge, the inside tube wall and particles were treated with a household anti-static agent. In measuring the bulk solids fraction ν_1 after the vibrations were stopped, a level particle surface was formed using the same procedure as described in the pouring experiments. **Figs. 2-6** show the improvement in solids fraction, $\left(\frac{\nu_1 - \nu_0}{\nu_1} \times 100\right)$ versus Γ for increasing values of a/d.

Our experiments reveal four trends in the behavior of ν versus Γ that depend on the level of the displacement amplitude. **Fig. 2** shows that for a/d = 0.04, the solids fraction increases with Γ, but the improvement is only about 3.3% at Γ = 5.1. Observations of the vibrated bed indicated that there was little or no bulk motion with the exception of some activity of the particles at the top surface for $\Gamma \geq 2$. We conjecture that at these excitation levels the bulk density increases through slow, cooperative particle rearrangements throughout the assembly, analogous to the 'push filling' mechanism suggested by An et al.[35]. When a/d is between 0.06 and 0.10, results in **Fig. 3a** show a maximum in bulk solids fraction ($\nu_m \approx$ 0.636, cor-

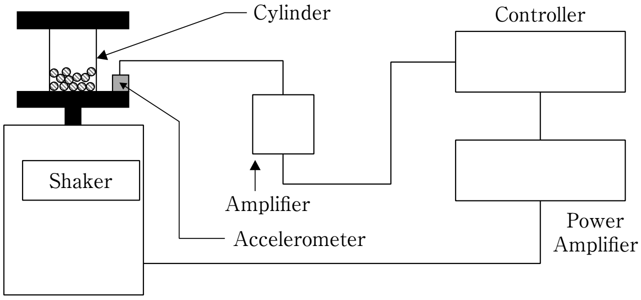

Fig. 1 Schematic of experimental apparatus.

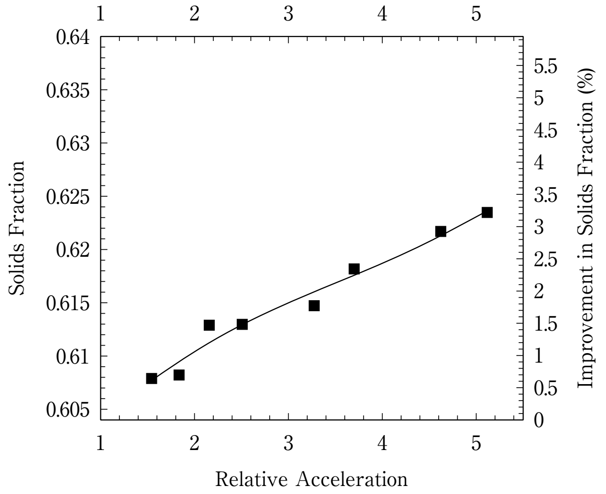

Fig. 2 Solids fraction versus relative acceleration at *a/d* = 0.04. The solid line is a best fit curve to show the trend.

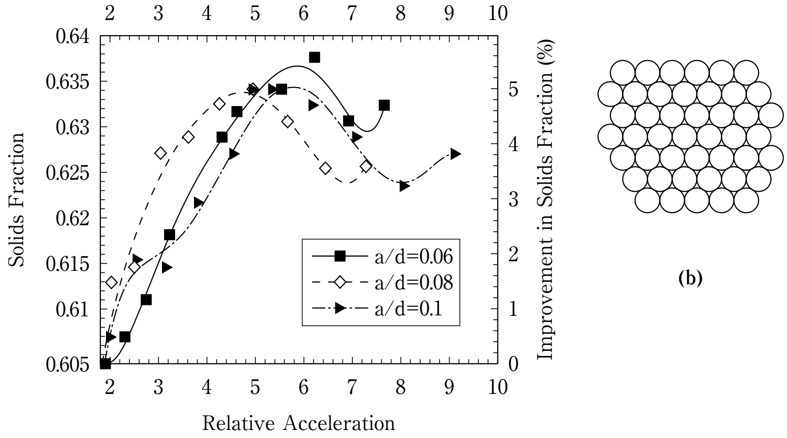

Fig. 3 (a) Solids fraction versus relative acceleration at *a/d* = 0.06, 0.08 and 0.10; The lines are best fit curves to show the trends in the data. (b) illustration of particle arrangement near the cylinder wall at Γc.

responding to an improvement > 5%) when Γ is between 5 and 7, followed by a slight expansion of the bed (or a reduction in v) with a further increase of Γ. Near the peaks (at $\Gamma=\Gamma_c$), particles near the cylinder walls were seen to remain in contact with each other and to travel downwards in a collective manner, a phenomenon indicative of convective motion that has been reported in other studies[38-46]. The movement of these wall particles became more pronounced as Γ was increased to Γ_c. Further observations made near the walls and on the surface at Γ_c revealed closed-packed arrangements of the particles as illustrated in Fig. 3b. We believe that the influence of the cylinder walls in the presence of the slow convection in this region at Γ_c is responsible for the creation of these structures, which in turn contribute to the overall increase in bulk solids fraction. It is worthwhile noting that Nowak et al.[32] also pointed out that the walls of the cylindrical container used in their experiments (aspect ratio $D/d \sim 9.4$) may have influenced the compaction process. In fact, they attained a substantially larger mean solids fraction (v= 0.656) than what is known as random close packing of spheres (v = 0.6366[6,22]).

Distinct oscillations (**Fig. 4**) in the solids fraction versus Γ were found when *a/d* = 0.16, where the improvement in the bulk density was generally less than 3.6%. At this amplitude level, convection could still be observed as particles adjacent to the walls moved downward. At the highest amplitude level used (*a/d* = 0.24), the solids fraction versus Γ remains almost constant and little improvement (approximately 0.5%) was attained (**Fig. 5**). At these conditions, a marked expansion of the bed depth occurred (analogous to other experiments reported in the literature[47]) and the system resembled a dense, energetic "gas" of

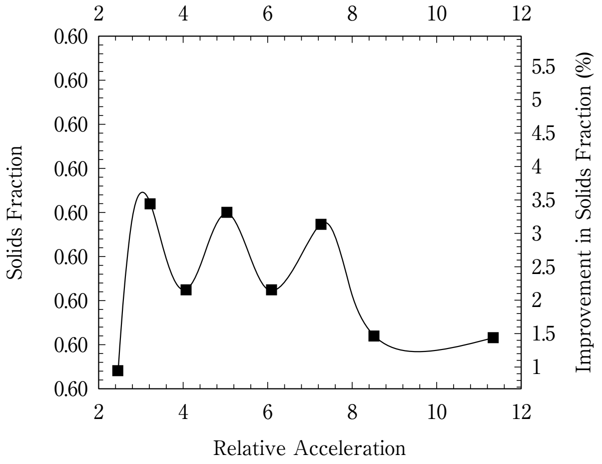

Fig. 4 Solids fraction versus relative acceleration at a/d = 0.16. The solid line is a best fit curve to show the trend.

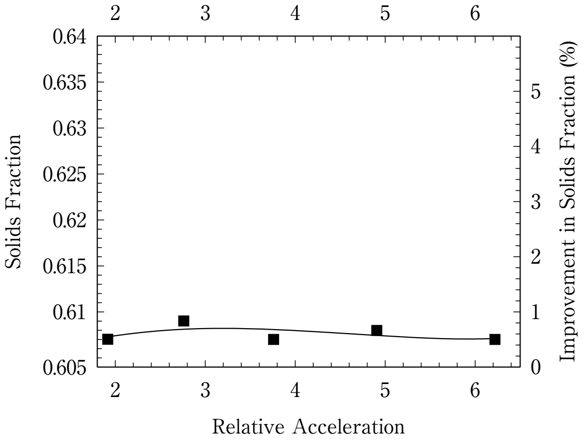

Fig. 5 Solids fraction versus relative acceleration at a/d = 0.24. The solid line is a best fit curve to show the trend.

particles (it required relatively little effort to insert a rigid bar into the vibrating mass). We were unable to see any particle convection near the cylinder walls in this case.

3. Discrete Element Simulations

The discrete element simulations reported in this paper employ the soft "partially latching spring model" developed by Walton et al. [48-50] for elastic-plastic collisions. This model features mechanisms of energy dissipation for both the normal (i.e., along the line of centers of the pair of colliding particles) and tangential directions. Energy loss in the normal direction is accomplished using linear springs that are activated as particles overlap and then move apart. Because the loading spring constant K_1 is smaller than the unloading (or restituting) spring of constant K_2, the normal relative separation velocity is smaller than the relative approach velocity, and this produces a constant effective restitution coefficient $e = \sqrt{K_1/K_2}$. For the flows simulated in this study, collision velocities were not of sufficient magnitude to warrant the use of a velocity-dependent restitution that is appropriate for particle velocities of the order of $1\,\mathrm{m/s}$ and greater. In the tangential direction the Walton-Braun model approximates Mindlin's and Deresiewicz's theory [51] for elastic spheres subjected to tangential loading. Dissipation is achieved through a tangential stiffness that decreases with tangential displacement until it is zero, at which point full sliding occurs at the friction limit μ. Although contacts that experience rotation coupled with tangential sliding are not a feature of this model, particles can rotate due to the transmission of tangential impulse.

The time step Δt through which the particle equations of motion are integrated is approximated from the normal force model by dividing twice the time spent in unloading period during a particle collision into n steps. It can be shown that $\Delta t = \frac{\pi e}{n}\sqrt{m/2K_1}$ where m is the particle mass and e is the restitution coefficient. The value selected for K_1 ensured that overlaps were less that approximately $0.01d$ in accordance with the behavior of real colliding particles, so that $\Delta t \sim 10^{-6}$s. The mass density of the simulated particles (ρ=1200 kg/m^3) corresponded to acrylic plastic to match the experimental material. The equations of motion of the N particles are integrated using a leap-frog method with a backward Euler approximation at t = 0. For the translational motion (rotation equations are analogous), the discretization is given by

$$\begin{cases} v_i^{t+1/2} = v_i^{t+1/2} + \dfrac{F_i^t}{2m_i}\Delta t, \quad t>0, \quad i = 1, 2, \quad \cdots N \\ x_i^{t+1} = x_i^t + v_i^{t+1/2}\Delta t \\ v_i^{-1/2} = v_i^0 - \dfrac{F_i^0}{4m_i}, \quad i = 1, 2, \cdots N \end{cases}$$

where **F** is the net force on the i^{th} particle.

In the results of our study described next, the computational cell was a rectangular box having a solid side walls and a floor whose motion was governed by $s(t)=a\sin(2\pi ft)$.

4. Simulation Results and Discussion

A poured assembly of spheres was obtained by initially positioning particles randomly within the computational cell, after which they were allowed to fall under the action of gravity for 1.5 seconds. This generated a stable configuration with a bulk solids fraction that did not change appreciably for runs of longer duration. We remark that the results of our pouring simulations[36] produced bulk solid fractions that were consistent with experimental measurements in the literature. The poured assembly was then used as the starting point for the vibration simulations. The assembly was energized by applying vertical, sinusoidal oscillations to the floor of the computational cell for three seconds, followed by a relaxation phase during which particles fell under gravity to a stable state. Although not reported in this paper, we found that the three seconds of vibration was sufficient for the system to reach steady-state conditions from time-averaged depth profiles of 'granular temperature' and solids fraction.

In what follows, the behavior of the bulk solids fraction as a function of amplitude and frequency is presented. In all cases, spheres were assigned a normal restitution coefficient e = 0.9, and friction coefficient μ_p = 0.1. As will be seen, the results were in reasonable qualitative agreement with the trends observed in our previously described experiments. In Section 4.2, a much larger system whose aspect ratio more closely matches the experiments is considered. Here, the simulated results are presented in the form of a chart that shows the improvement in density as a function of frequency and amplitude.

4.1 Vibration Frequency and Amplitude

Four amplitude ratios were considered (a/d = 0.02, 0.08, 0.24, 0.48) over frequencies ranging from 5Hz to 90Hz. Spheres were assigned a normal restitution coefficient e = 0.9, and friction coefficient μ_p = 0.1. These values were obtained from experiments of Louge [52] for acrylic spheres (i.e., μ_p = 0.096 ± 0.006, e=0.934 ± 0.009). Although we reduced the value of e somewhat to improve computational efficiency, this did not produce any significant changes in the qualitative trends reported in this paper. The selection of a shallow configuration (i.e., poured fill height of approximately 7d and $v_0 \approx$ 0.577) and an aspect ratio L/d = 9.4 minimized the system size (N = 600), so that greater computational efficiency was obtained. Despite the small system size, the qualitative trends obtained were consistent with those found in the physical experiments. Although not reported here, we also carried out studies in deeper beds and found similar behavior of the system's 'dynamic' state[36], which in turn impacts the densification upon relaxation.

The general trend in **Fig. 6** when a/d = 0.02 is very much the same as what took place in the physical experiments (see **Fig. 2**). Over the frequency range tested at this amplitude, there is a continual improvement in bulk solids fraction. When a/d = 0.08, the data shown in **Fig. 7** suggests a peak around 6% near $f \cong$ 50Hz; for greater frequencies, a reduction in solids fraction takes place. When the amplitude a/d is 0.24 (**Fig. 8**), the peak value occurs at approximately 40 Hz, and the curve decays thereafter until, near 80 Hz, no improvement in bulk density is possible at higher frequencies. The occurrence of the peak and decay afterwards is consistent with the experimental observations of Appolonia et al.[26]. Finally, at a/d= 0.48, the improvement in solids fraction is minimal (**Fig. 9**), and after a frequency of approximately 35 Hz, the system does not experience any densification upon relaxation. This trend is analogous to the experiments reported in **Fig. 5**.

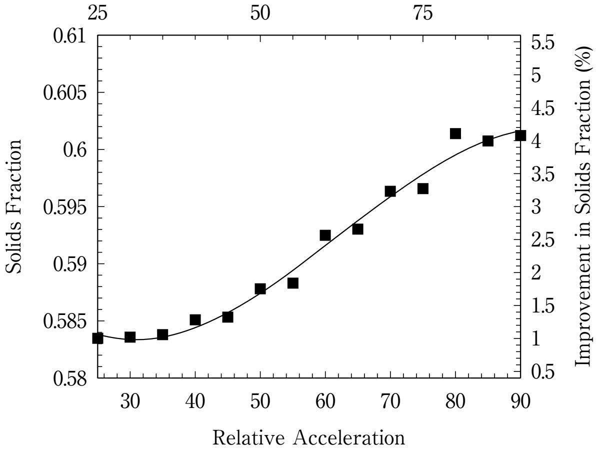

Fig. 6 Solids fraction behavior versus frequency at a/d = 0.02 and N = 600.

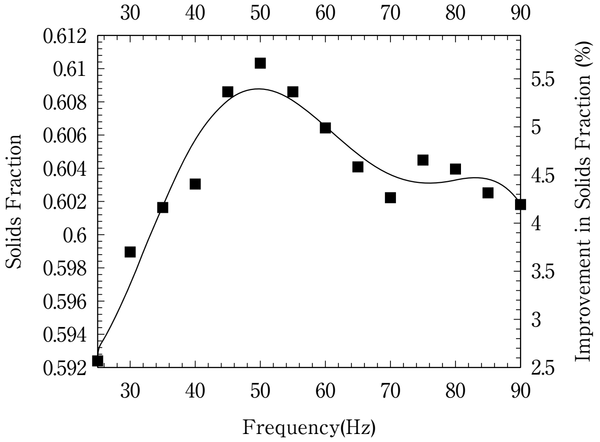

Fig. 7 Solids fraction behavior versus frequency at a/d = 0.08 and N = 600.

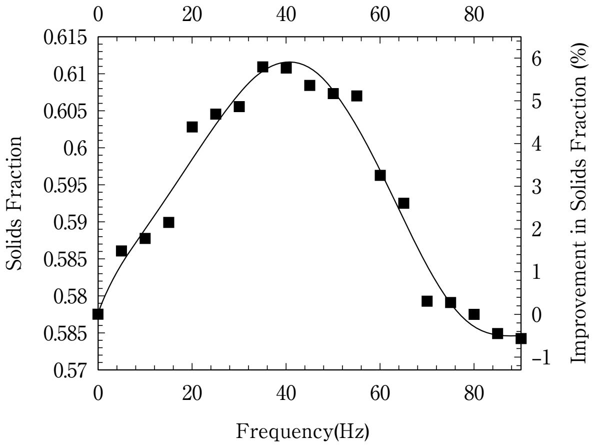

Fig. 8 Solids fraction behavior versus frequency at $a/d = 0.24$ and $N = 600$.

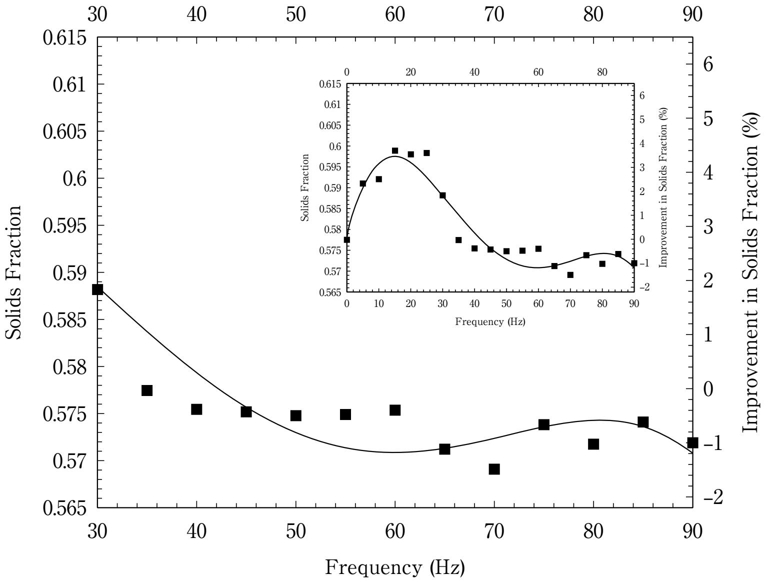

Fig. 9 Solids fraction behavior versus frequency at $a/d = 0.48$ and $N = 600$.

A comparison between the experiments (**Fig. 2-5**) and the simulation (**Fig. 6-9**) shows reasonable qualitative agreement. Furthermore, the maximum improvement in solids franction of approximately 6% agrees with the experimental measurements. Although there are quantitative differences between the simulated and experimental results (possibly attributed to boundary conditions and aspect ratio), the simulation does generate all of the important critical phenomena observed in the experiments.

4.2 Densification Phase Chart

We studied a system of $N = 8000$ spheres in a computational cell having an aspect ratio $L/d \approx 25$. In so doing, we were able to further validate the simulations in a system whose cross-sectional dimension was comparable to our experiments. The procedure previously described was followed to generate the initial poured assembly ($\nu_0 \cong 0.604$), which filled the cell to a depth of approximately 11d. Due to limited computational resources, we were unable to carry out studies for deeper beds at this aspect ratio, which would have permitted real quantitative comparisons with our experiments.

We ran a test to identify a specific value of the amplitude and frequency at which the relaxed bulk density was largest; this occurred at $a/d = 0.16$ and $f = 40$ Hz. With these parameters, the system was vibrated until the computed solids fraction curve flattened out (**Fig. 10**). An extrapolation of the date as $1/t \rightarrow 0$ yielded a solids fraction $\nu = 0.658$, in close agreement with the experimental results of Nowak et al. [53]. Arrangements of the particles adjacent to the side walls at $t = 13$s revealed the formation of hexagonally packed structures analogous to what was observed in

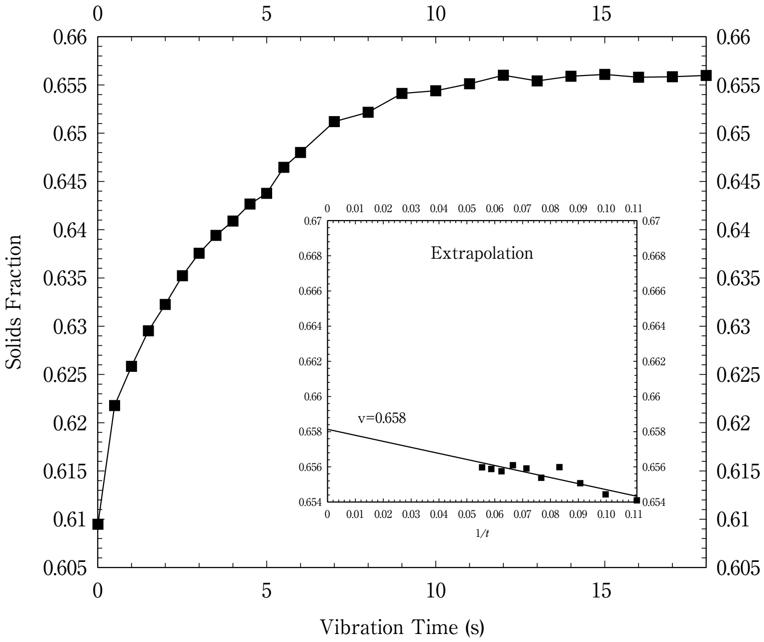

Fig. 10 Evolution of the solids fraction for an 8000 particle system (*L/d* = 25) vibrated at *a/d* =0.16 and *f* = 40 Hz. The extrapolated solids fraction (as $1/t \rightarrow \infty$) $v = 0.658$ is shown in the inset.

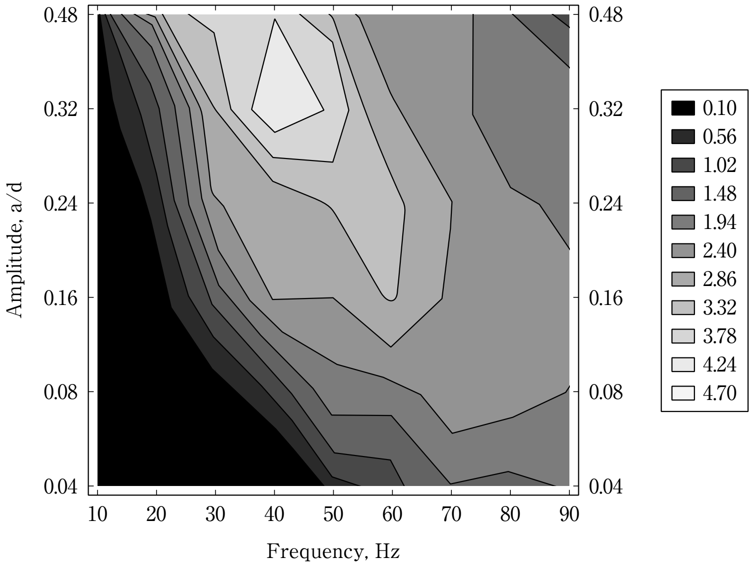

Fig. 11 Chart showing improvement in solids fraction as a function of vibration amplitude and frequency for an 8000 particle system in which *L/d* = 25.

our experiments

A series of case studies was carried out spanning vibration amplitudes and frequencies $0.02 \leq a/d \leq 0.48$ and $10\text{Hz} \leq f \leq 90\text{Hz}$. Our results are summarized in **Fig. 11** in the form of a chart showing the improvement in bulk solids fraction as a function of amplitude and frequency. Four distinct regions are visible corresponding to various levels of improvement as indicated by the gray scale. A region of optimal improvement (in the amplitude-frequency space) is clearly visible, a trend that is in agreement with our experiments. Although not presented in this paper, we also examined profiles of the system's granular temperature, solids fraction and ratio of lateral to vertical kinetic energy, which revealed common characteristics for each region[37]. At the poorest levels of improvement, the vibrated system was found to be in a relatively high energetic state which settled to a static configuration with little or no increase in bulk density. The full details of our investigation correlating the vibrated system with its relaxed density will be the subject of a future publication.

5. Conclusions

The densification behavior that takes place when a vertically oscillated system of uniform spheres is allowed to relax under gravity was investigated. The work finds its motivation in the industrial sector involved with the packaging of bulk solids. Experiments were carried out that exhibited clear trends regarding the influence of amplitude and frequency in achieving a state of optimal density. These trends were qualitatively reproduced in discrete element simulations that were extended further to a system having an aspect ratio comparable to the physical experiments. The results of the latter study were summarized in a 'phase' chart that revealed distinct frequency-amplitude regions which were characterized by various levels of the 'improvement' in the bulk density. Except for quantitative differences that depend on particle properties and mass overburden, we expect that similar patterns for the improvement would emerge for other materials.

6. Acknowledgements.

We acknowledge Union Carbide Corporation for the financial support of the Granular Science Laboratory and the research activities related to this paper. The authors also thank P. Singh, D. Blackmore, and J. Luke for their interest in this work and discussions, and O. Dybenko for help with the plots.

References

1) C. R. A. Abreu, F. W. Tavares, and M. Castier, "Influence of particle shape on the packing and on the segregation of spherocylinders via Monte Carlo simulations", *Powder Technology* **134**, 167-180 (2003).
2) D. J. Adams and A. J. Matheson, "Computation of dense random packings of hard spheres", *J. Chem. Phys.* **56**, 1989-1994 (1972).
3) R. F. Benenati and C. B. Brosilow, "Void Fraction Distribution in Beds of Spheres", *AICHE Journal* **8**, 359-361 (1962).
4) C. H. Bennett, "Serially deposited amorphous aggregates of hard spheres", *J. Appl. Phys.* **6**, 2727-2733 (1972).
5) J. D. Bernal and J. Mason, "Co-ordination of randomly packed spheres", *Nature* **188**, 910-911 (1960).
6) D. J. Cumberland and R. J. Crawford, "*The Packing of Particles*", Vol. 6 (Elsevier, 1987).
7) J. L. Finney, "Random packing and the structure of liquids. 1. The geometry of random close packing", *Proc. Roy. Soc. Lond. A* **319**, 479-493 (1970).
8) K. Gotoh, W. S. Jodrey, and E. M. Tory, "A random packing structure of equal spheres - statistical geometrical analysis of tetrahedral configurations" *Powder Technology* **20**, 233-242 (1978).
9) W. A. Gray, "*The Packing of Solid Particles*" (Chapman and Hall, Ltd., London, 1968).
10) M. J. Powell, "Computer-simulated random packing of spheres", *Powder Technology* **25**, 45-52 (1980).
11) C. A. Rogers, "The packing of equal spheres", *Proc. Lond. Math. Soc.* **8**, 609-620 (1958).
12) S. Torquato, T. M. Truskett, and P. G. Debenedetti, "Is Random Close Packing of Spheres Well Defined?", *Phys. Rev. Lett.* **84**, 2064-2067 (2000).
13) E. M. Tory, B. H. Church, M. K. Tan, and M. Ratner, "Simulated random packing of equal spheres", *Can. J. Chem. Eng.* **51**, 484-493 (1973).
14) W. M. Visscher and M. Bolsterli, "Random packing of equal and unequal spheres in two and three dimensionsn", *Nature* **239**, 504-507 (1972).
15) K. Z. Y. Yen and T. K. Chaki, "A dynamic simulation of particle rearrangement in powder packing with realistic interactions", *J. Appl. Phys.* **71**, 3164-3173 (1992).
16) W. Thompson, "On the division of space with minimum partitional area", *Phil. Mag.* **24**, 503-514 (1887).
17) C. S. Slichter, "Theoretical investigation of the motion of ground water," US Geol. Survey, 19th Annual Report, Part II (1899).
18) D. Hilbert and S. Cohn-Vossen, "*Anschauliche Geometrie*" (Springer Verlag, Berlin, 1932).
19) H. Heesch and F. Laves, "Uber dunne Kugelpackungen", *Z. Krist.* **85**, 443-453 (1933).
20) A. O. Oman and K. M. Watson, "Pressure drops in granular beds", *Natl. Patrol. News* **36**, 795-802 (1944).
21) G. D. Scott, "Packing of spheres", *Nature* **188**, 908-909 (1960).
22) G. D. Scott and D. M. Kilgour, "The density of random close packing of spheres", *British Journal of Applied Physics* **2**, 863 (1969).
23) N. Menon, "personnal communication", June 2, 2006.
24) P. E. Evans and R. S. Millman, "The Vibratory Packing of Powders", *Powder Met.* **7**, 50 (1964).
25) W. Macrae and W. A. Gray, "Significance of the properties of materials in the packing of real spherical particles", *Brit. J. Appl. Phys.,* 164-172 (1960).
26) D. D'Appolonia and E. D'Appolonia, "in *Determination of the maximum density of cohesionless soils*", 1967 (Jerusalem Academic Press), p. 1266-1268.
27) R. Dobry and R. V. Whitman, "Compaction of Sand on a Vertically Vibrated Table," Report No. 523, American Society of Testing Materials (1973).
28) M. Takahashi and S. Suzuki, "Numerical analysis of tapping behavior of ceramic powders", *Ceramic Bulletin* **65**, 1587 (1986).

29) J. B. Knight, C. G. Frandrich, C. N. Lau, H. M. Jaeger, and S. R. Nagel, "Density relaxation in a vibrated granular material", *Physical Review E* **51**, 3957-3963 (1995).

30) S. J. Linz, "Phenomenological Modeling of the Compaction Dynamics of Granular Systems", *Phys. Rev. E* **54**, 2925 (1996).

31) E. R. Nowak, A. Grushin, A. C. B. Barnum, and M. B. Weissman, "Density-noise power fluctuations in vibrated granular media", *Physical Review E* **63**, 020301 (2001).

32) E. R. Nowak, M. Povinelli, H. M. Jaeger, S. R. Nagel, J. B. Knight, and E. Ben-Naim, "in *Powders & Grains 97*", edited by R. Behringer and J. T. Jenkins (Balkema, Durham, NC, 1997), p. 377 - 380.

33) G. C. Barker and A. Mehta, "Vibrated powders: structure, correlations and dynamics", *Phys. Rev.* A **45**, 3435-3446 (1992).

34) A. D. Rosato and D. Yacoub, "Microstructure evolution in compacted granular beds", *Powder Technology* **109**, 255-261 (2000).

35) X. Z. An, R. Y. Yang, K. J. Dong, R. P. Zou, and A. B. Yu, "Micromechanical simulation and analysis of one-dimensional vibratory sphere packing", *Physical Review Letters* **95***,* 205502 (2005).

36) N. Zhang, "Doctoral dissertation Thesis", New Jersey Institute of Technology, 2004.

37) N. Zhang and A. D. Rosato, "Analysis of instantanteous dynamics states of vibrated granular materials", *Mechanics Research Communications* **31**, 525-544 (2004).

38) K. M. Aoki, T. Akiyama, Y. Maki, and T. Watanabe, "Convective roll patterns in vertically vibrated beds of granules", *Phys. Rev. E* **54**, 874-883 (1996).

39) J. A. C. Gallas, H. J. Herrmann, and S. Sokolowski, "Convection cells in vibrating granular media", *Physical Review Letters* **69**, 1371-1373 (1992).

40) J. B. Knight, E. E. Ehrichs, V. Y. Kuperman, J. K. Flint, H. M. Jaeger, and S. R. Nagel, "Experimental Study of Granular Convection", *Physical Review E* **54**, 5726 - 5738 (1996).

41) Y. Lan and A. D. Rosato, "Convection related phenomena in vibrated granular beds", *Physics of Fluids* **9**, 3615-3624 (1997).

42) C. Laroche, S. Douady, and S. Fauve, "Convective flow of granular masses under vertical vibrations", *J. Phys. France* **50**, 699-706 (1989).

43) J. Rajchenbach, "Dilatant process for convective motion in a sand heap", *Europhys. Lett.* **16**, 149 (1991).

44) A. D. Rosato and Y. Lan, "Granular-dynamics, modeling of vibration-induced convection of rough inelastic spheres", *Proceeding of the First International Particle Technology Forum, Denver CO (AIChE, New York, 1994)* (1994).

45) Y. Taguchi, "New origin of convective motion: elastically induced convection in granular materials", *Physical Review Letters* **69**, 1367-1370 (1992).

46) S. C. Yang and S. S. Hsiau, "Simulation Study of the Convection Cells in a Vibrated Granular Bed", *Chemical Engineering Science* **55**, 3627-3637 (2000).

47) C. R. Wassgren, "Vertical vibration of a bed of granular material in a container", *Journal of Applied Mechanics* **63**, 712-719 (1996).

48) O. R. Walton, Numerical simulation of inclined chute flows of monodisperse, inelastic, frictional spheres, *Mechanics of Materials*, **16**, 239-247(1993).

49) O. R. Walton, "in *Particulate Two-Phase Flow*", edited by M. C. Roco (Butterworths, Boston, 1992), p. 884-911.

50) O. R. Walton and R. L. Braun, "Stress calculations for assemblies of inelastic spheres in uniform shear", *Acta Mechanica* **63**, 73-86 (1986).

51) R. D. Mindlin and H. Deresiewicz, "Elastic spheres in contact under varying oblique forces", *J. Appl. Mech.* **20**, 327 (1953).

52) M. Y. Louge, (Cornell University, 1999), http://www.mae.cornell.edu/microgravity/impact-table.html

53) E. R. Nowak, J. B. Knight, E. B. Naim, H. M. Jaeger, and S. R. Nagel, "Density fluctuation in vibrated granular materials", *Physical Review E.* **57**, 1971-1982 (1998).

Author's short biography

Anthony D. Rosato, Ph.D.

Anthony Rosato received his PhD in Mechanical Engineering from Carnegie Mellon University in 1985. He has been at the New Jersey Institute of Technology since 1987 where he holds the rank of Professor of Mechanical Engineering. Dr. Rosato's research interests are in the broad field of particle technology, with a focus on computational modeling and experimental studies of granular flows related to the solids handling and processing industries. From 1995-1999, he served as the founding director of NJIT's Particle Technology Center, and he has been the director of the Granular Science Laboratory in the ME Department at NJIT since 1999. Dr. Rosato has held visiting appointments at Lawrence Livermore National Laboratory, Worcester Polytechnic Institute, the Lovelace Institutes (Albuquerque, NM), ESPCI in Paris and Stanford University. He is a Fellow of the ASME, Co-editor-in-chief of Mechanics Research Communications, and a member of the Academy of Mechanics, and Sigma Xi.

Dr. Ninghua Zhang

Ninghua Zhang received his PhD in 2004 from the New Jersey Institute of Technology, where he carried out experiments and particle-level simulations on density relaxation induced by vibrations. Before he began his doctoral studies in the United States, Dr. Zhang was employed as a project engineer in the glass and fiberglass industry in China. Here, he was involved in research and development related to manufacturing processes, and he also served as a liaison to several US companies. After 2004, he worked in the medical device field and currently, he is a design engineer for Oxford Plastics in New Jersey. Dr. Zhang is an affiliate of the Granular Science Laboratory in the Department of Mechanical Engineering at NJIT, where he is involved with several ongoing research projects.

Discharge of Size-Segregated Powders from a 2D-aerated Silo[†]

A. D'Arco, G. Donsì, G. Ferrari, M. Montesano and M. Poletto[1]
*Dipartimento di Ingegneria Chimica e Alimentare, Università degli Studi di Salerno**

Abstract

The effects of aeration on the discharge of silos loaded with initially segregated particles have been evaluated. Experiments were carried out on a two-dimensional laboratory-scale aerated silo, loaded according to either ideal or controlled natural segregation patterns. Two different systems of powders made up of two size cuts were tested, one system belonging to group A and the other to group B of the Geldart classification. One of the two cuts was colored to visualize the segregation changes and the solids flow during discharge. Time variations of the discharged solids discharged were evaluated by means of a rotating sample. Results of aerated discharge were compared with mass flow discharge. From analysis of the experimental results, it is possible to conclude that aerated discharges can effectively promote the uniform solids discharge of horizontally segregated solids of group A powders. In contrast, further segregation occurs for aerated discharges of group B powders below the minimum for fluidization.

Keywords: Silodischarge, Aerated powders, Segregation, Mixing

1. Introduction

Significant segregation due to size and density differences can occur during operation of silo filling (see, for example reference 3)) by ballistic effects if the solids are loaded into the silo by throwing them with a horizontal velocity component, as in the case where belt conveyors are used. In this case, larger and heavier particles travel longer distances, while finer particles are more significantly hindered by air drag and fall closer to the inlet. However, segregation also occurs with loading procedures characterized by vertical particle movement only, if the loading point is fixed, as it usually is in industrial applications. In this case, loading produces the formation of a heap on whose slopes the entering solids flow with a shearing motion. Also in this case, coarse solids tend to travel longer distances than fine particles and the result is a higher concentration of fines along the vertical of the filling point. To avoid uneven silo loading which might bring about static or flow problems to the silo, the solids loading point is generally located in axial position, and the fines therefore tend to concentrate along the silo axis[4)]. The case of silo filling by using very high solids rates is completely different, particularly when these are pneumatically conveyed. The presence of entrained air, in fact, can produce air circulating patterns in the empty portion of the silo and determines a preferential deposition of fines at the periphery[5)].

The effect of the segregation on the size distribution of the discharged solids depends on the solids flow regime during the hopper discharge. If the flow is of the funnel type, the motion occurs preferentially in the axial region of the hopper and the solids in this region are the first to leave the silo. In this case, the

---

[†] Accepted : August 14, 2006

* Via Ponte Don Melillo, I-84084 Fisciano (SA), Italy
[1] Corresponding author
TEL : +3908996 4132, FAX : +3908996 4057
E-mail: mpoletto@unisa.it

occurrence of horizontal size segregation produces variations of the size distribution over time. These may result in significant deviations of the product quality from its standards and in consequent losses of the product value. On the other hand, in mass flow silos, solids move almost uniformly towards the orifice and this leads to a significant reduction in time variation of the size distribution of the discharged solids[6, 7]. The solids in the discharging stream, however, are not mixed and some radial segregation persists. In multiple feeders in which the lines are fed at different distances from the hopper axis, this may lead to different particle size distribution[4] in the fed lines.

Quantitative approaches were proposed to evaluate the particle segregation that occurs during the silo loading procedures and apply to binary mixtures of solids with percolating fines[8]. Quantitative evaluation was also proposed to evaluate the effects of particle segregation on the fines concentration in the solids discharging from a mass flow hopper[9]. Furthermore the effect of the powder composition on the solids discharge rate was extensively discussed by Arteaga and Tuzun[10] and by Humby et al.[11]. Some interactions between silo segregation and discharge flow were discussed by Standish[12], Bates[13] and by Boss and Tukiendorf[14].

There are several techniques used to promote solids flow. One of these is air injection[15, 16], which has the considerable advantage of not requiring moving parts on the silo. It is suggested[17] that aeration can promote segregation and, therefore, it should be avoided in the cases where size segregation can occur easily. However, it was also known that the hopper aeration could change the solids discharge regime and promote mass flow[18] at aeration rates much smaller than that for which fluidization of the discharging solids occurs and for which the maximum solids discharge rates are attained. This work is a first step towards a quantitative evaluation of the effect of aeration on the discharge of horizontally segregated systems by directly evaluating the variation of the fines contents in the discharging solids. Tests were carried out with powders belonging both to Group A and B of the Geldart[1] classification for fluidization and its extension to silo flow[2].

2. Experimental

2.1 Apparatus

Experiments were carried out on a flat geometry silo in which the flow should qualitatively reproduce what happens in a silo slice of a three-dimensional geometry. A sampling device of the discharged solids was used to measure its discharge rate and its composition as a function of time. Figure 1 shows the silo coupled with the sampling device and the ancillary equipment.

2.1.1 2D silo

The silo internal dimensions are 180 mm in width, 10 mm in thickness and about 800 mm in height. The air is fed from two wind boxes located at either side of the central outlet slot at the bottom through two porous polymer distributing plates. . In order to achieve a symmetrical gas distribution, two electronic mass-flow controllers, MFC, independently regulate the desiccated air flow through the two distributing plates. The outlet slot is about 12 mm wide and 10 mm deep. The slot width increases downwards to avoid standpipe effects by allowing atmospheric pressure in the falling solids. The rear wall and side spacers are made of Perspex, whereas the front wall is made of tempered glass for improved visibility of the inventory. The outlet slide, OS, was manually operated in the first experiments, but was modified as indicated in Figure 1 to be pneumatically operated by the electro-pneumatic valve, PA. To reproduce the discharge conditions of non-aerated wedge-shaped hoppers, a pair of triangular wooden inserts was placed in symmetrical position inside the silo at both sides of the outlet. Three different pairs of inserts were used in order to reproduce discharge in wedges of 30, 15 and 5 degree half angles.

2.1.2 Sampling drum

The drum carries 16 sector compartments open at their tops. The drum is moved by a stepper motor, SM. The movement is programmed on the motor controller, SMC. In some experiments, a load cell (not indicated in Figure 1) supporting a bin collecting the discharging powder was used to measure the solids discharge rates.

2.1.3 Loading device

To carry out the loading procedure for heap segregation (cf. **2.3.1**), a wire was connected between the drum hub and the loading device LD as shown in Figure 1. In this configuration of the apparatus, the wire winds up on the drum hub with the motor rotation and raises the loading device at the desired velocity. The loading device comprises a funnel feeding a standpipe. The funnel can be loaded with the powder to fill the silo. The standpipe is a hollow steel stick with a square outside cross-section of 1 cm. It is about 1 m long and, therefore, its lower tip can reach the silo bottom when the loading device is lowered inside the silo. The tip of the standpipe is crossed by some nails whose role is to partially obstruct the powder flow at the exit, so that inside the standpipe, the powder flows in dense granular regime and it is not suspended in air or in free fall as would probably happen in a standpipe with an unobstructed exit. Two guides at the silo top keep the standpipe in the silo centre and in vertical position during its movement. The loading device and the wire were not present during discharge and the loading procedure for band segregation.

2.1.4 Image acquisition and automation

Sequences of the experiments carried out on the flat silo were recorded with the help of a digital reflex photo camera or with a digital video camera, DC in **Fig. 1**.

A system was developed to programmatically control the principal events in the discharge experiments:1) the initiation of the air feed,2) the valve opening,3) the sampling drum rotation and4) the start of the photo or video shooting. A personal computer equipped with a National Instruments I/O Data Acquisition Board (DAB) has been used. In particular two (0-5V) analog outputs simultaneously actuated have been used to open and set the air mass flow meters. Three of the eight digital channels (TTL signals) have been coupled with three switches to control the silo outlet opening and to trigger the camera. Two of these switches actuate the electro-pneumatic valve PA. The third switch closes the circuit that gives a command to the digital camera to start shooting. The stepper motor controller, SMC, used to move the sampling drum, is connected to the PC through a serial connection. This was used both to load the pro-

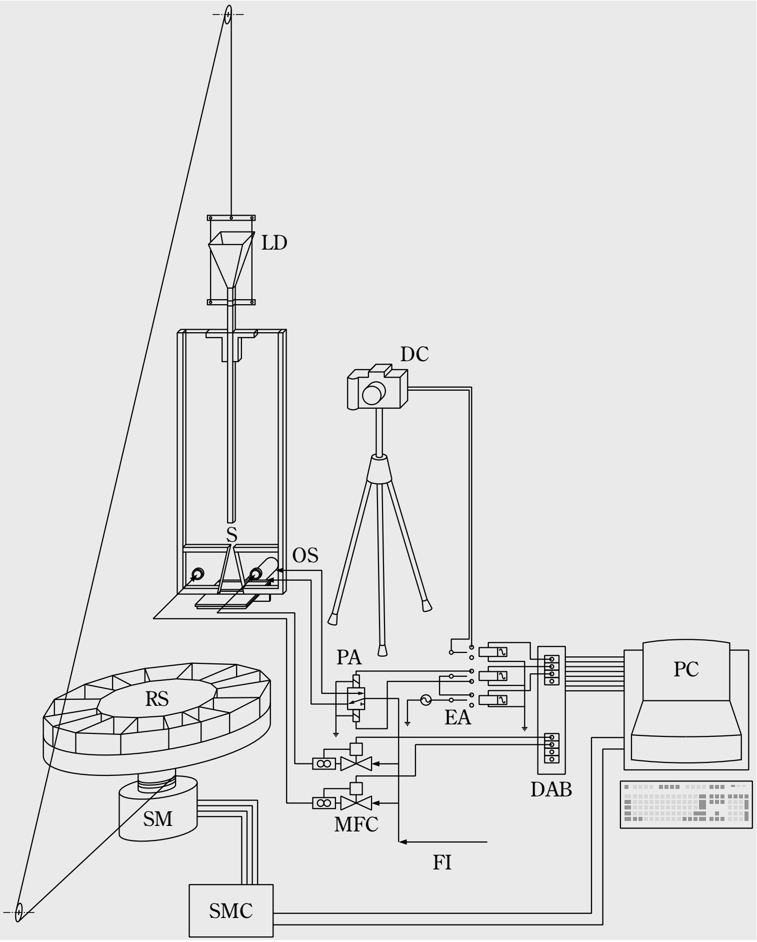

Fig. 1 Experimental apparatus: DAB, data acquisition board; DC, digital camera; EA, electric switches; FI, desiccated air feed; LD, silo loading device; MFC, mass flow controllers, OS, pneumatic actuator of the silo shutter; PA electro pneumatic valve for silo shutter actuators; PC, personal computer; RS; rotary sampling drum; S, silo; SM, stepper motor; SMC, controller of the stepper motor.

cedure for the motor rotation, before the discharge experiment, and to start it during the experiments. A Labview (National Instruments) procedure was developed to control the sequence of the 4 events described above.

2.2 Materials

The solids used were fresh Fluid Cracking Catalyst (FCC) particles and glass beads. Different cuts of these solids were used in the experiments. The main bulk and particle properties of these cuts are reported in **Table 1**. FCC powders are aeratable powders and accordingly belong to group A of the Geldart[1] classification, further modified by Geldart and Williams[2]. Glass beads, in contrast, are free-flowing coarser solids and belong to group B of the Geldart [1] classification. Some of these cuts were dyed to allow flow visualization and image analysis. In all the experiments, a couple of cuts were used to simulate the behavior of segregated powders. In **Table 1** and in the following text, these couples are named as Systems numbered Ⅰ to Ⅲ.

- System I was made up of two FCC cuts differing only by the color and was used with an ideal horizontal segregation pattern. The purpose was to validate the experimental procedure that will be described in the following text with other techniques[19], and to provide a reference behavior of aerated discharges without the effects of local variations of powder permeability due to size segregation.
- System Ⅱ was made up of two FCC cuts of significantly different sizes. These cuts do not segregate easily due to heap filling at the silo scale tested. These powders, however, have a fluid dynamic behavior similar to that shown by System I and were used to assess the effects of local permeability changes on the effectiveness of aeration.
- System Ⅲ was chosen from a wider set of pairs of glass bead cuts because of its ability to produce heap segregation while filling on the small scale silo of this study[20]. It was therefore tested with aerated discharge experiments starting from naturally segregated powders.

The compressed air fed to the MFCs used in the aerated silo is desiccated in a refrigerated unit.

2.3 Methods

2.3.1 Loading procedures

Two different loading procedures were used to obtain reproducible segregation patterns. A band segregation pattern reproduced an ideal horizontal segregation and was independent of the spontaneous powder segregation during silo loading. A further "natural" segregation pattern was made for more realistic results. In the band segregation pattern, the two size cuts of the system tested were loaded with perfect separation while in the "natural" segregation pattern, a mixture of the two cuts was loaded, inducing the formation of a heap which determines the segregation of the two size fractions.

Band segregation. This pattern is an ideal segregation pattern in which two equal quantities of the two cuts making up the examined system were loaded in the 2D silo separately in order to form three vertical bands: For systems Ⅱ, the central band was made up of the finest cut, the non-colored one. For system Ⅲ, the central band was also made up of the finest cut, that for this system, however, is the colored one. For system I, instead, the two cuts have the same size and the central band was always the non-colored one. The side bands were equally sized and each one had half the width of the central band. This pattern was obtained with the help of two square cross-sectional sticks corresponding exactly to the silo width. These were introduced vertically from the silo top where the separating boundary between the two cuts was intended to be. Their presence separated the silo volume so that the two cuts could there-

Table 1 Material properties

System name	Material	Color on images	d_p μm	80% range μm	ρ_p kg m^{-3}	U_{mf} mm s^{-1}	ε_{mf} -	Geldart group
System I	FCC	Natural	62	40 – 112	1960	1.8	0.59	A
	FCC	Dyed	62	40 – 112	1960	1.8	0.59	A
System II	FCC	Natural	40	28 – 62	1960	1.2	0.48	A
	FCC	Dyed	105	79 – 148	1960	6.5	0.64	A
System III	Glass	Dyed	93	71 – 128	2477	9.1	0.40	B
	Glass	Natural	350	265 – 488	2477	110	0.40	B

fore be accommodated separately. At the end of the procedure, the sticks were carefully withdrawn from the top, leaving the particulate material unmixed as shown in **Fig. 2** for System Ⅰ and System Ⅲ.

Heap segregation. This loading procedure was applied exclusively to system III. The loading device (LD in **Fig. 1**), was placed inside the silo with the tip close to the outlet. The two powder cuts, well mixed, were loaded in the funnel of the loading device. This was raised by rotating the stepper motor continuously so that the mixed powder could flow through the funnel standpipe. Flowing out the standpipe tip, the powder made a two-dimensional heap inside the silo. The two size cuts were chosen so that, in their flow on the heap slopes, the finest could percolate in between voids of the largest particle and concentrate around the silo axis. This produced a typical scheme of heap size segregation as shown in **Fig. 3** for two different silo shapes. In order to control the powder impact velocity, the stepper motor velocity was adjusted to keep the tip of the standpipe of the loading device a few centimeters above the top of the heap during the whole filling procedure. The segregation pattern obtained with this procedure was entirely reproducible.

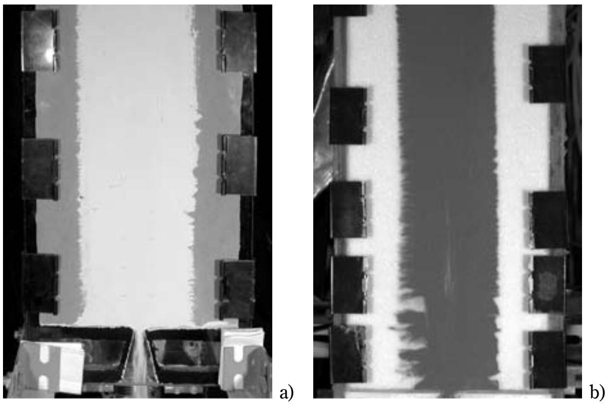
a)
b)

Fig. 2 Silo loaded according to the band segregation procedure for a) System I and b) System III.

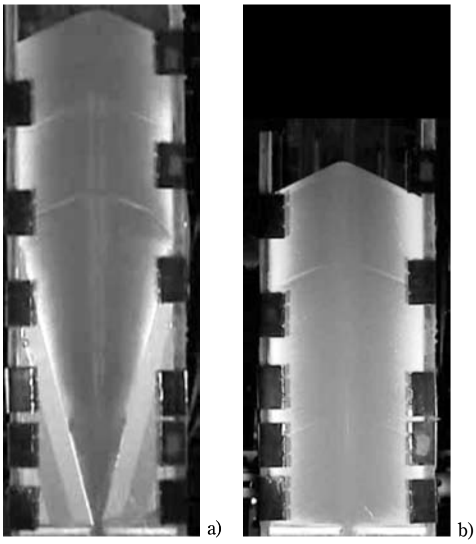
a)
b)

Fig. 3 Silo loaded according to the natural segregation procedure for System III: a) wedge-shaped hopper and b) flat-bottom hopper.

2.3.2 Discharge and sampling

For the experiments tested, the air fluidization rate of the discharging solids was considered the limiting aeration intensity. In fact, modification of the segregation and mixing phenomena beyond the minimum aeration for fluidization can seriously affect powder flow. It has to be considered, however, that the minimum aeration rate which is able to determine effective fluidization during the silo discharge is much larger than the minimum necessary to fluidize the solids in a closed silo. To carry out experiments at aeration rates between these two values and compare the results with those obtained at lower aeration rates, it was necessary to avoid any mixing effect derived from fluidization of the solids inside the closed silo before the outlet opening. For this reason, it was decided to minimize the time interval between the start of aeration and the outlet opening. In the first experiments, this was done by hand using a couple of operators who coordinated themselves in starting the aeration and opening the silo. Subsequently the whole apparatus was automated as described in the apparatus subsection above, and a Labview procedure almost simultaneously started the aeration, opened the silo outlet, started rotation of the sampling drum and triggered the shooting of the camera. In the sampling operation, the motor controller was programmed so that it periodically turned the drum at finite steps, and an empty compartment moved into position underneath the silo outlet at every fixed time interval, Δt_{so}. The frequency of the steps was generally adjusted so that the drum moved all the sixteen compartments underneath the outlet in a period similar to the discharge time of the silo. In any case, the stepper motor was programmed to stop as soon as the 16th compartment had reached the filling position.

2.3.3 Measurement of solids concentrations

Two different procedures were developed to measure the fractions of the two cuts contained inside a sub-sample.

For System Ⅲ, the two cuts could be easily separated by sieving each compartment content. This procedure was somewhat time-consuming for FCC powders and, therefore, was used only for experiments carried out with System Ⅲ. For System Ⅱ and Ⅲ sieving of the whole inventory was usually used to regenerate the material.

For cuts of different colors, in contrast, a colorimetric technique was developed. This technique required a sub-sampling of the solids collected in the compartments. At the end of the discharge, the solids collected in each compartment were mixed and a sample was taken to evaluate the fraction of the colored solids. To avoid size segregation, smaller samples were produced by letting the mixed solids discharge into the sampling drum from a small hopper through a small outlet orifice. This was rotated at high velocity so that the sampler could make several turns during the small hopper discharge and the sixteen sub-samples of about the same quantity (around 5g) obtained were all representative of the original mixture. One of these sub-samples was loaded in a Petri cap and put on a photographic table close to two other caps containing the samples of the two original unmixed cuts. A digital photo of the three caps was taken. The color intensity value in the HSI color encoding, averaged over the image of the solids contained in each cup, was used to correlate with the concentration. The relative intensity, Ir was calculated as:

$$I_r = \frac{I_s - I_d}{I_l - I_d} \qquad (1)$$

where I_s is the sample color intensity, I_l the color intensity of the light cut sample and I_d the color intensity of the dark cut sample. A calibration procedure based on samples of known concentration allowed calibration of the values of the measured relative intensity with the mass fraction of light solids, φ_u, contained in the sample with equations of the kind:

$$I_r = a + b \exp\ (c \cdot \varphi_u) \qquad (2)$$

Values of parameter a, b, and c are reported in **Table 2** for Systems Ⅰ and Ⅱ. Equation[2] was used to evaluate the fraction of light solids with the relative color intensity evaluated. The whole procedure is original but is essentially consistent with what was found by Realpe and Velasquez[21].

Table 2 Calibrated constants of eq. (2) for the colorimetric procedure

System name	a	b	c
System I	$-1.213\ 10^2$	$1.223\ 10^2$	$-7.991\ 10^{-4}$
System II	$-1.213\ 10^2$	$1.223\ 10^2$	$-8.193\ 10^{-4}$

The above procedures made it possible to obtain $n \le 16$ point time series of dark solids fractions in the sample. The n measurement of the non-colored fraction found in the i_{th} compartment, φ_{ui}, was validated with the help of the collected masses in each compartment, m_i, by comparing the overall mass of the same component, evaluated as $\Sigma\varphi_{ui}m_i$, with the mass of the non-colored component originally loaded into the silo. In all the experiments reported in the following text, these two values do not differ by more than a few percentage points. Sequences of non-colored solids fractions, φ_{ui}, for System I and of fines fraction for System Ⅱ ($\varphi_i = 1\text{-}\varphi_{ui}$) and for System Ⅲ ($\varphi_i = \varphi_{ui}$) will be used to describe the uniformity of the solids discharge. To provide a common basis, these sequences will be plotted as a function of the overall fraction of discharged solids. An overall estimate of the non-uniformity of the solids discharge will be obtained from the standard deviation, s, calculated from the φ_i series:

$$s = \sqrt{\frac{\Sigma(\varphi_i - \varphi_h)^2}{n}} \qquad (3)$$

where φ_T is the known amount of fines in the experiment and does not come from an averaging procedure of the n samples. Therefore, the consequences are 1) that the degrees of freedom of the χ^2 distribution represented by the sum in equation (3) is exactly n, and b) that s^2 is an unbiased estimator of the variance of the fines content in the container.

Locally averaged values of solids discharge rates were obtained by dividing the mass collected in each compartment in the range between the 2nd and the second last compartment used by the time interval between two subsequent steps in the discontinuous movement of the sampling drum used during the silo discharge. In some experiments, the solids discharge rates changed somewhat during silo discharge either due to bed height effect at aeration rates close to fluidization or to secondary effects induced by composition changes of the discharging mixture. Average solids flow rates calculated from the masses collected in the compartments between the 6th and the 10th position and the summary of the whole set of experimental conditions tested, with the 1 with the fines standard deviation are reported in **Table 3**.

Table 3 Experimental conditions tested

Sys.	Fine/ Coarse	Segr. Patt.	α °	U_{nf} mm s^{-1}	Δt_{so} s	W_s Kg s^{-1}	s
I	50/50	Band	90	0.00	3.75	0.0084	0.279
				3.31	0.56	0.085	0.173
				4.97	0.56	0.089	0.127
				6.62	0.41	0.093	0.129
				9.93	0.44	0.105	0.194
				13.2	0.41	0.106	0.237
II	50/50	Band	90	3.31	0.46	0.049	0.356
				6.62	0.75	0.077	0.322
				9.93	1.00	0.101	0.769
				13.2	0.70	0.101	0.159
III	50/50	Band	90	0.00	1.87	0.056	0.309
				19.9	0.75	0.095	0.339
				29.8	0.62	0.107	0.280
				39.8	0.62	0.113	0.269
				49.7	0.62	0.124	0.339
III	50/50	Heap	5	0.00	0.62	0.107	0.015
			15	0.00	1.12	0.059	0.055
			30	0.00	1.56	0.053	0.077
			90	0.00	1.56	0.040	0.066
			90	6.63	1.56	0.056	0.093
			90	26.5	1.31	0.093	0.207
			90	39.7	0.75	0.118	0.205
			90	49.7	1.12	0.129	0.194
			90	59.6	0.75	0.144	0.196
III	25/75	Heap	90	0.00	2.50	0.032	0.152
				26.5	1.00	0.064	0.137
				59.6	0.75	0.094	0.191
				82.8	0.62	0.121	0.182
				99.4	0.62	0.121	0.183

3. Results and Discussion

3.1 FCC powders (Systems I and II)

Fig. 4 to **Fig. 9** show results regarding the discharge of FCC powders of both Systems I and II discharged from a band-segregated silo. **Fig. 4** shows solids discharge rates for these two systems at increasing aeration. **Fig. 5** and **Fig. 6** show some pictures from the sequences taken from silo discharge. **Fig. 7** and **Fig. 8** show the sequences of the non-colored fraction (finest for system II) collected during the discharge in the compartments of the sampling drum series for Systems I and II respectively. In these figures, the fraction of the non-colored solids is plotted as a function of the cumulative value of the mass of solids discharged. Perfect mixing would correspond to flat lines at a value of around 50%. These figures instead show a consistent time variation of

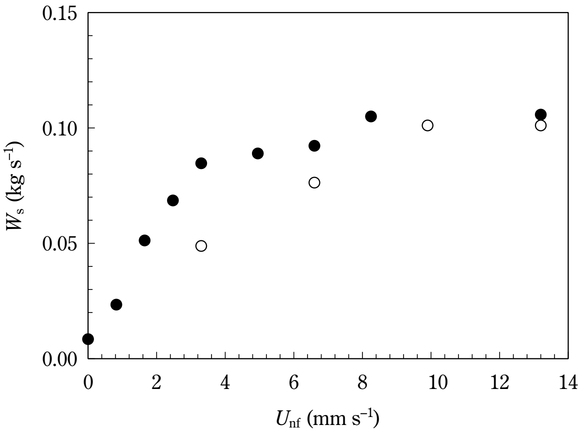

Fig. 4 FCC discharge rates vs aeration velocity for the flat silo: ●, System I; ○, System II.

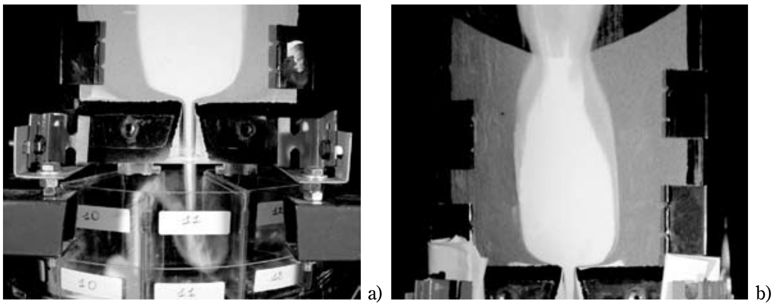

Fig. 6 Group A powders discharging at U_{nf}=6.62 mm s^{-1}. a) System I and b) System II

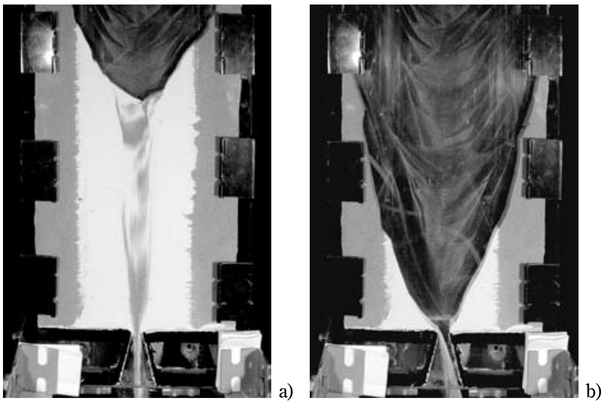

Fig. 5 System I discharging without aeration. a) during discharge; b) end of discharge.

the non-colored/fines fraction with time that will be discussed in the following paragraphs together with the observations arising from the other figures. **Fig. 9** reports values of the standard deviation s according to Equation 3.

A close look at **Fig. 4** confirms what is usually found for aerated discharge[22]. At low aeration rates, aeration promotes solids discharge rates while at high aeration rates, solids discharge rates attain a plateau value which coincides with the fluidization of the discharging solids and will therefore be addressed as U_{nfm}. The different bed permeabilities of Systems I and II justify different values of this velocity. The discharge behavior of these powders, as it appears from the discharge sequences and from the non-colored/fines fraction during discharge (**Fig. 7** and **Fig. 8**), is fairly similar for these two FCC systems.

From **Fig. 5** it appears that the non-aerated discharge is characterized by the formation of a deep funnel. In the first part of the silo emptying this determines the discharge of the material that was loaded in the silo center (lighter color cut) only. This circumstance appears in **Fig. 7** with ϕ_u values equal to 1. In the middle of discharge, the solids slide down from the silo top towards the central funnel where they tend to mix in proportions that, as reported in **Fig. 7**, are similar to the average value of 0.5. The last solids falling and, moreover, the solids left inside the silo at the end of the discharge appear richer in the colored cut.

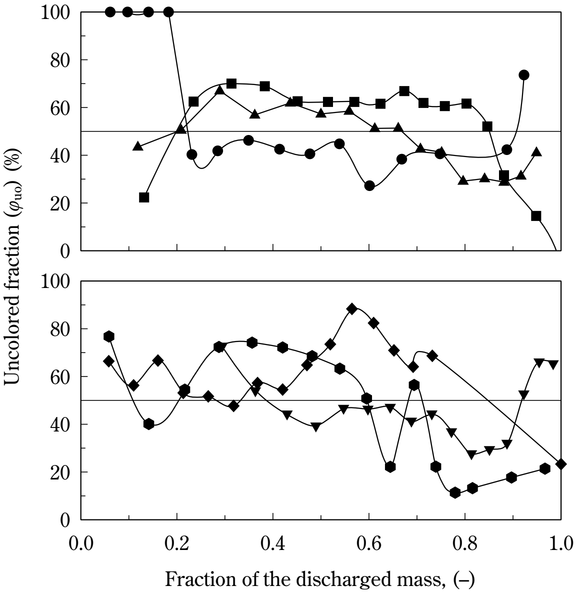

Fig. 7 Fraction of non-colored solids discharged as a function of the discharged mass at different aeration rates for System I, band segregation and 50/50 fine/coarse cut mass ratio: ●, U_{nf} = 0; ■, U_{nf} = 3.31 mm s^{-1}; ▲, U_{nf} =4.97 mm s^{-1}; ▼, U_{nf} = 6.62 mm s^{-1}; ◆, U_{nf} = 9.92 mm s^{-1}; ⬢, U_{nf} = 13.2 mm s^{-1}.

The effect of aeration on the solids flow field for these powders has been studied by Barletta *et al.*[19] and is to widen the width of the discharging funnel to a size close to the silo cross-section. **Fig. 6** refers to aeration rates of U_{nf} = 6.62mm s^{-1} for Systems I and II. The effect of aeration is to convey solids from the entire hopper section towards the exit. From these figures it is also possible to observe that the two cuts remain almost unmixed and show within the outlet

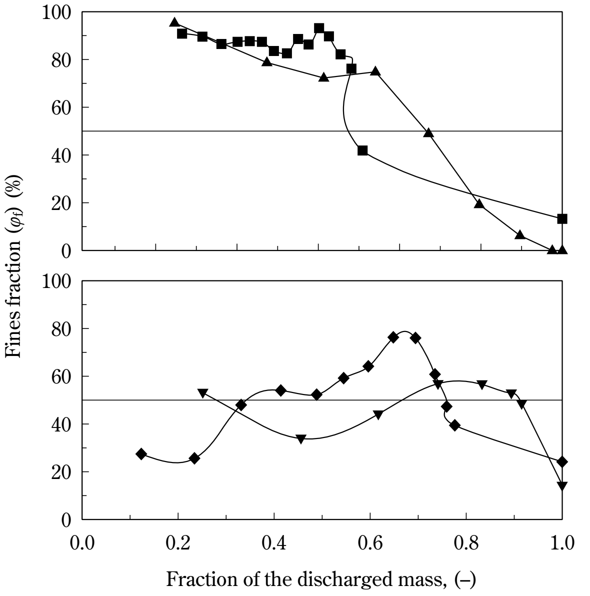

Fig. 8 Fraction of fine solids discharged as a function of the discharged mass at different aeration rates for System II, band segregation and 50/50 fine/coarse cut mass ratio: ■, U_{nf} =3.31 mm s^{-1}; ▲, U_{nf} =6.62 mm s^{-1}; ▼, U_{nf} = 9.93 mm s^{-1}; ◆, U_{nf} = 13.2 mm s^{-1}.

stream the same segregation that exists inside the silo. This means that the non-colored/fines fractions evaluated with the sampler can by no means be assumed to be representative of any local values solids fraction inside the silo. No evident changes in the discharge pattern are registered at increasing times since silo opening. Quantitative measurements, reported in the fines fraction during discharge in **Fig. 7** and **Fig. 8**, as well as the corresponding standard deviation calculated according to Equation 3 and shown in **Fig. 9**, suggest that for each system, an optimal nominal aeration rate value exists at which the sample averaged non-colored/fines minimizes its time variations. These values seem to coincide with those of U_{nfm} at 6 and 10mm s^{-1} for System I and II, respectively, indicating the onset of fluidization as an optimal condition to promote more time-uniform size distribution in the discharge of size-segregated powders of group A powders. At larger aeration rates, time variation of solids concentrations increase, probably due to the formation of gas bubbles in the fluidized powders inside the silo, which impairs the uniformity of the solids discharge.

3.2 Glass powders (System III)

Fig. 10 shows solids discharge rates for this system at increasing aeration and different initial segregation in the silo. In general, the effect of the aeration on the solids discharge rates of System III is

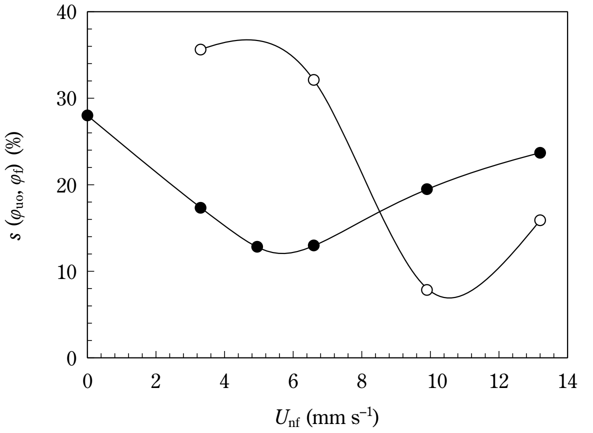

Fig. 9 FCC fines standard deviation vs aeration velocity: ●, System I; ○, System II.

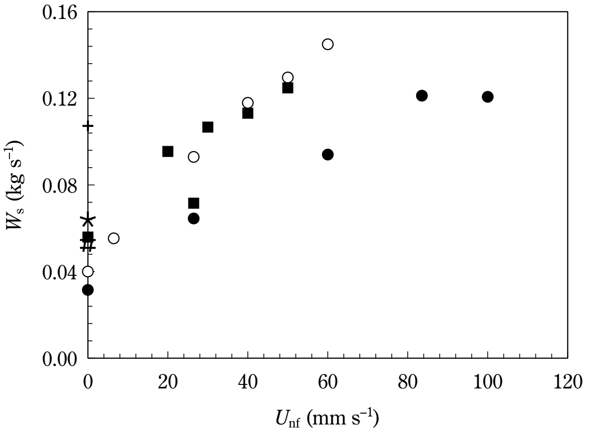

Fig. 10 System III discharge rates vs aeration velocity. Flat silo: ■, band segregation and 50/50 fine/coarse cut mass ratio; ○, natural segregation and 50/50 fine/coarse cut mass ratio; ●, natural segregation 25/75 fine/coarse cut mass ratio. Wedge-shaped silo and natural segregation, 50/50 fine/coarse cut mass ratio: ✚, 5° wedge angle; ∗, 15° wedge angle; #, 30° wedge angle.

qualitatively the same as that of Systems I and II. Not all the series of experiments were performed beyond the minimum fluidization nominal velocity during discharge, U_{nfm}, that was detected by observing bubble formation. So, if we cannot be sure that the plateau value has been reached in all cases, experiments carried out with heap segregation and 25/75 fine-to-coarse mass ratio suggest that the increments in the solids discharge rates produced for these powders by aeration are restricted to a factor of 4 or 5 rather than the factor of 10 shown by FCC powders. This is in agreement with what was previously observed for differences between the aerated discharge of Group A and Group B powders in non-segregated systems [23].

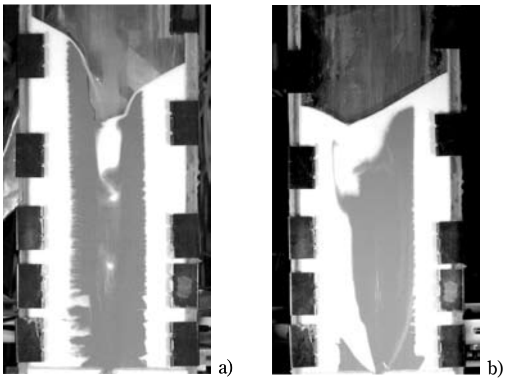

Figure 11 System III discharging from band segregation, 50/50 fine/coarse cut mass ratio: a) without aeration starting; b) at $U_{\mathrm{nf}} = 19.9\ \mathrm{mm\ s^{-1}}$.

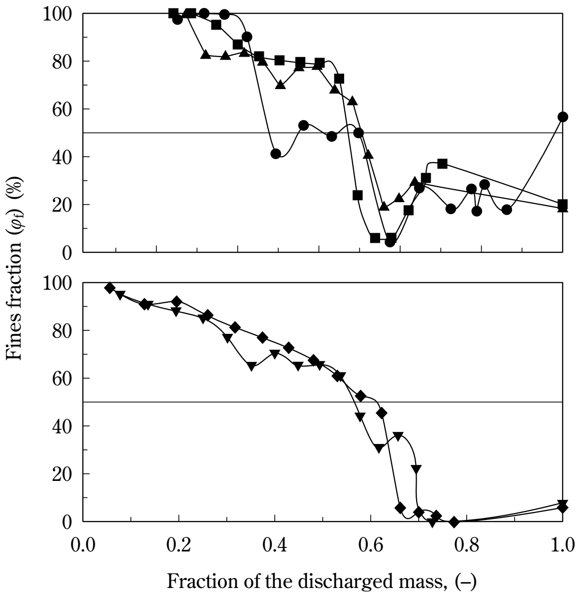

Fig. 12 Fraction of fine solids discharged as a function of the discharged mass at different aeration rates for System III, band segregation and 50/50 fine/coarse cut mass ratio: ●, $U_{\mathrm{nf}} = 0$; ■, $U_{\mathrm{nf}} = 19.9\ \mathrm{mm\ s^{-1}}$; ▲, $U_{\mathrm{nf}} = 29.8\ \mathrm{mm\ s^{-1}}$; ▼, $U_{\mathrm{nf}} = 39.8\ \mathrm{mm\ s^{-1}}$; ◆, $U_{\mathrm{nf}} = 49.7\ \mathrm{mm\ s^{-1}}$.

Band segregation. Fig. 11 shows some pictures taken from the discharge of glass powders starting from band segregation and 50/50 fines-to-coarse cuts ratio, and **Fig. 12** shows the fines fraction during discharge for the same situation. The discharge experiments of System III from band-segregated configurations show that the discharge behavior of this system is significantly different from what was observed with Systems I and II. Regarding non-aerated discharge (**Fig. 11a**), a sort of stable rat-hole forms during discharge which hinders any mixing effect in the initial part of the discharge. This is characterized by very high fines fractions in the relevant plot of **Fig. 12**. Some mixing occurs only when the rat-hole breaks, as it is evident in some intermediate points in the same plot of **Fig. 12**. The final part of the discharge is consequently dominated by high fractions of the coarse cut. Aeration of these solids clearly appears to be less effective in inducing a change in the solids motion. The consequence is the formation of a relatively narrow funnel characterized by unstable flow both at low and high aeration rates. Aeration tends to promote some higher degree of uniformity in the initial stages of discharge, but anticipates the complete discharge of the fines cut. This appears clearly from observation of the final part of the discharge and from the very low values of fines fraction in the final part of discharge appearing in the two plots of Figure 12 at the highest aeration rates ($U_{\mathrm{nf}} = 39.8$ and $49.7\mathrm{mm\ s^{-1}}$). The consequences are high values of the standard deviation of the fines fraction time series reported in **Fig. 18** for band segregation, which is randomly affected by aeration, with an overall negative trend.

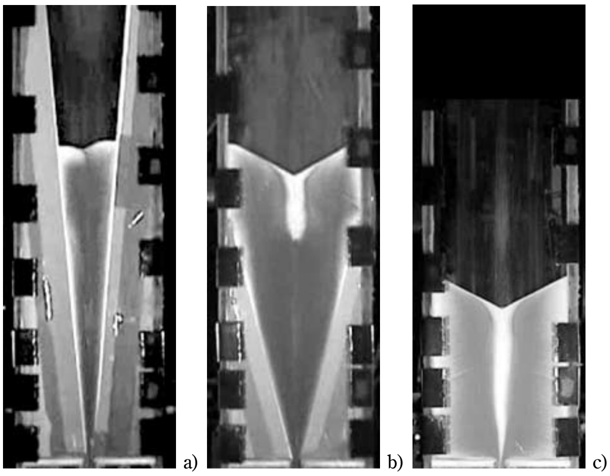

Fig. 13 System III discharging without aeration and starting from heap segregation, 50/50 fine/coarse cut mass ratio: a) from a 5° wedge hopper half-angle; b) from a 15° wedge hopper half-angle c) from a flat-bottom hopper.

Heap segregation. **Fig. 13** shows some pictures from the sequences taken from the discharge starting from heap segregation and 50/50 fine-to-coarse cut mass ratio in non-aerated silos with different wedge angles. Here, the migration of fines is clearly visible with the occurrence of brighter regions. This figure shows that size migration occurs during the discharge from a 15-half-angle wedge hopper and from the flat hopper. Insignificant fine migration is visible during the discharge from the 5-half-angle wedge hopper. **Fig. 14** shows some pictures from

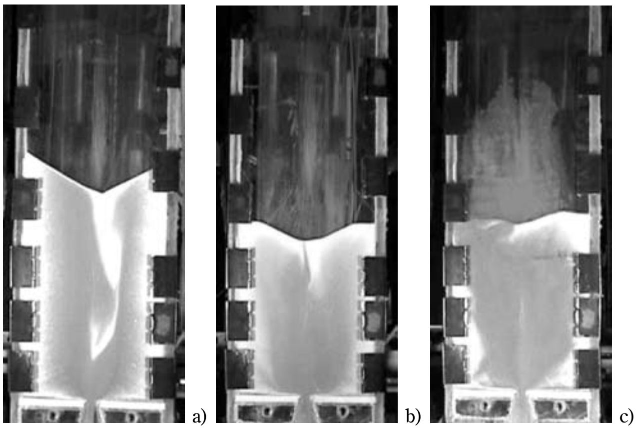

Fig. 14 System III discharging from heap segregation, 50/50 fines/coarse cut mass ratio at different aeration rates: a) U_{nf} = 6.62 mm s^{-1}; b) U_{nf} = 26.5 mm s^{-1}; c) U_{nf} = 49.7 mm s^{-1}.

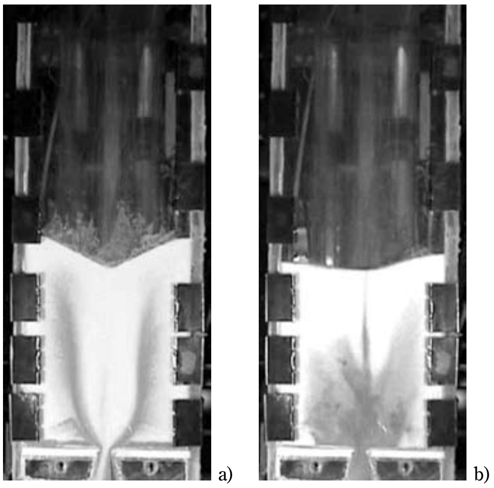

Fig. 16 System III discharging from heap segregation, 25/75 fine/coarse cut mass ratio at different aeration rates: a) U_{nf} = 26.5 mm s^{-1}; c) U_{nf} = 82.8 mm s^{-1}.

the sequences taken from the discharge starting from heap segregation and 50/50 fines-to-coarse cuts ratio. Pictures refer to increasing aeration. Also in this case, aeration results in larger funnels, but significant fines migration phenomena are visible at all aeration rates. **Fig. 15** shows the fines fraction sequences in all the discharge experiments starting from heap segregation and 50/50 fines-to-coarse cuts ratio. Here, the curves are all flat and around the 50% value, indicating a generally much better situation than in band-segregated experiments. The effect of aeration, however, is not very significant. **Fig. 16** shows some pictures from the sequences taken from the discharge starting from heap segregation and 25/75 fine-to-coarse cut mass ratio. Also in this case, the pictures refer to increasing aeration. These pictures show evident fines migration that appears also quantitatively in **Fig. 17**, which shows the fines fraction sequences. **Fig. 18** reports values of the standard deviation *s* according to Equation 3 for aerated discharge. **Fig. 19** summarizes values of the standard deviation *s* and the solids discharge rates for the different non-aerated discharge conditions.

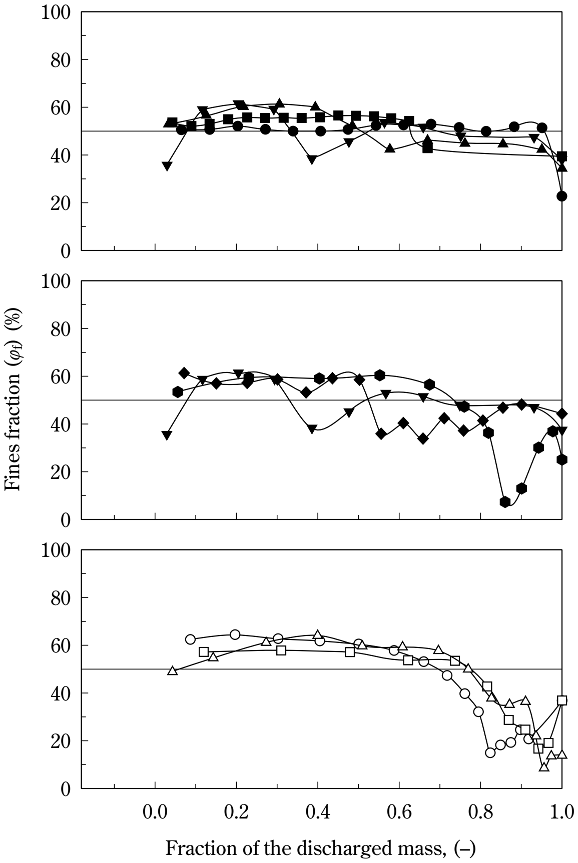

Fig. 15 Fraction of colored solids discharged as a function of the discharged mass for System III heap segregation and 50/50 fine/coarse cut mass ratio. U_{nf} = 0 : ●, 5° wedge; ■, 15° wedge; ▲, 30° wedge; ▼, flat bottom. Aerated discharge: ◆, U_{nf} = 6.63 mm s^{-1}; ⬢, U_{nf} = 26.5 mm s^{-1}; ●, U_{nf} = 39.7 mm s^{-1}; □, U_{nf} = 49.7 mm s^{-1}; △, U_{nf} = 59.6 mm s^{-1}.

In general, it is possible to say that when starting its discharge from a heap-segregated configuration, System III shows a completely different behavior than in band segregation. **Fig. 13** shows that, without aeration, a regular and continuous discharge sets in, during which a deep funnel develops at the silo axis. Stable sloping motion towards the silo center develops at the top of the discharging material. This motion, however, promotes further segregation of the fines that are released by the shearing solids before they reach the silo center, where only coarse

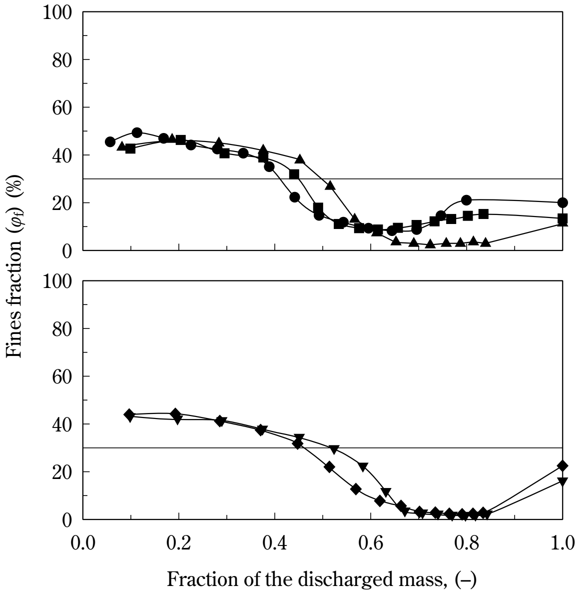

Fig. 17 Fraction of fine solids discharged as a function of the discharged mass at different aeration rates for System III for the flat silo, heap segregation and 25/75 fine/coarse cut mass ratio: ●, $U_{nf} = 0$; ■, $U_{nf} = 26.5$ mm s^{-1}; ▲, $U_{nf} = 59.6$ mm s^{-1}; ▼, $U_{nf} = 82.8$ mm s^{-1}; ◆, $U_{nf} = 99.4$ mm s^{-1}.

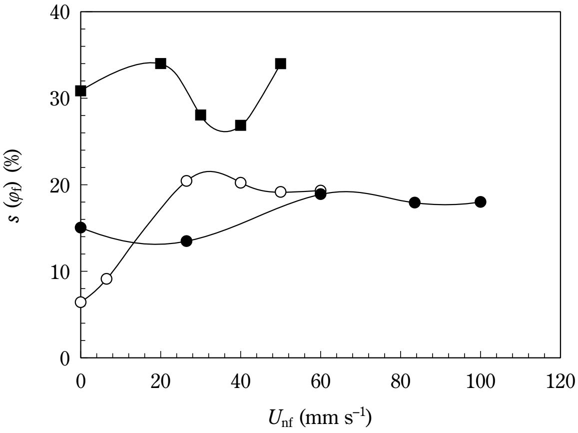

Fig. 18 System III fines standard deviations vs aeration velocity for the flat silo: ■, band segregation and 50/50 fine/coarse cut mass ratio; ○, natural segregation and 50/50 fine/coarse cut mass ratio; ●, natural segregation 25/75 fine/coarse cut mass ratio.

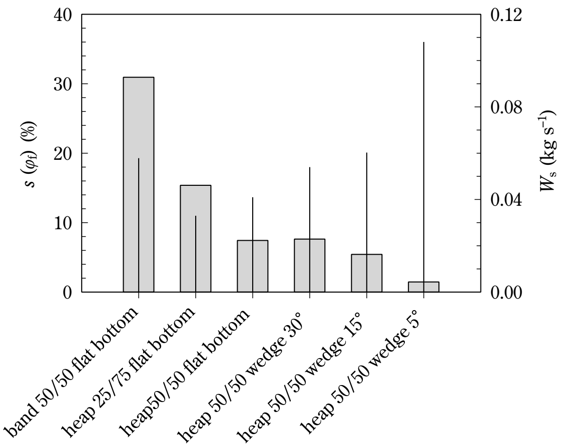

Fig. 19 System III fines standard deviations (gray histograms) and solid discharge rates (needles histograms) for different initial segregation patterns in the flat silo. In the label are reported in sequence: 1) the segregation procedure, 2) the fines to solids mass ratio, 3) the silo bottom shape.

solids arrive. This is clearly visible in **Fig. 13** as a bright core penetrating the discharging material. The discharging funnel, however, is sufficiently wide to withdraw solids also from the regions where fines are more concentrated. The resulting average fines fraction at the silo exit shown in **Fig. 15** indicates that its value is not very different from the overall fines content of the silo. Only some fluctuations are observed - due probably to flow instabilities. The final value of the standard deviation for this discharge in **Fig. 18** is relatively small. This result, however, seems a fortuitous combination of compensating effects that cannot be found in the similar discharge of the mixture with 25/75 fine-to-coarse cuts mass ratio and heap-segregated as shown in **Fig. 18** itself. Similarly to what happens in the discharge of band-segregated System III powders, the use of aeration leads to some widening of the discharging funnel. In the picture in **Fig. 14a** ($U_{nf} = 6.62$ mm s^{-1}), the shearing motion of the solids along the slopes at the powder top is less significant and some mixing occurs within the funnel. In the picture in **Fig. 14b** ($U_{nf} = 26.5$mm s^{-1}), i.e. relative to aeration close to the minimum for fluidization, some massive motion of fines towards the silo bottom is evident from the progressive paleness increase of the upper layers of the discharging solids inside the silo. This is even more evident in the picture in **Fig. 14c** ($U_{nf} = 49.7$mm s^{-1}). The discharge in this figure was carried out at aeration rates that lead to the formation of bubbles inside the silo and, therefore, exceed U_{nfm}. The bubbling inside the silo promotes some mixing that is reflected in the corresponding plot of fines fractions time series reported in **Fig. 15** by a smoother profile in the first portion of discharge. However, it is also characterized by a minimum in the fines fraction at the end of the discharge corresponding to the exit of the upper layer of solids. Even more pronounced effects of fines migration inside the silo and anticipated discharge are shown in the pictures in **Fig. 16a** ($U_{nf} = 26.5$mm s^{-1}) and **Fig. 16b** ($U_{nf} = 82.8$mm s^{-1}) relative to aerated discharge of System III mixtures with 25/75 fine-to-coarse cut mass ratio. The latter of these two figures, in particular, shows some bubbling inside the silo. Fines time series for this particular value of fine-to-coarse cut mass ratio in **Fig. 17** shows very limited variations of the aeration rate, as if the increased permeability of the system further reduced the effect produced by air flow. The air flow effect is in general limited to the overall fines standard deviation as reported in **Fig. 18**.

Non-aerated discharge with a wedge-shaped hopper was tested to compare other results with that of a mass flow hopper. Pictures of discharge reported in **Fig. 13** show that only the steepest hopper angle is able to give mass flow at which no significant segregation due to discharge is detected. In fact, the fines fraction time series for this experiment in **Fig. 15** is very close to the average fines fraction, and the corresponding standard deviation, with a value of about 1% reported in **Fig. 19**, is the smallest measured with this system. This condition is also the one that provides the largest solids discharge rate without aeration. It is worth noting that in general there is an inverse relationship between solids discharge rates and fines fraction standard deviations reported in these experiments.

4. Conclusions

The effects of aeration on the discharge of silos loaded with initially segregated particles have been investigated. The results confirm that the effect of aeration on promoting uniform flow properties in these systems strongly depends on the size of the particles to be discharged.

For Group A powders according to the Geldart[1)] classification, aeration significantly affects the solids flow field by changing the portion of the silo cross-section occupied by the funnel of the moving solids. Below the minimum aeration necessary to fluidize the discharging solids, aeration brings favorable effects. A minimum of the standard deviation for the fines fraction sequences appears at nominal aeration velocities equal to the minimum for fluidization during discharge, U_{nfm}. Comparison between System I (color segregation) and System II (size segregation) shows that the minimum of the standard deviation appears sharper for size-segregated powders.

For Group B[1)] powders, aeration does not significantly affect the solids flow field, and mass flow produced the most uniform fines fractions at the outlet during the discharge. The adverse effect of aeration can definitely be attributed to the promotion of further particle segregation during discharge that produces a separation of the fines in the upper layers of the discharging solids. Above U_{nfm}, aeration can produce intense and stable mixing of segregated powders.

Acknowledgements

This project was partially financed by Regione Campania within the framework defined by the Regional Law n.5/2002 on scientific research.

List of Symbols

a	parameter in eq. (2)
b	parameter in eq. (2)
c	parameter in eq. (2)
d_p	particle diameter, [m]
I_d	color intensity in the dark reference, [-]
I_l	color intensity in the light reference,[-]
I_r	relative color intensity according to eq. (1),[-]
I_s	color intensity in the sample, [-]
n	number of samples, [-]
U_{mf}	superficial velocity at the minimum for fluidization, [m s^{-1}]
U_{nf}	nominal superficial velocity, [m s^{-1}]
U_{nfm}	nominal superficial velocity at the minimum for fluidization, [m s^{-1}]
s	fraction of fines standard deviation
W_s	solids discharge rates, [kg s^{-1}]

Greek symbols

α	hopper half-angle [deg]
ε_{mf}	bed voidage at minimum for fluidization,[-]
φ_i	fraction of fines in compartment i, [-]
φ_u	fraction of non-colored particles, [-]
φ_{ui}	fraction of non-colored particles in compartment i, [-]
ρ_p	particle density, [kg m^{-3}]
Δt_{so}	time interval between samples, [s]

References

1) Geldart, D. Types of gas fluidization. *Powder Technol.*, **7**, 285-292 (1973).

2) Geldart, D. and Williams, J.C. 1985. Flooding from Hoppers: Identifying powders likely to give problems. *Powder Technol.*, **43**, 181-183.

3) Mosby, J., de Silva, S.R., and Enstad, G.G. Segregation of particulate materials. *KONA Journal*, **14**, 31-43(1996)

4) Salter, G.F., Bradley, M.S., Pittman, A.N. and Farnish,

R.J. Segregation of particulate solids. *From Powder to Bulk*, Proc. of *Int. Conf. on Powder and Bulk Solids Handling*, Jun. 13-15, London, United Kingdom, p. 479-495 (2000).

5) Arnold, P.C. On the influence of segregation on the flow pattern in silos. *Bulk solids handling*, **11**, 447-449 (1991).

6) Williams, J.C. Mixing and segregation in powders. In *Principles of Powder Technology.* Ed. M.J. Rhodes, Wiley, p.71-90 (1990).

7) Williams, J.C. The storage and flow of powders. In *Principles of Powder Technology.* Ed. M.J. Rhodes, Wiley, p.91-118 (1990).

8) Shinohara, K., Shoji, K. and Tanaka, T. Mechanism of segregation and blending of particles flowing out of a mass flow hopper. *Ind. Eng. Chem. Proc. Des. Dev.*, **9**, 174-180 (1970).

9) Shinohara, K., Shoji, K. and Tanaka, T. Mechanism of size segregation of particles in filling a hopper. *Ind. Eng. Chem. Proc. Des. Dev.*, **11**, 369-376m (1972).

10) Arteaga, P. and Tuzun, U. Flow of binary mixtures of equal density granules in hoppers – size segregation flowing density and discharge rates. *Chem. Eng. Sci.,* **45**, 205-223 (1990).

11) Humby, S., Tuzun, U. and Yu, B. Prediction of hopper discharge rates of binary granular mixtures. *Chem. Eng. Sci.,* **53**, 483-494 (1998).

12) Standish, N. Studies of size segregation in filling and emptying o hopper. *Powder Technol.*, **45**, 43-56 (1985)

13) Bates, L. Re-mixing of a segregated product during discharge from a mass flow silo. *Powder Handling Proc.* **10** (2), 135-138 (1998).

14) Boss, J. and Tukiendorf, M. The influence of filling modes upon mixing during discharge from a silo. *Powder Handling Proc.* **10** (4), 363-366 (1998).

15) Ferrari, G. and Bell, T.A. Effect of aeration on the discharge behavior of powders. *Powder Handling and Processing*, **10**, 269-274 (1998).

16) Dhodapkar, S. and Konanur, M. Selection of discharge aids for bins and silos- Part II. *Chem. Engng.* Oct., 71-82 (2005).

17) Bates, L. *User guide to segregation*. BMHB London (1997).

18) Barletta, D., Donsì, G., Ferrari, G. and Poletto, M. Visualisation of the particle velocity field by a high-speed video technique in a two-dimensional aerated bin. Proc. of the *4th World Conference on Particle Technology*, Sydney, Jul. 21-25, paper 265 (2002).

19) Barletta, D., D'Arco, A., Donsì, G., Ferrari, G. and Poletto, M. The use of aeration to obtain uniform flows of fine particles during the discharge from a hopper loaded with segregated solids. Proc. of *Fluidization XI*, Ischia (NA), Italy, May 9-14, p.707-714 (2004).

20) D'Arco, A. *Effects of aeration on time uniformity of the solids flow from silos loaded with radially segregated solids.* Doctorate Thesis, University of Salerno (2005).

21) Realpe, A. and Velasquez, C. Image processing and analysis for determination of concentrations of powder mixtures. *Powder Technol.*, **134**, 193-200 (2003).

22) Donsì, G., Ferrari, G. and Poletto, M. Gas pressure profiles inside a fluidized hopper discharging fine powders. Proc. of the 3rd *World Conf. on Particle Technolgy*, Brighton, UK, Jul. 6-9, paper 322 (1998).

23) Donsì, G., Ferrari, G. and Poletto, M. Distribution of gas pressure in a hopper discharging fine powders. *Chem. Eng. Sci.,* **52**, 4291-4302 (1997).

Author's short biography

Anna D'Arco

Anna D'Arco graduated in Chemical Engineering at the University of Salerno. She carried research on the aerated discharge of segregated powders at the Department of Chemical and Food Engineering where she received a Doctorate Degree in Chemical Engineering in the year 2005.

Giorgio Donsì

Giorgio Donsì is professor of Chemical Engineering since 1980. He is at the University of Salerno since 1984 where he has acted as the Dean of the Faculty of Engineering in the period from 1986 to 1995. He was elected rector in 1995 and occupied this position until year 2001. His scientific activity is mainly concerned with fluid dynamics of heterogeneous systems, fluidisation, fundamentals of the design of apparatuses for the food industry. He is author of about 180 papers in these fields.

Giovanna Ferrari

Giovanna Ferrari is professor of Chemical Engineering since 2000. She is at the University of Salerno since 1986. In the same University, she is responsible of the education programme in Chemical Engineering since 1998. Author of more than 120 papers in the field of powder technology and food process engineering, her research interests are focused on the following subjects: heat and mass transfer in particulate systems, characterisation of flow properties of powders, measurement and modelling of physical and transport properties of foods, design and characterisation novel technologies for food preservation.

Massimo Poletto

Massimo Poletto is Associate Professor of Chemical Engineering at the Faculty of Engineering of the University of Salerno since 2001. He graduated in Chemical Engineering in 1989. In 1993 he obtained a Doctoral Degree in Chemical Engineering at the University of Naples "Federico II". From 1994 to 2001 he was Assistant Professor in the present Faculty. His scientific interests regard the fluid dynamics and mechanics of dense granular systems, in particular fluidisation and the gravity flow of powders with and without the use of aeration. In the past he also was involved in research projects on the extraction with supercritical fluids. His work appears in more than 80 papers and conference presentations.

Fines Formation (and Prevention) in Seeded Precipitation Processes[†]

A.E.Lewis
Crystallization and Precipitation Unit, Department of Chemical Engineering, University of Cape Town[*]

Abstract

An overview of three studies on seeded precipitation in a fluidised bed reactor (FBR) is presented. The objective of using the FBR is to remove dissolved metals as precipitated metal salts onto a seed surface. For the nickel hydroxy-carbonate system ($S = \pm 10^5$), particle enlargement was found to occur by a combination of growth and aggregation. The concentration of fines correlated with the degree of supersaturation in the reactor, which suggests that fines formation was due to homogenous nucleation, attrition of rough growth precipitate, or a combination of the two. Reducing the local supersaturation by multiplying the feed points was found to be a successful fines control strategy.

For the mixed nickel/cobalt sulphide system, ($S = \pm 10^{11}$ for nickel and $\pm 10^{12}$ for cobalt), a significant quantity of fines was formed but these eventually aggregated onto the seeds. In contrast, for the copper sulphide system ($S = \pm 10^{34}$), the fines formed immediately but never aggregated onto the seed material and it was not possible to control the supersaturation levels to the extent that fines formation was avoided.

Keywords: Precipitation, Metal sulphide, Nucleation

1. Introduction

Although industrial applications of precipitation have a long history and precipitation has been studied scientifically since the 1930s, understanding of this operation is still very limited[1]. Industrially, precipitation reactions are generally carried out in very simple reactor systems. Probably over 90% of industrial precipitation processes are carried out in ordinary stirred tank reactors operated either batchwise or continuously[2]. Major problems, however, often occur in control of precipitation processes, specifically in understanding the effect of processing conditions on reactor performance and product characteristics such as precipitate morphology, purity and particle size distribution[3, 4, 1]. In addition, the design of industrial crystallisers is still experience-based[5], and geometric and time-dependent variations are not taken into account. It is therefore hardly surprising that these strategies fail almost without exception[6]. The problem is even more challenging in the field of industrial precipitation, where the default reactor design is a simple stirred tank, invariably quite inadequate for product control.

A significant amount of research has been conducted into the development of more efficient precipitation processes. The development of the seeded fluidised bed, or pellet reactor, offers a number of potential advantages over conventional precipitation options. The technology was initially employed for the softening of drinking water by calcium carbonate precipitation[7] and the removal of phosphates from waste water, producing calcium phosphate[8]. More recently, fluidised bed reactors have been used for the removal of metals (nickel, copper and zinc) from solution[9, 10, 11, 12] as carbonates or as sulphides. Kaksonen and co-workers[13] used biologically generated sulphide and alkalinity as the reagents to precipitate zinc and iron from acidic waste water in a fluidised bed reactor, whilst Esposito and co-workers[14] used the same sulphide source but precipitated only zinc from acidic waste water.

[†] Accepted: August 14, 2006

[*] Rondebosch, capetown, 7701, South Africa
TEL: 27-21-650-4091, FAX: 27-21-650-5501
E-mail: alison@chemeng.uct.ac.za

The seeded fluidised bed reactor can provide a suitable environment for a controlled precipitation process in a stable environment. The key feature is to promote heterogeneous nucleation of precipitate on the large surface area provided by the seed material by operating under controlled supersaturation conditions. Homogeneous nucleation, which produces very small particles (fines) that are difficult to remove from the process stream, is thus minimised. The fluid velocity in the reactor, typically between 10-35cm.s^{-1}, prevents the cementing together of the seed particles[12] but should also be sufficiently low to avoid attrition of the precipitate layer. As the thickness of the precipitate layer covering the seed particles increases, those pellets are more difficult to fluidise, and become segregated in the lower portion of the bed. This allows the larger pellets to be removed and replaced with fresh seed material.

The overall aim of this work is to characterise the mechanisms occurring in order to relate the effect of processing conditions on reactor performance and product characteristics (precipitate morphology, purity and particle size distribution).

2. Materials and Methods

2.1 Reactor design

A laboratory-scale fluidised bed reactor (**Fig. 1**) consisting of a borosilicate glass column, 150 cm high with an internal diameter of 2.5 cm, sealed from the atmosphere, was used. The reactor was filled with beach sand (95-97% SiO_2) (250-500 μm) as a seed material, to a resting height of 20, 70 or 90 cm. Reagent feed ports and sampling ports were situated at various positions along the length of the column. The base of the column consisted of a conical glass fitting, packed with glass beads of decreasing diameter (10^{-2} mm) that promoted uniform distribution of the upward flow and provided a support for the seeds.

A metal-rich sulphate solution, together with the re-circulation stream, was pumped into the reactor from the bottom of the column. The re-circulation stream helped to fluidise the bed. Air was excluded from the system, as air bubbles ascending through the column could result in the loss of seed material to the re-circulation or effluent streams. The column reactor was also sealed on the top to minimise losses to the atmosphere. The aqueous reagent (either sodium sulphide or sodium carbonate) was introduced via up to six inlet points on the side of the reactor. The inlet points were equally spaced, 10 cm apart, with the first point being 10 cm from the base of the reactor. The splitting of the reagent inflow reduced the local supersaturation around the inlet points. Up to eleven equally spaced sampling points on the side of the reactor were used to obtain data for column profiles. The first point was situated 15 cm from the base of the reactor with additional points at 10 cm intervals. Each sample port was sealed with a rubber septum and liquid samples were withdrawn from the centre of the column using a syringe and needle. A sample port 5 cm from the base of the column allowed the removal of coated seed particles for further analysis.

A pH probe (Hanna) was maintained at the level of the effluent port, above the maximum bed height, to monitor the effluent pH. All reagents ($NiSO_4.6H_2O$, $CoSO_4.7H_2O$, $CuSO_4.5H_2O$, $Na_2S.9H_2O$, and H_2SO_4) were analytical grade, obtained from Merck. Solutions were made up to required concentrations using distilled water. Liquid samples obtained from the sample ports, the recycle stream and the effluent stream were each filtered through a 0.22-μm ny-

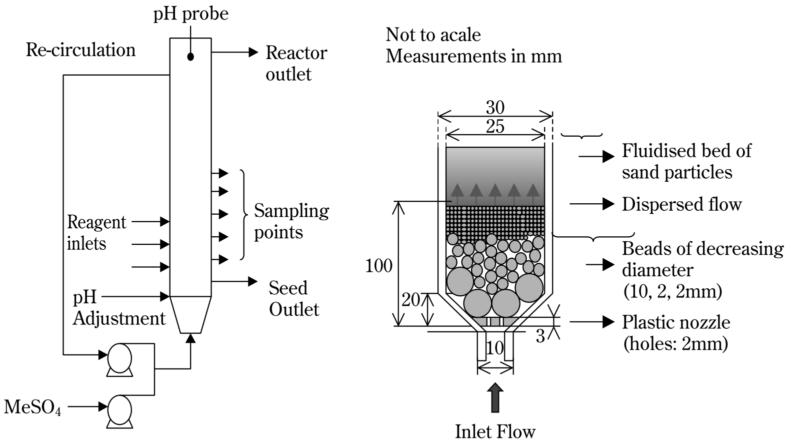

Fig. 1 Schematic representation of the seeded fluidised bed reactor.

Table 1 Experimental conditions for the three case studies

Variable	*FBR Ni(OH)CO₃*	*FBR Ni & CoS*	*FBR CuS*
Supersaturation (S)	Lowest	Moderate	Highest
Supersaturation (S)	1.05×10^{5}	2.42×10^{11} (Ni) 1.99×10^{12} (Co)	5.6×10^{34}
$[M^{2+}]$: $[Anion^{2-}]$ (mole:mole)	1 : 2	1 : 1	1 : 1
$[Co^{2+}]$total (ppm)	-	50	—
$[Ni^{2+}]$total (ppm)	100	120	—
$[Cu^{2+}]$total (ppm)	—	—	150
Inlet flow $Q_{feed} = Q_{/Reagent}$ (ml/min)	60	50	50
$Anion^{2-}$ concentration (ppm)	204	93	75.7
Reagent feed points	1, 2 and 6	3	3
Recycle Ratio : (Recycle flow/(Q_{feed} + $Q_{Reagent}$)	1.42; 1.67; 3.11	1	2.24
Retention time (sec)	97, 87, 55	212	131
Temperature (℃)	24 ± 2 ℃	23 ± 2℃	24 ± 2 ℃
pH	8.4-9.7	7.12-7.56	6.03-6.97
Resting bed height (cm)	20	70	90

lon membrane filter and analysed to determine pH (Cyberscan 2500 pH meter), and metal in solution (Varian SpectrAA-30 atomic absorption spectrophotometer). Unfiltered samples were used to determine the total metal concentration. The efficiency of the column was defined in terms of the metal removal efficiency as well as the metal conversion defined by equations (1) and (2). Fines were identified by the difference between the total and dissolved metal concentrations. For the nickel-hydroxy-carbonate process, the PSD of the fines was measured using an electro-zone sensing technique (Coulter Counter Multisizer III) in the detection range from 0.4 to 12.0 μm.

Metal removal efficiency:

$$\eta\ (\%) = \frac{M_{in} - M_{out,total}}{M_{in}} \times 100 \qquad (1)$$

M_{in} = metal concentration in the feed (ppm)
$M_{out,total}$ = metal concentration in the outlet (including fines) (ppm)

Metal conversion:

$$\eta\ (\%) = \frac{M_{in} - M_{out,dissolved}}{M_{in}} \times 100 \qquad (2)$$

M_{in} = metal concentration in the feed (ppm)
$M_{out,total}$ = outlet filtered metal concentration (excluding fines) (ppm)

The experimental conditions for the case studies are given in **Table 1**. All experiments were carried out a number of times under the same conditions to ensure reproducibility of the results. The supersaturations were calculated using OLI Analyser (OLI Systems Inc (2003)). In the OLI Analyser software, all of the solution equilibria are taken into account and the Ionic Activity Product is used to calculate the supersaturation. The Ksp values used to calculate the supersaturations were 6.4×10^{-18} for $Ni(OH)_2$ (no data was available in OLI for the hydroxy-carbonate species), $1\times10^{-19.4}$ for NiS and $1\times10^{-21.3}$ for CoS.

3. Case Study 1: Nickel hydroxy-carbonate precipitation

For the system with one reagent feed point (at 15 cm from the base), high levels of conversion and efficiency were measured, with both reaching 99% at the top of the column. See **Fig. 2**. The initial decrease in soluble nickel concentration and the presence of fines in the lower portions of the bed indicated the occurrence of homogeneous nucleation. The fines concentration as well as the pH decreased up the length of the bed, suggesting that the fines were aggregating onto the seeds. The pH decrease would account for the consumption of supersaturation caused by the process of aggregation.

The effect of increasing the number of feed points on the conversion, efficiency and fines concentration was also investigated, with two configurations being tested:

(a) 2FP with 2 reagent feed points (at H= 10 cm

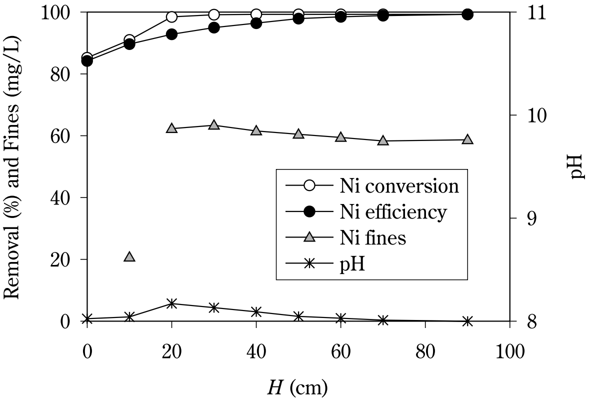

Fig. 2 Change in conversion, efficiency, fines concentration and pH with reactor height.

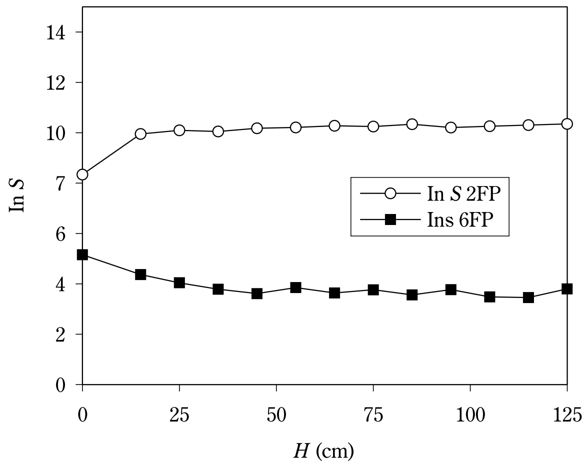

Fig. 4 Change in supersaturation with reactor height for 2FP and 6FP.

and 40 cm)

(b) 6FP with 6 reagent feed points (at H=10 cm, 20 cm, 40 cm, 50 cm, 80 cm and 90 cm).

The results in **Fig. 3** show that, for the 2FP case, the crystallisation efficiency varied between 60 and 90% with the fines formation ranging from 2 to 80mg/L. For the 6FP case, the crystallisation efficiency varied between 80 and 99% and the production of fines between 3 and 17mg/L. **Fig. 4** illustrates the change in relative supersaturation with bed height for the 2FP and 6FP configurations. It is clear that the global supersaturation is higher for the 2FP than for the 6FP case but, moreover, the stability of the supersaturation for the 2FP case is less.

For the 2FP configuration, the fines concentration up the bed was highly erratic and poorly controlled. Also, the two peaks observed in the fines formation correlate almost exactly with the reagent feed points. This could be accounted for by the high local supersaturation at the reagent feed points, which causes homogenous nucleation and results in the generation of fines. However, it is also possible that fines could be formed due to attrition in the bed.

Two plausible mechanisms can be proposed to account for fines formation and consumption. For the first mechanism, the reaction takes place in the immediate region near the feed point and nearly all the supersaturation is consumed to produce tiny crystals by primary nucleation. The remaining supersaturation is used for new growth onto the seeds and for aggregation of the fines onto the seeds.

The second mechanism is based on attrition or secondary nucleation mechanisms due to the turbulence in the bed and particle-particle or particle-wall collisions. Under conditions of high supersaturation, such as the 2FP configuration, the surface of the precipitate on the seeds became rough and thus additionally prone to attrition.

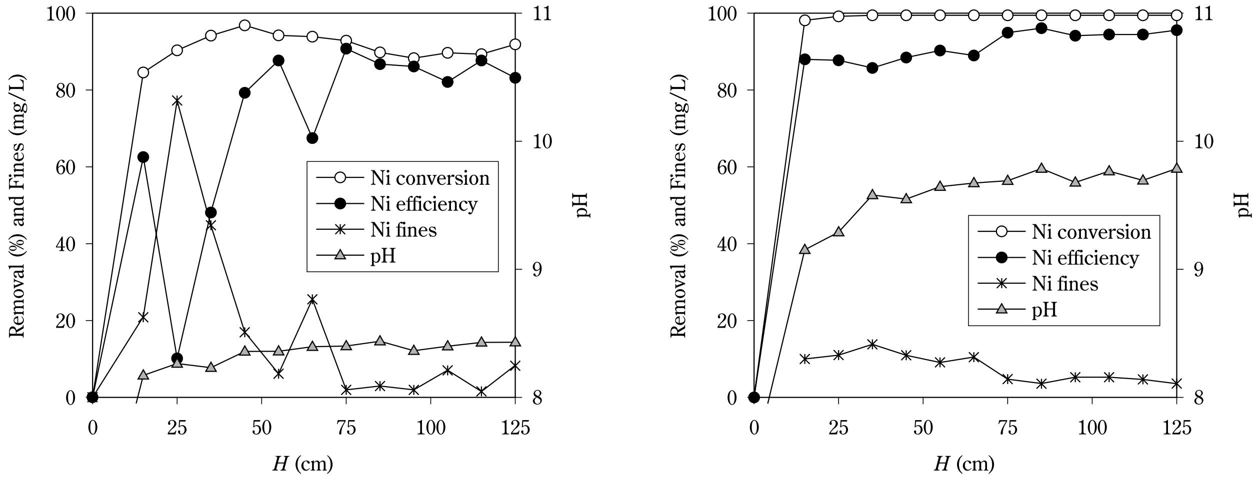

Fig. 3 Change in conversion, efficiency and fines concentration with reactor height for 2FP (left) and 6FP (right).

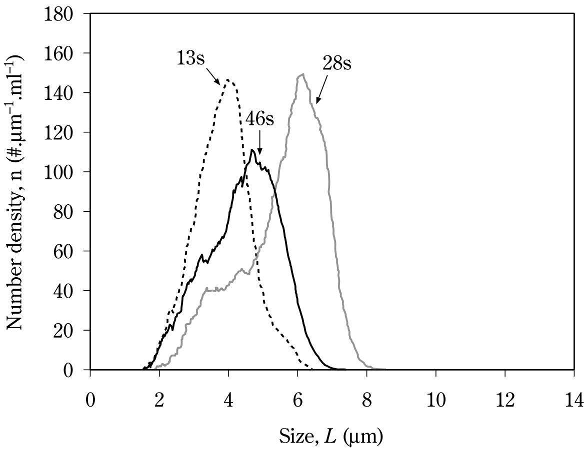

Fig. 5 Particle size distribution of fines in the fluidised bed reactor at various residence times.

Fig. 5 shows the effect of time on the PSD for the FP case, expressed as number density versus particle diameter. It was observed that, as the time increased i.e. from the bottom to the top of the column, the PSD broadened while its peak value shifted towards larger particle sizes with a slight increase in the particle number.

The observed shift of the peak size from 3.75 to 6.25 μm (between 13 and 28 s) is primarily due to the growth of tiny crystals to larger ones during their stay in the bed. However, in the same figure, after 46 s, the number of particles as well as their size decreased. The median diameter decreased from 6.25 to 4.75 μm. These decreases suggest that the larger fines are removed from the solution due to aggregation onto the surface of the seed.

From **Fig. 6**, it can be clearly seen that particles on the surface of the seed aggregated on the surface, but also grew into each other. The potential for generation of fines due to attrition of the rough layer aggregated onto the seed is also apparent, especially in the 2FP case. It can also be noticed that the coated layer on the seed surface is deeper with 6FP than with 2FP.

Conclusions:

Fines concentration could be correlated to the degree of supersaturation, and excess fines were produced because of the poor distribution of the supersaturation in the lower portion of the bed. However, aggregation of fines onto the seed material occurred up the length of the bed. At the higher supersaturation measured in the 2FP case, the surface of the precipitate on the seed crystals became rough and prone to attrition, thus releasing attrited particles as fines into solution.

The 6FP configuration demonstrated that splitting the feed could effectively reduce the local supersaturation and thus improve the removal efficiency of the nickel by preventing homogenous nucleation. In addition, the smoother growth surface on the seed particles was less susceptible to attrition. More details of these two case studies can be found in (9) and (15).

4. Case Study 2: Mixed nickel cobalt sulphide precipitation

For the mixed nickel-cobalt sulphide precipitation (carried out using three reagent feed points), a similar phenomenon of fines formation in the lower portion of the bed followed by slow aggregation of the fines onto the seeds in the upper regions of the bed was observed. Only the nickel results are shown in **Fig. 7**, the cobalt results being very similar. The aggregation process was accompanied by an increase in pH, which could be due to either an excess of sulphide in the system or to the transition-metal-mediated oxidation of the bisulphide ion in solution[16], which releases hydroxide ions. More details of this case

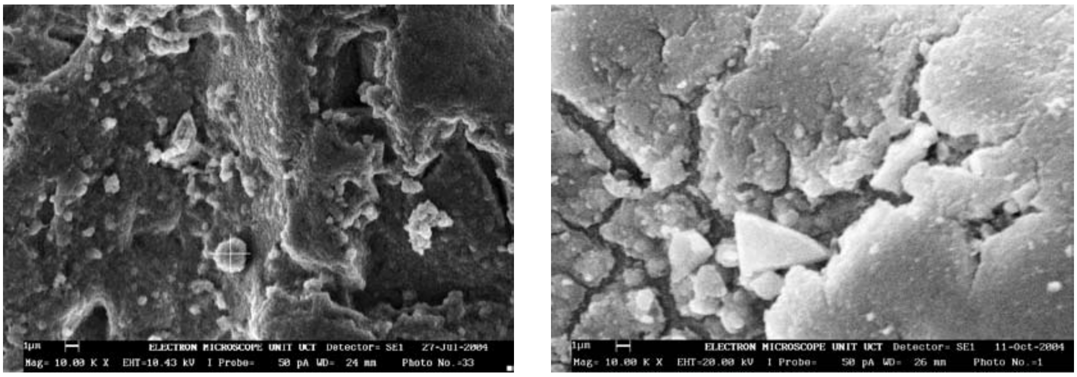

Fig. 6 SEM micrographs of silica grain showing the surface texture for 2FP (left) and 6FP (right).

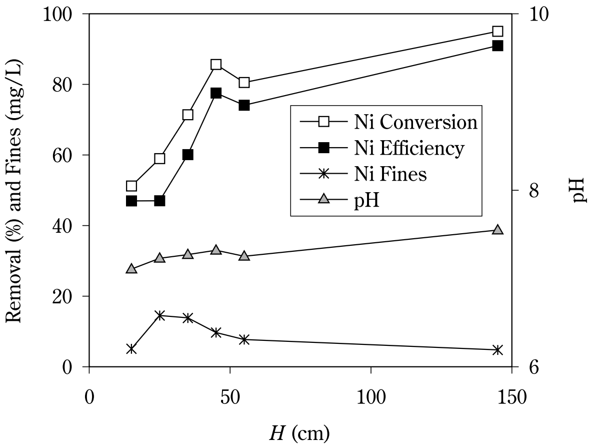

Fig. 7 Conversion, efficiency, fines concentration and pH for nickel in a mixed nickel-cobalt sulphide precipitation.

study can be found in (17).

5. Case Study 3: Copper sulphide precipitation

In contrast, for the copper sulphide case study illustrated in **Fig. 8**, fines were formed immediately but never aggregated onto the seed material. This contrasting behaviour compared with both the other case studies is most likely due to the extremely insoluble nature of copper sulphide and the resulting extremely high local supersaturation levels (10^{34}), which would be responsible for homogeneous nucleation and formation of fines. Because of the extremely insoluble nature of copper sulphide compared with the other two systems, the supersaturation is entirely consumed in the homogeneous nucleation process, with none remaining to achieve the fines aggregation observed in the other cases. More details of this case study can be found in Reference 18).

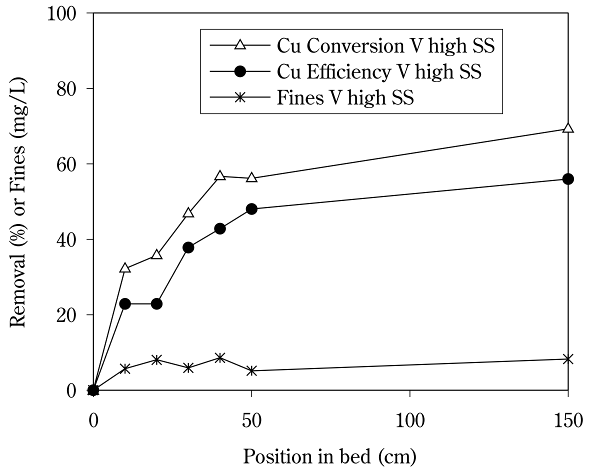

Fig. 8 Copper concentration in the reactor as a function of position in the bed.

6. Conclusions

For the nickel-hydroxy-carbonate system, the relatively lower global supersaturation resulted in high metal removal efficiencies. Fines were formed at the reagent injection point, but aggregated onto the seeds up the length of the bed. Splitting the reagent feed points allowed the local supersaturation to be better controlled, and fines formation due to both homogeneous nucleation and attrition was minimised.

For the nickel/cobalt sulphide system, despite the much higher global supersaturation, it was still possible to control fines formation by multiplying the reagent feed points. This resulted in fines formation and aggregation onto the seed material with time.

For the copper sulphide system, the extremely low solubility resulted in such high global supersaturation that it was not possible to control the fines. Once they had formed at the feed points, they did not aggregate in the reactor.

The overall conclusion from this work is that control of fines via supersaturation control is possible, to some extent, via strategies such as multiplying the number of reagent feed points. However, for systems with extremely low solubilities and high global supersaturations, this control parameter cannot be used to prevent fines formation in seeded precipitation processes such as these.

Acknowledgements

I would like to gratefully acknowledge the people who have contributed to this work, especially the students and Post Doctoral Fellows in the Crystallisation and Precipitation Unit at the University of Cape Town, who set up the reactors and generated the data in the laboratory. Warm thanks go to Damien Guillard, Karen Petersen, Rob van Hille, Ashton Swartbooi and Christian Taty Costodes, Thabang Pikane, Sagwadi Ngcamu and Traci Reddy. Thanks also to Miranda Waldron for her kind help with the SEM. I would also like to acknowledge the financial support of the National Research Foundation (NRF) and of the University Research Committee (URC) at the University of Cape Town (UCT).

References

1) Sohnel, O. and Garside, J., 1992. Precipitation: Basic

Principles and Industrial Application. Butterworth-Heinemann, Oxford.
2) Van Leeuwen, M., 1998. *Precipitation and Mixing*. Technical University of Delft, Delft.
3) Franke, J.and Mersmann, A., 1995. The Influence of the Operational Conditions on the Precipitation Process. *Chemical Engineering Science*, 50 (11), p1737-1753.
4) van Leeuwen, M., Bruinsma, O. and van Rosmalen, 1996. Three-zone approach for precipitation of barium sulphate. *Crystal Growth* , 166 p1004-1008.
5) Kramer, H., Dijkstra, J., Verheijen, P. and van Rosmalen, G., 2000. Modelling of industrial crystallizers for control and design purposes. *Powder Technology*, 108 (2-3), p185-191.
6) Kramer, H. J. M., Bermingham, S. K. and van Rosmalen, G. M., 1999. Design of industrial crystallisers for a given product quality. *J Cryst. Growth*, 198/199 p 729-737.
7) van Ammers, M., van Dijk, J. C.and Graveland, A., 1986. State of the art of pellet softening in the Netherlands. *Wat. Supply*, 4 p223-235.
8) Seckler, M., 1994. *Calcium phosphate precipitation in a fluidized bed*. Ph.D. Thesis, Delft University of Technology, The Netherlands, Delft University of Technology,.
9) Guillard, D. and Lewis, A. E., 2001. Nickel Carbonate precipitation in a fluidised bed reactor. *Industrial and Engineering Chemistry Research*, 40 (23), p5564-5569.
10) Zhou, P., Huang, J., Li, A. W. F. and Wei, S., 1999. Heavy metal removal from wastewater in fluidised bed reactor. *Wat. Res*, 33 (8), p1918-1924.
11) Wilms, D., 1988. Recovery of nickel by crystallisation of nickel carbonates in a fluidised bed reactor. *Proceedings of the VVT Symposium on Non-Waste Technology*, Espoo, Finland,.
12) Scholler, M., Van Dijk, J. C. and Wilms, D. A., 1987. Recovery of heavy metals by crystallisation in the pellet reactor. De Wall.; Van den Brink. (Ed.), Kluwer, Dordrecht. p294-303.
13) Kaksonen, A., Riekkola-Vanhanen, M. and Puhakka, J., 2003. Optimization of metal sulphide precipitation in fluidized-bed treatment of acidic wastewater. *Water Research*, 37 p255-266.
14) Esposito, G., Veeken, A., Weijma, J. and Lens, P., 2006. Use of biogenic sulphide for ZnS precipitation. *Separation and Purification Technology*, In Press, Corrected Proof (Available online 9 February 2006),.
15) Costodes, V.C.T. & Lewis, A.E. 2006, Reactive crystallisation of nickel hydroxy-carbonate in fluidized-bed reactor: Fines production and column design, *Chemical Engineering Science*, vol. 61, no. 5, pp. 1377 - 1385.
16) Lens, P. N. L. and Hulshoff Pol, L. (Eds), 2000. Environmental Technologies to Treat Sulphur Pollution: Principles and Engineering. IWA Publishing, London.
17) Lewis, A.E. & Swartbooi, A. 2006, Factors affecting metal removal in mixed sulphide precipitation, *Chemical Engineering and Technology*, vol. 29, no. 2, pp. 277-280.
18) van Hille, R.P., Petersen, K.A. & and Lewis, A.E. 2005, Copper sulfide precipitation in a fluidised bed reactor, *Chemical Engineering Science*, vol. 60, pp. 2571-2578.

Author's short biography

Professor Alison Lewis

Alison Lewis graduated with a BSc (Chem. Eng), MSc (Chem Eng) and PhD, all from the University of Cape Town. She is also a registered Professional Engineer. After two years working in industry, she joined the Chemical Engineering Department at UCT. In collaboration with colleagues at the Technical University of Delft, she established a specialisation in crystallisation and precipitation processes in the Chemical Engineering Department in 2000. The Crystallisation and Precipitation Unit is an accredited university research unit and its focus is primarily around precipitation systems related to the mineral processing industry.

Graduates from the Research Unit include: 1 PhD, 13 MSc and 47 Honours graduates. The publications include 36 international journal papers and books, 33 refereed international conference papers and 25 technical reports to industry.

Acoustic Methods for Particle Characterisation[†]

M. J. W. Povey
Procter Department of Food
Science,
The University of Leeds
Leeds, LS2 9JT, UK
University of Leeds[*]

Abstract

Acoustic and Ultrasonic Methods for Particle Characterisation have many advantages. They are generally non-invasive, can be non-contact, are safe and often are economic. However, it can be difficult to interpret data, and the expertise and commercial equipment necessary may be in short supply and inappropriate to commercial requirements. Nevertheless the potential for these techniques is immense, particularly with regard to the newly emerging field of nanotechnology. A less well-recognised but just as important requirement is the ability to characterise systems on length scales between the molecular and the macroscopic. It is not so well known that acoustics can provide information over a huge range of length scales, from a few nanometres (ultrasound spectrometry) up to geological scales. Commonsense approaches to the understanding of acoustics obscure the potential of the modality. Scattering theory underpins all the theory of acoustic propagation, and adopting this initially theoretical approach indicates a world of new information. At one level particles and structures may be sized, at another their molar compressibility obtained, at another their shape determined. Acoustic methods are complementary to light scattering techniques offering advantages where light scattering does not work ? optically opaque systems, mixtures with small refractive index differences, for example. So ultrasound spectrometry is uniquely well-suited to the characterisation of nanoparticle concentrates. In this article the theory of ultrasound propagation is outlined simply for a general audience, emphasising those aspects which provide the greatest potential for adoption of the modality in the particle characterisation community and briefly describing the relevant current commercial and laboratory equipment.

Keywords: Acoustic, Ultrasound, Stability, Size, Size distribution

1. Introduction

There is a great variety of particle characterisation methods; of size, of size distribution, of density, of molecular weight and so forth. So why is another set of methods needed? It is recognised that an area where particle characterisation is deficient is with regard to very small particles in concentrated systems. Clearly this is an issue in the area of nanoparticle production, for instance. There are other issues too, for example light scattering methods struggle if particles are coated, modifying their refractive index; or if there is more than one type of particle present. A good example of such a system which we have studied intensively is milk, which comprises several types of particles suspended in water. It is not difficult to satisfy yourself as to this fact, just compare skimmed and full-cream milk, both are white; this is because both the protein particles and the oil droplets are large and concentrated enough to scatter light, imparting a white colour on the product. Nevertheless, there must be powerful reasons to consider new techniques, invest in new equipment, train new experts

---

[†] Accepted : August 14, 2006

[*] Procter Department of Food Science The University of Leeds Leeds, LS2 9JT, UK
TEL: 0113 343 2963 , FAX: 0113 343 2982
Email: m.j.w.povey@leeds.ac.uk

and so on. But at a recent meeting of the Society of Chemical Industry in London it was baldly stated that there was no other technique to match ultrasound in the characterisation of nanoparticulate dispersions. Given the growing importance of this area we not surprisingly find a growing interest in ultrasound techniques for particle characterisation.

General introductions to ultrasound characterisation of particulate systems suspended in fluids can be found in works published by this author[1, 2] and by Kinsler and Frey[3].

2. Equipment for Acoustic and Ultrasound Measurement

There is a great variety of equipment and equipment types available. Techniques are classified as continuous, quasi-continuous and pulsed, referring to the way in which the sound is generated. The most common type of sound transducer employs a piezoelectric ceramic called lead zirconium titanate (PZT); however there are many other types of construction including electrically polarized plastics, single crystal materials such as quartz or lithium niobate, each offering differing advantages. Single frequency, frequency scanning or broad-band (simultaneous multiple frequencies) generation of sound is possible, typically over frequencies between a few Hz and 100 MHz, although a much wider range is possible. Sample volumes may vary between a few hundred microliter in resonant cell systems operating over a limited frequency range of between 7 and 15 MHz to 500 ml in a quasi-continuous, frequency sweeping spectrometer (1 MHz to 200 MHz).

The acoustic set-up of a quasi-continuous frequency sweeping spectrometer is schematically represented in **Fig. 1**. One transducer transmits a sound pulse that passes through the sample medium and is subsequently received by a second transducer. The sample medium is continuously stirred.

Ultrasound spectroscopy yields two types of measurable quantities; absorbance and velocity. Absorbance values A (in nepers) are derived from intensity measurements from the initial intensity $I_0(\omega)$ as a function of angular frequency $\omega\ (=2\pi f)$ and the measured intensity $I(\omega)$:

$$A(\omega)=\ln\left[\frac{I_0(\omega)}{I(\omega)}\right] \qquad [1]$$

The phase velocity is equal to the distance between the transducers, L, divided by pulse time of flight, Δt, of the sound pulse.

$$v\,(\omega)=\frac{L}{\Delta\, t(\omega)} \qquad [2]$$

The experimental measurements are always carried out relative to eference samples and samples. This can be achieved directly doing only one measurement on the sample and one measurement on the reference sample under the same conditions. The relative absorbance measured is then called the excess absorbance and also leads to the excess absorbance coefficient α_{xs}. The excess absorbance coefficient (Nepers/m) is independent of the instrument set-up and is a material property.

$$\alpha_{xs}(\omega)\equiv\left[A_{sample}(\omega)-A_{reference}(\omega)\right]/2L \qquad [3]$$

Here absorbance is normalised by the distance travelled by the pulse, in this case the first and second echoes are compared (**Fig. 1**) so the distance in this case is twice the cell width. It has been found that the measurement of the apparent excess absorbance can be carried out rapidly by selecting a suitable reference medium. The excess absorbance, α_{xs} is the absorbance that the sample exhibits over and above that of the reference sample. Usually water

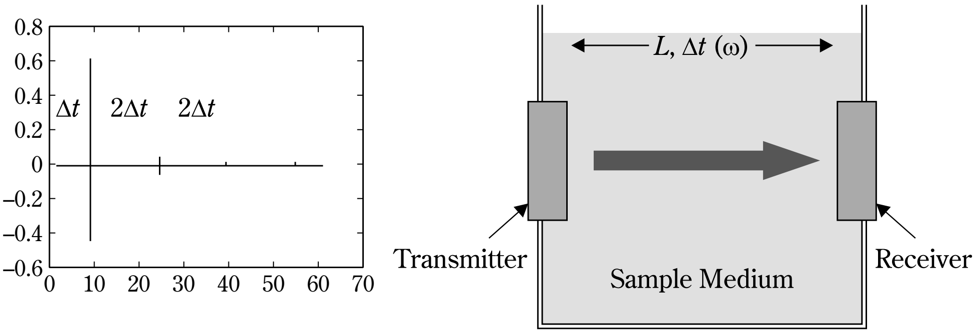

Fig. 1 Schematic representation of the spectrometer cell and pulse delay determination. Note that following the first 'echo', subsequently received echoes are reflected from the transmitter and consequently travel twice the distance taking twice the time.

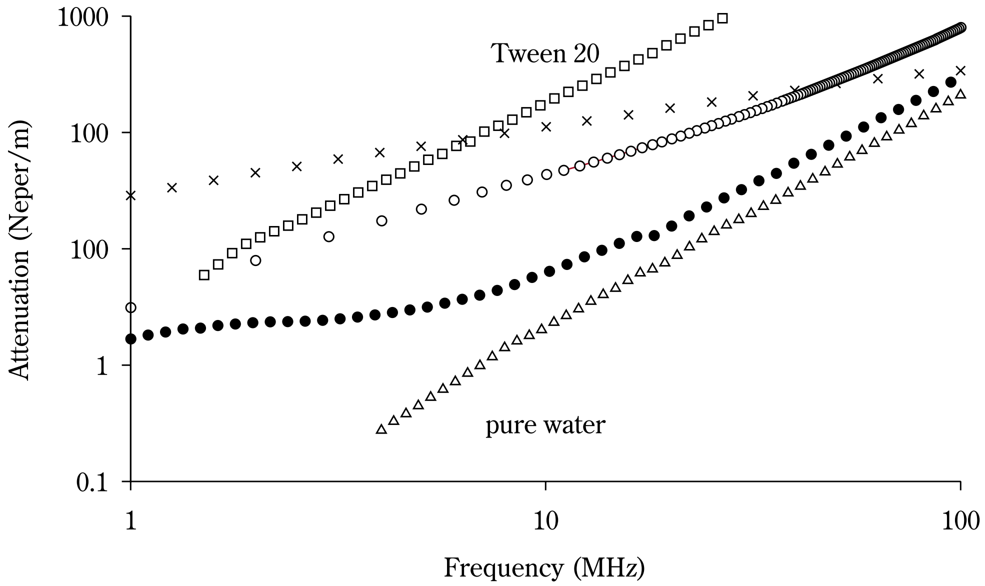

Fig. 2 Ultrasound attenuation plotted as a function of frequency for a surfactant solution, pure water, n-hexadecane and homogenised milk with a fat globule size of 1 μm at 25C. Water displays a power dependence on frequency of 2.01 and a pre-exponential factor of 0.02 whilst undiluted Tween 20 has an exponent of 1.69 and a pre-exponential factor of 3.59. Open triangles show the measured data in water purified by Millipore apparatus and open squares show the data for Tween 20. The open diamonds show the data for 4% Tween 20 dispersed in water; crosses are data for 20 % v/v n-hexadecane in water, D[3,2] = 1000 nm; circles are milk fat in water emulsion. (Data courtesy of Ran Huo, Valerie Pinfield and Stefan Meyer 4), University of Leeds).

is used as the reference sample. It is a more direct measure of processes that happen in the sample of interest and not in the reference sample. By choosing an appropriate reference sample, other effects can be selectively excluded.

One issue regarding ultrasound particle sizing has been the quantity of material needed to make the measurements, one well-known spectrometer requiring 500 ml. The reason for this is the requirement in ultrasound particle sizing for a very large frequency range of more than two decades. The attenuation of sound intensity as a function of distance is roughly proportional to the square of the frequency, so high frequencies require much shorter path lengths in order for a good signal-to-noise ratio, as compared with low frequencies. In water for example, measurements at 100 MHz require a few millimetres whilst at 1 MHz, hundreds of millimetres are required.

Water has one of the lowest attenuation factors of any liquid and it is quite a challenge to accurately measure the attenuation at low frequencies. In **Fig. 2** is plotted the spectrum of water purified in a millipore apparatus as measured in our laboratory on a Malvern Ultrasizer (Malvern Instruments, Malvern, UK). Note that in this instrument, the lowest measureable attenuation is around 0.1 Neper m^{-1} and the highest is around 1000 Neper m^{-1}. The instrument achieves this huge dynamic amplitude and frequency range through a combination of electronics and changing path length between transducers. In the case of the Malvern Ultrasizer, the measured attenuation spectrum is an absolute one, whereas in the case of other instruments, the spectrum is relative to a reference material. A wide frequency and attenuation range is essential if accurate particle sizing is to be done in a significant range of liquids and suspensions.

The need for a wide frequency range is illustrated in **Fig. 2** for a selection of materials. Note that while the pure materials (water and Tween20) exhibit straightforward power law dependence on frequency, the dispersions (Tween20 in water, homogenised milk and n-hexadecane in water) exhibit a far from straightforward frequency dependence. In the case of Tween20, the Tween micelles scatter sound by a thermal mechanism which has a complicated frequency dependence which nevertheless is predictable5) and with which the micelles can be sized6). The same is true of the milk and the casein nanoparticles in milk4). It is important to characterise the behaviour of the surfactant in the solvent if ultrasound particle sizing is to be carried out successfully.

Pulsed systems offer higher data acquisition rates, as high as ten measurements a second but lower bandwidths. Nevertheless, if averaged data is required, for example particle compressibility, solid content or a trend in size due to coalescence, then limited bandwidth, pulsed systems may be the best choice. An example of a miniaturised, limited bandwidth spectrometer using pulse techniques is given in reference[7]. A broadband transducer (1-10MHz) excites a pulse in a buffer rod within which it reverberates. Some of the sound escapes from the buffer rod into the sample within which it also reverberates; the same transducer both exciting and detecting the sound pulses. Comparison of the reverberation within the buffer rod and in the sample gives accurate velocity and attenuation data.

An even simpler system simply measures the reverberation time of sound pulses in a sample between pipe walls, generated and detected by the piezoelectric transducer embedded in the wall. This is a simple and robust system that can operate inline and be temperature-cycled between -15°C and 90°C, so is particularly suitable for crystallization studies[8, 9, 10].

3. Sizing nanoparticles

Solid particles can also be sized with attenuation spectroscopy. In **Fig. 3** is plotted the attenuation of sound at various frequencies between 100 kHz and 200 MHz for silica monodispersions of various sizes. Comparing **Fig. 3** with **Fig. 2** we may note that we have plotted the results obtained within the dynamic range of the Malvern Ultrasizer. Firstly note the complicated dependence on both size and frequency. This occurs because there are three scattering mechanisms at work, i.e. thermal scattering, visco-inertial scattering and elastic scattering, in addition to the frequency dependence of the attenuation inherent in each phase out of which the dispersion is composed. The width of the scattering peaks arises from the non-propagational nature of the thermal and shear waves which are excited by the particle in the acoustic field, the decay lengths of these waves scales inversely as the square root of the frequency. The situation is further complicated by multiple scattering which is responsible for the significant differences between the data for the dilute silica suspension in **Fig. 3** and the data for the concentrated suspension in **Fig. 4**; nevertheless, current ultrasound scattering theory is capable of predicting this behaviour from first principles[5]. In general, as the frequency increases so does the attenuation, as to be expected. However, this does not occur simply. Examination of **Fig. 3** indicates that little information about size distribution can be obtained for sizes below around 10 nm. But this does not mean that particles smaller than this are not detected. In fact a big advantage of ultrasound is that particles of all sizes are detected and contribute to the volume fraction, which is obtained independently from the spectra. So we can expect to obtain accurate values of the volume fraction, regardless of the size distribution. Examination of **Fig. 3** also indicates that the spectrum is very sensitive to particle size in the region 10 nm to 500 nm. In general there may not be a unique solution to the spectral inversion; several size distributions may satisfy a given spectrum. Here modelling of the spectrum is very useful because this allows a-priori knowledge of the distribution to constrain the range of solutions to the spectral inversion. Note in **Fig. 4** how increasing particle concentration increases the sizing range considerably.

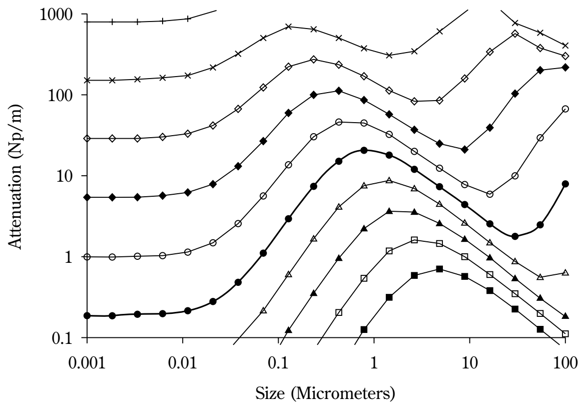

Fig. 3 Attenuation plotted against size and frequency for 2.24% v/v monosize silica suspended in water. Solid squares, 0.1 MHz; open squares, 0.233 MHz; solid triangles, 0.541 MHz; open triangles 1.26 MHz; closed circles, 2.93 MHz; open circles, 6.82 MHz; closed diamonds, 15.87 MHz; open diamonds, 36.94 MHz; crosses, 85.95 MHz; pluses, 200 MHz.

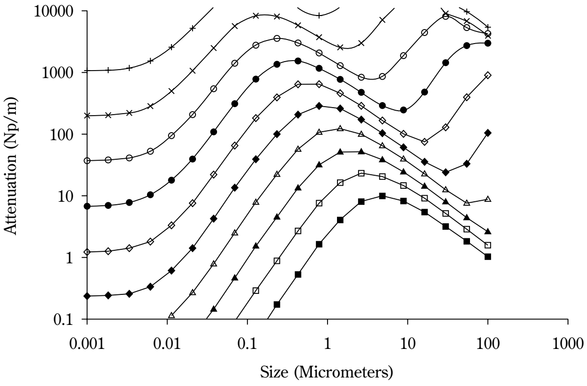

Fig. 4 Attenuation plots for 30% v/v monosize silica in water. Symbols as in **Fig. 3**.

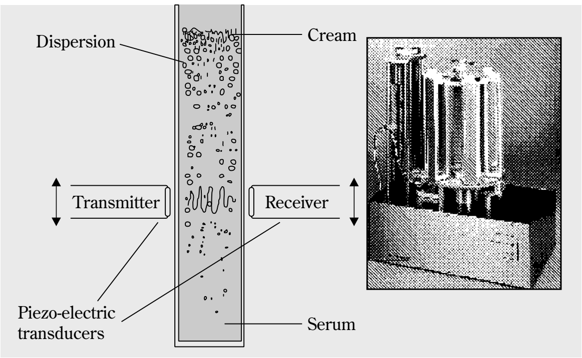

Fig. 5 Acoustiscan ultrasound scanner, diagram on left, picture on right[11].

4. Stability of Particulate Systems

The stability of particle dispersions is of particular concern to manufacturers and acoustic techniques offer a unique combination of ability to non-invasively characterise concentrated dispersions and to provide data which can be compared with mathematical models. This combination of techniques offers the prospect of product lifetime prediction, sometimes called shelf life[12, 13, 14, 15, 16, 17]. The Acoustiscan scanner (**Fig. 5**) employs a pulse echo technique similar to that of the FSUPER (Frequency scanning ultrasonic pulse echo reflectometer[7]). In the case of the Acoustiscan though, the transducers are moved using a stepper motor system, building up a spatial and temporal picture of the distribution of particles.

In **Fig. 6** the behaviour of an emulsion in which the density difference between the lighter dispersed phase and the heavier aqueous phase results in creaming is shown. We have shown that this type of behaviour is completely described by buoyancy and hydrodynamics and can model the behaviour precisely[13]. Fractionation occurs as the smaller particles are moved upwards in the backwash of the larger faster moving particles, resulting in the blurred-out interface between the cream (top) and the serum (bottom). This type of instability is actually unusual, largely because the particles interact through a variety of mechanisms - depletion flocculation, van der Waals forces, ionic forces, bridging flocculation, etc. In this case it is much harder to model the behaviour; an example of an emulsion which gels through depletion flocculation is given in **Fig. 7**. Note that there is a well-defined boundary between the cream and the serum; this arises because particles of all sizes are held within the flocs which then cream together, preventing the fractionation process seen in **Fig. 6**. This technique and approach permits the rapid prediction of dispersion stability because it is sensitive to the microscopic changes occurring which lead to product destabilisation.

5. Particle State and Solid Content

The speed of sound is extremely sensitive to the crystalline state of particles[8, 10]. This is because there is a large change in compressibility between the liquid and solid state. The density change is nothing like so great and as a result, we see a big change in the speed of sound through $v = {}^{1}/\sqrt{\kappa\rho}$. Since the speed of sound is measured in the UVM system with a pre-

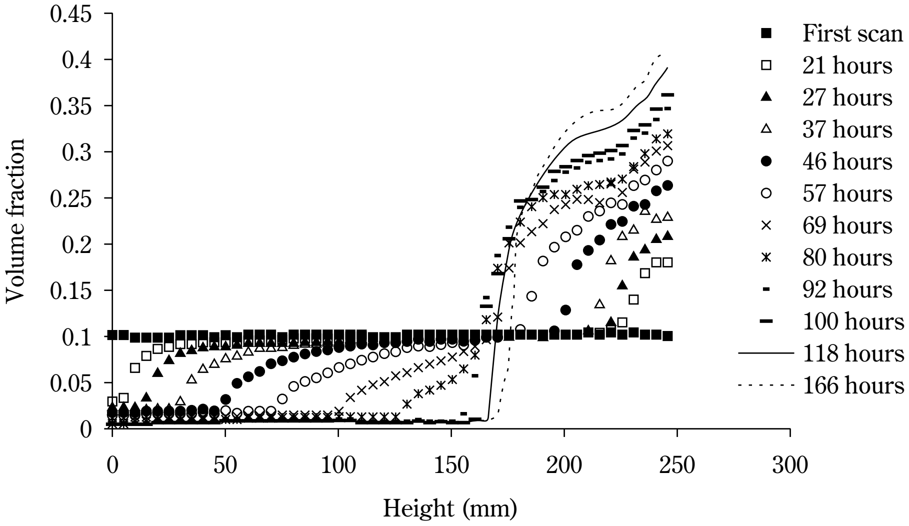

Fig. 6 Unhindered creaming of an oil-in-water emulsion measured using the Acoustiscan.

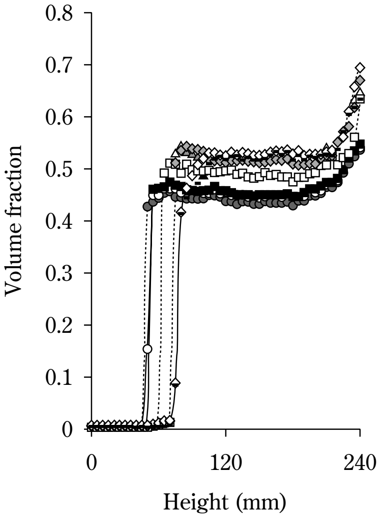

Fig. 7 Creaming and gelation in a flocculating oil-in-water emulsion. 35 wt % n-tetradecane oil-in-water emulsions containing 4 wt % sodium caseinate, 30 C, pH 6.8 . 0.5 μm. ●, after 52 h; o, after 64 h; ■, after 3 d; □, after 6 d; *, after 12 d; △, after 15 d; ▼, after 19 d; ◇, after 33 d.14)

cision of 0.1 ms^{-1} in 1500, we determine solid content to within 0.01 v/v or 1% v/v, regardless of particle size. This is a simple, rapid (10 measurements per second) and accurate method for determining particle state in concentrated dispersions of particles, no matter what their size. **Fig. 8** shows the solid content determined in a crystallisation n-hexadecane emulsion whose oil phase crystallizes at 2°C and melts at 18°C. This emulsion is very stable and can be cycled again and again between the crystalline and liquid states (**Fig. 9**). The method can distinguish between crystallization and the formation of a glass, since the two states of matter have totally different compressibilities.

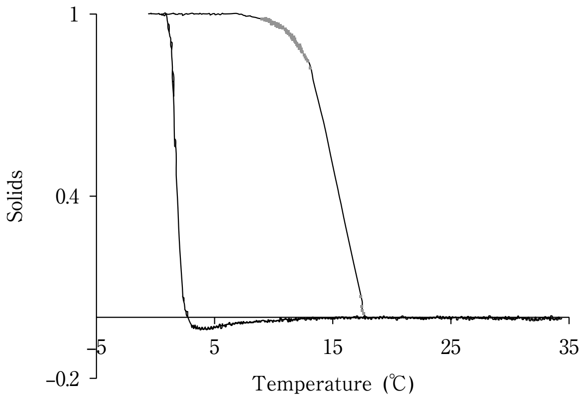

Fig. 8 Solid content of a 5% v/v n-hexadecane oil-in-water emulsion with D[3,2] = 123 nm.

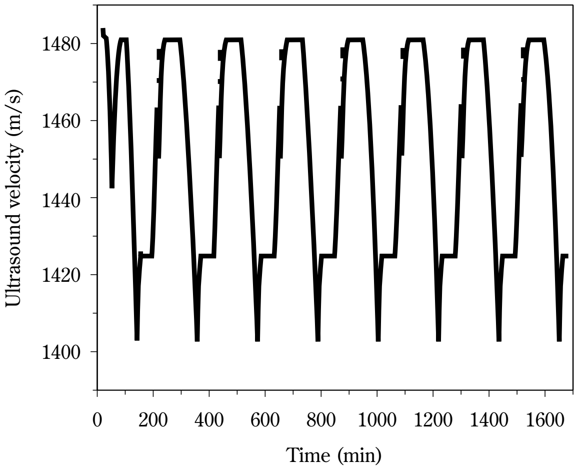

Fig. 9 Velocity data for the emulsion in ... cycled continuously between 0°C and 40°C, 7 times.

6. Conclusion

It is indeed surprising that ultrasound measurement is not used more widely in particle characterisation. This is particularly true when it is considered that for applications such as concentrated nanoparticle dispersions, there is no other technique which can be used to determine the state of the particle, the state of its surface or its size distribution. Nor is there any rival in the area of crystallization, particularly in the initial stages during nucleation. The answer to this question lies in the lack of commercially available equipment properly adapted to the needs of industry. However, such a situation is unlikely to last since the hurdles are not technical but practical. Equipment needs to become more versatile, more adaptable to manufacturing needs and less expensive; this is just a matter of time.

Acknowledgements

I am grateful to Dr Tarek Awad, Dr Valerie Pinfield and Miss Ran Huo of the University of Leeds for supplying data.

Reterences

1) Povey, M. J. W.: Ultrasonic techniques for fluids characterisation. (Academic Press, San Diego) 1997.
2) Povey, M. J. W.: Ultrasonics of food, Contemporary Physics, **39**. 1998 467-478.
3) Kinsler, L. E., Frey, A. R., Coppens, A. B., and Sanders, J. V.: Fundamentals of acoustics. (John Wiley and Sons, New York) 1982.

4) Meyer, S. Berrut, S. Goodenough, T. I. J. Rajendram, V. S. Pinfield, V. J. and Povey, M. J. W.: A comparative study of ultrasound and laser light diffraction techniques for particle size determination in dairy beverages, Measurement Science and Technology, **17**, 2006, 289-297.

5) Challis, R. E., Povey, M. J. W., Mather M. L. and Holmes, A. K.: The Use of Ultrasound in Characterising Colloidal Dispersions, Reports in Progress in Physics, **68**, 2005, 1541-1637.

6) Povey, M. J. W., Golding, M., Higgs, D. and Wang, Y.: Ultrasonic Spectroscopy Studies of Casein in Water, International Dairy Journal, **9**, 1999, 299-303.

7) Tong H. and Povey M. J. W.: Pulse echo comparison method with FSUPER to measure velocity dispersion in n-tetradecane in water emulsions, Ultrasonics, **40** 2002 37-41.

8) Povey M. J. W., Hindle S. A., Aarflot A. and Hoiland H.: Melting point depression of the surface layer in n-alkane emulsions and its implications for fat destabilization in ice cream, Crystal Growth & Design, **6**, 2006, 297-301.

9) Povey M. J. W., Hindle S. A., Kennedy J. D., Stec Z. and Taylor R. G.: The molecular basis for sound velocity in n-alkanes, 1-alcohols and dimethylsiloxanes, Physical Chemistry Chemical Physics, **5**, 2003 73-78.

10) Hindle, S., Povey M. J. W. and Smith K.: Kinetics of crystallization in n-hexadecane and cocoa butter oil-in-water emulsions accounting for droplet collision-mediated nucleation, Journal of Colloid and Interface Science, **232**, 2000, 370-380.

11) Nelson, P. V., Povey, M. J. W. and Wang, Y.: An Ultrasound Velocity and Attenuation Scanner for Viewing the Temporal Evolution of a Dispersed Phase in Fluids, Reviews of Scientific Instruments, **72**, 2001, 4234-4240.

12) Dickinson E., Ritzoulis C. and Povey M. J. W.: Stability of emulsions containing both sodium caseinate and Tween 20, Journal of Colloid and Interface Science, **212**, 1999, 466-473.

13) Pinfield V. J., Dickson E. and Povey M. J. W.: Modeling of combined creaming and flocculation in emulsions, Journa1 of Colloid and Interface Science, **186**, 1997, 80-89.

14) Dickinson E., Golding M. and Povey M. J. W.: Creaming and flocculation of oil-in-water emulsions containing sodium caseinate, Journal of Colloid and Interface Science, **185**, 1997, 515-529.

15) Pinfield V. J. and Povey M. J. W. and Dickinson E.: Interpretation of ultrasound velocity creaming profiles, Ultrasonics, **34**, 1996, 695-698.

16) Dickinson E., Ma J. G. and Povey M. J. W.: Creaming of concentrated oil-in-water emulsions containing xanthan, Food Hydrocolloids, **8**, 1994, 481-497.

17) Pinfield V. J., Dickinson E. and Povey M.J.W.: Modeling of concentration profiles and ultrasound velocity profiles in a creaming emulsion - importance of scattering effects, Journa1 of Colloid and Interface Science, **166**, 1994, 363-374.

Author's short biography

Malcolm J. W. Povey

BA, PhD, FInstP, CPhys, CEng
Professor of Food Physics
Procter Department of Food Science
The University of Leeds
Leeds, LS2 9JT, Great Britain
www.food.leeds.ac.uk/mp.htm
www.ultrasoundresearch.com

Malcolm Povey was born in 1947 in Wallasey, England. He studied physics at Lancaster University, graduating with a BA in 1970 and a PhD in 1973. He spent his postdoctoral period at Leeds University researching the effects of very high pressure on the bandstructure of alkali metal alloys and transferred to Food Science at Leeds in 1976. In Food Science he applied acoustical methods to the testing and evaluation of foods such as eggs, fruit, biscuits and milk.

Co-inventor of the 'Ultracane' and the Baker Petrolite 'Aggregation Monitor', he is internationally recognised as a leading researcher in the area of ultrasound, having pioneered its application to food. In 2003 his achievements were recognised by promotion to the Chair of Food Physics at Leeds.

Current research projects include nanoparticles for anti-microbial materials, nanocrystals, acoustic microscopy, product stability assessment, acoustics and ultrasonics for materials testing and novel ultrasound methods for characterising proteins. Most recently he developed in conjunction with Stable Microsystems methods for acoustically assessing the mechanical properties of materials including crispy foods such as biscuits.

He chairs the Hahn Prize Committee, the pre-eminent European food engineering and science prize.

An Experimental Study on the Fluidisation Behaviour of Geldart C Glass Powders[†]

K.Saleh[1], X.B.Cami, A.Thomas, P.Guigon
Chemical Engineering Department,
*CNRS-UMR 6067, Compiegne University of Technology**

Abstract

The main objective of this work was the study of the fluidisation behaviour of a glass powder in order to allow its application by electrostatic pulverisation. The high density and the small diameter of the original product lead to bed channelling and slugging. To avoid these inconsistency problems, different fluidisation-aid techniques were experimented with: incorporation of easy-to-fluidise large spherical glass particles into the glass powder, the use of mechanical agitation and the addition of four different types of flow conditioners (or glidants). Four batches containing 1 w/w% of different fluidisation additives (two containing hydrophilic additives and two hydrophobic additives) were tested. Fluidisation additives were Aerosils®, which are nano-sized silica products. The quality of fluidisation was determined by monitoring the pressure drop through the bed during fluidisation experiments at decreasing air velocities.

Two sizes of spherical glass particles were used as easy-to-fluidise particles. Nevertheless, the fluidisation was not obtained by means of this technique. Using the stirring system, a better but still poor fluidisation was achieved, although its quality was improved by adding flow conditioners. An insignificant influence of the stirring speed on fluidisation was observed when using the fresh powder or batches containing hydrophilic fluidisation additives. Moreover, the influence of the proportion of additive was tested in six batches containing 0.1, 0.2, 0.3, 0.4, 0.5, and 1 w/w% of the agent, which led to the most satisfactory improvement in fluidisation behaviour of the glass powder.

Keywords: Fluidisation, Fluidised bed, Glass powder, Flow conditioner, Agitation, Glidants

1. Introduction

One of industrial applications of fine glass powders is their electrostatic deposition on the surface of glass substrates such as sheets or decorative objects. Further heating of coated objects leads to subsequent sintering of the deposited layer of glass powder and formation of opaque patterns. However, dielectric properties of glass powders are inappropriate to their electrostatic application. Hence, the electrostatic deposition of glass powders requires their coating with suitable coating agents. The coating operation can be performed in a fluidised-bed coater (*e.g.* 1,2)), which should ensure a homogeneous covering of particles. In this technique, the fluidisation behaviour of powders to be coated is fundamental and decisive for the feasibility and the quality of coating. The main objective of this work is to study the fluidisation behaviour of a Geldart C-class powder derived from the grinding of recycled glass bottles. It is well known that this type of powder has poor flowability as well as poor fluidisation properties.

According to Geldart's classification[3)], fine powders could belong to two main groups with respect to their fluidisation behaviour: Group A particles that are considerably expanded before bubbling begins and Group C particles that are difficult or impossible to fluidise. This complexity is due to the interparticle forces that are greater than gravitational forces[4)]. In the absence of liquid bridges, adsorbed liquid layers and/or electrostatic forces, the most significant attractive interactions are van der Waals forces[4)]. Ac-

---

[†] Accepted: August 14, 2006

[*] BP 20259, 60205 Compiegne cedex, France
[1] Corresponding Author
TEL: +33-344235274, Fax: +33-344231980
E-mail: khashayar.saleh@utc.fr

cording to several investigations, interparticle forces play a key role on fluidisation behaviour of fine powders. For example, Lauga et al.[5] showed that there is a direct relationship between the expansion of Ni/SiO$_2$ aerogels in a fluidised bed and the interparticle interactions resulting from van der Waals forces. In addition, valuable information about the role of interparticle forces in the fluidisation of fine powders (class C) can be found in recent review articles of Yang[6] and Seville et al.[7]. There are several methods to improve a fine fluidisation process of Geldart C particles: adding easy-to-fluidise particles, fluidisation additives, agitation, vibration, centrifugation, acoustic field, magnetic field, etc. Easy-to-fluidise particles are generally powders belonging to class B having a size between 100 and about 1000 μm. Addition of this type of product to class C powders improves the fluidisation due to the mixing action of larger particles which can be assimilated to a mechanical agitator.

Another common solution to improve the fluidisation of very fine powders is the addition of small amounts of flow conditioners or *glidants*. This type of product is made up of submicron-size primary particles. Due to their small size, when adhered on the surface of core particles, primary particles behaves like a surface asperity. This leads to an increase in the minimum contact distance of two interacting particles, which in turn decreases the van der Waals forces[8, 9]. Silica-, alumina- and carbon-based glidants are the most widely used flow conditioners.

In this work, the effect of the addition of both easy-to-fluidise particles and flow conditioners as well as the use of agitation systems on the fluidisation behaviour of glass powders was studied.

The objective was to identify the optimal operating conditions for the fluidisation of glass powders allowing their further coating as well as a better understanding of the action mechanisms of glidants.

2. Definition of Fluidisation Criteria and Their Interpretation

A gas passing through a bed of powder exerts a friction force on particles that increases with the gas velocity. This results in a pressure drop between the entry and exit points of the bed. As illustrated in Fig. 1, a progressive increase of the pressure drop can be observed with increasing superficial gas velocity. Regarding the superficial gas velocity, U, two regimes can be distinguished: a fixed-bed region where pressure drop varies directly with the gas velocity, and a fluidised-bed zone where the pressure drop remains constant. The transition velocity between these two regimes is known as *minimal fluidisation velocity*, U_{mf}. **Fig. 1** summarises the fluidisation trends of more or less cohesive powders. For a perfect particulate fluidisation (*i.e.* each particle is individually suspended independently of surrounding particles) and in the absence of particle elutriation, the total friction force exerted on the bed ($\Delta P \cdot S$) is equal to the bed weight ($M \cdot g$). In addition, for an ideal fluidisation, the minimal fluidisation velocity, U_{mf}, can be determined by theoretical models or by semi-empirical correlations (e.g., Thonglimp[10]). Note that these models do not take into account the interparticle forces. For more cohesive particles, the fluidisation takes place through the suspension of ephemeral agglomerates rather than individual particles. This phenomenon does not affect the total pressure drop but leads to an increase in experimentally measured values of $U_{mf,exp}$. Finally, for more cohesive particles, slugging and channelling of the bed might occur. This leads to higher values of $U_{mf,exp}$, on the one hand, and to lower pressure drops on the other hand because the effective gas-particle contact area is reduced.

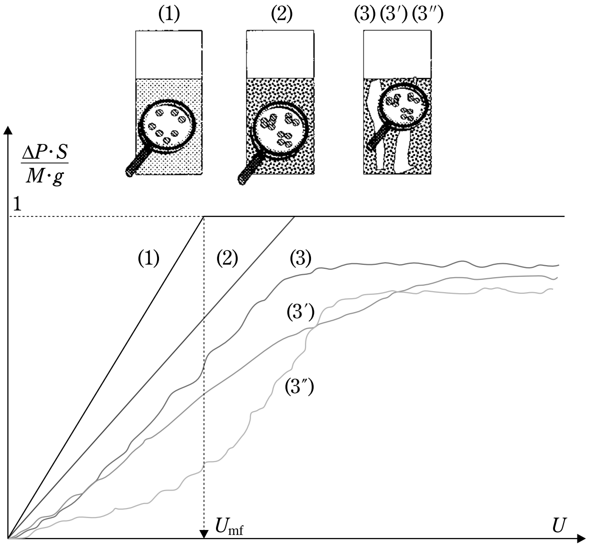

Fig. 1 Pressure drop profile (1. Homogeneous fluidisation of particles, 2. Homogeneous fluidisation of agglomerates, 3, 3′, 3″. Channelling and slugging fluidisation).

Accordingly, in addition to the minimal fluidisation velocity U_{mf}, the following criteria could be used to characterise the fluidisation behaviour of fine particles:

- Fluidisation index, *FI*

This parameter is the ratio of the minimum fluidisation velocity determined by a semi-empirical correlation valid for ideal fluidisation and the minimum fluidisation velocity experimentally determined:

$$FI = \frac{U_{mf,corr}}{U_{mf,exp}} \tag{1}$$

Obviously, *FI* depends on the empirical correlation used to calculate the minimum fluidisation velocity ($U_{mf,corr}$). *FI* is equal to unity for easy-to-fluidise particles ($>$100-200 μm) and tends towards zero for impossible-to-fluidise powders.

- Fluidisation quality, *FQ*

Fluidisation quality is defined as the dimensionless pressure drop through the bed:

$$FQ = \frac{\Delta P \cdot S}{M \cdot g} \tag{2}$$

An *FQ* equal to unity characterises a homogeneous fluidisation of either individual particles or ephemeral agglomerates. In contrast, channelling and slugging phenomena lead to poorer fluidisation qualities.

- Dynamic diameter of agglomerates, d_a

This parameter is an indication of the equivalent size of ephemeral agglomerates. d_a is a hypothetical diameter which allows matching predicted and experimentally measured values of U_{mf}, *i.e.* the agglomerate mean size necessary to have an *FI* equal to unity. d_a can be easily calculated once an adequate correlation is chosen.

Note that the ratio between the equivalent diameter of dynamic agglomerates and the elementary particles' mean size (d_a/d_p) is a rough and qualitative measure of interparticle cohesive forces: the more cohesive the powder is, the higher is the deviation of the ratio d_a/d_p from the unity. In fact, one might consider that d_a is the size of agglomerates which permits the interparticle forces to just be counterbalanced by break-up forces.

In this study, the semi-empirical correlation proposed by Thonglimp *et al.*[10] was used for prediction of $U_{mf,cor}$:

$$\frac{\rho_p U_{mf} d_p}{\mu} = \sqrt{31.6^2 + 0.0425 \cdot \frac{\rho_g(\rho_p-\rho_g) g d_p^3}{\mu^2}} - 0.0425 \tag{3}$$

Preliminary experiments conducted with perfectly fluidisable model glass beads showed that this correlation expects good $U_{mf,exp}$ values.

Generally, knowing the fluidisation criteria, one can roughly classify the fluidisation behaviour of cohesive powders as indicated in **Table 1**.

Table 1 Classification of behaviour of powders according to fluidisation criteria

FI	FQ	State
0.8 - 1	0.7 - 1	Homogeneous fluidisation of particles
<< 1	0.8 - 1	Homogeneous fluidisation of agglomerates
Very low	0.6 - 0.8	Non-homogeneous fluidisation

3. Experimental

3.1 Materials

A glass powder (GP) with a median mean diameter of 2.65 μm and a true density of 3100 kg/m^3 was used in this study. These parameters were measured using a Malvern Mastersizer analyser and a Helium pycnometer (Micromeretics, Accupyc 1330), respectively. The glass powder was prepared by milling recycled glass bottles. The higher density of this product with respect to the pure glass is due to impurities, in particular the presence of zinc oxide. The powder is cohesive, belonging to group C of Geldart's classification, which is characterised by a difficult fluidisation.

Two batches of easy-to-fluidise particles (EFP) were used. They were spherical glass beads with median mean diameters of 300 and 400 μm, respectively (ρ=2650 kg·m^3). Both batches belong to Geldart's group B and fluidise easily with bubbling starting at minimum fluidisation velocity.

As for flow conditioners, four different types of Aerosils® were used (**Table 2**). Aerosils® are made up of nano-size primary silica particles which are connected by solid bridges and which form non-dispersive *clusters* having a size several times greater than that of primary particles (**Fig. 2-a**). Due to their small size, the clusters in turn form secondary aggregates of a few micrometres, which can easily be fragmented and dispersed.

In this study, the size distribution of non-dispersive aggregates was measured using a Zetasizer from Malvern Instruments. Several liquid dispersants were tested but the most effective was found to be Ethanol. **Fig. 2-b** represents a typical curve of non-dispersive *clusters* size distribution. The mean sizes calculated from measured size distributions are reported in **Table 2**. As can be seen from data presented in this table, additives used here differ in the size of their primary particles and in their hydrophobe/hydrophile properties. Aerosil® 130 and Aerosil® 200 are both of hydrophilic nature but differ in the diameters of both

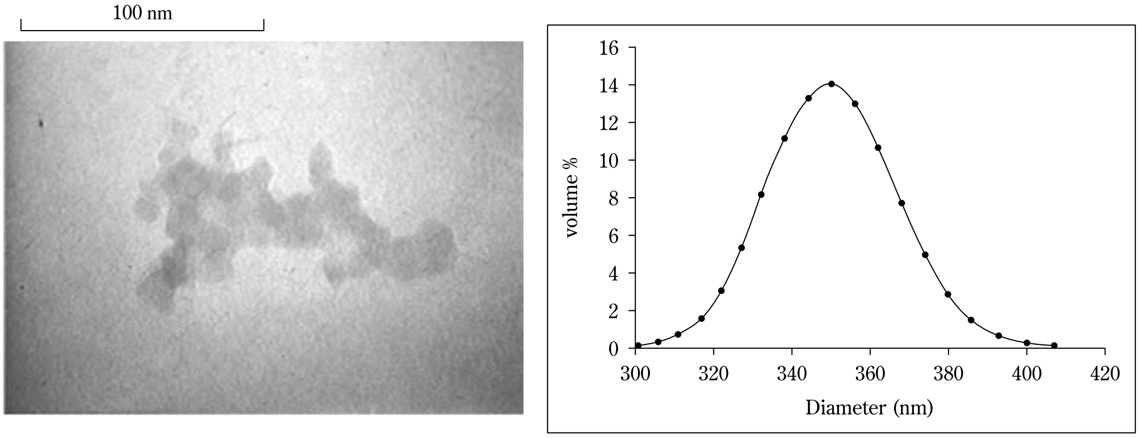

a) TEM image of an aggregate b) aggregate size distribution determined by PCS

Fig. 2 Size of non-dispersive aggregates (Aerosil® 812S).

Table 2 Fumed silica physico-chemical properties

Aerosil®	Primary particle size [a]	Aggregate average size [b]	BET Surface [a]	Tapped density [a]	Carbon content	Methanol wettability [a]
130	16 nm	320	130	50 g/L	—	—
200	12 nm	250	200	50 g/L	—	—
R972	16 nm	350	110	50 g/L	0.6-1.2 %	30%
R812S	12 nm	270	220	50 g/L	3-4%	60%

[a] supplier's specifications

[b] aggregate size determined by PCS

primary particles and non-dispersive aggregates. Aerosil® R 972 and Aerosil® R 812 S can be considered as hydrophobic homologous of Aerosil® 130 and Aerosil® 200, respectively. Indeed, these agents have sizes of primary and non-dispersive particles that are similar to those of Aerosil® 130 and 200, respectively, but their surface is treated by hydrophobic reagents, which are stable against hydrolysis.

3.2 Preparation of powders

A similar procedure was used to prepare both easy-to-fluidise and glidant-added mixtures. Each powder mixture was prepared using a Pro-C-epT® Mi-Pro high shear mixer (maximum volume: $1.2 \cdot 10^{-3}\ m^3$). The mixing was performed for 1 hour at a rotational speed of 200 rpm. Preliminary experiments showed that these conditions permit achievement of an optimal effect of the flow additive.

Easy-to-fluidise batches

Several binary mixtures of fresh fine powder (GP) and coarse particles (EFP) were prepared with coarse particle concentrations of 10, 20, 30, 40 and 50 w/w% (**Table 3**).

Glidant-added batches

Two series of glidant-added batches were prepared. In the first series, four batches were formulated each containing 1% w/w of different glidants. In the second series of batch formulation, five additional batches were prepared using Aerosil® R 812 S with different percentages: 0.1, 0.2, 0.3, 0.4 and 0.5%. This allows us to study the influence of additive percentage on fluidisation ability.

SEM micrographs presented in **Fig. 3** show a view of additive-free and glidant-added glass powders. It can be observed that the glass powder has an irregular shape and a wide size distribution. Agglomerates of powder are also observed. These characteristics reinforce poor fluidisation ability.

3.3 Experimental apparatus

In order to characterise the fluidisation behaviour of the prepared powder batches, home-made fluidisation equipment was used. This apparatus consists of a conventional fluidised column properly instrumented to monitor the operating conditions as well as the bed level and the pressure drop through the bed. The apparatus includes three main parts: the fluidisa-

Table 3 Summary of experiments and fluidisation criteria

Experiment number	Added (secondary) product	Weight percentage of additive	Bed mass (kg)	Stirring velocity (rpm)	U_{mf} (mm/s)	FI ($\times 10^4$)	FQ	d_a (μm)
1	—	—	1.0	—	—	—	—	—
2	—	—	1.0	65	1.97	40	0.89	72
3	—	—	1.0	110	1.97	40	0.94	71
4	—	—	1.0	160	1.78	44	0.91	70
5	Glass beads (300 μm)	50%	1.5	—	—	—	—	—
6	Glass beads (400 μm)	50%	1.5	—	—	—	—	—
7	Aerosil® 130	1	1.0	—	—	—	—	—
8	Aerosil® 130	1	1.0	65	0.90	87	0.94	48
9	Aerosil® 200	1	1.0	—	—	—	—	—
10	Aerosil® 200	1	1.0	50	0.62	117	0.98	39
11	Aerosil® 200	1	1.0	65	0.55	132	0.99	36
12	Aerosil® 200	1	1.0	80	0.64	113	0.99	41
13	Aerosil® R972	1	1.0	—	3.27	24	0.93	95
14	Aerosil® R972	1	1.0	65	0.86	91	0.97	49
15	Aerosil® R812S	0.1	0.9	—	3.37	23	0.89	100
16	Aerosil® R812S	0.2	0.9	—	3.43	23	0.88	102
17	Aerosil® R812S	0.3	0.9	—	2.26	35	0.89	83
18	Aerosil® R812S	0.4	0.9	—	2.18	36	0.88	81
19	Aerosil® R812S	0.5	1.0	—	2.06	38	0.95	75
20	Aerosil® R812S	1	1.0	—	2.13	37	0.96	75

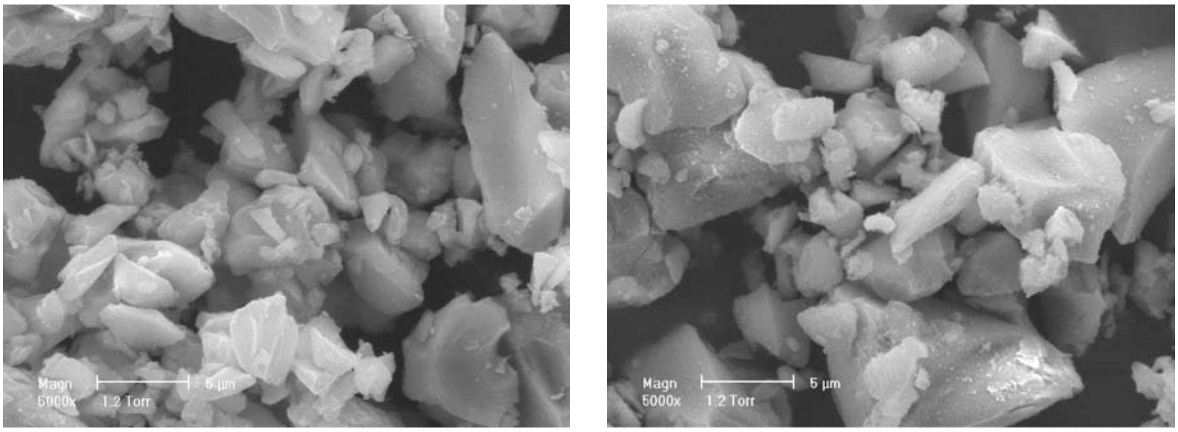

Fresh glass powder

glass powder + Aerosil® 200 (1% w/w)

Fig. 3 SEM images of fresh and glidant-added particles.

tion column, the air flow circuit and the acquisition device. **Fig. 4** shows a schematic diagram with some principal dimensions of the experimental set-up.

The fluidisation column is a Pyrex cylinder 100 mm in diameter and 500 mm in height. At the top of the column, an expanding freeboard section is mounted to permit minimisation of particle entrainment. The air stream exiting the freeboard section passes through a cyclone and elutriated particles are recovered. The air distributor is a metallic porous plate sandwiched between two filter papers. The distributor is placed between the fluidisation cylinder and the wind box, which is a $7.85 \cdot 10^{-3}$ m^3 cylindrical chamber. Before entering the bed, the compressed

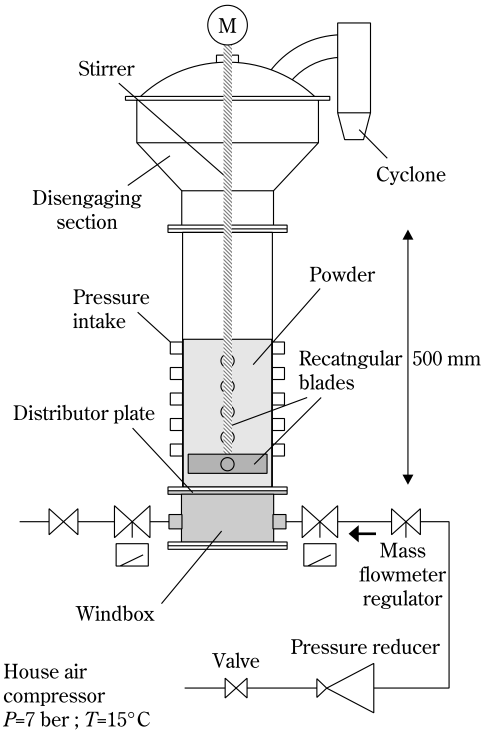

Fig. 4 Schematic diagram of experimental apparatus.

air passed through a filter, a pressure regulator and a mass flowmeter regulator. During each experiment, temperature and relative humidity inside the bed as well as pressure drops at different levels of the bed were monitored and recorded. Data acquisition was performed using a HP VEE® program. The program permitted selection of all electro valves to ensure the desired air flow rates for the predefined time intervals. Consequently, once the bed is charged, fluidisation trials are automatically carried out without any operator intervention. More detailed information on the experimental apparatus and acquisition system can be found elsewhere[11].

In addition, an agitation system was used in some trials. This system was composed of a motor, a rotating shaft and an agitator mobile which is made up of two rectangular blade stirrers (80 × 15 mm) placed at 20 mm from the air distributor.

3.4 Fluidisation experiments

The mass of each batch was fixed so that the condition $1.4 < H/D < 1.5$ was accomplished. Firstly, a determined initial mass of powder was introduced into the column in order to ensure a bed height of about 0.14-0.15 m. Prior to actual fluidisation tests, the bed was pre-conditioned to reduce the influence of initial bed packing . To this end, the air velocity was first increased and then decreased in steps of $0.1\ \mathrm{l \cdot min^{-1}}$ every 20 s. After each pre-conditioning cycle, the bed height was checked. If the bed was too high (or too low) a corresponding amount of powder was added (or removed) and the pre-conditioning was repeated.

Fluidisation properties were determined at decreasing air velocities. Firstly, the gas velocity was fixed at its maximum value. Then the gas stream was decreased gradually and the pressure drop was measured at each step after having maintained a constant gas velocity during 60 s at least. Between each step, the gas velocity was increased to its maximum value for 60 s. Each fluidisation test was repeated five times using exactly the same procedure. The reported values in this paper correspond to the mean value of all five runs. Note that the experimental values of minimum fluidisation velocity, $U_{mf,exp}$, were determined by plotting ΔP vs. U values in a log-log diagram as is recommended for fine powders of narrow size distribution (*e.g.* 12)). Such a presentation (not shown here) permits a better location of the transition point between the fixed state and fluidised bed.

4. Results and Discussion

Table 3 summarises the composition of all batches together with the operational conditions used during fluidisation experiments. As shown in this table, experiment no.°1 corresponds to the glass powder with no additives or mechanical agitation. Experiments 2 to 4 aimed show the effect of agitation speed on the fluidisation of glass powder. The effect of incorporating easy-to-fluidise particles was studied in experiments 5 and 6. Experiments 7 to 14 take into consideration the effect of the addition of 1% w/w of glidants, with or without agitation. Finally, experiments 15 to 20 emphasise the effect of the concentration of the glidant using Aerosil® R 812 S.

The characteristic fluidisation curve of fresh glass powder (**Fig. 5**) shows that the product does not fluidise even at gas velocities much higher than $U_{mf,cor}$ predicted by the correlation of Thonglimp *et al* ($8 \times 10^{-6}\ \mathrm{m.s^{-1}}$). Not one fluidisation property can be determined for this powder as the fluidisation state could not be established. Hence, auxiliary means must be used to promote the fluidisation of the glass powder.

4.1 Influence of agitation velocity

The effect of mechanical agitation on the fluidisation behaviour of the glass powder is also presented in **Fig. 5**. These results show that mechanical agita-

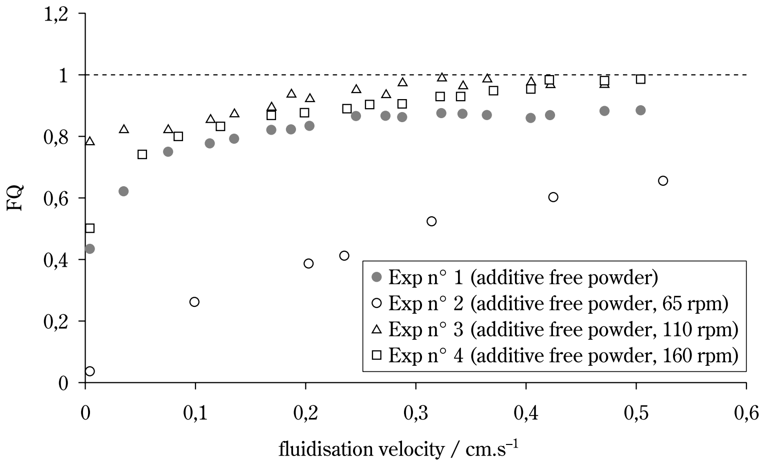

Fig. 5 Fluidisation curves for glass powder with and without mechanical agitation.

tion ensures a stable fluidisation operation with a relatively good quality. *FQ* values at 65 rpm range between 0.89 and 0.95 and are very close to unity at higher speeds. However, the fluidisation indexes are high (40×10^{-4} to 45×10^{-4}). This indicates that fluidisation takes place through suspension of aggregates rather than individual particles. The dynamic diameter of aggregates is about 70 μm.

These results reveal the importance of mechanical agitation in the feasibility of operation. However, the intensity of agitation does not play a significant role on fluidisation properties. As can be seen from **Fig. 5** and **Table 3**, an increase of rotational speed of agitation by a factor of 2 and 3 has no noticeable effect, neither on the quality of fluidisation nor on the fluidisation index, *FI*. This means that mechanical agitation improves the fluidisation by breaking up the channels and slugs and thereby ensuring a better distribution of the air stream within the bed. In contrast, mechanical agitation does not demolish dynamic aggregates. However, this observation might be modified if more shearing agitation systems are used (*e.g.* high shear blades).

4.2 Influence of the addition of easy-to-fluidise particles

Several batches containing easy-to-fluidise particles were used in this study. They differ in the mean size (300 and 400 μm) and the amount (10, 20, 30, 40, 50% w/w) of the coarse population. We limit ourselves to present the results obtained with mixtures containing 50% w/w easy-to-fluidise particles (**Table 3**). Note that due to the presence of coarse particles, the dynamic diameter of aggregates has no meaningful significance for these experiments. The results showed that the fluidisation of glass powders is possible by the addition of coarse particles. However, $U_{mf,exp}$ values were so high that great amounts of fine particles were elutriated. Although the $U_{mf,exp}$ decreased when using smaller easy-to-fluidise particles, its value still remained too high to avoid this phenomenon. A partial remedy to this problem is to decrease the mean size of the coarse population. However, in our case, even the use of 100-μm easy-to-fluidise particles did not ensure stable operation.

Another problem encountered with this technique is the segregation phenomenon, which appears at low gas velocities.

Consequently, compared to use of mechanical agitation, the addition of easy-to-fluidise particles does not seem to constitute a suitable technique for fluidisation of the glass powder used in this study. In fact, the operation lies between two undesired regimes, namely segregation and elutriation.

4.3 Influence of the addition of flow conditioners

Fluidisation characteristic curves of powders containing 1% w/w of two types of hydrophilic flow conditioners are presented in **Fig. 6**. These results reveal that the introduction of hydrophilic additives does not improve the fluidisation properties of the original powder. The characteristic curves are quite similar for additive-free powders and mixtures containing hydrophilic glidants. Fluidisation is only possible with the use of mechanical agitation. In this case, *FQ* values close to unity are obtained although *FI* remains low. For a given rotational speed, this enhancement is more pronounced for Aerosil® 200. This can be attributed to the higher size of non-dispersive aggregates

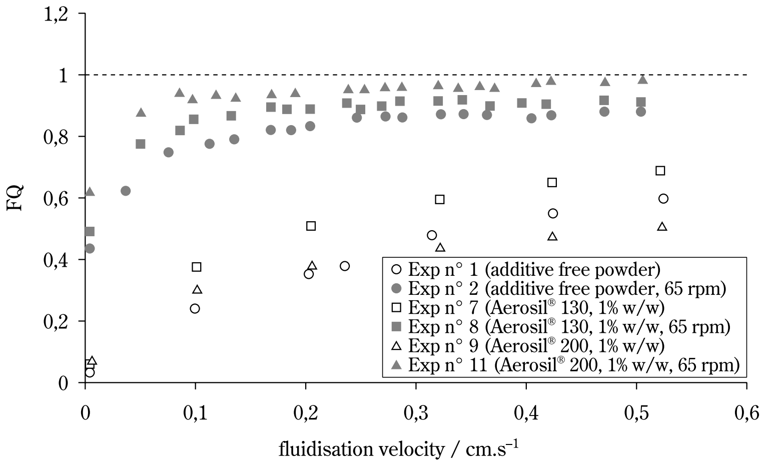

Fig. 6 Influence of adding hydrophilic additives with and without agitation.

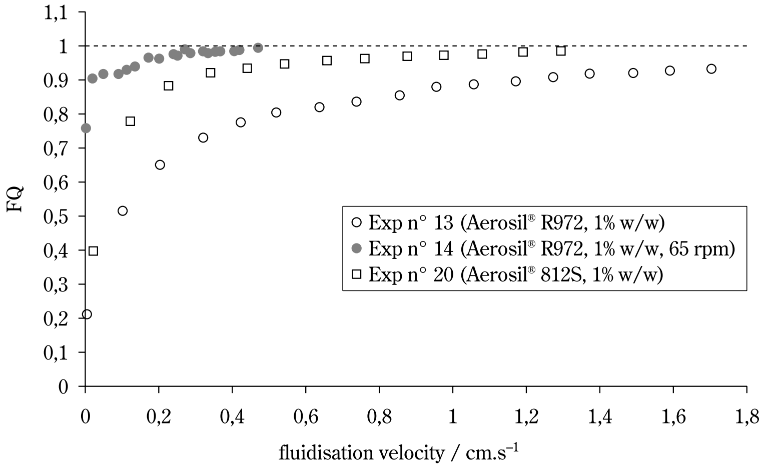

Fig. 7 Influence of adding hydrophobic additives.

for this additive compared to Aerosil® 130 (**Table 2**). This might lead to a more effective "opening" effect between particles and hence a more pronounced reduction of van der Waals forces.

The results presented in **Table 3** also confirm the observation made previously, *i.e.* the agitation rate (50, 65 and 80 rpm) has no influence on fluidisation properties.

The effects of the addition of hydrophobic agents on the fluidisation behaviour of the powder are presented in **Fig. 7**. These results confirm that the fluidisation enhancement in this case is largely better than that obtained by using hydrophilic agents. Using the agitation system and 1 w/w% of hydrophobic glidants, fluidisation qualities higher than 0.9 are obtained (0.93 and 0.97 for Aerosil R972 and R812S , respectively) (**Table 3**).

Furthermore, it can be seen that glass powders containing these two types of additives can fluidise even without mechanical agitation. However, for Aerosil R972, fluidisation criteria indicate that agitation is still beneficial to operation and that fluidisation deteriorates when agitation is turned off. The difference between the effectiveness of these additives might be attributed to the size of non-dispersive aggregates on the one hand and the hydrophobicity extent of products on the other hand. In fact, according to manufacturer's specifications, Aerosil R812S is more hydrophobic than R972. Consequently, this product can be more easily dispersed over the hydrophilic surface of glass powder. Indeed, SEM images of the surface of glass powders (**Fig. 8**) corroborate this assumption and show that Aerosil R812S is more evenly distributed at the surface of host particles. In addition, Aerosil R812S is made up of larger non-dispersive aggregates and is hence more suited to reducing interparticle forces.

Finally, it should be noted that a very marked ex-

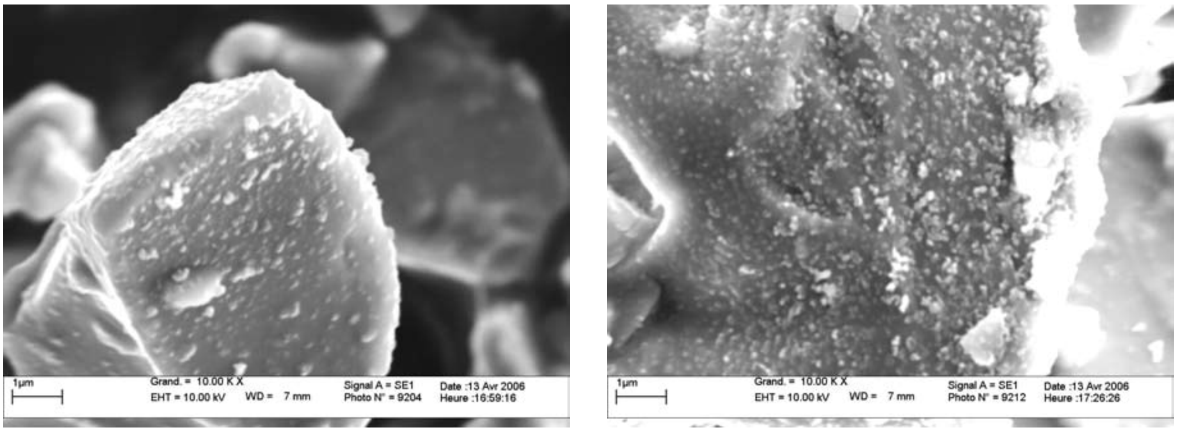

a) Aerosil® R972 (1% w/w) b) Aerosil® 812S (1% w/w)

Fig. 8 SEM images of hydrophobic additives on the surface of glass particles.

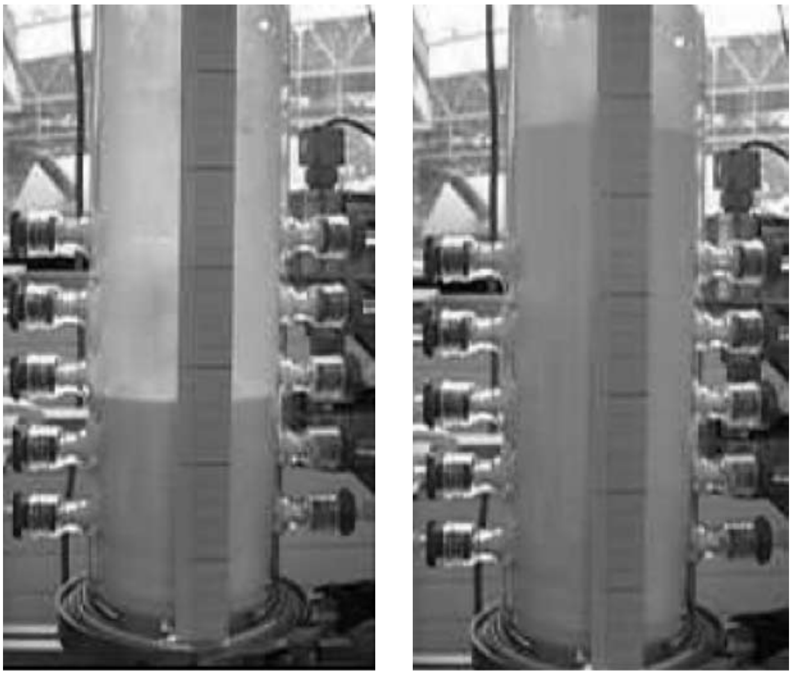

Fig. 9 Bed expansion of glass powder containing 1% w/w Aerosil® 812S.

pansion of the bed was obtained (H/H_0 = 2-2.5) when using Aerosil R812S as the additive (**Fig. 9**).

4.4 Influence of fluidisation additive rate

The additive rate is an important factor which influences the number of inserting particles. For example, during the investigation of flow properties of powder paints, Conesa et al.[11] reported that an optimal percentage of fluidisation additive exists beyond which the fluidisation is no longer enhanced or, in some cases, deteriorates. This optimal amount of additive depends on the physical properties of the original powder, the surface properties of both host and guest particles and the interactions between them, as well as the environmental conditions (temperature and humidity), process type and process-related variables.

The influence of the additive rate was investigated using batches formulated with the most effective glidant, *i.e.* Aerosil R812S, in different percentages (0.1, 0.2, 0.3, 0.4, 0.5 and 1 %w/w). Corresponding fluidisation curves are presented in **Fig. 10**. As can be seen, continuous improvement of *FQ* is obtained when the percentage of Aerosil increases up to 0.5%. Beyond this value, no significant improvement of fluidisation is observed.

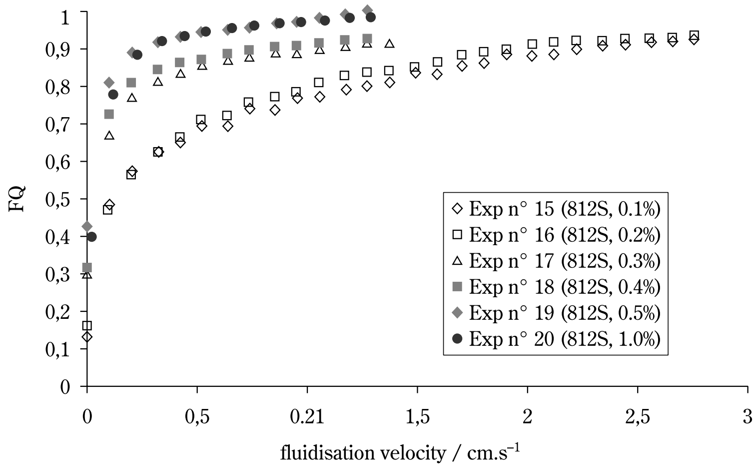

Fig. 10 Effect of the mass ratio of Aerosil® 812S on fluidisation behaviour of the glass powder.

5. Conclusions

The fluidisation behaviour of a class C glass powder was investigated. A fully automated experimental set-up was used to measure the fluidisation criteria: minimum fluidisation velocity, fluidisation quality, fluidisation index, and dynamic diameter of agglomerates.

The results showed that the introduction of easy-to-fluidise particles to fresh powder does not allow its fluidisation. However, the fluidisation was achieved using an agitation system but the agitation velocity had no significant effect on fluidisation ability.

The most remarkable effects were obtained when using flow conditioners. In particular, adding adequate amounts (0.5 to 1%) of a hydrophobic glidant (Aerosil R812S) led to a marked improvement of the fluidisation behaviour of glass powder so that it can be fluidised without any mechanical aid.

According to this study, it can be postulated that the effectiveness of glidants depends on two main parameters, namely the size of non-dispersive (inserting) aggregates and the hydrophobic extent of products. The size of inserting guest particles affects the gap between host particles and diminishes the attractive forces exerted between them. This conclusion was verified using both hydrophilic and hydrophobic glidants. As for the hydrophobicity of additives, this parameter doubly affects their effectiveness. Firstly, it plays a role on the dispersion of additives over the surface of host particles. A hydrophobic additive has more ease to spread over a hydrophilic support and *vice versa*. Secondly, van der Waals forces between two objects of opposite (hydrophobic/hydrophilic) natures are lower than two objects of similar nature. These considerations indicate that counteracting hydrophobic properties are needed to obtain the most pronounced improvement in powder flowability. More investigation are, however, needed to describe more precisely the exact role of the hydrophobic/hydrophilic nature of both support and additive powders.

Notations

d_a	dynamic agglomerate diameter, [m]
d_p	particle diameter, [m]
FI	fluidisation index, [-]
FQ	fluidisation quality, [-]
g	gravity acceleration, [$\mathrm{m \cdot s^{-2}}$]
H	bed height, [m]
M	mass of powder, [kg]
ΔP	pressure drop, [$\mathrm{kg \cdot m \cdot s^{-1}}$]
S	cross-sectional area of the bed, [$\mathrm{m^2}$]
U	superficial air velocity, [$\mathrm{m \cdot s^{-1}}$]
U_{mf}	minimum fluidisation velocity, [$\mathrm{m \cdot s^{-1}}$]
μ	viscosity, [$\mathrm{kg \cdot m^{-1} \cdot s^{-1}}$]
ρ	mass density, [$\mathrm{kg \cdot m^{-3}}$]

Subscripts:

Corr:	correlation
Exp	experimental
g	gas
a	aggregate
p	particle
0	initial

References

1) Hémati M., Cherif R., Saleh K. and Pont V.: Fluidised-

bed coating and granulation : influence of process-related variables and physico-chemical properties on growth kinetics, Powder Technology, **130** (2003) 18-34.

2) Saleh K., Chérif R. & Hémati M.: An experimental study of fluidized-bed coating: Influence of operating conditions on growth rate and mechanism, Journal of Advanced Powder Technology, Volume 10, No. 3, 255-278.
3) Geldart D.: Types of Gas Fluidisation, Powder Technology, **7** (1973) 285-292.
4) Visser J.: Van der Waals and the other cohesive forces affecting powder fluidisation, Powder Technology, **58** (1989) 1-10.
5) Lauga C., Chaouki J., Klvana D. and Chavarie C.: Improvement of the fluidisability of Ni/SiO_2 aerogels by reducing interparticle forces, Powder Technology **65** (1991) 461-468.
6) Yang W-C.: Fluidization of fine cohesive powders and nanoparticles - A review, J. Chin. Inst. Chem. Engrs Vol. 36, n° 1 (2005), 1-15.
7) Seville J.P.K, Willett C.D. and Knight P.C., Interparticle forces in fluidisation: a review, Powder Technology **113** (2000) 261-268.
8) Rumpf H.: Die Wissenschaft des Agglomerierens, Chemie-Ingenieur-Technik **46** (1) (1974) 1-11.
9) Meyer K. and Zimmermann I.: Effect of glidants in binary powder mixtures, Powder Technology **139** (2004) 40-54.
10) Thonglimp V., Hiquily N. and Laguerie C.: Vitesse minimale de fluidisation et expansion des couches de mélanges de particules solides fluidisées par un gaz, Powder Technology, **39** (1984) 223-239.
11) Conesa C., Saleh K., Thomas A., Guigon P., Guillot N.: Characterisation of Flow Properties of Powder Coatings Used in the Automotive Industry, KONA, **22** (2004), 94-106.
12) Kunii D. and Levenspiel O.: Fluidization Engineering, 2nd Edition (1991), Butterworth-Heinemann, ISBN 0-409-90233-0.

Author's short biography

Khashayar Saleh

Khashayar SALEH received a B.S. degree in Chemical Engineering from Sharif (Aryamehr) university of technology (Tehran/Iran) in 1992. He prepared a PhD thesis on the coating of fine powders in the Chemical Engineering Laboratory of Toulouse and obtained his doctor's degree in 1998 from Institut National Polytechnique de Toulouse (France). Dr Saleh is currently associate professor in the chemical engineering department of the Compiègne University of Technology. His work is focused on powder technology including size enlargement technology and powder's characterisation methods.

Xavier BERNAT CAMÍ

Xavier BERNAT CAMÍ is a Chemical Engineer from Rovira i Virgili University (Tarragona, Spain). He obtained a research Master in the field of Mass and Energy Transformation Processes from Compiègne University of Technology (Compiègne, France) in 2005. The research project of the Master was focused on the study of fluidisation ability of cohesive powders. Nowadays, he is a PhD student at Rovira i Virgili University (Tarragona, Spain). His current research is focused on wastewater treatment enhanced by membrane techniques. Concretely, he works with the recovery of homogeneous metallic catalysts, frequently used in advanced oxidation processes, with ultrafiltration ceramic membranes.

Aline Thomas

Aline THOMAS is a Ph.D student working in collaboration between the department of Chemical Engineering department of the Compiègne University of Technology (France) and the department of Materials and Painting Processes of the automotive company PSA Peugeot-Citroën. The subject of his research deals with the electrical behavior of powder coatings in order to characterize their electrostatic application in view of industrial applications.

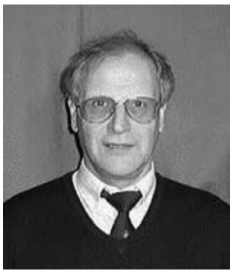

Pierre Guigon

Pierre Guigon is a Chemical Engineer from ENSIGC Toulouse (France 1971). Master of Engineering Science, UWO London Ontario, (Canada 1974), Docteur Ingénieur UTC Compiègne (France 1976), Docteur es Science UTC Compiègne (France 1978), Fellow of the Institution of Chemical Engineers. He is head of the Particle Technology Group at the Technical University of Compiègne. His research is in the field of particle suspensions (fluidization, pneumatic transport) and particle technology (communition and agglomeration).

Flowsheet Simulation of Solids Processes[†]

E.U. Hartge, M. Pogodda, C. Reimers, D. Schwier, G. Gruhn and J. Werther
Institute of Solids Process Engineering and Particle Technology Technical University Hamburg-Harburg[*]

Abstract

Flowsheeting program packages are now commonly used in chemical engineering for the design of processes involving fluids. The simulation of processes which involve solids or solids and fluids is not as advanced. In solids processing it is still common practice to design one apparatus separately from the other. There is a lack of suitable methods to combine single apparatus models to form a process and to treat this process as a whole. With the program package 'SolidSim', a simulation system especially designed for the simulation of processes including solids has been developed. At the present state of development, modules are available for classification, particle size reduction, crystallisation and dissolution, liquid-solid separation, gas-solid separation, agglomeration, reaction, drying, conveying and different general modules. The structure of the system is explained in detail and the application to a process for the treatment of contaminated sludge is shown.

Keywords: Solids process, Flowsheet simulation

1. Introduction

Today, flowsheeting program packages are commonly used in chemical engineering for the design of processes involving fluids (e.g. 1)). There are several established systems for the simulation of fluid processes. Among these are, for example, Aspen plus [2], Pro/II [3] or Chemcad [4].

The simulation of processes which involve solids is not as advanced, but it is common practice to design and optimise each apparatus separately from the others, neglecting its influence and dependence on the neighbouring processes. For simulation of the process, mathematical models for the individual units are used and the results are transferred manually from unit to unit. While this is feasible without significant loss of information for several units in series, it fails if there is a recycle loop which feeds back an outlet stream of one unit into another unit placed upstream. In that case, the simulation of the whole flowsheet has to be done iteratively, which is not or only in a very limited way possible by manual sequencing. In each case, simulating a process by this method is quite a time-consuming process.

Furthermore, the simulation unit by unit permits finding optimal operating conditions for each unit operation or apparatus. But such a sequential optimization of individual units will not necessarily lead to a global optimum for the whole process.

The reason for the gap between the simulation of fluid and of solids processes is basically the need for a more complex description of the solids. In addition to the parameters needed to characterise a fluid, for solids the dispersity has to be described, e.g. by the particle size. The description of the dispersity usually requires a distributed parameter, thus increasing the complexity of the information to be transferred between the different units of a flowsheet. A more detailed discussion of this problem will be given in the

---

[†] Accepted : August 14, 2006

[*] 021073 Hamburg-Harburg, Deniekesh, 15, Germany
[1] Corresponding author
TEL: +49-40-428783039, FAX: +49-40-428782678
Email: werkher@tuhh.de

following sections of the paper.

While most of the simulation systems for fluid processes also offer some basic support for the simulation of solids processes, they are mostly used exclusively for the simulation of fluid processes. On the other hand, there are some specialised flowsheet simulation systems for solids processes, e.g. USimPac[5], JKSimMet[6], PMP FBSim[7], SoProSim[8], AggFlow[9], Rockworks[10] and METSIM[11]. These packages are either limited to physical non-thermal and non-reactive processes or to quite narrow industrial sectors, e.g. ore or earth processing or metallurgy. Quite often the interaction between the solids and the surrounding fluid is neglected.

Against this background, the simulation program SolidSim was developed by a group of 11 institutes from 9 German universities. The aim of this development was a generally applicable flowsheet simulation system, providing all the structures necessary for the description of solids and the simulation of solids processes, including physical treatment, thermal treatment and also for reactions. The system should not be restricted to solids processes only, but it should also be possible to extend the system towards fluid processes. Further requirements were easy handling via a graphical user interface and the interoperability with other simulation systems. The latter was achieved by implementing a standardised interface as defined by the Cape Open Laboratory Network (CO-LaN,[12]). At the moment, the simulation package is for steady-state simulation only.

2. Simulation of Solids Processes

The most obvious difference to the simulation of fluid processes is the necessity of using distributed attributes to describe solids. The most important but not the only attribute is the particle size. The introduction of a distributed parameter, which usually has to be discretized, increases the number of variables by an order of magnitude or even more.

Since the fate of a particle in many processes depends on its particle size, some other parameters describing the particle may depend on the particle size. For example, when particles are dried in a dryer with a perfect plug flow of solids, the remaining humidity inside a particle will depend on the particle size, unless all particles are completely dried. Large particles will have a higher moisture content than the smaller ones. Thus, we need the moisture content as a particle-size dependent attribute. To extend the example of the dryer, we may now assume that there is no plug flow of the solids, but for the solids the dryer might behave like a stirred tank. In that case the particles of each particle size will underlie a residence-time distribution. The particles with a short residence time will have quite a high residual moisture, while particles of the same particle size which stay for a longer period in the dryer will have a lower moisture content. Thus, the moisture content in each individual class will be a distributed parameter. This distribution of the moisture content will again be size-dependent as the average moisture of the fines will be lower than that of the coarse particles. Similar secondary distributions will result if the particle undergoes a reaction.

While for the drying example, the secondary distribution might not be very important and could be replaced by average values, for the processing of ores, the content of metal in the ore as a secondary attribute could be crucial for the whole concentrating process.

Generally, in flowsheeting simulation programs different phases are distinguished. Here, the term phase is defined as ‘a stable or metastable collection of compounds with a homogeneous composition, which can be distinguished from other phases through the presence of physical interfaces that separate states of matter with different characteristics, such as density. Each phase has an associated state of aggregation, i.e. gaseous, liquid or solid’[13]. The requirement of a physical interface allows multiple liquid phases, e.g. oil and water, but only one gaseous phase. Also for solids, a physical interface can hardly be defined. Therefore all different types of solids belong to the same phase and the type of solid is only one more attribute in the attribute hierarchy. Looking onto the stream of solids entering an apparatus, this makes sense. For example, a gas cyclone does not distinguish between different types of solids as long they have the same size and density, or, to be more precise, the same terminal velocity. It would make no sense to feed the different types of solids one after the other to the cyclone model, since they interact and will influence each other. The cyclone model does not even require the information on the solids type; it needs only information about the terminal velocity. While the model of the cyclone will calculate the separation according to this primary attribute, there is also an implicit change of the other dependent attributes. If a compound A consists of heavier and larger particles than a second compound B, compound A will be enriched in the underflow of the cyclone, while compound B will be enriched in the fines carried out together with the gas. This implicit change of any dependent attribute has to be calculated by the system.

As for the example of the gas cyclone, it is a general problem when dealing with mixtures of solids that most models of apparatus or unit operations for solids are derived for one type of solids with a constant density only. For classification processes, the particle size is then usually used as the dispersity attribute to which separation rates are assigned. But examination of the physical mechanism of the classification process often yields that it is not the size that is the governing parameter, as in the case of the gas cyclone, but the terminal velocity. To allow simulation of the classification of mixtures of solids, the models therefore have to be rewritten such that the fractional separation efficiency is indeed a function of the governing parameter. Only if there is no interaction between the particles, a model can be taken as published and the different types of solids can be fed individually to the model and be mixed again at the outlet.

3. Structure of Solidsim

Generally, flowsheet simulation programs may be classified into two groups, block-oriented programs and equation-oriented programs. The former resemble the manual sequencing of individual models for the different units as described above, but with automation of the information transfer between the blocks. Loops are solved iteratively by calculating the units or blocks within the loop repeatedly. The equation-oriented systems put all the model equations for the different units of a flowsheet into one big equation system and solve the whole system with a suitable solver.

The block-oriented approach has the disadvantage that it cannot be used for dynamic simulations due to excessive computing times. On the other hand, the equation-oriented approach puts high demands on the solver. For fluid processes, the equation systems may already become very large with several tens of thousands of variables and equations. With the distributed attributes necessary for solids processes, the size of the equation system will increase even more, reaching the limits of computational resources available today. Even more important, the inclusion of population balances will change the nature of the equation system to a system of partial and ordinary integro-differential equations[14]. Up to now for very large systems of this type, no generally applicable solvers are available. This forced the decision to design SolidSim as a block-oriented system.

The program system is divided into four major parts:

- the simulation environment, which provides the basis of the whole system,
- the stream objects, which transport and manage the inserted stream information and
- the model library with the unit models,
- the property package, that provides the physical data and the phase equilibrium for the materials in the stream objects.

For the interconnection between these basic elements, the interfaces as defined by the CAPE-OPEN standard[13] are used as far as possible. The not yet completely publicly available version 1.1 of the standard was used. A sketch of the structure is shown in **Fig. 1**. The plugs and sockets denoted by Thermo^{SE} have been extended within the present work for the treatment of solids (SE = Solid Extension). The extension allows easy handling of distributed properties.

Additionally, in **Fig. 1**, the communication with other simulation packages is indicated. Using the CAPE-OPEN standard, a detailed flowsheet simulated with SolidSim may be used as one module in an external CAPE-OPEN-compliant simulation environment, using the standard interfaces for the communication. Another possibility for use of the functionality of other simulation packages in connection with SolidSim is to incorporate modules from other packages as unit models into the SolidSim environment. Very important is the possibility to use external property packages inside SolidSim, since the development of a detailed property package was not within the focus of the present work, and only a very basic property package is part of the SolidSim system. Tests with

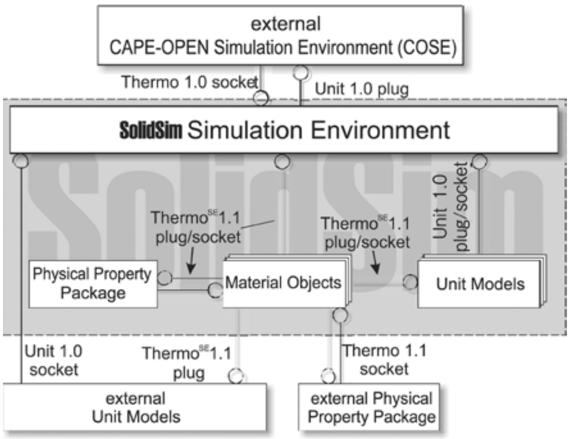

Fig. 1 Structure of the SolidSim program system.

the program package ASPEN+(12.1) of Aspentech have been carried out successfully. The connection with property packages via the Cape-Open interfaces has been tested with Aspen Properties[15)], Infochem's Multiflash[16)] and with Simulis Thermodynamics[17)]; all packages have been used successfully to provide the fluid data necessary for simulation.

The Material Stream Object

One major development task in the present work was the development of the stream objects, i.e. the structures to store the current status of a material stream connecting two subsequent models or units in the flowsheet. The stream objects have to provide the models with all properties of the incoming materials, i.e. fluids and solids. The schematic structure of the material stream object is depicted in **Fig. 2**. The material stream is described by overall properties such as temperature, pressure and total flow. The matter of the stream is divided into different phases each characterised by an ID and the state of aggregation. Required properties are the phase fraction (concentrated) and the composition (distributed). In addition, further phase properties can be defined as either concentrated or distributed. A typical distributed property is the particle size distribution, while e.g. the density will typically be a concentrated parameter. In some cases, however, the density might also be a distributed parameter, e.g. in the case of soil, which in detail consists of different materials, but which may be treated within the simulation system as one single compound. In general, the user has to decide for each attribute whether it is necessary to describe it by a distribution or if it is sufficient to use a single value as a concentrated parameter. The system is not restricted to a limited list of properties, but the user is allowed to introduce any new property to the system, as long as at least one unit model makes use of this property.

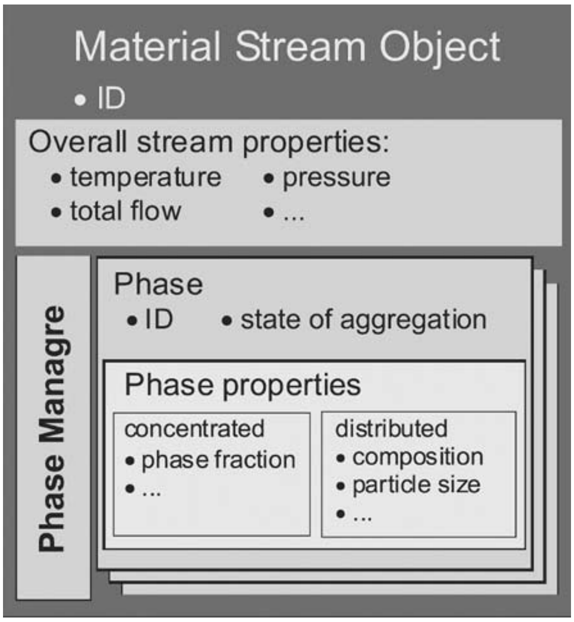

Fig. 2 Structure of the material stream object.

While for the implementation of the fluid part and for the storage of concentrated properties existing approaches could be used, the implementation of the solids part with the distributed properties had to be newly developed.

The design goal was a structure which allows the efficient storage of and access to complex hierarchies of nested and dependent distributed solids properties. In addition, the stream object should be able to provide the information to the unit models in an appropriate manner, i.e. it should only give the information needed by the module, hiding all additional complexity.

For the storage and access of a hierarchy of attributes a tree structure is often used. But this kind of structure requires rearrangement of the tree if the hierarchical dependencies change. Since during a simulation run, the hierarchical structure changes from unit to unit, this causes a significant computational overhead. Therefore, instead of the tree structure, the data in SolidSim is stored in an n-dimensional matrix, with n being the number of dependent attributes. As an example, a matrix for three distributed attributes (i, j, k) is shown in **Fig. 3**. In this matrix, each cell represents the mass fraction ΔQ_3 of the matter of a phase that can be described by the combination of the different property classes. The highlighted cell represents the mass fraction of all particles which can be described by the 2nd class of attribute i, the 5th class of attribute j and the 1st class of attribute k.

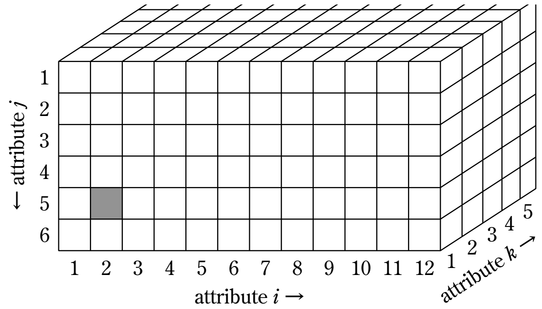

Fig. 3 Matrix-representation of distributed properties. As an example, the mass fraction $\Delta Q_3(2,5,1)$ is shown as a shaded square.

For the sum of all entries in the matrix, it holds that.

$$\sum \Delta Q_3(i, j, k)=1 \tag{1}$$

This structure allows access to all combinations of attributes in any arbitrary sequence without any resorting.

As a solution for the problem of attributes being implicitly changed between entrance and outlet of a unit as described above for the example of a gas cyclone, a movement matrix has been introduced. Instead of directly writing the changed attributes to the outlet streams, taking care of all dependent attributes, the unit model only has to fill a movement matrix, which includes only attributes which are explicitly changed. The dimension of the movement matrix is equal to two times the number of explicitly changed attributes. For the example of the cyclone, the explicitly changed attribute would be the terminal velocity only, thus the dimension of the morement matrix is equal to two. In cases where only one attribute is explicitly changed, the movement matrix is a square matrix (c.f. **Fig. 4**) quite similar to a breakage matrix known from comminution. It assigns the material in a certain class at the inlet to any of the defined classes at the outlet. For a classification, only the fields on the diagonal will be filled, all the other fields will be zero. The values $T_{i,j}$ with $i = j$ on the diagonal are the fractional separation efficiencies. For size reduction, the matrix will have non-zero values only in the lower left triangle ($T_{i,j}$ with $i \geq j$), for an agglomeration process, only the upper right half ($T_{i,j}$ with $i < j$) will be filled with non-zero values. Only the transformation matrix is computed by the model of a unit and then passed back to the material stream object. This will apply the transformation matrix to the whole attribute matrix, thus ensuring that all implicit changes of dependent attributes are correctly calculated.

		outlet					
		0	1	2	3	4	5
inlet	0	$T_{0,0}$	$T_{0,1}$	$T_{0,2}$	$T_{0,3}$	$T_{0,4}$	$T_{0,5}$
	1	$T_{1,0}$	$T_{1,1}$	$T_{1,2}$	$T_{1,3}$	$T_{1,4}$	$T_{1,5}$
	2	$T_{2,0}$	$T_{2,1}$	$T_{2,2}$	$T_{2,3}$	$T_{2,4}$	$T_{2,5}$
	3	$T_{3,0}$	$T_{3,1}$	$T_{3,2}$	$T_{3,3}$	$T_{3,4}$	$T_{3,5}$
	4	$T_{4,0}$	$T_{4,1}$	$T_{4,2}$	$T_{4,3}$	$T_{4,4}$	$T_{4,5}$
	5	$T_{5,0}$	$T_{5,1}$	$T_{5,2}$	$T_{5,3}$	$T_{5,4}$	$T_{5,5}$

Fig. 4 Structure of a movement matrix

Model Library

The model library is basically a collection of independent software modules containing one or several models for a certain apparatus or a unit operation. For each apparatus, models of different complexity and different requirements with respect to the input data are used. This allows the use of different models in different stages of the design process, e.g. in an early design phase quite simple models which need only a few data that are easy to measure or estimate, and more complex models with higher requirements with respect to the data to simulate or optimise an existing plant. Models from the open literature have been selected for implementation. The models have been chosen together with experts from industry, based on their experience with the models applied to industrial units. Most of the models had to be rewritten such that they depend on the parameters which really determine the physical process, e.g. as mentioned above, the models for gas cyclone and hydrocyclone have been rewritten to employ the terminal velocity as the independent parameter instead of the combination of particle size and density.

While in fluid processing the absolute geometry of an apparatus usually has only a minor effect on the result and is therefore neglected in most simulations systems, for many of the solids-processing units, the geometry directly affects the result of the process; for example the cut size of a gas cyclone is not only affected by the velocities and solids loading, but depends directly on the absolute diameter of the cyclone. Due to this influence, most of the modules require information about the geometry of the apparatus, in some modules even two calculation modes are implemented, one with a user-defined absolute geometry (simulation mode) and another in which the geometry is calculated by the module itself (design mode).

The software modules were implemented as COM objects, so that they can be added and removed during runtime. They communicate with the simulation environment via the Cape-Open Unit 1.0 plug/socket and with the connected streams via the extended Thermo^{SE} 1.1 plug and socket (**Figs. 1**, **5**). The Unit 1.0 interface is mainly used to control the program logic and execution sequence, the Thermo^{SE} 1.1 interface is used to query all information about the materials involved. In the case of solids processes,

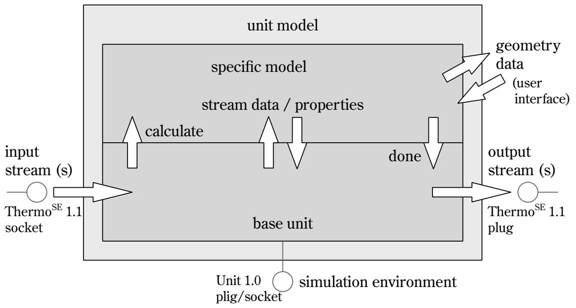

Fig. 5 Internal structure and interfaces of a unit model.

additional information, e.g. on the geometry of the apparatus is usually necessary; such information has to be queried from the user by the user interface provided by each module. Usually only parameters purely related to the apparatus should be queried this way. Since some models rely on parameters which are a combination of material properties and machine parameters, this rule cannot be followed strictly. In such cases, these combined parameters also have to be queried from the user.

In order to facilitate the development of unit models, a 'base unit class' has been implemented which forms the common basis of all the modules (**Fig. 5**). The task of this base unit is twofold. First it should hide all implementation details for the communication between the different software components from the engineering-oriented developer of the unit model.

The second task is to provide and ensure a minimal functionality, e.g. to copy input to output streams, to check mass balances, to provide methods for connecting streams to the ports of the apparatus, etc. In the simplest case, the model implementer should only have to implement specific calculation and initialisation routines and to provide some basic information about entrance and exit ports.

The model library is still far from being complete, but it already covers the most important areas of particle technology. It contains modules for classification and separation, size reduction and size enlargement, drying, particle generation by crystallization and also for a gas-solids reactor. **Table 1** gives a list of solids processing steps for which models have been developed together with the name of the responsible project partner. The implementation of further solids processing steps as independent modules is either planned or already in progress.

Another possibility to extend the model library is to create aggregate units. These aggregate units combine existing modules as a sub-flowsheet, which afterwards can be used as a new unit model. This approach allows, for example the creation of a module for a circulating fluidised bed simply by combining a fluidised-bed module with the cyclone module. Another example which has already been tested is the creation of a module of a classifier mill, which has been simulated by the combination of a crusher and a sifter.

Table 1 Solids processing modules in SolidSim

Processing step	Responsible partner
Separation, classification	Werther, Hamburg
Filtration of fluids	Ripperger, Kaiserslautern
Gas filtration	E. Schmidt, Wuppertal
Separation processes in centrifuges	Stahl & Nirschl, Karlsruhe
Agglomeration, granulation	Mörl, Magdeburg
Crushing in mills	Peukert, Erlangen
Convection drying	Tsotsas, Magdeburg
Crystallisation, dissolving	Kind, Karlsruhe
Gas-solid reactions in fluidised beds	Werther, Hamburg
Liquid spraying	Walzel, Dortmund
Dosing and conveying	Wirth, Erlangen

4. Application of Solidsim

The application of the developed system shall be demonstrated with two examples. The first one, a closed grinding circuit, is quite simple. It consists of only two units and needs as the only attributes the material and the particle size distribution to describe the solids. The second example is a process for the physical treatment of contaminated sludge. This example is much more complex, it consists of 9 major units plus several auxiliary units such as mixing points, splitters and pumps. Furthermore, a controller is involved.

Simulation of a Closed Grinding Cicuit

Size reduction is usually done in a closed circuit, i.e. a combination of a mill or crusher and classifier, which sends the coarse material back to the size reduction step. This combination of the size reduction unit and the classification unit might either consist of two independent units or alternatively one single unit.

Fig. 6 shows a screenshot of SolidSim with a flowsheet of a closed milling circuit. The feed is coal with a particle size distribution ranging from about 50μm to 10 mm as shown in the screenshot. The sieve has a mesh width of 0.8 mm, the mill used in this example

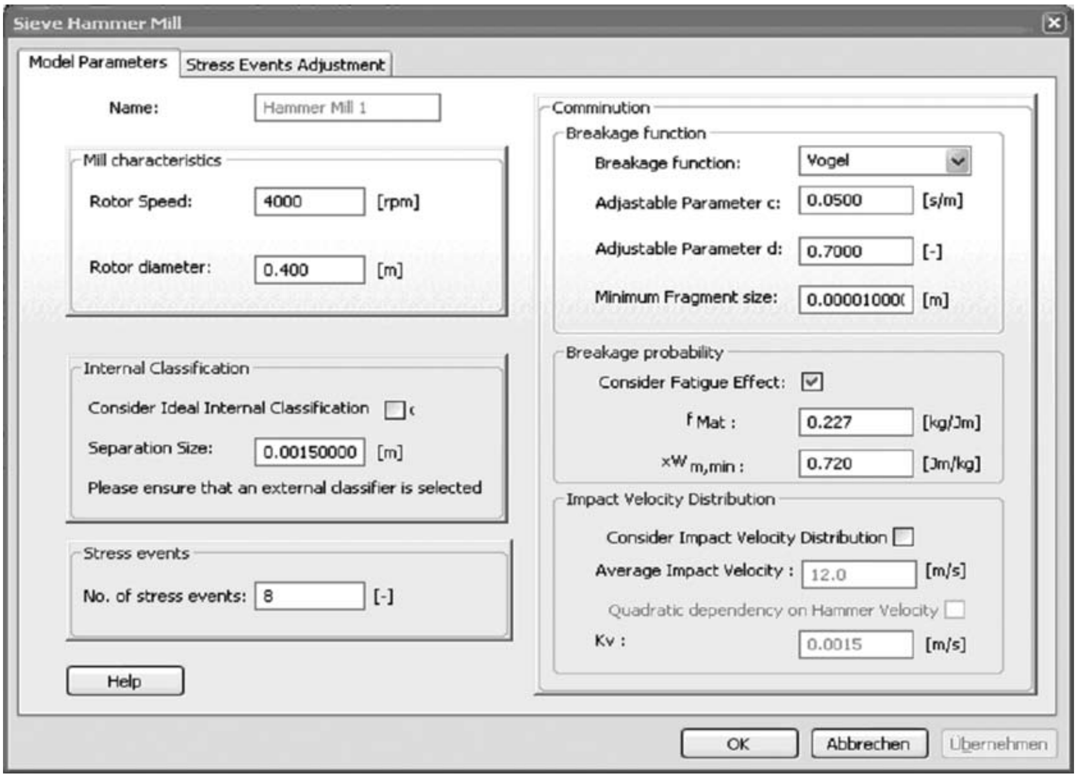

Name: Hammer Mill 1

Mill characteristics
Rotor Speed: 4000 [rpm]
Rotor diameter: 0.400 [m]

Internal Classification
Consider Ideal Internal Classification ☐
Separation Size: 0.00150000 [m]
Please ensure that an external classifier is selected

Stress events
No. of stress events: 8 [-]

Comminution
Breakage function
Breakage function: Vogel
Adjustable Parameter c: 0.0500 [s/m]
Adjustable Parameter d: 0.7000 [-]
Minimum Fragment size: 0.00001000([m]

Breakage probability
Consider Fatigue Effect: ☑
f_{Mat}: 0.227 [kg/Jm]
$xW_{m,min}$: 0.720 [Jm/kg]

Impact Velocity Distribution
Consider Impact Velocity Distribution ☐
Average Impact Velocity: 12.0 [m/s]
Quadratic dependency on Hammer Velocity ☐
Kv: 0.0015 [m/s]

Fig. 6 Parameterization of the module "hammer mill"

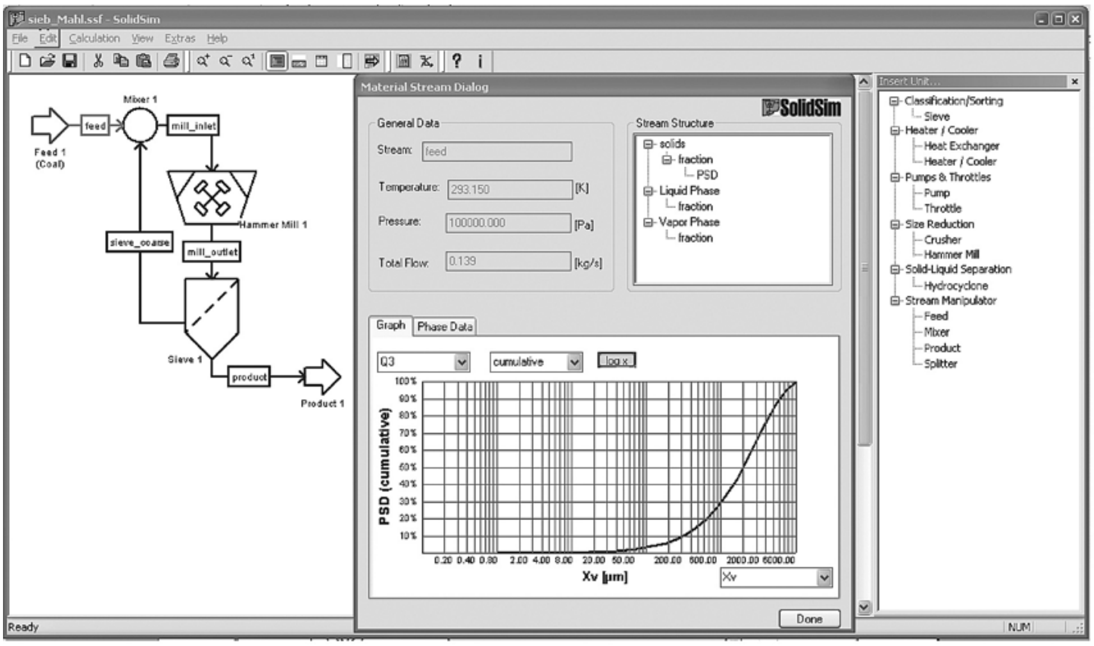

General Data
Stream: feed
Temperature: 293.150 [K]
Pressure: 100000.000 [Pa]
Total Flow: 0.139 [kg/s]

Stream Structure
- solids
  - fraction
    - PSD
- Liquid Phase
  - fraction
- Vapor Phase
  - fraction

Fig. 7 Screen shot of SolidSim with a closed milling circuit.

is a hammer mill. The model used for the simulation of the hammer mill is based on the work by Vogel and Peukert[18), 19)], the description of the classification with the sieve is based on a classification function by[20)]. A detailed description of the models can be found in[21)]. The parameterization dialog of the mill can be seen in **Fig. 7**.

It takes about 30s to iteratively solve this problem. The results of the simulation are as shown in **Figs. 8** and **9**. In **Fig. 8**, the particle size distribution of the product is plotted, whereas **Fig. 9** gives an overview on the different streams in the flowsheet. In this case the total mass flow, the mass flow of solids (which is equal to the total mass flow since no fluid has been defined) and the medium particle size x_{50} (last column) for all the streams are shown. The simulation yields that the recycle stream has a mass flow nearly twice the size of the feed mass flow.

Using the SolidSim system for this simulation allows the configuration of the circuit to be easily changed. While in the first version of the circuit, the feed enters the mill first, for the second version as shown in **Fig. 10**, the feed flow enters the sieve first, thus removing the fines before entering the mill. The calculated results are shown at the bottom of **Fig. 10**. The simulations show that in this case, the flow through the mill is slightly reduced, while the throughput through the sieve is increased. In addition, the PSD of the product is changed minimally; the product has a slightly higher medium size x_{50}.

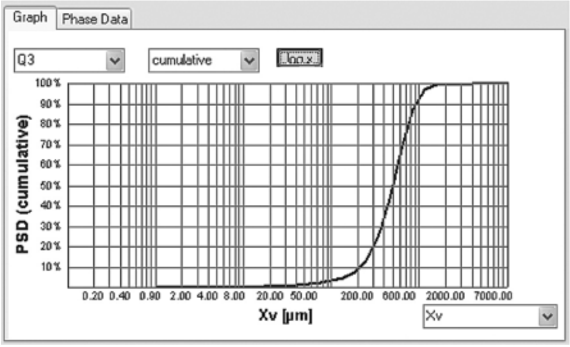

Fig. 8 Result of the simulation of the flowsheet according to **Fig. 6**, particle size distribution of the product.

Name	Total flow	Phase flow	avg. distr. Props (solid phase)
		solids (S)	*PSD*
	kg/s	kg/s	m
feed	0.13889	0.13889	0.001986
mill_inlet	0.36089	0.36089	0.001183
mill_outlet	0.36089	0.36089	0.0007829
sieve_coarse	0.222	0.222	0.001041
product	0.13889	0.13889	0.0005092

Fig. 9 Result of the simulation of the flowsheet according to **Fig. 6**, screenshot of the stream overview.

Simulation of a Soil Washing Process

As a second, more complex example, SolidSim has been applied to a special soil washing process, namely the physical treatment of contaminated harbour sludge. The process has been developed by the authors' group which has been in operation in Hamburg [22, 23] for several years. This process takes advantage of the fact that the extent of contamination

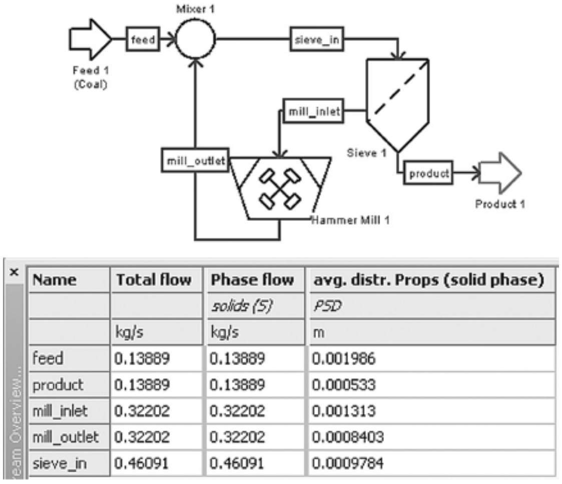

Name	Total flow	Phase flow	avg. distr. Props (solid phase)
		solids (S)	*PSD*
	kg/s	kg/s	m
feed	0.13889	0.13889	0.001986
product	0.13889	0.13889	0.000533
mill_inlet	0.32202	0.32202	0.001313
mill_outlet	0.32202	0.32202	0.0008403
sieve_in	0.46091	0.46091	0.0009784

Fig. 10 Modified circuit with screenshot of the stream overview.

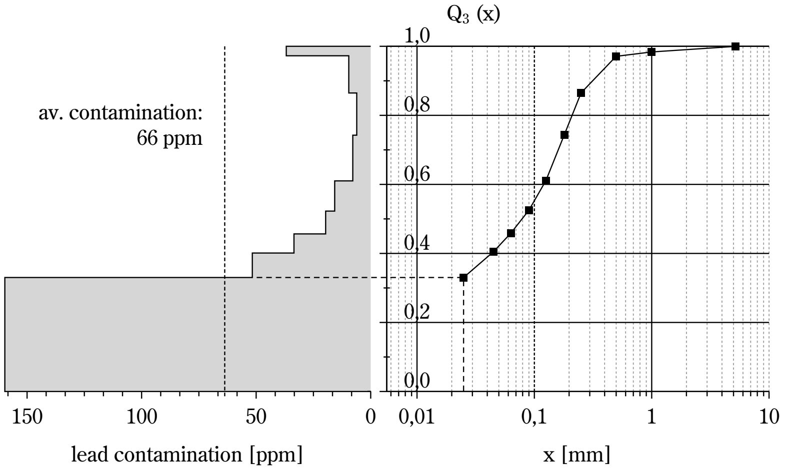

Fig. 11 Size-dependent contamination of dredged sludge (harbour of Hamburg) with lead. On the right side, the cumulative mass distribution of the particle size is plotted.

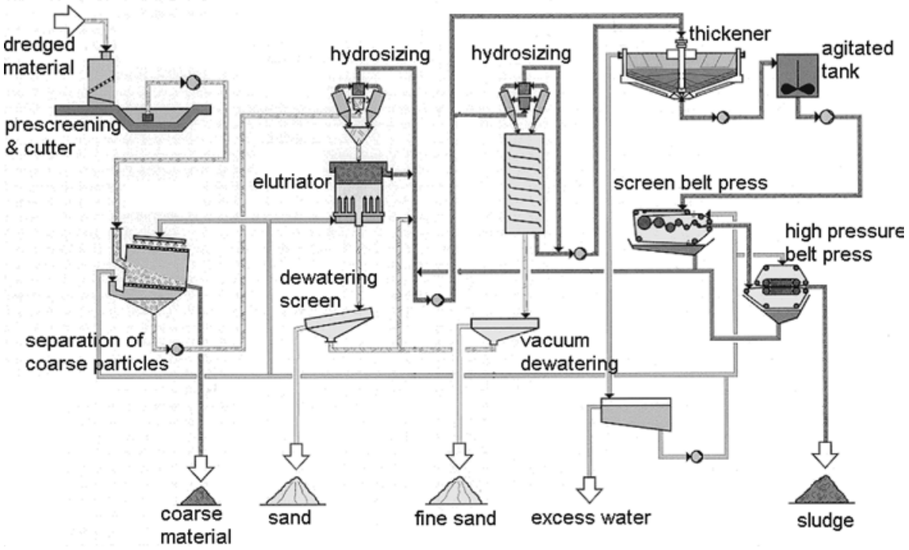

Fig. 12 Flowsheet for the mechanical dewatering and separation of harbour sediments.

depends on the particle size. This is illustrated in **Fig. 11**. In the right-hand part of the graph, the cumulative mass distribution of the particle size is plotted. On the left side, the contamination of the different particle size classes is shown. It can be seen that the fraction of particles with a size below 25μm making up about 35% of the mass has a lead concentration of about 160 ppm. The area of the bars in the left part of the diagram is proportional to the mass fraction of contaminants of the respective class in the total contamination. Thus, removing the fine particles with $d_p < 25\mu$m will remove only about 35% of the mass but more than 80% of the contamination, resulting in a highly contaminated fraction of fines and a coarse fraction with a low concentration of lead.

The technical process for this classification and dewatering as it is employed in Hamburg is shown in **Fig. 12**. It consists of several sieves, hydrocyclones, an elutriator, screen belt presses and some other units. The models used for the simulation of the different units may be found in reference 21). With the fairly large number of units and several recycles of the process water with fines, this process is certainly too complex for manual simulation. Furthermore, it demonstrates the use of a dependent attribute which is in this case the particle-size-dependent contamination. Simulation with SolidSim allows prediction of the influence of changes of operating conditions or the influence of a change of a single unit on performance of the whole process.

It also allows finding suitable operating parameters to keep the sand fractions below given contamination limits when the dredged sludge changes or even to improve the process by performing several simulation runs with variations of the operating parameters or of the flowsheet itself. Up to now, no mathematical optimization feature is implemented, but the structure of the program allows for a respective extension of the system in the future.

Fig. 13 shows a screenshot of SolidSim with the flowsheet of the process. The process has been simulated with a mass flow at the entrance of 9 kg/s fluid and 1 kg/s solids. **Fig. 14** shows as results of the simulation the particle size distribution and the distribution of the lead contamination for both the sand fraction and the sludge.

The results show that 52% of the solids fed to the process remain in a highly contaminated “sludge” product, while the remaining 48% are collected in the less contaminated products “coarse material”, “sand”, and “fine sand”. These latter materials may be reused for road building or other purposes, whereas the sludge has to be dumped in a landfill for hazardous waste. The separation process reduces the required disposal volume by roughly 50%.

5. Conclusions

The complex description of solids with their distributed and dependent attributes puts special demands on systems for flowsheet simulation. With the package SolidSim, a system has been developed that meets these requirements. It is the result of the joint effort of specialists from university and indus-

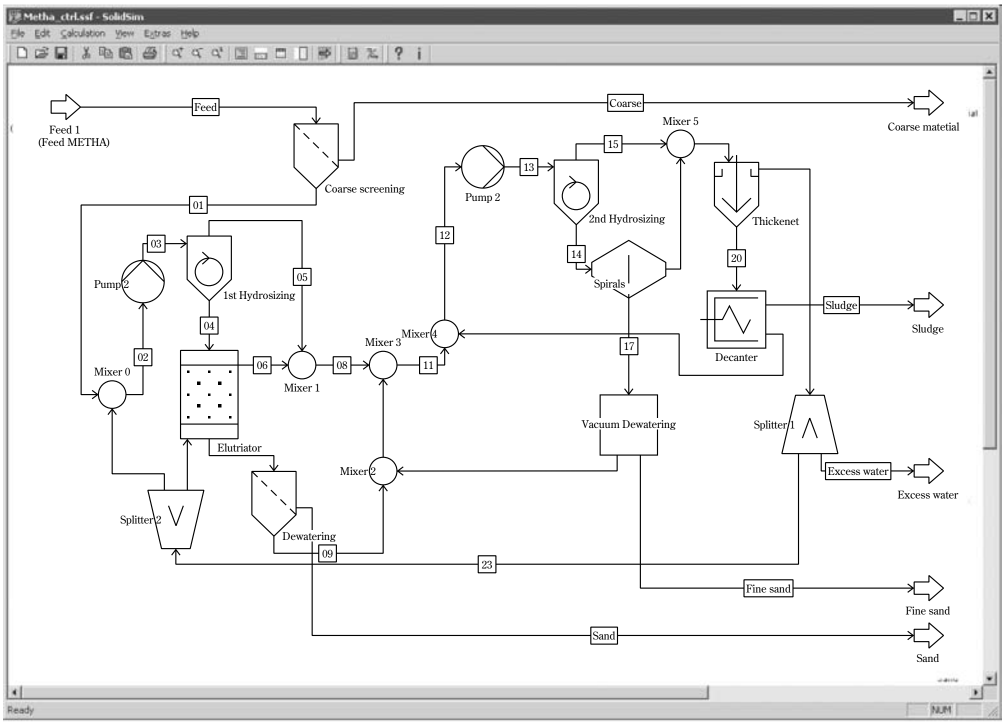

Fig. 13 SolidSim flowsheet for the mechanical dewatering and separation of harbour sediments.

try. First applications with complex solids processes show its ability to support the engineer in designing and improving solids processes. At the moment, the system is not yet in a marketable state. It needs some improvement in stability and also a further extension of the model library. This further development of the system is in progress with the financial support of an industrial consortium [24].

Acknowledgements

Financial support of this work by the Association of Industrial Research Institutions (Arbeitsgemeinschaft industrieller Forschungsvereinigungen – AiF) under grant no. 94 ZBG/1-12 and by the industrial consortium IK SolidSim is gratefully acknowledged.

Bibliography

1) Seider, W. D., J. D. Seader, and D. R. Lewin, : Process design principles: synthesis, analysis and evaluation: John Wiley & Sons, 1999.
2) Aspentech: Aspen Plus, http://www.aspentech.com/includes/product.cfm?IndustryID=0&ProductID=69, 2006.
3) simsci-esscor: Pro II, http://www.simsci-esscor.com/us/eng/products/productlist/proII/default.htm, 2006.
4) Chemcad: Chemcad, http://www.chemstations.net/, 2006.
5) USIM PAC, http://www.svedala-cisa.com/usimpac/upac.htm, 2006.
6) JKSimMet, http://www.jksimmet.com/, 2006.
7) Grainsoft: PMP Sim, http://www.grainsoft.com/index.htm, 2006.
8) Wilichowski, M., T. Pawletta, : SoProSim - A Tool for the flowsheet-orientated Simulation of Classification Processes, in: Pratsinis, S. E., Schulz, H., Strobel, R. & Schreglmann, C. (Eds.), Proceedings of International Congress for Particle Technology PARTEC 2004. Nuremberg: 2004, Proceedings on CD.
9) Bedrock Software: AGGflow, http://www.aggflow.com/, 2006.
10) Rockware Inc.: Rockworks, http://www.rockware.com/catalog/pages/rockworks2004.html, 2006.
11) metsim: MetSim, http://www.metsim.com/, 2006.
12) CO-LaN: CO-Lan, www.co-lan.org, 2006.
13) CO-LaN consortium: Thermodynamic and Physical Properties v1.1, http://www.colan.org/Spec%2011/CO%20Thermo%201.1%20Specification.pdf, 2005.
14) Moltz, S.: Reduktion populationsdynamischer Modelle, Dusseldorf: VDI-Verlag, 2004.
15) Aspentech: Aspen Properties, http://www.aspentech.com/includes/product.cfm?IndustryID=0&ProductID=77, 2006.
16) Infochem: Infochem Multiflash, http://www.infochemuk.com/product/products.htm, 2006.
17) ProSim: Simulis Thermodynamics, http://www.prosim.net/prod_simulist.html, 2006.
18) Vogel, L. and W. Peukert, : Modelling of grinding in

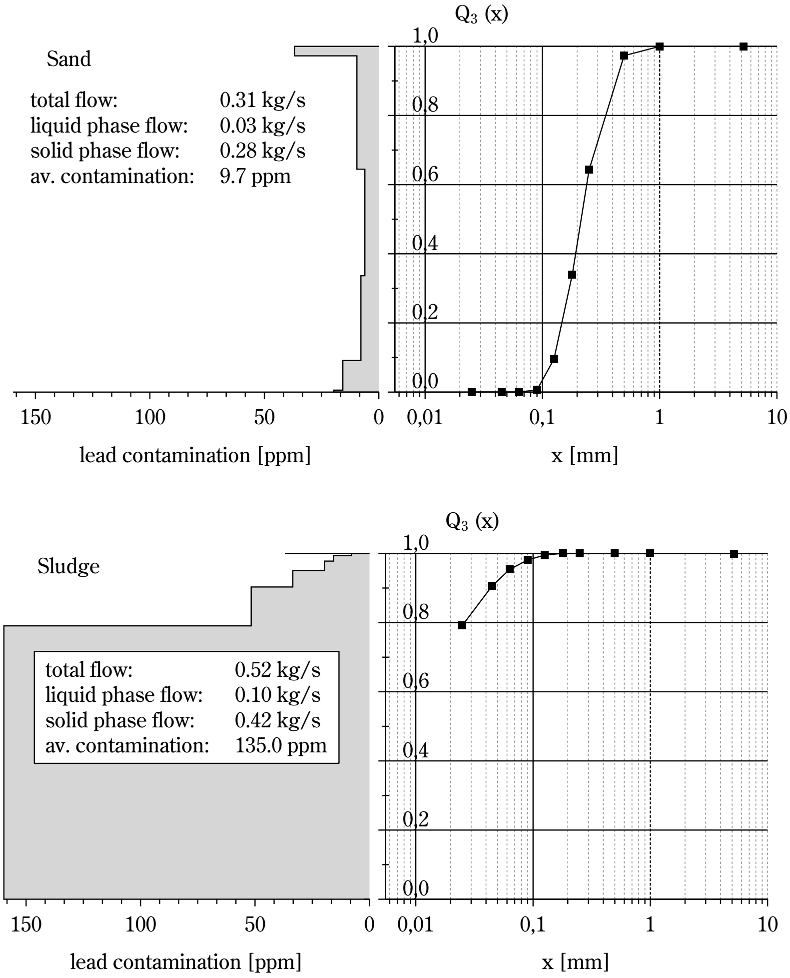

Fig. 14 Simulation results: particle size distributions and distribution of contamination in the two products "sand" and "sludge".

an air classifier mill based on a fundamental material function, KONA Powder and Particle, 21, 2003, 109-120.

19) Vogel, L. and W. Peukert, : Breakage behaviour of different materials - construction of a mastercurve for the breakage probability, Powder Technology, 129, 2003,

20) Rogers, R. S. C.: A Classification Function for Vibrating Screens, Powder Technology, 31, 1982, 135-137.

21) Werther, J., G. Gruhn, M. Kind, L. Morl, W. Peukert, S. Ripperger, E. Schmidt, H. Nirschl, E. Tsotsas, P. Walzel, and K.-E. Wirth, Fliesschema-Simulation von Feststoffprozessen - Schlussbericht, http://www.solidsim.de/Abschlussbericht/SolidSimAbschlussbericht.pdf, 2005.

22) Detzner, H. D., L. Kitschen, and W. Weimerskirch, Erste Grossanlage zur Aufbereitung von Hafensedimenten, Aufbereitungstechnik, 34, 1994, 4-6.

23) Werther, J., R. Hilligardt, U. Kalck, and J. Weber, : Investigation on the mechanical treatment of dredged material, in: Wolf, K., van den Brink, W. J. & Colon, F. J. (Eds.), Contaminated Soil '88. Kluwer Academic Publishers, Dordrecht, 1988, 1285-1294.

24) SolidSim, www.Solidsim.de, 2006.

Author’s short biography

Ernst-Ulrich Hartge

Dr.-Ing. Ernst-Ulrich Hartge is Senior Scientist at the Institute for Solids Process Engineering and Particle Technology of the Hamburg University of Technology. His research interests are in the field of fluidization technology and its application to combustion and chemical processes. Another major field of his work is the development of a system for the flowsheet simulation of complex solids processes.

Matthias Pogodda

Dipl.-Ing. Matthias Pogodda is currently a research fellow in the Institute of Solids Process Engineering and Particle Technology of the Hamburg University of Technology. The main focus of his work is the development of the flow sheet simulation system ‚SolidSim’, which is especially designed for the simulation of complex solids processes. He is also conducting research in the field of data reconciliation and instrumentation network design of solids processes.

Claus Reimers

Claus Reimers is currently a research fellow in the Institute of Solids Process Engineering and Particle Technology at Hamburg University of Technology, working on the development of a flow-sheeting system for complex solids processes, called SolidSim. His research is focused on the optimization of solids processes.

Daniel Schwier

Daniel Schwier is currently a research fellow at the Institute of Solids Process Engineering and Particle Technology at the Hamburg University of Technology. His research topic is the treatment of inaccuracies of parameters and models in the flowsheet simulation of solids processes.

Günter Gruhn

Professor Günter Gruhn was (till 2003) the head of the Department of Process and Plant Engineering at the Hamburg University of Technology. His research interests were mainly directed towards flowsheeting and optimisation of complex process systems, design and operation (scheduling) of multi product plants for manufacturing fine chemicals and optimal production control of petrochemical plants.

Joachim Werther

Professor Joachim Werther is the head of the Institute of Solids Process Engineering and Particle technology at the Hamburg University of Technology. His research interests are mainly directed towards fluidization technology and its application for industrial processes, towards classification of particles and towards the physical treatment of contaminated solids. A further major field of research is the development of advanced simulation tools for the flowsheet simulation of processes involving solids.

Drug Delivery System Using Biodegradable Nanoparticles Carrier[†]

Do Hun Lee and Ik Joong Kang[1]
Department of Chemical & Bio Engineering,
*Kyungwon University**

Abstract

Recently, many biochemists have identified that chitosan is not rejected by the body and that it can improve the effective and safe delivery of drugs and vaccines with its absorptive power. Also, it has been known that chitosan is suitable for controlled drug release thanks to its advantages of biodegradability and bio-compatibility. As the interest into the extension of human life and personal health has been increased, the pharmaceutical and medical worlds have been making efforts to develop more sustained and effective drug release property in a body. This study investigated the individual drug characteristics and drug release behavior by manufacturing the chitosan patch using insulin, a drug used for treating diabetes, at a low temperature, and further tried to find the optimal condition by adding the skin activating agent to the chitosan patch using NOD (Non Obese Diabetic) mice. According to the analysis using the chitosan-insulin drug and the skin-activating agent, a dramatic decrease in the blood glucose level was achieved. An experiment was performed in vivo by utilizing chitosan nanoparticles as a biopolymer to control the drug delivery rate at an optimal concentration, pH and temperature. It was also observed that the experiment of the drug delivery by nanoparticles containing insulin could effectively lower the blood glucose of the mouse.

Keywords: Drug delivery system, Nanoparticles, Chitosan, Biopolymer

1. Introduction

As one of the most important and essential researches to develop convenient and effective drugs in the medical industry, more focus has been paid on the non-injection or parenteral drug. The study on drug release in the medical industry can be said to be one the most effective ways to stand up against side effects including: a) angioma due to an intramuscular and intravenous injection, b) allergies and mental stresses that are originated from other kinds of immune disorders on the skin, c) drug dissolution induced from the oral administration. The meaning of the drug release study is linked directly with the dignity of human beings in terms of reducing the pain of drug delivery. This study is valuable as a noble delivery method of the drug. This study has been increasingly applied to various fields including the inhibitor of partial nerves for local anesthesia, medical supplies for kids, and substitutes for the existing drug. Unlike the existing direct medication sought only after the treatments, a recent trend of drug manufacturing is toward longer lasting effects with less pain and less quantity. This field has been considered as one of the most prospective fields of the medical industry, and thus has been enormously invested in to develop the complex drug delivery system that releases multi-functional, compound and compact drugs. As the effect of a medicine appears in proportion to the drug concentration in the blood, it is necessary to control the curve of the blood concentration with

---

[†] Accepted : August 14, 2006
* Sungnam 461-701, KOREA
[1] Corresponding author
TEL :+82-31-750-5357 FAX :+82-31-750-5363
E-mail: ijkang@kyungwon.ac.kr

various pharmaceutical technologies. Hence, it is essential that the behavior of the drug in a body should be controlled by various technologies to perform the stable and effective medication on the selective area [1-3]. Throughout the world, the United States and Japan have set spurs to the development of the drug delivery system over the last 20 years thanks to their bio-technologies and genetic technologies. Considering the rapid growth in the patents application of the drug forms, the Korean pharmaceutical industry is also displaying interest in the development of new drugs through the new types of drug forms. Presently, several success stories have been announced and they have already started manufacturing and marketing the treatments of arthritis using the new technologies. An ideal drug delivery system can be achieved by materials that have no chemical changes and that satisfy the conditions of biodegradability and bio-compatibility of the nanoparticles carrier, the biodegradable speed of the carrier and the delivery speed of the drug [4, 5]. Another reason that the drug delivery system has come into the spotlight is because of shorter development periods and lower costs compared to the development of a new drug [6-8]. As the effect of a general medicine appears in proportion to the drug concentration in the blood, it is necessary to control the curve of the blood concentration with various pharmaceutical technologies. Especially, it is essential to maximize the drug delivery on the target areas using special technologies rather than controlling the drug concentration in the blood, in which an anti-cancer medicine and a genetic material are expected to generate severe side effects when delivered to the normal tissue. Therefore, it is also necessary to control the drug behavior in a body in order to effectively perform a stable treatment on the desired areas [9, 10]. This kind of drug form, which is designed for optimal treatments, is called the Drug Delivery System (DDS). The development of the drug forms originated because the necessities of new types of drug forms are on the rise based on the biotechnology, which is considered to be a breakthrough when development of materials with new chemical structures are at the height of their prosperity [11, 12]. Drugs are administered through injection, mouth, transdermal, and a mucous membrane, but the drug delivery system is invented to improve the way of drug administration. The drug delivery system raised a question in the existing pharmaceutical medication methodology (the drug forms and application methods), and moves toward the goal of optimization of drug therapy by handling the medical supplies as "the science of medication methodology", not only as "materials". In other words, it is designed so that the desired amount of drug can reach the desired area with the desired concentration. For example, when an antiphlogistic agent is administrated through the mouth for the treatment of arthritis, the drug will work upon the joint but will give rise to side effects on the other areas. Against this backdrop, the drug delivery system intends to design the drug forms to reduce this side effect and to maximize the remedial result [13-16]. Drugs are processed in the form that can display the most convenient and efficient medical action, and then are administered in a body through various ways. The administered drug is released from its form, and is absorbed into blood, which is then delivered to each organ through the bloodstream and finally is eliminated through metabolism and urination. All drugs will work upon the desired area (receptor) in a body while they will give rise to side effects on the other areas [17-22].

When the characteristic length of a high molecular substance is controlled in the size of a nanometer, several functions are displayed, which cannot be seen in the ordinary material. The material designed to have a stable structure in the size of a nanometer can lead the newly-advanced materials in the field of life science and environmental industry on its own or as a composite material mixed with other materials, as well as replacing the existing high-functional materials. As nanoparticles containing insulin are available in wide application using the chitosan that attracts public attention as the last biomass, they can be widely applied to the industry as well as to academic research [23-27]. Chitosan or poly (D-glucosamine) is the polymer consisting of chitin that is partially deacetylated. Chitosan can be easily made from chitin, a natural polymer, which is derived from the cuticles of insect species or Crustaceans such as crabs and shrimp. Chitin exists in nature with the largest amount but cellulose. Chitosan has various useful characteristics including high chemical resistance, big thermal stability, affinity with dyes and metal ions, and bio-compatibility. Over the last 20 years, these kinds of characteristics have been widely applied to chemical engineering, biomedicine, waste water treatment, the collection and recycling of metal, functional membranes, and the controlling of metal ions in a body [28-33]. As chitosan dissolves in an acidic solution, has reactive amino suitable for chemical changes, and is harmless to people, the functional polymer made from chitosan can be an excellent ion exchange resin or an absorbent. Hence, it can be widely applied to medical supplies, as a remover of agrichemicals and heavy metals, waste water treatments, etc. [34, 35]. As chitosan nanoparticles manufactured in the present study have a low production cost, bio-compatibility and low toxicity, research on this subject has been widely conducted [36-38].

The present study investigated the release characteristics *in vitro* and *in vivo* after manufacturing penicillin and insulin using chitosan at a low temperature. Each process is optimized with its temperature, pH, time, etc. for making the optimal drugs. Then, their release characteristics in accordance with the drug concentration are investigated. The drug is processed in the form that can be easily applied and that can display its optimal medical action. Then, it is administered in a body through various routes. The administered drug is released from its form, and is absorbed into blood, which is then delivered to each organ through the bloodstream and finally is eliminated through metabolism and urination. All the drugs will work upon the desired area (receptor) in a body while they will give rise to side effects on the other areas [19]. The present study investigated its release effect in a body using insulin that contains chitosan. In addition, it also investigated its release characteristics *in vitro* and *in vivo* after manufacturing insulin using chitosan, a biodegradable polymer, at a low temperature. Each process is optimized with its temperature, pH, time, etc. for making the optimal drugs. Then, their release characteristics in accordance with the drug concentration are investigated. People who have diabetes suffer from pain and financial loss, for insulin is administered through an injection. However, this pain can be relieved when the drug is administered through a mucous membrane in the nose using the chitosan nanoparticles. This study confirmed that drug delivery system using the biodegradable nanoparticles carrier are effective in drug release and can lower the blood glucose level..

2. Experimental

2.1 Reagent and Device

NOD (Non Obese Diabetic) mice in their 3rd, 5th and 7th weeks were bought from Korea Taconic Co., Ltd. for the experiment (**Fig. 1**). Norvolin-R was bought from Korea Green Cross Corporation, while glycerol, chitosan and acetic acid were bought from Sigma-Aldrich that won recognition for its degree of purity. Chitosan was gained from chitin after being deacetylated (95% of deacetylation), which was bought from Aldrich. Its molecular weight for the experiment was about 30,000-50,000 and 100,000-120,000.

2.2 *In vitro* and *In vivo* Experiments using the Chitosan Patch

2.0g of chitosan, 30mℓ of distilled water and 1mℓ of acetic acid are put into the 50mℓ sterilized vial and they are stirred regularly. Then, it is stabilized at 40 ℃ for three days. Next, it is blended with penicillin-G and insulin, respectively for their suitable concentration and stabilized at 4℃ for a week. For the in vitro experiment using the chitosan patch, the stabilized chitosan drug is put into a container of stainless steel with 13㎠ of surface area and a size of 5㎤. Then, its surface is fixed with a sterile dressing of the same size. The fixed drug is neutralized in the solution that is set at pH 8 using NaOH, and then is soaked in the distilled water until just before the experiment. After that, it is put into 1l of phosphate buffer solution ($KHCO_3$: 9g/l, K_2HPO_4: 1.4g/l, KH_2PO_4: 1.1g, pH 7.4) and then is kept at 37℃ by the constant temperature system. If the buffer solution reaches over pH 7.4 during the experiment, set it at 7.4 with the HCI 0.1M. Next, the chitosan drug is put into this buffer solution, and the supernatant should be stirred at the speed of 100rpm. The reagent is sampled three times at the interval of 1, 2, 4, 8, 12 and 24 hours. The values are averaged and their concentration is measured at 290_ which is the inflection point of 290_ with U.V

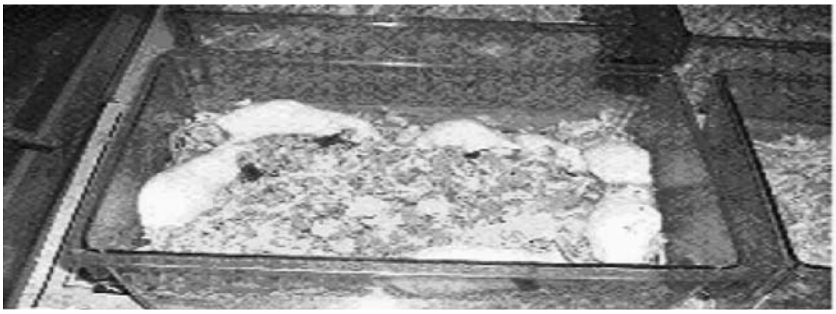

Fig. 1 NOD mice for in vivo experiment.

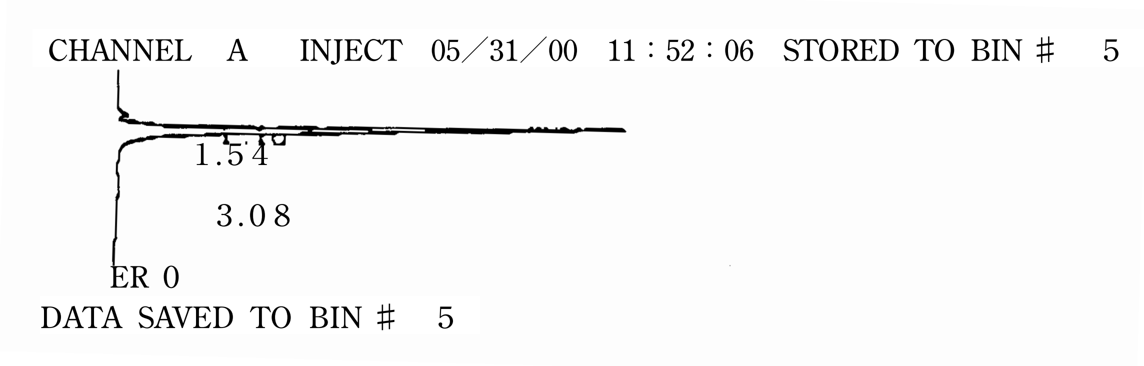

```
CHANNEL  A   INJECT  05/31/00  11:52:06  STORED TO BIN #   5
      1.54
        3.08
ER 0
DATA SAVED TO BIN #   5
```

Fig. 2 Insulin Isolation for in vitro Drug Release System.

(HP-8435).

For the *in vivo* experiment using the chitosan patch, its effect is analyzed after adding the skin activating agent. First of all, put each chitosan with different molecular weight (M, W: 50,000, 120,000; hereinafter called C1 and C2) into the sterilized vial together with distilled water and acetic acid. Then, it is stabilized at 40℃ for three days. When the skin activating agent (glycerol, DMSO, DMF) is added, the same amount of distilled water is reduced for making the initial chitosan solution, while the rest of the process remains the same. Each insulin concentration of 10 IU and 20 IU is blended with the prearranged chitosan solution. Then, exactly 1mℓ of manufactured drug is put into the container (2.5㎝ in diameter, 0.25 ㎝ in height) using a syringe, which is soaked in 0.1 M of NaOH solution for 10 seconds. Then, it is put into the small amount of distilled water of 4 ℃ and is kept refrigerated. Drugs are apt to decompose, so prepare it within one hour prior to the experiment. The arranged drug is wrapped hard around the abdominal region of the mouse with sanitary tape, so that it is well fixed to observe the difference of the drug release. The blood glucose level is analyzed using SURE STEP Plus (see **Fig. 2**), which is a blood glucose test meter manufactured by LifeScan, Inc., USA. The test strips for the experiment are code 9, also from LifeScan, Inc. The insulin concentration is analyzed using the HPLC system of Waters Corporation. Particle size and zeta potential are analyzed using Zeta-plus from Brookheaven Instruments Corporation, while the formation of nanoparticles are confirmed using AFM from PSIA Corp. (see **Fig. 3**). The insulin concentration is measured using C-18 as a separate column and is analyzed using HPLC (HP-5420) from Waters Corporation, USA (see **Fig. 4**).

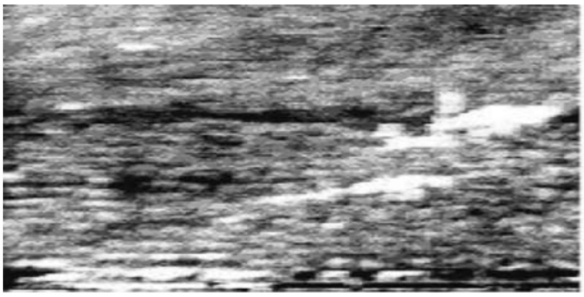

Fig. 3 AFM Pictures of the Nanoparticles.

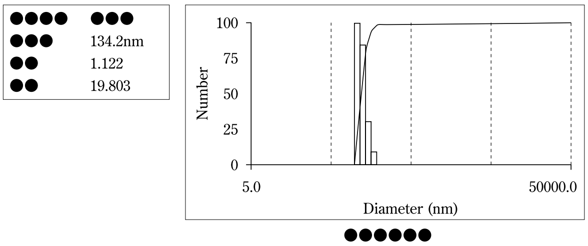

σ (nm)	G (d)	C (d)	σ (nm)	G (d)	C (d)	σ (nm)	G (d)	C (d)
55.3	0	0	338.1	0	99	1970.6	0	100
65.0	0	0	388.3	0	99	2318.1	0	100
76.5	0	0	458.8	0	99	2726.8	0	100
90.0	0	0	537.4	0	99	3207.8	0	100
105.9	100	44	632.1	0	99	3773.6	0	100
124.6	84	52	743.6	0	99	4439.1	0	100
146.5	50	55	874.8	0	99	5222.0	0	100
172.4	0	55	1029.0	0	99	6142.0	0	100
202.8	0	55	1210.5	2	100	7226.3	0	100
238.5	0	99	1424.0	0	100	8600.8	0	100
280.8	0	99	1675.1	0	100	10000.0	0	100

Fig. 4 Nanoparticle Size Analysis using Zeta-potential Analyzer.

2.3 Manufacturing the Chitosan Nanoparticles Containing Insulin

For the *in vivo* experiment using the chitosan nanoparticles, these nanoparticles are manufactured by putting regular sized chitosan into the sterilized vial together with other materials including insulin, distilled water and acetic acid, which is then blended and is kept refrigerated for three days for stabilization. Then, it is completely dissolved in the Tripolyphosphate solution and is stabilized at room temperature. Next, it is reacted by adding glycerin for about 10 minutes, and its pH is measured. After that, it is centrifuged for 15 minutes. The centrifuged solution is frittered with a micro pipette. Then, the nanoparticles are confirmed with the Particle size analyzer, Zeta potential and Atomic Force Microscopy (AFM). After measuring the blood glucose level once from the arranged blood of a mouse, nano-chitosan solution is administered to the mucous membrane of a NOD mouse using a micro pipette. The number of administration varies: once, five times and seven times. For a chitosan solution containing 100 μℓ /ml of insulin, 0.3g (1%) of chitosan is put into the sterilized vial, which is evenly soaked with 1.2mℓ of insulin using a micro pipette and then is kept refrigerated for over four hours. Next, it is blended with 28.35mℓ of distilled water and then is combined with 0.15mℓ of acetic acid, which is completely dissolved using the glass rod and Voltex Mixer before being kept refrigerated. 0.09g of Tripolyphosphate (hereinafter called TPP) solution is completely dissolved in 29.91mℓ of distilled water and is kept refrigerated. With these two solutions, first put 25mℓ of chitosan solution into a new vial (50mℓ) and 10mℓ of TPP solution is added using the micro pipette, which are completely blended for five minutes. Five minutes later, 100 μℓ of glycerin is added and stirred for 10 minutes, which is put into two micro tubes (1.7mℓ) up to 0.9mℓ respectively. This tube is centrifuged with a centrifugal separator set at 15,000rpm for 15 minutes. Then, the supernatant is separated from the centrifuged solution and is analyzed with the HPLC system. The analyses are performed twelve times at the beginning and then after 1 hour, 2 hours, 4 hours, 8 hours, 12 hours, 1day, 2 days, 3 days, 4 days, 5 days, 6 days, and 7 days. The reagents containing chitosan nanoparticles are composed of the insulin concentration (μℓ /mℓ) of 100, 75, 50 and 30 respectively, and the composition of each reagent is as follows (see **Table 1**):

Table 1 The Composition of Nanoparticles

Insulin Concentration (μℓ/mℓ)	100	75	50	30
Chitosan (g)	0.3	0.3	0.3	0.3
Distilled Water(mℓ)	28.35	28.65	28.95	29.19
Insulin (mℓ)	1.2	0.9	0.6	0.36
Acetic Acid(mℓ)	0.15	0.15	0.15	0.15

3. Results and Discussion

Fig. 5 shows the drug release concentration at Penicillin-G 0.1, 0.3, 0.5, and 0.7 % in vitro. The value shows a relatively slow increase, in other words, a relatively stable increase. The value is more stable when its concentration is higher. Also, it is identified that transformation occurs when mixing chitosan and penicillin at over 30℃. This should be considered when mixing these two materials. Through this experiment, it is observed that chitosan allows the drug release to be stabilized. Therefore, it is estimated that chitosan and its derivatives are quite useful when conducting drug release experiments.

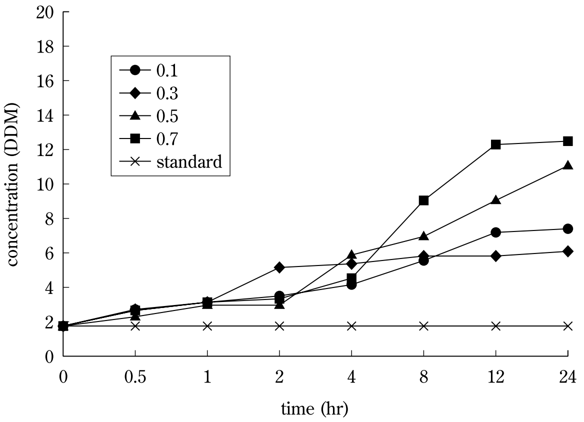

Fig. 5 Drug Release Concentration at Penicillin 0.1, 0.3, 0.5, and 0.7%.

Figu. 6 shows the blood glucose level in NOD mice in accordance with three different hypodermic injections. For NOD mice in the control group, the blood glucose level does not fall below 200 mg/dl. The hypodermic injection was administered by 2 IU/Mouse (0.057 IU/g) and 5 IU/Mouse (0.143 IU/g) based on the 35g of NOD mice. For the hypodermic injection on 5 IU/Mouse, the lowest blood glucose level (40 mg/dl) is observed after four hours of ad-

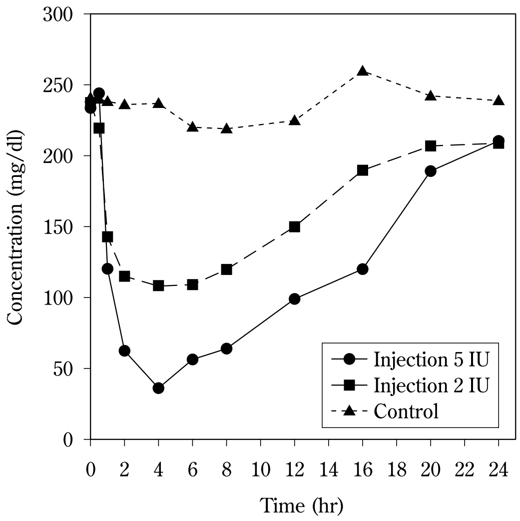

Fig. 6 Effects of Hypodermic Injection on Blood Glucose Level in NOD-mouse.

ministration, which is not a desirable value compared to that of the normal mouse. It is 2IU hypodermic injection that has similar effect with the blood glucose level (110-120 mg/dl) of a normal mouse. This value is the suitable blood glucose level that should be gained from the drug patch.

Fig. 7 displays the effects of transdermal insulin delivery by a chitosan patch (Chsn1= MW; 50,000, Chsn2= MW; 120,000) on the blood glucose level. As shown in the **Fig. 7** chitosan 1 is more effective in its insulin delivery than chitosan 2.

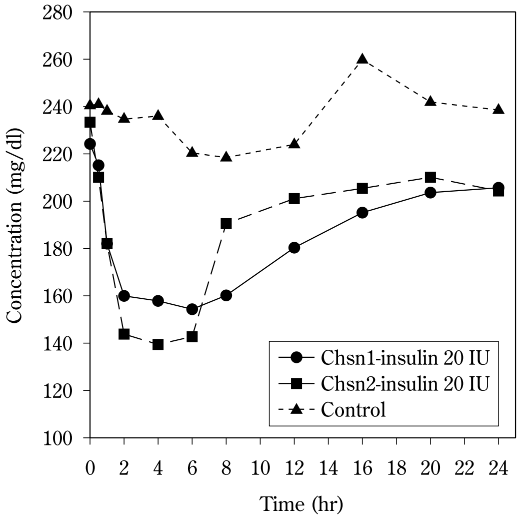

Fig. 7 Effects of transdermal insulin delivery by a chitosan patch on blood glucose levels in NOD-mouse (chsn1=mw: 50,000, chsn2 = mw: 120,000).

As **Fig. 8** shows, the effects of DMSO molecular weight on the blood glucose level of NOD-mouse are investigated in order to find the most suitable DMSO concentration. As **Fig. 11** shows, the higher the DMSO concentration is, the higher the blood glucose level becomes. It is estimated that when the DMSO concentration reaches over a certain level, drug delivery is difficult due to the increase of skin reaction. The result found that DMSO2 (0.85 mg/ml), showing the most suitable blood glucose level of 135 mg/dℓ, is the optimal concentration of the skin activating agent. Unlike the hypodermic injection, this is because the drug is administered every three hours and then is given one hour of restoration period before re-administrating the drug. Compared to drug administration through a hypodermic injection, drug administration through an insulin patch achieves 8% of drug delivery on the aspect of insulin, and maintains a reasonably low blood glucose level.

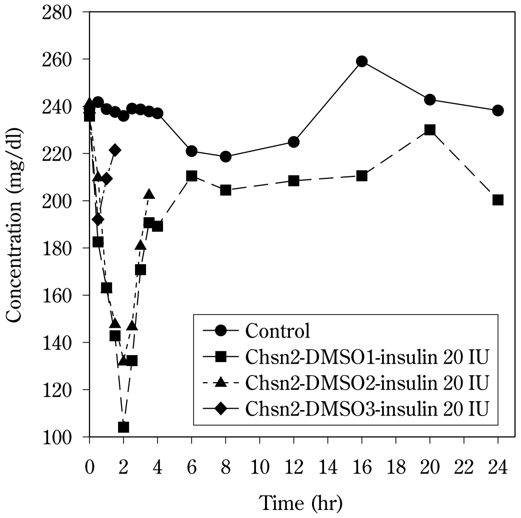

Fig. 8 Effect of DMSO molecular weight on blood glucose level of NOD-mouse *in vivo*. (DMSO1: 1.7 mg/mℓ, DMSO2: 0.85 g/mℓ, DMSO3: 3.4 g/mℓ).

Fig. 9 shows the blood glucose level change of a mouse at dietary state in vivo depending on the chitosan nanoparticles that contain various insulin concentrations (10 IU, 7.5 IU, and 5.0 IU). As shown in **Fig. 9**, when the insulin concentration is increased, the blood glucose level is decreased. The variation of the three curves is significant because the intake of each mouse varies among the several elements to change the blood glucose level (i.e. food intake, activities and the level of stress).

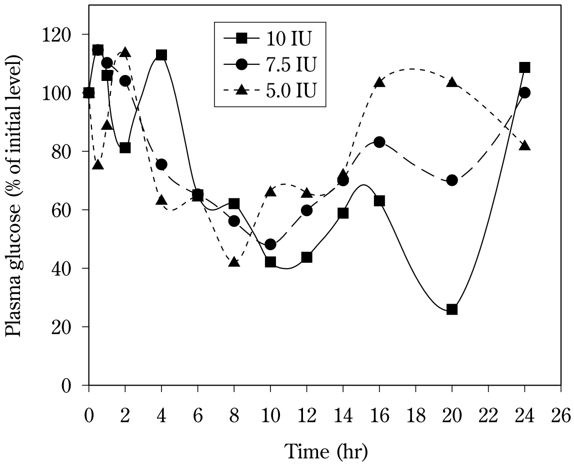

Fig. 9 Nanoparticles effect on blood glucose level change of mouse at dietary state *in vivo*.

Fig. 10 is an experiment to find the insulin transportation by nanoparticles. The mice are left eight hours without food, and then their blood glucose level change is observed for 24 hours. In this experiment, the insulin concentration of the nanoparticles is relatively lower than the prescribed diet because if a mouse is administrated with the same amount of insulin during hunger, it may go into shock. As shown in **Fig. 10**, the blood glucose level is lowered in the order of 7.5 IU, 5.0 IU, and 3.0 IU, and unlike the prescribed diet, their blood glucose level is stabilized four hours later, which is an ideal result.

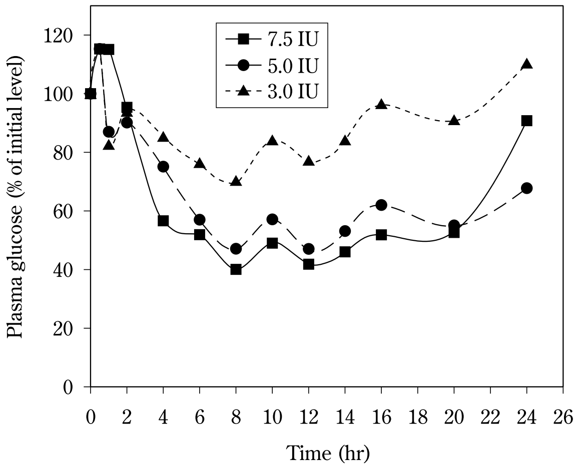

Fig. 10 Nanoparticles effect on blood glucose level change of mouse at abstention state *in vivo*.

4. Conclusions

During the *in vitro* experiment, it was found that chitosan can release the drug at a constant level, and that it is pertinent to apply chitosan and its derivatives for drug release experiments. Also, the mixture of chitosan and penicillin is transformed when made at over 30℃, which should be considered before mixing these two materials.

During the *in vivo* experiment using the chitosan-insulin patch, the author found that it can release the drug at a relatively constant level, and that chitosan is effective for drug release experiments. In addition, the author observed that a high molecular chitosan raises the efficiency as a drug release carrier more than a low molecular chitosan, and that the amount of drug release may be controlled depending on the condition. Chitosan containing insulin releases less drug when stored at a low temperature, and the insulin drug is decomposed over time. It is necessary to perform systematic research on this matter in the future. When comparing the skin activating agents, the author found that DMSO is the most effective in vivo.

For the *in vivo* experiment using the chitosan nanoparticles containing insulin, the blood glucose level does not fall below 200mg/ml among the NOD mice in the control group. It is the curve of 2 JU that has the most approximate value for our drug patch. It shows the decrease of blood glucose level for Insulin 10 IU and 20 IU NOD mice in case of chitosan 1 and 2 with different molecular weight (MW; 50,000, MW; 120,000). Chitosan 2 shows somewhat better characteristics. When manufacturing the chitosan solution, the skin activating agent is added for the experiment. The result found that DMSO displays the best decrease on the blood glucose level. With DMSO, the value drops up to 104mg / dℓ , which is lower than we expected. However, the blood glucose level is increased up to 270 mg/dℓ. It is estimated that DMSO may cause stress accompanied by stigmas. Against this backdrop, the author conducted DMSO experiments with different concentrations. The result found that as the DMSO concentration is increased, the skin reacts against the drug due to skin irritation. Based on the above experiments, the author summarizes the results as follows:

1. Capital Chitosan manufactured with over 95% degree of purity performs a relatively stable drug release during *in vitro* and *in vivo* experiments, and that it is reasonable to apply the chitosan derivatives for the drug release experiments.
2. With the chitosan patches, the blood glucose level is lowered the best when the skin activating agent, DMSO, is added.
3. It is possible to manufacture nanoparticles of 100-200 nm with the biodegradable high molecular weight chitosan, and the manufactured nanoparticles are highly efficient as a drug release carrier.
4. For insulin absorption through a mucous membrane, only a small amount of chitosan nanoparticles can maintain the stable blood glucose level of 100-120 mg/dl.
5. It is estimated that insulin absorption is increased through the chitosan nanoparticles because the nanoparticles can expand the connection of the epithelian cells loosely.

References

1) T. C. Yang, R. R. Zall, *Ind. Eng. Chem. Prod. Res. Dev.*, **23**, 168 (1984).
2) M. L. Gonzalez, M. A. Holgado and C. Sanchez, *Intern. J. Pharm.*, **232**(1), 225 (2002).
3) D. Marchi, et al., *Horm Res*, **41**(2), 93 (1994).
4) R. K. Campbell, , et al., *Ann Pharmacother*, **30**, 1263 (1996).
5) S. Kang, et al., *Diabetes Care*, **14**, 942 (1991).
6) D. C. Howey, et al., *Diabetes*, **43**, 396 (1994).
7) D. C. Howey, et al., *Clin Pharmacol Ther.*, **58**, 459 (1995).
8) E. W. Terbraak , et al., *Diabetes Care*, **19**, 1437 (1996).
9) E. Torlone, et al., *Diabetologia*, **37**, 713 (1994).
10) N. D. .Stephen and K. G. Daryl, *Diabetologia*, **9**, 25

(1997).
11) S. Watnasirichaikul, N. M. Davies, T. Rades, I. G. Tucker, *Pharm. Res.*, **17**(6), 684 (2001).
12) H. Tozaki, J. Nishioka, J. Komoike, N. Okada, T. Fujita, S. Muranishi, S. I. Kim, *J. Pharm. Sci.*, **90**(1), 89 (2001).
13) M. J. Coloma, H. J. Lee, A. Kurihara, E. M. Landaw, R. J. Boado, S. L. Morrison,W. M. Pardridge, *Pharm. Res.*, **17**(3), 266 (2000).
14) A. M. Lowman, M Morishita, M. Kajita, T. Nagai, N. A. Peppas, *J. Pharm. Sci.*, **88**(9),933 (1999).
15) K. Iwanaga, S. Ono, K. Narioka, M. Kakemi, K. Morimoto, S. Yamashita, Y. Namba,N. Oku, *J. Pharm. Sci.*, **88**(2), 248 (1999).
16) J. M. Barichello, M. Morishita, K. Takayama, T. Nagai, *Intern. J. Pharm.*, **184**(2), 189 (1999).
17) C. R. Rao, A. K. Cheetham, *J. Mat. Chem.*, **11**(12), 2887 (2001).
18) K. Ito, S. Kondo, M. A. Kuzuya, *Chem. Pharm. Bull.*, **49**(12), 1615 (2001).
19) C. L. Garcia, D. Sarubbi, E. Flanders, D. O'Toole, J. Smart, C. Newcomer, *Pharm.Res.*, **18**(12), 1685 (2001).
20) C. S. Kwok, P. D. Mourad, L. A. Crum, B. D. Ratner, J. *Bio. Mat. Res.*, **57**(2), 151(2001).
21) K. C. Gupta, N. V. Mageti, R. Kumar, *J. Mat. Sci.*, **12**(9), 753 (2001).
22) K. Kurita, M. Hayakawa, Y. Nishiyama, M. Harata, *Carbo. Polymers*, **47**(1), 7 (2002).
23) E. B. Pereira, H. F. De Castro, F. F. De Moraes, G. M. Zanin, *Appl. Biochem. Biotech.*,**91**(3), 739 (2001).
24) S. A. Onkop, *Intern. J. Pharm.*, **194**(1), 1 (2001).
25) F. L. Mi, H. W. Sung, S. S. Shyu, *Carbo. Polymers*, **48**(1), 61 (2002).
26) R. A. Muzzarelli, M. B. Mattioli, M. Miliani, C. Muzzarelli, F. Gabbanelli, G. Biagini,*Carbo. Polymers*, **48**(1), 15 (2002).
27) T. Senda, Y. He, Y. Inoue, *Polymer Intern.*, **51**(1), 33 (2002).
28) F. L. Mi, Y. B. Wu, S. S. Shyu, J. Y. Schoung, Y. B. Huang, Y. H. Tsai, J. Y. Hao, *J. Biomed. Mat. Res.*, **59**(3), 438 (2002).
29) Y. H. Kim, S. H. Gihm, C. R. Park, K. Y. Lee, T. W. Kim, I. C. Kwon, H. Chung, S.Y. Jeong, *Bioconju. Chem.*, **12**(6), 932 (2001).
30) K. Kofuji, T. Ito, Y. Murata, S. Kawashima, *Bio. Pharm. Bull.*, **24**(2), 205 (2001).
31) L. Yang, W. W. Hsiao, P. Chen, *J. Membr. Sci.*, **197**(1), 185 (2002).
32) G. C. Steenkamp, K. Keizer, H. W. Neomagus, H. M. Krieg, *J. Memb. Sci.*, **197**(1), 147 (2002).
33) S. Fukushima, S. Kishimoto, S. Horai, K. Miyawaki, S. Kamiyabu, Y. Kamata, Y. Yamaoka, Y. Takeuchi, *Biol. Pharm. Bull.*, **24**(9), 1027 (2001).
34) J. Q. Liu, C. Kolar, T. A. Lawson, W. H. Gmeiner, *J. Org. Chem.*, **66**(17), 5655 (2001).
35) M. H. Qvist, U. Hoeck, B. Kreilgaard, F. Madsen, S. Frokjaer, *Intern. J. Pharm.*,**231**(2), 253 (2002).
36) C. L. Garcia, D. Sarubbi, E. Flanders, D. O'Toole, J. Smart, *Pharm. Res.*, **18**(12), 1685 (2001).
37) Y. S. Rhee, J. G. Choi, E. S. Park, S. C. Chi, *Intern. J. Pharm.*, **228**(1), 161 (2001).
38) H. H. Tonnesen, *Intern. J. Pharm.*, **225**(1), 1 (2001).

Acknowledgement

This research was supported by the Kyungwon University TIC Research Fund in 2005.

Author's short biography

Do Hun Lee

He graduated with a master of engineering in Chemical Engineering from Kyungwon University in Korea in 2001. He is a researcher in Dongbu Fine Chemicals from 2001.

Ik Joong Kang

Dr. Ik Jong Kang is a professor at Kyungwon University in Korea. He has been at Kyungwon University since 1990. He graduated with a ph.D. in Chemical Engineering from Korea University in 1989. He has served as a researcher in KRICT, visiting professor at University of Washington from 1994 to 1995, and at University of Florida from 2003 to 2004. Dr. Kang's major research interests include drug delivery systems using biodegradable materials and its application in medicine and cosmetics.

KAPSEL: Kyoto Advanced Particle Simulator for ELectrohydrodynamics
—Toward Direct Numerical Simulations of Colloidal Dispersions—[†]

R. Yamamoto[1], **K. Kim**[2], **and Y. Nakayama**[3]
Department of Chemical Engineering, Kyoto University[*]

Abstract

We have released a colloid simulator named KAPSEL implemented the "Smoothed Profile (SP) method" which has been developed by ourselves for direct numerical simulations of particulate flow providing a way to couple continuum fluid dynamics with rigid-body dynamics through smoothed profile of colloidal particle. KAPSEL enebles us to simulate multi-component fluids, such systems as charged colloids in electrolyte solutions. Dynamics of colloidal dispersions is solved as much computational cost as required for solving non-particulate flows. KAPSEL computes the fluid velocity and the electrostatics potential by solving both Navier–Stokes and Poisson equations directly. The time evolutions of the colloidal particles and the density of counter ions are then determined by solving Newton's equation of motion and advection-diffusion equation, respectively, in a consistent manner so that the electro-hydrodynamic coupling can be fully taken into account. The electrophoretic mobility of spherical colloidal particles is calculated in several situations including those in concentrated dispersions. The comparisons with theories show excellent quantitative agreements.

Keywords: Colloidal dispersion, Simulation, Rheology, Electrophoresis, Hydrodynamics, Sedimentation

1. Introduction

Interparticle interactions in colloidal dispersions mainly consist of thermodynamic potential interaction and hydrodynamic interactions 2). Whereas the former works in both static and dynamic situations, the latter works solely in dynamic situation. Although the thermodynamic interactions in static situations have been studied extensively and summarized as a concept of effective interactions, the nature of dynamic interactions are poorly understood. Since the hydrodynamic interaction is essentially long-ranged, many-body, it is extremely difficult to study its role by means of analytical way alone. Numerical simulations can aid to investigate fundamental role of the hydrodynamic interaction in colloidal dynamics.

Between November 2002 and March 2006, the "Development of Hybrid Molecular Dynamics Simulation Project,"[4] sponsored by the Japan Science and Technology Agency,[5] was carried out initially at the Department of Physics and Astrophysics,[6] Graduate School of Science, Kyoto University and later at the Department of Chemical Engineering,[7] Graduate School of Engineering, Kyoto University. As the ma-

---

[†] Accepted: June 23, 2006

[*] Kyoto 615-8510, Japan

[1] Corresponding author,
TEL&FAX: +81-75-383-2682
E-mail: ryoichi@cheme.kyoto-u.ac.jp

[2] Present address: Institute for Molecular Science, Okazaki 444-8585, Japan

[3] Present address: Department of Chemical Engineering, Kyushu University, Fukuoka 819-0395, Japan

[4] http://www-tph.cheme.kyoto-u.ac.jp/hymd/index-e.html

[5] http://www.jst.go.jp/EN/

[6] http://www.scphys.kyoto-u.ac.jp/index-e.html

[7] http://www.cheme.kyoto-u.ac.jp/english/

jor objective of this project, we developed a reliable and efficient numerical method, called smoothed profile (SP) method 5) 6) 10) and 11), to resolve the hydrodynamic interactions acting on solid particles immersed in complex host fluids. In the SP method, the original sharp boundaries between colloids and host fluids are replaced with diffuse interfaces with finite thickness ξ. This simple modification greatly improve the performance of numerical computations since it enables us to use the fixed Cartesian grid even for problems with moving boundary conditions.

In 2006, we have released a program package named KAPSEL, the Kyoto Advanced Particle Simulator for Electrohydrodynamics, which is based on the SP method and applicable to several electrohydrodynamic phenomena such as electrophoresis of charged colloidal particles. The entire KAPSEL source code is viewable on the web[8] and anyone agreeing to the “OCTA Free Software License Agreement”[9] can download it freely for use. This document outlines the basic principles of the SP method and tutorials describing how to install and execute KAPSEL using a few sample test cases. The latest information will be appearing online, so the reader is recommended to refer to the web if the instructions described in this paper return unsuccessful results.

2. Installation

2.1 Installation of OCTA

KAPSEL is designed to be used as an add-on engine of “OCTA[10],” an integrated simulation system for soft materials developed by the joint project of industry and academia funded by Ministry of Economy, Trade and Industry (METI), Japan. To use KAPSEL, one needs a graphical user interface called “Gourmet” distributed within the “OCTA” program package, whose newset version[11] can be obtained from the web. One must install “OCTA” properly by following the installation procedure of “OCAT” on each machine.

Because KAPSEL needs library called “libplatform,” whose source codes are attached to “Gourmet” to implement data input/output through UDF files, one must follow the instructions below to build “libplatform” on each machine in advance of compilation of KAPSEL.

Linux: For Linux machines, follow the instruction below to build “libplatform.”

```
% cd /usr/local/OCTA2006/GOURMET_2006
% tar xvfpz gourmet*_src.tar.gz
% cd src
% make
% make install
```

Windows: For Windows machines, first install the free software Cygwin[12] that emulates UNIX on the Windows. In doing so, be sure to include “gcc,” “gcc-mingw,” and “make.” Subsequently, start up the Cygwin shell and build “libplatform” as follows.

```
% ln -s /cygdrive/c/OCTA2006/ /usr/local/.
% cd /cygdrive/c/OCTA2006/GOURMET_2006
% ./GOURMET2006_SRC.EXE
% cd src
% make -f Makefile.cygmingw
% make -f Makefile.cygmingw install
% cd ../lib/cygwin
% ln -s ../win32/libplatform.a .
```

Mac: For MacOS X machines, follow the instruction below to build “libplatform.” Here we assume “OCTA2006” is installed in “/Application/OCTA/” and two environment variables, “PATH” and “PF_FILES” , are set properly.

```
% cd /Application/OCTA/GOURMET_2006/src
% make
% make install
```

2.2 Installation of KAPSEL

The complete source codes of the latest version of KAPSEL can be obtained from the web as a “gzipped-tar” archive file under the name of “kapsel.tar.gz.” The file can be decompressed into the “./kapsel/” using the following command.

```
% tar xvfpz kapsel.tar.gz
```

Linux and Windows: The compilation of KAPSEL can be made as follows using the supplied “Makefile” without any changes.

```
% cd kapsel
% make
```

Mac: For MacOS X machines, put the following in the “Makefile,” and then perform “make.”

```
ARCH=macosx
CC=gcc
CXX=g++
```

---

[8] http://www-tph.cheme.kyoto-u.ac.jp/kapsel/

[9] http://octa01.t.u-tokyo.ac.jp/OCTA/license_eng.html

[10] http://octa.jp/

[11] At this moment, the newest version is “OCTA2006.” We further assume “OCTA2006” is properly installed.

[12] http://cygwin.com/

```
CCOPT=-DMACOSX -03 -fno-inline
LINKS=-lm -lplatform
```

2.3 User support

The BBS of the OCTA home page http://octa.jp contains the bulletin board of KAPSEL. Enter questions or bug reports about KAPSEL in the bulletin board.

3. Rheology of Colloidal Dispersions

Although the rheology of suspensions is important in terms of practical application, its theoretical generalization is too complex a process. (For example, refer to Ref. 2) In the low concentration limit of colloidal particles, the theoretical result shows that the apparent viscosity of a suspension η_{eff} increases as given in equation (1) (see 2), for example.),

$$\frac{\eta_{eff}}{\eta}=1+\frac{5}{2}\varphi, \tag{1}$$

where η denotes the viscosity of the solvent and φ the volume fraction of the colloidal particles. This is Einstein's well-known viscosity equation, although it only holds for the range with the volume fraction $\varphi << 0.1$. As the particle concentration increases, the effect of particle interactions becomes visible with changes in particle structures resulting from the interaction, vitrification and crystallization occurring. This makes it difficult to predict the rheology of a suspension theoretically on the basis of the basic laws. Although affected by the aforementioned difficulties, the importance of the subject means a number of experimental studies have been performed, with several empirical or semi-empirical formulas for the apparent viscosity having been proposed to summarize such studies. (See the Doughherty-Krieger equation 3), Refs. 4), and references therein.)

As the particle concentration increases, the involvement of diverse effects other than the colloid volume fraction in the phenomena necessitates analysis of an individual phenomenon rather than the formation of a cohesive theory. The Smoothed Profile (SP) method provides a simulation method allowing solvent-induced many-body interactions between colloidal particles to be calculated directly; it also allows the rheology of various kinds of suspensions to be analyzed. KAPSEL so far allows simulation and rheology measurement in a simple shear flow condition to be performed for a monodisperse system in a Newtonian fluid.

3.1 Basic Equations

3.1.1 Equation of Motion of Colloidal Particles

Let us consider the motion of N spherical particles in a Newtonian fluid. The position, velocity, and angular velocity $\{\boldsymbol{R}_i, \boldsymbol{V}_i, \boldsymbol{\Omega}_i\}$ of the ith colloidal particle having mass M_p evolve over time according to the equations of motion:

$$\dot{\boldsymbol{R}}_i=\boldsymbol{V}_i, \tag{2}$$

$$M_p\dot{\boldsymbol{V}}_i=\boldsymbol{F}_i^H+\boldsymbol{F}_i^{other}, \tag{3}$$

$$\boldsymbol{I}_p\cdot\dot{\Omega}_i=\boldsymbol{N}_i^H, \tag{4}$$

$\boldsymbol{I}_p=(2/5)\,M_pa^2\boldsymbol{I}$ denotes the moment of inertia of the colloidal particle, with $\boldsymbol{I}$ denoting the unit tensor. In the above equations, $\boldsymbol{F}_i^H$ and $\boldsymbol{N}_i^H$ respectively denote the force and torque received by the colloidal particle from the fluid, expressing the momentum balance. For the implementation of this calculation, see Refs. 5, 6). $\boldsymbol{F}_i^{other}$ denotes direct interaction between colloidal particles and buoyancy.

3.1.2 Solvent Motion: Navier-Stokes Equation in Shear Flow

Solvent motion is in the form of incompressible flow ($\nabla\cdot\boldsymbol{v}=0$). The velocity field $\boldsymbol{v}$ of the entire system of the solvent and the colloidal particles follows the Navier-Stokes equation:

$$(\partial_t+\boldsymbol{v}\cdot\nabla)\boldsymbol{v}=-\frac{1}{\rho}\nabla p+\nu\nabla^2\boldsymbol{v}+\phi\boldsymbol{f}_p+\boldsymbol{f}^{shear}, \tag{5}$$

ρ, $\eta=\rho\nu$, and p denote the density, viscosity, and pressure of the solvent, respectively. The body force $\phi\boldsymbol{f}_p$ takes into account the solid/non-slip boundary condition on surfaces of colloidal particles. For the detailed implementation, see Ref. 5, 6).

3.2 Rheology Measurement

The external force $\boldsymbol{f}^{shear}$ controls v_x so that it is kept at the profile of a simple shear flow given by

$$v_x=S\left(\frac{L_y}{2}-y\right). \tag{6}$$

In equation (6), S denotes the shear rate. This driving method is the product of the application of the Schumacher and Eckhardt method 9), devised for uniform flow, to the Smoothed Profile (SP) method[13]. In this driving method, periodic boundary conditions are applied in the flow direction (x-) and span direc-

---

[13] To solve a simple shear flow problem, we can use a method involving giving the velocity/force at the boundary wall as the boundary conditions, Rogallo's moving grid method 8, 9), analogous to the Lees-Edwards boundary condition in molecular dynamics simulation, and another method; however, we used the aforementioned calculation method, in which grids do not distort and no boundary problems occur.

tion (z-), while a free-slip boundary condition ($\partial_y v_{x,z}(y=0, L_y)=0$) is imposed on the upper and lower walls. The upper and lower walls are non-transparent, that is, condition $v_y(y=0, L_y)=0$ holds. In the SP method, $\boldsymbol{f}^{shear}$ is applied as feedback during each step of calculation after the advection of colloidal particles and fluid is completed.

The apparent viscosity of a suspension is defined by

$$\eta_{eff}=\frac{\sigma^{eff}_{xy}}{S}, \tag{7}$$

where S (denoting the shear rate) is a control parameter, and the macroscopic shear stress σ^{eff}_{xy} is evaluated on the basis of the calculation data. Let us derive a stress calculation method for a suspension. To facilitate the explanation, the case of a uniform fluid is initially considered. Subsequently, the case of a colloidal dispersion (SP method) is described.

3.2.1 Uniform fluids

Let us write the equations of motion for the shear flow of uniform fluid as follows:

$$\nabla\cdot\boldsymbol{v}=0, \tag{8}$$

$$\rho\dot{\boldsymbol{v}}=\nabla\cdot\boldsymbol{\sigma}+\rho\boldsymbol{f}^{shear}. \tag{9}$$

In equation (9), $\boldsymbol{f}^{shear}$ denotes the external force field per unit mass that exerts shear on the system. This gives the definition of macroscopic stress in the following form:

$$\boldsymbol{\sigma}^{eff}=\frac{1}{V}\int d\boldsymbol{x}\boldsymbol{\sigma}. \tag{7}$$

This can be calculated through the volume integral of local stresses $\boldsymbol{\sigma}$.

Let us consider evaluating $\boldsymbol{\sigma}^{eff}$ by using external force $\rho\boldsymbol{f}^{shear}$. Using an identity of second order

$$\boldsymbol{\sigma}=[\nabla\cdot(\boldsymbol{\sigma}\boldsymbol{x})]^{T}-\boldsymbol{x}\nabla\cdot\boldsymbol{\sigma}, \tag{11}$$

the following equations are obtained:

$$\int d\boldsymbol{x}\boldsymbol{\sigma}=\int d\boldsymbol{x}\Big[[\nabla\cdot(\boldsymbol{\sigma}\boldsymbol{x})]^{T}-\boldsymbol{x}\nabla\cdot\boldsymbol{\sigma}\Big] \tag{12}$$

$$=\int d\boldsymbol{x}[-\boldsymbol{x}\nabla\cdot\boldsymbol{\sigma}] \tag{13}$$

$$=\int d\boldsymbol{x}\Big[\boldsymbol{x}\left(\rho\boldsymbol{f}^{shear}-\rho\dot{\boldsymbol{v}}\right)\Big] \tag{14}$$

$$=\int d\boldsymbol{x}\boldsymbol{x}\rho\boldsymbol{f}^{shear}-\frac{d}{dt}\int d\boldsymbol{x}\rho\boldsymbol{v}. \tag{15}$$

Here, we drop the surface term and use the incompressible condition ($\nabla\cdot\boldsymbol{v}=0$). In the steady state, since the change in the total momentum is zero, we ultimately obtain

$$\boldsymbol{\sigma}^{eff}=\frac{1}{V}\int d\boldsymbol{x}\boldsymbol{x}\rho\boldsymbol{f}^{shear}. \tag{16}$$

3.2.2 SP Method for Particle Dispersion

Let us formally write the equation of the momentum of suspension in shear flow as follows:

$$\frac{d}{dt}(\rho_t\boldsymbol{v})=\nabla\cdot\boldsymbol{\sigma}^{suspension}+\rho_t\boldsymbol{f}^{shear}, \tag{17}$$

$$\rho_t=(1-\phi)\rho_f+\phi\rho_p. \tag{18}$$

In equation (17), $\boldsymbol{\sigma}^{suspension}$ denotes the stress of the suspension. Since this $\boldsymbol{\sigma}^{suspension}$ cannot be calculated directly, the formula to be obtained through the integration of stress (10) cannot be implemented.

On the other hand, the SP-method-based equation for the velocity field of a suspension under a shear flow condition is given by

$$\dot{\boldsymbol{v}}=\frac{1}{\rho}\nabla\cdot\boldsymbol{\sigma}+\phi\boldsymbol{f}_p+\boldsymbol{f}^{shear}. \tag{19}$$

Comparing this with equation (17), we obtain

$$\frac{1}{\rho_t}\nabla\cdot\boldsymbol{\sigma}^{suspension}=\frac{1}{\rho}\nabla\cdot\boldsymbol{\sigma}+\phi\boldsymbol{f}_p, \tag{20}$$

From this, we obtain

$$\boldsymbol{\sigma}^{eff}=\frac{1}{V}\int d\boldsymbol{x}\boldsymbol{x}\rho_t\boldsymbol{f}^{shear} \tag{21}$$

as an expression of the stress of the suspension. Although this contains the position vector explicitly, the macroscopic shear stress to be measured is free from how the origin of the system of coordinates is defined. This is compatible with the fact that the translational motion of the entire system is not driven by $\boldsymbol{f}^{shear}$. This fact will be confirmed in the following. When the origin of coordinates is shifted to a position expressed by $\boldsymbol{x}=\boldsymbol{x}'+\boldsymbol{x}_0$, we obtain

$$\int d\boldsymbol{x}(\boldsymbol{x}'+\boldsymbol{x}_0)\rho_t\boldsymbol{f}^{shear}=\int d\boldsymbol{x}\boldsymbol{x}'\rho_t\boldsymbol{f}^{shear}+\boldsymbol{x}_0\int d\boldsymbol{x}\rho_t\boldsymbol{f}^{shear}. \tag{22}$$

Since the external force $\boldsymbol{f}^{shear}$ is controlled such as to produce a shear flow, rather than a translational motion of the entire system, $\int d\boldsymbol{x}\rho_t\boldsymbol{f}^{shear}=0$. The SP method uses equation (21) to evaluate macroscopic stress.

3.3 UDF Description

3.3.1 Input Parameters

Selecting "Shear_Navier_Stokes" for "constitutive_eq" makes it possible to simulate the motion of colloidal particles in a Newtonian fluid under shear flow[14]. In the following, the variables to be specified in an input

---

[14] Simulation can be performed similarly when other alternatives for "constitutive_eq" are selected: for example, "Navier_Stokes" for the motion of colloidal particles in a Newtonian fluid, such as gravitational sedimentation of particles, and "Electrolyte" for the motion of charged colloids, electrophoresis in an external electric field, and similar.

UDF file are described.

The section "constitutive_eq.Shear_Navier_Stokes" specifies the characteristics of the solvent:

- constitutive eq.Shear Navier Stokes.DX...Grid width Δ as the unit quantity for length.
- constitutive eq.Shear Navier Stokes.RHO... Density of the solvent.
- constitutive eq.Shear Navier Stokes.ETA... Viscosity of the solvent.
- constitutive eq.Shear Navier Stokes.Shear rate... Shear rate.

The section "particle_spec[]," specifies the characteristics concerning the particle:

- particle spec[].Particle number... Number of particles.
- particle spec[].MASS RATIO... Ratio of the density of the particles to that of the fluid.

The pieces of information on the particle radius and boundary thickness are entered as follows:

- A_XI... Boundary thickness ξ. When "Shear_Navier_Stokes" is selected, at least $\xi \geq 1$ must be selected.
- A··· Particle radius.

The section "gravity," enter the pieces of information on gravity:

- gravity.G... Gravitational acceleration.
- gravity.direction... Select the direction in which to apply gravity.

Specify the type of Lennard-Jones potential for interparticle force.

- EPSILON... the energy unit for the Lennard-Jones potential.
- LJ powers... the power exponent of the Lennard-Jones potential.

The section "mesh," specifies the simulation size (The current version is only compatible with a periodic boundary condition in a rectangular parallelepiped cell.):

- mesh.NPX... The size in the x-direction is $L_x=2^{NPX}$.
- mesh.NPY... The size in the y-direction is $L_y=2^{NPY}$.
- mesh.NPZ... The size in the z-direction is $L_z=2^{NPZ}$.

The section "time_increment," specifies the time increment:

- time_increment... When you select "auto," specify the time increment upper limit $T_{dump}=\rho/\eta k_{max}^2$, where k_{max} is the wave number determined by the grid width DX. When you select "manual," specify the value manually.
- time_increment.auto.factor... The time increment is specified as $\Delta t=T_{dump} \times$ factor.
- time_increment.manual.delta_t··· Enter Δt manually.

The section "switch," specifies the simulation condition:

- switch.ROTATION... Select "ON" to solve an equation of motion for particle rotation.
- switch.HYDRO_int... Select "Correct" to solve a Navier-Stokes equation for a fluid; for "Shear_Navier_Stokes," however, the "Correct" switch is the only one implemented.
- switch.Stokes... Select "with advection" to take the inertia term into consideration when solving a Navier-Stokes equation. Select "w/o advection" to perform Stokes approximation not taking the inertia term into consideration; for "Shear_Navier_Stokes," however, the option "w/o advection" is not implemented yet.
- swithch.LJ truncate... When handling force between particles arising from the Lennard-Jones potential, select "OFF" for a normal form containing the attractive force term, "ON" for repulsive force, not containing the attractive force term, or "NONE" when no force is applied at all.
- switch.INIT_distribution... With this switch, select the initial configuration of particles from "uniform_random" (random), "random_walk" (shifted from a square lattice randomly), "FCC" (on an FCC lattice), "BCC" (on a BCC lattice), and "user_specify" (the coordinates and velocity are user-specified.). When you select "user_specify," enter the initial particle position and velocity into "user_specify.Particles[].R" and "user_specify.Particles[].v," respectively. If the number of lists to be entered is smaller than that specified in "Particle_number," increase "user_specify.Particles[]" by implementing the "Edit→Add an array Element" operation on "Gourmet" or edit the UDF file directly.
- switch.FIX_CELL... Set the direct current component of the full velocity at zero, $\boldsymbol{v}_{k=0}=0$. To introduce gravitational acceleration to measure the settling velocity, set this to "ON."

The section "output," specifies the pieces of information on the data output:

- output.GTS... Number of data output interval steps.
- output.Num_snap...Frequency of data output; in other words, the total number of steps is specified by GTS × Num_snap.
- output.AVS... Select "ON" to carry out data output in the AVS format.
- output.AVS.ON.Out_dir... Insert the directory for outputting AVS format data. For example, when "data" is specified, it is necessary to create the "./data" and "./data/avs/" directories in advance. The AVS field file is outputted to the "./data/" direc-

tory under the filename of "data.fld"; the data file is outputted to the "./data/avs/" directory under the filename of "data_*.dat." The number of steps is entered in the asterisk *.

- output.AVS.ON.FileType... Select between "Binary" and "ASCII" for formatting the AVS data file.
- output.UDF... Select "ON" for output UDF.

As many pieces of record data of the coordinates and velocities of particles as specified in "output. Num_snap" are stored after "Particles[]" of the output UDF.

In the section "resume," select from the following options to resume an interrupted calculation for the resume UDF:

- resume.caclucation... Select "NEW" to start a new calculation. Select "CONTINUE" to restart calculation after reading the pieces of information concerning the number of calculation steps, particle coordinates, velocity, angular velocity, solvent velocity field, and ion density field obtained at the end of the previous calculation. The data is saved in a location below "resume.CONTINUE.Saved_Data" of the restart UDF file. In this case, calculation is resumed with the restart UDF created at the end of the previous calculation being used as the input UDF. How to use this input UDF will be described in detail in Section 5.5.

3.3.2 Units of Space and Time

The grid width Δ is used as the unit of length.

The following points should be noted concerning the unit of time:

- A system of units is adopted that makes the relation $\rho=\eta=\Delta=1$ hold in the Navier-Stokes equation.
- When the entries RHO=A, ETA=B, and DX=C are made in the input udf file, the maximum wave number $k_{\max}$ is given using C, with the upper limit of the time increment given as $T_{\mathrm{dump}} = (A/B)/k_{\max}^2$ on the basis of the diffusion time of the momentum. The time increment Δt is adjusted by $T_{\mathrm{dump}} \times$ factor. However, the unit for time itself is the same as in the case of $\rho = \eta = \Delta = 1$.

4. Electrophoresis of Charged Colloids

When colloidal particles are dispersed in a solvent with very large permittivity such as water, ions are emitted from leaving groups on colloid surfaces, with the particle surfaces becoming charged. The emitted ions are electrostatically attracted to particle surfaces, and at the same time, are diffused by thermal fluctuation and form a cloud-like ionic atmosphere called an electric double layer around the colloidal particles. The properties of a colloidal disperse system in equilibrium are described by a Poisson-Boltzmann equation. The Debye-Hückel approximation, obtained by linearizing the Poisson-Boltzmann equation, allows an unobstructed understanding to be obtained. In contrast, in so-called electrokinetic phenomena, such as electrophoresis, the behavior of particles and ionic distribution is determined by competition between hydrodynamic and electrostatic interactions. As a result of the competition, the ionic distribution becomes incapable of following the motion of particles, with electric double layers distorted out of spherical symmetry, resulting in a non-equilibrium state. The only means to analyze such a complex state is to introduce a theoretically simple approximation. In addition, even computer-based simulation has seldom yielded a correct reproduction.

To overcome this situation, this project involved developing a new simulation method called the Smoothed Profile (SP) method 5, 10, 6, and 11). In the SP method, colloids are handled as particle pictures. In contrast, the solvent and ions are presented as a coarse-grained density field in the state of a continuum. In a continuum picture, the interface between a colloidal particle and a solvent, usually expressed through a step function, is expressed safely on a fixed orthogonal grid, using an interface function to overcome difficulties in numerical calculation. Accordingly, the SP method uses both particle and continuum pictures to describe their degrees of freedom and the interaction between them with physical correctness. This is an outstanding feature of the SP method that allows multi-scaled complex phenomena to be analyzed. In addition, the SP method solves hydrodynamic interactions by carrying out direct numerical calculations of a Navier-Stokes equation 5, 6). To implement these calculations, we constructed a formalism to consistently solve the three degrees of freedom, namely, colloidal particles (the Newton's equation of motion), ion distribution (an advection-diffusion equation), and a solvent velocity field (the Navier-Stokes equation), based on the assumption of a smooth interface function. Using this, we firstly succeeded in simulating electrophoresis quantitatively 11). In the following section, the basic equations taken into consideration in KAPSEL are described, with a brief mention of the underlying theory.

4.1 Basic Equations

As described in the Refs. 6, 11), let us take a general view of the basic electrohydrodynamics equations necessary for simulation. N colloidal particles with a radius of a, dispersed in an electrolytic solvent, are considered. The permittivity of the solvent ϵ is assumed to be spatially uniform. The SP method expresses the interface between a particle and solvent in the form of a smooth function $\phi(\boldsymbol{r}) \in [0,1]$ of finite thickness ξ. On a fixed orthogonal grid, the particle domain is expressed by $\phi=1$, the solvent domain by $\phi=0$, and the interface domain by $0<\phi<1$. Other methods using $\phi(\boldsymbol{r})$ on an orthogonal grid are proposed by Tanaka-Araki 12) and Kajishima et al. 13). Introducing an interface function allows remarkably improved calculation efficiency in comparison with the finite element method using nonstructural lattices. The surface of a colloidal particle is assumed to be charged uniformly and the quantity of charge per particle to be Ze. In an ordinary continuum picture, the particle surface charge distribution is expressed using a delta function. Consequently, a suitable boundary-compatible lattice is used in the finite element method; which significantly encumbers the calculation efficiency. In contrast, the SP method also uses a smooth distribution for this particle surface charge distribution $eq(\boldsymbol{r})$. For example, when we use the differential of the first order of the interface function ϕ, $eq(\boldsymbol{r})$ is expressed as

$$eq(\boldsymbol{r}) = \frac{Ze|\nabla\phi(\boldsymbol{r})|}{4\pi a^2}. \tag{23}$$

Just as the interface function $\phi(\boldsymbol{r})$ is structured such as to be reduced to a step function with $\xi \to 0$, $q(\boldsymbol{r})$ is structured such as to be reduced to a delta function with $\xi \to 0$.

4.1.1 Advection-diffusion Equation

Let us define the density distribution C_α of α type ions with a valence of Z_α in the entire calculation domain as shown below:

$$C_\alpha(\boldsymbol{r},t) = (1-\phi(\boldsymbol{r},t))C^*_\alpha(\boldsymbol{r},t). \tag{24}$$

The domain where ions exist is expressed by $(1-\phi)$. $C^*_\alpha(\boldsymbol{r},t)$ is the auxiliary variable for calculation, being defined as smooth throughout the entire calculation domain. C^*_α in the colloid domain ($\phi=1$) has no physical meaning. The total charge distribution, including the particle surface charge distribution, is given by

$$\rho_e(\boldsymbol{r}) = e\sum_\alpha Z_\alpha C_\alpha(\boldsymbol{r}) + eq(\boldsymbol{r}). \tag{25}$$

In the equation, the initial distribution is constructed such as to meet the electrical neutrality condition $\int \rho_e d\boldsymbol{r} = 0$.

The time evolution of the auxiliary ion density C^*_α is assumed to follow the advection-diffusion equation

$$\partial_t C^*_\alpha = -\nabla\cdot C^*_\alpha \boldsymbol{v} + \Gamma_\alpha \nabla\cdot(C^*_\alpha \nabla\mu_\alpha). \tag{26}$$

This equation consists of two terms, one expressing the advection, due to the solvent velocity field $\boldsymbol{v}$, and the other expressing the diffusion due to the gradient of the chemical potential μ_α. Since C^*_α follows the advection-diffusion equation, $\int d\boldsymbol{r} C^*_\alpha$ is conservative.

The absence of ion permeation into colloidal particles is considered to be the condition for the component normal to the interface of the ion diffusion flow rate to become zero. In other words, it is expressed by $\boldsymbol{n}\cdot\nabla\mu_\alpha=0$ 6, 11). In this equation, $\boldsymbol{n}$ denotes the (outward) normal vector on the particle surface. Using the interface function, $\boldsymbol{n}$ can be expressed in the form of $\boldsymbol{n} = -\nabla\varphi/|\nabla\varphi|$. Γ_α is the Onsager transport coefficient of an α-type ion, being related to the friction and diffusion coefficients of the ion as $f_\alpha = 1/\Gamma_\alpha$, $D_\alpha = k_B T \Gamma_\alpha$. The chemical potential of the ion is assumed to be expressed in the form 16):

$$\mu_\alpha = k_B T \ln C^*_\alpha + Z_\alpha e(\Psi - \boldsymbol{E}\cdot\boldsymbol{r}). \tag{27}$$

In the equation, $\boldsymbol{E}$ denotes the external electric field, and the electrostatic potential $\Psi(\boldsymbol{r})$ is obtained by solving the Poisson equation

$$\epsilon\nabla^2\Psi = -\rho_e. \tag{28}$$

This chemical potential assume a Poisson-Boltzmann distribution in equilibrium.

4.1.2 Navier-Stokes Equation

Solvent flow is incompressible ($\nabla\cdot\boldsymbol{v}=0$). The velocity field $\boldsymbol{v}$ of a solvent follows the Navier-Stokes equation

$$\rho(\partial_t + \boldsymbol{v}\cdot\nabla)\boldsymbol{v} = -\nabla p + \eta\nabla^2\boldsymbol{v} - \rho_e(\nabla\Psi - \boldsymbol{E}) + \phi \boldsymbol{f}_p. \tag{29}$$

In the equation, ρ, η, and p denote the density, the viscosity of a solvent, and pressure, respectively. Note here that electrostatic force $-\rho_e(\nabla\Psi - \boldsymbol{E})$ acts on the fluid. The external force term $\phi\boldsymbol{f}_p$ ensures the rigidity of a particle. In other words, $\phi\boldsymbol{f}_p$ takes the non-slip boundary conditions of the particle surface into consideration. The details are defined in Refs. 5, 6).

4.1.3 Equation of Motion of Colloidal Particles

The position, velocity, and angular velocity of the ith colloidal particle having mass M_p evolve over time according to the equations of motion

$$\dot{\boldsymbol{R}}_i = \boldsymbol{V}_i, \tag{30}$$

$$M_p\dot{\boldsymbol{V}}_i = \boldsymbol{F}_i^H + \boldsymbol{F}_i^{other}, \quad \boldsymbol{I}_p\cdot\dot{\Omega}_i = \boldsymbol{N}_i^H. \tag{31}$$

In equation (31), $\boldsymbol{F}_i^H$ denotes the force actingon the particle induced by the fluid, expressing the momentum balance between the solid and fluid 6); $\boldsymbol{F}_i^{other}$ denotes the force due to the potential between particles, such as the Lennard-Jones potential. The rotational motion of the particles is also taken into consideration, though not described here 6). The above are the equations necessary for the simulation.

4.2 Electric Double Layer

4.2.1 Poisson-Boltzmann Equation

The basis for quantitative treatment of the structure of an electric double layer is the Poisson-Boltzmann equation. Let us determine the equilibrium distribution of ions under equation (27) for the case where the external electric field does not exist ($\boldsymbol{E}=0$). When the chemical potential has become uniform, that is, μ_α=constant, we obtain

$$C^*_\alpha(\boldsymbol{r})=\bar{C}_\alpha\exp\left(-\frac{Z_\alpha e\Psi(\boldsymbol{r})}{k_BT}\right) \tag{32}$$

as the equilibrium ion distribution. This is a Boltzmann distribution under the electrostatic potential Ψ. Combined this with equation (28), called the Poisson-Boltzmann equation.

4.2.2 Debye-Hückel Approximation and Debye Screening Length

Let us consider a spherical colloidal particle in a z:z-symmetry electrolytic solvent. The Poisson-Boltzmann equation for this condition is given by 2)

$$\nabla^2\Psi(\boldsymbol{r})=\frac{2ze\bar{C}}{\epsilon}\sinh\left(\frac{ze\Psi(\boldsymbol{r})}{k_BT}\right). \tag{33}$$

The boundary conditions at a point at infinity are $\Psi|_{r=\infty}=0$ and $C^*|_{r=\infty}=\bar{C}$. The boundary condition on the surface of the particle is given by

$$\nabla\Psi|_{\mathrm{surface}}=-\frac{\sigma e}{\epsilon}, \tag{34}$$

where the surface charge density is given by $\sigma e=Ze/4\pi a^2$. In other words, a boundary condition of constant surface charge is considered. A method of approximation, in which $ze\Psi/k_BT\ll 1$ is assumed and equation (33) is linearized, is called the Debye-Hückel approximation.
It gives

$$\nabla^2\Psi(r)=\frac{2z^2e^2\bar{C}}{k_BT\epsilon}\Psi=\kappa^2\Psi. \tag{35}$$

In connection with this equation, the constant having a length dimension

$$\kappa^{-1}=\frac{1}{\sqrt{8\pi\lambda_B z^2\bar{C}}} \tag{36}$$

is called the Debye screening length. In equation (36), $\lambda_B=e^2/4\pi k_BT_\varepsilon$ is called the Bjerrum length. In an ordinary electrolyte,

$$\kappa^{-1}=\frac{1}{\sqrt{4\pi\lambda_B\Sigma_\alpha Z^2_\alpha\bar{C}_\alpha}} \tag{37}$$

holds. Since the system is spherically symmetric, it is sufficient to consider the radius $r=|\boldsymbol{r}|$ only, then we obtain

$$\frac{d^2\Psi}{dr^2}+\frac{2}{r}\frac{d\Psi}{dr}=\kappa^2\Psi. \tag{38}$$

The general solution of this equation is given by a Yukawa-type potential

$$\Psi(r)=\Psi_0\frac{a}{r}\exp[-\kappa(r-a)]. \tag{39}$$

The electrostatic force arising from colloidal charge is screened to the extent of κ^{-1}. the Debye screening length κ^{-1} can be considered the distance at which a balance is struck between the effect of the Coulomb force, via which a surface charge attracts an ion of the opposite sign, and the thermal diffusion tending to scratch out the local presence of an ion. For this reason, κ^{-1} can be regarded as the thickness of an electric double layer. When the temperature is high and hence the thermal energy k_BT is large, κ^{-1} becomes large. In addition, as the ionic strength ($\Sigma_\alpha Z^2_\alpha\bar{C}_\alpha/2$) increases, the screening effect increases and κ^{-1} decreases. For example, let us consider the bulk salt concentration $\bar{C}$ throughout a z:z-symmetric electrolytic solvent. With the medium assumed to be water with a temperature of 25℃, the Bjerrum length is given by λ_B=0.72nm; substituting the actual value into equation (36), we obtain

$$\kappa^{-1}=\frac{0.3}{z\sqrt{\bar{C}}}(\mathrm{nm}). \tag{40}$$

When $z=1$ and $\bar{C}$=0.1M, κ^{-1}=1nm; and when $z=1$ and $\bar{C}$= 0.001M, κ^{-1}=10nm.

The surface potential $\Psi(r=a)=\Psi_0$ is determined on the basis of the boundary condition $d\Psi/dr(r=a)=-\sigma e/\epsilon$. Ψ and the surface charge density σe are related by

$$\sigma e=\epsilon\kappa\Psi_0(1+(\kappa a)^{-1}). \tag{41}$$

In other words, as the surface charge increases, the surface potential increases linearly. The Debye-Hückel approximation cannot be applied to locations where the surface potential is high. In reality, as the surface charge increases, the increase in the surface potential becomes more difficult. The relation for this situation can be obtained by solving the nonlinear Poisson-Boltzmann equation. Approximate solutions for a 1:1 electrolyte solvent are proposed by Loeb-Overbeaak-Wiersema 2) and Oshima-Healy-White 15).

4.3 Backgrounds of Electrophoresis

When an electric field $\boldsymbol{E}$ is applied from outside, a colloidal particle charged to Ze is subjected to the electrostatic force $Ze\boldsymbol{E}$, and starts moving. Although the particle is accelerated by the electrostatic force, it is subject to viscous resistance from the fluid;

and reaches the steady velocity V when a balance is struck between the electrostatic force and the viscous resistance. Assuming the viscous resistance to be Stokes resistance, $6\pi\eta aV$, this allows the balance between forces to be written in the form of

$$ZeE=6\pi\eta aV. \tag{42}$$

From this, the electrophoresis mobility

$$\frac{V}{E}=\frac{Ze}{6\pi\eta a} \tag{43}$$

is derived. However, this is unsuitable, and the actual electrophoresis mobility is smaller than this value. This is due to the lack of consideration of the motion of the ion atmosphere and electrostatic force, despite the electrostatic force acting on the ion atmosphere around the colloid. Accompanied by the motion of the ion atmosphere, colloid migration exhibits a much slower migration velocity. In addition, if the electric double layer distorts out of spherical symmetry, the resulting force must be taken into consideration. This will make theoretical consideration extremely complicated. For this reason, several analyses of electrophoresis have been made on simplified models 2).

4.3.1 Smoluchowski Theory

In the case of $\kappa a \gg 1$, where the radius of a particle a considerably exceeds the thickness of an electric double layer κ^{-1}, Smoluchowski's equation is applicable. Since the thickness of an electric double layer is infinitely small in this case, the particle surface can be regarded as a plane with the curvature of the particle surface neglected. An external electric field Ex, parallel to the plane (assumed to be in the x-direction), is assumed to be applicable. When the motion of the fluid is observed from above the particle, in a coordinate system fixed to the latter, the fluid, apart from the particle, should have a velocity of $-V$. Considering the balance between the viscous resistance and the electrostatic force, we obtain

$$\eta\frac{\partial^2 v_x}{\partial y^2}=\sum_{\alpha} eC_{\alpha}E_x=0. \tag{44}$$

Since the ion distribution is related to the second order differentiation of the electrostatic potential through the Poisson equation, the following relation holds:

$$\eta\frac{\partial^2 v_x}{\partial y^2}=\epsilon\frac{\partial^2 \Psi}{\partial y^2}E_x. \tag{45}$$

Performing integration under the boundary conditions whereby the velocity gradient, potential gradient, and potential are all equal to zero for $y \to \infty$, this yields

$$\eta\,[v_x(y)+V]-\epsilon E\Psi(y)=0. \tag{46}$$

Subsequently, we obtain Smoluchowski's equation

$$\frac{V}{E}=\frac{\epsilon\zeta}{\eta} \tag{47}$$

because the velocity is zero at the particle surface ($y=0$). In equation (47), the zeta potential ζ is originally defined as the potential at the slip plane, but it is replaced by the potential at the particle surface $\Psi(0)$.

4.3.2 Hückel Theory

Let us consider a limit opposite to the condition represented by Smoluchowski, $\kappa a \ll 1$, at which the particle is extremely small compared with the thickness of the electric double layer. In other words, when Ze is a limit of a point charge, Hückel's equation is applicable. When the potential on the particle surface is replaced by the Coulomb potential

$$\zeta=\frac{Ze}{4\pi\epsilon a}, \tag{48}$$

Hückel's equation

$$\frac{V}{E}=\frac{2}{3}\frac{\epsilon\zeta}{\eta} \tag{49}$$

is obtained.

4.3.3 Henry and O'Brien-White Theories

For an ordinary κa value, Henry's equation

$$\frac{V}{E}=f(\kappa a)\frac{\epsilon\zeta}{\eta} \tag{50}$$

is known as a coupler of equations (47) and (49). $f(\kappa a)$ is called Henry's coefficient, being defined as follows:

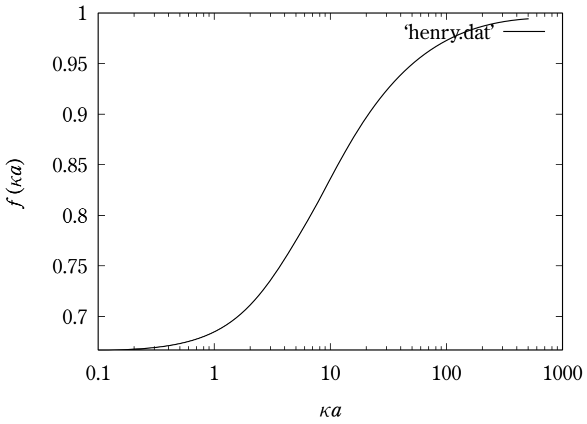

Fig. 1 Henry's coefficient $f(\kappa a)$.

$$f(\kappa a)=1-5\exp(\kappa a)E_7(\kappa a)+2\exp(\kappa a)E_5(\kappa a) \qquad (51)$$

$$=\frac{2}{3}+\frac{(\kappa a)^2}{24}-\frac{5(\kappa a)^3}{72}-\frac{(\kappa a)^4}{144}+\frac{(\kappa a)^5}{144}+\left[\frac{(\kappa a)^4}{12}-\frac{(\kappa a)^6}{144}\right]\exp(\kappa a)E_1(\kappa a). \qquad (52)$$

In equation (51), E_n (κa) is an exponential-integral function of the nth order. Smoluchowski's equation corresponds to $f=1(\kappa a\rightarrow\infty)$ and Hückel's equation to $f=2/3$ $(\kappa a\rightarrow 0)$. (**Fig. 1**)

Henry's equation (50) is a linear relation to the zeta potential, applicable only when the zeta potential is low. As the zeta potential increases, consideration of the deformation effect of the electric double layer (called the relaxation effect) becomes necessary. Using numerical analysis, O'Brien and White have proposed, for ordinary κa and ζ values, the relationship between the electrophoretic mobility and the zeta potential 16). Subsequently, Ohshima, Healy, and White have proposed an analytical equation for the range of $\kappa a\geq 10$ 17).

4.4 UDF Description

4.4.1 Input Parameters

Selecting "Electrolyte" as "constitutive_eq" allows the simulation of motion of charges colloids and an electrophoretic phenomenon under an external electric field[15]. In the following, the variables to be specified in an input UDF file are described.

Enter pieces of information on the solvent and ion distribution in the section "constitutive_eq.Electrolyte":

- constitutive_eq.Electrolyte.DX... Grid width Δ as the unit quantity for length
- constitutive_eq.Electrolyte.RHO... Solvent density.
- constitutive_eq.Electrolyte.ETA... Solvent viscosity.
- constitutive_eq.Electrolyte.kBT... Thermal energy at the temperature T.
- constitutive_eq.Electrolyte.Dielectric cst... Solvent permittivity.
- constitutive_eq.Electrolyte.Init_profile... Choose between "Uniform" and "Poisson_Boltzmann." When you choose "Boltzmann," note that considerable time may be needed in induction periods of simulations to handle a multi-particle problem, in particular.
- constitutive_eq.Electrolyte.Add_salt... When you use "saltfree," consider a single component of ion having the sign opposite to that of the particle surface. If you use "salt," consider two types of ions, positive and negative.
- constitutive_eq.Electrolyte.Add_salt.saltfree.Valency_counterion... Valency of a counterion.
- constitutive_eq.Electrolyte.Add_salt.saltfree.Onsager_coeff_counterion... Onsager transport coefficient of a counterion.
- constitutive_eq.Electrolyte.Add_salt.salt.Valency_positive_ion... Valency of a positive ion.
- constitutive_eq.Electrolyte.Add_salt.salt.Valency_negative ion... Valency of a negative ion.
- constitutive_eq.Electrolyte.Add_salt.salt.Onsager_coeff_positive_ion... Onsager transport coefficient of a positive ion.
- constitutive_eq.Electrolyte.Add_salt.salt.Onsager_coeff_negative_ion... Onsager transport coefficient of a negative ion.
- constitutive_eq.Electrolyte.Add_salt.salt.Debye_length... Specifying the Debye screening length causes the corresponding salt concentration to be specified.
- constitutive_eq.Electrolyte.Electric_field... Choose between "ON" and "OFF" of the external electric field.
- constitutive_eq.Electrolyte.Electric_field.ON... Choose between DC (direct current electric field) and AC (alternating current electric field).
- constitutive_eq.Electrolyte.Electric_field.ON.DC.Ex... Intensity of the x-direction electric field; the same applies in the case of an alternating current electric field.
- constitutive_eq.Electrolyte.Electric_field.ON.DC.Ey... Intensity of the y-direction electric field; the same applies in the case of an alternating current electric field.
- constitutive_eq.Electrolyte.Electric_field.ON.DC.Ez... Intensity of the z-direction electric field; the same applies in the case of an alternating current electric field.
- constitutive_eq.Electrolyte.Electric_field.ON.AC.Frequency... Frequency of an alternating current electric field.

The section "particle_spec[]," specifies pieces of information on the particle type:

- particle_spec[].Particle_number... Number of particles.

---

[15] Simulations can be performed also when alternatives to the above parameters are selected for "constitutive_eq" : for example, "Navier_Stokes" for the motion of colloidal particles in a Newtonian fluid, such as gravitational sedimentation of particles and "Shear_Navier_Stokes" for the motion of colloidal particles in a Newtonian fluid under a shear flow condition, rheology of a dispersion system, and similar.

- particle_spec[].MASS_RATIO... Specific weight of a particle relative to the fluid.
- particle_spec[].Surface_charge... Total amount of particle surface charges.

Enter the pieces of information on the particle radius and interface thickness into the following locations:

- A_XI... Interface thickness ξ. When "Electrolyte" is selected, the differential of the first order of the interface function $\nabla\phi$ is used; consequently, the thickness of the smallest interface is $\xi=2$.
- A... Particle radius.

The section "gravity," specifies the pieces of information on gravity:

- gravity.G... Gravitational acceleration.
- gravity.direction... Select the direction in which gravity is applied.

Determine the type of the Lennard-Jones potential for interparticle force.

- "EPSILON"... Specify the unit for the energy of the Lennard-Jones potential.
- "LJ_powers"... Specify the power exponent of the Lennard-Jones potential.

The section "mesh," specifies the simulation size (The current version is compatible only with a periodic boundary condition in a rectangular parallelepiped cell.):

- mesh.NPX... The size in the x-direction is $Lx=2^{NPX}$.
- mesh.NPY... The size in the y-direction is $Ly=2^{NPY}$.
- mesh.NPZ... The size in the z-direction is $Lz=2^{NPZ}$.

The section "time_increment," specifies the time increment:

- time_increment... When you select "auto," specify the time increment upper limit $T_{\mathrm{dump}}=\min(\rho/\eta k^2_{\mathrm{max}}, 1/k_B T\,\Gamma_\alpha\, k^2_{\mathrm{max}})$, where k_{max} is the maximum wave number determined by the grid width DX. When you select "manual," specify the value manually.
- time_increment.auto.factor··· The time increment is specified as $\Delta t=T_{\mathrm{dump}}\times$ factor using "factor," the value to be entered.
- time_increment.manual.delta_t··· Enter the Δt value manually.

The section "switch," specifies the simulation conditions:

- switch.ROTATION... Select "ON" to solve an equation of motion for particle rotation.
- switch.HYDRO int... Select "Correct" to solve a Navier-Stokes equation for a fluid; for "Electrolyte," however, the "Correct" switch is the only one implemented.
- switch.Stokes... Select "with advection" to take the inertia term into consideration when solving a Navier-Stokes equation. Select "w/o advection" to perform a Stokes approximation not taking the inertia term into consideration; for "Shear_Navier_Stokes," however, the option "w/o advection" is not implementedyet.
- swithch.LJ_truncate... When handling force between particles arising from the Lennard-Jones potential, select "OFF" for a normal form containing the attractive force term, "ON" for repulsive force not containing the attractive force term, or "NONE" when no force is applied at all.
- switch.INIT_distribution... With this switch, select the initial configuration of particles from "uniform_random" (random), "random_walk" (shifted from a square lattice randomly), "FCC" (on an FCC lattice), "BCC" (on a BCC lattice), and "user_specify" (the coordinates and velocity are user-specified.). When you select "user_specify," enter the initial particle position and velocity into "user_specify.Particles[].R" and "user_specify.Particles[].v," respectively. If the number of lists to be entered is smaller than that specified in "Particle_number," increase "user_specify.Particles[]" by carrying out the "Edit → Add an array Element" operation on "Gourmet" or edit the UDF file directly.
- switch.FIX_CELL... Set the direct current component of the full velocity at zero, that is, $v_{k=0}=0$. To introduce gravitational acceleration to measure the settling velocity, set this to "ON."

The section "output," specifies the pieces of information on the data output:

- output.GTS... Number of data output interval steps
- output.Num snap... Number of times of data output; in other words, the number of total steps is specified by "GTS × Num_snap."
- output.AVS... Select "ON" to carry out data output in the AVS format.
- output.AVS.ON.Out_dir... Insert the directory for outputting AVS format data. For example, when "data" is specified, the "./data" and "./data/avs/" directories must be created in advance. The AVS field file is outputted to the "./data/" directory under the filename of "data.fld"; and the data file is outputted to the "./data/avs/" under the filename of "data_*.dat." The number of steps is entered in the asterisk*.
- output.AVS.ON.FileType... Select between "Binary"

and "ASCII" for formatting the AVS data file.

- output.UDF... Select "ON" for output UDF.

The number of pieces of record data of coordinates and velocities of particles specified in "output. Num_snap" is stored after "Particle[]" of the output UDF.

In the section "resume," select from the following options to resume an interrupted calculation for the resume UDF:

- resume.caclucation... Select "NEW" to start a new calculation. Select "CONTINUE" to restart calculation after reading the pieces of information on the number of calculation steps, particle coordinates, velocity, angular velocity, solvent velocity field, and ion density field obtained at the end of the previous calculation. The data is saved in a location below "resume.CONTINUE.Saved_Data" of the restart UDF file. In this case, calculation is resumed with the restart UDF created at the end of the previous calculation being used as the input UDF. How to use this input UDF will be described in detail in Section 5.5.

4.4.2 Units of Space and Time

The grid width Δ is used as the unit of length.

The following points should be noted for the unit of time:

- A system of units is adopted that makes the relation $\rho=\eta=\Delta=1$ hold in the Navier-Stokes equation.
- If the entries RHO=A, ETA=B, and DX=C are made in the input UDF file, the maximum wave number k_{max} is given using C, with the upper limit of the time increment given as $T_{dump}=(A/B)/k_{max}^2$ on the basis of the diffusion time of the momentum. The time increment Δt is adjusted by T_{dump} × factor. However, the unit for time itself is the same as in the case of $\rho=\eta=\Delta=1$.
- In the case of "Electrolyte," use either $(A/B)/k_{max}^2$ or $(1/k_B T\Gamma_{\alpha})/k_{max}^2$ as T_{dump}, whichever is smaller. Use a unit for time so that $\rho=\eta=\Delta=1$ holds.

5 Tutorial

5.1 How to Run KAPSEL

KAPSEL is executed as follows:

```
% kapsel -Iinput.udf -Ooutput.udf -Ddefine.udf
-Rrestart.udf
```

KAPSEL is executed by using -I to designate the input UDF, -O to designate the output UDF, -D to designate the definition UDF, and -D to designate the restart UDF. Note that no option can be omitted. The restart UDF will be described in Section 5.5.

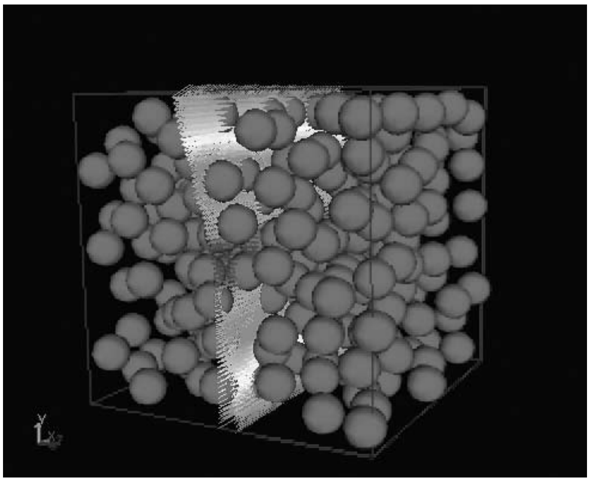

Fig. 2 Flow of a suspension under shear; arrows indicate the velocity field on a plane normal to the flow.

5.2 Sample Simulations

5.2.1 Particle Dispersion under Shear

"shear.udf" can be used as a sample input UDF file; to be more specific, initially ensure that "./data" and "./data/avs/" have been created, and then execute the following:

```
% kapsel -Ishear.udf -Ooutput.udf -Ddefine.udf
-Rrestart.udf
```

In this example (shown in **Fig. 2**), calculation is carried out on the assumption that the mesh size is 64 × 64 × 64, the shear rate S=0.01, the particle radius a=4, the interface thickness ξ=1, and the number of particles is 288. Under this condition, the particle volume fraction φ is 0.29.

With "Shear_Navier_Stokes" selected as "constitutive_eq," the data as shown below is outputted in the standard error output:

```
#1:dev_sigma_yx 2:shear_rate_obs 3:shear_rate ...
0.00647023 -0.00449194 0.01 ...
.
.
.
```

The data in the second and the eighth columns show the temporal shear rate and the temporal shear stress, respectively. Since the data in the 17th column represents the shear strain multiplied by L_y, one may draw the stress-strain curve by plotting "−$8" versus "−$17/L_y," where "$$n$" denotes the data in the nth column. The data in each column is accumulated over

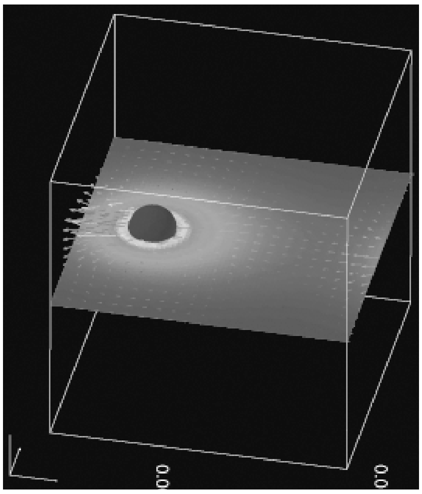

Fig. 3 A colloidal particle (colored blue) in electrophoretic motion under an external electric field applied in the +x direction; in the figure, light and shade represent the electric charge density distribution and the arrows the solvent velocity fields.

simulation time excluding the initial one fourth of the total duration, and the averaged value is printed in the last line.

5.2.2 Electrophoresis: a single particle

To obtain an example of calculation for the simulation of single-particle electrophoresis, use “sample1.udf” as a sample input UDF file; to be more specific, first make sure that “./data” and “./data/avs/” have been created, and then execute the following:

```
% kapsel -Isample1.udf -Ooutput.udf -Ddefine.udf
-Rrestart.udf
```

In this example, a 1:1 electrolytic solvent is considered in a mesh size of $64 \times 64 \times 64$, and the calculation is carried out on the assumption that the radius a=5, the interface thickness ξ=2, the colloidal charge Z=−100, the electric field E_x=0.1, and the Debye screening length κ^{-1}=10. **Fig. 4** shows the evolution of the migration velocity over time. The figure shows that a steady velocity is realized at the point of equilibrium between the electrostatic force and the fluid resistance.

5.2.3 Electrophoresis: many particles

The simulation of electrophoresis with the number of particles assumed to be 32 can be calculated with “sample2.udf.” Other parameters are identical to those in the previons case where the number of particles is one.

5.2.4 Electrophoresis: +/- binary particles

The electrophoresis of a mixed system, in which 64 positively charged colloidal particles and as many

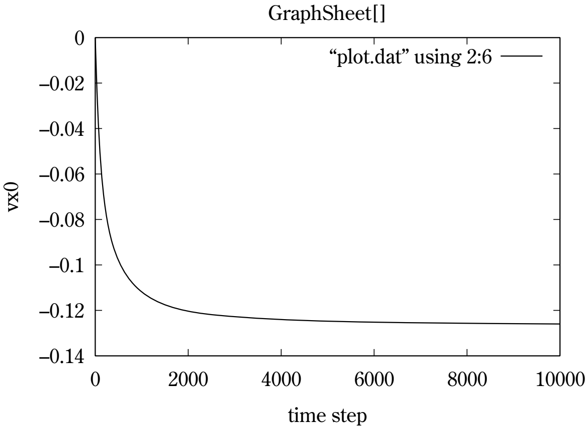

Fig. 4 Evolution of the migration velocity of a colloidal particle over time.

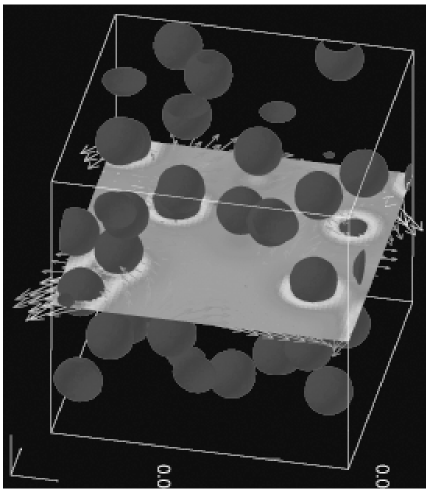

Fig. 5 A colloidal particle (colored blue) in electrophoretic motion under an external electric field applied in the +x direction.

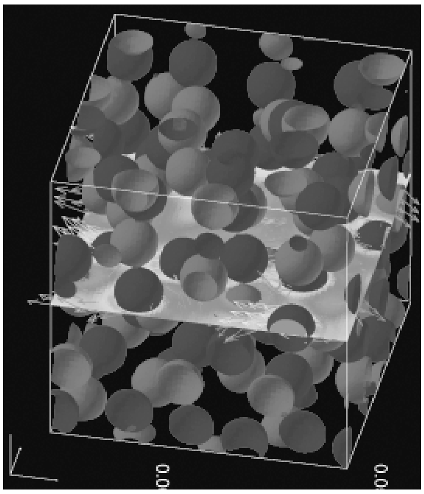

Fig. 6 Positively charged colloidal particles (colored red) and negatively charged colloidal particles (colored blue) in electrophoretic motion under an external electric field applied in the +x direction; positive-signed colloids migrate in the +x direction and negative-signed ones in the -x direction.

negatively charged particles exist, can be calculated with “sample3.udf.” Other parameters are identical to those in the previous cases.

5.3 Visualization

5.3.1 Using AVS/Express

With “output.AVS” set at “ON,” an AVS-format file is outputted. Using AVS/Express[16] to read the “avs_charge.v” file and designating the field file “data.fld” as the “Read_field” module allows the particles, solvent velocity field, and charge distribution to be visualized respectively. The particles are displayed in colors according to the surface charge value *Ze*. The visualization shown in **Figs. 3, 5**, and **6** is obtained by using AVS/Express with “avs_charge.v.”

5.3.2 Using “Gourmet”

When one starts up “Gourmet” to read “output.udf,” loads a Python script “show_field.py” supplied with KAPSEL on the Python panel of “Gourmet,” and executes “Run,” the graphic window opens to visualize the particles, solvent velocity field, and charge density distribution[17]. And clicking on the playback button at the bottom of the graphic window causes animation to start. Since particles are visualized on the basis of the particle coordinate data outputted to the output UDF as record data, setting “output.UDF” at “ON” is necessary. Since the solvent velocity field and the charge density distribution have read “Binary” files outputted in the AVS format, it is necessary to set “output.AVS” at “ON” and “output.AVS.ON.FileType” at “Binary.”

5.4 Plotting Data: gnuplot

Using “gnuplot[18],” it is possible to plot the time series of the position and velocity of a particle in graph form on the basis of the record data outputted to UDF 1).

When one starts up “Gourmet” to read “output.udf,” loads a Python script “plot.py” supplied with KAPSEL on the Python panel of “Gourmet,” and executes “Run,” one can create a graph sheet on the basis of the record data storing the positions and velocities of particles. To plot those data, change the check mark placed on “Tree” in the “View” box to “Table,” select “GraphSheet” in the list of variables, and browse the “GraphSheet” data. Subsequently, executing the “Make” operation on the “Plot” panel of “Gourmet” and executing the “Plot” operation allows the graph shown in **Fig. 4** to be drawn. If an excessive number of line types hinders an easy view of a graph, one may delete unnecessary portions from the “plot” command created in the editor of the “Plot” panel. How to call “gnuplot” from “Gourmet” is described in detail in Chapter 3 of the document 1).

5.5 Restart UDF

Select “NEW” in “resume.Calculation” in the input UDF and end the calculation in the sequence

```
% kapsel -Iinput.udf -Ooutput.udf -Ddefine.udf
-Rrestart.udf
```

and the pieces of information concerning the number of steps, particles, solvent velocity field, and ion distribution at the end of the calculation will be outputted to “restart.udf.” To restart calculation using these pieces of data, follow the steps below:

1. Copy “restart.udf” to “input.udf.”
2. Open “input.udf” on “Gourmet” and select “CONTINUE” in “resume.Calculation.”
3. Specify and store the number of steps to be calculated as a single unit after increasing “output.Num_step.”
4. If the sequence

```
% kapsel -Iinput.udf -Ooutput.udf -Ddefine.udf
-Rrestart.udf
```

is followed again, the data is read from “input.udf” to restart calculation.

5. For both the AVS data and “output.udf,” the output data of the resumed calculation can be added with the previously calculated data as it is.
6. The data at the completion of calculation is stored in “restart.udf” again; therefore, repeating the steps above allows calculation to be continued.

5.6 Known Problems

1. When “Electrolyte” is selected for “constitutive_eq,” a segmentation error or abortion may occur at the time of ending a program run (at the time of manipulating the restart UDF file) depending on the machine used. However, the result of the execution itself seems to pose no problems.
2. “show_field.py” seems not to work normally on “Gourmet_2003.”
3. KAPSEL that has been built in the Windows Cygwin + MinGW environment seems to end due to errors during execution. When “MinGW” is not used,

---

[16] http://www.avs.com/

[17] Versions earlier than “Gourmet_2003” have some glitches and it has been shown that this script does not work normally. In such cases, use the supplied Python script “particleshow.py” for visualization. The solvent velocity field and the charge density distribution are not displayed; only particles are displayed.

[18] http://www.gnuplot.info/

no problems occur.

References

1) Doi, M. and Y. Nishio: “Graphical User Interface GOURMET Operation’s Manual”, OCTA Users Group, Tokyo, Japan (2005), http://octa.jp.

2) Russel, W.B., D.A. Saville, and W.R. Schowalter: “Colloidal Dispersions”, Cambridge University Press, Cambridge, England, (1989).

3) Krieger, I.M.:. Rheology of monodisperse latices, Adv. Colloid Interface Sci., 3. 111 (1972).

4) Hsueh, C.H. and P.F. Becher: Effective viscosity of suspensions of spheres, J. Am. Ceram. Soc., 88. 1046 (2005).

5) Nakayama Y. and R. Yamamoto: Simulation method to resolve hydrodynamic interactions in colloidal dispersions, Phys. Rev. E, 71. 036707 (2005).

6) Nakayama, Y., K. Kim, and R. Yamamoto: Simulating (electro)hydrodynamic effects in colloidal dispersions: smoothed profile method, http://arxiv.org/abs/cond-mat/0601322 (2006).

7) Schumacher J. and B. Eckhardt: On statistically stationary homogeneous shear turbulence, Europhys. Lett., 52. 627 (2000).

8) Rogallo, R.S.: Numerical experiments in homogeneous turbulence: NASA Tech. Memo., 81315 (1981).

9) Onuki, A: A new computer method of solving dynamic equations under externally applied deformations, J. Phys. Soc. Jpn., 66. 1836 (1997).

10) Kim, K. and R. Yamamoto: Effcient simulations of charged colloidal dispersions: A density functional appraoch, Macromol. Theory Simul., 14. 278 (2005).

11) Kim, K., Y. Nakayama, and R. Yamamoto: Direct Numerical Simulations of Electrophoresis of Charged Colloids, Phys. Rev. Lett., 96. 208302 (2006).

12) Tanaka H. and T. Araki: Simulation method of colloidal suspensions with hydrodynamic interactions: Fluid particle dynamics, Phys. Rev. Lett., 85. 1338 (2000).

13) Kajishima, T., S. Takiguchi, H. Hamasaki, and Y. Miyake: Turbulence structure of particle-laden flow in a vertical plane channel due to vortex shedding, JSME Int. J. Ser. B, 44. 526 (2001).

14) Barrat, J.-L. and J.-P. Hansen: “Basic Concepts for Simple and Complex Liquids”, Cambridge University Press, Cambridge, England (2003).

15) Ohshima, H., T. W. Healy, and L. R. White: Accurate analytic expressions for the surface charge density/surface potential relationship and double-layer potential distribution for a spherical colloidal particle, J. Colloid Interface Sci., 90. 17 (1982).

16) O’Brien, R. W. and L. R. White: Electrophoretic mobility of a single colloidal particle, J. Chem. Soc. Faraday Trans. 2, 74. 1607 (1978).

17) Ohshima, H., T. W. Healy, and L. R. White: Approximation analytic expressions for the electrophoretic mobility of spherical colloidal particles and the conductivity of their dilute suspensions, J. Chem. Soc. Faraday Trans. 2, 79. 1613 (1983).

Author's short biography

Kang Kim

Kang Kim obtained his B.Sc., M.Sc. and Ph.D degrees from Kyoto University in 1998, in 2000 and in 2003, respectively. He then joined a research project, "Hybrid Molecular Dynamics Simulation for Soft Matters," as a post doctoral fellow under the direction of Prof. R. Yamamoto until June, 2006. He is currently a Research Associate at Institute for Molecular Science. His research interests include computer simulations for analyzing dynamics in simple and complex liquids.

Yasuya Nakayama

Yasuya Nakayama received his PhD in Informatics from Kyoto University in 2003, MSc from Kyoto University in 2000 and BSc from Kyushu University in 1998. He joined a research project, "Hybrid Molecular Dynamics Simulation for Soft Matters," as a post doctoral fellow under the direction of Prof. R. Yamamoto till October, 2005. Currently he is a Research Associate at Kyushu University. His current activities are focused on physics and simulations of dispersions and polymer processing.

Ryoichi Yamamoto

Ryoichi Yamamoto received his PhD in Engineering from Kyoto University in 1996, MEn and BEn from Kobe University in 1992 and 1988. He became a Research Associate at Kobe University (1994) and moved to Department of Physics, Kyoto University where he became a Research Associate (1996) and a Lecturer (2000). He is an Associate Professor at Department of Chemical Engineering, Kyoto University since 2004. He concerns mainly to understand the nature of unique properties of soft matters and complex fluids by using computer simulations. He is interested also in developments of new simulation methods applicable to complex materials.

Effects of NaOH Concentration on Zeolite Synthesis from Fly Ash with a Hydrothermal Treatment Method[†]

K. Fukui[1], T. Nishimoto, M. Takiguchi and H. Yoshida
Department of Chemical Engineering,Graduate School of Enginnering,Hiroshima University[*]

Abstract

Effects of NaOH concentration on the crystal structure and the reaction rate of the zeolite synthesized from fly ash with a hydrothermal treatment method was investigated. The fly ash or the mixture of fly ash and silica powder was hydrothermal treated using NaOH aqueous solutions of various concentrations.

As a result, a decrease in the NaOH concentration raises the selectivity of phillipsite to the generated zeolite, and lessens that of hydroxysodalite. The reaction rates of them increase consistently with the NaOH concentration. It is clarified that the dependence of crystal structure of generated zeolite on NaOH concentration is not only induced by the dependence of the dissolution rates of silicate ion and aluminate ion from fly ash on it. The fraction of additive silica powder required to synthesize phillipsite selectively increases with increase in the NaOH concentration, and the required treatment time decreases with it.

Keywords: Fly ash, Zeolite, Phillipsite, Hydroxysodalite, Sodium hydroxide

1. Introduction

In Japan, the amount of fly ash emitted from thermo-electric power stations, etc. stood at approximately 5,800,000 tons in 1991 and exceeded 10,000,000 tons in 2000, and is expected to increase dramatically[1)]. Approximately 50% of the fly ash emitted is utilized in the cement/concrete industry and civil engineering/construction industry, and the remainder is disposed by landfill. The “Law for the Promotion of Effective Utilization of Resources” was established in Japan in 2000, which designates fly ash as a specified byproduct, and promotes the reuse of fly ash to alleviate the depletion of resources and environmental pollution. In this context, a commercially feasible method is needed to be able to recycle fly ash into products of greater value[2)].

Methods have been proposed for efficient utilization of fly ash through the synthesis of zeolite (phillipsite) by hydrothermal treatment[3-7)]. However, because synthesized phillipsite deposits on the surface of unreacted fly ash, it is difficult to separate the phillipsite from unreacted fly ash and obtain a phillipsite product featuring sufficiently high performance. Another problem is the occurrence of hydroxysodalite as a byproduct depending on the properties of the fly ash used. However, through studying the effects of the particle size and composition of raw fly ash on the generation speed and crystal phase of zeolite[8)] and a technique to selectively synthesize only phillipsite from fly ash whose silica content is low[9)], we found that a phillipsite product whose performance is equivalent to that of phillipsite synthesized from a pure raw material can be stably synthesized with fly

---

[†] This report was originally printed in J. Soc. Powder Technology, Japan, 40, 497-504 (2003) in Japanese, before being translated into English by KONA Editorial Committee with the permission of the editorial committee of the Soc. Powder Technology, Japan

[*] 1-4-1, Kagamiyama, Higashi-Hiroshima 739-8527, Japan

[1] Corresponding author
TEL&FAX: +81-82-424-7715
E-mail: kfukui@hiroshima-u.ac.jp

ash of various properties.

In this study, we investigated the effects of the concentrations of aqueous NaOH solution used in hydrothermal treatment on the crystal phase of the zeolite being generated[10], and determined the conditions for selectively synthesizing phillipsite more rapidly than in conventional techniques.

2. Test Method

As raw powder, the fly ash emitted from Shin-Onoda Electric Power Station, The Chugoku Electric Power Co., Inc. was used and silica powder was added to the raw fly ash. The properties of these substances are summarized in **Table 1**. The silica component in the raw fly ash was 51.0%, which means that the silica content in the raw material was relatively low. The dissolution rate constants k_{Si}, k_{Al} at 373K for soluble Si species (such as silicate ion) and soluble Al species (such as aluminate ion) given in **Table 1** were determined by measuring the time-dependent changes in the concentrations of both chemical species types C_{Si} and C_{Al} in the aqueous NaOH solution prepared by dissolving 40.0 g of the fly ash in 1.0 L of 2.0 N aqueous NaOH solution in 313-343K, by calculating the dissolution rate constants at various temperatures in this temperature range using Equations (1) and (2), and then developing an Arrhenius plot from the results of the calculation[8].

$$\frac{\mathrm{d}C_{Si}}{\mathrm{d}t}=k_{Si}\,m_{FA}\,(C_{S,Si}-C_{Si}) \tag{1}$$

$$\frac{\mathrm{d}C_{Al}}{\mathrm{d}t}=k_{Al}\,m_{FA}\,(C_{S,Al}-C_{Al}) \tag{2}$$

where, m_{FA} stands for the mass of fly ash, $C_{S,Si}$ means the saturated concentration of soluble Si species and $C_{S,Al}$ represents the saturated concentration of soluble Al species.

Also, by approximating, with the equation below, the dissolution behavior of silica powder with a solution prepared by dissolving 8.2 g of silica powder in 1.0 L of 2.0 N aqueous NaOH solution, the dissolution rate constant of the silica powder k°_{Si} was determined[9].

$$\frac{\mathrm{d}C_{Si}}{\mathrm{d}t}=k^{\circ}_{Si}\,m_{Si}\,(C_{S,Si}-C_{Si}) \tag{3}$$

where, m_{Si} represents the mass of silica powder.

Fig. 1 schematically illustrates the experimental apparatus used for the hydrothermal synthesis reaction.First, 40.0 g of raw fly ash or the raw material mixture prepared by adding silica powder to raw fly ash was suspended in 1.0 L of aqueous NaOH solution kept at a reaction temperature of 373K, thereby hydrothermal treatment was performed. The concentration of the aqueous NaOH solution was varied from 1.0 to 5.0 N, while the reaction pressure was kept at 1.0×10^5 Pa and the stirrer speed was maintained at 250 rpm.After a certain period, the reaction vessel was allowed to cool to an ordinary temperature in atmosphere, and then the suspension was filtrated. The powder product filtered off was thoroughly rinsed with distilled water, and was allowed to dry at 393K for 48 hours. As a result, the powder product consisted of unreacted fly ash and newly generated zeolite.

The properties of the so-obtained powder were evaluated based on the ammonium ion equilibrated adsorption mass and crystal structure of the powder. The ammonium ion equilibrated adsorption mass was determined by allowing 200 ppm aqueous ammonium chloride solution to pass a column filled with 0.5 g of the product at a rate of 1.0 mL/min, and then by measuring the ammonium ion concentration

Table 1 Properties of tested fly ash and additive silica powder

		Fly ash	Silica powder
Component	SiO_2 (wt%)	51.0	100.0
	Al_2O_3 (wt%)	37.0	0
	Others (wt%)	12.0	0
Median diameter (µm)		2.0	2.0
Composition		$Al_6Si_2O_{13}$ Al_2SiO_5 SiO_2	Amorphous silica
Dissolution rate constant (2N NaOHaq., 373K)			
	SiO_4^{4-} $(kg^{-1}s^{-1})$	2.0×10^{-3}	3.0×10^{-2}
	$Al(OH)_4^-$ $(kg^{-1}s^{-1})$	1.8×10^{-2}	———

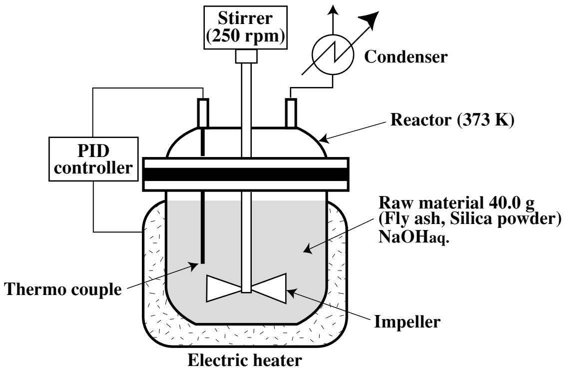

Fig. 1 Schematic diagram of experimental apparatus.

of the passed solution with an ion-meter (Horiba, F23)[9]. The crystal structure of the product was determined using an X-ray diffraction system (Rigaku, RINT-2000).Furthermore, the Si species concentration and Al species concentration in the reaction solution of the hydrothermal treatment (aqueous NaOH solution) were measured using an atomic absorption spectroscope (Shimadzu, AAG-6400G), and the measurement values were respectively taken as the soluble Si species concentration and soluble Al species concentration.

3. Test Results and Discussion

Fig. 2 provides an XRD peak chart for a product that was obtained by subjecting 40.0 g of fly ash alone to hydrothermal treatment for 12 hours in 1.5–3.0 N aqueous NaOH solution.

The higher the concentration of the aqueous NaOH solution used for hydrothermal treatment, the lower the peak intensity of the unreacted fly ash. This indicates that with a higher concentration of aqueous NaOH solution, the proportion of unreacted fly ash in the powder product is smaller. In the region lower than 2.5 N, the peaks of zeolite are peaks for phillipsite ($Na_6Al_6Si_{10}O_{32}$-$3.5H_2O$) and hydroxysodalite ($Na_4Al_3Si_3O_{12}OH$), while at 3.0 N, only a peak for hydroxysodalite is present. With a powder product obtained through hydrothermal treatment with a higher concentration aqueous NaOH solution, the peak intensity for hydroxysodalite is higher and that for phillipsite is lower.

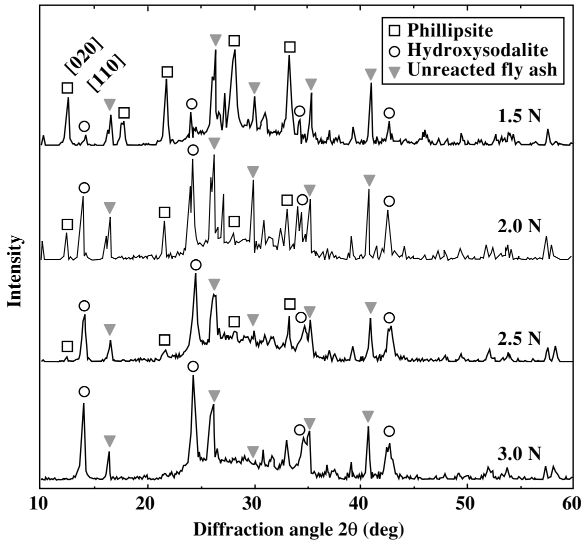

Fig. 2 XRD peak charts for products treated with various NaOHaq.concentrations (Treatment time=12hr).

Fig. 3 illustrates the interrelation existing with the powder product, obtained from 12-hours long hydrothermal treatment, among the peak intensity of interplanar spacing 4.1 Å ([020]plane) for phillipsite, the peak intensity of interplanar spacing 6.3 Å ([110]plane) for hydroxysodalite, the ammonium equilibrated adsorption mass and NaOH concentrations. With a greater NaOH concentration, the peak intensity for hydroxysodalite simply increases. At the same time, the peak intensity for phillipsite reaches maximum at 1.5 N, and decreases with a higher NaOH concentration, and reaches zero at 3.0 N or higher NaOH concentration. Since the ammonium adsorption mass with hydroxysodalite is much smaller than that with phillipsite[9], the tendency of the ammonium ion equilibrated adsorption mass is similar to the tendency in the variation of peak intensity with phillipsite. If the value of peak intensity is taken as an index of the mass of produced zeolite, the proportion of phillipsite to produced zeolite is highest with hydrothermal treatment with 1.0 N aqueous NaOH solution, and the mass of the produced phillipsite is greatest when 1.5 N aqueous NaOH solution is used.

Next, **Fig. 4** graphically illustrates the correlation between the XRD peak intensity with the powder product obtained from the hydrothermal treatment of fly ash in 1.0–2.5 N aqueous NaOH solutions and the hydrothermal treatment time.

With either phillipsite or hydroxysodalite, the higher the NaOH concentration, the shorter the time elapsed before the beginning of crystallization as

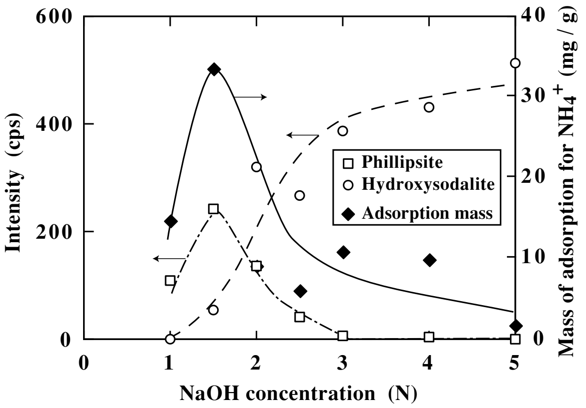

Fig. 3 XRD intensity and adsorption mass of NH_4^+ for products as a function of NaOHaq.concentration (Treatment time=12hr).

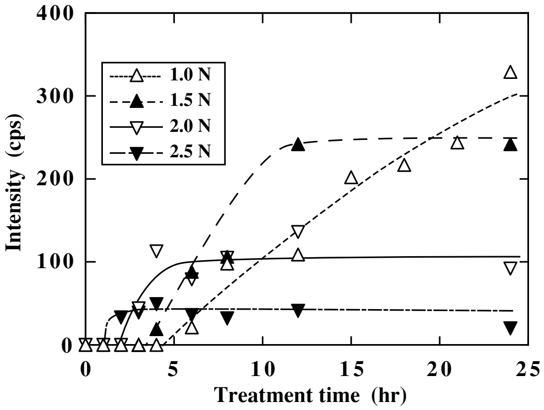

(a) Phillipsite [020]

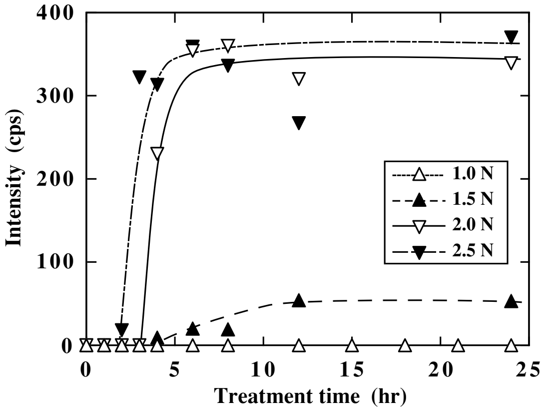

(b) Hydroxysodalite [110]

Fig. 4 Change in XRD peak intensity of products with treatment time for various NaOH concentrations.

well as the time before the completion of reaction at which the peak intensity levels off. Also, the gradient of peak intensity after the beginning of crystallization is greater with a higher NaOH concentration. From this finding, it can be judged that a higher NaOH concentration leads to a greater powder production rate for both phillipsite and hydroxysodalite as well as to earlier completion of the reaction. However, it is apparent that a higher NaOH concentration at the same time leads to a smaller proportion of phillipsite in the zeolite product and a greater proportion of hydroxysodalite, which is a byproduct. One possible reason for a smaller production mass with 1.0 N NaOH solution as shown in **Fig. 3** is that the reaction was not complete because the hydrothermal treatment time was 12 hours.

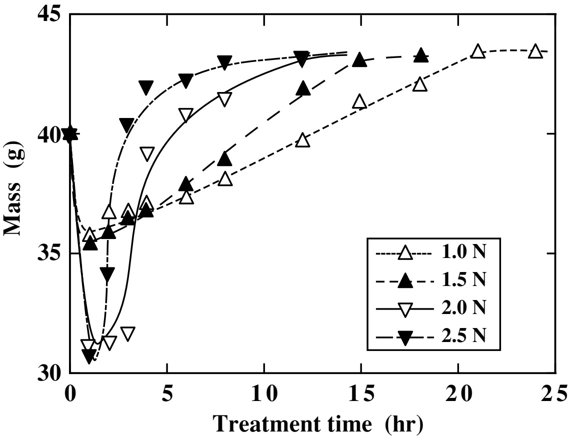

Fig. 5 Change in mass of products with treatment time for various NaOH concentrations.

Fig. 5 graphically illustrates the correlation between the mass of the powder product and the hydrothermal treatment time. With any NaOH concentration, the mass of the powder product first decreases and then increases as the treatment time elapses.

After leveling off, the mass remains virtually the same with all the NaOH concentrations. However, it is apparent that with a higher NaOH concentration, the magnitude of reduction in the mass of the powder product is small and the time elapsed after the increase in mass has leveled off and until the reaction is complete is shorter. These findings indicate that the dissolution rates of soluble Si species (such as silicate ion) and soluble Al species (such as aluminate ion) released from fly ash are greater with a higher NaOH concentration.

Fig. 6 graphically illustrates the time-dependent variation in soluble Si species concentration and soluble Al species concentration in the reaction liquid resulting from hydrothermal treatment with 1.5–2.5 N aqueous NaOH solutions. With any NaOH concentration, the concentrations of soluble Si species simply increase and gradually reach the same value.

Incidentally, the concentration of soluble Al species increases as the treatment time elapses, and eventually maximizes, and decreases to near-zero. Also, with a higher NaOH concentration, the time span during which the concentration of soluble Al species drops to zero is shorter. These findings indicate that zeolite production is promoted with a higher NaOH concentration.

The zeolite generation reaction from fly ash is considered to consist of a dissolution process for soluble Si species and soluble Al species from fly ash, and a zeolite generation process with both species. As illustrated in **Figs. 5** and **6**, when the concentration of NaOH used for the hydrothermal process is varied,

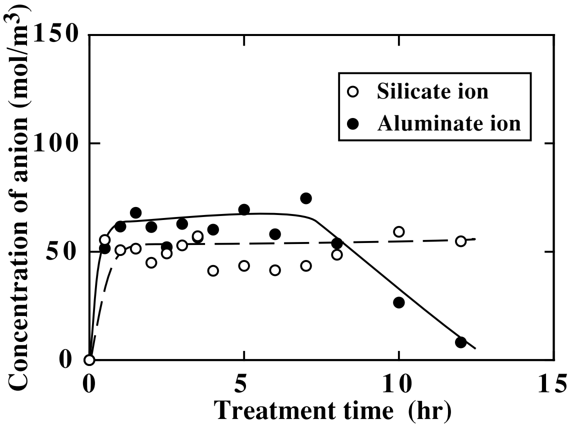

(a) NaOHaq. = 1.5 N

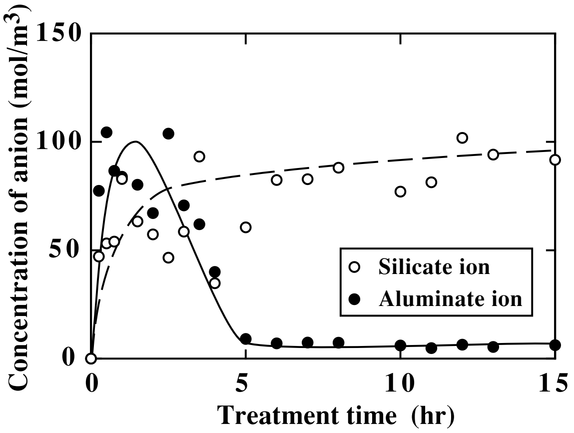

(b) NaOHaq. = 2.0 N

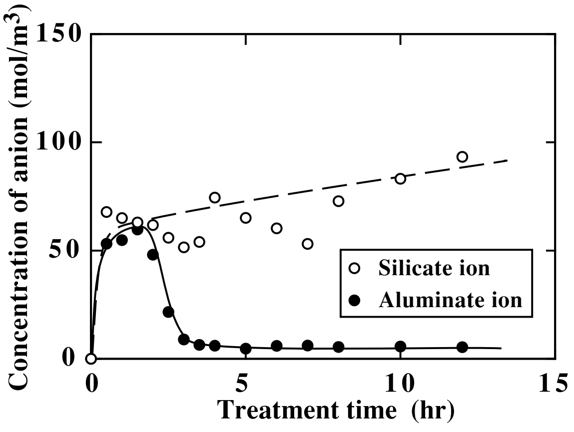

(c) NaOHaq. = 2.5 N

Fig. 6 Change in anion concentration in NaOHaq. with treatment time for various NaOHaq.concentrations.

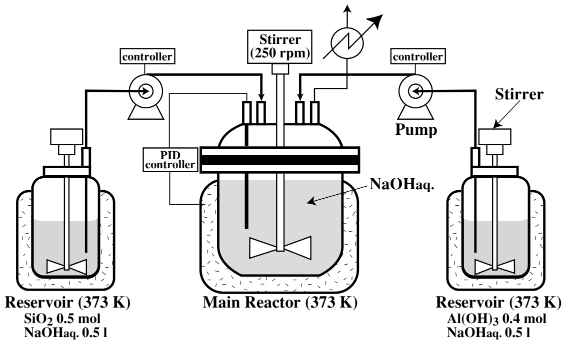

Fig. 7 Experimental set-up for hydrothermal synthesis from pure raw materials.

the rates of dissolution of soluble Si species and soluble Al species from fly ash vary. Because of this, the reason for the change in the crystal phase of the produced zeolite depending on the NaOH concentration may result from the variation in the dissolution rates. We investigated this using the experimental set-up illustrated in **Fig. 7**. The reaction system comprises a main reactor, an Si source reservoir and an Al source reservoir. Aqueous SiO_2-NaOH solution and aqueous Al $(OH)_3$-NaOH solution were poured into the main reactor at arbitrary rates with pumps in order to simulate the dissolution of soluble Si species and soluble Al species from fly ash. Also, the controllers were adjusted so that the mass of aqueous NaOH solution in the main reactor was 1.0 L at the time point at which the supply of the raw material solutions was stopped. Reaction conditions other than those mentioned above were the same as those for treatment of fly ash. Incidentally, the supply rates for raw material solutions were adjusted so that the concentrations of soluble Si species and soluble Al species in the main reactor, when the hydrothermal reaction did not take place, satisfied the variations in concentrations defined by the following equations, wherein K_{Si} represents the Si source supply rate constant and K_{Al} stands for the Al source supply rate constant.

$$\frac{dC_{Si}}{dt}=K_{Si}\ (C_{S,Si}-C_{Si}) \tag{4}$$

$$\frac{dC_{Al}}{dt}=K_{Al}\ (C_{S,Al}-C_{Al}) \tag{5}$$

Hydrothermal synthesis was performed with aqueous NaOH solutions of different concentrations while the pure raw materials were fed into the main reactor under the conditions that satisfied $K_{Si}=2.0\times10^{-5}s^{-1}$ and $K_{Al}=7.2\times10^{-4}s^{-1}$, total supplied moles number $M_{Si}=0.12$ mol ($m_{Si}=7.2\times10^{-3}$ kg) and total supplied moles number $M_{Al}=0.11$ mol ($m_{Al}=8.6\times10^{-3}$ kg). The XRD peak charts for the so-obtained powder products are given in **Fig. 8**. Note that even though the raw material supplying conditions were unchanged,

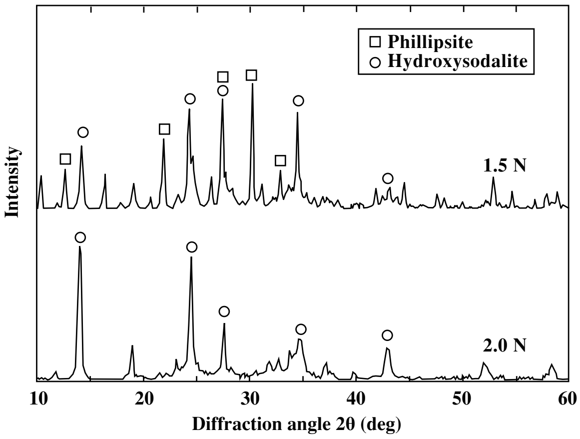

Fig. 8 XRD peak charts for products treated with various NaOHaq. concentrations ($K_{Al}=7.2\times10^{-4}$ s^{-1}, $K_{Si}=2.0\times10^{-5}$ s^{-1}, M_{Al}=0.11mol, M_{Si}=0.12mol, Treatment time=12hr).

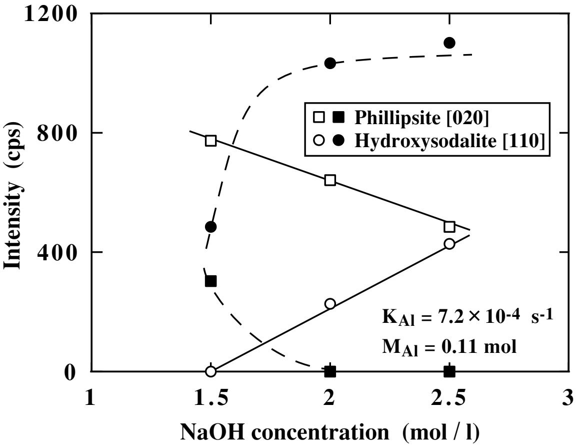

Fig. 9 Peak intensity of products synthesized from pure raw materials as a function of NaOH concentration for various experimental conditions (○□: M_{Si}/M_{Al}=1.2, K_{Si}/K_{Al}=0.11,●■: M_{Si}/M_{Al}=1.0, K_{Si}/K_{Al}=0.03).

powder products of different crystal phases were obtained. That is, the peaks of both phillipsite and hydroxysodalite phases are present when 1.5 N aqueous NaOH solution was used, while only hydroxysodalite occurred when the concentration of the aqueous NaOH solution used was 2.0 N.

Fig. 9 illustrates the correlation between NaOH concentrations and XRD peak intensities of the powder products, in cases where pure raw materials were supplied under the same conditions as those for the dissolution behavior from fly ash as well as in cases where the raw materials supply conditions were as summarized in **Fig. 8**. Under both sets of supply conditions, the peak intensity for phillipsite was low and the peak intensity for hydroxysodalite was high with a higher NaOH concentration, and, consequently, it is apparent that even when the raw material supply conditions remain unchanged, hydroxysodalite as a byproduct tends to occur with a higher NaOH concentration. Judging from these findings, when synthesizing zeolite from fly ash, the dissolution rate dependency of soluble Si species and soluble Al species released from fly ash on NaOH concentration does not constitute a major cause of NaOH concentration-dependency of the crystal phase of produced zeolite.

Next, we studied a method to inhibit the occurrence of hydroxysodalite as a byproduct when fly ash was subjected to hydrothermal treatment with high-concentration aqueous NaOH solution. Previously we showed that when 2.0 N aqueous NaOH solution is used, the occurrence of hydroxysodalite is inhibited by adding silica powder of a greater dissolution rate into the fly ash of low silica content [8, 9].

In the present study, we prepared 40.0 g of mixture by adding silica powder into fly ash, and subjected the mixture to 12-hour long hydrothermal treatment with aqueous NaOH solutions of various concentrations. **Fig. 10** illustrates the interrelation between the mass of added silica powder and the XRD peak intensity of the resultant powder products, and **Fig. 11** summarizes the correlation between the mass of added silica powder and the ammonium ion equilibrated adsorption mass for the resultant powder products. In hydrothermal treatment with aqueous NaOH solution of any concentration, the peak intensity for the phillipsite in the powder product is higher and the peak intensity for the hydroxysodalite is lower with a greater mass of the added silica powder. It is also apparent that with a higher concentration of aqueous NaOH solution, a greater mass for silica powder is necessary to inhibit the occurrence of hydroxysodalite. Therefore, even when hydrothermal treatment is performed with a high-concentration aqueous NaOH solution, phillipsite only can be selectively synthesized by using a raw material consisting of fly ash with the addition of silica powder. Incidentally, the pattern of ammonium ion equilibrated adsorption mass is similar to that for the peak intensity of phillipsite, and the adsorption mass simply increases with a higher NaOH concentration.In addition, the mass of ammonium ion adsorption is greater with hydrothermal treatment using an aqueous NaOH solution of lower concentration.Furthermore, as indicated by

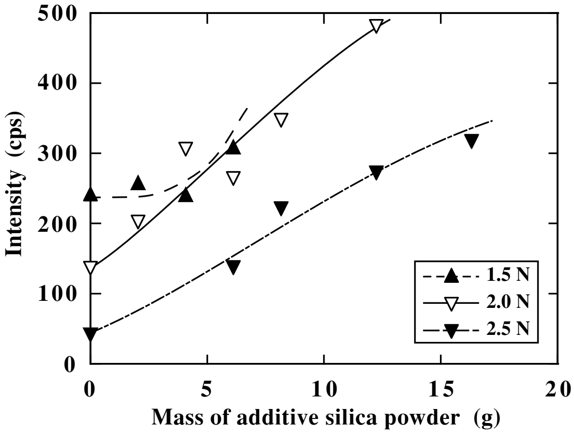

(a) Phillipsite [020]

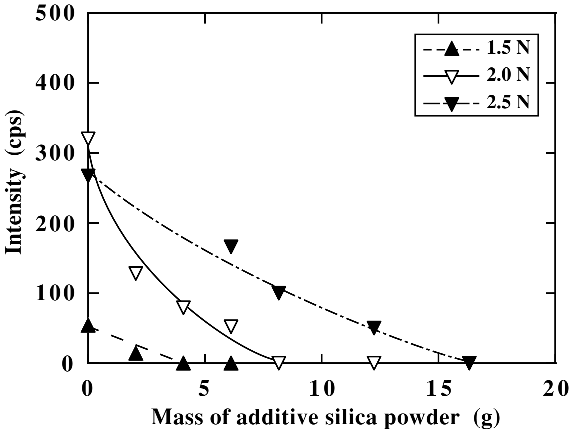

(b) Hydroxysodalite [110]

Fig. 10 XRD peak intensity of products as a function of additive silica mass for various NaOHaq. concentrations (Treatment time=12hr, Fly ash+Silica powder=40.0g).

the arrows in **Fig. 11**, the adsorption masses of ammonium for the powder products at a minimum silica powder addition that still inhibits the occurrence of hydroxysodalite are almost the same.

Fig. 12 illustrates the interrelation between the hydrothermal treatment time and the peak intensity for phillipsite in the powder product in the case where hydrothermal treatment was performed by adding the minimum mass of silica powder needed for inhibiting the occurrence of hydroxysodalite. Similar to the case where fly ash only was used as a raw material, a higher-concentration aqueous NaOH solution used for hydrothermal treatment leads to a quicker start to crystallization, a quicker completion of the hydrothermal reaction, and a steeper gradient of peak intensity after the start of crystallization.

Fig. 13 illustrates ammonium ion equilibrated adsorption masses with powder products that underwent hydrothermal treatment until the timings that are regarded as the completion of the reaction. In this chart, the adsorption masses for the powder products obtained under various conditions are virtually the same; therefore, it is possible to obtain powder products of similar adsorptivity not containing hydroxysodalite by controlling the proportion of silica components in the raw material, regardless of the concentration of the aqueous NaOH solution used for hydrothermal treatment.

Based on these findings, we determined the interrelation among the NaOH concentration, the silica powder mass that must be added to synthesize phillipsite only and the necessary hydrothermal treat-

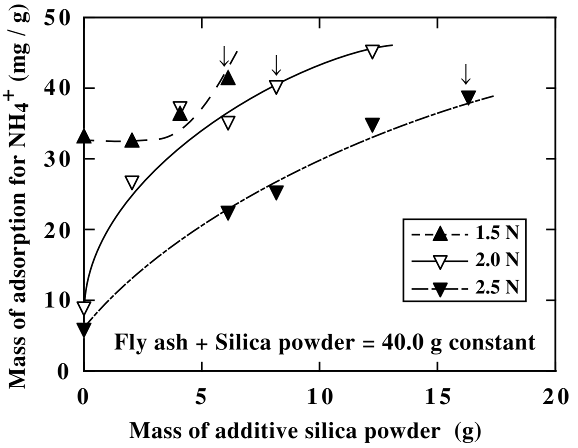

Fig. 11 Adsorption mass of NH_4^+ for products as a function of additive silica mass for various NaOHaq. concentrations (Treatment time=12hr, Fly ash+Silica powder=40.0g).

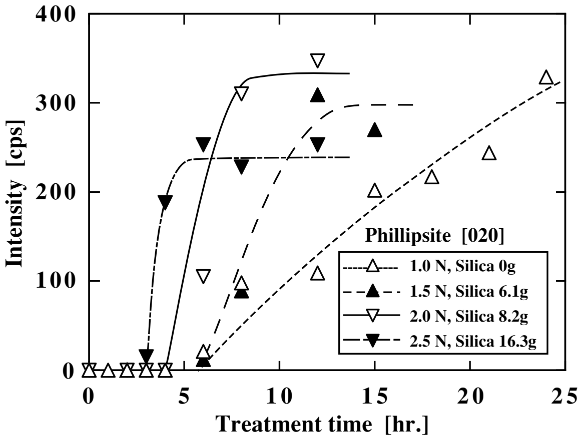

Fig. 12 Change in phillipsite peak intensity of products with treatment time for various NaOHaq. concentrations (Fly ash+Silica powder=40.0g).

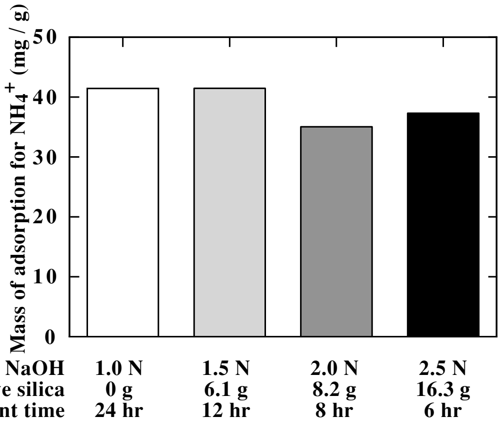

Fig. 13 Adsorption mass of NH_4^+ for products synthesized under various experimental conditions.

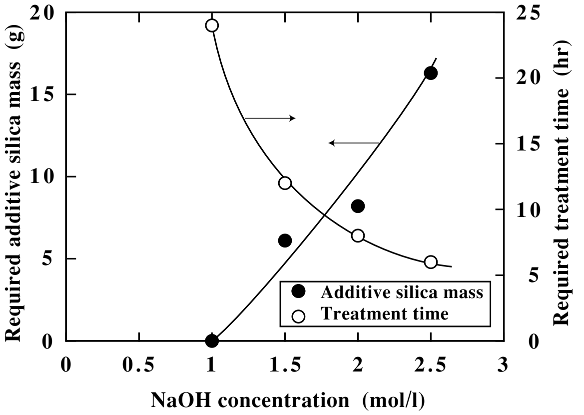

Fig. 14 Required additive silica mass and required treatment time for synthesizing phillipsite as a function of NaOHaq. concentration (Fly ash+Silica powder=40.0g).

ment time, and the resultant interrelation is summarized in **Fig. 14**. With a higher NaOH concentration, the silica powder mass that must be added to synthesize phillipsite only is greater, and the time needed to complete the reaction is shorter. Therefore, we can selectively synthesize phillipsite in a shorter time by adding a greater amount of silica powder into fly ash and subjecting the mixture to hydrothermal treatment with high concentration aqueous NaOH solution.

4. Conclusion

1) With a higher NaOH concentration in the hydrothermal treatment liquid, the proportion of phillipsite in the powder product will be lower and the proportion of hydroxysodalite will be higher.
2) With a higher NaOH concentration in the hydrothermal treatment liquid, the time elapsed before the start of the crystallization of zeolite will be shorter, and the zeolite crystal generation rate will be greater.
3) Phillipsite only can be selectively synthesized by using a raw material comprising fly ash with the addition of silica powder even when hydrothermal treatment is performed with high concentration aqueous NaOH solution, and with a higher NaOH concentration, the necessary silica powder mass increases.
4) When phillipsite is selectively synthesized by using a mixture of fly ash and silica powder as a raw material, the phillipsite generation rate increases with a higher NaOH concentration in the hydrothermal treatment liquid, thereby the treatment time can be shortened.

Acknowledgement

The present study was sponsored by Hosokawa Powder Technology Foundation.

Nomenclature

C_{Al}: concentration of $Al[OH]_4^-$ $[mol/m^3]$
C_{Si}: concentration of SiO_4^{4-} $[mol/m^3]$
$C_{S,Al}$: saturated concentration of $Al[OH]_4^-$ $[mol/m^3]$
$C_{S,Si}$: saturated concentration of SiO_4^{4-} $[mol/m^3]$
k_{Al}: dissolution rate constantof $Al[OH]_4^-$ from fly ash $[kg^{-1}\ s^{-1}]$
k_{Si}: dissolution rate constant of SiO_4^{4-} from fly ash $[kg^{-1}\ s^{-1}]$
$k°_{Si}$: dissolution rate constant of SiO_4^{4-} from additive silica $[kg^{-1}\ s^{-1}]$
K_{Al}: feed rate constantof $Al[OH]_4^-$ $[s^{-1}]$
K_{Si}: feed rate constantof SiO_4^{4-} $[s^{-1}]$
m_{FA}: mass of fly ash $[kg]$
m_{Si}: mass of additive silica powder $[kg]$
m_{Al}: mass of aluminium hydroxide powder $[kg]$
M_{Al}: total molar of fed $Al[OH]_4^-$ $[mol]$
M_{Al}: total molar of fed SiO_4^{4-} $[mol]$
t: treatment time $[s]$

References

1) Kankyou Gijyutsu Kyoukai and Nihon Fly Ash Kyoukai ed.: “Coal Ash Handbook”, pp. II-4 (1995).
2) Kankyou Gijyutsu Kyoukai and Nihon Fly Ash Kyoukai ed.: “Coal Ash Handbook”, pp. II-219 (1995).
3) Haruna,J.: “Japan Patent”, 01-24014 (1989).
4) Haruna,J.: “Japan Patent”, 03-45512 (1991).

5) Kato,Y., K.Kakimoto, H.Ogawa, M.Tomari and E.Sakamoto: “An Application of Hydrothermal Crystallized Coal Ashes to Waste Water Treatment 1”, Industrial Water, **33**, 27-33 (1986).

5) Touyama,Y., K.Katayama and M.Meguro: “NH_4^+−Adsorption Characteristics of Zeolites Synthesized from Fly Ashe”, J.of Chem. Soc. of Japan, **2**, 136-140 (1996).

6) Querol,X., F.Plana, A.Alastuey and A.Lopez-Soler: “Synthesis Na-zeolites fromfly ash”, Fuel, **76**, 793-799 (1997).

7) Scott,J., D.Guang, K.Naeramitmarnsuk, M.Thabuot and R.Amal: “Zeolite Synthesis from Coal Fly Ash for the Removal of Lead Ions from Aqueous Solution”, J.Chem. Technology and Biotechnology, **77**, 63-69 (2002).

8) Fukui,K., H.Yoshida, H.Sakaguchi and M.Arita: “Zeolite Synthesis from Coal Fly Ash Prepared by Hydrothermal Treatment Method and Effect of Particle Size on its Reaction Mechanism”, Kagaku Kogaku Ronbunshu, **25**, 987-992 (1999).

9) Fukui,K., M.Kinugawa, T.Nishimoto and H.Yoshida,: “Effect of Fly Ash Content on Zeolite Synthesis from Coal Fly Ash Prepared by Hydro-thermal Treatment Method”, Kagaku Kogaku Ronbunshu, **28**, 155-160 (2002).

10) Suyama,Y., S.Hanada, F.Miyaji and N.Kayahara,: “Synthesis and Properties of FA-Zeolite-Sepiolite Composite Adsorbent”, J.Ceram. Soc. Japan, **109**, 155-161 (2001).

Author’s short biography

Kunihiro Fukui

Kunihiro Fukui received his bachelor’s and master’s degree in Chemical Engineering from Kyoto University in 1991 and 1993. He got his Ph.D in Chemical Engineering from Kyoto University in 1998. He has been a Associate Professor of Chemical Engineering Department at Hiroshima University since 2005, followed by his career of a Research Instructor. His major research interests are accurate size classification, measurement method of particle size distribution and synthesis of functional material from industrial waste.

Takashi Nishimoto

He received his bachelor’s and master’s degree in Chemical Engineering from Hiroshima University. He is now working as a engineer of Ryomei Giken Co., LTD.

Mayumi Takiguchi

She received his bachelor’s and master’s degree in chemical Engineering from Hiroshima University. He is now working as a engineer of Sumitomo Dow LTD.

Hideto Yoshida

Hideto Yoshida has been a Professor of Chemical Engineering Department at Hiroshima University since 1994. His major research interests are fine particle classification, numerical simulation of cyclone separator, cut size control of classifier.

Effects of Frictional Force on the Formation of Colloidal Particle Monolayer During Drying—Study Using Discrete Element Method—[†]

H. Nishikawa[1], **M. Fujita, S. Maenosono, Y. Yamaguchi and T. Okudo**
Department of Chemical System Engineering, The University of Tokyo[*]

Abstract

This paper presents the effect of frictional force between colloidal particles and a solid substrate on the formation of particle monolayer by a numerical simulation. Discrete Element Method is employed to simulate the dynamics of colloidal particles trapped in liquid film. Forces such as capillary immersion force, van der Waals force and frictional force are included in the simulation model. Isotropic ordering factor and non-dimensional boundary length are introduced to quantify the structures of colloidal particles. In the case where the diameter of colloidal particles ranges from 100nm to 1000nm, the monolayer structures depend strongly on the frictional constant between a particle and a solid substrate. On the other hand, in the case where diameter is about 10nm, large domains of hexagonal close-packed structuers are formed because of the Brownian force.

Keywords: Particle Monolayer, Discrete Elment Method, Substrate Friction

1. Introduction

In material nanotechnology, techniques for arranging nanoparticles/colloidal particles in a regular pattern are required. For example, a two-dimensional array (monolayer) involving nanoparticles/colloidal particles is used as a mask for lithography[1)]. Methods for forming a two-dimensional array include the Langmuir-Blodgett (LB) process, self-assembled monolayer (SAM) process, electrophoretic process and liquid membrane process. The liquid membrane process in which a colloidal dispersion solution is applied to and allowed to dry on a solid substrate is a promising processes. In a drying process within the liquid membrane process, when the liquid membrane is thinner than the particle diameter, a meniscus is formed between particles, thereby a long-distance attractive force known as a lateral capillary force occurs between particles. Mainly by this force, a particle group collects through a self-assembly phenomenon. Other than the lateral capillary force, various factors affect the arrangement structure of a particle group. Examples of these factors include the Brownian force, frictional drag from a substrate and the DLVO force. Clarifying the relation between various factors and resultant structures will make it possible to draw up a guideline for efficient preparation of material.

In order to form a colloidal particle membrane through a liquid membrane process, two-dimensional arrays consisting of polystyrene latex particles or protein particles have been produced as in the case of a series of studies by Nagayama et al.[2-4)]

The correlation between process conditions and the structure of particles has been studied[5,6)]; how-

---

[†] This report was originally printed in J. Soc. Powder Technology, Japan, 41 (6), 465-472 (2004) in Japanese, before being translated into English by KONA Editorial Committee with the permission of the editorial committee of the Soc. Powder Technology, Japan

[*] 7-3-1, Hongo, Bunkyo-ku, Tokyo 113-8656, Japan

[1] Corresponding author
TEL: +81-82-424-7715 FAX:
E-mail: hiroyuki.nishikawa@mizuho-ir.co.jp

ever, the various factors that affect the structure have not been studied comprehensively because experiments in which each of a plurality of processes is independently varied are difficult. Nevertheless, with the advance in computer simulations the dynamics of particles can now be directly tracked, and a multiplicity of processes can be studied while varying particular parameters independent of other parameters. We have simulated a colloidal particle arrangement process[8-10] based on a liquid membrane process, considering the Brownian force, frictional drag from a substrate and the DLVO force by adopting a discrete element method (DEM)[7]. As a result, we have found that the actual arrangement structure quantitatively matches those experimentally obtained and have shown that this simulation technique is useful as a means of estimating the structure of particles. In the present study, we focus on the effect of friction from a substrate, which poses a significant effect in an actual system. We perform a series of calculations for particle diameters in a wider range of 10–1000nm and varied the decrease rate of liquid membrane thickness, and studied the correlation between the frictional drags from substrates, particle diameters and drying rates of solvents and the structures.

2. Simulation Technique

2.1 Motion equation for particles

In a system where a group of particles move within a plane, the motion equation used for individual particles in a translational motion is the Langevin's equation that is used in nonequilibrium Brownian dynamics[11].

$$m\frac{dv_i}{dt}=F_i-\xi v_i+F_{eff}^{B} \tag{1}$$

A rotational motion for individual particles can be expressed by the law of angular momentum.

$$I\frac{dw_i}{dt}=M_i \tag{2}$$

Fi includes an inter-particle contact force, a lateral capillary force and a frictional drag from a substrate, each considered in the DEM. ξ represents the Stoke's drag coefficient. In our system, the particles are partially immersed in a solvent, and the proportion of immersed particles varies depending on the height of the liquid membrane. Therefore, we took the proportion of the horizontal projected area of the region of the particles immersed in the solvent to the whole area as s, and then defined x using the following formula:

$$\xi=s\times 6\pi\alpha\eta \tag{3}$$

For time quadrature of a motion equation, the predictor-corrector velocity Verlet method used in the molecular dynamics was employed. This scheme features the 2nd order accuracy for time steps, and can be applied when the force acting on particles, determined by calculating the predicted velocity, is a function of position-velocity. Thus, this method is suitable for our model that incorporates a drag from a solvent and a frictional drag from a substrate.

2.2 Forces acting on particles

2.2.1 Brownian oscillating force

When in a liquid membrane, particles are in contact with a solvent, and are therefore subjected to the Brownian force that is derived from the thermal agitation of the solvent. The Brownian force is obtained as a probable random force in accordance with normal distribution. When the entire surface of individual particles is fully immersed in a solvent, the Brownian force of particles moving in a two-dimensional plane can be expressed by the formulas below:

$$\left\langle F^{B}(t)\right\rangle=0 \tag{4}$$

$$\left\langle F^{B}(t)\cdot F^{B}(t)\right\rangle=\frac{24\pi\alpha\eta K_B T}{\Delta t} \tag{5}$$

In a manner identical to that for the Stoke's drag, the effective Brownian force was defined, assuming that particles were partially immersed in a solvent, by using the following formula:

$$F_{eff}^{B}(t)=s\times F^{B}(t) \tag{6}$$

2.2.2 Inter-particle contact force

When particles come into contact with each other, viscoelasticity occurs between particles. With DEM, this force is simulated with the Voigt model, which consists of a spring for representing an elasticity term and a dashpot for representing a viscosity term, wherein the spring and dashpot are situated in parallel. Incidentally, each contact force is determined after division in the normal direction and the tangential direction, wherein a friction slider is inserted in the tangential direction to represent the frictional drag between particles.

2.2.3 Lateral capillary force

The lateral capillary force working between two particles in a liquid membrane can be, if these particles are colloidal particles, approximated with the following formula[12] (**Fig. 1**).

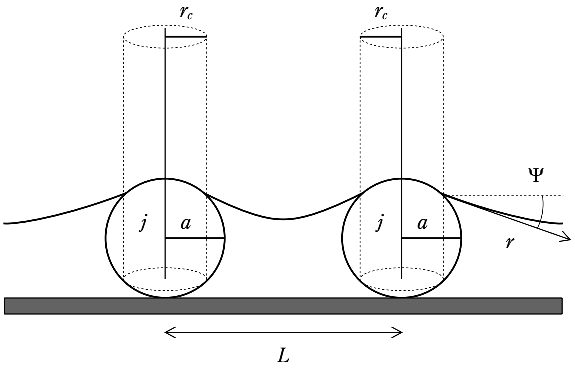

Fig. 1 Capillary immersion force between two particles.

$$F^m = \frac{2\pi\gamma Q^2}{L} \tag{7}$$

where, Q is a capillary charge, and is defined by the formula below:

$$Q = r_c \sin\psi \tag{8}$$

(where r_c stands for the radius of a circle defined by the interfaces of three phases (particles, solvent, air).) For an actual system, an effective lateral capillary force from a multiplicity of particles needs to be calculated. For this purpose, we determined an effective lateral capillary force, considering the screening effect[9].

When the particle diameter is about 10 nm, a liquid membrane cannot stably exist on a solid substrate. As a result, with a greater inter-particle distance, the meniscus will be cut off and the lateral capillary force seems to fail to function. Therefore, assuming that the meniscus can be approximated with a parabola, the meniscus cut-off distance[10] is approximated using the following formula:

$$L_{cut} = \frac{4h}{\tan\psi} + 2rc \tag{9}$$

(where h represents the height of interfaces of three phases above the surface of the substrate, provided that the height of the interfaces of three phases is assumed to be common with all the particle types.)

When an inter-particle distance is greater than this value, the lateral capillary force is taken as 0.

When the particle diameter is approximately 1 μm, a flat liquid surface seems to occur even though the particles are far apart from each other. As a result, the meniscus cut-off distance will be underestimated. However, in the present study, we studied the effect of particle diameter, and concluded that application of the same model not governed by a particle diameter was needed; therefore, we considered the effect of cut-off of the meniscus.

2.2.4 Frictional drag from substrate

When the vertical component of surface tension is not 0, particles receive static friction and dynamic friction from a substrate. A DLVO force is present between a substrate and particles. For convenience, we supposed that a substrate was inactive to particles. Also, we assumed that the maximum static frictional coefficient and the maximum dynamic frictional coefficient take the same value, and that the frictional drags are governed by the classic Coulomb frictional drag. A static frictional drag is represented by the following formula[10]:

$$\begin{aligned} F^f &= -F_0 & &; |F_0| < \mu_{ps} Z \\ F^f &= -\mu_{ps} Z \frac{F_0}{|F_0|} & &; |F_0| > \mu_{ps} Z \end{aligned} \tag{10}$$

At the same time, a dynamic frictional drag is defined as:

$$F^f = -\mu_{ps} Z \frac{v_i}{|v_i|} \tag{11}$$

where,

$$Z = 2\pi\gamma Q \tag{12}$$

When the magnitude of the resultant of forces other than the frictional drags acting on particles is not greater than the magnitude of maximum static frictional drag, the particles remain motionless.

2.2.5 Van der Waals force

Van der Waals force deriving from fluctuation in induced dipole of atoms occurs between particles. The magnitude of the van der Waals force working between particles is defined by the following formula[13]:

$$F^{vdw} = \frac{Aa}{12(L-2a)^2} \tag{13}$$

When particles are situated in a solvent, an electrostatic repelling force acts between the particles. In the present study, we supposed that the effect of frictional drag from a substrate could be more clearly defined through calculation with a purer system, and did not included the term for an electrostatic repelling force.

2.3 Simulation conditions

In the present study, we assumed monodispersed colloidal silica particles as colloidal particles and water as a solvent*). The calculation cell was in the form of a square with one edge measuring 40D, while cyclic boundary conditions were set in two directions. The number of particles within the cell was adjusted

Table 1 Physical conditions for the simulations

Parameter	Value
Young's modudus of a particle	7.3×10^{10} (Nsm^{-2})
Poisson ratio of a particle	0.173
Viscosity of liquid, η	8.91×10^{-4} (Nsm^{-2})
Surface tension of liquid, γ	7.20×10^{-2} (Nm^{-1})
Evaporation speed of liquid	1.0×10^{-2} (ms^{-1})
Hamaker constant, A	8.3×10^{-21} (J)
Contact angle between a particle and liquid	20 (degree)
Zata potential	0 (mV)

to 1296. This setting coincided with a coverage ratio of 0.702. **Table 1** summarizes the calculation conditions including the physical properties of the particles and solvents. The actual calculation was performed by converting various amounts into nondimensional values including representative values of particle diameter α, solvent surface tension γ and particle mass m.

In the initial state, the particles were arranged at random and their initial velocity was set to 0 so that they did not collide with each other, and the thickness of the liquid membrane was the same as the diameter of particles.

The calculation was repeated until the meniscus was cut off with every particle pair as the height of the liquid membrane decreased.

For the present study, the viscous drag from a fluid acting on particles was expressed using the Stokes drag model. In contrast with an actual system, an effective viscous drag is significantly large because of factors including the lubrication effect, which is important when particles are in closer vicinity. As a result, when the Stokes drag model is employed, the particle move velocity is overestimated. Incidentally, with the our system, the "proportion of particle movement velocity to liquid surface decrease velocity" governs the degree of aggregation of a particle group. Accordingly, we compensated for the overestimation in particle move velocity with an increased liquid surface decrease velocity of 1.0×10^{-2} ms^{-1} in order to maintain the above-mentioned proportion at a value obtained from the experiment and to quantitatively express the self-assembly process of particles during the drying process.

2.4 Analysis for arrangement structure

In order to evaluate particle arrangement structures, two indices, that is, an ordering factor and a nondimensional boundary length, were introduced[10].

2.4.1 Ordering factor

Delaunay triangles are obtained by subjecting an arrangement structure to the Voronoi polygonal division, and by connecting particles with line segments that are vertical to the edges of Voronoi polygons. Then, the triangles formed by connecting the centers of all the particles involved are gathered, and polygons composed of these triangles are considered. If the surroundings of particles are most densely packed, the resultant polygons will be regular hexagons. Then, the proportion of the so-formed regular hexagons to all the particles is defined as an ordering factor.

We call this index the Isotropic Ordering Factor (IOF).

2.4.2 Nondimensional boundary length

The characteristics of a particular arrangement structure that cannot be evaluated with an ordering factor can be evaluated using an index that is characterized by the boundary length of an aggregated body. To determine the boundary length of an aggregated body, the coordination numbers of the particles involved are utilized, wherein a coordination number is defined as "a number of other particles with which a given particle is in contact". As to individual particles, the region not in contact with other particles corresponds with the boundary of the aggregated body. (A shorter boundary length means more progressed aggregation with a particle group.) A Nondimensional Boundary Length (NBL) is defined using the following formula:

$$NBL=\frac{1}{6n}\sum_{\kappa}(6-\kappa)N(\kappa) \tag{14}$$

With formula (14), the solution is 1 with the initial state; 0.83 when all the particles take the form of dimer; and 0 when all the particles form the most densely packed structure.

---

*) When the solvent is water, the minimum thickness of the liquid membrane that can be stably present on a substrate is approximately 100 nm, and it is impossible to obtain a liquid membrane whose thickness measures several nm. For the present study, we assumed a solid substrate that had a high-energy surface to allow a several nm thick liquid membrane to stably exist.

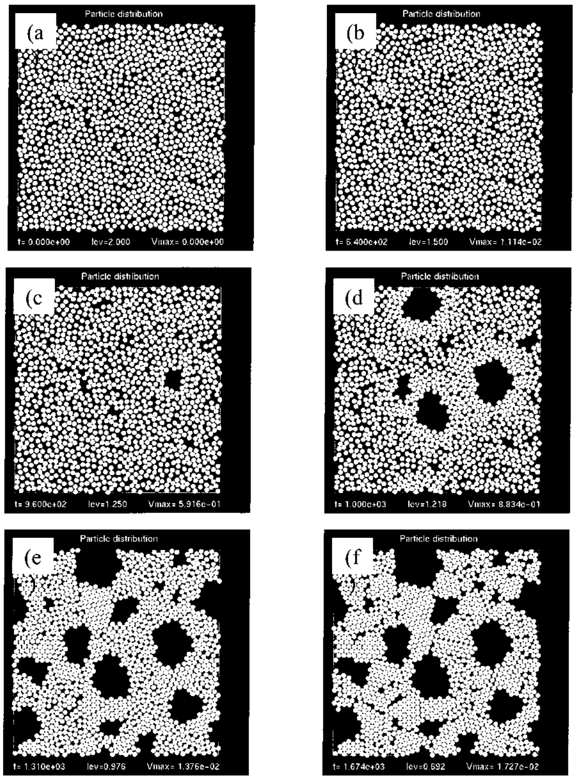

Fig. 2 Snapshots of colloidal particles calculated for D=100nm and μ_{ps}=0.1. (a)h=2.000, (b)h=1.500, (c)h=1.250, (d)h=1.218, (e) h=0.976, (f)h=0.692.

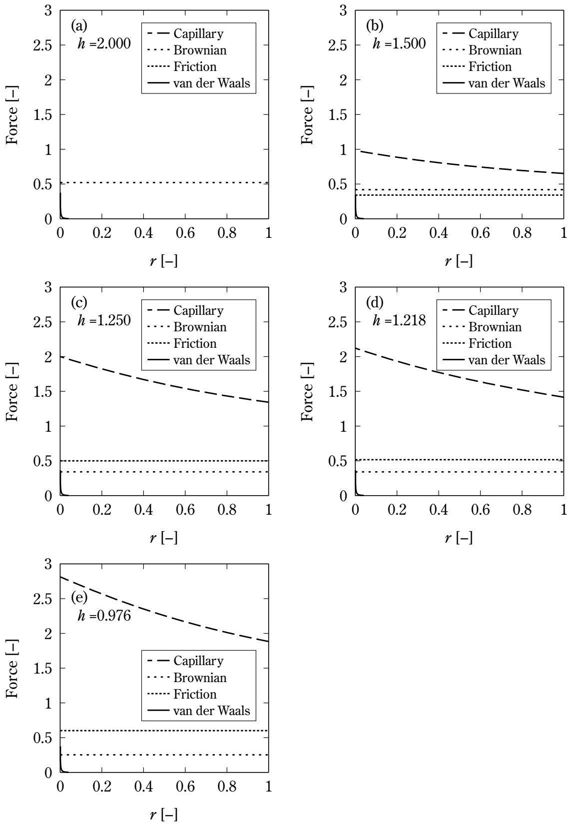

Fig. 3 Force curve for D = 100nm and μ_{ps}=0.1, (a)h=2.000, (b)h=1.500, (c) h=1.250, (d) h=1.218, (e) h=0.976.

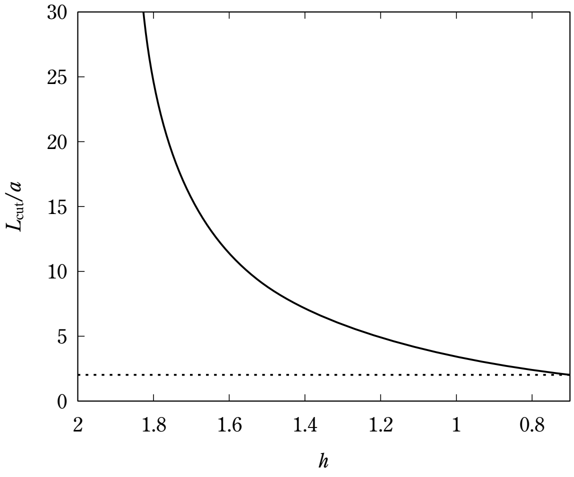

Fig. 4 Cut-off distance of capillary immersion force with h.

3. Result and Discussion

3.1 Examples of arrangement process

Fig. 2 illustrates several snapshots for the arrangement process where D=100 nm and μ_{ps}=0.1. (t represents a nondimensional time, *lev* a liquid membrane thickness and *V*max the absolute value of the maximum velocity of particles.)

Fig. 3 illustrates the distance-dependency of the magnitude of nondimensional forces associated with the snapshots in **Fig. 3**, and **Fig. 4** shows plotting of the interrelation between the liquid membrane thickness and meniscus cut-off distance. Note that the Brownian forces in **Fig. 3** are standard deviations of force.

Fig. 2(a) illustrates the initial state, where the particles appear to have been randomly distributed. When the liquid membrane thickness drops below the particle diameter, a meniscus occurs between particles, thereby a lateral capillary force acts between particles. At the same time, because the component perpendicular to the surface tension is no longer 0, the frictional drag from a substrate also acts on particles.

Fig. 2(b) is a snap shot for h=1.500. Several particles are in contact with adjacent particles, forming dimers while most particles remain apart from other particles. From **Fig. 3(b)**, the lateral capillary force appears to be dominant; however, because the screening effect is introduced, the effective lateral capillary force is smaller than 1/10 the two-body force. Consequently, the resultant force consisting of the lateral capillary force and the Brownian oscillating force is not greater than the frictional drag from a substrate, and the particles cannot move. With certain particles, the resultant force consisting of the lateral capillary force and the Brownian force is greater than the frictional drag from a substrate, thereby these particles come into contact with adjacent particles. Then, these particles remain motionless as they remain in contact with other particles owing to the frictional drag from a substrate and the van der Waals force.

When the level of the liquid membrane drops to h=1.2 (**Fig. 2 (c), (d)**), a plurality of regions that lack particles occur (voids), and these voids grow rapidly.

In particular, certain particles around these voids may have the most densely packed structure. As the effect of the lateral capillary force is greater (**Fig. 3(c), (d)**), more particles gradually start moving; and at the same time, the size of the voids becomes greater. In particular, the effective lateral capillary force acting on the particles around the voids greatly increases, thereby aggregation of particle groups occurs. When the height of the liquid membrane decreases to about h=0.976, several domains and larger voids appear, and aggregation seems to be virtually completed. At this time, the Brownian force further decreases (**Fig. 3(e)**). On the other hand, when the meniscus cut-off distance drops below two times the particle diameter (**Fig. 4**), the meniscus between domains is cut off, the effective lateral capillary force acting on the particles around each domain increases, thereby the particles around each domain are forced into each domain. Typically by this effect, rearrangement takes place, leading to the final state (**Fig. 2(f)**). When **Fig. 2(e)** is compared with **Fig. 2(f)**, clearer boundaries are found in **Fig. 2(f)**. For a two-dimensionally arranged membrane formed by a liquid membrane process too, it seems that when the liquid membrane thickness decreases and the liquid membrane between domains is cut off, the grain boundaries develop.

3.2 Effect of frictional drag from substrate on the arrangement process

Fig. 5 illustrates a time-dependent change in NBL for D=100 nm and μ_{ps}=0.0–1.0. If there is no frictional drag from a substrate (μ_{ps}=0.0), and when $1.4<h<2.0$, the NBL simply decreases.

This seems to be because the particle groups come into contact with each other owing mainly to the lateral capillary force, and once the particle groups are in contact with each other, the van der Waals force acts between the particles, thereby the particles do not come off from other particles. Then, domains consisting of the most densely packed particle groups are formed, and aggregation does not progress further; as a result, the value of NBL remains unchanged. However, the NBL again decreases when $0.8<h<1.0$. This seems to be because, as mentioned in Sec. **3.1**, a meniscus between domains is cut off, leading to development of particle rearrangement in the domains.

If a substrate provides drag and when $1.9<h<2.0$, the NBL temporarily decreases, and then remains at a particular value. This is because the effective lateral capillary force does not exceed the frictional drag from a substrate, and, as a result, the particles remain motionless. Then, when the thickness of the liquid membrane decreases and the effective lateral capillary force exceeds the frictional drag from a substrate, aggregation proceeds. However, with a greater μps, the start of domain formation delays. In other words, the meniscus cut-off distance is shorter and

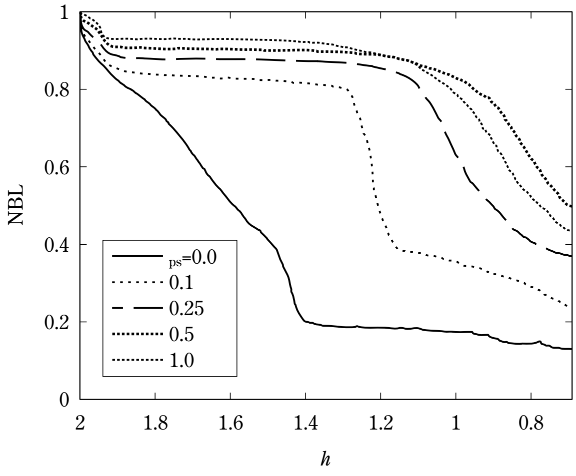

Fig. 5 NBL with h for D = 100nm and μ_{ps}=0.0 - 1.0.

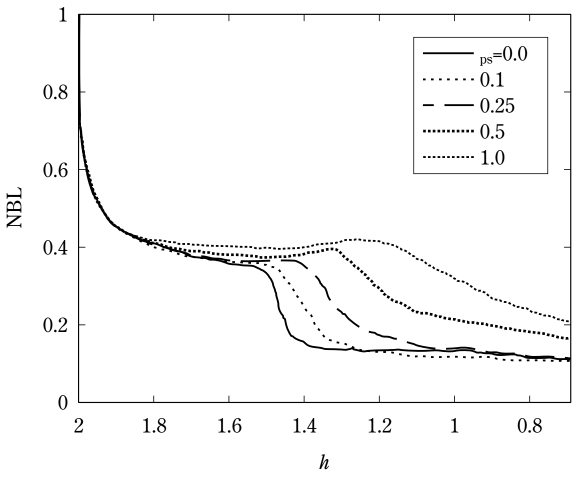

Fig. 6 NBL with h for D = 10nm and μ_{ps}=0.0 - 1.0.

the time elapsed before completion of drying is also shorter, the NBL in the final state is much greater.

Fig. 6 illustrates time-dependent change in the NBL for D=10 nm and μ_{ps}=0.0–1.0. Regardless of whether or not the frictional drag from a substrate is present, the NBL drops to about 0.4 when 1.9<h<2.0. This is because many particles are in contact with each other due to the Brownian force to form a network structure. At this time point, however, there are few domains that are most densely packed. If μ_{ps}=0.0, 0.1 or 0.25, and when 1.2<h<1.5 and the effective lateral capillary force is greater, the formation of denser domains begins.

Consequently, the NBL again decreases, and drops to about 0.10. On the other hand, if μ_{ps}=0.5 or 1.0, and when h<1.4, progress of aggregation is slower. Nevertheless, when compared with the case where D=100 nm, and when μ_{ps} is the same, the case where D=10 nm exhibits an apparently smaller NBL in the final state as well as the formation of domains.

3.3 Effect of frictional drag from the substrate and particle diameter on the arrangement structure

Fig. 7 shows snapshots for the terminal state for D=10 or 100 nm, μ_{ps}=0.0, 0.25 or 0.5. For μ_{ps}=0.0 (**Fig. 7(a)(i), (b)(i)**), no significant difference is found between the case with D=100 nm and the case with D=10 nm, and there are a plurality of domains and voids with both cases.

When D=100 nm, the region of domains is smaller with greater μ_{ps} (**Fig. 7(a)(ii), (iii)**). With greater μ_{ps}, the height of the liquid membrane, which is mainly governed by the lateral capillary force, is smaller. More specifically, the meniscus cut-off distance is smaller and the time span where aggregation develops is shorter; as a result, drying ends though the formation of domains does not fully take place.

When D=10 nm and even though μ_{ps}=0.25, larger domains exist (**Fig. 7(b)(ii)**). At μ_{ps}=0.5, the domains are smaller (**Fig. 7(b)(iii)**) but are still larger compared with the case for D=100 nm. This is because the Brownian force exceeds the frictional drag from a substrate, and, as a result, the particles move at random, promoting aggregation.

Consequently, although a frictional drag from a substrate is present, greater domains are formed.

Fig. 8 illustrates the dependency of IOF on a substrate frictional drag coefficient in the final state for D=10−1000 nm and μ_{ps}=0.0−1.0. If D>50 nm, the IOF value decreases with a greater μ_{ps} and becomes closer to 0. Incidentally, if D=10 nm, and when 0.0<μ_{ps}<0.25, the IOF value is greater than 0.35, and larger domains are formed. When μ_{ps}>0.5, the IOF value is smaller; however, the IOF value for a same μ_{ps} is still significantly large. In other words, the motion of particles is inhibited by a frictional drag from the substrate; when D<25 nm, the effect of the Brownian force is significantly exhibited, and the ordering factor increases. In our study, the effect of the Brownian force was apparent only in the case of D<25 nm. It may be possible to determine conditions that allow

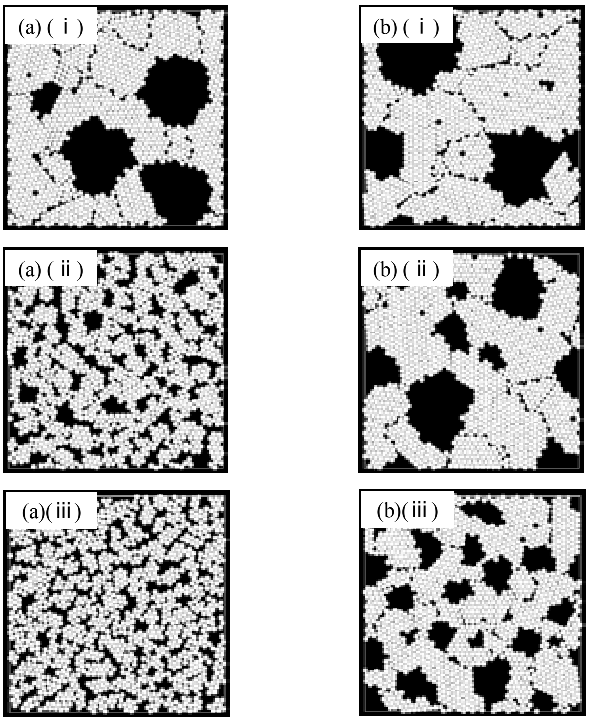

Fig. 7 Snapshots of colloidal particles at the final state.
(a) D = 100nm. (i) μ_{ps} = 0.0, (ii) μ_{ps} = 0.25, (iii) μ_{ps} = 0.5 ;
(b) D = 10nm. (i) μ_{ps} = 0.0, (ii) μ_{ps} = 0.25, (iii) μ_{ps} = 0.5.

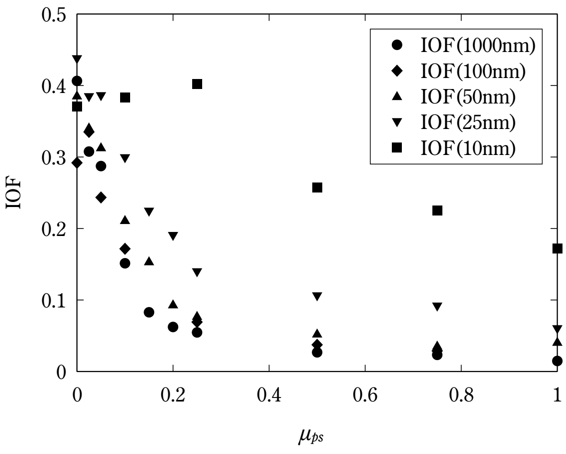

Fig. 8 IOF of the final siate for D = 10 -1000nm and μ_{ps} = 0.0 - 1.0.

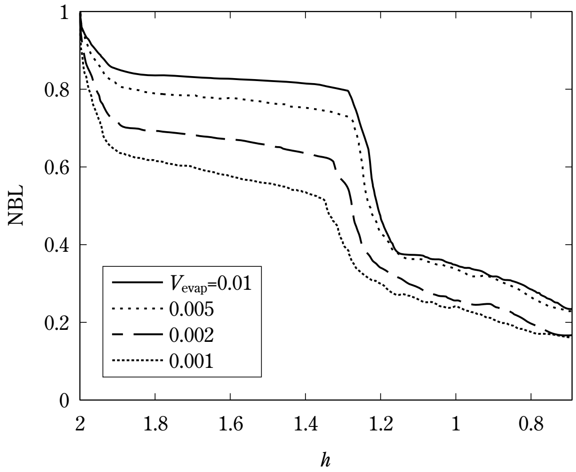

Fig. 9 NBL with h for D=100nm, μ_{ps}=0.1 and V_{evap} = 1.0 × 10^{-3}-1.0× 10^{-2} m s^{-1}.

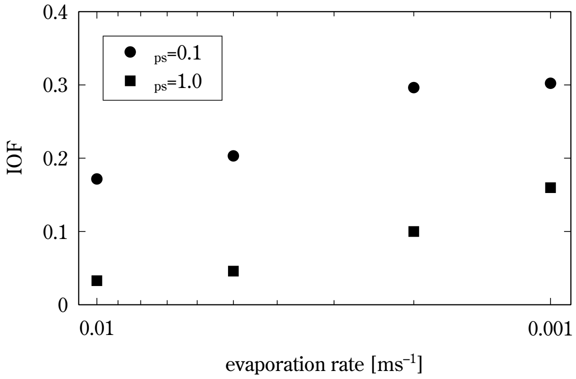

Fig. 10 IOF for D = 100nm, μ_{ps}= 0.1, 1.0 and V_{evap} = 1.0 × 10^{-3} 1.0 × 10^{-2} m s^{-1}.

the formation of greater domains in the cases where the particle diameter is 25 nm or greater, by searching for the conditions that allow the Brownian force to work effectively.

3.4 Effect of frictional drag from the substrate and the liquid membrane thickness decrease speed on the arrangement structure

Fig. 9 illustrates the time-dependent change in the NBL for the liquid membrane thickness decrease rates of 1.0, 2.0 and 5.0 × 10^{-3} ms^{-1} when D=100 nm and μ_{ps}=0.1. With a lower liquid membrane thickness decrease rate and when $1.9<h<2.0$, the degree of decrease in NBL is greater.

This is because more particles come into contact with other particles due to a longer time in which the Brownian force can work efficiently. Then, the NBL remains at a constant value, and again decreases when $1.3<h<1.4$. With the same h, a lower liquid membrane thickness decrease rate leads to a lower NBL value.

Fig. 10 shows the IOF values of the arrangement structures obtained from D=100 nm, μ_{ps}=0.1 and 1.0. As to two frictional coefficients, a lower liquid membrane thickness decrease rate leads to a greater IOF value. It appears to be possible that by further decreasing the liquid membrane decrease rate, domains are formed that are comparable with those formed when there is no frictional drag from a substrate.

3.5 The coefficient of friction between the substrate and particles in the experiment

In the present study, we examined the effect of the friction from a substrate on arrangement structures of particles. The coefficient of friction between colloidal particles in liquid and a substrate as well as the mechanism of friction between colloidal particles in liquid and a substrate are unknown. One example of results from studies in this field is a report where frictional drags between latex particles (particle diameter 100 or 300 nm) and a mica substrate in water were measured by LFM (Lateral Force Microscopy)[14]. According to this report, if a frictional drag is compatible with Coulomb's law, the frictional coefficient should be in the order of 1. The reason why the frictional coefficient takes such a value, although a mica substrate is very smooth in the atomic order, is unknown. And, it is likely that with other systems too (in particular, systems with rough-surfaces substrates), the coefficient of friction between particles and a substrate is not 0. Therefore, we cannot ignore the effect of the substrate involved.

4. Conclusion

We have modeled an arrangement process for colloidal particles with a liquid membrane process, and have studied the effect of frictional drag from a substrate on arrangement structure of particle groups. When a particle diameter is 100 nm or greater, the frictional drag from a substrate inhibits movement of the particles, thereby the coefficient of friction between a substrate and particles significantly affects the arrangement structure. On the other hand, when a particle diameter is about 10 nm, the Brownian force promotes particle movement, thereby densely packed domains are obtained even though the frictional drag from a substrate is present. Even if the ordering factor is otherwise small, the drying rate may be lowered so that the forces including a lateral capillary force are allowed to act on particles for a sufficiently long time so as to improve the ordering factor.

Acknowledgement

The present study was performed as a part of the "Nanotechnology program—Nanoparticles synthesis and function-endowing project" funded by NEDO.

Nomenclature

A	Ⅱ a maker constant of a particle	[J]
a	radius of a particle	[m]
D	diameter of a particle	[m]
I	inertial moment of a particle	[kg · m^2]
F^B	Brownian force acting on a particle	[N]
F^B_{eff}	effective Brownian force acting on a particle	[N]
F_o	Total force acting on a particle except friction	[N]
F_i	external force acting on a particle	[N]
F^m	capillary force acting between two particles	[N]
F^f	frictional force from a solid substrate	[N]
F^{vdW}	van der Waals force acting on a particle	[N]
H_c	height of meniscus	[m]
k	coordinate number	[−]
k_B	Boltzmann constant	[J · K^{-1}]
L	inter-particle distance	[m]
L_{cut}	cut-off distance of capillary force	[m]
m	mass of a particle	[kg]
M	rotational moment of a particle	[kg · m^2 · s^{-2}]
n	number of particles	[−]
$N(k)$	number of particles, the coordinate number of which is k	[−]
Q	capillary charge	[m]
r_c	radius of contact circle of three-phase interface	[m]
s	he ratio of the part of a particle immersed in liquid to that of the whole particle	[−]
T	absolute temperature	[K]
Δt	iteration time	[s]
v_i	velocity of the i-th particle	[m · s^{-1}]
γ	surface tension of liquid	[N · m^{-1}]
Ψ	meniscus slope angle at three-phase interface	[s^{-1}]
μ_{ps}	frictional Constant between a particle and a substrate	[−]
v	velocity of a particle	[−]
ω	angular velocity of a particle	[s^{-1}]
ζ	coefficient of Stokes drag force	[kg · s^{-1}]

References

1) Burmeister, F., W. Badowsky, T. Braun, S. Wicprich. J. Boneberg and P. Leiderer: Colloid Monolayer Lithography -A Flexible Approach for Nanostructuring of Surfaces, *Applied Surface Science*, 144-145, 461-466 (1999).
2) Denkov, N. D., O. D. Velev, P. A. Kralchevsky, I. B. Ivanov, H. Yoshimura and K. Nagayama: "Tow-dimensional Crystallization", *Nature*, **361**, 26-26 (1993).
3) Micheletto, R., H. Fukuda. and. M. Ohtsu: "A Simple Method for the Production of a Two-Dimensional. Ordered Array of Small Latex Particles", *Langmuir*, **11**, 333-3336 (1995).
4) Nagayama, K., "Two-Dimensional Self-Assembly of Colloids in Thin Liquid Films", *Colloids and Surfaces*, **109**, 363-374 (1996).
5) Rakers, S., L. F. Chi and H. Fuchs: "Influence of the Evaporation Rate on the Packing Order of Polydisperse Latex Monofilms" *Langmuir*, **13**, 7121-7224 (1997).
6) Ronder, S. C., P. Wedin and L. Bergstrom: "Effect of Electrolyte and Evaporation Rate on the Structural Features of Dried Silica Monolayer Films", *Langmuir*, **18**, 9324-9333 (2002).
7) Cundall, P. A. and O. D. L. Strack: "A Discrete Numerical Model for Granular Assemblies", *Geotechnique*, **29**, 47-65 (1979).
8) Maenosono, S., Dushkin C. D., Yamaguchi Y., Nagayama K. and Tsuji Y.: "Effect of Growth Conditions on the Structure of Two-Dimensional Latex Crystals: Modeling", *Colloid and Polymer Science*, **217**, 1152-1161 (1999).
9) Nishikawa, H., S. Maenosono, Y. Yamaguchi and T. Okubo: "Self-Assembling Process of Colloidal Particles into Two-Dimensional Arrays Induced by Capillary Immersion Force: A Simulation Study with Discrete Element Method", *Journal of Nanopartiele Research*, **5**. 103-110 (2003).
10) Fujita, M., H, Nishikawa, T. Okubo and Y. Yamaguchi: "A Multiscale Simulation on Two-dimensional Self-Organization of Nanopartieles in a Liquid Film", submitted to *Japanese Journal of Applied Physics*.
11) Russel, W. B., D. A. Saville and W. R. Schowalter: "Colloidal Dispersions", Cambridge University Press (1989).
12) Kralchevsky, P. A. and K, Nagayama: "Capillary Forces between Colloidal Particles", *Langmuir*, **10**. 23-36 (1994).
13) Israelachivili, J. N.: "Intermolecular and Surface Forces", Academic Press, 1992.
14) Yuan, Y. and A. M. Lenhoff: "Measurement of Mobility of Adsorbed Colloids by Lateral Force Microscopy", *Journal of Colloid and Interface Science*, **267**, 350-359 (2003).

Author's short biography

Hiroyuki Nishikawa

Hiroyuki Nishikawa obtained his Master Degree (2001) in Fundamental Chemistry at Chiba University and his Doctor Degree (2006) in Chemical System Engineering at University of Tokyo. He is now working for Mizuho Information & Research Institute, Inc. as a consultant at Engineering Service Department.

Masahiro Fujita

Dr. Masahiro Fujita was born on December 2, 1964 in Ehime prefecture, Japan. He attended the University of Tokyo where he received the degree of Bachelor of Engineering in Naval Architecture in 1988 and the degree of Doctor of Engineering in aeronautics in 1993. After studying, he worked for Mitsubishi Research Institute, Inc. for six years as a staff researcher at Simulation Engineering Department, where he was responsible for computational fluid dynamics in diverse fields. From 2000 to 2002, he worked for Intelligent Modeling Laboratory, the University of Tokyo as a Research Associate for Center of Excellence, where he was involved in flow visualization using virtual reality technology. In 2002, he joined in Nanomaterial Center, Institute of Engineering Innovation, the University of Tokyo as a research scientist, where he was involved in simulation of solid-liquid multiphase flow in materials nanotechnology. In 2005, he was assigned to Assistant Professor of Department of Chemical System Engineering, School of Engineering, the University of Tokyo. He has an extensive background in engineering field and is familiar with a variety of simulation technology. He has also experience in research of project management method when he was at Mitsubishi Research Institute, Inc.

Shinya Maenosono

Education	
Ph.D. University of Tokyo in Chemical System Engineering	2002
B.Eng. University of Tokyo in Precision Engineering	1993

Professional Employment	
Associate Professor, School of Materials Science, Japan Advanced Institute of Science and Technology	2006-
Assistant Professor, Department of Chemical System Engineering, University of Tokyo	2000-2006
Researcher, Production Engineering Department, Fuji Photo Film Co.,LTD.	1999-2000
Researcher, Yokohama Research Center, Mitsubishi Chemical Corporation	1993-1999

Yukio Yamaguchi

1975 Master degree from the University of Tokyo
1975 Join to Mitsubishi Chemical Corporation
1982 Engineer degree from Massachusetts Institute of Technology
2000 Professor of the University of Tokyo

Author's short biography

Tatsuya Okubo

Tatsuya Okubo is a professor of chemical system engineering at the University of Tokyo. He received his BS, MS and PhD degrees in chemical engineering from the University of Tokyo in 1983, 1985, and 1988, respectively. He joined the faculty of Kyushu University as a research associate in 1988, and moved to the University of Tokyo in 1991. Following the research associate position for two years in the University of Tokyo, he spent one year at California Institute of Technology as a visiting associate. He was promoted to an assistant professor in 1994 and an associate professor in 1997. He has been a full professor since April 2006. His research interests are in materials chemistry and engineering, particularly in synthesis, processing and application of nanoporous materials such as zeolites and mesoporous silica and nanostructured materials. He received Young Investigator award from the Society of Chemical Engineers of Japan in 1993, and had been selected as a PRESTO Investigator of JST twice in 1997-2000 and 2002-2006. Okubo can be reached by e-mail at okubo@chemsys.t.u-tokyo.ac.jp.

Influence of Habit Modifiers on Particle Shape in a Crystallization Process[†]

K.Kadota, K.Takase, A.Shimosaka, Y.Shirakawa[1] and J.Hidaka
Department of Chemical Engineering and Materials Science, Doshisha University[*]

Abstract

For crystallization in solution, the method of changing particle shape by adding the impurities called habit modifiers has been attracted attention as a fabrication process of functional particles. The method is complicated due to many controlling parameters, such as supersaturation, concentration, kinds of impurities, etc. It needs to clarify the mechanism of crystal growth for the control of crystal shape. Therefore, the influence of impurities on crystal growth has been examined by experiments and simulations. In the experiment, the technique by differential scanning calorimeter (DSC) was used for measuring the properties of clusters with changing the habit modifiers. In adding habit modifiers, the number of clusters increased. The formation of clusters was investigated by molecular dynamics (MD) simulation. This simulation result agreed with the experiment result and then the formation of clusters which assembled remarkably around impurities was demonstrated by simulation.

Keywords: Molecular dynamics, Crystallization, Particle shape, Habit modifiers, Sodium chloride

1. Introduction

In order for a functional material associated with a powder material to function as designed, the individual particles consisting of the powder material are required to possess the intended characteristics. To achieve this, many studies have been conducted on particle configuration control techniques for controlling chemical composition, size and size distribution, surface parameters and shapes of particles, under the unique concept of "particle design"[1]. Among the important particle parameters, particle shape is particularly important as it significantly affects physical and chemical characteristics including fluidity, solubility and the electromagnetic characteristics of powder materials. In this context, there have long been attempts at controlling particle shapes to provide particles in powder materials with useful functions in various industrial fields including photographic materials[2], magnetic materials[3] and medicine[4].

For precision control of particle shapes, industrial crystallization techniques are used which employ crystal habit modifiers that can offer relatively diverse variations in crystal shapes. However, though used in a diverse range of industrial fields, crystallization techniques require many sequences of trial and error processes to determine specific industrial crystallization conditions that help provide intended crystal shapes since shape change mechanisms for particles crystallized with crystal habit modifiers are unknown. This issue arises from insufficient molecular level elucidation in crystal growth mechanisms[5]. Recent reports state that in crystallization processes, solute clusters occur, and deposit on crystal surfaces, thereby significantly affecting crystal growth[6, 7].

Therefore, for the elucidation of crystal shape change mechanisms with crystal habit modifiers, a microscopic study into cluster formation in a supersaturated solution is necessary.

To this end, by performing a crystallization experiment and by adopting the molecular dynamics technique that can provide microscopic information,

---

[†] This report was originally printed in J. SOC. Powder Technology, Japan, **41**(6), 431-439(2004) befor being translated into English by KONA Editorial Committee with the permission of the editorial committee of the Soc. Powder Technology, Japan

[*] 1-3, Miyakodani, Tatara, Kyotanabe
Kyoto, Japan 610-0321

[1] Corresponding author
TEL: +81-774-65-6648　FAX：+81-774-65-6842
E-mail: yshiraka@mail.doshisha.ac.jp

we studied the effect of crystal habit modifiers on the shapes of crystals that grew in solutions. First, we studied the effect of crystal habit modifiers on the shape change of crystals using a fluidized crystallizer, determined the interrelation existing among the parameters of clusters occurring in a supersaturated solution (cluster size, number of occurring crystals, etc.), supersaturation ratio and crystal habit modifier types, and then through MD simulation, studied the supersaturation state that is difficult to observe by experiments as well as the solution structures resulting from the addition of crystal habit modifiers.

2. Experiment Method

2.1 Crystallization for sodium chloride crystals

The fluidized crystallizer for our experiment is schematically illustrated in **Fig. 1**. This apparatus consists of a head tank, a cooler and a crystallization tank. Sodium chloride (purified salt from The Salt Industry Center of Japan, purity 99.5%) was dissolved in 8×10^{-3} m^3 of distilled water to provide a mother liquor. During the experiment, the mother liquor was kept at 303K, and excess sodium chloride crystals were placed at the bottom of the head tank so that the mother liquor remained a saturated aqueous solution. Then, the saturated aqueous solution was converted into a supersaturated aqueous solution by cooling it from 303K to 297K, and the resultant supersaturated aqueous solution was supplied to the crystallization tank.

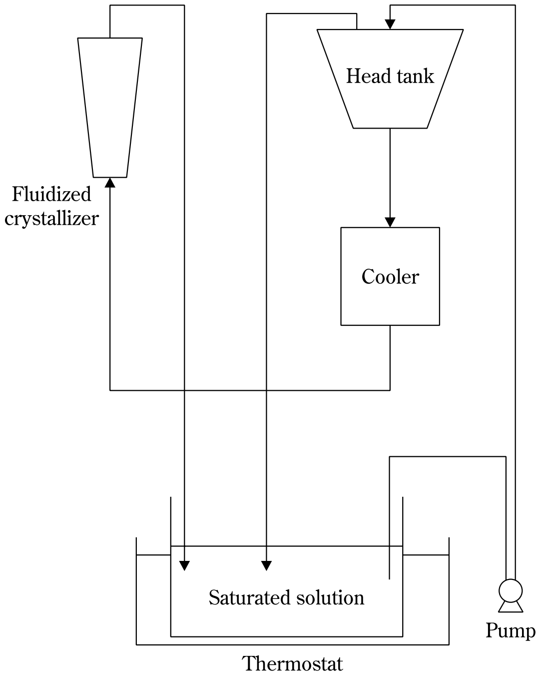

Fig.1 Schematic diagram of experimental apparatus

Table 1 Operating condition on fluidized crystallizer

Radius of seed crystal	2.50-3.00	(10^{-4}m)
Crystallization time	1.08	(10^4s)
Crystallization temperature	300 ± 3	(K)
Flow rate	5.0	(10^{-6}m^3/s)
Supersaturation ratio	1.8×10^{-3}	(–)

The aqueous solution overflowing from the tank and the crystallization tank was recovered in the mother head tank and again converted into a saturated aqueous solution whose temperature was 303K. In the crystallization tank, 20×10^{-3} kg of sodium chloride seed crystals, whose size and shape were adjusted as required, were placed in the crystallization tank. The flow rate was adjusted to a constant level at 0.3×10^{-3} m^3/min such that the seed crystals could float in the crystallization tank. Under these conditions, the seed crystals were allowed to grow, and then a crystal habit modifier was added, thereby change in crystal shapes was studied. The conditions of the experiment are summarized in **Table 1**. The crystal habit modifiers were Cu^{2+} and Mn^{2+} as cations and NO_3^-, Cl^- and SO_4^{2-} as anions. The purity of each crystal habit modifier was 99.9% (Kojundo Chemical Laboratory), and was added in the amount of 0.01 M in the form of salt (MX, M=Cu^{2+}, Mn^{2+}, X=SO_4^{2-}, NO_3^-, Cl^-).

2.2 Interfacial energy measurement by thermal analysis

Cluster parameters were determined through thermal analysis during a cooling process for supersaturated solutions containing crystal habit modifiers[8]. The analyzer was a differential scanning calorimeter DSC (MAC Science, Model DSC3300S). With the analyzer, aqueous sodium chloride (Kojundo Chemical Laboratory, purity 99.98%) solution containing a crystal habit modifier was analyzed. First, 1.00×10^{-9}–3.00×10^{-9} m^3 of aqueous sodium chloride solution saturated at 323K was loaded into a platinum specimen cell, and the cell was set in the calorimeter. To allow the existing cluster in the solution to be fully disaggregated, the cell was maintained for 5 minutes at 353K which was 30K higher than the saturation temperature, and was quenched at the rate of 0.33 K/s.

During this course, crystallization heat occurred while the crystals precipitated from the resultant supersaturated solution, thereby the calorimetric change was measured.

3. Behavior of Aqueous Sodium Chloride Solution Investigated by MD Simulation

Interaction potentials between the water and ion and between the ion and ion were calculated with the equations below, and the parameters proposed by Koneshan et al. were adopted[9].

$$u(r_{ij})=4\varepsilon_{ij}\left[\left(\frac{\sigma_{ij}}{r_{ij}}\right)^{12}-\left(\frac{\sigma_{ij}}{r_{ij}}\right)^{6}\right]+\frac{q_i q_j}{r_{ij}} \quad (1)$$

$$\sigma_{ij}=\frac{(\sigma_i+\sigma_j)}{2}, \quad \varepsilon_{ij}=\sqrt{\varepsilon_i \varepsilon_j} \quad (2)$$

The first term in the right-hand member in Eq. (1) represents the Lennard-Jones potential. The second term stands for the Coulomb potential, and was calculated with the Ewald method, where i and j stand for the ion type and rigid body molecule type, respectively. ε_{ij} and σ_{ij} are amounts having an energy unit and a length unit, respectively, and were determined according to the Lorentz-Berthelot law provided by Eq. (2). The parameters are listed in **Table 2**.

A translational motion of particles was defined by applying Newton's equation of motion to numerical integration by the velocity Verlet method, while a rotational motion was defined by subjecting Euler's equation of motion to numerical integration by the leap-frog method. Periodic boundary conditions were applied to the cell, and the SPC/E rigid body rotator model (Extended Simple Point Charge model), which well simulates a liquid structure and diffusion constant, was adopted for the water molecules[9]. The time interval for one step was 0.1 fs. The length of the basic cell was assumed to be 22.5×10^{-10} m, and the calculation was executed for 4.5 M saturated solution and 6.5 M, 9.0 M, 12.0 M and 15.0 M supersaturated aqueous sodium chloride solutions. To investigate the effect of crystal habit modifiers, calculations were made for Cu^{2+} and Mn^{2+}, each with the 9.0 M aqueous sodium chloride solution. The concentration of each Cu^{2+} and Mn^{2+} was set to 0.01 M, and the solution containing Cu^{2+} and the solution containing Mn^{2+} were each allowed to reach the thermal equilibrium state at a particular temperature, and were then cooled down. Additionally, to investigate the effect of periodic boundary conditions, a series of similar calculations were performed for settings where the length of the basic cell in a 9.0 M supersaturated aqueous sodium chloride solution was assumed to be 52×10^{-10} m, thereby the dependency of cluster sizes and size distribution on the cell size were studied.

The potential parameters of Cu^{2+} and Mn^{2+} used as crystal habit modifiers in the present study were determined through an interpolation or extrapolation technique, based on the σ values and radii of the ions whose parameters were reported[9].

Table 2 Pair potential function paramenters for aqueous NaCl solution

Atom/ion	$\sigma(10^{-10}$m)	ε(kJ/mol)	Charge(e)
O	3.169	0.6502	−0.8476
H	—	0.4184	+0.4238
Na^+	2.583	0.4184	+1.0
Cl^-	4.400	0.4184	-1.0
Cu^{2+}	1.832	0.4184	+2.0
Mn^{2+}	1.501	0.4184	+2.0

4. Result and Discussion

4.1 Result of experiment

4.1.1 Shape change of sodium chloride crystal

Fig. 2 shows an SEM photograph of a sodium chloride crystal obtained from an aqueous solution to which manganese sulfate as a crystal habit modifier was added. The crystal shape of sodium chloride generally varies from regular hexahedron to octahedron when a crystal habit modifier is added[10]. In the present study, the process of change in crystal shape into an octahedron was also verified. As for the three lattice planes of the sodium chloride crystal, that is, the {111}, {110} and {100} plane, the speed of crystal growth is slower in this order. In other words, the

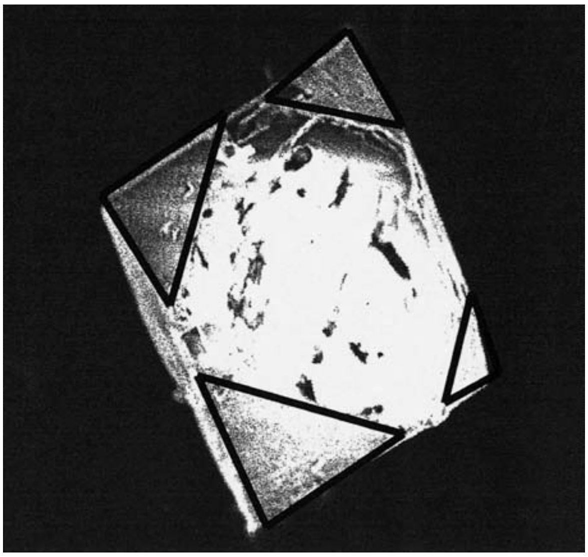

Fig.2 SEM photograph of NaCl grown in aqueous solution with $MnSO_4$

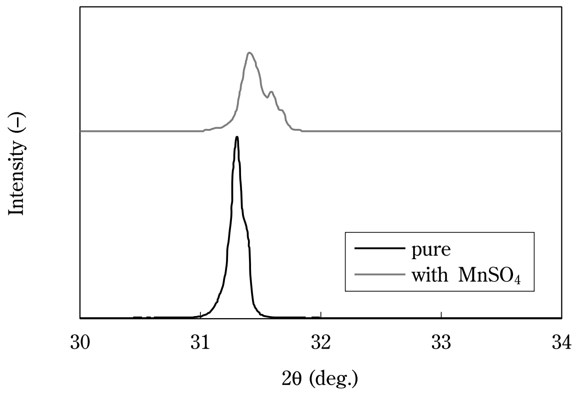

Fig.3 XRD patterns for NaCl

crystal growth with the {100} plane is slowest, and this plane occurs as the outer shape of the crystal. To sum up, sodium chloride crystals are usually regular hexahedrons consisting of {100} planes. The reason why the crystal shape of sodium chloride changes when a particular crystal habit modifier is added to a site of crystal growth is because the crystal habit modifier is adsorbed in the step of a particular lattice plane, leading to variation in the relative ratio of growth speeds of the lattice planes[10]. **Fig. 3** illustrates the result of X-ray diffraction for sodium chloride crystals when manganese sulfate as a crystal habit modifier was added to seed crystals. The X-ray diffractometer was the RINT2500 from Rigaku. Since a new peak occurred when manganese sulfate was added, it seems that the shape of the sodium chloride crystals varied owing to the deposition of Mn^{2+} on the crystal surface.

4.1.2 Formation of cluster

To be able to determine cluster parameters from the results of thermal analysis with a DSC, the relation between the measurement result and the cluster parameters needs to be clarified. As plotted in **Fig. 4**, a segment up to the formation of the critical nucleus is defined as a cluster[8), 11)], and the maximum values for the radius and total number of constituent ions for the critical cluster immediately before nucleus formation as well as the excess free energy at that time point are taken as the cluster parameters.

In order for a cluster to occur in a supersaturated solution, the energy barrier Δg defined by the following equation needs to be exceeded[11)].

$$\Delta g = 4\pi r^2 \sigma_s - nkT \ln(C/C^*) \qquad (3)$$

where, Δg; free energy difference associated with the formation of a cluster, r: radius of the cluster, σ_s; interfacial energy of the cluster, n; number of solute molecules constituting the cluster, k; Boltzmann constant, T; saturation temperature, C: solute concentration, C^*; saturation concentration. If the volume of one solute molecule is taken as v, then n can be defined as:

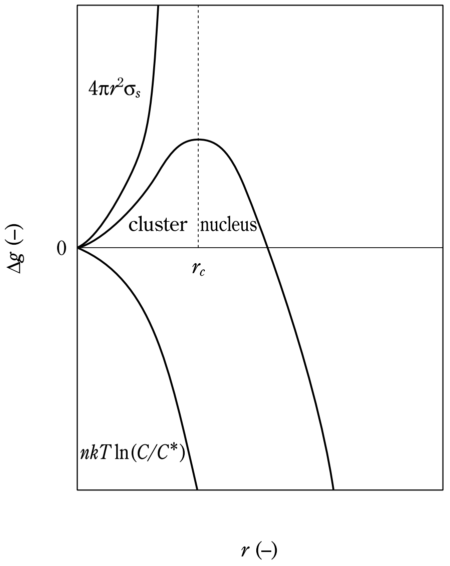

Fig.4 Classical theory of nucleation

$$n = \frac{4\pi r^3}{3v} \qquad (4)$$

If Eq. (4) is substituted in Eq. (3), and when Δg takes a maximum value, then $d\Delta g/dr = 0$. Therefore, the radius of cluster r_c in the critical state can be expressed by the following equation:

$$r_c = 2\sigma_s v / kT \ln(C/C^*) \qquad (5)$$

If the increase in the resultant maximum of Δg_{max} can be expressed as:

$$\Delta g_{max} = 4\pi r_c^2 \sigma_s - \frac{4\pi r_c^3 kT}{3v} \ln\left(\frac{C}{C^*}\right) \qquad (6)$$

As a result, the supersaturation dependency of n and Δg_{max} can be defined as:

$$n = \frac{4\pi}{3v}\left[\frac{2\sigma_s T}{kT \ln(C/C^*)}\right]^3, \quad \Delta g_{max} = \frac{16\pi\sigma_s^3}{3}\left[\frac{v}{kT\ln(C/C^*)}\right]^2 \qquad (7)$$

By determining the interfacial energy σ_s, the cluster parameters can be calculated. The nucleation rate R_N can be expressed as follows[8)]:

$$R_N = k_N \exp\left[-\frac{16}{3}\pi\left(\frac{\sigma_s}{kT}\right)^3\left(\frac{v}{\ln(C/C^*)}\right)^2\right] \qquad (8)$$

Incidentally, when assuming that N critical clusters occur in a solution whose volume is V during a waiting time θ_t from the start of cooling to the occurrence of clusters, the nucleation rate R_N can be expressed by the following equation:

$$R_N = \frac{1}{V}\frac{N_{obs}}{\theta_t} \tag{9}$$

Therefore, if both members in Eq. (9) are converted into logarithms and Eq. (8) is substituted, the following equation will be obtained:

$$\log\theta_t V = -\log\frac{k_N}{N_{obs}} + \frac{1}{2.303}\cdot\frac{16}{3}\pi\left(\frac{\sigma_s}{kT}\right)^3\left(\frac{v}{\ln(C/C^*)}\right)^2 \tag{10}$$

Consequently, by plotting the relation between $\theta_t V$ and $1/\log_2(C/C^*)$, and by reading the inclination of the resultant straight line, the interfacial energy σ_S can be determined.

Fig. 5 illustrates the relation between θV and $1/\log^2(C/C^*)$ for pure aqueous sodium chloride solution. The thus-obtained interfacial energy was substituted in Eqs. (6) and (7), and the resultant cluster parameters are listed in **Table 3**. From this result, it is understood that the average number of solute molecules that constitute a sodium chloride cluster is 3.7. According to the report of Rajiv et al., the approximate number of solute molecules that constitute a sodium chloride cluster is 4[12], and this agrees with well the result of our experiment.

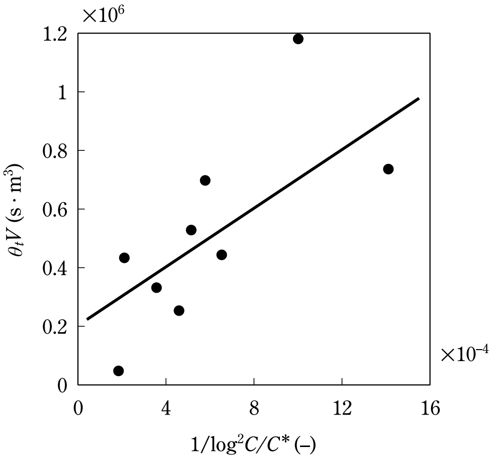

Fig.5 Relationship between $1/\log^2 C/C^*$ and $\theta_t V$ in NaCl solution

Table 3 Values of clusters parameters

S=1.015	σ(10^4J/m^2)	$2r$(10^{-10}m)	n(–)	Δg(10^{-22}J/ion)
Pure NaCl	5.70	4.51	3.7	1.22
$Cu(NO_3)_2$	14.7	11.6	62.4	20.7
$CuCl_2$	14.5	11.5	60.3	20.0
$CuSO_4$	15.2	12.1	69.8	23.2
$Mn(NO_3)_2$	20.0	15.8	157.9	52.4
$MnCl_2$	18.4	14.5	122.4	40.6
$MnSO_4$	22.0	17.4	210.8	69.9

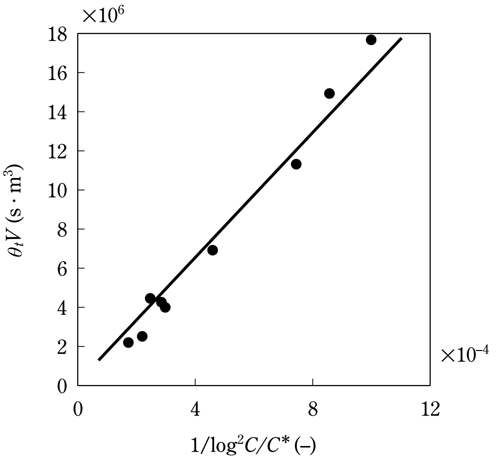

Fig.6 Relationship between $1/\log^2 C/C^*$ and $\theta_t V$ in NaCl solution with $CuSO_4$

Fig. 6 shows the result obtained from the addition of copper sulfate as a crystal habit modifier. The cluster parameters for this case were determined and the result is summarized in **Table 3**. The cluster size with the addition of a crystal habit modifier is apparently larger than the cluster size without the addition of a crystal habit modifier. When the effects of two cation types are compared with each other, the addition of Mn^{2+} resulted in a larger cluster size compared with the addition of Cu^{2+}. Also, from the aspect of anion types, the cluster size is greater in the order of SO_4^{2-}, NO_3^- and Cl^-. These results are microscopically discussed in Sec. **4.2.4** using the MD simulation technique.

4.2 Simulation results

4.2.1 Validity of simulation method

To investigate the validity of the MD simulation method used for the present study, we determined the pair distribution function and mean square displacement between Na^+ and Cl^- in 4.5 M equilibrated saturated aqueous sodium chloride solution. **Fig. 7** provides the result of pair distribution function, while **Table 4** lists diffusion coefficients of Na^+ and Cl^- ions obtained from the inclination of mean square displacement. These values well match the values in the previous work[13], and this fact means that our simulation technique and the parameters adopted are relevant.

4.2.2 Effect of supersaturation on clusters

Cluster formation in a solution is triggered by concentration fluctuation of solute molecules. Thus, it is possible that a portion of extremely high concentra-

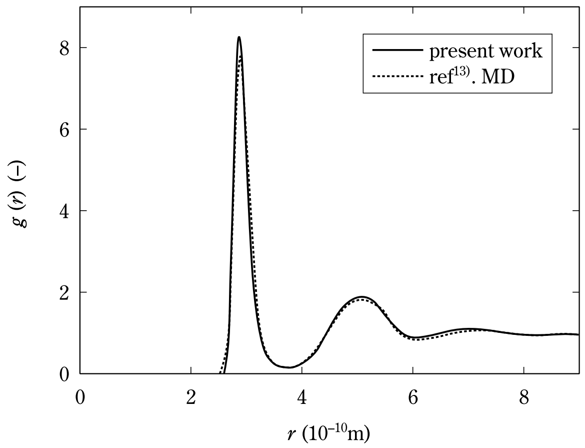

Fig.7 Pair distribution function for sodium ion-chloride ion in 4.5M equilibrium NaCl solution

Table 4 Diffusion coefficient D in 4.5M aqueous NaCl solution at 298K

	Na^+ ($10^{-9}m^2/s$)	Cl^- ($10^{-9}m^2/s$)	H_2O ($10^{-9}m^2/s$)
present work	0.67	0.76	1.42
reference[13]	0.64	0.78	1.45

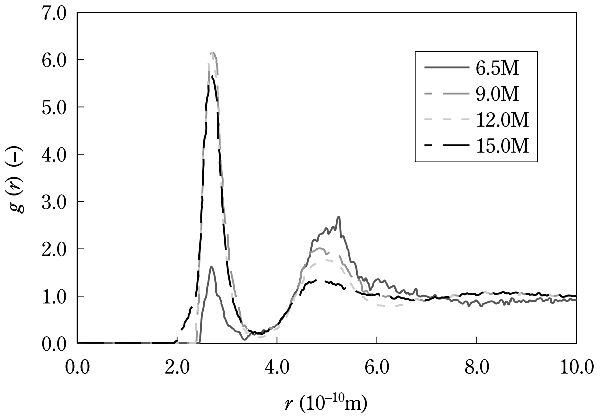

Fig.8 Pair distribution function for sodium ion-chloride ion at each concentration

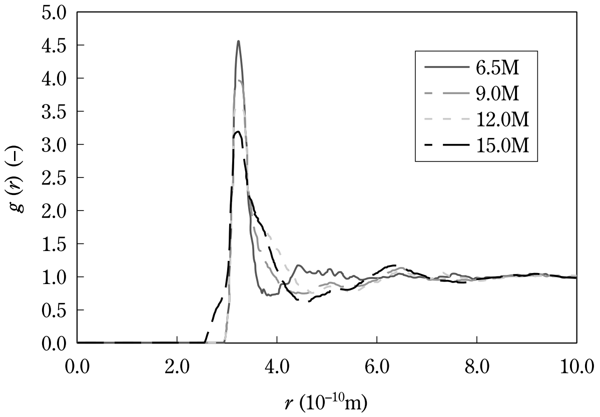

Fig.9 Pair distribution function for sodium ion-oxygen ion at each concentration

tion can locally exist. Solutions whose concentration ranged from 4.5 M to 15.0 M were cooled down, and the resultant pair distribution functions between Na^+ and Cl^- are plotted in **Fig. 8**, and the similar functions between O^- and Na^+ are shown in **Fig. 9**. With higher concentrations, the first peaks in pair distribution functions between Na^+ and Cl^- are apparently greater. In contrast, the first peaks in pair distribution functions between O^- and Na^+ are smaller with higher concentrations.

This seems to be because the respective ions in sodium chloride having hydration structure in a lower concentration became dehydration as the concentration increased, resulting in cluster formation. Therefore, we investigated the numbers of clusters and size distributions of clusters with lower and higher concentrations. The results are summarized in **Figs. 10** and **11**. Note that the clusters in our simulation are defined as particles in the first peaks in pair distribution functions. The time-dependent change in the numbers of clusters is apparent in **Fig. 10**. In other words, the formation and disintegration of clusters always continue to occur in a supersaturated solution. With a higher concentration, the distribution of cluster sizes tends to be larger.

4.2.3 Effect of cell size

Calculation was performed with 9.0 M supersaturated solution in a system having a large cell size.

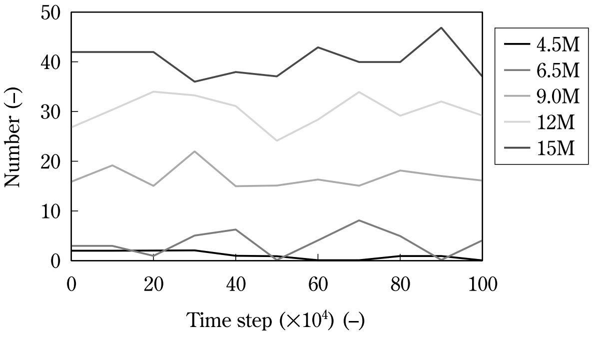

Fig.10 Time dependence of total number of clusters

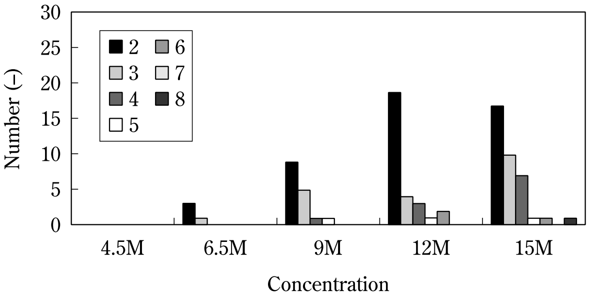

Fig.11 Size distribution of clusters at 1000000 step

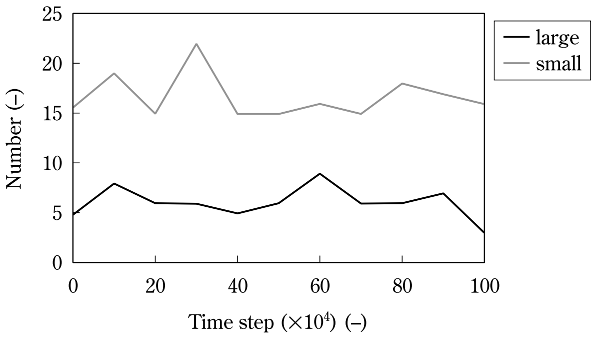

Fig.12 Time dependence of total number of clusters

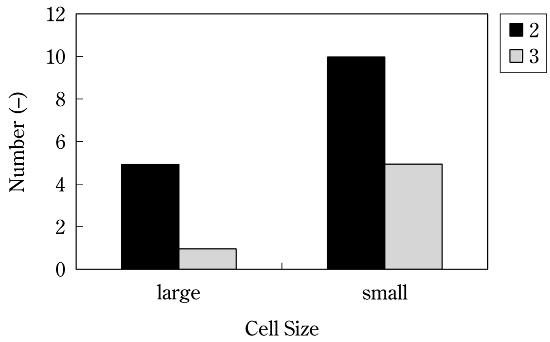

Fig.13 Size distribution of clusters at 1000000 step

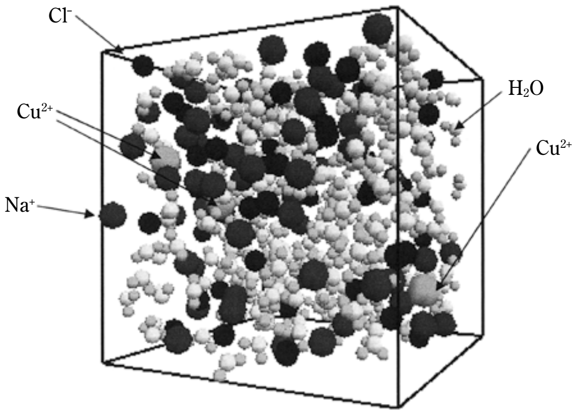

(a) NaCl solution

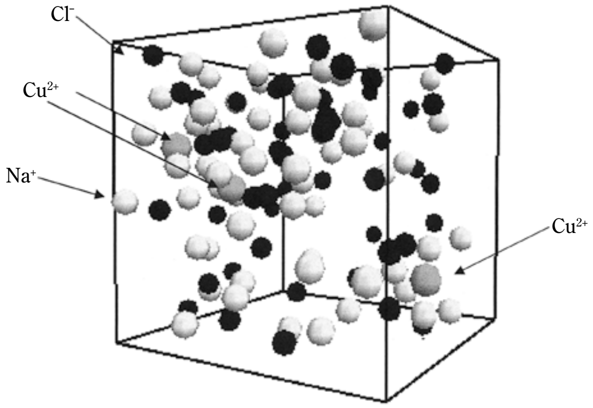

(b) Without water

Fig.14 Effect of habit modifiers for NaCl solution in MD simulation

First, the time-dependent change in the numbers of clusters is illustrated in **Fig. 12**, and the resultant cluster distributions are shown in **Fig. 13**. The numbers of clusters decreased with a larger cell size. This seems to be because a smaller system was affected by periodic boundary conditions. However, **Fig. 13** shows that there was a little change in the size distribution of clusters. As a result, it should be understood that the results obtained from our simulation provide quantitatively useful information.

4.2.4 Effect of crystal habit modifiers on cluster formation

Based on the above-mentioned findings, we performed simulation with 9.0 M supersaturated aqueous sodium chloride solution to which Cu^{2+} or Mn^{2+} as a crystal habit modifier was added. **Fig. 14** schematically illustrates the state of the solution containing added Cu^{2+}. **Fig. 15** shows a comparison of pair distribution functions between Na^+ and Cl^- with pure 9.0 M aqueous sodium chloride solution and pair distribution function with aqueous sodium chloride solution containing a crystal habit modifier. Compared with the pure aqueous sodium chloride solution, the

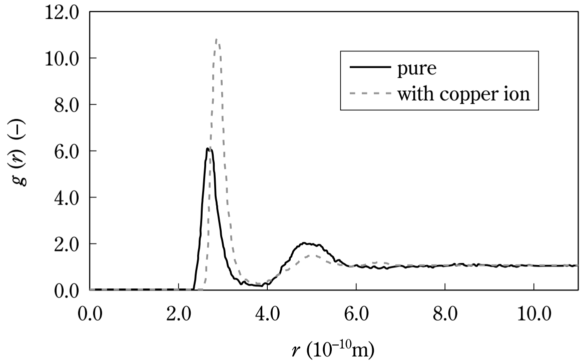

(a) Cu^{2+}

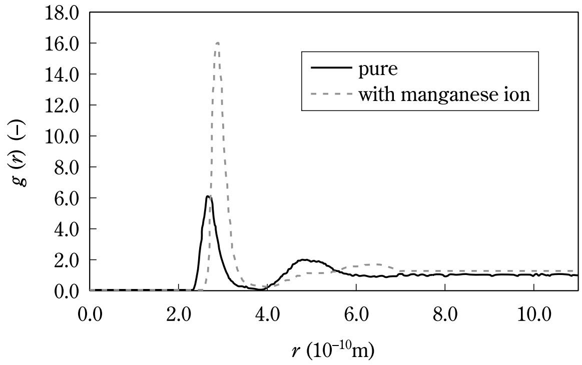

(b) Mn^{2+}

Fig.15 Comparison of pair distribution function between pure NaCl solution and solutions with modifier solution containing a crystal habit modifier features an apparently greater first peak in pair distribution function. This is because the formation of clusters is promoted by an added crystal habit modifier. **Fig. 16** provides a comparison in the total numbers of clusters, and **Fig. 17** shows a comparison in the size distributions of clusters. As a result of the addition of a crystal habit modifier, the total number of clusters is greater. From this fact, we were confident that the addition of a crystal habit modifier contributes to an increase not only in the total number of clusters, but also in the crystal sizes. Incidentally, from **Fig. 14**, cluster formation is very much apparent around a crystal habit modifier. In other words, the reason why the addition of a crystal habit modifier causes clusters to grow larger is that Na^+ and Cl^- ions approach crystal habit modifier ions, thereby forming clusters. Also, we confirmed through the behavior of ions in the simulation that when Mn^{2+} was added, dramatic cluster formation occurred around Mn^{2+} ions.

That is, the larger cluster sizes with the addition of Mn^{2+} shown in **Fig. 17** appear to result from strong attraction by the Mn^{2+} ions. This Cation effect well matches the finding obtained from the DSC.

5. Conclusion

Using a fluidized bed crystallizer, we performed a series of crystal growth experiments with aqueous sodium chloride solution types containing a crystal habit modifier (MX, $M=Cu^{2+}$, Mn^{2+}, $X=SO_4^{2-}$, NO_3^-, Cl^-). During this process, the anion and cation types in the crystal habit modifier were systematically varied. The surfaces of the resultant crystals with an X-ray diffraction analysis technique, were analyzed and, as a result, found that the surface of each crystal incorporated anions of the crystal habit modifier, and the shape of each crystal was changed. Also, cluster parameters with a DSC were measured, and, as a result, learned that a crystal habit modifier can increase the numbers of ions that constitute clusters.

Furthermore, we investigated cluster formation in various solutions by adopting an MD technique. First, considering localized fluctuation in concentration, MD simulation for cluster formation with several supersaturated solutions were performed, thereby learning that the total number of clusters increases and size distribution is wider with a greater supersaturation ratio.

We also clarified that like in a series of experiments, the addition of a crystal habit modifier causes cluster formation to be promoted and the numbers of ions constituting the clusters to increase, and in terms of the effect of cations, that the cluster size around the crystal habit modifier ions is greater with the addition of Mn^{2+} as compared with the addition of Cu^{2+}. From the above-mentioned findings, it should be understood that clusters deriving from a crystal habit modifier significantly affect shape change in crystals. This information is extremely useful in particle shape control with a crystal habit modifier.

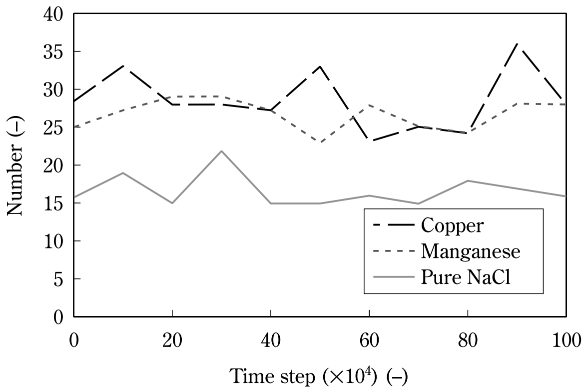

Fig.16 Time dependence of total number of clusters

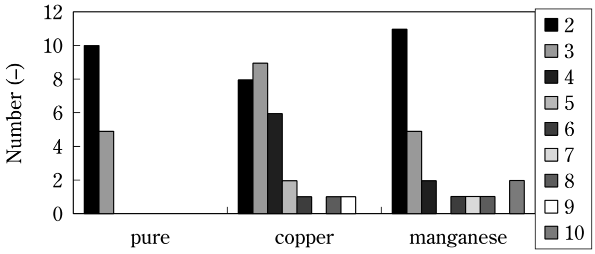

Fig.17 Size distribution of clusters at 1000000 step

Acknowledgement

We would like to express our sincere thanks to our fellow participants in the joint research effort conducted by local joint academic circles in the Kyoto Prefecture region since a certain portion of the present study has been financially supported as part of the "Development of infrastructure technology for the creation of functional fine particles."

Nomenclature

C : concentration of NaCl [kg/m^3]
C^* : equilibrium saturation concentration [kg/m^3]
D : diffusion coefficient [−]
k : Boltzmann constant [J/k]
m : exponent number [−]
n : number of molecules in a critical nucleus [−]

N_{obs} : number of nuclei for θ [−]

q : electrical charge [−]

r : radius of nucleus [m]

r_c : radius of critical nucleus [m]

R_N : nucleation rate [−]

t : crystallization time [s]

T : absolute temperature [K]

v : volume of crystal [kg/m^3]

V : volume of vessel [kg/m^3]

θ_t : waiting time [s]

φ_c : Coulomb energy [eV]

σ : parameter related to ion radius [m]

σ_s : specific energy of crystal compared with its solution [J/ion]

Δg : free energy change in formation of a critical nucleus [J/ion]

References

1) Yamamoto, H.:"Crystallization Behavior and Functionalities of Pharmaceutical and Food Materials", *J. Crystal. Growth. Jpn.*, **23**, 422-429 (1996)

2) J.E.Maskasky:"The Seven Different Kinds of Crystal Forms of Photographic Silver Halids", *J.Imag.Sci*, **30**, 247-254 (1986)

3) Yonemochi, Y., M. Kimata, K. Yoshimoto, M. Hasegawa, M. Tsukada, H. Kamiya:"Preparation of Micro-Size Monodispersed Hematite Particles by Gel-Sol Method", *J. Soc. Powder Technol., Jpn.*, **40**, 150-156 (2003)

4) Momonaga, M., K. Onishi and H. Yazawa:"Additive Effect and Scale-up in Selective Crystallization of Sodium Cefazolin Polymorphs", *Kagaku Kougaku Ronbunshu*, **18**, 553-561 (1992)

5) Sato K.,:"Yoeki karano Kesshouseicho", p1-6, Kyoritsu Shuppan

6) Sazaki, G., H. Ooshima, J. Kato, Y. Harano and N. Hirokawa:"Mechanism of crystallization of enzyme protein themolysin", *J. Crystal. Growth.*, **130**, 357-367 (1993)

7) Matsuoka, M.:"Nucleation and Crystal Growth: Phenomena and Modelling", *J. Cryst. Grow. Jpn.*, **24**, 30-39 (1997)

8) Harano, Y., K. Nakano:"Nucleation Rate of Potassium Chlorate from Quiescent Supersaturated Aqueous Solution", *J. Chem. Eng. Jpn.*, **9**, 373-377 (1976)

9) S.Koneshan, Jayendren, C.Rasaiah, R.M.Lynden-Bell, and S.H.Lee:"Solvent Structure, Dynamics and Ion Mobility in Aqueous Solution at 25℃ " *J. Phys. Chem. B*, **102**, 4193-4204 (1998)

10) Hokura, K., A.Yoshio:"Kaitei Shoseki", p.25, Kagaku Kougyosha (1987)

11) Marios D. Demetriou, Nasr M. Ghoneim, Adrienne S. Lavine:"Effects of nucleation transience on crystallization kinetics under strongly nonequilibrium conditions", *J. Chem. Phys.*, **23**, 10739-10743 (2002)

12) Rajiv M. G., A. S. Myerson:"Effect of impurities on cluster growth and nucleation", *J. Crysalt. Growth.* **126**, 216-222 (1993)

13) Shehasis C., Amalendu Chandra:"Molecular Dynamics Simulation of aqueous NaCl and KCl solutions; Effect of ion concentration on the single particle, pair, and collective dynamical properties of ion and water molecules"*J. Chem. phys.*, **115**, 3732-3741 (2001)

Author’s short biography

Kazunori Kadota

Kazunori Kadota is Ph. D. course of the Department of Chemical Engineering and Materials Science at Doshisha University, where he also received his B. S. (2002) and M. S. (2004) degrees. His research interests include the crystallization.

Keiichi Takase

K. Takase graduated with a degree in Department of Applied Chemistry from Osaka Institute of Technology (1994) and received his Ph. D. form Molten Salt Chemistry at Niigata University in 2000.

Atsuko Shimosaka

Dr. Atsuko Shimosaka has been a Lecture of the Department of Chemical Engineering and Materials Science at Doshisha University since 1993. Her research interests are focused on the mechanical analysis of granular behavior and computer simulated design of functional materials. Currently, she is an editor of the Journal of The Society of Powder Technology, Japan.

Yoshiyuki Shirakawa

Y. Shirakawa graduated with a degree in Solid State Physics from Niigata University (1988), where he also received his Ph. D. (1993). He then took a position in post doctorate research, and studied the structure and electronic properties of non-crystalline materials for one year. He subsequently continued on at Niigata University as a research associate in Fundamental Science and Technology. Afterwards he became a research associate in Materials Science and Processing at Osaka University (1 995-1 998). Since 1998 he has been working in the Department of Chemical Engineering and Materials Science at Doshisha University, where he has been committed in understanding of the interface effects and development of nanoparticle composite materials.

Jusuke Hidaka

Prof. Jusuke Hidaka has been at Doshisha University, Japan since 1976. His major research interests are focused on the mechanical analysis of powder flow using computer simulation, and the classification and instrumentation of powder industrial processes using acoustic emission. He is the vice president of The Society of Powder Technology, Japan.

Effect and Behavior of Liquid Additive Molecules in Dry Ultrafine Grinding of Limestone[†]

M. Hasegawa[1], M. Kimata and M. Yaguchi
Department of Chemistry and Chemical Engineering
Yamagata University[*]

Abstract

The effect of liquid additives such as alcohol and glycol on the ultrafine grinding of limestone was investigated by using a vibration rod mill. Liquid additives used in the present work were three alcohols and two glycols with different alkyl groups. The experiments were carried out by a batch operation, and the change in specific surface area of limestone with grinding time was measured by BET adsorption method. The behavior of methanol molecules added as an additive was traced by monitoring the temperature and pressure in the grinding pot during grinding. The results showed that alcohols and glycols promote the ultrafine grinding of limestone, and that the maximum specific surface area of limestone obtained with additives is proportional to the amount of the additive. The stepwise addition of a small amount of additive was more effective rather than adding the whole amount at once in increasing the grinding rate of limestone. It was also found that the degradation of crystal structure of limestone was controlled by the addition of alcohol. The grinding status of limestone could be traced by monitoring the temperature in the grinding pot, and the measurement of pressure change in grinding pot revealed that the additive molecules are chemisorbed on fresh surface of limestone created by the grinding.

Keywords: Grinding Aid, Limestone, Ultrafine Grinding, Alcohol, Pressure Change, Temperature Change

1. Intoroduction

It is known that grinding is one of unit operations with the lowest energy efficiency. Grinding aids which can improve the efficiency of the grinding remarkably with a small amount addition should more positively be applied to the grinding operations, especially to dry ultrafine grinding with higher energy consumption, from the viewpoint of energy conservation. Although the greatest problem in the use of grinding aids is contamination of product ground by additives, it can be solved through selecting or designing an appropriate additive that has no detrimental effect on downstream processing or the final product.

In the cement industry, grinding aids have been studied and used practically for a long time. However, grinding aids have scarcely been utilized in fields other than the cement industry, because of the undesirable contamination of the product and the lack of instruction in application of grinding aids. In most of the studies on grinding aids, the effects of grinding aids have been discussed to get the fine powders of micron sizes, but there are only a few reports[1, 2] as to ultrafine powders with submicron size.

In our laboratory, the effects of various liquid additives on dry ultrafine grinding of some minerals, such as feldspar[3], quartz[4] and alumina[5], have been

---

[†] This report was originally printed in J. Soc Powder Technology, Japan, **42**, 178-184 (2005) in Japanese, before being translated into English by KONA Editorial Committee with the permission of the editorial committee of the Soc. Powder Technology, Japan

[*] 4-3-16, Jonan, Yonezawa 992-8510, Japan

[1] Corresponding author
TEL&FAX: +81-238-26-3162
E-mail: mhase@yz.yamagata-u.ac.jp

investigated to apply grinding aids to dry ultrafine grinding process. In this paper, the same experiments on limestone were successively carried out to accumulate the data of additive effects and to investigate the addition methods of additives. Furthermore, the measurements of the temperature and pressure in grinding pot were also attempted to elucidate the behavior of limestone powder and additive molecules in grinding pot during grinding.

2. EXPERIMENTAL

A grinding apparatus and grinding conditions were the same as used in the previous paper[5]. The apparatus was a vibration rod mill with two grinding pots with an internal volume of about 1.0 liter. Grinding media loaded in the pot were rods with dimensions of 11 × 11 mm in diameter and length. Both the pots and the rods were made of silicon nitride for the importance of wear-resistance. A desired amount of solid sample (weight 89.4g, fractional sample filling 0.11) were charged to the pot filled with rods (weight 1371g, fractional rod filling 0.8). The addition methods of additives were carried out by two ways, a collective addition of the whole amount at the start of grinding and stepwise addition of a small amount (1ml) every one hour. All the experiments were conducted in a batchwise closed system for a required time considering the volatilization of additives and moisture in atmosphere.

A solid sample used in this work was limestone from Okayama and its density was 2.70×10^3 kg/m^3. The sample was crushed previously with a jaw crusher and a stamp mill, and then was prepared to particle size below 200mesh (74μm). The specific surface area of the limestone sample before grinding was 9.89×10^2 m^2/kg. Three kinds of alcohols and two kinds of glycols were used as liquid additives, as shown in **Table 1**. These additives were special grade reagents (Kanto Chem. Co., Inc.) and used without further purification.

After grinding for a required time, the specific surface area of the ground products sampled by cone and quartering was measured by the BET adsorption method (Micromeritics Co., Flowsorb II). The temperature degassing before the measurement was 200 ℃.

The temperature in grinding pot, as shown in **Fig. 1**, was measured by setting a thermocouple, which did not touch the grinding pot wall and rods,

Table 1 Liquid additives used

additives	Molecular formula	Molecular weight	Boiling point[K]
Methanol	CH_3OH	32.0	337.8
Ethnol	C_2H_3OH	46.1	351.5
1-Propanol	$(CH_3)_2CHOH$	60.1	370.2
Ethylene glycol	$HOCH_2CH_2OH$	62.1	470.4
Propylene glycol	$CH_3CH(OH)CH_2OH$	76.1	460.5

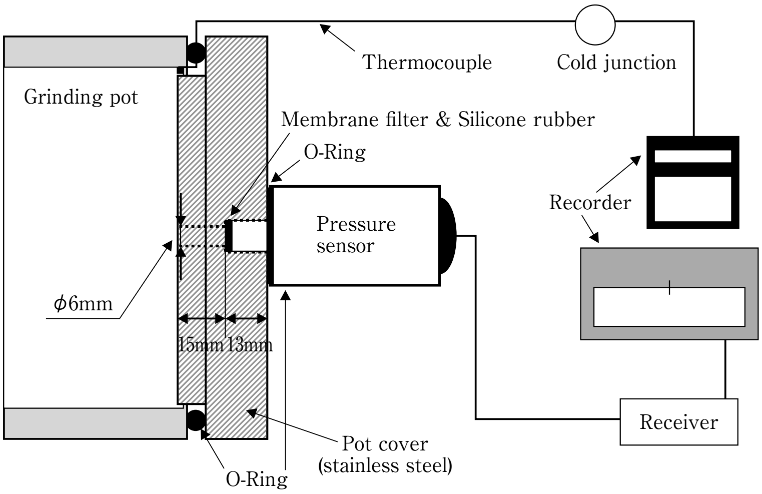

Fig. 1 Measurement method of the pressure and temperature in grinding pot.

through a silicone ling packed the grinding pot. To measure the gage pressure in grinding pot a small pressure sensor (Yokogawa M&C Co., FP-201) was also attached to center in the pot cover made of stainless steel. Data of temperature and pressure obtained were recorded to a industrial chart multi-recorder (Yokogawa Electric Co., μR1000) and a pen recorder (Yokogawa Electric Co., Type3066), respectively.

3. RESULTS AND DISCUSSION

3. 1 Effect of liquid additives as grinding aid

Figs. 2 and **3** show the variations of the specific surface area of limestone as a function of grinding time at the various addition amounts (1～8ml) of methanol and ethanol, respectively. Each plot in the figures is an independent experiment. The result without an additive (0ml) is also shown in these figures. The specific surface area without an additive was at most about 8.5 times as large as the area before grinding over the grinding time from 4-8 h, and hardly increased with subsequent grinding and inversely decreased. On the other hand, the results with alcohol additives indicated that both two alcohols were effective as grinding aids and that the specific surface areas increased with an increase in the addition amount of alcohol at the same grinding time. However, at all addition amounts of additives the increasing rate of specific surface area gradually slowed down at long grinding time, and then the specific surface area maintained a constant value or decreased. Although the maximum value of specific surface area and the grinding time at the maximum value differed with the amount of additives, the both showed a tendency to increase with the amount of additive. These agreed roughly with the results on three organic oxides in previous papers[3-5].

Fig. 4 shows the variations of the specific surface area of limestone as a function of grinding time at the different addition amounts of ethylene glycol. From **Fig. 4**, ethylene glycol was found to be one of effective grinding aids as well as alcohols. We also confirmed the effectiveness of grinding aid for propylene glycol. At the addition amount of 8 ml the specific surface area after grinding for 72 h, which was not shown in **Fig. 4**, was almost equal to that at the grinding time of 48 h. Consequently, the maximum value of specific surface area with ethylene glycol was estimated to reach at the grinding time between 48 h and 72 h, which was the same as that with alcohol additives. The horizontal solid lines at the specific surface area of 11000 m^2/kg in **Figs. 2, 3** and **4** were equivalent to the specific surface area diameter of around 0.2 μm assuming ground limestone particles

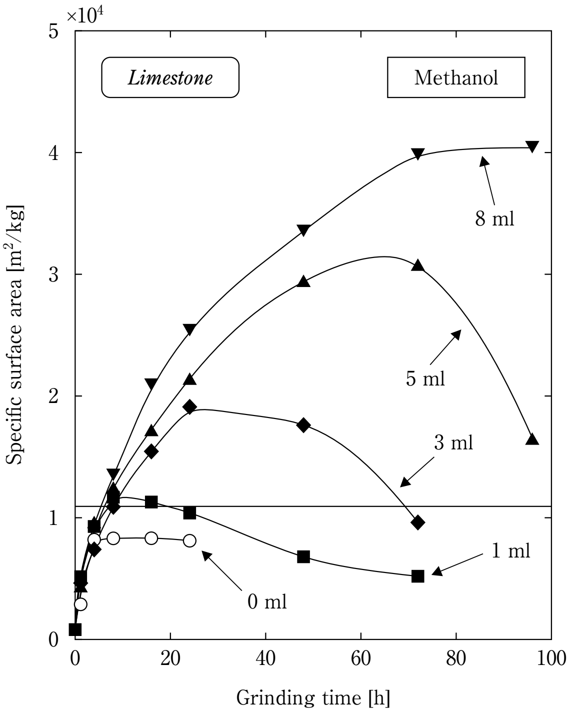

Fig. 2 Variations of specific surface area of limestone as a function of grinding time with the addition amount of methanol.

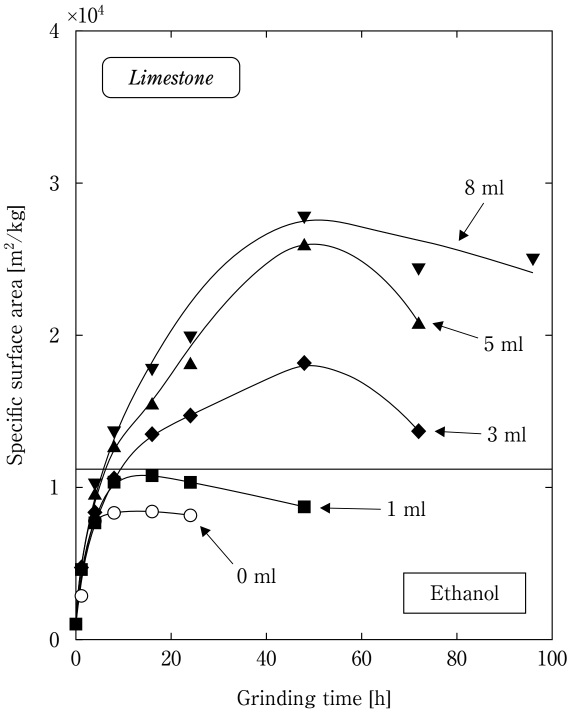

Fig. 3 Variations of specific surface area of limestone as a function of grinding time with the addition amount of ethanol.

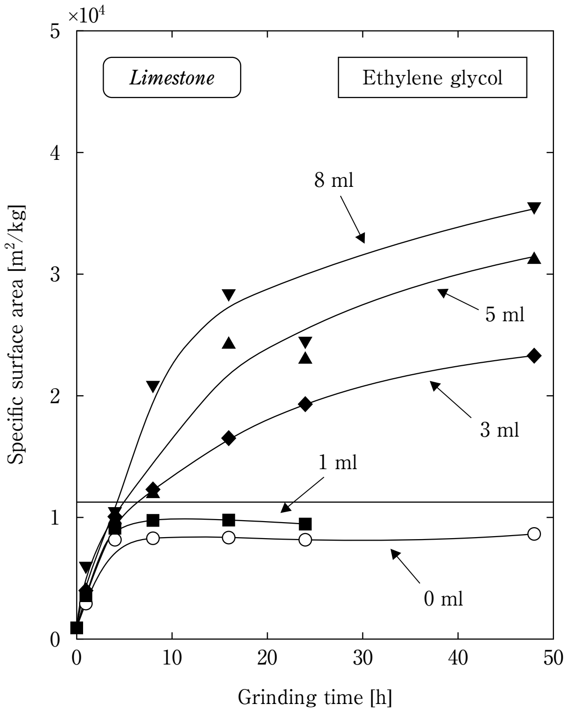

Fig. 4 Variations of specific surface area of limestone as a function of grinding time with the addition amount of ethylene glycol.

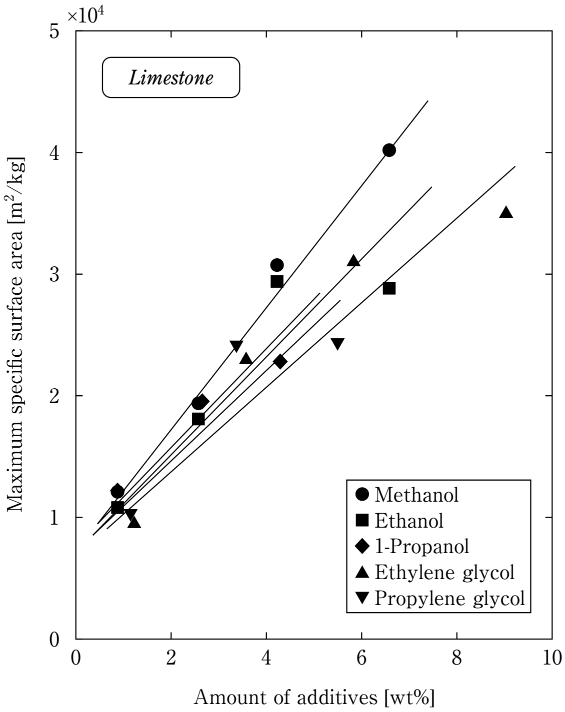

Fig. 5 Relationships between maximum specific surface area and the amount of additives.

to be spheres. Thus, the ultrafine grinding of limestone implied to be achieved sufficiently in this work.

Fig. 5 shows the relationships between the maximum specific surface area and the weight percentage of amount of additives for limestone sample. The results with propylene glycol are not contained in the figure because the specific surface area does not reach clearly a maximum value. As can be seen from the figure, the maximum specific surface area obtained with any additive was found to be linearly proportional to the amount of additives within the experimental range in this work. The slope of lines differed with the kinds of additives and the slopes with alcohol additives were larger than that with glycol. These tendencies were also in accord with results in the previous papers[3-5].

3. 2 Effect of addition method of liquid additives

The effect of grinding aids is not only to increase the maximum specific surface area, but also to increase a grinding rate at the initial stage of grinding. From **Figs. 2, 3** and **4**, the initial grinding rate was found hardly to change with the different amount of additives. In general, a whole amount of grinding aids have been collectively added at the start of grinding, but in this work a novel addition method which stepwise added a small amount of additives, 1ml, was attempted to investigate the effect of the addition methods of additives.

The results with methanol additive are shown in **Fig. 6**. The Data with stepwise and collective addition of methanol are represented by broken lines and solid lines, respectively. When the total amount of additives was the same, the specific surface areas with stepwise addition were larger than that with collective addition at the grinding time longer than 4 h. The results with ethanol additive showed also a similar tendency. It was found that the stepwise addition method could reach a certain value of the specific surface area with the shorter grinding time. The effect of stepwise addition is considered to be due to the favorite dispersion state of additives in the initial grinding stage. Therefore, it is suggested that the addition method, which increases the amount of additives with the increasing the specific surface area, may be more advantageous.

Fig. 7 shows the scanning electron micrographs of limestone before and after grinding for 24h : (a) original before grinding; (b) after grinding without an additive; (c) after grinding with collective addition of 3ml methanol; and (d) after grinding with stepwise addition of 3ml methanol. For the product without an additive (b), a large amount of the agglomerates of

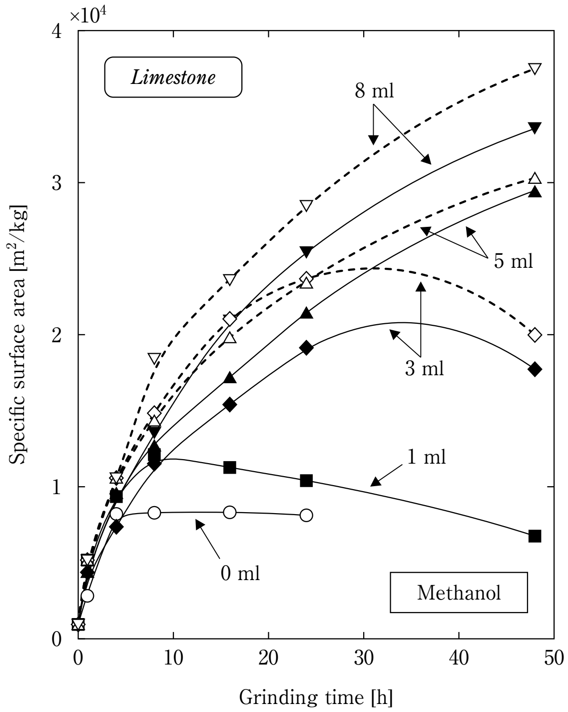

Fig. 6 Effect of the addition method of methanol on specific surface area of limestone.

the fine powder ground were observed. On the other hand, there were hardly agglomerates in the products with methanol additive (c) and (d), and those micrographs revealed the presence of limestone powder with submicron size. Compared with the collective addition method, the stepwise addition method was found to give the fineness and good dispersion of product ground.

3. 3 Effect of liquid additive on crystalline structure of product

The crystalline structure of limestone ground with collective addition of ethanol was examined by means of a powder X-ray diffraction apparatus. **Fig. 8** shows the variations of peak intensity ratio in (104) lattice plane, which had the greatest diffraction intensity, with grinding time. The intensity ratio was taken as the value divided by the intensity before grinding. The parameter in figure was the amount of ethanol. In ordinary grinding operation, the crystallinity of solid sample lowered and the peak intensity decreased as the grinding proceeded. From the **Fig. 8**, the intensity ratios in all cases decreased with grinding time, especially the intensity ratio without an additive remarkably decreased at the grinding time of 8h. After grinding for 8h, the specific surface area without an additive must reach a maximum, when the grinding in pot will be in equiliburium. On

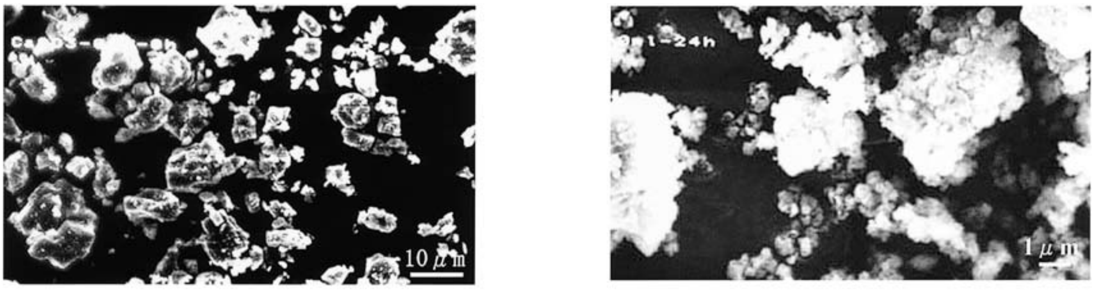

(a) Limestone powder before grinding

(b) Product without additives

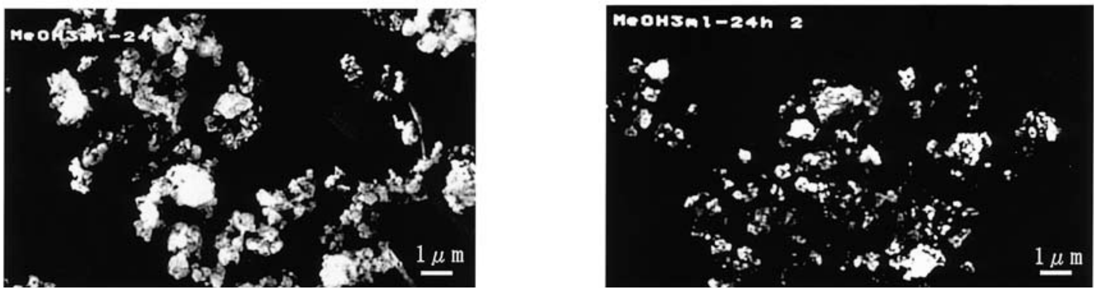

(c) Product with collectively addition of menthanol (3ml)

(d) Product with stepwise addition of menthanol (3ml)

Fig. 7 Electron scanning micrographs of limestone before and after grinding for 24 hours, (a) before grinding (b) after grinding without additives (c) with collective addition of methanl (d) with stepwise addition of methanol.

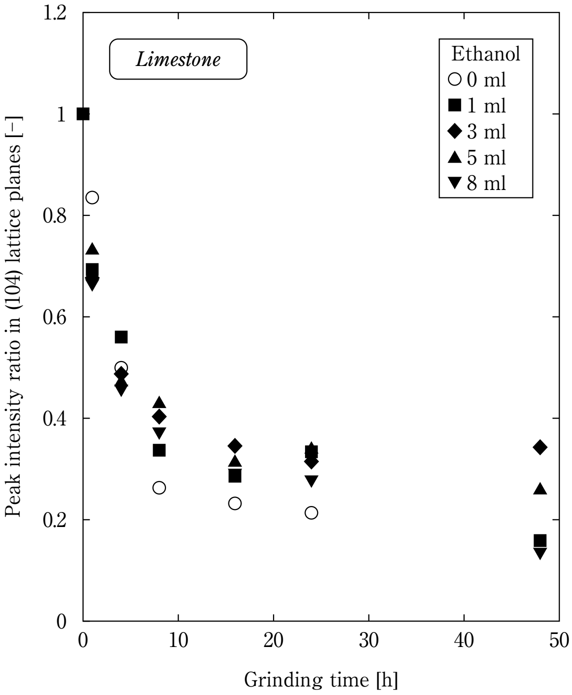

Fig. 8 Plots of peak intensity ratio in (104) lattice plane vs. grinding time.

the other hand, the decrease in intensity ratios with ethanol additive was found to be smaller than that without an additive at the grinding time longer than 8h. Although the specific surface area with ethanol additive was about twice that without an additive at the grinding time of 24h because the addition of ethanol promoted the grinding of limestone, the decrease in the intensity ratio was inversely controlled. With ethanol additive, the crystallinity of limestone degraded to some extent when the specific surface area reached a maximum at the grinding time longer than about 48h. This suggested that the grinding energy is dissipated to degrade the crystalline structure of limestone when the grinding is in equiliburium or negative grinding occurs.

3. 4 Variations of temperature and pressure in grinding pot

In vibrating ball mill, most of the mechanical energy given to grind a solid sample converts into a thermal energy due to the collision and rubbing between solid sample and grinding media, grinding media themselves, and pot wall and media[6]. **Fig. 9** shows the results of the temperature measurement in the grinding pot when the different amount of ethanol was collectively added. The variations of temperature were shown as the temperature difference with a room temperature. Four photographs of **(a) - (d)** in **Fig. 9** were the inside state of the pot immediately after grinding at each grinding condition. Without ethanol additive, the temperature in the pot increased rapidly with the grinding time from the start of grinding and rose to about 39℃ at the grinding time of 5h, which was about 18℃ in terms of the temperature difference with room temperature. The high temperature difference was kept on until grinding finished. The specific surface area without ethanol reached a maximum at grinding time of 4h and then grinding

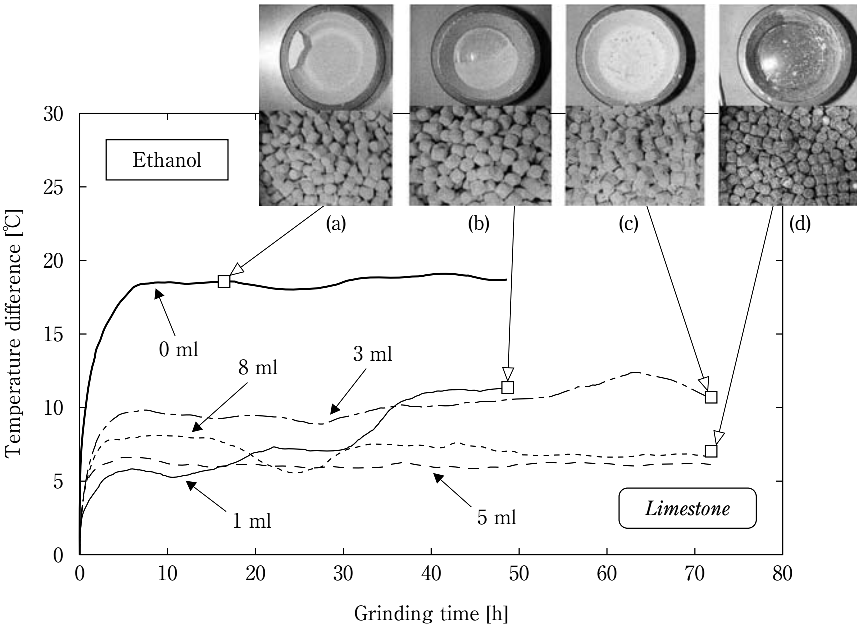

Fig. 9 Variations of the temperature and status in grinding pot as a function of grinding time with different amount of ethanol.

scarcely proceeded. Consequently, it is considered that a rise of temperature in pot is attributed to the grinding equilibrium at the initial grinding stage. In the photograph (a) without ethanol after 16h, in fact, the thick coating layer of limestone powder was observed on the pot inside wall and grinding media.

On the other hand, it was found that the temperature difference at the various amount of ethanol was remarkably lower than that without an additive. The specific surface area at the addition amount of 1ml and 3ml reached a maximum at the grinding time of 16h and 48h, respectively, and the temperature differences gradually increased with grinding time since then. Although at the addition amount of 8ml the specific surface area hardly increased at the grinding time longer than 48h, a negative grinding phenomenon did not appear clearly and the coating layer of limestone powder on the pot wall and grinding media could not confirm also, as can be seen from **Fig. 9 (d)**. It is obvious that the ethanol addition contributed to keeping the dispersibility of limestone powder and controlled the agglomerate of powder themselves and the adhesion of powder to pot wall. Thus, the variation of temperature in pot was found to reflect adequately the grinding state in pot during grinding.

Fig. 10 shows measurement results on the temperature (broken line) and pressure (solid line) in the grinding pot with the collective addition of ethanol 1ml and 3ml. The abscissa of the figure is the grinding time, and left and right ordinates show the gage pressure and temperature in pot, respectively. We traced the temperature and pressure change in the pot added methanol, which was set in a constant temperature tank, and confirmed the validity of a trial pot cover prior to grinding experiments. As the temperature in pot increased after the start of grinding, as can be seen in the figure, the pressure with each amount of methanol also increased rapidly because the vapor pressure of methanol increased. At the addition amount of 1ml the specific surface area reached a maximum at the grinding time of about 8h. The temperature increased also up to the grinding time of 8h, but the pressure rapidly decreased after grinding for about 2h. Although the pressure in pot without grinding increases in proportional to the temperature rise, the reduction of pressure with grinding can be explained by the adsorption of methanol molecules on the fresh surface of limestone created by the grinding. In the case of 1ml addition, the pressure in pot became lower than atmospheric pressure at the grinding time longer than 8h and then showed a constant pressure regardless of some variations of the temperature. This indicates that methanol molecules adsorbed on limestone powder surface do not desorb, that is, methanol molecules chemisorb evidently. In the experiment at the addition amount of 1ml, in fact, the pot cover could not be opened easily due to the lower of pressure in pot after grinding.

The maximum specific surface area at the addition amount of 3ml reached at the grinding time of 24h. Then, the temperature in pot was relatively stable around 15℃ , but the pressure in pot was gradually decreased and kept at a constant pressure at the grinding time longer than 40h. In the case at the addition amount of 5ml and 8ml, whose data were not

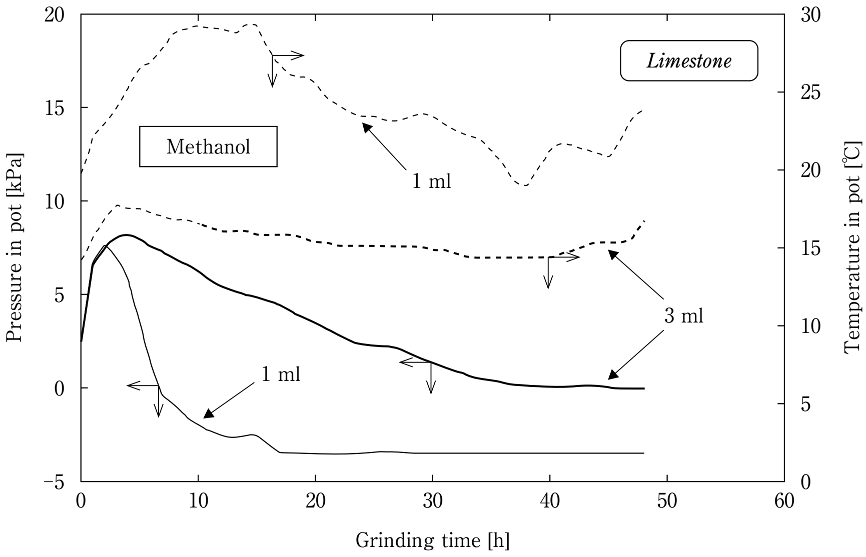

Fig. 10 Variations of the temperature and pressure in grinding pot as a function of grinding time with the addition of methanol.

shown here, the greater amount of methanol, the higher initial pressure in pot. The change of pressure, however, was found to maintain a constant if there was no change of temperature in pot. The methanol molecules, therefore, will evaporate by the corresponding amount to the quantity of molecules adsorbed on powder. The results with ethanol additive showed also a similar tendency to those with methanol additive.

4. CONCLUSION

The dry ultrafine grinding of limestone was carried out with the liquid additives, three alcohols and two glycols, and the influence of the amount and addition method of additives on the grinding effect was investigated by using a vibration rod mill. The temperature and pressure in grinding pot was also measured to elucidate the behavior of solid sample and additive molecules. The results obtained are as follows:

1) All additives used are satisfactorily effective as grinding aids, and the ultrafine grinding of limestone is easily achieved by means of additives.

2) The maximum specific surface area with additives is proportional to the amount of the additive within the experimental range in this work.

3) To increase the initial grinding rate, the stepwise addition method of a small amount of additive is more effective rather than adding the whole amount at once at the start of grinding.

4) The degradation of crystalline structure of limestone can be controlled by the addition of liquid additives.

5) The grinding status can be estimated by monitoring the changes of temperature and pressure in grinding pot during grinding.

6) The additive molecules are chemisorbed on the fresh surface of limestone created by the grinding.

References

1) Pollmanns, J., G.J.Pollmans, H.Hoberg and F.U.Schneider: "Ultrafine Grinding with Solid Additives", Proceeding of XVIII International Mineral Processing Congress, pp. 219-226, Sydney (1993).

2) Ohsawa, T., S.Yasue, A.Suganuma and T.Hamada: Preprint of 33rd Autumn meeting of the Soc. of Chem. Eng., Japan, pp. 205, Yonezawa (1998).

3) Hasegawa, M.and Y.Kanda : "The Effect of Alcohol Grinding Aids on Ultrafine Grinding of Feldspar", *J.Soc. Powder Technol., Japan*, **30**, 570-575 (1993).

4) Hasegawa, M., M.Kimata, M.Shimane, T.Shoji and M.Tsuruta: "The Effect of Liquid Additives on Dry Ultrafine Grinding of Quartz", *Powder Technol.*, **114**, 145-151 (2001).

5) Hasegawa, M., M.Kimata and T.Shoji: "The Effect of Liquid Additives and Behavior of Alumina Powder in Ultrafine Grinding of Alumina", *J.Soc. Powder Technol. Japan*, **39**, 736-742 (2002).

6) Arai, Y.: "Huntai no Zairyo Kagaku", p. 84, Baifukan (1987).

Author's short biography

Masahiro Hasegawa

Dr. Masahiro Hasegawa is Professor of the Department of Chemistry and Chemical Engineering at Yamagata University. He received his PhD from Tohoku University in 1987. His research interests are in the field of fine particle productions by breaking down and building up processes, and included the design of grinding aids, mechanochemical reaction, functional composite particles, photocatalytic particles with magnetism.

Author's short biography

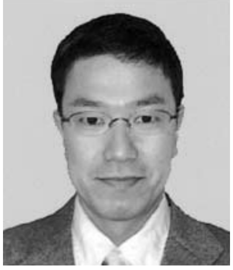

Mitsumasa Kimata

Dr. Mitsumasa Kimata is an Associate Professor in the Department of Chemistry and Chemical Engineering at Yamagata University. He received his PhD in Materials Science and Energy Engineering and MS in Chemical Engineering from Yamagata University in 1997 and 1991, respectively. He has served as a researcher or a Research Associate at Ube-Nitto Kasei Co., Kanagawa Institute of Technology, the University of Birmingham, and Yamagata University. In 2006 he became an Associate Professor at Yamagata University. His research interests are monodisperse nanoparticles, sol-gel method, photocatalyst, surface potential, powder property, mechanochemical reaction, and ultrafine grinding.

Masakazu Yaguchi

Masakazu Yaguchi received his Batchelor degree on Chemistry and Chemical Engineering and Masters degree in Materials Science and Engineering from Yamagata University in 2000 and 2002, respectively. He currently works on Engineering Department at Taiheiyo Cement Corporation.

Vapor Phase Preparation and Some Properties of Carbon Micro-Coils (CMCs)†

X.Chen and S.Motojima[1]
Department of Applied Chemistry, Faculty of Engineering,
*Gifu University**

Abstract

Carbon microcoils (CMCs) have an interesting 3D-helical/spiral form with a coil diameter of micrometer orders and a coil length of mm orders. Pulverized CMCs are generally embedded into polymer matrix to form CMC/polymer composites for various applications. The CMCs are very interested as a possible candidate for electromagnetic absorbers, remote microwave heating elements, microwave visualization materials, tactile and nearness sensors, chiral catalyst, etc. In this review, the preparation conditions, morphology, some properties and possible applications of the CMCs are briefly introduced.

Keywords: Carbon microcoil, Ceramic microcoil, Acetylene, Tactile sensor, Electromagnetic absorber

1. Introduction

Materials with bulk, plate, thin films, powder, or straight fiber-like morphologies are now commonly available. However, Substances or materials with 3D-helical/spiral structure are not commercially available. Recently, the vapor growth of helical-coiled carbon nanotubes or nanofibers are reported and have attracting attentions in biotechnology and nanotechnology. Motojima and coworkers have prepared regularly coiled carbon fibers (carbon microcoils, "CMCs") with 3D-helical/spiral structures with high reproducibility and high coil yield, and the preparation conditions, microstructures, growth mechanisms, and some properties were intensively examined. These results are comprehensively introduced in reviews[1-3].

In this review, we will briefly introduce the preparation processes, morphologies, microstructures, and some properties of the CMCs and ceramic microcoils/microtubes. We also introduce the potential applications of the CMCs.

2. Preparation and morphology of carbon microcoils (CMCs)

The carbon microcoils (CMCs) is obtained by the catalytic pyrolysis of acetylene at 700-800℃. The CMCs grew vertically on the substrate surface on which catalyst powder was painted. On the other hand, the irregular CMCs with larger coil diameters and larger coil gap; super-elastic CMCs, than that of regular CMCs grew horizontally on the substrate surface. Using Fe-based alloys, Au, Pd/Pt, etc., as a catalyst, a single-helix CMC with large coil gap can be obtained. Under optimum reaction conditions, the purity or content of the CMCs in the deposits was almost 100%.The micro-coiling morphology of the CMCs is formed by the rotation of a catalyst grain that is exclusive growing point for the CMCs. The coiling (rotating) speed is about one cycle per second around the coil axis. The CMCs with various coiling morphology; regular coils, irregular coils, double

---

† This report was originally printed in J. Soc. Powder Technology, Japan, 42, 715-720 (2004) in Japanese, before being translated into English by KONA Editorial committee with the permission of the editorial committee of the Soc. Powder Technology, Japan

* 1-1, Yamagido, Gifu 501-1193, Japan

[1] Corresponding author
TEL: +81-58-293-2621　FAX: +81-58-293-5012
E-mail: motojima@apchem.gifu-u.ac.jp

coils, single coils, twist nanocoils, etc., can be obtained depending on the reaction conditions. Almost all of the CMCs are double-coiled forms in which two fibers entwine with each other such as the double helix structure of a DNA. The amount of the CMCs having right- and left-clockwise coiled forms are about the same. There are two forms of a carbon fiber cross section from which the CMC is formed; circular or elliptic-forms, and rectangular or ribbon-like-forms. We call the former coils as "circular-coils" and the latter coils as flat coils. **Fig. 1a** shows regular double-helix circular CMCs with a constant coil diameter of 5 μm and without any coil gap throughout one coil. **Fig. 1b** shows the regular double-helix flat CMCs with a constant coil diameter of 10 μm. The CMCs has generally high elasticity and can be extended up to 2-15 times original coil length and then elastically contracts to an original coil length, depending on the coil diameters, fiber diameters and cross section forms of carbon fibers from which coils is formed. Generally, the circular coils have higher elasticity than that of flat coils. **Fig. 2** shows the pulverized CMCs (CMC powder) with short coil length of 15-25 μm using a high speed smashing machine. The CMC powder is embedded into polymer matrix to form CMC/polymer composites of various forms of beads, sheets, filaments, etc., for various applications. It was found using XRD, Raman scattering, electron diffraction, and TEM examinations that the as-grown CMCs have almost amorphous structures comparable to that of activated carbon. It was also found that the as-grown CMCs can be graphitized by high temperature heat-treatment, and the graphite coils with herring born structure is obtained at above 2500℃ heat-treatment.

3. Modification of CMCs to various ceramic coils

The as-grown CMCs can be easily vapor phase metallized and/or nitided to form micro-coils of metal carbides and nitrides with full preservation of the coiling morphology of the CMCs. Using very regular-coiled carbon coils without a coil gap, micro-tube of MC_x/C (carbon coil) /MC_x~MC_x (MC_x: metal carbide) or MN_x/C/MN_x~MN_x (MN_x: metal nitride) can be obtained. These modification processes is shown in **Fig. 3**. **Fig. 4** shows TiO_2 microcoils obtained by CVD coating of TiO_2 layers on the CMCs templates

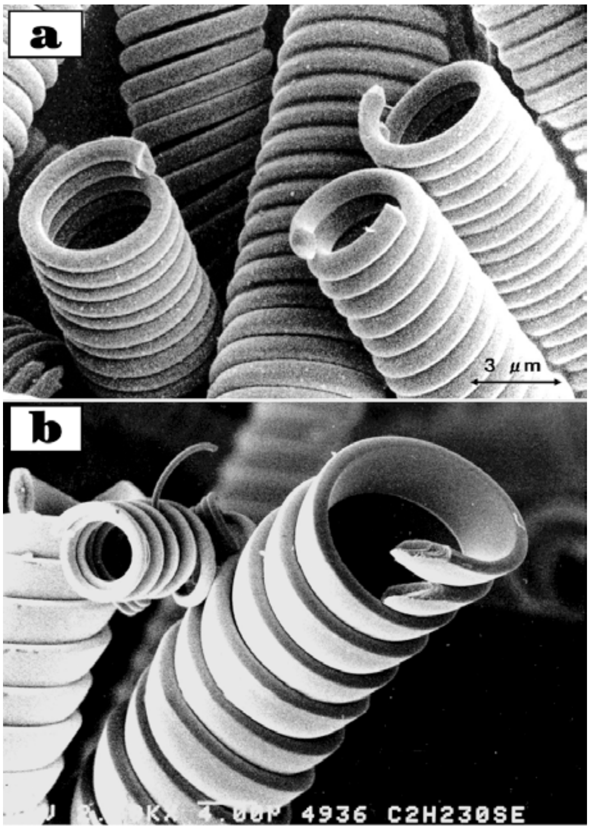

Fig. 1 Rupture terminals of double-helix CMCs.
(a) Circular CMCs, (b) flat-CMCs.

Fig. 2 Pulverized CMCs (CMC powder) .

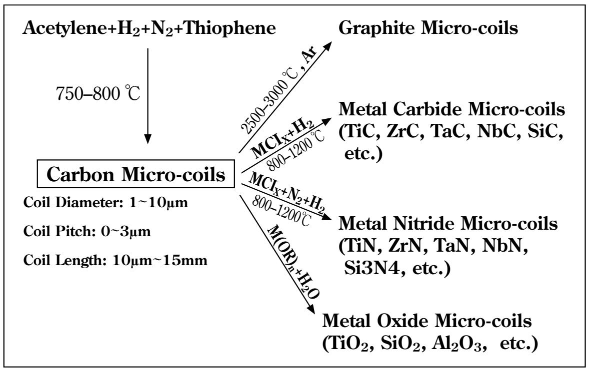

Fig. 3 Modification process of CMCs to graphite coils and various ceramic coils/tubes.

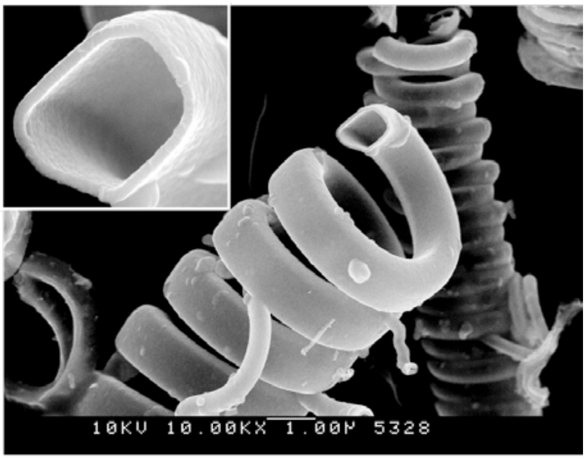

Fig. 4 Coiled TiO_2 microtube obtained by a CVD coating of TiO_2 layers on CMC-template.

followed by oxidation process.

4. Properties

4.1 Composition and physical properties

The as-grown carbon coils is composed of 97.2～98.2 wt% C, 0.6～1.0 wt% O, 1.0～1.4 wt% H, 0.08~0.09 wt% S and 0.25 wt% Ni. **Table 1** shows density, specific surface area, and average pore size.

4.2 Electric Properties

The bulk (powder) electrical resistivity of the as-grown CMCs decreases with increasing the bulk density, and is 1-10Ω・cm for 0.3 g/cm^3 and 0.1- 0.2 Ω・cm for 0.6 g/cm^3. The resistivity of the bulk carbon coils can be decreased steeply with the surface coating by carbon, TiC, TiN, ZrC, NbC, or TaC, but not by graphitizing at high temperature heat-treatment. The as-grown CMC can be easily elastically extended under small applied load. The electrical resistivity linearly increases by the extension and decreases by the contraction, probably caused by the formation of inner stress under the extension process.

4.3 Electromagnetic properties

It is reasonably considered that micro-coiling morphology of the CMCs is the most effective and ideal one for the generation of inductive current by Faraday's Law under the irradiation of electromagnetic (EM) wave resulting in effective absorption of EM wave. **Fig. 5** shows the reflection loss of EM waves of 10-110 GHz region by the CMC (1wt%) /PMMA foamed plate. It can be seen that the reflection loss shows above -20 dB (above 99 % absorption) at wide frequency ranges of 50-110 GHz. These results indicate that the carbon coils is a promising candidate as a novel EM absorber, especially in the GHz range, because of its micro-coiling morphology. The thin sheet containing CMCs (10 wt%) /PMMA beads was heated in a microwave oven (2.45 GHz) and the heat increase by the absorption of EM waves were measured by a IR thermography. It was observed that the temperature increased at each separations of 60 mm from the right side, and no temperature increases was observed between them. The separation was responsible to a half wavelength of 2.45 GHz. That is, microwave and their distribution within a microwave oven can be visualized by CMCs sheets, while the EM wave cannot be observed by naked eyes.

4.4 Chemical properties

The carbon coil becomes oxidize at about 450℃ in air, and the weight significantly decreased with increasing temperature and burn out at 700℃ . On the other hand, the graphite micro-coils obtained by the

Table 1 Density, specific surface area an pore diameter of the as-grown carbon coils

External EM field (AC, 60 Hz)	Bias valtage (V)	Density (g/cm^3)	Specific surface area (m^3/g)	Pore dismenter (nm)
with	without	1,7234	100-140	3～4
	DC650	1,8398		
		1,8019		
	AC1300	1,7431		
without	without	1,7431	70-130	3～4
	DC 650	1,7978		
	AC1300	1,7901		
Ref.	nanotubo			
(carbon filters)	VGCF	2,0817	20-30	
	PAN	1,7402	2-10	
	Pitch	2,0154	1-10	

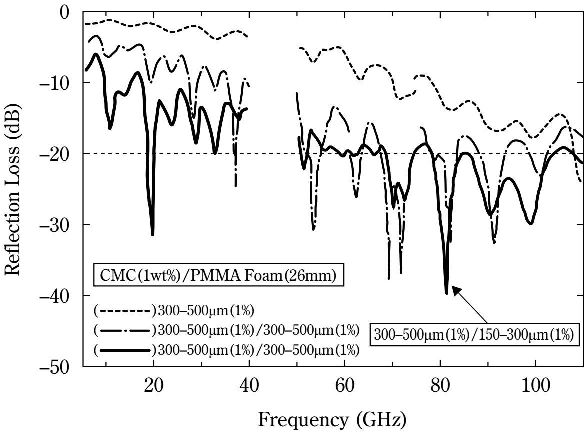

Fig. 5 Reflection loss of CMC (1wt%) /PMMA foam.

heat treatment of as-grown carbon coils at 3000℃ for 6 hrs in $CO+CO_2$ becomes oxidize at about 700℃ in air.

4.5 Bio-activation properties

The highly-purified as-grown CMCs were added in skin cell (Pam 212) and collagen (mRNA) and the propagation or activation effect of CMCs were examined. It was observed that the skin cell formation was promoted by 160% versus control (without addition of CMCs) by the 1000 ng/ml addition. The collagen formation was also increased by 1.14 times versus control by the 1000 ng/ml addition. These results suggest that the CMCs can effectively activate the cell propagation. Accordingly, as-grown CMCs are commercialized as an additive in cosmetics.

4.6 Tactile and nearness sensing properties

The CMCs have high elasticity and can be easily extended and contracted under small applied loads. It was found that electrical parameters such as resistivity (R), inductance (L), capacitance (C), impedance (Z), phase angle (θ) changed under the extension or contraction. The elastic CMCs was uniformly embedded into elastic polysilicone, and the change in electrical parameters were examined under applied small loads. **Fig. 6** shows the change in L parameter of the CMC (1wt%)/ polysilicone elements under applied load. It can be seen that the large change in L signal under applied 1mgf is observed, and the signal strength increases with increasing applied load. The change in electrical parameters was also observed in accessing of some substances. That is, the CMC/ polysilicone elements have high tactile and nearness sensing property comparable to human skin, and the detection limit is below 1mgf (ca.1Pa).

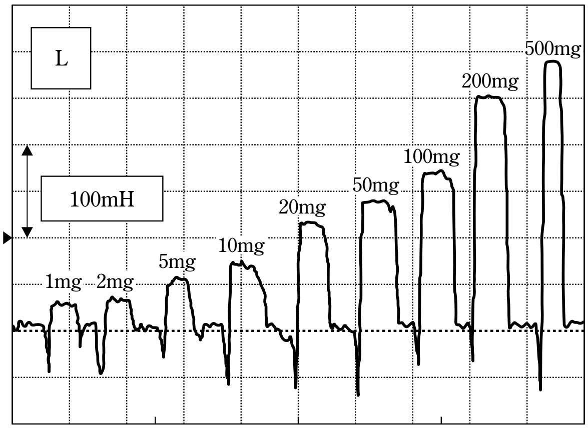

Fig. 6 Change in L (inductance) parameter of CMC (1wt%) thin sensor element under applied load.
Thickness of element: 0.1 mm.

5. Conclusions

Carbon microcoils (CMCs) have an interesting 3D-helical/spiral form with a coil diameter of micrometer orders and a coil length of mm orders. The CMCs can be easily pulverized without rupturing their coiling morphologies. The pulverized CMCs are generally embedded into polymer matrix to form CMC/polymer composites for using in various applications. The CMCs and ceramic microcoils have many novel functionalities, and are very interested as a possible candidate for electromagnetic absorbers, remote microwave heating elements, microwave visualization materials, hydrogen absorber, field emitter, micro sensors, chiral catalyst, capacitors, energy converters, etc.

References

1) S. Motojima, Y. Hishikawa and H. Iwanaga, Recent Res. Develop.Mater. Sci., 3, 633-662 (2002).
2) S. Motojima and X. Chen, Encyclepedia Nanosci. Nanotech, (ed. by H. S Nalwa, 2004), vol. 6, pp. 775-794.
3) S. Motojima and X. Chen, Bull. Chem. Soc. Jpn., (in press).

Author's short biography

Dr. Xiuqin Chen

Dr. Xiuqin Chen received M.E. degree from Xiamen University, China in 1987. She was promoted to a professor of Huaqiao University, China in 2000. She received a Ph. D. degree from a Gifu University in 2000. She served at Gifu University as an invited researcher in 2001, a postdoctoral fellowship for foreign researchers of JSPS (2002-2004), and a special researcher of Gifu University (2005~).

Author's short biography

Seiji Motojima

Seiji Motojima In 1977, he received the Ph. D. degree from the Nagoya University. He became an assistant professor in 1971, associate professor in 1982, and professor in 1990 at Gifu University. He has received several awards for his research excellence from various societies, such as The Chemical Society of Japan, The Ministry of Education, Culture, Sports, Science and Technology, The Jpn, Res. Ins. Mater. Technol., Port for Techno-Democracy, etc. His current research focus is creation and characterization of 3D-helical/spiral materials, especially of carbon microcoils (CMC) with novel functions.

The 40th Symposium on Powder Technology

The 40th Symposium on Powder Technology was held on August 29, 2006 at Hotel Laforet Tokyo in Tokyo under the sponsorship of the Hosokawa Powder Technology Foundation and with the support of Hosokawa Micron Corporation. The symposium was very successful as usual with the attendance of 151 including 26 academic people. The main subject was "Processing and Applications of Nanoparticles as a Key to Practical Use of Nanotechnology".

The 40th Symposium on Powder Technology

Subject: Processing and Applications of Nanoparticles as a Key to Practical Use of Nanotechnology

Session 1 Chairperson: Prof. Ko Higashitani (Kyoto Univ.)

• Manufacturing Process of Pharmaceutical Microparticles Assisted with Nano-structure Construction (KONA Award Lecture)	Prof. Yoshinobu Fukumori (Kobe Gakuin Univ.)
• Organic-Inorganic Nano-Hybrid Materials	Prof. Yoshiki Chujo (Kyoto Univ.)

Session 2 Chairperson: Prof. Makio Naito (Osaka Univ.)

• Preparation of Electronic Ceramic Dick Layer of Fine Particle Crystalline by Dry Process and Its Application	Prof. Mitsuteru Inoue (Toyohashi Univ. of Technology)
• Application of Porous Materials to Electrochemical Functional Interface Prepared by Using Nanoparticles	Prof. Kiyoshi Kanemura (Tokyo Metropolitan Univ.)

Session 3 Chairperson: Prof. Kiyoshi Nogi (Osaka Univ.)

• Nanoparticles Fine Pitch Wiring for Printed Electronics	Prof. Katsuaki Suganuma (Osaka Univ.)
• Development and Application of Nanoparticle Dispersion and Composite Process	Dr. Takehisa Fukui (Hosokawa Powder Technology Research Institute)

The 14th KONA Award

KONA Award sponsored by Hosokawa Powder Technology Foundation is given to the scientists or groups who have achieved excellence in the researches related to the basic powder technology. The 14th award has been presented to Professor Yoshinobu Fukumori of Kobe Gakuin University.

Prof. Fukumori received his M.S and Ph.D from Kyoto University in 1971 and 1977. In 1976 he joined the Faculty of Pharmaceutical Science of Kobe Gakuin University. In 1995 he became a full professor of Kobe Gakuin University. His research activity is concerned with spouted bed processing of micro particles and development of micro and nano-particulate systems fro drug delivery. The fluidized/spouted bed coating processes are favorably applied to pharmaceutical particles. He has been producing many types of functional pharmaceutical particulate system for the purpose of efficient drug delivery, including the enteric-coated particles and the sustained-, prolonged- and delayed-release systems. However, the current coating technology has a limit in the size of the particles that can be processed. He has been established and well experienced only for particles larger than 200μm. The extension of the coating technology to a smaller size range has been challenged by him and his group. The research that he has made so far are as follows:

- Analysis of agglomeration phenomena of fine particles ;
- Optimization of coating operations and processor construction ;
- Development of large-scale processor ;
- Additives and formulation for coating fine particles;
- Release modifiers for microcapsules ;
- Novel aqueous polymeric suspensions for coating fine particles ;
- Micro-agglomeration technology ;

The results of these researches have been applied for developing various controlled-release systems such as

- Thermo-sensitively drug-releasing microcapsules with nano-structured membranes and with multi-layered structure ;
- Biodegradable, biocompatible microcapsules of proteins ;
- Microparticles carrying nanoparticulate drug to be nano-dispersed in GI tract ;
- Colon-specific delivery system for peptides ;

Further, his micro and nano-particle processing technology has been applied to drug/atom delivery systems for cancer therapies as follows :

- Delayed-releasing, self-dispersable microcapsules for cancer chemoembolization therapy ;
- Microcapsules for gadolinium neutron capture therapy of cancer ;
- Lipid nanoparticles for i.v. injections in gadolinium neutron capture therapy of cancer ;
- Chitosan nanoparticles for i.t. injections in gadolinium neutron capture therapy of cancer.

The 14th KONA Award has been given to his remarkable achievement of many years.

Academic publication concerning powder technology in Japan (2005)(2006)

Content Extract: Journal of the Society of Powder Technology, Japan, Vol. 42 (2005)

No.1

ORIGINAL PAPERS

REVIEW

LECTURE SERIES

No. 2

ORIGINAL PAPERS

REVIEW

REVIEW : FRONTIER RESEARCH SERIES

LECTURE SERIES

No. 3

REVIEW

ORIGINAL PAPERS

No. 4

ORIGINAL PAPERS

REVIEW

LECTURE SERIES

No.5

ORIGINAL PAPERS

SHORT COMMUNICATION

REVIEW

REVIEW : FRONTIER RESEARCH SERIES

LECTIJRE SERIES

No. 6

REVIEW

ORIGINAL PAPERS

SHORT COMMUNICATION

ORIGINAL PAPERS

REVIEW : FRONTIER RESEARCH SERIES

No. 7

ORIGINAL PAPERS

REVIEW

LECTURE SERIES

DOCTORAL THESIS INTRODUCTION

No. 8

ORIGINAL PAPERS

REVIEW

LECTURE SERIES

DOCTORAL THESIS INTRODUCTION

No. 9

ORIGINAL PAPERS

REVIEW

ORIGINAL PAPER

REVIEW

REVIEW : FRONTIER RESEARCH SERIES

DOCTORAL THESIS INTRODUCTION

No. 10

ORIGINAL PAPERS

REVIEW

LECTURE SERIES

DOCTORAL THESIS INTRODUCTION

No. 11

ORIGINAL PAPERS

REVIEW

REVIEW : FRONTIER RESEARCH SERIES

LECTURE SERIES

DOCTORAL THESIS INTRODUCTION

No. 12

ORIGINAL PAPERS

REVIEW

LECTURE SERIES

DOCTORAL THESIS INTRODUCTION

Content Extract: Journal of the Society of Powder Technology, Japan, Vol. 43 (2006)

No. 1

ORIGINAL PAPERS

REVIEW

LECTURE SERIES

DOCTORAL THESIS INTRODUCTION

No. 2

ORIGINAL PAPERS

REVIEW

REVIEW : FRONTIER RESEARCH SERIES

LECTURE SERIES

DOCTORAL THESIS INTRODUCTION

No. 3 Special Issue of the 41st Summer Symposium
“Recent Research and Development in Powder and Electrostatics”

ORIGINAL PAPERS

REVIEWS

No. 4

ORIGINAL PAPERS

REVIEW

LECTURE SERIES

DOCTORAL THESIS INTRODUCTION

No. 5

ORIGINAL PAPERS

REVIEWS

REVIEW : FRONTIER RESEARCH SERIES

LECTURE SERIES

DOCTORAL THESIS INTRODUCTION

No. 6 Special Issue of 41st Particle Technology Meeting
"Supercritica1 Fluid Technology for Pharmaceutica1 Applications and Nano Drug Delivery Systems"

REVIEW

ORIGINAL PAPERS

REVIEW

REVIEW : FRONTIER RESEARCB SERIES

DOCTORAL THESIS INTRODUCTIONS

No. 7

ORIGINAL PAPERS

REVIEW

LECTURE SERIES

DOCTORAL THESIS INTRODUCTION

No. 8

ORIGINAL PAPERS

REVIEW

REVIEIV : FRONTIER RESEARCH SERIES

LECTURE SERIES

DOCTORAL THESIS INTRODUCTION

No. 9 Special Issue of 43rd Symposium on Powder Science and Technology

ORIGINAL PAPERS

REVIEW

DOCTORAL THESIS INTRODUCTION

No. 10

ORIGINAL PAPERS

REVIEW

REVIEW : FRONTIER RESEARCH SERIES

LECTURE SERIES

DOCTORAL THESIS INTRODUCTION

Development of the Model for Dispersion of Adhesive Particles and the Dynamic

No. 11　Special Issue of 50th Anniversary

No. 12

ORIGINAL PAPERS

REVIEW

LECTURE SERIES

DOCTORAL THESIS INTRODUCTION

Content Extract : Kagaku Kogaku Ronbunshu Vol. 31 (2005)

No.1

Transport Phenomena and Fluid Engineering

Particle Engineering

Separation Engineering

Chemical Reaction Engineering

Energy

Environment

General Research and Others

No. 2

Physical Properties and Physical Chemistry

Transport Phenomena and Fluid Engineering

Particle Engineering

Chemical Reaction Engineering

Process Systems Engineering and Safety

Biochemical, Food and Medical Engineering

Materials Engineering and Interfacial Phenomena

Energy

No.3

Transport Phenomena and Fluid Engineering

Separation Engineering

Micro and Nano Systems

Materials Engineering and Interfacial Phenomena

Energy

Environment

No.4

Physical Properties and Physical Chemistry Transport

Separation Engineering

Chemical Reaction Engineering

Process Systems Engineering and Safety

Energy

Environment

No.5

Physical Properties and Physical Chemistry Transport

Transport Phenomena and Fluid Engineering

Particle Engineering

Separation Engineering

Process Systems Engineering and Safety

Biochemical, Food and Medical Engineering

Micro and Nano Systems

Energy

Environment

No.6

Transport Phenomena and Fluid Engineering

Separation Engineering

Thermal Engineering

Chemical Reaction Engineering

Process Systems Engineering and Safety

Biochemical, Food and Medical Engineering

Micro and Nano Systems

Energy

Environment

Content Extract : Kagaku Kogaku Ronbunshu Vol. 32 (2006)

No.1

Special Issue [Application of Computer Chemistry to Chemical Engineering]

- Molecular Design of Highly Efficient Extractants for Separation of Lanthanides and Actinides by Computational Chemistry
  Kazuya Uezu, Jun-Ichiro Yamagawa and Masahiro Goto …… 1
- Quantitative Structure-Property Relationship of Extraction Behavior of Sugars Using Molecular Modeling
  Kazuharu Yoshizuka, Michiaki Matsumoto and Kazuo Kondo …… 6
- Transport Properties of Condensable and Non-condensable Gas Mixtures through Microporous Silica Membranes Studied with Molecular Dynamics Simulation
  Tomohisa Yoshioka, Toshinori Tsuru and Masashi Asaeda …… 11
- Molecular Simulation Study on Adsorption of Methanol/Water Mixed Gases in Mesoporous Silicas with Surface Modification
  Shin-ichi Furukawa, Naoki Aoyama, Toshihiro Nishiumi, Tomoshige Nitta, Hideaki Takahashi and Masayoshi Nakano …… 18
- Prediction of Phase Equilibria for Water1Light Hydrocarbon Systems at High Temperatures and Pressures by Cubic Equation of State with Information from Molecular Simulation
  Yusuke Shimoyama, Yoshio Iwai, Yasuhiko Arai, Tomoya Tsuji and Toshihiko Hiaki …… 25
- Development of Pressure Controlled Grand Canonical Ensemble Monte Carlo for Efficient Estimation of Solubility in Polymer
  Hiromitsu Takaba, Hideki Hayashi and Shin-ichi Nakao …… 31
- Two-Dimensional Monte Carlo Simulations of a Colloidal Dispersion Composed of Rod-like Ferromagnetic Particles in the Absence of an Applied Magnetic Field
  Masayuki Aoshima and Akira Satoh …… 39

Transport Phenomena and Fluid Engineering

- Analogy-Based Evaluation of Heat and Mass Transfer Characteristics in a Falling Liquid Film along a Vertical Absorber with spirally wound Fir-Finned Tube
  Kazushige Nakao, Eiichi Ozaki, Tsuneo Yumikura, Masaki Ikeuchi, Goro Yamanaka and Yushi Hirata …… 48
- Development of Desulphurization Plants Using Spray Drop Simulation Model
  Yoshihiro Kajibata, Yasuo Miwa and Yusaku Sakata …… 59

Separation Engineering

- Enrichment of Protein/Enzyme Solution by Membrane-Supported Gels
  Akira Suzuki, Tamae Yoshida, Hideshi Seki and Hideo Maruyama …… 66
- Degradation of Acetaldehyde Adsorption Performance of Impregnated Activated Carbons
  Toshiaki Hayashi, Mikio Kumita and Yoshio Otani …… 72
- Prediction of Non-Ideal Binary Gas Adsorption Equilibria of Volatile Organic Compounds by the Thermodynamic Non-ideal Adsorbed Solution Model
  Shuji Himeno, Kenichi Okubo and Shoichi Fujita …… 79

Chemical Reaction Engineering

- Emulsion Polymerization of Styrene Under Indirect Ultrasonic Irradiation1
  Daisuke Kobayashi, Hideyuki Matsumoto and Chiaki Kuroda …… 88

Environment

- Flotation Separation of SiC from Wastes in the Silicon Wafer Slicing Process
  Junji Shibata, Norihiro Murayama and Kengo Nagae …… 93
- Enhancement of Chloride Volatilization of Zn, Pb and Cu from Molten Fly Ash under Reduced Pressure
  Shigeo Mizuno, Katsuya Nakayama, Takahiro Kawachi, Yoshihiro Kojima, Fujio Watanabe, Hitoki Matsuda, and Mitsuru Takada …… 99

No.2

Transport Phenomena and Fluid Engineering

- Stability of Cellular Foam Formed from Anionic and Cationic Surfactant Aqueous Solution
  Kae Fujita and Toshiro Miyahara …… 103

Particle Engineering

- Fluidized Bed Medium Separation (FBMS) of Cl-Containing Plastics in Home Electric Appliance Shredder Residue
  Mikio Yoshida, Jun Oshitani, Ken-ichi Kaname and Kuniaki Gotoh …… 115

Separation Engineering

- General Convective Drying Model for Multi-material Based on Approximations of Receding Critical Moisture Plane and Linear Driving Force

Thermal Engineering

Biochemical, Food and Medical Engineering

Energy

Environment

General Research and Others

No.3

Transport Phenomena and Fluid Engineering

Particle Engineering

Separation Engineering

Thermal Engineering

Chemical Reaction Engineering

Biochemical, Food and Medical Engineering

Micro and Nano Systems

Materials Engineering and Interfacial Phenomena

Environment

No.4

Transport Phenomena and Fluid Engineering

Particle Engineering

Separation Engineering

Chemical Reaction Engineering

Biochemical, Food and Medical Engineering

Energy

No.5

Transport Phenomena and Fluid Engineering

Separation Engineering

Thermal Engineering

Energy

Environment

No.6

Transport Phenomena and Fluid Engineering

Separation Engineering

Thermal Engineering

Process Systems Engineering and Safety

Biochemical, Food and Medical Engineering

Materials Engineering and Interfacial Phenomena

Energy

Environment

Content Extract : Journal of Aerosol Research Vol.20 (2005)

No.1

Feature Articles

－High Temperature Dust Collection Technology－

Research Paper

Series Article

－Varieties of Pathological Lesions Induced by Aerosol－

No.2

Feature Articles

－Synthesis and Control of Nano-functional Materials by Aerosol Process－

Research Paper

Technical Paper

Series Article

－Varieties of Pathological Lesions Induced by Aerosol－

No.3

Feature Articles

－Nanoparticles and Their Heath Effects－Nanomaterials in Environments and Industries－

Technical Paper

Research Paper

Series Article
－Varieties of Pathological Lesions Induced by Aerosol－

No.4

Feature Articles
－Nature and Atmospheric Aerosols－Traditional Subjects with New Insights－

Research Paper

Technical Paper

Letter

Series Article
－Varieties of Pathological Lesions Induced by Aerosol－

Content Extract : Journal of Aerosol Research Vol.21 (2006)

No.1

Feature Articles

－Application of Aerosol to Medical Field－Recent Trend of Inhalation Therapy－

Research Paper

Technical Paper

Note

No.2

Feature Articles

－Present Status, Problems and Future Activities on Atmospheric Environmental Problems in South East Asian Developing Countries－

Technical Paper

Research Paper

No.3

Feature Articles

－Science of Functional Plasma and Its Advanced Application Technology－

Research Paper

GENERAL INFORMATION

HISTORY OF THE JOURNAL

KONA journal has been published by the Council of Powder Technology, Japan. (CPT), from No.1 to No.12 issues, under the sponsorships of Hosokawa Micron Corporation (No.1 to No.9) and Hosokawa Powder Technology Foundation (No.10 to No.12).

The CPT has been established in 1969 as a non-profit organization to enhance the activities of research and development on powder science and technology in Japan under the sponsorship of Hosokawa Micron Corporation. In 1983, the CPT has decided to issue an international journal named "KONA", which publishes the excellent articles appeared in Japanese journals concerning powder science and technology, after translated into English, throughout the world. After the seventh volume issued in 1989, the CPT has changed its policy to internationalize the "KONA" from the 8th issue (1990) and on by incorporating the monographs originally written in English from the authors throughout the world. Immediately, the present editorial board including Asian, Americas' and European Blocks has been organized.

From the 13th issue and on, the Hosokawa Powder Technology Foundation has taken over the role of KONA publisher from the CPT in 1995 (No.13) and the Foundation has entrusted the editorial duty to the present KONA editorial board organized by the CPT without requesting any shift in our present editorial policies. This switching of publisher has been simply and only to make the aim and scope of the Foundation definite. Essentially no change has been observed in continuously editing and publishing this journal except in the designation on a part of the journal cover.

AIMS AND SCOPE OF THE JOURNAL

KONA Journal is to publish the papers in a broad field of powder science and technology, ranging from fundamental principles to practical applications. The papers discussing technological experiences and critical reviews of existing knowledge in specialized areas will be welcome.

These papers will be published only when they are judged, by the Editor, to be suitable for the progress of powder science and technology, and are approved by any of the three Editorial Committees. The paper submitted to the Editorial Secretariat should not have been previously published except the translated papers which would be selected by the Editorial Committees.

CATEGORY OF PAPERS

- Invited papers
  Original research and review papers invited by the KONA Editorial Committees.
- Contributed papers
  Original research and review papers submitted to the KONA Editorial Committees, and refereed by the Editors.
- Translated papers
  Papers translated into English, which were previously published in other languages, selected by the KONA Editorial Committees with the permission of the authors and / or the copyright holder.

SUBMISSON OF PAPERS

Papers should be sent to each KONA Editorial Secretariat.

- Asia / Oceania Editorial Secretariat
  Mr. T. Kawamura
  Hosokawa Powder Technology Foundation
  1-9 Shoudai Tajika, Hirakata, 573-1132 JAPAN
- Europe / Africa Editorial Secretariat
  Dr. P. van der Wel or Mrs. P. Krubeck
  Hosokawa Micron GmbH
  Welserstr. 9-11, 51149 Köln
  P.O. Box 920262, 51152 Köln
  GERMANY
- Americas Editorial Secretariat
  Dr. C.C. Huang
  Hosokawa Micron Powder Systems
  10 Chatham Road, Summit, NJ 07901 USA

PUBLICATION SCHEDULE

KONA is published once a year.

SUBSCRIPTION

KONA is distributed free of charge to senior researchers at universities and laboratories as well as to institutions and libraries in the field throughout the world. The publisher is always glad to consider the addition of names of those who wish to obtain this journal regularly to the mailing list. Distribution of KONA is made by each Secretariat.

Free electronic publication of KONA is available in http://www.kona.or.jp

INSTRUCTIONS TO AUTHORS

(1) Manuscript format

- Two copies should be submitted to the Editorial Secretariat, in double-spaces typing on pages of uniform size.
- Authorship is to give authors' names, and the mailing address where the work has been carried out on the title page.
- Abstract of 100-180 words should be given at the beginning of the paper.
- Nomenclature should appear at the end of each paper. Symbols and units are listed in alphabetical order with their definitions and dimensions in SI units.
- Literature references should be numbered and listed together at the end of paper, not in footnotes. Please give information as in the following examples:
  1) Carslaw, H.C. and J.C. Jaeger: "Conduction of Heat in Solids", 2nd ed., Clarendon Press, Oxford, England (1960).
  2) Howell, P.A.: US Patent, 3,334,603 (1963).
  3) Rushton, J.H., S. Nagata and D.L. Engle: AlChEJ., 10. 294 (1964).
  4) Seborg, D.E.: Ph.D. Dissertation, Princeton Univ., N.J., U.S.A. (1969).
- Original figures with each single copy should be submitted, on separate sheets. Authors' names and figure numbers are marked in the corner.
- Figure numbers and captions are listed on a separate sheet.
- Place of figure insertion is to be indicated in the margin of the manuscript.
- Tables should be typed on separated sheets.
- Author's short biography and photograph should be attached.
- For data and text submissions we accept PC-format floppy and CD-ROM discs with unformatted text files in ASCII code. Files in Microsoft Word format are also acceptable. When submitting images, please insure that the files are compatible with Adobe Photoshop and have a resolution of at least 350 dpi.

(2) Reprints

- The authors shall receive 50 free reprints. Additional reprints will be furnished when ordered with return of galley proofs.

(3) Publication policy

- Original papers submitted for publication become immediately the property of the Hosokawa Powder Technology Foundation and remain so unless withdrawn by the author prior to acceptance for publication or unless released by the Editor. The original papers in KONA should not be reproduced or published in any form without the written permission of the Hosokawa Foundation. The Hosokawa Foundation does not claim the copyright for translated papers.

HOSOKAWA MICRON

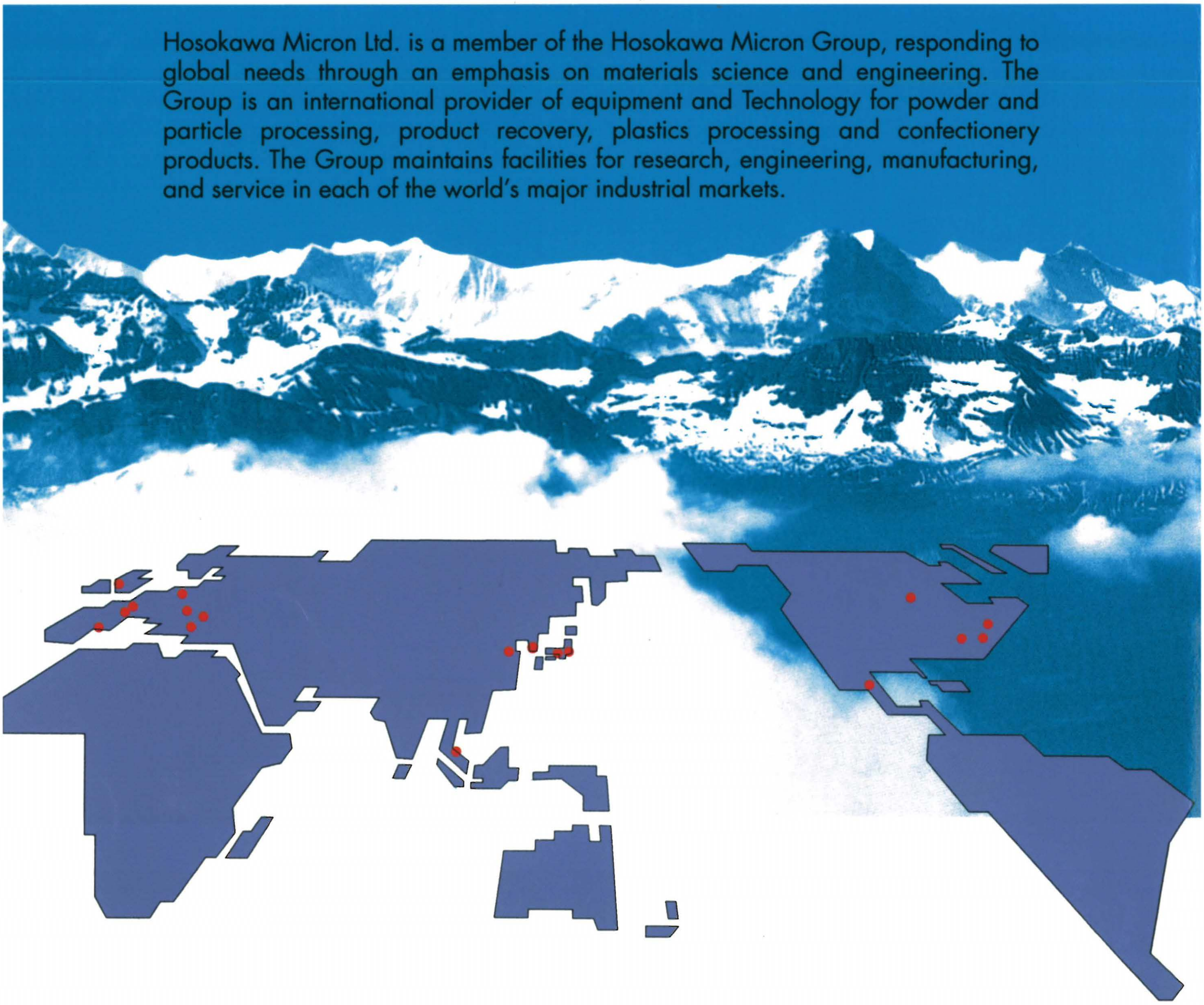

Hosokawa Micron Ltd. is a member of the Hosokawa Micron Group, responding to global needs through an emphasis on materials science and engineering. The Group is an international provider of equipment and Technology for powder and particle processing, product recovery, plastics processing and confectionery products. The Group maintains facilities for research, engineering, manufacturing, and service in each of the world's major industrial markets.

Process Technologies for Tomorrow

HOSOKAWA MICRON

Headquarter Locations;
HOSOKAWA MICRON CORPORATION
http://www.hosokawamicron.co.jp